

The Effects of Wall Inertia and Axial Bending on Instabilities in Flow Through an Elastic-Walled Tube

A thesis submitted to the School of Mathematics
of the University of East Anglia in partial fulfilment
of the requirements for the degree of Doctor of Philosophy

Martin Christopher Walters
February 2016

© This copy of the thesis has been supplied on condition that anyone who consults it is understood to recognise that its copyright rests with the author and that use of any information derived there from must be in accordance with current UK Copyright Law. In addition, any quotation or extract must include full attribution.

© Copyright 2015
Martin Christopher Walters

Abstract

In certain parameter regimes, steady flow through flexible tubes is unstable to self-excited oscillations. Whittaker *et al.* (2010, Proc. Roy. Soc. A 466) solved an asymptotic model for the onset of self-excited oscillations in a long, thin-walled, flexible tube clamped between two rigid tubes, with a large axial tension. This work neglected effects such as wall inertia, axial bending, and in-plane shear forces. Whittaker (2015, IMA J. Appl. Math.) reintroduced in-plane shearing and found a shear-relaxation boundary layer at the tube ends.

In this thesis, wall inertia and axial bending are reintroduced into these models. In Chapter 2, wall inertia terms are added to the governing equations for the wall mechanics, and a new ‘tube law’ describing the wall motion is derived. Combining this with a description of the fluid mechanics, the effect of wall inertia on the oscillations is quantified. Wall inertia is found to be a destabilising effect.

In Chapters 3–7, axial bending is reintroduced allowing ‘clamped’ boundary conditions to be satisfied at the tube ends. Three different regimes dependent on the dimensionless length and wall thickness of the tube are found. Chapters 4–5 concentrate on the two regimes where the shear layer found by Whittaker (2015) must be considered. An axial bending boundary layer that induces higher-order corrections to the shear layer and bulk solution is found in these regimes. In Chapters 6–7, a final regime is considered where the shear layer no longer needs consideration, but a new model for the wall mechanics is needed. Deriving and solving a linearised 2D model for bending a semi-infinite block under tension, corresponding to a 2D cross-section of the tube wall, a new transverse shear-relaxation layer is found. This boundary layer allows clamped boundary conditions to be satisfied and induces higher-order corrections to the bulk solution.

Acknowledgements

Firstly, I would like to thank my supervisor Dr Robert Whittaker for his constant support, guidance, patience and wealth of knowledge. I am truly grateful for all of the time you have given to help my work be the best it can be. I would also like to thank the University of East Anglia for funding my PhD, as well as all the staff within the School of Mathematics for all their help throughout both my undergraduate and postgraduate studies.

I wish to thank my office mates, in particular Julian and John for their support and constant source of entertainment. I also thank all of the people I have met and worked with throughout the Ziggurat Challenge. Tuesday nights won't be the same without the chaos of attempting to get all the teams and officials in the right place every ten minutes! Additionally, I thank all the people at the UEA, Norfolk, and Great Yarmouth and Waveney fencing clubs for all the amazing times I have had with them and for providing much needed distractions from my work.

I wish to thank all of the friends I have made over the past eight years in Norwich. In particular, I thank Rick, Luca, Nicola, James, Neil, Guy, Megan, Blaise, Fran, Yannis, Holly and Rob for being there for me through thick and thin, and for all the countless laughs I have had with you.

Finally, I would like to thank my parents and sister for all of the love and support they have given and for never losing faith in me. I am forever grateful for everything you have done for me, and without you I would never have been able to make it this far.

Contents

List of Figures	xii
List of Tables	xvii
1 Introduction	1
1.1 Background	1
1.1.1 Applications	1
1.1.2 Experimental Studies	4
1.1.3 Development of a Tube Law	6
1.1.4 One-Dimensional Models	7
1.1.5 Two-Dimensional Models	9
1.1.6 Three-Dimensional Models	11
1.1.7 The Sloshing Mechanism	12
1.1.8 Sloshing Instability in Three-Dimensional Flow	13
1.2 Overview	14
2 Effect of Wall Inertia on Flow Through an Elastic-Walled Tube	19
2.1 Introduction	19
2.2 Mathematical Set-up	20
2.2.1 Problem Description	20
2.2.2 Dimensionless Groups and Parameter Regime	22
2.2.3 Non-dimensionalization	22
2.3 A Tube Law to Model the Wall Mechanics	24
2.3.1 Lagrangian Surface Coordinates, Deformation Notation and Tensor Notation	24
2.3.2 Kirchhoff–Love Shell Equations and Constitutive Laws . .	26
2.3.3 Scaling and Non-Dimensionalization	28
2.3.4 Leading-Order Force-Balance Equations	30

2.3.5	Curvature and Shear Components in terms of the Deformations, and the Relationships Between the Deformations	31
2.3.6	Reducing the Governing Equations to a Single Equation for η	31
2.3.7	Applying a Fourier Expansion of η	32
2.3.8	Decomposition of η	33
2.3.9	The Tube Law	34
2.4	Fluid Mechanics	34
2.5	Combined System for Fluid-Structure Interaction	35
2.5.1	Governing ODEs	35
2.5.2	Boundary and Matching Conditions	36
2.6	Solving the Governing ODEs for the Normal Modes	36
2.6.1	Solution in the Rigid Sections of the Tube	37
2.6.2	General Solution in the Flexible Section of the Tube	37
2.6.3	Determining the Eigenfrequencies of the Model	38
2.6.4	Comparing the Eigenfrequencies for Different values of M	40
2.6.5	The Effect of Wall Inertia on \tilde{p} , \tilde{w} and \tilde{A}	41
2.7	Stability Criterion and Growth Rate	46
2.7.1	Fluxes and Fluid Energy	46
2.7.2	Oscillatory Energy in the Tube Wall	47
2.7.3	Simplification of \tilde{E}_s in (2.131)	49
2.7.4	Determining the Growth Rate and Stability Criterion	51
2.8	Asymptotic Solution for $M \gg 1$	53
2.8.1	Leading-Order Solution	54
2.8.2	First-Order Solution	55
2.8.3	Asymptotic Approximation for Re_c	57
2.8.4	Asymptotic Approximation for Λ	61
2.9	Conclusions	65
2.A	Proof That the Eigenfrequencies are Real	68
3	Introducing an Axial-Bending Boundary Layer	70
3.1	Introduction	70
3.2	Theory of Singular Limits and Boundary Layers	72
3.2.1	Definition of a Singular Problem	72
3.2.2	Singular Differential Equations	73
3.2.3	Introducing a Boundary Layer	73

3.2.4	Approximation in the Outer Layer	74
3.2.5	Approximation in the Boundary Layer	75
3.2.6	Matching the Outer and Boundary Layer Approximations	76
3.2.7	Comparisons of the Exact Solution and the Asymptotic Approximations	77
3.2.8	Applications to Adding the Effects of Axial Bending to the Model in Chapter 2	78
3.3	Mathematical Set-up for the Elastic-Walled Tube	79
3.4	Types of Boundary Conditions at the Tube Ends	81
3.5	Consideration of the Shear-Relaxation Layer Found by Whittaker (2015)	84
3.6	Finding an Estimate for the Bending Boundary-Layer Width	86
3.7	The Different Regimes	89
3.8	Overview of Chapters 4–7	90
4	The Bending Boundary Layer in Regime I_a	92
4.1	Introduction	92
4.2	Mathematical Set-up	94
4.3	Consideration of the Inner Shear-Relaxation Layer by Whittaker (2015)	95
4.4	Estimating The Sizes of the Deformations in the Bending Layer	96
4.5	Boundary and Matching Conditions	97
4.6	Tensor Notation and Constitutive Laws	98
4.7	Force-Balance Equations	100
4.8	Normal Force-Balance Equation	101
4.9	Azimuthal Force-Balance Equation	105
4.10	Axial Force-Balance Equation	106
4.11	Leading-Order Area Change in the Bending Layer	107
4.12	Corrections to the Inner Shear-Layer Solution	108
4.13	Corrections to the Outer Shear-Layer and Bulk-Layer Solutions .	112
4.14	Conclusions	114
4.A	General Solutions for the Deformations in the Inner Shear Layer	116
4.A.1	Recasting the System in Terms of the Stresses	116
4.A.2	Determining the Leading-Order Stresses	117
4.A.3	Determining the First-Order Correction to \tilde{S} in the Inner Shear Layer	118
4.A.4	General Solutions of the Leading-Order Deformations .	118

5 The Bending Boundary Layer in Regime I_b	120
5.1 Introduction	120
5.2 Mathematical Set-up	122
5.3 Tensor Notation and Constitutive Laws	124
5.4 Consideration of the Outer Shear-Relaxation Layer by Whittaker (2015)	126
5.5 Force-Balance Equations	129
5.6 Boundary and Matching Conditions	136
5.7 Re-casting the Problem in Terms of the Stresses	136
5.8 Determining the Sizes of the Stresses in the Bending Layer	138
5.9 Solution in the Limit of a Circular Cross-Section ($\sigma_0 \rightarrow \infty$)	139
5.10 Asymptotic Analysis for $\tilde{\mathcal{F}} \ll 1, \delta_B \ll 1$	141
5.10.1 Leading-Order Solution	142
5.10.2 First-Order Solution	146
5.10.3 Second-Order Solution	147
5.11 Bending-Layer Deformations	149
5.12 Leading-Order Area Change in the Bending Layer	151
5.13 Corrections to the Outer Shear-Layer Solution	153
5.14 Corrections to the Bulk-Layer Solution	159
5.15 Conclusions	161
5.A Reformulation in Terms of Stress Variables	164
5.B Limit of a Circular Cross-Section ($\sigma_0 \rightarrow \infty$)	166
5.B.1 Governing Equations as ($\sigma_0 \rightarrow \infty$)	166
5.B.2 Fourier Representation	167
5.B.3 General Solution	168
5.B.4 Applying Boundary and Matching Conditions	169
5.B.5 Full Solution of the Modes	169
6 The Boundary Layer in Regime II	172
6.1 Introduction	172
6.2 Mathematical Set-Up	174
6.2.1 Set-Up of the Semi-Infinite Block	174
6.2.2 Lagrangian Representation of the System	176
6.2.3 Tensor Notation	177
6.2.4 Governing Equation and Boundary Conditions	177
6.3 Constitutive Law for σ	178
6.3.1 A Modified Saint Venant–Kirchhoff Model	178

6.3.2	Approximations for \mathcal{G} , \mathcal{G}^T and $\det(\mathcal{G})^{-1}$	178
6.3.3	Linearising the Problem	179
6.3.4	A Linearised Constitutive Law for σ	180
6.4	Linearising the Governing Equation and Boundary Conditions	181
6.4.1	Boundary Conditions on Boundaries $\bar{\gamma}_2$ and $\bar{\gamma}_4$	181
6.4.2	Boundary Condition on Boundary $\bar{\gamma}_3$	183
6.4.3	The Linearised Problem	184
6.5	Numerical Solution	185
6.5.1	Evaluating the Integrals in (6.52)	186
6.5.2	Rewriting the Problem in Terms of E and ν	187
6.5.3	Variational Form of the Problem	189
6.6	Analytical Treatment	190
6.6.1	Eliminating u_2 from the Governing Equation	190
6.6.2	Eliminating u_2 from the Boundary Conditions	191
6.6.3	Governing System for u_1	193
6.6.4	General Solution for \hat{u}_1	195
6.6.5	Determining the Decay Rate Ω	196
6.6.6	General Solutions for u_1 and u_2	197
6.6.7	Applying the Remaining Conditions	199
6.7	Far-field Approximation for $x_2 \rightarrow \infty$	200
6.8	Comparison of Analytical and Numerical Results	201
6.9	The Effect of Varying Axial Tension on the Deformations	205
6.9.1	Effect of Varying $\bar{\mathcal{F}}$ on the Decay Rate and Boundary-Layer Width	205
6.9.2	Effect of Varying $\bar{\mathcal{F}}$ on u_1^∞	207
6.9.3	Fundamental-Mode Approximation for u_1^∞	208
6.9.4	Behaviour of u_1^∞ for Small and Large $\bar{\mathcal{F}}$	209
6.10	Applying the 2D Model to the Elastic-Walled Tube	212
6.10.1	Summary of the Set-up of the Elastic-Walled Tube	212
6.10.2	Relating the Coordinate Systems and Deformations in the 2D and 3D models	214
6.10.3	An Expression for ξ^*	216
6.10.4	Area Change at the Exit of the Boundary Layers	218
6.10.5	Matching the Boundary-Layer Area Change to the Bulk Solution	219

6.10.6 Corrections to the Original Boundary Conditions in the Bulk Layer	220
6.11 Physical Interpretation	222
6.12 Conclusions	226
6.A Deriving the Boundary Condition (6.71) as $x_2 \rightarrow \infty$	230
6.B Asymptotic Analysis of the Fundamental Decay Rate Ω_0	234
6.B.1 Decay Rate Ω_0 as $\bar{\mathcal{F}} \rightarrow \infty$	235
6.B.2 Decay Rate Ω_0 as $\bar{\mathcal{F}} \rightarrow 0$	236
6.C Finding the Solution of the Biharmonic Equation	241
6.C.1 Solution for $\phi(x)$	241
6.C.2 A Biorthogonality Relation Between the Eigenfunctions $\phi_n(x)$	242
6.C.3 Determining the Constants A_n	245
6.C.4 Application to the Semi-Infinite Block Under Tension	246
7 A 1D Model for Bending a Semi-Infinite Block Under Tension	247
7.1 Introduction	247
7.2 Mathematical Set-Up	249
7.3 Application of Kirchhoff–Love Shell Theory	250
7.4 A 1D Model Derived from the Averaged Cauchy’s Momentum Equation	254
7.5 Deriving a 1D Model from the System (6.88)–(6.93)	256
7.5.1 Governing Equations, Boundary and Integral Conditions .	257
7.5.2 Eliminating $u_1^{(2)}$ and $u_1^{(4)}$ from the Governing Equations .	260
7.5.3 General Solution for $u_1^{(0)}$	261
7.5.4 General Solutions for $u_1^{(2)}$ and $u_1^{(4)}$	262
7.5.5 Finding the Full Solution of the 1D Model	263
7.5.6 Comparing the Decay Rates in the 1D and 2D models .	264
7.5.7 Comparing the Deformations in the 1D and 2D models .	266
7.5.8 Matching the 1D Model to the 2D Model	273
7.6 Behaviour of u_1 for Small x_2	280
7.7 Conclusions	280
7.A Deriving a 1D Model from the Averaged Cauchy’s Momentum Equation	284
7.A.1 Averaged Force-Balance and Moment-Balance Equations .	284
7.A.2 Deriving the 1D Model	286
7.A.3 Solution of the System (7.93)–(7.96)	288

8 Conclusions and Future Work	290
8.1 Conclusions	290
8.2 Recommendations for Future Work	299
Bibliography	302

List of Figures

1.1	The set-up of a Starling Resistor.	4
1.2	A sketch of a typical experimental measurement of the tube law.	5
1.3	A sketch of the 2D channel introduced by Pedley (1992).	10
1.4	The set-up of the tube in the Whittaker <i>et al.</i> (2010c) model.	15
2.1	The set-up used by Whittaker <i>et al.</i> (2010c).	21
2.2	The set-up of the undeformed, elliptical, elastic-walled tube.	25
2.3	A depiction of the angles $\theta^{*\alpha}$	27
2.4	Graphs of the first five normal modes of \tilde{p}_n , for different values of M	43
2.5	Graphs of the first five normal modes of $i\tilde{w}_n$, for different values of M	44
2.6	Graphs of the first five normal modes of \tilde{A}_n , for different values of M	45
2.7	The critical Reynolds number $Re_c/\ell\alpha$ against M	52
2.8	The gradient of the growth rate $\ell\alpha^2\partial\Lambda/\partial Re$ against M	53
2.9	Asymptotic expansions and semi-analytical solutions for the first four eigenfrequencies ω_n as functions of M	58
2.10	Asymptotic expansions and semi-analytical solutions for the axial mode shapes of the pressure \tilde{p}_n for the first four modes. . .	59
2.11	Asymptotic expansions and semi-analytical solutions for the critical Reynolds number $Re_{cn}/\ell\alpha$ for the first four modes, as functions of M	61
2.12	Asymptotic expansions and semi-analytical solutions for the gradient of the growth rate $\ell\alpha^2\partial\Lambda_n/\partial Re$ for the first four modes, as functions of M	64

3.1	A physical representation of the clamped, pinned and sliding boundary conditions applied to a shell.	71
3.2	The exact solution and leading-order approximations of the boundary-value problem (3.2), (3.3) in the outer and boundary layers.	78
3.3	The set-up of the undeformed, elliptical, elastic-walled tube as used by Whittaker (2015).	79
3.4	The pinned and clamped boundary conditions to be satisfied at the interfaces between the rigid and elastic regions of the tube. .	83
3.5	Solutions for the Fourier coefficients of the first Fourier modes of the in-plane stresses in the shear-relaxation layer, in the limit of a circular cross-section.	85
3.6	Solutions for the Fourier coefficients of the first Fourier modes of the deformations in the shear-relaxation layer, in the limit of a circular cross-section.	85
3.7	The different cases of the problem of introducing an axial-bending boundary layer.	89
4.1	The arrangement of the boundary layers in regime I_a	93
4.2	The set-up of the undeformed, elliptical, elastic-walled tube. . . .	94
4.3	The first $n = 1$ modes of the approximations of $\hat{\zeta}$ in the original inner shear layer studied by Whittaker (2015), in the bending layer, and in the corrected inner shear layer.	111
4.4	The first $n = 1$ modes of the approximations of $\hat{\eta}$ in the original inner shear layer studied by Whittaker (2015), in the bending layer, and in the corrected inner shear layer.	112
4.5	The first $n = 1$ modes of the approximations of $\hat{\zeta}$ in the original inner shear layer studied by Whittaker (2015), in the bending layer, and in the corrected inner shear layer.	113
5.1	The arrangement of the boundary layers in regime I_b	121
5.2	The set-up of the undeformed, elliptical, elastic-walled tube. . . .	122
5.3	The first $n = 1$ modes of the leading-order approximations of \tilde{N} , \tilde{S} , $\tilde{\Sigma}$ in the bending layer and outer shear layer.	145
5.4	The numerical solution of the first $n = 1$ mode of the function $C_n(z_B)$	153

5.5	The first $n = 1$ modes of the approximations of $\hat{\zeta}$ in the original outer shear layer studied by Whittaker (2015), in the bending layer, and in the corrected outer shear layer.	157
5.6	The first $n = 1$ modes of the approximations of $\hat{\eta}$ in the original outer shear layer studied by Whittaker (2015), in the bending layer, and in the corrected outer shear layer.	158
5.7	The first $n = 1$ modes of the approximations of $\hat{\zeta}$ in the original outer shear layer studied by Whittaker (2015), in the bending layer, and in the corrected outer shear layer.	159
5.8	The leading-order solutions for the first $n = 1$ Fourier coefficients $\alpha_1, \beta_1, \gamma_1$ in the expansions for the stresses $\tilde{N}, \tilde{S}, \tilde{\Sigma}$	170
5.9	The leading-order axial behaviour of the solutions for the first $n = 1$ mode of the deformations $\hat{\xi}, \hat{\eta}, \hat{\zeta}$	171
6.1	Two-dimensional cross section of the tube wall in the normal and axial directions near the clamped edge.	173
6.2	The set-up of the semi-infinite block subject to the deformation \mathbf{u} and axial tension \mathbb{F}	175
6.3	Components of the unit tangent vector \mathbf{t} and unit outward normal \mathbf{n} of boundary γ_2	183
6.4	The linearised problem of a semi-infinite block being bent under axial tension.	185
6.5	The decay rates Ω_n of the first four modes of the deformations u_1, u_2 , against $\bar{\mathcal{F}}$	198
6.6	The numerical solutions and analytical approximations for $u_1 - u_1^\infty$ and $u_2 - u_2^\infty$ across x_1 for fixed values of x_2	203
6.7	The numerical solutions and analytical approximations for $u_1 - u_1^\infty$ and $u_2 - u_2^\infty$ across x_2 for fixed values of x_1	204
6.8	The boundary-layer width $\tilde{\delta}_B = 1/\Omega_0$ of the fundamental mode against $\bar{\mathcal{F}}$	206
6.9	The numerical value of u_1^∞ against $\bar{\mathcal{F}}$	208
6.10	The numerical solution for u_1^∞ for small $\bar{\mathcal{F}}$	210
6.11	The numerical solution for u_1^∞ for large $\bar{\mathcal{F}}$	211
6.12	The set-up of the tube used by Whittaker <i>et al.</i> (2010c).	213
6.13	Orientation of the coordinates (x_1, x_2) and $(x^*, z^* - z_+^*)$, as well as the deformations u_1, u_2 and ξ^* , relative to a 2D cross-section of the tube wall, near the rigid-flexible wall boundary at $z^* = z_+^*$. .	216

6.14	The numerical solution of u_2 in the x_1 -direction for small and large $\bar{\mathcal{F}}$, for fixed values of x_2	223
6.15	The numerical solution of $u_2^{(n)}$ in the x_1 -direction for $\bar{\mathcal{F}} = 10$ (large $\bar{\mathcal{F}}$), for fixed values of x_2	225
6.16	The numerical solutions of u_2 , du_2/dx_1 , and $du_2^{(n)}/dx_1$, in the x_2 -direction for fixed values of x_1 , for $\bar{\mathcal{F}} = 10$ (large $\bar{\mathcal{F}}$).	226
6.17	Sketch of the different shapes of u_2 for small and large $\bar{\mathcal{F}}$	227
6.18	The asymptotic approximations (6.233) of Ω in the limit $\bar{\mathcal{F}} \rightarrow 0$	238
7.1	The linearised problem of a semi-infinite block being bent under axial tension.	249
7.2	The numerical solutions for $\partial u_1 / \partial x_2$ and $-\partial u_2 / \partial x_1$ across x_1 for $x_2 = 5$, in the case of small and large $\bar{\mathcal{F}}$	253
7.3	The boundary-layer width $\tilde{\delta}_{CM} = \bar{\Lambda}^{-1}$, obtained from the 1D model in Appendix 7.A, against $\bar{\mathcal{F}}$	255
7.4	The fundamental decay rate Ω_0 from the 2D model and the decay rates r_+ , r_- and C_1/C_0 from the 1D model, against $\bar{\mathcal{F}}$	265
7.5	The decay rates Ω_1 , Ω_2 and Ω_3 of the first, second and third modes from the 2D model, and the decay rate r_+ from the 1D model, against $\bar{\mathcal{F}}$	266
7.6	The numerical and analytical solutions for u_1 in the 2D and 1D models respectively, when $\bar{\mathcal{F}} = 0.001$	269
7.7	The numerical and analytical solutions for u_1 in the 2D and 1D models respectively, when $\bar{\mathcal{F}} = 1$	270
7.8	The numerical and analytical solutions for $u_1(x_1, x_2) - u_1(0, x_2)$ in the 2D and 1D models respectively, in the x_1 -direction, when $\bar{\mathcal{F}} = 1000$	271
7.9	The numerical and analytical solutions for u_1 in the 2D and 1D models respectively, in the x_2 -direction, when $\bar{\mathcal{F}} = 1000$	272
7.10	The analytical solution for u_1 in the 1D model (dashed lines) in the x_1 and x_2 -directions, for $\bar{\mathcal{F}} = 0.001$, $A_2 = 0.03$, $A_4 = 2.51$, $A_6 = -2.5629$ and $B_2 = 0.01$	277
7.11	The analytical solution for u_1 in the 1D model (dashed lines) in the x_1 and x_2 -directions, for $\bar{\mathcal{F}} = 1$, $A_2 = 0.03$, $A_4 = 0.01$, $A_6 = -0.04053$ and $B_2 = 0.15$	278

List of Tables

2.1	Eigenfrequencies for different values of M with $\mathcal{F} = 0.01$	40
2.2	Eigenfrequencies for different values of M with $\mathcal{F} = 0.1$	41
2.3	Eigenfrequencies for different values of M with $\mathcal{F} = 1$	41
4.1	Scaling estimates for the dominant terms contributing to the normal force-balance equation in regime I_a	102
4.2	Scaling estimates for the dominant terms contributing to the azimuthal force-balance equation in regime I_a	103
4.3	Scaling estimates for the dominant terms contributing to the axial force-balance equation in regime I_a	104
5.1	Scaling estimates for the dominant terms contributing to the normal force-balance equation in regime I_b	133
5.2	Scaling estimates for the dominant terms contributing to the azimuthal force-balance equation in regime I_b	134
5.3	Scaling estimates for the dominant terms contributing to the axial force-balance equation in regime I_b	135
6.1	The eigenvalues Ω_n of the decay rate in the x_2 -direction for different values of $\bar{\mathcal{F}}$	197
8.1	Summary of the boundary layers needed to satisfy the full clamped boundary conditions in regimes I_a , I_b and II	298

Chapter 1

Introduction

1.1 Background

1.1.1 Applications

Fluid flow through elastic-walled tubes occurs in many biological systems. In the human body, the cardiovascular, respiratory and digestive systems all use flexible tubes to transport various fluids around the body. As such, the study of flows in elastic tubes is important in understanding the different phenomena that occur in these biological vessels.

In the cardiovascular system, the propagation of pulse waves in the arteries is vital for transporting blood to organs and tissues within the body. This is a well known and understood example, and one-dimensional models have been formed (see McDonald, 1974; Lighthill, 1975; Pedley, 1980) which are able to adequately explain many properties of the problem. The analysis of this problem is helped by the fact that under normal conditions the arteries have a positive transmural (internal minus external) pressure, which allows them to retain a relatively stiff, inflated state. However many blood vessels, such as the veins above the heart and outside the skull have a negative transmural pressure, which causes the vessels to buckle and collapse non-axisymmetrically. These vessels are much more flexible in their buckled state and small changes in fluid pressure can cause large changes in the cross-sectional area. This leads to strong interaction between the fluid and solid mechanics, which induces many interesting phenomena such as flow limitation and self-excited oscillations.

The collapse of blood vessels and the subsequent effects can be used in many situations. For example the collapse of blood vessels is believed to be a part of auto-regulation of blood flow to many internal organs (Rodbard &

Takacs, 1966; Rodbard, 1966). This auto-regulation is particularly significant within vessels in subjects with long necks, such as in the giraffe jugular vein studied by Pedley *et al.* (1996). Venous collapse is also used in exercise to allow muscular compression of leg veins to pump blood against gravity to the heart, and the external compression of veins in lower limbs is used to prevent deep-vein thrombosis (Kamm, 1982; Olson *et al.*, 1982). The collapse of vessels can also have adverse consequences. For example, the dynamic flow-induced collapse of blood vessels downstream of atherosclerotic stenoses has been proposed as a mechanism of plaque rupture by Binns & Ku (1989) and Ku (1997). This plaque rupture can lead to serious effects such as heart attacks and strokes.

A number of different kinds of flow-induced instabilities have been observed within collapsed blood vessels. One example occurs in blood pressure measurement, where the brachial artery is compressed by a cuff around the upper arm. Initially, the pressure within the cuff is large enough to collapse the brachial artery entirely, restricting the flow of blood through the artery. The pressure in the cuff is then slowly decreased allowing pockets of blood to pass through the collapsed segment of the artery, forcing the opposite walls of the vessel to open and then close, and generating audible noises called "Korotkoff sounds" (Bertram *et al.*, 1989; Ur & Gordon, 1970). Other examples include oscillations in the coronary blood vessels which were observed during open-heart surgery (Tsuji *et al.*, 1978), and oscillations of the external jugular vein, collapsed due to a low hydrostatic pressure, which give rise to cervical venous hum (Danahy & Ronan, 1974).

In the respiratory system, the airways have a certain degree of flexibility which again allows fluid-structure interaction and gives rise to yet more phenomena. One example occurs during forced expiration. Here, contraction of the expiratory muscles increases the pressure that drives air out of the peripheral airways. However, if this driving pressure increases past a certain level, the proximal airways start to collapse. The reduction of the cross-sectional area of these airways then increases the fluid velocity, and the Bernoulli effect reduces the internal fluid pressure leading to further airway collapse. This results in flow limitation and 'negative effort dependence', where an increase in expiratory effort beyond a particular level leads to reduction in expiratory flow rate.

Self-excited oscillations also occur in the airways and are believed to cause

a number of respiratory noises. It is thought that flutter instabilities are the cause of respiratory wheezes during forced expiration (Gavriely *et al.*, 1984, 1989), and controlled flow-induced vibrations of the vocal chords are used in speech production and can be modelled as a collapsible tube system (Berke *et al.*, 1991). Additionally, bird song is generated using oscillations of a set of membranes in the avian syrinx, and experimental and theoretical evidence has been provided by Fee *et al.* (1998) pointing towards the primary mechanism of these oscillations being a dynamic flow-structure interaction.

Snoring sounds in humans are also generated with flow induced instabilities. Initially, the Bernoulli effect can induce collapse and closure of the upper airway, characterized with a simple lumped-parameter model by Gavriely & Jensen (1993). When in this collapsed state, flow-induced instabilities of the pharyngeal wall can yield noise production. A distributed collapsible-tube model of this process was developed by Aittokallio *et al.* (2001). Along with the instabilities of the airway wall, flow-induced flutter of the soft palate generates an independent form of noise production. This has been modelled by Huang (1995) as a flexible cantilevered elastic plate that moves as air flows past it.

Further examples of fluid flow through elastic-walled tubes can be found in the digestive system. In micturition, the urethra behaves like a passive collapsible tube and exhibits flow limitation effects (Griffiths, 1969, 1971). This is different from the ureter and other deformable vessels in the digestive system that transport fluids using peristalsis. A model for this process has been developed by Carew & Pedley (1997). More examples of biological applications can be found in the reviews by Heil & Jensen (2003) and Grotberg & Jensen (2004).

Although many of the applications of flow through collapsible tubes are biological, some industrial applications can also be found. One example is the development of flexible micro-channels that can be utilized to ensure satisfactory micro-mixing of confluent streams (Selverov & Stone, 2001; Yi *et al.*, 2002; Hsiung *et al.*, 2007). More industrial applications include gas and oil flow through steel submarine pipes and flexible tubes transporting fluids in machinery.

1.1.2 Experimental Studies

Experimental data of fluid flow through elastic-walled tubes is usually obtained using a Starling Resistor (Knowlton & Starling, 1912), which is shown in Figure 1.1. This comprises an elastic tube which is clamped between two rigid tubes and enclosed in a chamber with a fixed pressure. Fluid is driven through the tubes, either by applying a controlled pressure difference between the ends of the rigid tubes, or by using a volumetric pump to fix a specific flux at one end.

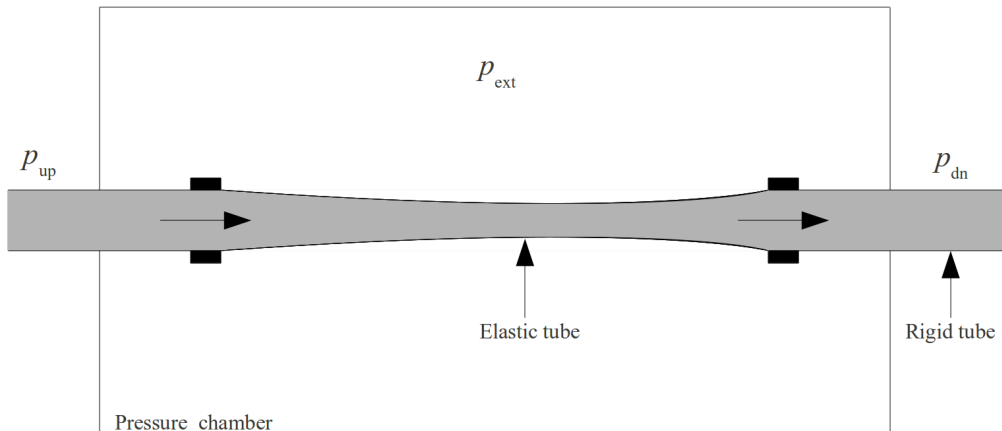


Figure 1.1: The set-up of a Starling Resistor. An elastic tube is clamped between two rigid tubes and is contained in a pressure chamber with fixed pressure p_{ext} . Flow is driven through the tube using a controlled pressure difference $p_{\text{up}} - p_{\text{dn}}$ between the two ends. Flow can also be driven through the tube by using a volumetric pump to set a particular flux at either end. The pressure p_{ext} in the chamber can be modified to control the degree of collapse of the elastic tube.

If the transmural pressure over the tube wall in the Starling Resistor becomes sufficiently large and negative, the elastic tube buckles non-axisymmetrically. Once the elastic tube reaches this buckled state, it becomes highly compliant and small changes in the transmural pressure can cause large changes in the tube shape and cross-sectional area. This leads to phenomena such as flow limitation and self-excited oscillations, which have been observed in many experimental studies of the Starling Resistor, for example within the studies conducted by Conrad (1969).

The relationship between the transmural pressure and cross-sectional area, also known as a ‘tube law’, has been investigated experimentally by Kececioglu *et al.* (1981), and a sketch of their experimental measurement of the tube law, along with the typical cross-sectional shapes of the tube wall may be viewed in

Figure 1.2. From the figure, we see that at a high enough transmural pressure the tube takes an almost circular shape, and the change in the cross-sectional area is predominantly due to axisymmetric stretching. When the transmural pressure is reduced to some negative value, the tube buckles into an elliptical shape. Here, changes to the cross-sectional area are then predominantly due to bending rather than stretching, allowing the tube to be more compliant than in its circular state. Further reduction of the transmural pressure forces the opposite sides of the tube wall to come into contact, first at a point, and then along a line. In these states, the tube becomes less compliant as strong bending forces now appear at the bulbous end of each lobe of the tube, resisting further area reductions.

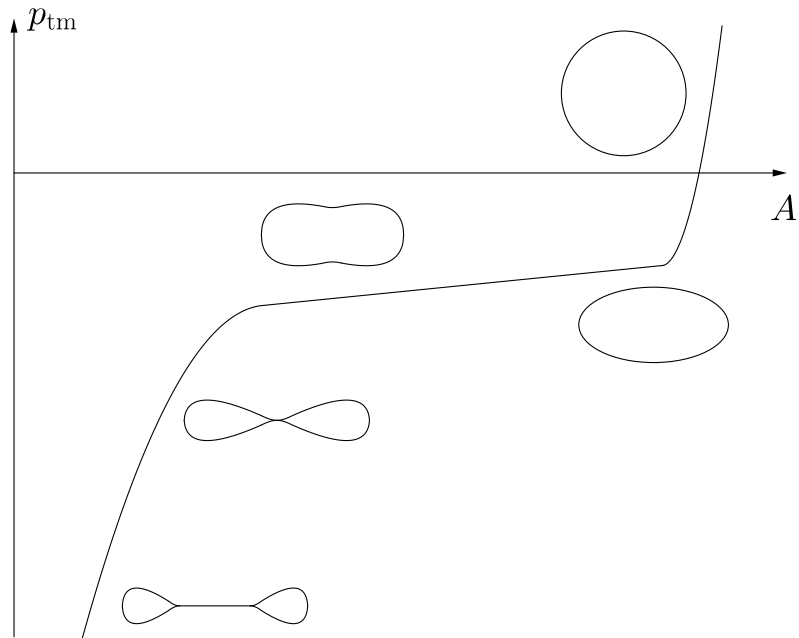


Figure 1.2: A sketch of a typical experimental measurement of the tube law relating the transmural pressure p_{tm} to the cross-sectional area A of the tube, based on the measurements taken by Kececioglu *et al.* (1981). Also shown are sketches of the typical shapes of the cross-section as p_{tm} varies.

Experiments by Bertram and coworkers (e.g. Bertram, 1986; Bertram *et al.*, 1990, 1991) have characterized the Starling Resistor system in the greatest detail, and in particular, they have determined regions of parameter space where the system produces spontaneous oscillations. These oscillations occur in distinct frequency bands and are strongly dependent on the properties of the rigid sections of the tube. Additionally, Ohba *et al.* (1997) developed flow visualizations of self-excited oscillating flow through a Starling Resistor that

show a single central jet downstream of the elastic tube, and experiments conducted by Kounanis & Mathioulakis (1999) point towards the onset of self-excited oscillations being associated with the symmetry of flow downstream of the elastic tube breaking. Furthermore, in the case where the tube is buckled into a two-lobed cross-section, flow visualizations have been created by Bertram & Godbole (1997) displaying axially decaying twin jets downstream of the collapsible tube with a region of reversed flow in between. Other relevant early experimental studies can be found in the review by Bertram (2003).

A great deal of recent experimental work has focused on the onset of self-excited oscillations in the Starling Resistor in a specific parameter regime. In this regime, large-amplitude, low-frequency oscillations, where the tube is open for the majority of the period so the cross-sectional area remains near its maximum value, are observed. These oscillations, also known as LU-type oscillations were observed by Bertram *et al.* (1990) and experiments by Bertram & Nugent (2005), Bertram & Tscherrey (2006), Bertram (2008) and Truong & Bertram (2009) have uncovered many features of these oscillations. Further details of these experimental studies, and of others investigating the LU-type oscillations, may be found in the review by Heil & Hazel (2011).

1.1.3 Development of a Tube Law

In order to derive models describing the wall mechanics of the elastic-walled tube within the Starling Resistor, investigations have been carried out to determine appropriate expressions for a tube law relating the transmural pressure $p_{\text{tm}} = p_{\text{int}} - p_{\text{ext}}$ (where p_{int} , p_{ext} represent the internal and external pressure of the tube respectively) to the cross-sectional area A of the tube. The simplest expressions proposed for the tube law are based on the assumption that the cross-sectional area A at a given axial position is determined entirely by the properties of the tube (usually taken to be axially uniform) and the transmural pressure p_{tm} at the same axial position. These expressions usually have the following form

$$p_{\text{tm}} = P(A), \quad (1.1)$$

where P is some function.

Many simple power law and polynomial models have been suggested for $P(A)$ based on fitting to numerical data such as that constructed by Shapiro (1977) and Elad *et al.* (1987), as well as based on fitting to experimental data

like that found by Kececioglu *et al.* (1981). However, these simple tube laws that only give the transmural pressure as a function of the local area do not take into account any axial forces arising between neighbouring cross sections due to axial variation of the cross-sectional shape of the tube.

McClurken *et al.* (1981) first considered adding extra terms to the tube law (1.1) to account for axial stretching and bending forces. They assumed that these effects would contribute additively to $P(A)$ so that

$$p_{\text{tm}} = P(A) + P_T + P_B, \quad (1.2)$$

where P_T , P_B represent the effects of axial stretching and bending respectively. To determine the form of P_T , McClurken *et al.* modelled a cross-section of the collapsed tube as two parallel lines joined by semi-circles at each end. In doing so, they were then able to calculate the effect of axial tension on the straight surfaces and this was related to an equivalent pressure change. This yielded the relation

$$P_T = \frac{kT}{(A_0 - A)^{\frac{1}{2}}} \frac{\partial^2 A}{\partial z^2}, \quad (1.3)$$

where k is some constant, T is the axial tension, A_0 is the cross-sectional area of the tube in its undeformed state, and z is the axial coordinate. Similarly, an expression was derived for P_B that was proportional to $\partial^4 A / \partial z^4$.

Reyn (1987) later considered applying membrane theory to calculate the effect of axial tension in inflated axisymmetric tubes. For small amplitude deformations, the axial tension is determined to again have an additive effect on the tube law as in (1.2), with $P_T \propto T \partial^2 A / \partial z^2$. Reyn then assumed that this form for P_T could still be applied to non-axisymmetrically buckled tubes.

The tube laws derived by both McClurken *et al.* (1981) and Reyn (1987) are based on the tube taking idealised geometries. However, there is no guarantee that these tube laws will hold in other regimes. More recently, Whittaker *et al.* (2010d) were able to derive a tube law rationally from shell theory valid for small-amplitude, long-wavelength deformations of a thin-walled elliptical tube. Details of the derivation of this tube law are found later in §2.3.

1.1.4 One-Dimensional Models

Early elastic-walled-tube experiments (reviewed by Bertram, 2003) found a vast array of different types of oscillations spanning over a large range of frequencies. However, the mechanisms involved in developing self-excited oscillations are still not fully understood. In order to gain a better

understanding of these mechanisms, one-dimensional models were used in early theoretical analyses.

These one-dimensional models use three quantities to describe the system: the mass flux or flow rate of the fluid within the tube, the cross-sectional area of the tube and the transmural pressure, all as functions of an axial coordinate. Three partial differential equations are then used as governing equations for the system. The equations themselves are derived from conservation of mass, conservation of axial momentum and some tube law, and typically take the following forms

$$\frac{\partial A}{\partial t} + \frac{\partial(wA)}{\partial z} = 0, \quad (1.4)$$

$$\rho \left(\frac{\partial w}{\partial t} + w \frac{\partial w}{\partial z} \right) = -\frac{\partial p_{\text{tm}}}{\partial z} - F, \quad (1.5)$$

$$p_{\text{tm}} = P(A) - T \frac{\partial^2 A}{\partial z^2}. \quad (1.6)$$

Here z is again the axial coordinate, t is time, $A(z, t)$ is the cross-sectional area of the tube, $w(x, t)$ and $p_{\text{tm}}(x, t)$ are the cross-sectionally averaged axial velocity of the fluid and transmural pressure, ρ is the constant fluid density, T is the axial tension applied to the tube wall, and $P(A)$ is just some function. The parameter $F \geq 0$ represents viscous dissipation, which can be either distributed frictional losses or quasi-steady losses in a region of separated flow. If we have distributed frictional losses, F takes the form $F = F(w, A)$. However, Cancelli & Pedley (1985) suggested that if we have quasi-steady losses in a region of separated flow downstream of the collapsible tube, F should take the form $F = (\chi - 1)\rho w \partial w / \partial z$, where $\chi = 1$ upstream of the separation point, and $0 < \chi < 1$ downstream of the separation point. Further terms representing wall inertia, wall damping and bending stiffness can be added to the tube law (1.6) and these terms can have an important effect in the stability of the flow-structure interactions that occur.

Using equations (1.4)–(1.6), one-dimensional models have been able to predict many of the phenomena found experimentally within the Starling Resistor. By neglecting frictional effects in equations (1.4)–(1.6), Cancelli & Pedley (1985) were able to predict choking, where the cross-sectional area $A \rightarrow 0$ in a finite time. However, by including viscous dissipation in equation (1.5), either through the $F = (\chi - 1)\rho w \partial w / \partial z$ term suggested by Cancelli & Pedley (1985) or by including a distributed frictional term as considered by Hayashi *et al.* (1998), a rich variety of self-excited oscillations can be modelled.

The inclusion of viscous dissipation effects and subsequent prediction of these self-excited oscillations has been incorporated into many one-dimensional models, such as the models by Cancelli & Pedley (1985), Jensen (1992), Matsuzaki *et al.* (1994) and Hayashi *et al.* (1998). These oscillations are found to occur in distinct frequency bands, as observed in experiments, and Jensen (1990) found that this was because the oscillations occur as normal modes of the system, with each having a discrete number of wavelengths along the elastic-walled tube. Jensen (1992) also found that nonlinear mode interactions yield complex dynamical behaviour similar to that seen experimentally.

These kinds of one-dimensional models are still widely used to model networks of collapsible tubes (Bull *et al.*, 2005; Fullana & Zaleski, 2009; Venugopal *et al.*, 2009), and are able to capture qualitative effects such as the onset of self-excited oscillations that are observed in higher-dimensional models, as demonstrated by Stewart *et al.* (2009). However, these one-dimensional models are also prone to some disadvantages. Firstly, although these models provide significant insights to the mechanisms occurring within elastic-walled tubes, they fail to match quantitatively with experimental results. Secondly, the form of the conservation of axial momentum equation (1.5) and the tube law (1.6) are not derived rationally from higher-order systems, and instead ad hoc closure assumptions are required to incorporate different effects such as viscous dissipation and the form of the tube law. Finally, this 1D framework is not guaranteed to capture all known modes of instability within collapsible tube systems, such as Tollmien-Schlichting (TS) waves or travelling-wave flutter (TWF), both studied by Carpenter & Garrad (1985, 1986).

1.1.5 Two-Dimensional Models

In the 1980s and 1990s, work focused on the development of two-dimensional models of flow through elastic-walled tubes. Two classes of model are generally used, with the first describing small-amplitude instabilities in spatially uniform, unbounded elastic-walled channels. These models are based on the Orr-Sommerfeld equation, and by incorporating the effects of wall inertia, damping, bending stiffness and tension, multiple modes of instability are found. The three most commonly found modes are Tollmien-Schlichting waves, travelling-wave flutter and static divergence, although other modes of instability have also been found. For example, Davies & Carpenter (1997)

found a strongly unstable interaction between TS and TWF modes, LaRose & Grotberg (1997) discovered a long-wavelength instability of developing flow in a collapsible channel, and Walsh (1995) identified a long-wave flutter mode that occurs when there is significant coupling between transverse and longitudinal wall strain. Additionally, another type of mode has been found that grows using an energy transfer from the mean flow to the channel wall, developed from Reynolds stresses within a critical layer. This group of instabilities is reviewed in more detail by Shankar & Kumaran (1999) and Kumaran (2000, 2003).

The second class of two-dimensional model is based on the model system constructed by Pedley (1992), which may be seen in Figure 1.3. This system contains a two-dimensional channel, where one wall has a segment replaced by a flexible membrane under longitudinal tension. Fluid is driven through the channel by a fixed pressure drop between the two ends of the channel, and the transmural pressure over the membrane determines the shape of the membrane.

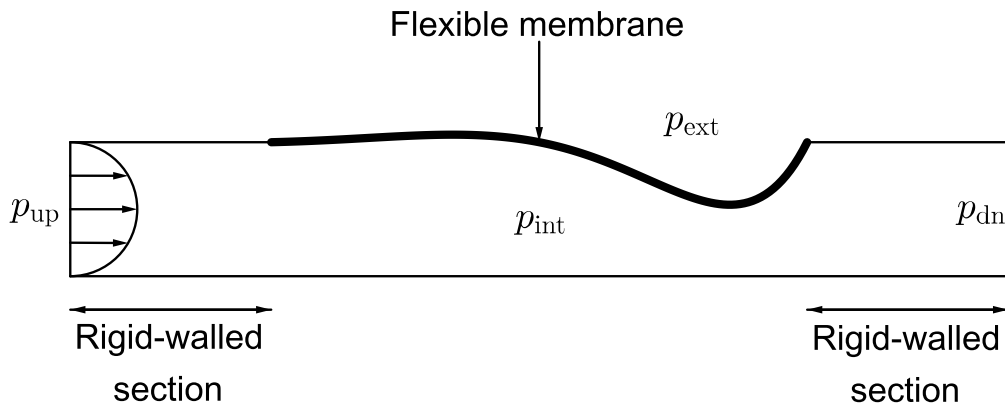


Figure 1.3: A sketch of the 2D channel introduced by Pedley (1992). A finite 2D channel, with part of the upper wall replaced by a flexible membrane under tension, has fluid driven through it from left to right using a controlled pressure difference $p_{up} - p_{dn}$. The transmural pressure (internal pressure p_{int} minus external pressure p_{ext}) determines the shape of the membrane.

Much work using this model system has focused on regimes where deflections of the flexible membrane are small compared to the channel width. For example, by assuming the flow has a Reynolds number Re of $Re \gg 1$, Guneratne (1999) found that when there is zero external pressure ($p_{ext} = 0$) and the membrane tension T is reduced from an initially large value, a static divergence instability gives rise to static eigenmodes. Guneratne also found

that when $p_{\text{ext}} \neq 0$ and the tension T is lowered, the system passes through regions of parameter space where single, multiple or no steady solutions occur. Later on, Huang (2001) used numerical simulations of the linearized Navier–Stokes equations to examine this system when the flexible membrane has inertia, damping and relatively low tension, and the external pressure is set to allow a uniform steady solution to exist. In doing so, it was seen that the system can yield static divergence and flutter (dependent on membrane inertia) instabilities that are affected by the upstream and downstream boundary conditions.

Many Navier–Stokes simulations of steady laminar flows in Pedley’s 2D channel have also been conducted (e.g. Rast, 1994; Luo & Pedley, 1995, 1996; Shim & Kamm, 2002), and these have predicted properties such as steady asymmetric membrane configurations, flow separation downstream of the collapsible segment, and sometimes a long-wavelength standing wave in flow downstream of the elastic region. Luo & Pedley (1996) demonstrated that these steady flows can become unstable to self-excited oscillations when there is a sufficiently high Reynolds number or a sufficiently low membrane tension. They also found the surprising result that the dominant viscous dissipation occurs in viscous boundary layers on the walls upstream of the flexible membrane, as opposed to downstream of the membrane where propagating waves known as “vorticity waves” occur. Later on, Luo & Pedley (1998) showed that introducing wall inertia to the model destabilises a high-frequency flutter mode, and Luo & Pedley (2000) discovered that the primary instability becomes more stable when an upstream flux is prescribed rather than a pressure drop across the channel. More examples and details about 2D models in both unbounded and bounded channels may be seen in the reviews by Heil & Jensen (2003), Grotberg & Jensen (2004) and Heil & Hazel (2011). Additionally, details of other alternative instability mechanisms that can occur in bounded channels may be seen in Stewart *et al.* (2009).

1.1.6 Three-Dimensional Models

Although there are no fully three-dimensional analytical models developed that describe the Starling Resistor system, Heil and coworkers have been able to use finite-element methods coupling non-linear Kirchhoff–Love shell theory (allowing large deformations and small strains) to an internal 3D Navier–Stokes flow to investigate this system further. By restricting attention to Stokes flows

or lubrication theory, Heil & Pedley (1996) and Heil (1997) demonstrated how non-axisymmetric buckling of the tube contributes to non-linear pressure-flow relations that yield flow limitation via purely viscous mechanisms. The Stokes-flow simulations carried out by Heil (1997) were also found to be in excellent agreement with experimental data.

Hazel & Heil (2003) later extended these simulations to model 3D flows with a Reynolds number of a few hundred, within non-uniformly buckled tubes. In doing so, they simulated twin jets emerging from a 2-lobed throat, with reversed flow in between. Further downstream, these jets were found to then thicken and merge, and the properties exhibited by these jets were found to be in agreement with experiments by Bertram & Godbole (1997).

The simulations discussed here all assume that the flow through the Starling Resistor has fourfold symmetry. However, experiments by Kounanis & Mathioulakis (1999) reveal a flow downstream of the constriction with only twofold symmetry. It is as yet unclear whether this symmetry breaking contributes to a further mechanism of instability in the Starling Resistor.

1.1.7 The Sloshing Mechanism

In this thesis a particular family of oscillations, generated by a simple instability mechanism, is considered. This mechanism was first determined by Jensen & Heil (2003) by studying the 2D system constructed by Pedley (1992), and depicted in Figure 1.3, in a parameter regime where the tension in the wall is large, using a combination of asymptotic analysis and numerical simulation. Within this regime high-frequency oscillations, which are governed by a dynamic balance between fluid inertia and large elastic restoring forces, are formed. The oscillations of the wall periodically displace fluid from the flexible region of the tube into the rigid regions, which results in axial sloshing flows in the rigid parts of the tube. If the amplitude of these sloshing flows is greater in the upstream rigid section than in the downstream rigid section, then there will be a net influx of kinetic energy into the system. If this influx exceeds additional losses, such as viscous dissipation (most of which is found in the boundary layers near the tube walls) and work done by the pressure at the tube ends, then the system can extract energy from the flow to drive any instabilities. Jensen & Heil (2003) used asymptotic techniques to obtain predictions for the frequency and growth rates of any arising instabilities. They also found their predictions for the critical Reynolds number at which oscillations develop to be

in good agreement with numerical simulations.

1.1.8 Sloshing Instability in Three-Dimensional Flow

Whittaker *et al.* (2010a,b) showed that the essential components of the sloshing instability mechanism found by Jensen & Heil (2003) are still present in a three-dimensional flow. However, for efficient extraction of energy from the mean flow to occur, it is necessary that the tube performs oscillations about a non-axisymmetric mean state¹. This was shown by Heil & Waters (2008) and Whittaker *et al.* (2010a). Hence, this instability is most likely to occur when either a tube with an initially axisymmetric cross section has buckled non-axisymmetrically or a tube's undeformed cross section is not circular. This is in agreement with experimental results showing that self-excited oscillations most readily develop in tubes which are in a strongly buckled steady-state configuration (Bertram, 2008).

In the first case, where an initially axisymmetric tube has buckled non-axisymmetrically, Heil & Boyle (2010) confirmed the existence of self-excited oscillations arising from the sloshing mechanism. This was done by constructing numerical simulations of flows in initially axisymmetric elastic-walled tubes, and more details of this investigation may be found in the review by Heil & Hazel (2011).

The second case, where the tube has a non-circular undeformed cross section, was investigated further by Whittaker *et al.* (2010c). Here, the fluid behaviour in response to the wall motion (studied by Whittaker *et al.*, 2010a) and the wall behaviour in response to the fluid pressure (studied by Whittaker *et al.*, 2010d) were combined to derive a model for the 3D Starling Resistor system. Asymptotic methods were then used to reduce the model to a single 1D ODE for the fluid pressure as a function of the axial coordinate. To describe the wall behaviour, a 'tube law' linking the transmural pressure with the cross-sectional area of the tube was used. Unlike the tube laws used in previous one-dimensional models discussed in §1.1.4, this tube law was derived rationally from shell theory for an elliptical tube by Whittaker *et al.* (2010d). The model that was formed by Whittaker *et al.* (2010c) is valid for long-wavelength,

¹This is because in a tube with circular cross section, the area changes induced by small-amplitude deformations are only quadratic in the displacement amplitude. The sloshing flows caused by the displacements are then an order of magnitude smaller, giving a much smaller influx of kinetic energy.

high-frequency, small-amplitude oscillations of a thin-walled, initially elliptical elastic tube under large axial tension. The predictions made by the model for the mode shapes, frequencies and growth rates of the oscillations, as well as the critical Reynolds number at which oscillations arise, were found to be in good agreement with direct numerical simulations. However, some effects such as wall inertia, axial bending, and normal and in-plane shear forces have been neglected to simplify the mathematics within the model.

Another drawback of the Whittaker *et al.* (2010c) model is the type of boundary conditions satisfied at the ends of the elastic-walled tube in the Starling Resistor. As the elastic-walled tube is clamped onto two rigid tubes, canonical ‘clamped’ boundary conditions, forcing the displacement and axial gradient of the tube wall to be zero, should be applied at the tube ends. However, in the model derived by Whittaker *et al.* (2010c), the axial-order of the model is not high enough to satisfy these conditions and instead the Dirichlet parts of the non-canonical ‘sliding’ boundary conditions, which only set the normal and azimuthal displacements to be zero at the tube ends, are satisfied. Whittaker (2015) reintroduced in-plane shear forces to the Whittaker *et al.* (2010c) model, and found a shear-relaxation boundary layer near the tube ends. This shear layer allowed the Dirichlet parts of the ‘pinned’ boundary conditions, which fix the normal, azimuthal and axial displacements to be zero, to be satisfied at the tube ends. However, the inclusion of these in-plane shear forces did not raise the axial-order of the model enough for the clamped boundary conditions to be satisfied.

1.2 Overview

In this thesis, the model by Whittaker *et al.* (2010c) is expanded to include the effects of wall inertia, axial bending and normal shear forces. The impact that these effects have on the self-excited oscillations generated by the Whittaker *et al.* (2010c) model is then evaluated.

The original set-up used in the Whittaker *et al.* (2010c) model is depicted in Figure 1.4. Here, we have a tube of length L , wall thickness d and circumference $2\pi a$, with an initially elliptical cross section, comprised of an elastic-walled tube clamped between two rigid-walled tubes. The elastic-walled tube has incremental Young’s modulus E and Poisson’s ratio ν , and is subject to an axial tension force F . A fluid is then driven through the tube using a volume

flux condition at the downstream end, and the elastic-walled tube is susceptible to deformations from forces arising from the transmural pressure. Whittaker *et al.* (2010c) combined separate models for the tube wall and the fluid flow to form a one-dimensional ODE governing the oscillatory components of the cross-sectional area variation, transmural pressure, and axial velocity of the fluid. These oscillatory components are all written as functions of axial position. The frequency of the oscillations appears as an eigenvalue within the model, and countably many oscillatory modes, each with their own distinct eigenfrequency, are found to exist. The growth rates and stability criteria of these oscillations are found by considering the energy balance of the system. In the Whittaker *et al.* (2010c) model, the parameters are set so that the tube is long and thin walled, the applied axial tension force is large, the fluid has a similar density to the tube wall, and the mean fluid flow has a high Reynolds number whilst still being laminar. The resulting deformations are then considered to be small in amplitude. This parameter regime can be applied to blood vessels in the cardiovascular system with a large and negative transmural pressure, such as the veins above the heart and outside the skull.

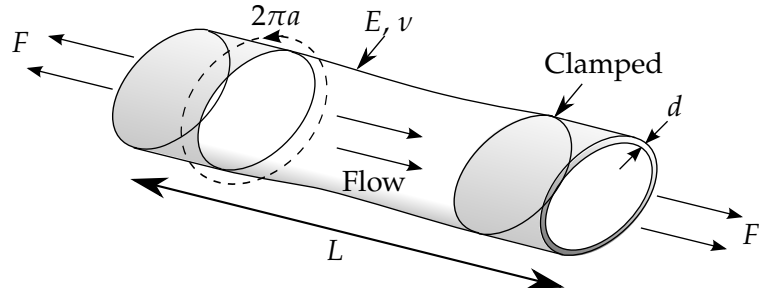


Figure 1.4: The set-up of the tube in the Whittaker *et al.* (2010c) model. This tube is comprised of an initially elliptical elastic-walled tube clamped between two rigid tubes, and fluid flows from left to right, due to a volume flux condition at the downstream end.

In Chapter 2, wall inertia is added to the model by Whittaker *et al.* (2010c). This is done by reintroducing the wall inertia terms (neglected in the Whittaker *et al.* (2010c) model) to the force-balance equations governing the mechanics of the tube wall. Using the force-balance equations, a new ‘tube law’ (similar to the tube law derived by Whittaker *et al.* (2010d)) which relates the transmural pressure to the cross-sectional area of the tube is derived. Combining this with the fluid mechanics of the problem, a combined system for the interaction between the tube wall and the fluid is constructed. Solving this system,

countably many oscillatory modes for the instabilities are found and their frequencies are determined. The stability criterion and growth rates of the modes of the oscillations are also determined and it is found that the inclusion of wall inertia destabilises the system. Finally, asymptotic approximations describing the properties of the oscillations are derived in the case of large wall inertia.

In Chapters 3–7, we expand the Whittaker *et al.* (2010c) model to include the effects of axial bending. Initially, the model derived by Whittaker *et al.* (2010c) is unable to satisfy the canonical ‘clamped’ boundary conditions which should be set at the ends of the elastic-walled tube. It is found that terms representing axial bending are needed within the model in order for the clamped boundary conditions to be satisfied. These terms are only significant at leading order near the elastic-walled tube ends and as such, a boundary layer where axial bending effects are significant is introduced.

In Chapter 3, an estimate for the width of this axial-bending boundary layer is derived using a toy model. Using this estimate, the problem is found to split into multiple cases dependent on the relative sizes of the estimate, the tube wall thickness and the shear-relaxation boundary layers studied by Whittaker (2015). The first case occurs when the estimate of the bending boundary-layer width is larger than the tube wall thickness. In this scenario, it is found that the shear-relaxation boundary layer (which is split into an inner and outer layer) derived by Whittaker (2015) has a significant effect on the solution of the model and must be considered. This case then splits into two regimes: regime I_a , where the bending layer is estimated to be smaller than both the inner and outer shear-relaxation layers, and regime I_b , where the bending layer is expected to be larger than the inner shear layer, but still smaller than the outer shear layer. The final case, regime II , occurs when the estimate of the bending boundary-layer width is smaller than the tube wall thickness. In this regime, the shear-relaxation boundary layer no longer has a significant effect on the solution of the model and does not need to be considered. However, a different model is needed to describe the mechanics of the tube wall.

Chapter 4 concentrates on the first case, regime I_a . Here the shear-relaxation layer modelled by Whittaker (2015) must be considered, and in this regime it is predicted by the toy model in Chapter 3 that the bending-layer width is larger than the tube wall thickness but smaller than both the shear layers modelled by Whittaker (2015). In this scenario, Kirchhoff–Love shell theory which is used to

model the wall mechanics in the bulk of the tube in Chapter 2 can also be used to model the wall mechanics here. It is also expected that the bending layer is situated at the ends of the elastic-walled tube and matches onto modified inner and outer shear-relaxation layers, which in turn match onto the bulk layer. Solving the governing system within this bending layer, the bending-layer width is found to be in agreement with the prediction from the toy model in Chapter 3, and the leading-order deformations and area variation within the bending layer are calculated. The corresponding corrections to the inner shear layer are then calculated and the maximum order at which corrections apply to outer shear layer and bulk layer are also evaluated.

In Chapter 5, regime I_b is considered. As in regime I_a , the shear-relaxation layer studied by Whittaker (2015) must be considered. The toy model in Chapter 3 predicts in this case that the width of the bending layer is larger than both the tube wall thickness and the inner shear layer, but smaller than the outer shear layer. In this case, Kirchhoff–Love shell theory can once again be used to model the wall mechanics. It is also found that the inner shear layer is no longer needed in this scenario as its effects are incorporated into the bending layer. As such, the bending layer is found to again be situated at the ends of the elastic-walled tube. This bending layer then matches onto a modified outer shear layer, which in turn matches onto the bulk layer. When the model considered here is written in terms of the deformations of the tube wall, a leading-order degeneracy is found. To solve this problem, the model is instead written and solved in terms of the in-plane stresses of the tube wall, up to second order. In solving this model, the bending layer is found to have a different width to that predicted by the toy model in Chapter 3. This is because azimuthal stretching mechanisms which cannot be captured by the toy model contribute at leading order in this regime. However, the width of the bending layer is still found to be in between the sizes of the inner and outer shear layers. Using the expressions for the stresses, the deformations in the bending layer are calculated up to first order and the area change within the bending layer is numerically determined. The corrections to the outer shear layer are then calculated, and the maximum order at which corrections apply to the bulk layer is evaluated.

Chapter 6 considers the final case, regime II . Here, the shear-relaxation layer studied by Whittaker (2015) no longer has a significant effect on the bulk layer and does not need to be considered. The toy model in Chapter 3 predicts in

this regime that the bending layer will be smaller than the tube wall thickness, and thus Kirchhoff–Love shell theory can no longer be used to model the bending layer. Instead, as azimuthal variation is expected to be slow on the predicted scale of the bending layer, a linearised two-dimensional model of bending a semi-infinite block under tension is considered. This semi-infinite block corresponds to a two-dimensional cross-section of the tube wall in the normal and axial directions. This model is then solved numerically, and analytical techniques are also applied to determine asymptotic approximations of the boundary-layer width, and far-field approximations of the normal and axial deformations up to the amplitude of the deformations. It is found in the case corresponding to regimes I_a and I_b that the boundary-layer width derived from this model agrees with the estimate provided by the toy model in Chapter 3. However, in the case corresponding to regime II, a boundary layer with a much larger width than predicted is found. This boundary layer, which is found to have a width larger than the block thickness, is determined to be a new transverse shear-relaxation boundary layer. It is noted that this shear layer is different from the shear layer studied by Whittaker (2015), which arises from shear in the azimuthal direction. This 2D model is then used to model a transverse shear layer at the ends of the elastic-walled tube, and the corrections to the boundary conditions in the bulk layer due to this shear layer are calculated.

In Chapter 7, the 2D model for bending a semi-infinite block under tension, derived in Chapter 6, is considered further. Since the boundary layer found in Chapter 6 for regime II has a width larger than the block thickness, it is possible that Kirchhoff–Love shell theory (or another approximation applying the property that the wall thickness is the smallest geometric parameter) could be used to derive a one-dimensional model for the problem. Three different 1D models are derived and evaluated in this chapter, and through this analysis, more information about the wall mechanics within the new boundary layer is determined. It is found that only one of these models can accurately capture the behaviour of the deformations in the far-field, but even this model cannot accurately capture the deformations near the clamped end of the block. We find that this is due to a two-dimensional effect which is not incorporated into the 1D models.

Finally, in Chapter 8 some concluding remarks and recommendations for further work to be carried out on the models derived here are provided.

Chapter 2

The Effect of Wall Inertia on the Instability of Flow Through an Elastic-Walled Tube

2.1 Introduction

In this chapter, we will expand the model derived by Whittaker *et al.* (2010c) to include the effects of wall inertia on the self-excited oscillations generated within an elastic-walled tube with initially elliptical cross section. A description of the mathematical set-up used by Whittaker *et al.* (2010c) is provided in §2.2. In §2.3, we extend the work done by Whittaker *et al.* (2010d) to generate a tube law which takes into account inertia of the tube wall and relates the cross-sectional area of the tube to the transmural pressure. This tube law will be acquired from shell theory for an elliptical tube. We will then combine this tube law with the fluid mechanics investigated by Whittaker *et al.* (2010a,b) (and provided in §2.4) to create the leading-order governing ODE's for the system in §2.5.

Once the governing ODE's are derived, we then solve them for both the frequency of the oscillations and the oscillatory pressure field in §2.6. Using the solutions for the frequencies of the oscillations and the oscillatory pressure, we then calculate the corresponding axial velocity of the fluid and cross-sectional area of the tube. Once this has been accomplished, we quantify the effect wall inertia has on the frequency and mode shapes of the oscillations.

In §2.7, we investigate the time-averaged energy budget of the system and use this to determine expressions for the growth rates of the oscillations, as

well as expressions for the critical Reynolds numbers needed for each mode to become unstable. Using these expressions, we will evaluate the effect of wall inertia on the stability and growth rate of each mode and determine which mode is the most unstable and has the highest growth rate for a given wall inertia value. Finally in §2.8, we will investigate the case when we have large wall inertia and calculate asymptotic solutions for the frequency of the oscillations, the oscillatory pressure and the critical Reynolds number and growth rate of the oscillations.

2.2 Mathematical Set-up

2.2.1 Problem Description

We adopt the same set-up as Whittaker *et al.* (2010c) and depicted in Figure 2.1. A tube of length L and circumference $2\pi a$ with an initially elliptical axial cross-section is considered. The tube is set so that the tube axis is aligned with the z^* -axis and the ellipticity of the tube is set by a parameter σ_0 . Using this parameter, the major and minor radii are given by $ac \cosh(\sigma_0)$ and $ac \sinh(\sigma_0)$, where we have

$$c = \frac{\pi \operatorname{sech}(\sigma_0)}{2E(\operatorname{sech}(\sigma_0))}, \quad (2.1)$$

and the complete elliptic integral of the second kind $E(\phi)$ is defined as

$$E(\phi) = \int_0^{\frac{\pi}{2}} (1 - \phi^2 \sin^2 \theta)^{\frac{1}{2}} d\theta. \quad (2.2)$$

The constant c has been chosen to force the circumference to be $2\pi a$. Using the values of the major and minor radii, the cross-sectional area in the undeformed state is calculated to be

$$A_0^* = \pi a^2 c^2 \cosh(\sigma_0) \sinh(\sigma_0) = a^2 \frac{\pi^3 \tanh(\sigma_0)}{4[E(\operatorname{sech}(\sigma_0))]^2}. \quad (2.3)$$

The tube is split into three regions: two rigid sections occupying $0 < z^*/L < z_1$ and $z_2 < z^*/L < 1$, and an elastic-walled section within $z_1 < z^*/L < z_2$ which is clamped onto the rigid tubes at $z^* = z_1 L, z_2 L$. The elastic-walled region is susceptible to deformations from forces arising from the transmural (internal minus external) pressure. It is assumed that the elastic wall behaves linearly elastically over the range of deformations we consider here, and has thickness d , mass per unit area m , Poisson's ratio ν and incremental Young's

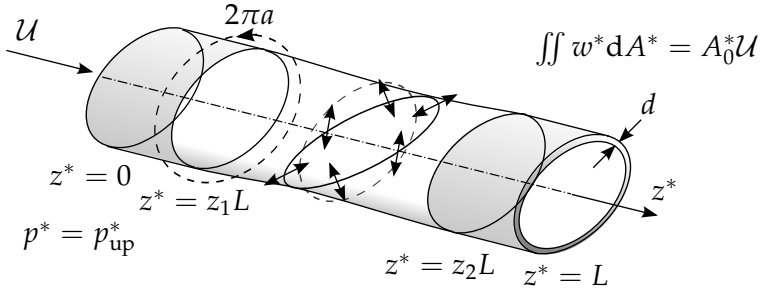


Figure 2.1: The set-up used by Whittaker *et al.* (2010c). An initially elliptical elastic-walled tube is clamped between two rigid tubes, and fluid flows from left to right, due to a volume flux condition at the downstream end.

modulus E . Using these parameters, we define the extensional stiffness D and the bending stiffness K of the tube wall as

$$D = \frac{Ed}{1 - \nu^2}, \quad K = \frac{Ed^3}{12(1 - \nu^2)}. \quad (2.4)$$

An axial tension force F is applied at the ends of the elastic-walled tube, giving rise to a uniform axial pre-stress of $F/(2\pi ad)$ in the undeformed configuration.

Within the tube, a fluid with density ρ and viscosity μ is driven through the tube using a steady axial volume flux with size $A_0^* \mathcal{U}$ at the downstream end $z^* = L$. The pressure is also fixed to be $p^* = p_{\text{up}}^*$ at the upstream end $z^* = 0$. By prescribing the flow rate at the downstream end, we ensure that no kinetic energy is lost there, which in turn, along with the fixed upstream pressure, ensures that the instability mechanism is at its most potent. Outside the tube, there is a constant external pressure p_{ext}^* , which acts on the tube.

As in the Whittaker *et al.* (2010c) model, we will consider oscillations of the fluid and tube wall with typical timescale T and amplitude $b(t^*) \ll a$, where t^* is dimensional time. The key variables we will use to describe the system are the fluid pressure p^* , the axial velocity of the fluid w^* and the cross-sectional area A^* of the tube. In the parameter regime we shall be considering, it is found that the transverse velocity components do not appear at leading order.

By assuming that oscillations involve a balance between forces from the azimuthal bending of the tube wall and axial fluid inertia, we can estimate a timescale T by equating the inertial pressure scale $\rho L^2 b/(aT^2)$ associated with oscillations of the fluid with the pressure scale Kb/a^4 associated with azimuthal bending. Doing so, we find

$$T = \left(\frac{\rho a^3 L^2}{K} \right)^{\frac{1}{2}}. \quad (2.5)$$

2.2.2 Dimensionless Groups and Parameter Regime

We now describe the dimensionless groups involved in this problem. We first have the three geometric ratios

$$\delta = \frac{d}{a}, \quad \ell = \frac{L}{a} \quad \text{and} \quad \Delta(t^*) = \frac{b(t^*)}{a}, \quad (2.6)$$

which correspond to the wall thickness, tube length and oscillation amplitude respectively. We also have two groups related to the fluid mechanics. Here, these are represented as the Womersley number α and the Strouhal number St , defined by

$$\alpha^2 = \frac{\rho a^2}{\mu T} = \left(\frac{\rho K}{a \ell^2 \mu^2} \right)^{\frac{1}{2}} \quad \text{and} \quad St = \frac{a}{U T} = \left(\frac{K}{\rho a^3 \ell^2 U^2} \right)^{\frac{1}{2}}. \quad (2.7)$$

The Womersley number represents the relative importance of unsteady inertia to viscous effects and the Strouhal number represents the relative importance of unsteady to convective inertia. Using these, we can define the Reynolds number Re as

$$Re = \frac{\rho U a}{\mu} = \frac{\alpha^2}{St}. \quad (2.8)$$

The final groups we define that are related to the tube wall are the dimensionless axial force \mathcal{F} and the dimensionless mass M defined by

$$\mathcal{F} = \frac{a F}{2 \pi K \ell^2}, \quad M = \frac{m a^4}{K T^2} \equiv \frac{m}{\rho a \ell^2}. \quad (2.9)$$

The dimensionless axial force \mathcal{F} is the ratio of the restoring forces $Fb/2\pi aL^2$ from tension effects to the restoring forces Kb/a^4 from azimuthal bending. The dimensionless mass M is the ratio of wall inertia mb/T^2 forces to the azimuthal bending Kb/a^4 forces or equivalently the forces $\rho a \ell^2/T^2$ due to the fluid inertia.

Here, we will consider a parameter regime where the tube wall is thin, under a large axial tension and generates small-amplitude, high-frequency, long-wavelength oscillations, so we have

$$\Delta(t) \ll 1, \quad \alpha \gg 1, \quad \ell St \gg 1, \quad \ell \gg 1, \quad \delta \ll 1, \quad \text{and} \quad \mathcal{F} = O(1). \quad (2.10)$$

2.2.3 Non-dimensionalization

We now non-dimensionalize the variables involved, starting by scaling dimensional time t^* with $t^* = Tt$. The transverse lengths are

non-dimensionalized using the typical radial scale a , and the axial length and the cross-sectional area are non-dimensionalized as follows

$$z^* = Lz, \quad A_0^* = a^2 A_0, \quad A^* = a^2 A. \quad (2.11)$$

It is assumed that the area $A(z, t)$ varies harmonically in time with dimensionless frequency ω and amplitude $\Delta(t)$. The pressure drop in the fluid and non-zero external pressure mean that the transmural pressure has a steady, axially varying component which deforms the tube wall slightly. Oscillations then occur about this deformed steady configuration. Hence, we can write

$$A(z, t) = A_0 + \frac{1}{\alpha^2 \ell St} \bar{A}(z) + \Delta(t) \operatorname{Re}(\tilde{A}(z) e^{i\omega t}) + \dots, \quad (2.12)$$

where A_0 is the cross-sectional area in the undeformed state, $\bar{A}(z)$ is the change in area due to the steady component of the transmural pressure and $\tilde{A}(z)$ is the (potentially complex) axial mode shape of the change in area due to the oscillations of the wall. The scaling for the steady area variation is chosen so that the ratio $\Delta \alpha^2 \ell St$ between the steady and oscillatory area variations matches with the ratio between the steady and oscillatory components of the pressure found later in (2.13).

We decompose the pressure and axial velocity of the fluid into steady and oscillatory components and non-dimensionalize as

$$p^* - p_{\text{up}}^* = \frac{\mu L \mathcal{U}}{a^2} \bar{p} + \frac{\rho L^2 b}{a T^2} \operatorname{Re}(\tilde{p}(z) e^{i\omega t}) + \dots, \quad (2.13)$$

$$w^* = \mathcal{U} \bar{w} + \frac{L b}{a T} \operatorname{Re}(\tilde{w}(z) e^{i\omega t}) + \dots. \quad (2.14)$$

As in the expression (2.12) for the dimensionless area, overbars denote steady components whereas tildes denote the complex axial mode shapes of the oscillatory components. The pressure has been non-dimensionalized using the viscous scale $\mu L \mathcal{U} / a^2$ for the steady component and the inertial scale $\rho L^2 b / a T^2 \equiv \Delta K / a^3$ for the oscillatory component. The velocity has been non-dimensionalized using scales for the mean flow and wall motion. The oscillatory components have the same frequencies as the wall motion and as discussed in §2.4, the large aspect ratio of the system results in the leading-order oscillatory pressure \tilde{p} and leading-order oscillatory axial velocity \tilde{w} being uniform in the cross-section of the tube.

The steady external pressure is non-dimensionalized as

$$p_{\text{ext}}^* - p_{\text{up}}^* = \frac{\mu L \mathcal{U}}{a^2} \bar{p}_{\text{ext}}. \quad (2.15)$$

Using this and the expression (2.13) for the fluid pressure $p^* - p_{\text{up}}^*$, we may define the dimensional transmural pressure p_{tm}^* as

$$\begin{aligned} p_{\text{tm}}^* &= p^* - p_{\text{ext}}^* = (p^* - p_{\text{up}}^*) - (p_{\text{ext}}^* - p_{\text{up}}^*) \\ &= \frac{\mu L \mathcal{U}}{a^2} (\bar{p} - \bar{p}_{\text{ext}}) + \frac{\rho L^2 b}{a T^2} \text{Re}(\tilde{p}(z) e^{i\omega t}) + \dots \end{aligned} \quad (2.16)$$

The transmural pressure is then non-dimensionalized as

$$p_{\text{tm}}^* = \frac{\Delta K}{a^3} p_{\text{tm}}. \quad (2.17)$$

Applying this to the expression (2.16) for p_{tm}^* , we find the non-dimensional transmural pressure p_{tm} is given by

$$p_{\text{tm}} = \frac{1}{\Delta \alpha^2 \ell S t} (\bar{p} - \bar{p}_{\text{ext}}) + \text{Re}(\tilde{p}(z) e^{i\omega t}) + \dots \quad (2.18)$$

Finally, energy and energy fluxes are non-dimensionalized using

$$\rho \mathcal{U}^2 a^2 L \quad \text{and} \quad \rho \mathcal{U}^3 a^3. \quad (2.19)$$

These are based on the kinetic energy and kinetic energy fluxes in the steady flow.

2.3 A Tube Law to Model the Wall Mechanics

We now proceed to derive a tube law relating the transmural pressure with the cross-sectional area of the tube by following the procedure used by Whittaker *et al.* (2010d). The main difference is that terms which relate to wall inertia are also included in the derivation of the tube law.

2.3.1 Lagrangian Surface Coordinates, Deformation Notation and Tensor Notation

We first introduce a new coordinate system that takes into account the deformations arising in the tube wall. We parameterize the midplane of the tube wall with dimensional Lagrangian coordinates (x^1, x^2) , which are measures of arc length in the azimuthal and axial directions respectively, in the undeformed state¹. We also introduce two dimensionless Lagrangian

¹Note that the superscripts denote coordinate directions and are not to be mistaken for powers.

surface coordinates, $\tau \in [0, 2\pi)$ and $z \in [0, 1]$. These are related to (x^1, x^2) by $dx^1 = ah(\tau)d\tau$ and $dx^2 = a\ell dz$, where

$$h(\tau) = c(\sinh^2(\sigma_0) + \sin^2 \tau)^{\frac{1}{2}} = c \left(\frac{1}{2} \cosh 2\sigma_0 - \frac{1}{2} \cos 2\tau \right)^{\frac{1}{2}}.$$

We now introduce the dimensionless functions $\xi(\tau, z, t)$ and $\eta(\tau, z, t)$ to represent the normal and tangential displacements of the wall, as well as the dimensionless functions $\zeta_a(z, t)$ and $\zeta(\tau, z, t)$ to represent the components of the axial displacements due to an overall shift in the axial direction and a deformation about this shift. Using these functions along with our coordinate system, we can define the position of the wall midplane \mathbf{r} in the deformed state as follows,

$$\mathbf{r} = \mathbf{r}_0(\tau, z) + \frac{\Delta(t)a}{h(\tau)} (\xi(\tau, z, t)\hat{\mathbf{n}} + \eta(\tau, z, t)\hat{\mathbf{t}}) + \Delta(t)a\ell \left(\frac{1}{\ell^2} \zeta(\tau, z, t) + \delta^2 \zeta_a(z, t) \right) \hat{\mathbf{z}}. \quad (2.20)$$

Here, \mathbf{r}_0 is the initial position of the surface element and the vectors $\hat{\mathbf{n}}$, $\hat{\mathbf{t}}$ and $\hat{\mathbf{z}}$ are unit vectors in the normal, azimuthal and axial directions of the undeformed tube, respectively. The components ξ , η , ζ and ζ_a of the deformation \mathbf{r} are depicted in Figure 2.2.

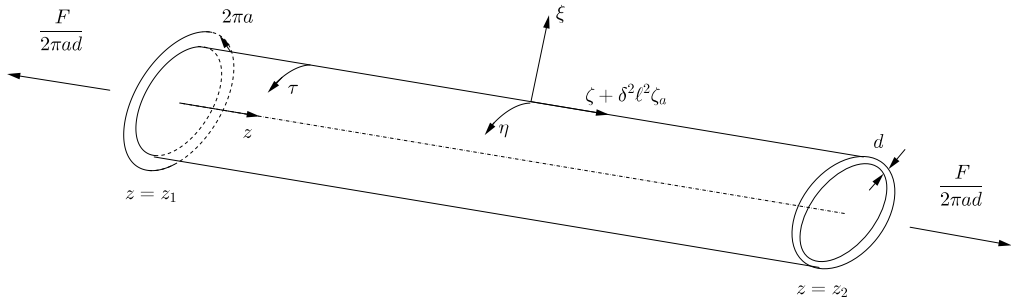


Figure 2.2: The set-up of the undeformed, elliptical, elastic-walled tube, similar to that used by Whittaker *et al.* (2010d). The midplane of the tube wall is parameterized by the dimensionless coordinates (τ, z) , and the displacements of the wall are described by the components ξ , η , $\zeta + \delta^2 \ell^2 \zeta_a$ of the deformation \mathbf{r} , given by (2.20).

With the definition of \mathbf{r} , we can define the basis vectors in the deformed state to be

$$\mathbf{a}_\alpha = \frac{\partial \mathbf{r}}{\partial x^\alpha}, \quad (2.21)$$

where the indices span over $(1, 2)$. We also define the unit normal to the tube wall at each point to be

$$\mathbf{a}_3 = \frac{\mathbf{a}_1 \times \mathbf{a}_2}{|\mathbf{a}_1 \times \mathbf{a}_2|}, \quad (2.22)$$

as well as the metric tensor

$$a_{\alpha\beta} = \mathbf{a}_\alpha \cdot \mathbf{a}_\beta, \quad (2.23)$$

and the curvature tensor

$$b_{\alpha\beta} = \mathbf{a}_3 \cdot \frac{\partial \mathbf{a}_\alpha}{\partial x^\beta}. \quad (2.24)$$

2.3.2 Kirchhoff–Love Shell Equations and Constitutive Laws

The Kirchhoff–Love shell equations in covariant differential form (Flügge, 1972; Søndergaard, 2007) are now used as a starting point for the derivation of our tube law. These are

$$N^{\alpha\beta} b_{\alpha\beta} + \nabla_\alpha Q^\alpha + f^3 = m\ddot{\mathbf{r}}^3, \quad (2.25)$$

$$\nabla_\beta N^{\beta\alpha} - b_\gamma^\alpha Q^\gamma + f^\alpha = m\ddot{\mathbf{r}}^\alpha, \quad (2.26)$$

$$\nabla_\beta M^{\beta\alpha} - Q^\alpha + g^\alpha = i\ddot{\theta}^{*\alpha}. \quad (2.27)$$

In these equations, $N^{\alpha\beta}$, $M^{\alpha\beta}$ and Q^α represent in-plane stress, the in-plane bending moment and the normal shear stress respectively, f^α are tangential body forces, f^3 is a normal body force, g^α are body moments and ∇_α is a two-dimensional covariant derivative in the direction \mathbf{a}_α . We also have \mathbf{r}^α as the component of \mathbf{r} in the \mathbf{a}_α direction. Finally, $\ddot{\theta}^{*\alpha}$ denotes the angular acceleration about an axis passing through the tube wall in the \mathbf{a}_α direction, and i is the moment of inertia about the same axis. The angles $\theta^{*\alpha}$ of rotation that the tube wall takes about axes passing through the material in the \mathbf{a}_α direction are depicted in Figure 2.3. Equations (2.25) and (2.26) represent equilibrium of forces in the \mathbf{a}_3 and \mathbf{a}_α directions respectively, while equation (2.27) represents the equilibrium of moments about the two axes in the plane of the tube wall.

The moment of inertia i for an element of the tube wall is that of a rod of length d and mass m orientated to be normal to the shell surface. Hence, we have

$$i = \frac{1}{12}md^2. \quad (2.28)$$

We now use (2.27) to eliminate Q^α from (2.25) and (2.26). Substituting in the components of \mathbf{r}^α and assuming that any external forces come only from the transmural pressure p_{tm}^* , so $f^\alpha = g^\alpha = 0$ and $f^3 = p_{\text{tm}}^*$, we obtain the following

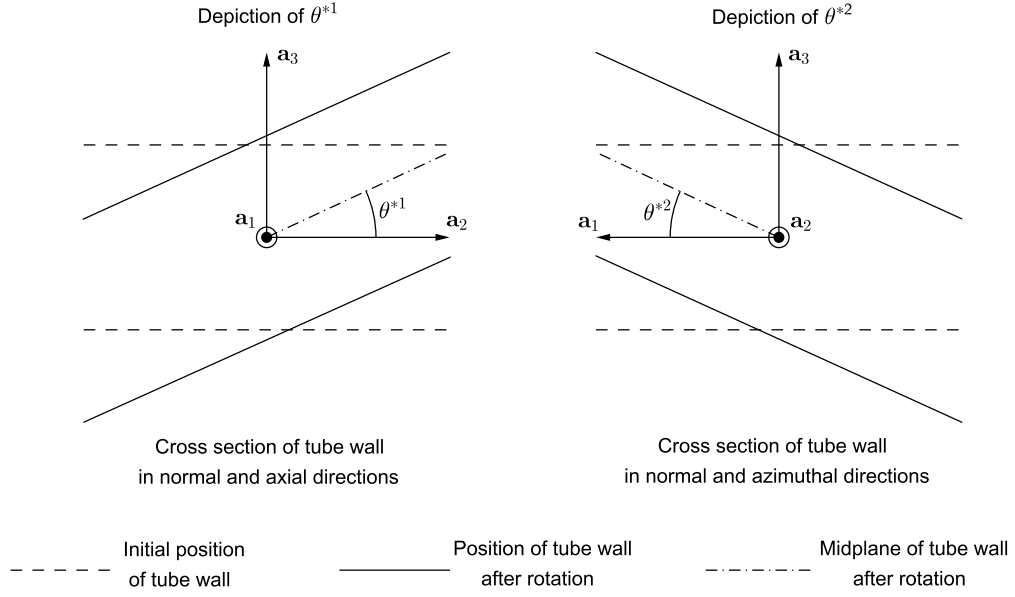


Figure 2.3: A depiction of the angles $\theta^{*\alpha}$ of rotation that the tube wall takes about axes passing through the material in the \mathbf{a}_α direction.

equations

$$\nabla_\alpha \nabla_\beta M^{\alpha\beta} + N^{\alpha\beta} b_{\alpha\beta} - \frac{1}{12} \nabla_\alpha m d^2 \ddot{\theta}^{*\alpha} + p_{\text{tm}}^* - \frac{m}{T^2} \left(\frac{\Delta(t)a}{h(\tau)} \right) \frac{d^2 \xi}{dt^2} + \dots = 0, \quad (2.29)$$

$$\nabla_\beta N^{\beta 1} - b_\gamma^1 \nabla_\beta M^{\beta\gamma} + \frac{1}{12} b_\gamma^1 m d^2 \ddot{\theta}^{*\gamma} - \frac{m}{T^2} \left(\frac{\Delta(t)a}{h(\tau)} \right) \frac{d^2 \eta}{dt^2} + \dots = 0, \quad (2.30)$$

$$\nabla_\beta N^{\beta 2} - b_\gamma^2 \nabla_\beta M^{\beta\gamma} + \frac{1}{12} b_\gamma^2 m d^2 \ddot{\theta}^{*\gamma} - \frac{m \Delta(t) a \ell}{T^2} \left(\frac{1}{\ell^2} \frac{d^2 \zeta}{dt^2} + \delta^2 \frac{d^2 \zeta_a}{dt^2} \right) + \dots = 0. \quad (2.31)$$

It is noted that we will also have terms dependent on $\dot{\Delta}$ and $\ddot{\Delta}$. However these are assumed to be negligible due to the amplitude of the oscillations changing on a longer time scale than the oscillations themselves.

We now introduce the in-plane strain and bending strain tensors which characterize the deformation of the wall material

$$\gamma_{\alpha\beta} = \frac{1}{2} (a_{\alpha\beta} - \bar{a}_{\alpha\beta}), \quad \kappa_{\alpha\beta} = -b_{\alpha\beta} + \bar{b}_{\alpha\beta} + 2\bar{b}_\alpha^\delta \gamma_{\delta\beta}, \quad (2.32)$$

where overbars denote the values of the quantities in the undeformed state.

Using linear constitutive laws (Flügge, 1972, section 9.4), we can relate $N^{\alpha\beta}$

and $M^{\alpha\beta}$ to $\gamma_{\alpha\beta}$ and $\kappa_{\alpha\beta}$ by

$$\begin{aligned} N^{\alpha\beta} &= \delta_2^\alpha \delta_2^\beta \frac{F}{2\pi a} + D[(1-\nu)\gamma^{\alpha\beta} + \nu\gamma_\lambda^\lambda a^{\alpha\beta}] \\ &\quad + K \left\{ \frac{(1-\nu)}{2} [2a^{\beta\delta}b^{\alpha\gamma} + a^{\beta\gamma}b^{\alpha\gamma} + a^{\alpha\delta}b^{\beta\gamma} - b_\lambda^\lambda(a^{\alpha\delta}a^{\beta\gamma} + a^{\alpha\gamma}a^{\beta\delta})] \right. \\ &\quad \left. + \nu[a^{\alpha\beta}b^{\gamma\delta} + a^{\gamma\delta}b^{\alpha\beta} - a^{\alpha\beta}a^{\gamma\delta}b_\lambda^\lambda] \right\} \kappa_{\lambda\delta}, \end{aligned} \quad (2.33)$$

$$\begin{aligned} M^{\alpha\beta} &= K[-(1-\nu)(b_\gamma^\alpha\gamma^{\gamma\beta} - b_\lambda^\lambda\gamma^{\alpha\beta}) - \nu(b^{\alpha\beta} - b_\lambda^\lambda a^{\alpha\beta})\gamma_\mu^\mu \\ &\quad + \frac{1}{2}(1-\nu)(\kappa^{\alpha\beta} + \kappa^{\beta\alpha}) + \nu a^{\alpha\beta}\kappa_\lambda^\lambda], \end{aligned} \quad (2.34)$$

where δ_j^i is the Kronecker delta. Equations (2.33) and (2.34) are found by substituting the plane stress form of Hooke's law into the definitions of $N^{\alpha\beta}$ and $M^{\alpha\beta}$, rewriting in terms of $\gamma_{\alpha\beta}$ and $\kappa_{\alpha\beta}$ and neglecting higher-order δ terms.

2.3.3 Scaling and Non-Dimensionalization

Our next step is to non-dimensionalize (2.29), (2.30) and (2.31) which will allow us to determine which terms appear at leading order in the governing equations. We proceed to use the scalings and non-dimensionalizations found by Whittaker *et al.* (2010d) to simplify our equations.

First, we recall the scalings (2.9), (2.17) for the axial force F , mass per unit area m and transmural pressure p_{tm}^* . Next, we scale the curvature tensor both in the deformed and undeformed states. In the undeformed state, we scale as

$$\bar{b}_\alpha^\beta = \frac{1}{a} \begin{bmatrix} \bar{B}(\tau) & 0 \\ 0 & 0 \end{bmatrix}, \quad (2.35)$$

due to the only curvature in the undeformed state being the azimuthal curvature, which has size $O(1/a)$. Using this, we scale the curvature tensor in the deformed state as

$$b_\alpha^\beta = \bar{b}_\alpha^\beta + \frac{\Delta(t)}{ah(\tau)} \begin{bmatrix} \beta(\tau, z) & O(\ell^{-1}) \\ O(\ell^{-1}) & \frac{1}{\ell^2} \frac{\partial^2 \zeta}{\partial z^2} \end{bmatrix}. \quad (2.36)$$

Now, we scale the in-plane and bending strains starting with $\gamma_{\alpha\beta}$, which may be written as

$$\gamma_{\alpha\beta} = \Delta(t) \begin{bmatrix} O(\delta^2, \ell^{-2}) & \frac{1}{\ell}(s(z) + O(\delta^2, \ell^{-2})) \\ \frac{1}{\ell}(s(z) + O(\delta^2, \ell^{-2})) & \frac{1}{\ell^2} \frac{\partial \zeta}{\partial z} + \delta^2 \frac{d\zeta_a}{dz} + \dots \end{bmatrix}, \quad (2.37)$$

where $s(z)$ is the leading-order component of the shear strain which is independent of τ . We scale $\kappa_{\alpha\beta}$ as follows

$$\kappa_{\alpha\beta} = \frac{\Delta(t)}{a} \begin{bmatrix} -\frac{1}{h}\beta + O(\delta^2, \ell^{-2}) & \frac{1}{\ell}O(1) \\ \frac{1}{\ell}O(1) & -\frac{1}{\ell^2 h} \frac{\partial^2 \xi}{\partial z^2} \end{bmatrix}. \quad (2.38)$$

The axial bending term found in κ_{22} is found to be too small to contribute at leading order on the axial scale considered here and will be neglected. However we later reintroduce this axial bending term in Chapters 3–7 by considering smaller axial scales where the bending term becomes significant at leading order.

The in-plane stress $N^{\alpha\beta}$ is scaled as

$$N^{\alpha\beta} = \frac{K}{a^2} \begin{bmatrix} 0 & 0 \\ 0 & \ell^2 \mathcal{F} \end{bmatrix} + \frac{\Delta(t)K}{a^2} \begin{bmatrix} \tilde{N}(\tau, z) & \ell \tilde{S}(z) + \dots \\ \ell \tilde{S}(z) + \dots & \tilde{\Sigma}(\tau, z) \end{bmatrix}, \quad (2.39)$$

where

$$\tilde{N}(\tau, z) = \frac{a^2 D}{\Delta(t)K} (\gamma_{11} + \nu \gamma_{22}) = \frac{12\gamma_{11}}{\Delta(t)\delta^2} + 12\nu \left(\frac{1}{\delta^2 \ell^2} \frac{\partial \zeta}{\partial z} + \frac{d\zeta_a}{dz} \right) \quad (2.40)$$

is the dimensionless hoop stress,

$$\tilde{\Sigma}(\tau, z) = \frac{a^2 D}{\Delta(t)K} (\gamma_{22} + \nu \gamma_{11}) = \nu \tilde{N} + 12(1 - \nu^2) \left(\frac{1}{\delta^2 \ell^2} \frac{\partial \zeta}{\partial z} + \frac{d\zeta_a}{dz} \right) \quad (2.41)$$

is the dimensionless axial stress and

$$\tilde{S}(z) = \frac{a^2 D}{\Delta(t)K} \gamma_{12} = \frac{12(1 - \nu)s(z)}{\delta^2 \ell^2} \quad (2.42)$$

is the leading-order dimensionless shear stress. We also scale the bending moment $M^{\alpha\beta}$ as

$$M^{\alpha\beta} = -\frac{\Delta(t)K}{a} \begin{bmatrix} \frac{1}{h}\beta + O(\delta^2, \ell^{-2}) & O(\ell^{-1}) \\ O(\ell^{-1}) & O(\ell^{-2}) \end{bmatrix}. \quad (2.43)$$

We now evaluate the covariant derivatives that arise in (2.29), (2.30) and (2.31). At leading order, these are

$$\nabla_1 = \frac{1}{ah} \frac{\partial}{\partial \tau} + O(\ell^{-1}), \quad \nabla_2 = \frac{1}{a\ell} \frac{\partial}{\partial z} + O(\ell^{-2}). \quad (2.44)$$

We must also evaluate one of the higher-order terms in the derivative of $N^{\alpha\beta}$ due to the large factor multiplying \mathcal{F} in the definition (2.39) of $N^{\alpha\beta}$. The full expression for the derivative of $N^{\alpha\beta}$ is

$$\nabla_\alpha N^{\alpha\beta} = \frac{\partial N^{\alpha\beta}}{\partial x^\alpha} + \Gamma_{\gamma\alpha}^\alpha N^{\gamma\beta} + \Gamma_{\gamma\alpha}^\beta N^{\alpha\gamma}, \quad (2.45)$$

where the Christoffel symbol is given by $\Gamma_{\mu\nu}^\beta \equiv a^{\alpha\beta} \mathbf{a}_\alpha \cdot \mathbf{a}_{\mu,\nu}$. As each component of $\Gamma_{\mu\nu}^\beta$ is $O(\Delta)$ at most, we only need to consider the terms involving N^{22} , which is the only component of $N^{\alpha\beta}$ that is non- $O(\Delta)$. Hence the relevant Christoffel symbols are Γ_{21}^1 , Γ_{22}^1 and Γ_{22}^2 . Whittaker *et al.* (2010d) calculated these to be

$$\Gamma_{21}^1 = \frac{1}{a\ell} \frac{\partial \gamma_{11}}{\partial z} + \dots = \frac{\Delta(t)}{a\ell} \left[\frac{\delta^2}{12} \frac{\partial \tilde{N}}{\partial z} - \nu \left(\frac{1}{\ell^2} \frac{\partial^2 \zeta}{\partial z^2} + \delta^2 \frac{d^2 \zeta_a}{dz^2} \right) \right] + \dots, \quad (2.46)$$

$$\Gamma_{22}^1 = \frac{\Delta(t)}{a\ell^2 h} \frac{\partial^2 \eta}{\partial z^2} + \dots, \quad (2.47)$$

$$\Gamma_{22}^2 = \frac{\Delta(t)}{a\ell} \left(\frac{1}{\ell^2} \frac{\partial^2 \zeta}{\partial z^2} + \delta^2 \frac{d^2 \zeta_a}{dz^2} \right) + \dots \quad (2.48)$$

Finally, the angles $\theta^{*\alpha}$ of rotation that the tube wall takes about axes passing through the tube wall in the \mathbf{a}_α directions are scaled as

$$\theta^{*1} = \frac{\Delta}{\ell} \theta^1, \quad \theta^{*2} = \Delta \theta^2, \quad (2.49)$$

where the angles θ^α are $O(1)$. These scalings are determined by taking the ratio of the size of the normal deformations to the length scales in the axial and azimuthal directions.

2.3.4 Leading-Order Force-Balance Equations

Substituting the scalings (2.9), (2.17), (2.35)–(2.49) into the force-balance equations (2.29)–(2.31), and retaining only leading-order terms in Δ , δ and ℓ^{-1} , we find the following

$$\bar{B}\tilde{N} + \frac{\mathcal{F}}{h} \frac{\partial^2 \zeta}{\partial z^2} - \frac{1}{h} \frac{\partial}{\partial \tau} \left(\frac{1}{h} \frac{\partial}{\partial \tau} \left(\frac{\beta}{h} \right) \right) + p_{\text{tm}} + \frac{M}{h} \ddot{\xi} = 0, \quad (2.50)$$

$$\frac{1}{h} \frac{\partial \tilde{N}}{\partial \tau} + h \frac{d\tilde{S}}{dz} + \frac{\mathcal{F}}{h} \frac{\partial^2 \eta}{\partial z^2} + \frac{\bar{B}}{h} \frac{\partial}{\partial \tau} \left(\frac{\beta}{h} \right) + \frac{M}{h} \ddot{\eta} = 0, \quad (2.51)$$

$$\begin{aligned} \frac{1}{\ell} \frac{\partial}{\partial z} \left(\nu \tilde{N} + 12(1 - \nu^2) \left(\frac{1}{\delta^2 \ell^2} \frac{\partial \zeta}{\partial z} + \frac{d\zeta_a}{dz} \right) \right) + \mathcal{F} \ell \frac{\delta^2}{12} \frac{\partial \tilde{N}}{\partial z} \\ + \mathcal{F} \ell (2 - \nu) \left(\frac{1}{\ell^2} \frac{\partial^2 \zeta}{\partial z^2} + \delta^2 \frac{d^2 \zeta_a}{dz^2} \right) + M \ell \left(\frac{1}{\ell^2} \ddot{\zeta} + \delta^2 \ddot{\zeta}_a \right) = 0. \end{aligned} \quad (2.52)$$

We note that the angular inertia terms have now vanished. This is because during the scaling these terms have become $O(\delta^2)$.

2.3.5 Curvature and Shear Components in terms of the Deformations, and the Relationships Between the Deformations

Now, \bar{B} , β and \tilde{S} are evaluated in terms of the dimensionless deformation functions ξ , η , ζ and ζ_a . Whittaker *et al.* (2010d) found the relations to be

$$\begin{aligned}\bar{B} &= -\frac{c^2 \sinh(2\sigma_0)}{2h^3}, & \beta &= -\frac{2}{c^2 \sinh(2\sigma_0)} \frac{\partial}{\partial \tau} \left(1 + \frac{\partial^2}{\partial \tau^2} \right) \eta, \\ \tilde{S} &= \frac{12(1-\nu)}{\delta^2 \ell^2} \frac{d}{dz} \left(\frac{1}{2\pi} \int_0^{2\pi} \eta d\tau \right).\end{aligned}\quad (2.53)$$

Whittaker *et al.* (2010d) also found the following to hold at leading order

$$\xi \sinh(2\sigma_0) + \frac{2h^2}{c^2} \frac{\partial \eta}{\partial \tau} - \eta \sin(2\tau) = 0, \quad (2.54)$$

$$\frac{\partial \eta}{\partial z} + \frac{\partial \zeta}{\partial \tau} = \frac{h}{2\pi} \frac{d}{dz} \int_0^{2\pi} \eta d\tau. \quad (2.55)$$

Equation (2.54) is known as the inextensibility condition and can be used to eliminate ξ from our equations in favour of η . We can also use (2.55) to rewrite ζ in terms of η .

2.3.6 Reducing the Governing Equations to a Single Equation for η

The governing equations (2.50)–(2.52) are now reduced to a single equation to be solved for η . Eliminating the hoop stress \tilde{N} between (2.50) and (2.51) and substituting in the expressions (2.53) gives

$$\begin{aligned}\mathcal{L}(\beta) &= p_{tm} C_p h + h \frac{d^2}{dz^2} \mathcal{R}(\eta) + \mathcal{F} \left[\left(C_n + C_{n'} \frac{\partial}{\partial \tau} \right) \frac{\partial^2 \xi}{\partial z^2} + \frac{\partial^2 \eta}{\partial z^2} \right] \\ &\quad - M \left[\left(C_n + C_{n'} \frac{\partial}{\partial \tau} \right) \ddot{\xi} + \ddot{\eta} \right],\end{aligned}\quad (2.56)$$

where we have introduced the linear operators \mathcal{L} and \mathcal{R} defined by

$$\mathcal{L}(\beta) = \frac{2}{c^2 \sinh 2\sigma_0} \left(\frac{\partial^3}{\partial \tau^3} + L_2 \frac{\partial^2}{\partial \tau^2} + L_1 \frac{\partial}{\partial \tau} + L_0 \right) \beta, \quad (2.57)$$

$$\mathcal{R}(\eta) = \frac{12(1-\nu)}{\delta^2 \ell^2} \frac{1}{2\pi} \int_0^{2\pi} \eta d\tau, \quad (2.58)$$

as well as the coefficients

$$L_2 = -\frac{3 \sin(2\tau)}{\cosh(2\sigma_0) - \cos(2\tau)}, \quad (2.59)$$

$$L_1 = -\frac{(2 \cos^2(2\tau) + 8 \cosh(2\sigma_0) \cos(2\tau) - 9 - \cosh^2(2\sigma_0))}{(\cosh(2\sigma_0) - \cos(2\tau))^2}, \quad (2.60)$$

$$L_0 = \frac{3 \sin(2\tau) (\cosh^2(2\sigma_0) - 5 + 4 \cosh(2\sigma_0) \cos(2\tau))}{(\cosh(2\sigma_0) - \cos(2\tau))^3}, \quad (2.61)$$

$$C_p = \frac{3 \sin(2\tau)}{\sinh(2\sigma_0)}, \quad (2.62)$$

$$C_n = \frac{2 \sin(2\tau)}{\sinh(2\sigma_0)}, \quad (2.63)$$

$$C_{n'} = \frac{\cosh(2\sigma_0) - \cos(2\tau)}{\sinh(2\sigma_0)}. \quad (2.64)$$

We now use (2.54) and (2.53b) to eliminate ξ and β from (2.56). Doing so, we obtain

$$\mathcal{L}(\mathcal{K}(\eta)) - h \frac{\partial^2}{\partial z^2} \mathcal{R}(\eta) - \mathcal{F} \frac{\partial^2}{\partial z^2} \mathcal{J}(\eta) + M \mathcal{J}(\dot{\eta}) = p_{\text{tm}}(z, t) C_p h. \quad (2.65)$$

Here we have introduced two more linear operators \mathcal{K} and \mathcal{J} , which are given by

$$\mathcal{K}(\eta) = \frac{-2}{c^2 \sinh(2\sigma_0)} \frac{\partial}{\partial \tau} \left(1 + \frac{\partial^2}{\partial \tau^2} \right) \eta, \quad (2.66)$$

$$\begin{aligned} \mathcal{J}(\eta) = & -\frac{(\cosh(2\sigma_0) - \cos(2\tau))^2}{\sinh^2(2\sigma_0)} \frac{\partial^2 \eta}{\partial \tau^2} - \frac{3(\cosh(2\sigma_0) - \cos(2\tau)) \sin(2\tau)}{\sinh^2(2\sigma_0)} \frac{\partial \eta}{\partial \tau} \\ & + \frac{2 \sinh^2(2\sigma_0) + 3 \sin^2(2\tau) - (\cosh(2\sigma_0) - \cos(2\tau))^2}{\sinh^2(2\sigma_0)} \eta. \end{aligned} \quad (2.67)$$

It is noted that (2.65) is an equation to be solved for η , forced by p_{tm} . By examining (2.65), it is seen that the right-hand side is odd and π -periodic in τ . Hence, the form of the operators on the left-hand side of (2.65) implies that η is also odd and π -periodic in τ . Using this property, we have that $\mathcal{R}(\eta) = 0$.

2.3.7 Applying a Fourier Expansion of η

As the solution of (2.65) is symmetric, we find it convenient to express η as a Fourier series. As η is odd in τ , we only keep the sine terms. Hence, our series is

$$\eta = \sum_{n=1}^{\infty} e_n(z, t) \sin(2n\tau), \quad (2.68)$$

where $e_n(z, t)$ are the Fourier coefficients of η . Substituting the expansion (2.68) into (2.65), we obtain

$$\mathcal{L}(\mathcal{K}(\eta)) = p_{\text{tm}}(z, t)C_p h + \mathcal{F} \sum_{m=1}^{\infty} C_{Tm}(\tau) e_m''(z, t) - M \sum_{m=1}^{\infty} C_{Tm}(\tau) \frac{\partial^2}{\partial t^2} e_m(z, t), \quad (2.69)$$

where ' is the differential with respect to z and $C_{Tm}(\tau)$ is defined by

$$\begin{aligned} C_{Tm}(\tau) = \frac{1}{\sinh^2 2\sigma_0} \Big\{ & \sin(2m\tau) \left[3 \sin^2 2\tau + 2 \sinh^2 2\sigma_0 \right. \\ & \left. + (4m^2 - 1)(\cosh 2\sigma_0 - \cos 2\tau)^2 \right] \\ & - 6m(\cosh 2\sigma_0 - \cos 2\tau) \cos(2m\tau) \sin 2\tau \Big\}. \end{aligned}$$

2.3.8 Decomposition of η

As the first term on the right-hand side of (2.69) represents forcing of azimuthal bending due to the transmural pressure, whereas the second and third terms represent axial tension and wall inertia effects, η is now decomposed into parts to better represent these different effects. We define two functions $\eta^{(P)}(\tau)$ and $\eta_m^{(T)}(\tau)$ that satisfy

$$\begin{aligned} \mathcal{L}(\mathcal{K}(\eta^{(P)})) &= C_p h, \\ \mathcal{L}(\mathcal{K}(\eta_m^{(T)})) &= C_{Tm}. \end{aligned}$$

Doing this, we can substitute $\mathcal{L}(\mathcal{K}(\eta^{(P)}))$ and $\mathcal{L}(\mathcal{K}(\eta_m^{(T)}))$ into equation (2.69). As \mathcal{L} and \mathcal{K} are linear and the solution for η is unique (shown by Whittaker *et al.*, 2010d), we obtain the following equation for η

$$\eta(\tau, z) = p_{\text{tm}}(z, t)\eta^{(P)}(\tau) + \mathcal{F} \sum_{m=1}^{\infty} \eta_m^{(T)}(\tau) e_m''(z, t) - M \sum_{m=1}^{\infty} \eta_m^{(T)}(\tau) \frac{\partial^2}{\partial t^2} e_m(z, t). \quad (2.70)$$

We now define Fourier series for $\eta^{(P)}$ and $\eta_m^{(T)}$ as

$$\begin{aligned} \eta^{(P)}(\tau) &= \sum_{n=1}^{\infty} E_n^{(P)} \sin(2n\tau), \\ \eta_m^{(T)}(\tau) &= \sum_{n=1}^{\infty} E_{mn}^{(T)} \sin(2n\tau), \end{aligned}$$

where $E_n^{(P)}$ and $E_{mn}^{(T)}$ are the Fourier coefficients of $\eta^{(P)}$ and $\eta_m^{(T)}$ respectively. Substituting these into equation (2.70) and equating coefficients, we get the following set of equations for $e_n(z, t)$ in terms of $E_n^{(P)}$ and $E_{mn}^{(T)}$

$$e_n(z, t) = p_{\text{tm}}(z, t)E_n^{(P)} + \mathcal{F} \sum_{m=1}^{\infty} E_{mn}^{(T)} e_m''(z, t) - M \sum_{m=1}^{\infty} E_{mn}^{(T)} \frac{\partial^2}{\partial t^2} e_m(z, t). \quad (2.71)$$

2.3.9 The Tube Law

Now, we assume that the deformations in the tube wall that arise from the transmural pressure $p_{\text{tm}}(z, t)$ and the axial pre-stress \mathcal{F} can be modelled by the first Fourier mode of η , $\eta^{(P)}$ and $\eta_m^{(T)}$. It has been shown by Whittaker *et al.* (2010d) that the sizes of the higher-order Fourier coefficients are much smaller than the sizes of the first-order Fourier coefficients, and because of this our assumption is justified. Making this assumption, we can truncate equation (2.71) after $m = 1$ giving us

$$e_1(z, t) = E_1^{(P)} p_{\text{tm}}(z, t) + \mathcal{F} E_{11}^{(T)} \frac{\partial^2 e_1}{\partial z^2} - M E_{11}^{(T)} \frac{\partial^2 e_1}{\partial t^2}. \quad (2.72)$$

Whittaker *et al.* (2010d) have also shown the following relation between $e_1(z, t)$ and the cross-sectional area $A(z, t)$

$$\frac{A(z, t) - A_0}{A_0} = \frac{6\Delta e_1(z, t)}{c^2 \sinh^2 2\sigma_0}, \quad (2.73)$$

By rearranging (2.73) to give $e_1(z, t)$ in terms of $A(z, t)$ and substituting into (2.72), the following equation for $p_{\text{tm}}(z, t)$ is obtained

$$p_{\text{tm}}(z, t) = \frac{k_0}{\Delta A_0} (A(z, t) - A_0) - \frac{k_2 \mathcal{F}}{\Delta A_0} \frac{\partial^2 A(z, t)}{\partial z^2} + \frac{k_2 M}{\Delta A_0} \frac{\partial^2}{\partial t^2} (A(z, t) - A_0), \quad (2.74)$$

where k_0 and k_2 are given by

$$k_0 = \frac{c^2 \sinh^2(2\sigma_0)}{6E_1^{(P)}}, \quad k_2 = \frac{c^2 \sinh^2(2\sigma_0) E_{11}^{(T)}}{6E_1^{(P)}}. \quad (2.75)$$

Equation (2.74) is our tube law relating the transmural pressure and cross-sectional area of the tube. As this tube law is linear, we can decompose it into steady and oscillatory components. Using (2.12), (2.18), and taking just the oscillatory component of (2.74), we obtain

$$\tilde{p}(z) = \frac{k_0}{A_0} \tilde{A}(z) - \frac{k_2 \mathcal{F}}{A_0} \frac{d^2 \tilde{A}(z)}{dz^2} - \frac{k_2 M \omega^2}{A_0} \tilde{A}(z). \quad (2.76)$$

2.4 Fluid Mechanics

We now turn our focus to the fluid mechanics of the system. As we are dealing with an incompressible viscous fluid, the flow is governed by the Navier-Stokes equations (Batchelor, 1967)

$$\rho \left(\frac{\partial \mathbf{v}}{\partial t} + \mathbf{v} \cdot \nabla \mathbf{v} \right) = -\nabla p_{\text{tm}}^* + \mu \nabla^2 \mathbf{v} + \mathbf{f}, \quad (2.77)$$

$$\nabla \cdot \mathbf{v} = 0. \quad (2.78)$$

Here \mathbf{v} is the total dimensional velocity of the fluid, and \mathbf{f} represents any other body forces. In our model, only the axial components of the velocity contribute at leading order. Using a long-wavelength approximation and the property that the oscillatory component of the axial velocity has a high frequency, Whittaker *et al.* (2010c) showed that the oscillatory axial velocity has a plug flow profile in the core, with passive Stokes layers near the tube wall. Whittaker *et al.* (2010c) also determined that at leading order, the oscillatory axial velocity \tilde{w} and oscillatory pressure \tilde{p} are uniform in the cross-section, which is common in long-wavelength approximation theory. Hence, we have $\tilde{w} = \tilde{w}(z)$, $\tilde{p} = \tilde{p}(z)$ at leading order. Finally, Whittaker *et al.* (2010c) calculated the leading-order oscillatory components of the continuity and axial momentum equations to be

$$A_0 \frac{d\tilde{w}}{dz} + i\omega \tilde{A} = 0, \quad (2.79)$$

$$i\omega \tilde{w} = -\frac{d\tilde{p}}{dz}. \quad (2.80)$$

By eliminating \tilde{w} in equations (2.79)–(2.80), the following relationship between \tilde{p} and \tilde{A} is calculated

$$\tilde{A} = -\frac{A_0}{\omega^2} \frac{d^2 \tilde{p}}{dz^2}. \quad (2.81)$$

2.5 Combined System for Fluid-Structure Interaction

2.5.1 Governing ODEs

Using the oscillatory component (2.76) of the tube law obtained from the wall mechanics and the relation (2.81) derived from the fluid mechanics, we now form the governing ODEs for each section of the tube. Eliminating \tilde{A} between (2.76) and (2.81), we obtain

$$k_2 \mathcal{F} \frac{d^4 \tilde{p}}{dz^4} + (M\omega^2 k_2 - k_0) \frac{d^2 \tilde{p}}{dz^2} - \omega^2 \tilde{p} = 0. \quad (2.82)$$

This is the governing ODE for flow inside the flexible region of the tube, situated at $z_1 < z < z_2$.

To find a governing ODE for the flow inside the rigid sections of the tube, $0 < z < z_1$ and $z_2 < z < 1$, we first of all apply the constraint

$$\tilde{A} = 0,$$

as the cross-sectional area in the rigid parts of the tube is fixed. Using the relation (2.81) between \tilde{A} and \tilde{p} , the governing ODE in the rigid sections is

found to be

$$\frac{d^2\tilde{p}}{dz^2} = 0. \quad (2.83)$$

2.5.2 Boundary and Matching Conditions

By applying physical conditions, we determine the boundary conditions that must be satisfied at the ends of the tube as well as the matching conditions at the interfaces between the flexible and rigid sections of the tube. At $z = z_1, z_2$, we must have continuity of pressure and continuity of axial volume flux. As the axial volume flux is proportional to \tilde{w} and hence $d\tilde{p}/dz$, (see (2.80)) we have

$$[\tilde{p}]_{-}^{+} = \left[\frac{d\tilde{p}}{dz} \right]_{-}^{+} = 0, \quad \text{at } z = z_1, z_2. \quad (2.84)$$

At the points where the elastic wall is clamped onto the rigid parts of the tube, we must have $\tilde{A} = 0$. Hence, using equation (2.81), we obtain the conditions

$$\frac{d^2\tilde{p}}{dz^2} = 0, \quad \text{at } z = z_1, z_2. \quad (2.85)$$

In this model, we have fixed the total pressure at $z = 0$ as constant. As this constraint is a steady condition, any oscillations in pressure must have zero amplitude at the upstream end. Thus, we must have

$$\tilde{p} = 0 \quad \text{at } z = 0. \quad (2.86)$$

Finally, the axial volume flux has been fixed at $z = 1$. Because of this, the amplitude of the mode shape \tilde{w} of the oscillatory axial velocity must be zero at $z = 1$. By using this in equation (2.80), we find the final boundary condition

$$\frac{d\tilde{p}}{dz} = 0 \quad \text{at } z = 1. \quad (2.87)$$

2.6 Solving the Governing ODEs for the Normal Modes

Solutions for the governing equations (2.82) in $z_1 < z < z_2$ and (2.83) in $0 < z < z_1$ and $z_2 < z < 1$, subject to the boundary and matching conditions (2.84)–(2.87), are now sought. We solve this system for the oscillatory pressure \tilde{p} and the unknown frequency ω of the oscillations.

2.6.1 Solution in the Rigid Sections of the Tube

In the rigid sections of the tube ($0 < z < z_1$ and $z_2 < z < 1$), we have the governing equation (2.83)

$$\frac{d^2\tilde{p}}{dz^2} = 0.$$

First, we solve this equation in the upstream rigid section of the tube $0 < z < z_1$. Doing so, and applying the boundary condition (2.86) we find

$$\tilde{p} = Gz \quad \text{in } 0 < z < z_1, \quad (2.88)$$

where G is constant. We also use the boundary condition (2.87) to solve the governing equation (2.83) in the downstream rigid part of the tube $z_2 < z < 1$. Doing so, the following solution is obtained

$$\tilde{p} = H \quad \text{in } z_2 < z < 1, \quad (2.89)$$

where H is some constant.

Using these solutions and the fact that \tilde{p} and $d\tilde{p}/dz$ are continuous across the interfaces between the rigid and flexible sections of the tube from (2.84), we determine new boundary conditions for the flexible region of the tube. From (2.88) we have

$$\tilde{p} = Gz_1, \quad \frac{d\tilde{p}}{dz} = G, \quad \text{at } z = z_1. \quad (2.90)$$

Eliminating G within (2.90), we find

$$z_1 \frac{d\tilde{p}}{dz} - \tilde{p} = 0 \quad \text{at } z = z_1. \quad (2.91)$$

Using equation (2.89), we also find

$$\frac{d\tilde{p}}{dz} = 0 \quad \text{at } z = z_2. \quad (2.92)$$

2.6.2 General Solution in the Flexible Section of the Tube

To simplify the following mathematics and the boundary conditions, we introduce a new variable \mathcal{Z} defined as

$$\mathcal{Z} = \frac{z_2 - z}{z_2 - z_1}. \quad (2.93)$$

Rewriting the governing ODE (2.82) in terms of \mathcal{Z} and rearranging, we obtain

$$\frac{d^4\tilde{p}}{d\mathcal{Z}^4} + \frac{(M\omega^2 k_2 - k_0)(z_2 - z_1)^2}{k_2 \mathcal{F}} \frac{d^2\tilde{p}}{d\mathcal{Z}^2} - \frac{\omega^2(z_2 - z_1)^4}{k_2 \mathcal{F}} \tilde{p} = 0. \quad (2.94)$$

The boundary conditions (2.85), (2.91), (2.92) then become

$$\frac{d^2\tilde{p}}{d\mathcal{Z}^2} = 0 \quad \text{at} \quad \mathcal{Z} = 0, 1, \quad (2.95)$$

$$\frac{z_1}{z_2 - z_1} \frac{d\tilde{p}}{d\mathcal{Z}} + \tilde{p} = 0 \quad \text{at} \quad \mathcal{Z} = 1, \quad (2.96)$$

$$\frac{d\tilde{p}}{d\mathcal{Z}} = 0 \quad \text{at} \quad \mathcal{Z} = 0. \quad (2.97)$$

The governing equation (2.94) is a fourth-order ODE with constant coefficients. This is solved by looking for solutions of the form $\tilde{p} = e^{\lambda\mathcal{Z}}$ and solving the resulting polynomial for λ . It may be shown (see Appendix 2.A) that the eigenfrequencies ω are always real and non-zero. As the coefficient of \tilde{p} in (2.94) is strictly negative, the polynomial for λ always has one pair of real solutions and one pair of imaginary solutions. We find the general solution of (2.94) to be

$$\tilde{p}(\mathcal{Z}) = A \cosh g\mathcal{Z} + B \sinh g\mathcal{Z} + C \cos h\mathcal{Z} + D \sin h\mathcal{Z}, \quad (2.98)$$

where A, B, C and D are constants to be found, and g^2, h^2 are defined as

$$g^2 = \frac{(k_0 - M\omega^2 k_2)(z_2 - z_1)^2}{2k_2 \mathcal{F}} \left(1 + \sqrt{1 + \frac{4\omega^2 k_2 \mathcal{F}}{(k_0 - M\omega^2 k_2)^2}} \right), \quad (2.99)$$

$$h^2 = \frac{(k_0 - M\omega^2 k_2)(z_2 - z_1)^2}{2k_2 \mathcal{F}} \left(-1 + \sqrt{1 + \frac{4\omega^2 k_2 \mathcal{F}}{(k_0 - M\omega^2 k_2)^2}} \right), \quad (2.100)$$

for $k_0 > M\omega^2 k_2$ and

$$g^2 = \frac{(k_0 - M\omega^2 k_2)(z_2 - z_1)^2}{2k_2 \mathcal{F}} \left(1 - \sqrt{1 + \frac{4\omega^2 k_2 \mathcal{F}}{(k_0 - M\omega^2 k_2)^2}} \right), \quad (2.101)$$

$$h^2 = \frac{(k_0 - M\omega^2 k_2)(z_2 - z_1)^2}{2k_2 \mathcal{F}} \left(-1 - \sqrt{1 + \frac{4\omega^2 k_2 \mathcal{F}}{(k_0 - M\omega^2 k_2)^2}} \right), \quad (2.102)$$

for $k_0 < M\omega^2 k_2$. These different definitions for g and h , which depend on the sign of $k_0 - M\omega^2 k_2$, are needed to ensure that g always corresponds to the real solutions of λ , while h always corresponds to the imaginary solutions of λ . We note for future reference that as $\omega \rightarrow \infty$, $g = O(1)$ while $h = O(\omega)$.

2.6.3 Determining the Eigenfrequencies of the Model

We now calculate the possible frequencies ω that can occur in this model. Applying the four boundary conditions (2.95)–(2.97), to (2.98), we find four homogeneous equations. Writing these in matrix form, we obtain

$$\tilde{B}\mathbf{b} = \mathbf{0},$$

where

$$\tilde{B}^T = \begin{pmatrix} \frac{z_1}{z_2 - z_1} g \sinh g + \cosh g & g^2 \cosh g & 0 & g^2 \\ \frac{z_1}{z_2 - z_1} g \cosh g + \sinh g & g^2 \sinh g & g & 0 \\ -\frac{z_1}{z_2 - z_1} h \sinh h + \cosh h & -h^2 \cosh h & 0 & -h^2 \\ \frac{z_1}{z_2 - z_1} h \cosh h + \sinh h & -h^2 \sinh h & h & 0 \end{pmatrix}, \quad \mathbf{b} = \begin{pmatrix} A \\ B \\ C \\ D \end{pmatrix},$$

and \tilde{B}^T denotes the transpose of \tilde{B} . To obtain a non-trivial solution for the constants in \mathbf{b} , we must have that $\det \tilde{B} = 0$. Calculating the determinant of \tilde{B} and simplifying, it is found that

$$z_1 \left[2gh(1 - \cosh g \cos h) + (g^2 - h^2) \sinh g \sinh h \right] - (z_2 - z_1) \frac{g^2 + h^2}{gh} \left[g \sinh g \cos h + h \cosh g \sinh h \right] = 0. \quad (2.103)$$

This equation was first derived in the Whittaker *et al.* (2010c) model, but for different definitions of g and h that neglected wall inertia.

Normally we would proceed by substituting the definitions (2.99)–(2.102) of g and h into (2.103), which yields an equation in a single unknown ω . However we instead use a different method which allows us to more easily see the behaviour of (2.103) for certain values of h . First, we obtain an expression for ω in terms of g and h by considering the product of (2.99) and (2.100)

$$\omega^2 = \frac{g^2 h^2 k_2 \mathcal{F}}{(z_2 - z_1)^4}. \quad (2.104)$$

We also take the difference between (2.99) and (2.100) to find another relationship between g and h . Using (2.104) to eliminate ω in this relationship, we obtain

$$g = \left[\frac{\frac{k_0(z_2 - z_1)^2}{k_2 \mathcal{F}} + h^2}{1 + \frac{Mh^2 k_2}{(z_2 - z_1)^2}} \right]^{\frac{1}{2}}. \quad (2.105)$$

It is noted that using (2.101) and (2.102) instead of (2.99) and (2.100) in these calculations yields the same results. We now use (2.105) to eliminate g from the eigenvalue equation (2.103), giving us an equation to be solved for a single unknown h . Solving numerically using Maple, we find countably many solutions for h . The relationship (2.105) is then used to recover g and finally (2.104) is used to find the eigenfrequencies. We denote the n th eigenfrequency as ω_n , with ω_1 being the fundamental mode.

We have seen that as $\omega \rightarrow \infty$, $g \rightarrow O(1)$ and $h \rightarrow O(\omega)$. Hence, for large ω the eigenvalue equation (2.103) is approximately

$$-z_1 h^2 \sinh(g) \sin(h) - \frac{(z_2 - z_1) h^2}{g} \cosh(g) \sin(h) = 0. \quad (2.106)$$

By examining this, we expect to find solutions at $h \simeq n\pi$, where n is an integer. This approximation for the roots is used when calculating the numerical solutions for the eigenfrequencies.

2.6.4 Comparing the Eigenfrequencies for Different values of M

We now determine the eigenfrequencies ω_n of the model for different axial tensions \mathcal{F} and different masses of the tube wall M . In Tables 2.1–2.3, these eigenfrequencies have been calculated, with values $z_1 = 0.1$, $z_2 = 0.9$ and $\sigma_0 = 0.6$ which set the tube geometry. Using the value for σ_0 , we also derive $k_0 = 11.07487$, $k_2 = 1.70441$ and $A_0 = 2.73060$. These parameters have been chosen to be the same as in the Whittaker *et al.* (2010c) model.

It is seen from the tables that the inclusion of a non-zero wall inertia parameter M significantly reduces the values of the eigenfrequencies ω_n for the higher-order modes, even when M is small. However for the fundamental modes, the effect of wall inertia is only significant when M reaches 0.1. Finally, it is noted that for larger values of M , the eigenfrequencies increase much more slowly when the wave number is increased.

M	ω_1	ω_2	ω_3	ω_4	ω_5
0	6.108	19.06	33.80	50.86	70.67
0.001	6.091	18.60	31.61	44.81	57.98
0.01	5.948	15.55	21.62	25.74	29.14
0.1	4.912	7.728	8.563	9.274	10.03
1	2.389	2.639	2.792	2.985	3.210

Table 2.1: Eigenfrequencies for different values of M with $\mathcal{F} = 0.01$, $z_1 = 0.1$, $z_2 = 0.9$ and $\sigma_0 = 0.6$.

M	ω_1	ω_2	ω_3	ω_4	ω_5
0	6.991	25.73	54.31	94.37	146.5
0.001	6.970	25.08	50.68	82.96	120.0
0.01	6.795	20.82	34.41	47.54	60.37
0.1	5.545	10.24	13.64	17.23	20.87
1	2.638	3.514	4.481	5.565	6.694

Table 2.2: Eigenfrequencies for different values of M with $\mathcal{F} = 0.1$, $z_1 = 0.1$, $z_2 = 0.9$ and $\sigma_0 = 0.6$.

M	ω_1	ω_2	ω_3	ω_4	ω_5
0	11.80	59.41	144.3	268.1	431.4
0.001	11.76	57.88	134.6	235.6	353.3
0.01	11.45	47.96	91.30	135.1	177.8
0.1	9.259	23.63	36.29	49.08	61.51
1	4.360	8.148	11.96	15.86	19.75

Table 2.3: Eigenfrequencies for different values of M with $\mathcal{F} = 1$, $z_1 = 0.1$, $z_2 = 0.9$ and $\sigma_0 = 0.6$.

2.6.5 The Effect of Wall Inertia on \tilde{p} , \tilde{w} and \tilde{A}

Using the values of the eigenfrequencies ω_n , we determine the corresponding normal modes of the pressure \tilde{p}_n , the axial velocity \tilde{w}_n and the area \tilde{A}_n . We first find \tilde{p}_n by substituting our eigenvalues into equation (2.98). Then substituting \tilde{p}_n in equations (2.80) and (2.81) allows us to find the corresponding \tilde{w}_n and \tilde{A}_n .

In Figure 2.4, the first five normal modes of \tilde{p}_n have been normalised with the following conditions

$$\int_0^1 |\tilde{p}'_n|^2 dz = 1, \quad \tilde{p}'_n(0) > 0, \quad (2.107)$$

and plotted for different values of M . From the figure, we can see that there is almost no observable change in the fundamental mode for any of the values of M . However for higher-order modes, there are notable differences when M reaches values of size 0.1 and 1. In these cases, rather than oscillating about

$\tilde{p}_n = 0$, waves start shifting to larger values of \tilde{p}_n as z increases along the axial direction of the tube.

In Figure 2.5, the first five normal modes of $i\tilde{w}_n$ have been plotted using the normalised modes of \tilde{p}_n from before. We see that there is very little difference between the modes for $M = 0, 0.01$. However, in the cases where $M = 0.1$ and $M = 1$, like the modes of the pressure \tilde{p}_n , the higher-order modes oscillate about a non-zero value of $i\tilde{w}_n$ as you move along the z -axis.

Finally, in Figure 2.6, the first five normal modes of \tilde{A}_n have been plotted, again using the normalised modes of \tilde{p}_n calculated before. As before, it is seen that there is not much difference between the modes when $M = 0$ and $M = 0.01$. However, in the cases $M = 0.1$ and $M = 1$, it can be seen that the fundamental mode \tilde{A}_1 tends towards being symmetric about $z = 0.5$. It is also noted that unlike the modes for the pressure \tilde{p}_n and axial velocity \tilde{w}_n , the higher-order modes for the area oscillate about $\tilde{A}_n = 0$ as you move along the z -direction, for all values of M .

It is noted that in all of the figures, there are differences in the amplitude of the modes as M varies. However, as we are solving a linear problem, the amplitudes are arbitrarily set by the normalisation condition (2.107). As such, this variation in amplitude is not a significant result.

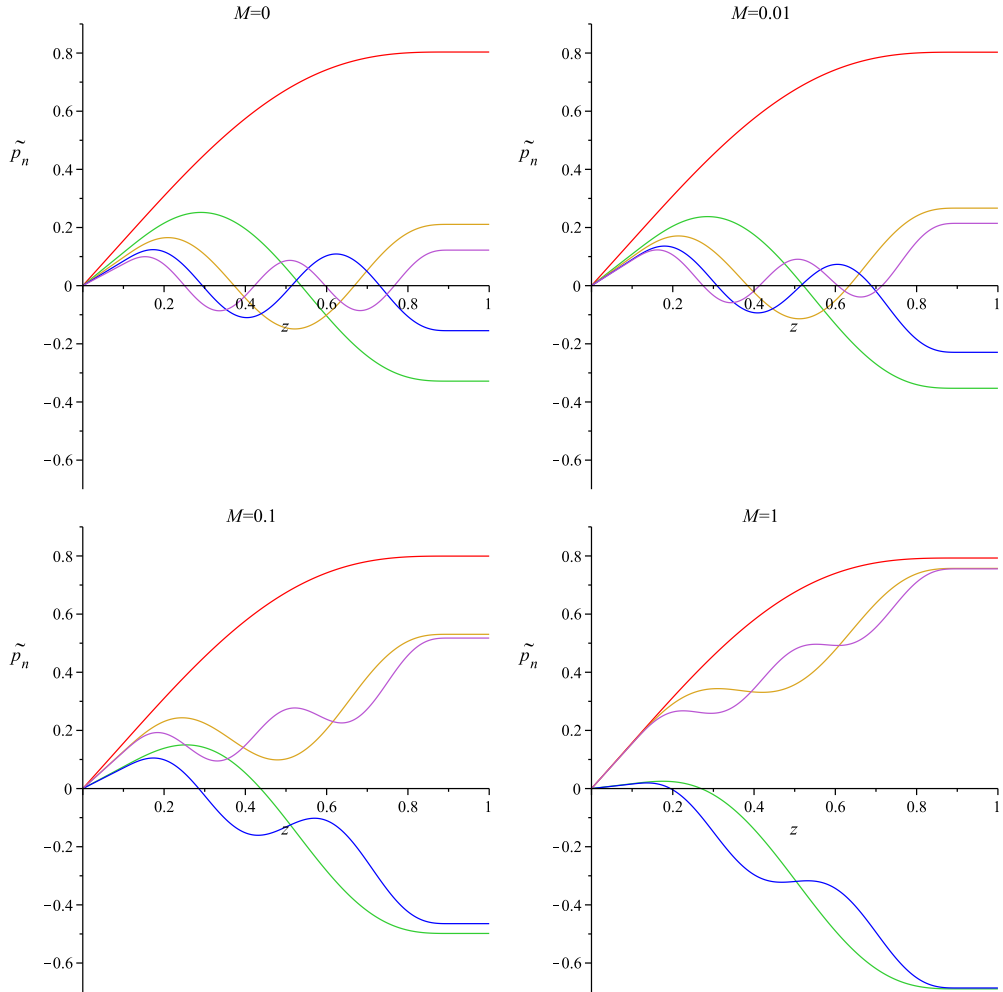


Figure 2.4: Graphs of the first five normal modes of \tilde{p}_n , for different values of M in the case $\mathcal{F} = 1$, $z_1 = 0.1$, $z_2 = 0.9$ and $\sigma_0 = 0.6$. These have been normalised such that $\int_0^1 |\tilde{p}'_n|^2 dz = 1$ and $\tilde{p}'_n(0) > 0$. The red, green, yellow, blue and purple curves correspond to the fundamental, second, third, fourth and fifth modes respectively.

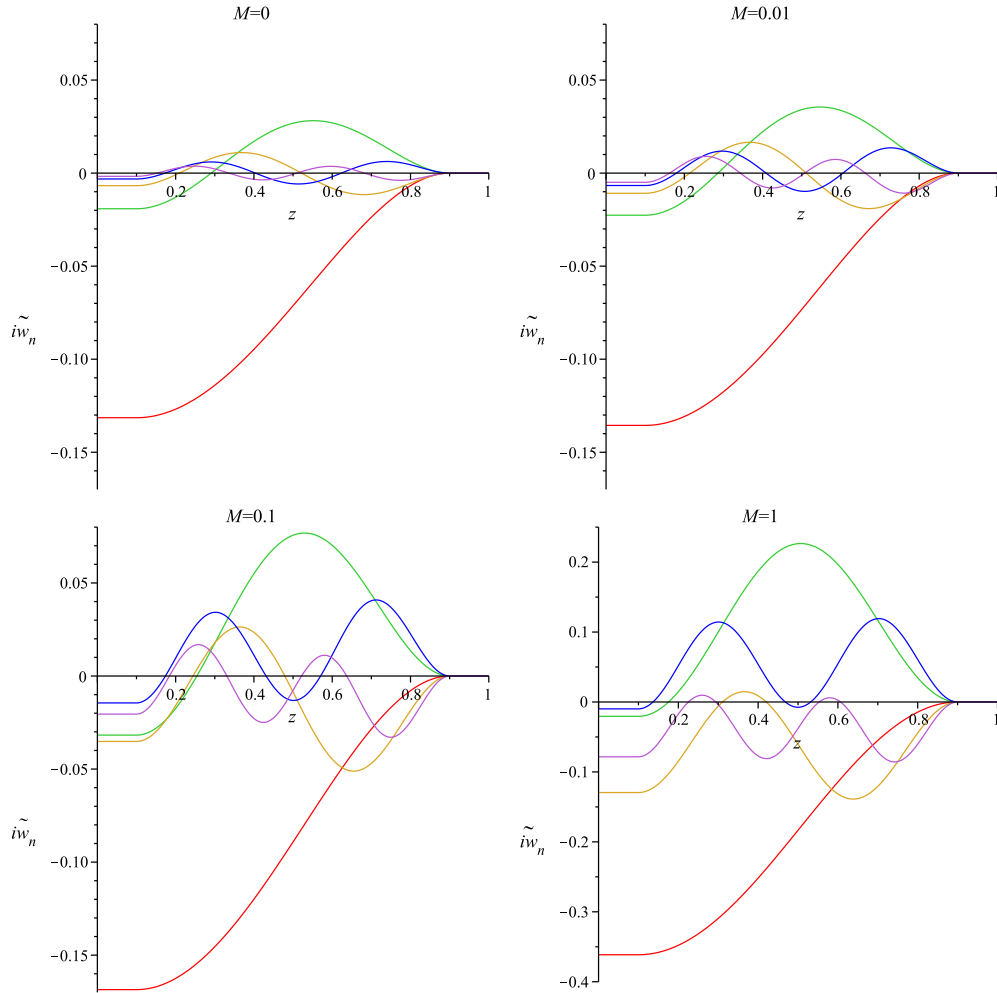


Figure 2.5: Graphs of the first five normal modes of $i\tilde{w}_n$, for different values of M in the case $\mathcal{F} = 1$, $z_1 = 0.1$, $z_2 = 0.9$ and $\sigma_0 = 0.6$. These have been calculated using the normalised modes of \tilde{p}_n plotted in Figure 2.4. The red, green, yellow, blue and purple curves correspond to the fundamental, second, third, fourth and fifth modes respectively.

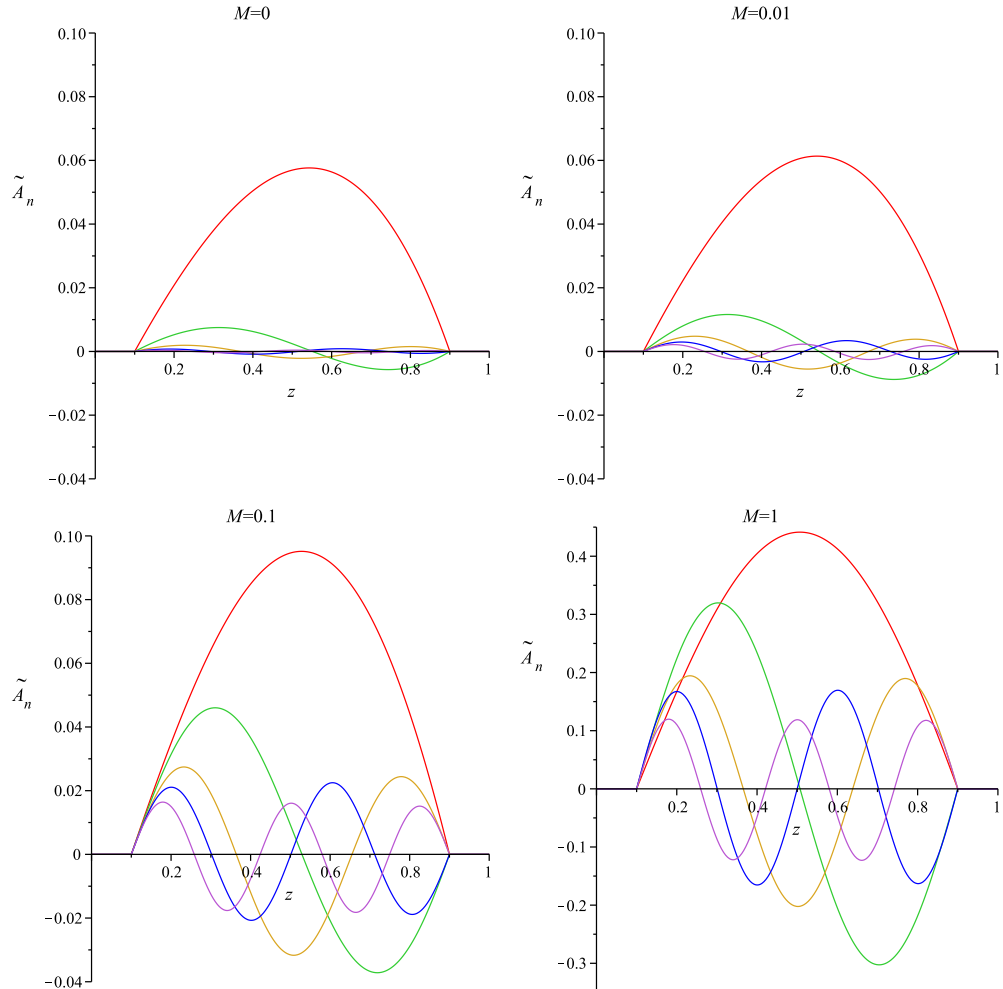


Figure 2.6: Graphs of the first five normal modes of \tilde{A}_n , for different values of M in the case $\mathcal{F} = 1$, $z_1 = 0.1$, $z_2 = 0.9$ and $\sigma_0 = 0.6$. These have been calculated using the normalised modes of \tilde{p}_n plotted in Figure 2.4. The red, green, yellow, blue and purple curves correspond to the fundamental, second, third, fourth and fifth modes respectively.

2.7 Stability Criterion and Growth Rate

We proceed to derive an expression for the growth rate of the oscillations, as well as the critical mean flow rate at which oscillations first occur, using the energy budget of the system. Whittaker *et al.* (2010c) found the following relation using the energy budgets for the fluid and tube wall

$$\frac{d}{dt}(\tilde{\mathbb{E}}_s + \tilde{\mathbb{E}}_f) = \frac{1}{\ell St}(\mathcal{K} - \mathcal{S} - \mathcal{D}). \quad (2.108)$$

Here, $\tilde{\mathbb{E}}_s$ is the total dimensionless energy due to oscillations in the tube wall and $\tilde{\mathbb{E}}_f$ is the dimensionless oscillatory kinetic energy in the fluid, both averaged over a period of the oscillations. We also have \mathcal{K} as the mean flux of kinetic energy through the ends of the tube, \mathcal{S} as the mean rate of working by pressure forces that arise at the tube ends due to oscillatory flow, and \mathcal{D} as the mean rate of dissipation by the oscillatory flow. The energies and fluxes have been non-dimensionalized using the scalings (2.19).

2.7.1 Fluxes and Fluid Energy

Whittaker *et al.* (2010a) and Whittaker *et al.* (2010c) showed that \mathcal{K} , \mathcal{S} , \mathcal{D} and $\tilde{\mathbb{E}}_f$ are given by

$$\mathcal{K} = \frac{3}{4}\pi\ell^2 St^2 \Delta^2 |\tilde{w}(0)|^2, \quad (2.109)$$

$$\mathcal{S} = \frac{1}{4}\pi\ell^2 St^2 \Delta^2 |\tilde{w}(0)|^2, \quad (2.110)$$

$$\mathcal{D} = \frac{\pi\ell^3 St^3 \Delta^2 (2\omega)^{\frac{1}{2}}}{2\alpha} \int_0^1 |\tilde{w}(z)|^2 dz, \quad (2.111)$$

$$\tilde{\mathbb{E}}_f = \frac{\Delta^2 St^2 A_0 \ell^2}{4} \int_0^1 |\tilde{w}(z)|^2 dz. \quad (2.112)$$

These values are in terms of the fluid flow and so are unchanged in the presence of wall inertia here. Using the relation (2.80) between \tilde{w} and \tilde{p} , it is found that the expressions (2.109)–(2.112) may be rewritten in terms of \tilde{p} as the following

$$\mathcal{K} = \frac{3}{4\omega^2}\pi\ell^2 St^2 \Delta^2 |\tilde{p}'(0)|^2, \quad (2.113)$$

$$\mathcal{S} = \frac{1}{4\omega^2}\pi\ell^2 St^2 \Delta^2 |\tilde{p}'(0)|^2, \quad (2.114)$$

$$\mathcal{D} = \frac{\pi\ell^3 St^3 \Delta^2 (2\omega)^{\frac{1}{2}}}{2\alpha\omega^2} \int_0^1 |\tilde{p}'(z)|^2 dz, \quad (2.115)$$

$$\tilde{\mathbb{E}}_f = \frac{\Delta^2 St^2 A_0 \ell^2}{4\omega^2} \int_0^1 |\tilde{p}'(z)|^2 dz. \quad (2.116)$$

Hence, the only term in (2.108) that needs to be evaluated now is $\tilde{\mathbb{E}}_s$.

2.7.2 Oscillatory Energy in the Tube Wall

As a starting point for deriving an expression for \dot{E}_s , we consider the following expression for the rate of working in the tube wall due to pressure forces

$$\frac{dE_s^*}{dt^*} = \iint_{\text{TubeWall}} p_{\text{tm}}^* \frac{\partial \mathbf{r}}{\partial t^*} \cdot \hat{\mathbf{n}} dS. \quad (2.117)$$

Here, E_s^* is the total dimensional energy in the tube wall due to the dimensional transmural pressure p_{tm}^* , dS is an element of the midplane of the tube wall, t^* is once again dimensional time, \mathbf{r} is the position of the wall midplane in the deformed state, as defined in (2.20), and $\hat{\mathbf{n}}$ is a unit vector normal to the tube wall. The expression (2.117) for the dimensional rate of working in the tube wall dE_s^*/dt^* comes from integrating the product of the force from the transmural pressure and the normal component of the velocity of the tube wall, over the midplane of the tube wall.

Inserting the appropriate limits for the integration within (2.117) and noting that p_{tm}^* is independent of τ , it is found that

$$\frac{dE_s^*}{dt^*} = \int_0^L p_{\text{tm}}^* \int_0^{2\pi} \frac{\partial \mathbf{r}}{\partial t^*} \cdot \hat{\mathbf{n}} a h(\tau) d\tau dz^*. \quad (2.118)$$

Whittaker *et al.* (2010d) found the following relation between the dimensional area change $A^* - A_0^*$ in the tube wall and the deformation $\mathbf{r} - \mathbf{r}_0$ of the tube wall

$$A^* - A_0^* = \int_0^{2\pi} (\mathbf{r} - \mathbf{r}_0) \cdot \hat{\mathbf{n}} a h(\tau) d\tau + O(\Delta^2). \quad (2.119)$$

By differentiating this relation with respect to t^* (noting that A_0^* and \mathbf{r}_0 are constants and thus vanish), neglecting terms quadratic and higher order in Δ , and substituting into (2.118), we obtain

$$\frac{dE_s^*}{dt^*} = \int_0^L p_{\text{tm}}^* \frac{\partial A^*}{\partial t^*} dz^*. \quad (2.120)$$

The expression (2.120) is now non-dimensionalized using the scalings (2.11) for the axial length and cross-sectional area, (2.17) for the transmural pressure, (2.19) for the energy and $t^* = Tt$ for time. Applying these scalings, the following is calculated

$$\frac{dE_s}{dt} = \Delta S t^2 \ell^2 \int_{z_1}^{z_2} p_{\text{tm}} \frac{\partial A}{\partial t} dz, \quad (2.121)$$

where E_s is the dimensionless energy in the tube wall due to the transmural pressure. We note that $\partial A / \partial t = 0$ in the rigid regions of the tube and thus we only need to take the integral within (2.121) over the region $z_1 < z < z_2$.

We now convert (2.121) into an expression solely in terms of the area A . This is done by applying the tube law (2.74) which relates the transmural pressure p_{tm} to A . Substituting the tube law into (2.121), it can be shown that

$$\frac{dE_s}{dt} = \frac{St^2\ell^2}{A_0} \int_{z_1}^{z_2} k_0(A - A_0) \frac{\partial A}{\partial t} - k_2 \mathcal{F} \frac{\partial^2 A}{\partial z^2} \frac{\partial A}{\partial t} + k_2 M \frac{\partial^2 A}{\partial t^2} \frac{\partial A}{\partial t} dz. \quad (2.122)$$

By integrating the second term of (2.122) by parts, it can be shown that

$$\begin{aligned} - \int_{z_1}^{z_2} k_2 \mathcal{F} \frac{\partial^2 A}{\partial z^2} \frac{\partial A}{\partial t} dz &= \left[-k_2 \mathcal{F} \frac{\partial A}{\partial z} \frac{\partial A}{\partial t} \right]_{z=z_1}^{z=z_2} + \int_{z_1}^{z_2} k_2 \mathcal{F} \frac{\partial A}{\partial z} \frac{\partial^2 A}{\partial t \partial z} dz, \\ &= \int_{z_1}^{z_2} k_2 \mathcal{F} \frac{\partial A}{\partial z} \frac{\partial^2 A}{\partial t \partial z} dz, \end{aligned} \quad (2.123)$$

where the boundary terms vanish as $\partial A / \partial t = 0$ at $z = z_1, z_2$. Substituting this into (2.122) and noting that

$$\begin{aligned} (A - A_0) \frac{\partial A}{\partial t} &= \frac{1}{2} \frac{\partial}{\partial t} (A - A_0)^2, & \frac{\partial A}{\partial z} \frac{\partial^2 A}{\partial t \partial z} &= \frac{1}{2} \frac{\partial}{\partial t} \left(\frac{\partial A}{\partial z} \right)^2, \\ \frac{\partial^2 A}{\partial t^2} \frac{\partial A}{\partial t} &= \frac{1}{2} \frac{\partial}{\partial t} \left(\frac{\partial A}{\partial t} \right)^2, \end{aligned}$$

we obtain

$$\frac{dE_s}{dt} = \frac{St^2\ell^2}{2A_0} \int_{z_1}^{z_2} \frac{\partial}{\partial t} \left[k_0(A - A_0)^2 + k_2 \mathcal{F} \left(\frac{\partial A}{\partial z} \right)^2 + k_2 M \left(\frac{\partial A}{\partial t} \right)^2 \right] dz. \quad (2.124)$$

Integrating this expression with respect to t , we find

$$E_s = \frac{St^2\ell^2}{2A_0} \int_{z_1}^{z_2} k_0(A - A_0)^2 + k_2 \mathcal{F} \left(\frac{\partial A}{\partial z} \right)^2 + k_2 M \left(\frac{\partial A}{\partial t} \right)^2 dz + C, \quad (2.125)$$

where C is some constant dependent on the steady deformation of the tube wall.

We now recall the expression (2.12) of the cross-sectional area $A(z, t)$

$$A(z, t) = A_0 + \frac{1}{\alpha^2 \ell St} \bar{A}(z) + \Delta(t) \operatorname{Re}(\tilde{A}(z) e^{i\omega t}).$$

Substituting this into (2.125), we find the following expression for E_s in terms of the steady area change \bar{A} and the oscillatory area change \tilde{A}

$$\begin{aligned} E_s &= \frac{St^2\ell^2}{2A_0} \int_{z_1}^{z_2} k_0 \left[\frac{1}{\alpha^2 \ell St} \bar{A} + \Delta \operatorname{Re}(\tilde{A} e^{i\omega t}) \right]^2 - \Delta^2 M \omega^2 k_2 \left[\operatorname{Re}(\tilde{A} e^{i\omega t}) \right]^2 \\ &\quad + k_2 \mathcal{F} \left[\frac{1}{\alpha^2 \ell St} \frac{\partial \bar{A}}{\partial z} + \Delta \operatorname{Re} \left(\frac{\partial \tilde{A}}{\partial z} e^{i\omega t} \right) \right]^2 dz + C. \end{aligned} \quad (2.126)$$

Using (2.126), it is possible to determine the mean energy \mathbb{E}_s in the tube wall due to transmural pressure. This is done by taking an average of E_s over the timescale of a single oscillation as follows

$$\mathbb{E}_s = \langle E_s \rangle = \frac{\omega}{2\pi} \int_0^{\frac{2\pi}{\omega}} E_s dt. \quad (2.127)$$

It can be shown that if a function $\mathbb{A}(z, t)$ has the form $\mathbb{A}(z, t) = \bar{\mathbb{A}}(z) + \text{Re}(\tilde{\mathbb{A}}(z)e^{i\omega t})$, then $\langle \mathbb{A}^2 \rangle$ is calculated to be

$$\langle \mathbb{A}^2 \rangle = \bar{\mathbb{A}}^2 + \frac{1}{2} |\tilde{\mathbb{A}}|^2. \quad (2.128)$$

By taking a time average of the expression (2.126) and applying the property (2.128), \mathbb{E}_s is determined to be

$$\begin{aligned} \mathbb{E}_s = & \frac{St^2\ell^2}{2A_0} \int_{z_1}^{z_2} k_0 \left(\frac{1}{\alpha^4\ell^2St^2} \bar{\mathbb{A}}^2 + \frac{\Delta^2}{2} |\tilde{\mathbb{A}}|^2 \right) + \frac{\Delta^2 M \omega^2 k_2}{2} |\tilde{\mathbb{A}}|^2 \\ & + k_2 \mathcal{F} \left(\frac{1}{\alpha^4\ell^2St^2} \left(\frac{\partial \bar{\mathbb{A}}}{\partial z} \right)^2 + \frac{\Delta^2}{2} \left| \frac{\partial \tilde{\mathbb{A}}}{\partial z} \right|^2 \right) dz + C. \end{aligned} \quad (2.129)$$

Hence, \mathbb{E}_s may be decomposed into components due to the steady and oscillatory area changes of the tube. Thus, the dimensionless energy $\tilde{\mathbb{E}}_s$ in the tube wall due to the oscillations is given by

$$\tilde{\mathbb{E}}_s = \frac{\Delta^2 St^2\ell^2}{4A_0} \int_{z_1}^{z_2} (k_0 + M\omega^2 k_2) |\tilde{\mathbb{A}}|^2 + k_2 \mathcal{F} \left| \frac{\partial \tilde{\mathbb{A}}}{\partial z} \right|^2 dz. \quad (2.130)$$

In order to combine this with the expressions (2.113)–(2.116) for the other terms in the energy budget equation (2.108), it is convenient to rewrite $\tilde{\mathbb{E}}_s$ in terms of \tilde{p} . This is done using the relation (2.81) between $\tilde{\mathbb{A}}$ and \tilde{p} and it can be shown that

$$\tilde{\mathbb{E}}_s = \frac{\Delta^2 St^2 A_0 \ell^2}{4\omega^4} \int_{z_1}^{z_2} (k_0 + M\omega^2 k_2) \tilde{p}'' \tilde{p}''^\dagger + k_2 \mathcal{F} \tilde{p}''' \tilde{p}'''^\dagger dz, \quad (2.131)$$

where $'$ denotes a derivative with respect to z and † denotes the complex conjugate.

2.7.3 Simplification of $\tilde{\mathbb{E}}_s$ in (2.131)

It is possible to now use the expression (2.131) for $\tilde{\mathbb{E}}_s$ in the energy budget relation (2.108) to determine the growth rate and stability criterion of the oscillations. However, it is found that (2.131) can be simplified further to form a more convenient expression for $\tilde{\mathbb{E}}_s$. The details of this simplification are now provided.

Firstly, by integrating the second term of (2.131) by parts, it is calculated that

$$\int_{z_1}^{z_2} k_2 \mathcal{F} \tilde{p}''' \tilde{p}'''^\dagger dz = \left[k_2 \mathcal{F} \tilde{p}''' \tilde{p}'''^\dagger \right]_{z=z_1}^{z=z_2} - \int_{z_1}^{z_2} k_2 \mathcal{F} \tilde{p}''' \tilde{p}'''^\dagger dz. \quad (2.132)$$

From (2.85), we know that $\tilde{p}'' = 0$ at $z = z_1, z_2$ and thus the first term on the right-hand side of (2.132) vanishes. Substituting this into (2.131) allows us to obtain

$$\tilde{\mathbb{E}}_s = \frac{\Delta^2 St^2 A_0 \ell^2}{4\omega^4} \int_{z_1}^{z_2} (k_0 + M\omega^2 k_2) \tilde{p}'' \tilde{p}''^\dagger - k_2 \mathcal{F} \tilde{p}''' \tilde{p}'''^\dagger dz. \quad (2.133)$$

We further simplify the expression (2.133) for $\tilde{\mathbb{E}}_s$ by considering the governing ODE (2.82) in the elastic-walled region $z_1 < z < z_2$ of the tube. Rearranging (2.82), it can be shown that

$$-k_2 \mathcal{F} \tilde{p}''' = (M\omega^2 k_2 - k_0) \tilde{p}'' - \omega^2 \tilde{p}. \quad (2.134)$$

As the integral in (2.133) is between $z = z_1$ and $z = z_2$, we may substitute (2.134) into (2.133) to obtain

$$\tilde{\mathbb{E}}_s = \frac{\Delta^2 St^2 A_0 \ell^2}{4\omega^2} \int_{z_1}^{z_2} 2Mk_2 \tilde{p}'' \tilde{p}''^\dagger - \tilde{p} \tilde{p}''^\dagger dz. \quad (2.135)$$

By integrating the second term of (2.135) by parts, it is found that

$$\tilde{\mathbb{E}}_s = \frac{\Delta^2 St^2 A_0 \ell^2}{4\omega^2} \int_{z_1}^{z_2} |\tilde{p}'|^2 + 2Mk_2 |\tilde{p}''|^2 dz - \left[\tilde{p} \tilde{p}'^\dagger \right]_{z=z_1}^{z=z_2}. \quad (2.136)$$

It is possible to evaluate the boundary term using the boundary conditions (2.91), (2.92). Rearranging (2.91), it is found that $\tilde{p} = z_1 \tilde{p}'$ at $z = z_1$. We also have $\tilde{p}' = 0$ at $z = z_2$ from (2.92). Applying these to the boundary term in (2.136), it can be shown that

$$- \left[\tilde{p} \tilde{p}'^\dagger \right]_{z=z_1}^{z=z_2} = z_1 |\tilde{p}'|^2 \Big|_{z=z_1}. \quad (2.137)$$

In §2.6, it was found that \tilde{p} behaves linearly in the region $0 < z < z_1$. As such, we must have that \tilde{p}' takes a constant value in $0 < z < z_1$. Using this property, it is seen that the right-hand side of (2.137) is equal to the integral of $|\tilde{p}'|^2$ over the region $0 < z < z_1$. Thus, we have

$$- \left[\tilde{p} \tilde{p}'^\dagger \right]_{z=z_1}^{z=z_2} = \int_0^{z_1} |\tilde{p}'|^2 dz, \quad (2.138)$$

and $\tilde{\mathbb{E}}_s$ may be written as

$$\tilde{\mathbb{E}}_s = \frac{\Delta^2 St^2 A_0 \ell^2}{4\omega^2} \int_{z_1}^{z_2} |\tilde{p}'|^2 + 2Mk_2 |\tilde{p}''|^2 dz + \int_0^{z_1} |\tilde{p}'|^2 dz. \quad (2.139)$$

As the integrals in the expressions (2.113)–(2.116) for the other terms in the energy budget relation (2.108) are over the entire length of the tube $0 < z < 1$, it is convenient to rewrite (2.139) in terms of an integral with the limits $z = 0, 1$. From (2.89), it is seen that \tilde{p} is constant in the region $z_2 < z < 1$. As such, we must have $\tilde{p}' = 0$ when $z_2 < z < 1$. It is also seen from (2.83) that in the rigid parts of the tube $0 < z < z_1$ and $z_2 < z < 1$, we have $\tilde{p}'' = 0$. Using these properties, it is observed that

$$\int_0^{z_1} 2Mk_2 |\tilde{p}''|^2 dz = \int_{z_2}^1 2Mk_2 |\tilde{p}''|^2 dz = \int_{z_2}^1 |\tilde{p}'|^2 dz = 0.$$

Hence, rewriting (2.139), we obtain the following simplified expression for \tilde{E}_s

$$\tilde{E}_s = \frac{\Delta^2 St^2 A_0 \ell^2}{4\omega^2} \int_0^1 |\tilde{p}'|^2 + 2Mk_2 |\tilde{p}''|^2 dz. \quad (2.140)$$

2.7.4 Determining the Growth Rate and Stability Criterion

Now that we have calculated the dimensionless oscillatory energies in the wall and fluid, we can use these along with (2.108) to find expressions for the growth rate of the oscillations as well as the stability criterion. Using the expressions (2.116), (2.140) for \tilde{E}_f , \tilde{E}_s in terms of \tilde{p} , we see that

$$\tilde{E}_s + \tilde{E}_f = \frac{\Delta^2 St^2 A_0 \ell^2}{2\omega^2} \int_0^1 |\tilde{p}'|^2 + k_2 M |\tilde{p}''|^2 dz. \quad (2.141)$$

Using the definitions (2.113)–(2.115) for \mathcal{K} , \mathcal{S} and \mathcal{D} in terms of \tilde{p} , we find

$$\mathcal{K} - \mathcal{S} - \mathcal{D} = \frac{\Delta^2 St^2 \ell^2 \pi}{2\omega^2} \left[|\tilde{p}'(0)|^2 - \frac{\ell St (2\omega)^{\frac{1}{2}}}{\alpha} \int_0^1 |\tilde{p}'(z)|^2 dz \right]. \quad (2.142)$$

Substituting (2.141)–(2.142) into (2.108) and evaluating the differential on the left-hand side, we obtain

$$\frac{d\Delta}{dt} = \left[\frac{\pi}{2A_0} \left(\frac{\frac{|\tilde{p}'(0)|^2}{\ell St} - \frac{(2\omega)^{\frac{1}{2}}}{\alpha} \int_0^1 |\tilde{p}'(z)|^2 dz}{\int_0^1 |\tilde{p}'(z)|^2 + k_2 M |\tilde{p}''(z)|^2 dz} \right) \right] \Delta. \quad (2.143)$$

Hence, the amplitude of the oscillations grows or decays exponentially and we may write

$$\Delta(t) = \Delta_0 e^{\Lambda t},$$

where Δ_0 is the initial amplitude of the oscillations, and the growth rate Λ is given by

$$\Lambda = \frac{\pi}{2A_0} \left(\frac{\frac{|\tilde{p}'(0)|^2}{\ell St} - \frac{(2\omega)^{\frac{1}{2}}}{\alpha} \int_0^1 |\tilde{p}'(z)|^2 dz}{\int_0^1 |\tilde{p}'(z)|^2 + k_2 M |\tilde{p}''(z)|^2 dz} \right). \quad (2.144)$$

When $\Lambda = 0$, neutrally stable oscillations are obtained. We define the critical Reynolds number Re_c to be the Reynolds number (defined by $Re = \alpha^2/St$) at which $\Lambda = 0$. Using the expression (2.144) for the growth rate, we find

$$Re_c = \frac{\alpha\ell(2\omega)^{\frac{1}{2}}}{|\tilde{p}'(0)|^2} \int_0^1 |\tilde{p}'(z)|^2 dz. \quad (2.145)$$

Using this expression for Re_c , the growth rate Λ may be written as

$$\Lambda = \frac{\pi(Re - Re_c)|\tilde{p}'(0)|^2}{2A_0\ell\alpha^2 \int_0^1 |\tilde{p}'(z)|^2 + k_2M|\tilde{p}''(z)|^2 dz}. \quad (2.146)$$

By evaluating Re_c and Λ numerically, we may plot both as functions of M . Doing so, we find that the size of the critical Reynolds number for the first and third modes are comparable, and the sizes for the second and fourth modes are also comparable. In Figure 2.7, Re_c is plotted against M for the first four eigenmodes of \tilde{p} . From the plots, we see there are significant differences in the behaviour of the odd ($n = 1, 3, 5, \dots$) and even ($n = 2, 4, 6, \dots$) modes as M increases. The main difference is that the critical Reynolds number Re_c for a given α and ℓ (which depend on the properties of the fluid and geometry of the tube wall) decreases with increasing M for odd modes. Thus, odd modes become more unstable for higher wall inertia. However, for even modes, Re_c increases rapidly for increasing M , implying even modes become more stable for higher wall inertia. We also see that in the case $0 \leq M \leq 1$ the mode with the smallest Re_c and therefore the most unstable, is the fundamental mode.

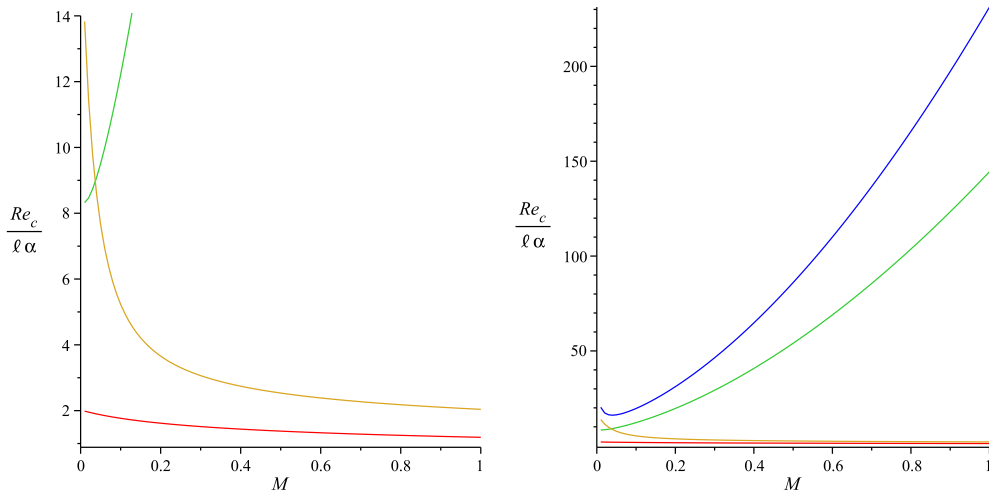


Figure 2.7: The critical Reynolds number $Re_c/\ell\alpha$ against M , with $z_1 = 0.1$, $z_2 = 0.9$, $\sigma_0 = 0.6$, for mode numbers $n = 1$ (red), $n = 2$ (green), $n = 3$ (yellow) and $n = 4$ (blue).

In Figure 2.8, we have plots of $\partial\Lambda/\partial Re$, again for the first four eigenmodes. For all four modes, as M increases, the gradient of Λ for a given A_0 , α and ℓ decreases. However this decrease is larger for even modes than for odd modes. We also see that when $0 \leq M \leq 1$, the fundamental mode is the mode that has the highest growth rate by a significant margin. Finally, we note that for both even modes, $\Lambda \rightarrow 0$ very quickly as we increase M .

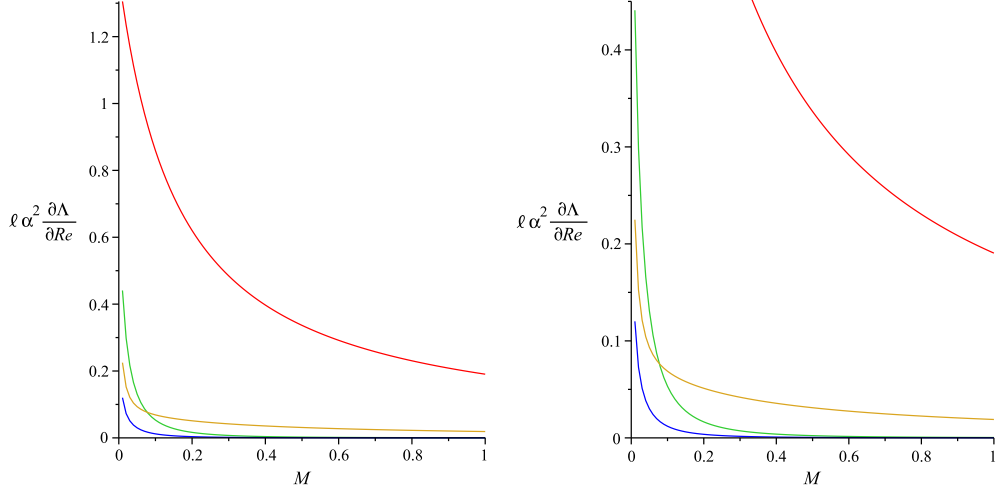


Figure 2.8: The gradient of the growth rate $\ell\alpha^2\partial\Lambda/\partial Re$ against M , with $z_1 = 0.1$, $z_2 = 0.9$, $\sigma_0 = 0.6$, for mode numbers $n = 1$ (red), $n = 2$ (green), $n = 3$ (yellow) and $n = 4$ (blue).

2.8 Asymptotic Solution for $M \gg 1$

To better understand the behaviour of the different modes, we turn our attention to finding asymptotic expansions for the eigenfrequencies ω_n , the corresponding modes of the oscillatory pressure \tilde{p}_n , the critical Reynolds number Re_c and the growth rate Λ , valid when $\epsilon = 1/M \ll 1$. In the governing equation (2.82) for the flexible part of the tube, when M is large, we expect the $d^4\tilde{p}/dz^4$ and $d^2\tilde{p}/dz^2$ terms to balance. Thus, we expect $\omega_n = O(M^{-\frac{1}{2}})$. We also need $\tilde{p}_n = O(1)$ to satisfy the normalisation condition (2.107) which will be imposed. Hence, we consider expansions of the form

$$\omega_n = M^{-\frac{1}{2}} (\omega_{n0} + \epsilon\omega_{n1} + \dots) \quad \tilde{p}_n(z) = p_{n0}(z) + \epsilon p_{n1}(z) + \dots \quad (2.147)$$

where ω_{n0} , ω_{n1} , $p_{n0}(z)$, $p_{n1}(z)$ are $O(1)$, and n denotes the n th eigenmode. We now find the leading and first-order approximations of ω_n and \tilde{p}_n in each of the section of the tube.

In the flexible region of the tube $z_1 \leq z \leq z_2$, the governing equation (in terms of \mathcal{Z}) is (2.94). Substituting in the expansions (2.147) gives

$$\begin{aligned} (p_{n0}'''' + \epsilon p_{n1}'''' + \dots) + \frac{[(\omega_{n0} + \epsilon \omega_{n1} + \dots)^2 k_2 - k_0](z_2 - z_1)^2}{k_2 \mathcal{F}} (p_{n0}'' + \epsilon p_{n1}'' + \dots) \\ = \frac{\epsilon(\omega_{n0} + \epsilon \omega_{n1} + \dots)^2 (z_2 - z_1)^4}{k_2 \mathcal{F}} (p_{n0} + \epsilon p_{n1} + \dots), \end{aligned} \quad (2.148)$$

where ' now denotes $d/d\mathcal{Z}$.

2.8.1 Leading-Order Solution

At leading order in the elastic-walled region of the tube $z_1 \leq z \leq z_2$, we obtain the ODE

$$p_{n0}'''' + \lambda_0^2 p_{n0}'' = 0, \quad (2.149)$$

where

$$\lambda_0^2 = \frac{(\omega_{n0}^2 k_2 - k_0)(z_2 - z_1)^2}{k_2 \mathcal{F}}. \quad (2.150)$$

We find that for non-trivial solutions, we must have $\lambda_0^2 > 0$. Thus, we find the general solution to be

$$p_{n0}(\mathcal{Z}) = A_0 \mathcal{Z} + B_0 + C_0 \cos(\lambda_0 \mathcal{Z}) + D_0 \sin(\lambda_0 \mathcal{Z}), \quad (2.151)$$

where A_0, B_0, C_0 and D_0 are constants to be found. By applying the boundary conditions (2.95)–(2.97), we find

$$p_{n0}(\mathcal{Z}) = D_0 \left[\sin(\lambda_0 \mathcal{Z}) + \lambda_0 (1 - \mathcal{Z}) + \frac{\lambda_0 z_1}{z_2 - z_1} (1 - (-1)^n) \right], \quad (2.152)$$

$$\lambda_0 = n\pi. \quad (2.153)$$

Here D_0 is an arbitrary constant setting the amplitude of the modes. Substituting (2.153) into (2.150) we find

$$\omega_{n0} = \left(\frac{n^2 \pi^2 \mathcal{F}}{(z_2 - z_1)^2} + \frac{k_0}{k_2} \right)^{\frac{1}{2}}. \quad (2.154)$$

In the upstream rigid region of the tube $0 \leq z \leq z_1$, the flow is governed by (2.88). With this, the matching condition (2.84) and (2.152), we find

$$p_{n0}(z) = \left[\frac{D_0 \lambda_0}{z_2 - z_1} (1 - (-1)^n) \right] z \quad \text{in } 0 \leq z \leq z_1. \quad (2.155)$$

In the downstream rigid section of the tube $z_2 \leq z \leq 1$, flow is governed by (2.89). Using this with the matching condition (2.84) and (2.152) gives

$$p_{n0}(z) = D_0 \lambda_0 \left[1 + \frac{z_1}{z_2 - z_1} (1 - (-1)^n) \right] \quad \text{in } z_2 \leq z \leq 1. \quad (2.156)$$

Hence, the leading-order solution for \tilde{p}_n is

$$p_{n0}(z) = \begin{cases} \left[\frac{D_0 \lambda_0}{z_2 - z_1} (1 - (-1)^n) \right] z & 0 \leq z \leq z_1 \\ D_0 \left[\sin(\lambda_0 \frac{z_2 - z}{z_2 - z_1}) + \lambda_0 \frac{z - z_1}{z_2 - z_1} + \frac{\lambda_0 z_1}{z_2 - z_1} (1 - (-1)^n) \right] & z_1 \leq z \leq z_2 \\ D_0 \lambda_0 \left[1 + \frac{z_1}{z_2 - z_1} (1 - (-1)^n) \right] & z_2 \leq z \leq 1 \end{cases} \quad (2.157)$$

Finally to set the initial amplitude of the oscillations we apply the normalisation condition (2.107). Doing so, we obtain

$$D_0 = \frac{z_2 - z_1}{\lambda_0 (z_1(1 + (-1)^{n+1})^2 + \frac{3}{2}(z_2 - z_1))^{\frac{1}{2}}}.$$

In the equation (2.157) for p_{n0} , each region has a term dependent on $(-1)^n$. Because of this, the leading-order pressures behave differently for odd and even modes. We note that in the upstream region $0 \leq z \leq z_1$, odd modes have a linear rise in pressure whereas even modes have a value of zero. We also note that in the downstream region $z_2 \leq z \leq 1$, the leading-order approximation (2.157) has one fixed value for odd modes and another different fixed value for even modes.

2.8.2 First-Order Solution

Our next step is to calculate the first-order approximations of ω_n and \tilde{p}_n . We start by considering the solution in the flexible region $z_1 \leq z \leq z_2$. By evaluating (2.148) at $O(\epsilon)$, we obtain the following ODE

$$p_{n1}'''' + \lambda_0^2 p_{n1}'' = \frac{\omega_{n0}^2 (z_2 - z_1)^4}{k_2 \mathcal{F}} p_{n0} - \lambda_1 p_{n0}'' \quad (2.158)$$

where

$$\lambda_1 = \frac{2\omega_{n0}\omega_{n1}k_2(z_2 - z_1)^2}{k_2 \mathcal{F}}. \quad (2.159)$$

The general solution of (2.158) is found to be

$$p_{n1}(\mathcal{Z}) = A_1 \mathcal{Z} + B_1 + C_1 \cos(\lambda_0 \mathcal{Z}) + D_1 \sin(\lambda_0 \mathcal{Z}) + f_1 \mathcal{Z} \cos(\lambda_0 \mathcal{Z}) + g_1 \mathcal{Z}^3 + h_1 \mathcal{Z}^2, \quad (2.160)$$

where

$$\begin{aligned} f_1 &= \frac{D_0}{2\lambda_0^3} \left(\frac{\omega_{n0}^2 (z_2 - z_1)^4}{k_2 \mathcal{F}} + \lambda_0^2 \lambda_1 \right), \\ g_1 &= -\frac{D_0 \omega_{n0}^2 (z_2 - z_1)^4}{6\lambda_0 k_2 \mathcal{F}}, \\ h_1 &= \frac{D_0 \omega_{n0}^2 (z_2 - z_1)^4}{2\lambda_0 k_2 \mathcal{F}} \left(1 + \frac{z_1}{z_2 - z_1} (1 - (-1)^n) \right), \end{aligned}$$

and A_1 , B_1 , C_1 and D_1 are constants to be found. Applying the boundary conditions (2.95)–(2.97), we obtain

$$\begin{aligned} B_1 &= A_1 \left(\frac{z_1}{z_2 - z_1} ((-1)^n - 1) - 1 \right) - g_1 \left(1 + \frac{6}{\lambda_0^2} + \frac{3z_1}{z_2 - z_1} \right) \\ &\quad - h_1 \left(1 + \frac{2}{\lambda_0^2} + \frac{2z_1}{z_2 - z_1} \right), \\ C_1 &= \frac{2h_1}{\lambda_0^2}, \\ D_1 &= -\frac{A_1 + f_1}{\lambda_0}, \\ \lambda_1 &= \frac{2}{D_0 \lambda_0} (6g_1(-1)^n + 2h_1((-1)^n - 1)) - \frac{\omega_{n0}^2 (z_2 - z_1)^4}{\lambda_0^2 k_2 \mathcal{F}}. \end{aligned} \quad (2.161)$$

Here, A_1 is still to be determined by the normalisation condition (2.107). Substituting (2.161) into (2.159) allows us to find

$$\omega_{n1} = \frac{1}{2\omega_{n0} k_2} \left[\frac{2k_2 \mathcal{F} (6g_1(-1)^n + 2h_1((-1)^n - 1))}{D_0 \lambda_0 (z_2 - z_1)^2} - \frac{\omega_{n0}^2 (z_2 - z_1)^2}{\lambda_0^2} \right]. \quad (2.162)$$

We now look at the asymptotic expansion in the rigid parts of the tubes. In $0 \leq z \leq z_1$, we use (2.88) as well as the matching condition (2.84) and (2.160) to find the first-order pressure p_{n1} in the rigid upstream part of the tube to be

$$p_{n1}(z) = \frac{z}{z_1} \left[A_1 + B_1 + f_1(-1)^n + g_1 + h_1 \left(1 + \frac{2}{\lambda_0^2} (-1)^n \right) \right] \quad \text{in } 0 \leq z \leq z_1. \quad (2.163)$$

In $z_2 \leq z \leq 1$, we apply the matching condition (2.84) and (2.160) to (2.89). This gives the asymptotic solution for p_{n1} in the downstream region as

$$p_{n1}(z) = B_1 + \frac{2h_1}{\lambda_0^2} \quad \text{in } z_2 \leq z \leq 1. \quad (2.164)$$

By combining (2.160), (2.163) and (2.164), we find the first-order solution for \tilde{p}_n as

$$p_{n1}(z) = \begin{cases} \frac{z}{z_1} \left[A_1 + B_1 + f_1(-1)^n + g_1 + h_1 \left(1 + \frac{2}{\lambda_0^2} (-1)^n \right) \right] & 0 \leq z \leq z_1 \\ A_1 \mathcal{Z} + B_1 + C_1 \cos(\lambda_0 \mathcal{Z}) + D_1 \sin(\lambda_0 \mathcal{Z}) \\ \quad + f_1 \mathcal{Z} \cos(\lambda_0 \mathcal{Z}) + g_1 \mathcal{Z}^3 + h_1 \mathcal{Z}^2 & z_1 \leq z \leq z_2 \\ B_1 + \frac{2h_1}{\lambda_0^2} & z_2 \leq z \leq 1 \end{cases}, \quad (2.165)$$

where A_1 is still unknown. Finally, in order to satisfy the normalisation

condition (2.107), A_1 is set as

$$A_1 = \frac{1}{\frac{3}{2} + \frac{z_1}{z_2 - z_1} (1 - (-1)^n)^2} \left[(1 - (-1)^n) \left(f_1(-1)^n - g_1 \left(\frac{6}{\lambda_0^2} + \frac{3z_1}{z_2 - z_1} \right) \right. \right. \\ \left. \left. - h_1 \left(\frac{2}{\lambda_0^2} (1 - (-1)^n) + \frac{2z_1}{z_2 - z_1} \right) \right) + f_1 \left(\frac{1}{4} - (-1)^n \right) \right. \\ \left. - g_1 \left(1 - \frac{6}{\lambda_0^2} (-1)^n \right) - h_1 \right].$$

To test the accuracy of our leading and first-order approximations for ω_n and \tilde{p}_n we plot them against the semi-analytical solutions found earlier in §2.6. In Figure 2.9, this has been done for the first four eigenfrequencies ω_n of our model. It is seen from the figure that there is good agreement between the asymptotic and semi-analytically calculated frequencies. We also see that unusually, the asymptotic solution is better for the higher modes (particularly at lower values of M). The reason for this stems from the second term in the governing ODE (2.82) in the flexible part of the tube. This term depends on $M\omega^2$ and becomes the dominant term in the regime $M \gg 1$. However, as our value for ω increases, a lower value of M is needed for this term to become dominant. Hence for the higher eigenfrequencies, a lower value of M is required for dominance and the approximation approaches the semi-analytical solution at smaller values of M .

In Figure 2.10, the semi-analytically obtained \tilde{p}_n , and the approximation (2.147) for \tilde{p}_n up to leading and first-order have been plotted for the first four modes, with $M = 1$. From this we observe that there is good agreement between the approximations and the semi-analytical solution, particularly in the case with the first-order approximation.

2.8.3 Asymptotic Approximation for Re_c

Now that we have asymptotic approximations for the eigenfrequencies ω_n and the modes $\tilde{p}_n(z)$ of the pressure up to leading order, we may use these approximations to derive asymptotic approximations for the critical Reynolds number Re_c and the growth rate Λ , in the case of large M .

We begin with deriving an approximation for Re_c . Substituting the approximations (2.147) for ω_n , $\tilde{p}_n(z)$ into the expression (2.145) for Re_c , it is found that the critical Reynolds number Re_{cn} for the n^{th} mode is given by

$$Re_{cn} = \frac{\alpha \ell \sqrt{2} \epsilon^{\frac{1}{4}} (\omega_{n0} + \epsilon \omega_{n1} + O(\epsilon^2))^{\frac{1}{2}}}{(p'_{n0}(0) + \epsilon p'_{n1}(0) + \epsilon^2 p'_{n2}(0) + O(\epsilon^3))^2}. \quad (2.166)$$

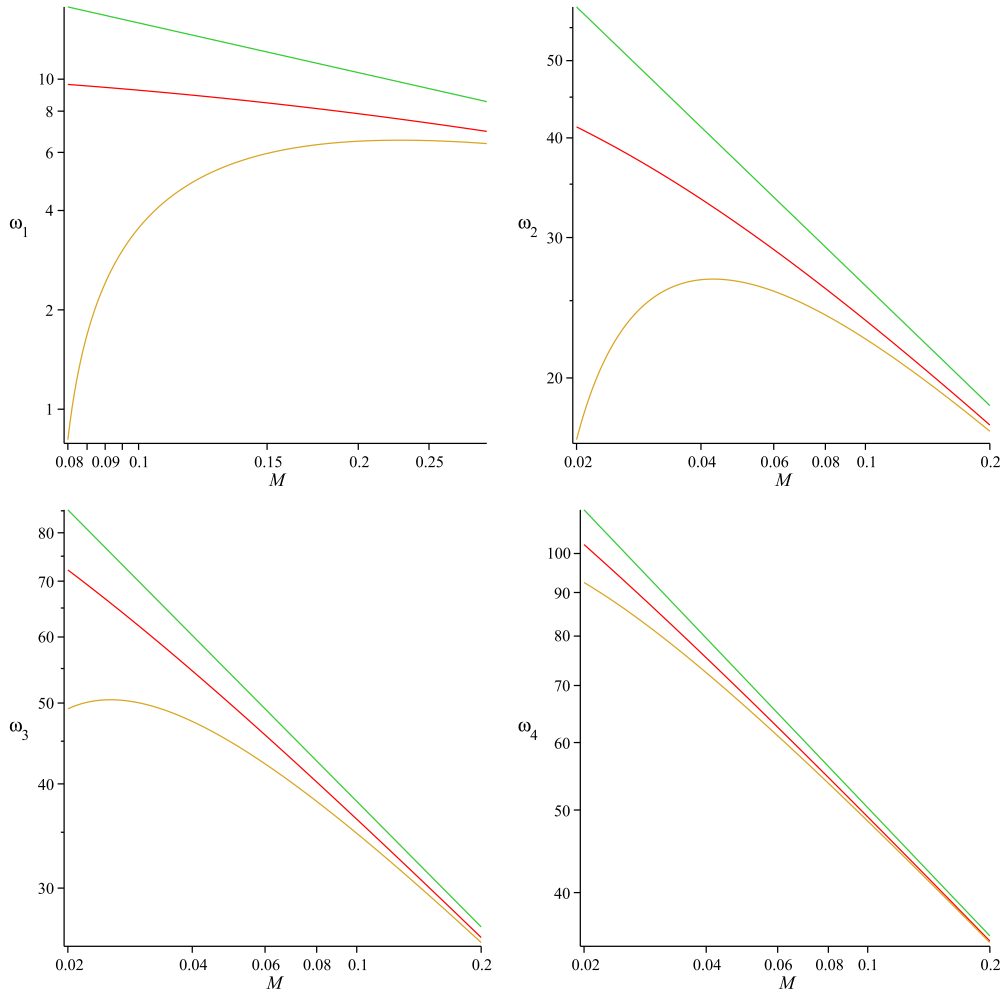


Figure 2.9: The semi-analytical eigenfrequencies ω_n (red) calculated in §2.6, along with the leading-order (green) $M^{-\frac{1}{2}}\omega_{n0}$ and first-order (yellow) $M^{-\frac{1}{2}}(\omega_{n0} + M^{-1}\omega_{n1})$ asymptotic expansions as functions of M for the first four eigenfrequencies.

We note that in the current scenario, the normalisation condition (2.107) sets the integral within (2.145) to have a value of 1. By examining the expression (2.157) for p_{n0} , it is seen that $p'_{n0}(0)$ is zero for even modes and non-zero for odd modes. As such, we obtain different asymptotic expansions for Re_{cn} when n is odd and even.

When n is odd, we may rewrite (2.166) in the following way

$$Re_{cn} = \frac{\alpha\ell\sqrt{2}\epsilon^{\frac{1}{4}}\omega_{n0}^{\frac{1}{2}} \left(1 + \epsilon\frac{\omega_{n1}}{\omega_{n0}} + O(\epsilon^2)\right)^{\frac{1}{2}}}{\left(\frac{dp_{n0}(0)}{dz}\right)^2 \left(1 + \epsilon\frac{p'_{n1}(0)}{p'_{n0}(0)} + O(\epsilon^2)\right)^2}. \quad (2.167)$$

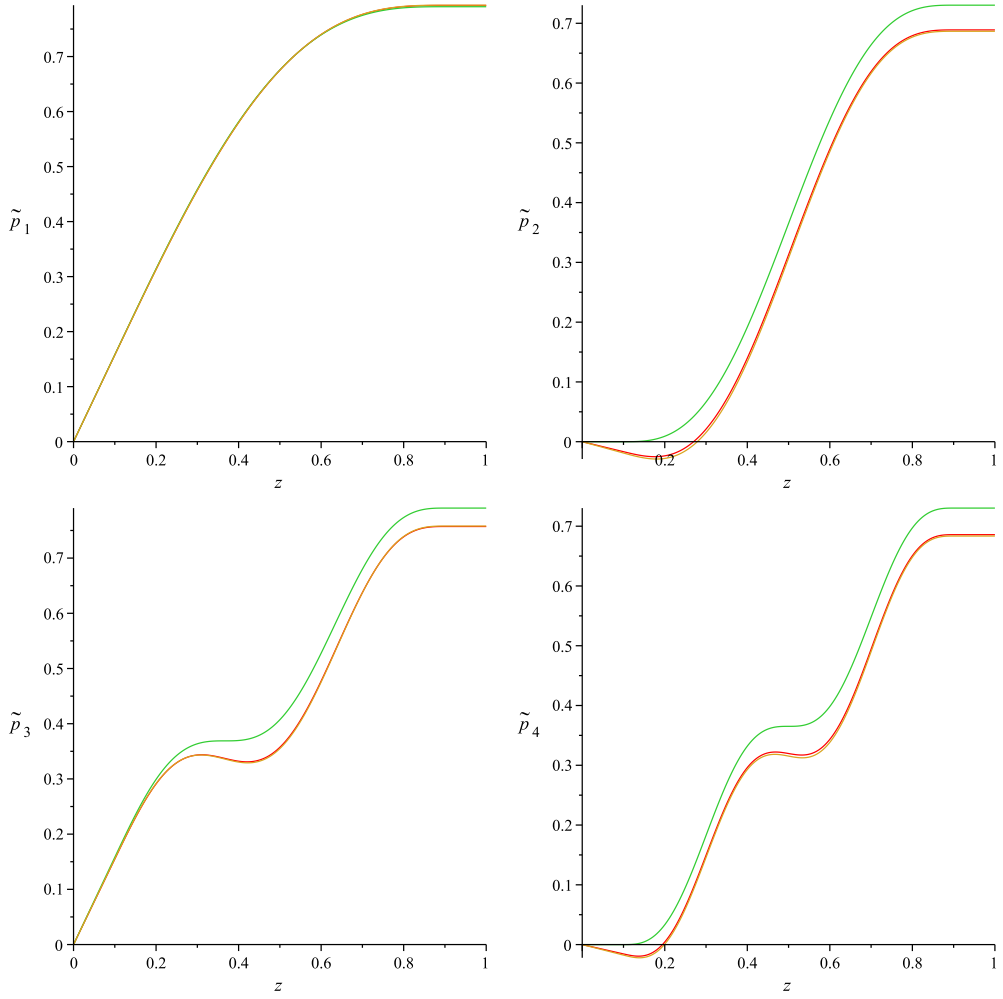


Figure 2.10: The semi-analytical mode shapes of the pressure \tilde{p}_n (red) calculated in §2.6, along with the leading-order (green) \tilde{p}_{n0} and first-order (yellow) $\tilde{p}_{n0} + M^{-1}\tilde{p}_{n1}$ asymptotic expansions when $M = 1$ for the first four eigenmodes.

It is possible to apply the Binomial Theorem to find

$$\left(1 + \epsilon \frac{\omega_{n1}}{\omega_{n0}} + O(\epsilon^2)\right)^{\frac{1}{2}} = 1 + \epsilon \frac{\omega_{n1}}{2\omega_{n0}} + O(\epsilon^2), \quad (2.168)$$

$$\left(1 + \epsilon \frac{p'_{n1}(0)}{p'_{n0}(0)} + O(\epsilon^2)\right)^{-2} = 1 - \frac{2\epsilon p'_{n1}(0)}{p'_{n0}(0)} + O(\epsilon^2). \quad (2.169)$$

Substituting these into (2.167), the asymptotic approximation of Re_{cn} up to first order for odd modes is found to be

$$Re_{cn} = \frac{\alpha \ell \sqrt{2} \epsilon^{\frac{1}{4}} \omega_{n0}^{\frac{1}{2}}}{\left(\frac{dp_{n0}(0)}{dz}\right)^2} \left[1 + \epsilon \left(\frac{\omega_{n1}}{2\omega_{n0}} - \frac{2p'_{n1}(0)}{p'_{n0}(0)}\right) + O(\epsilon^2)\right] \quad \text{for odd } n. \quad (2.170)$$

For even n , $p'_{n0}(0) = 0$ and (2.166) can be written as so

$$Re_{cn} = \frac{\alpha \ell \sqrt{2} \epsilon^{-\frac{7}{4}} \omega_{n0}^{\frac{1}{2}} \left(1 + \epsilon \frac{\omega_{n1}}{\omega_{n0}} + O(\epsilon^2)\right)^{\frac{1}{2}}}{\left(\frac{dp_{n1}(0)}{dz}\right)^2 \left(1 + \epsilon \frac{p'_{n2}(0)}{p'_{n1}(0)} + O(\epsilon^2)\right)^2}. \quad (2.171)$$

Again, by using the Binomial Theorem, it can be shown that

$$\left(1 + \epsilon \frac{p'_{n2}(0)}{p'_{n1}(0)} + O(\epsilon^2)\right)^{-2} = 1 - \frac{2\epsilon p'_{n2}(0)}{p'_{n1}(0)} + O(\epsilon^2). \quad (2.172)$$

By substituting this and (2.168) into (2.171), the asymptotic expansion of Re_{cn} up to first order for even modes is shown to be

$$Re_{cn} = \frac{\alpha \ell \sqrt{2} \epsilon^{-\frac{7}{4}} \omega_{n0}^{\frac{1}{2}}}{\left(\frac{dp_{n1}(0)}{dz}\right)^2} \left[1 + \epsilon \left(\frac{\omega_{n1}}{2\omega_{n0}} - \frac{2p'_{n2}(0)}{p'_{n1}(0)}\right) + O(\epsilon^2)\right] \quad \text{for even } n. \quad (2.173)$$

We note that in order to determine the first-order approximation of Re_{cn} for even modes, an expression for $p_{n2}(z)$ would be needed. However, to determine this expression, we would need to solve the governing system up to second order. This would require a lot of working and as such is not attempted here. Instead, we will evaluate the accuracy of just the leading-order approximation of the critical Reynolds number for even modes.

Immediately, we see that the approximations (2.170), (2.173) for Re_{cn} have different behaviours for odd and even modes. The leading-order approximation (2.170) for odd modes behaves as $Re_{cn} \sim \epsilon^{1/4} = M^{-1/4}$ whereas for even modes, the leading-order approximation (2.173) behaves as $Re_{cn} \sim \epsilon^{-7/4} = M^{7/4}$. From these behaviours, it can be deduced that as M increases, Re_{cn} decreases for odd modes and increases for even modes, agreeing with the behaviours found in §2.7.4.

To further test the accuracy of the approximations (2.170), (2.173), we plot them against the semi-analytical results of Re_{cn} found in §2.7.4. In Figure 2.9, the leading and first-order approximations (2.170) of $Re_{cn}/\ell\alpha$ for the fundamental and third modes, and the leading-order approximations (2.173) of $Re_{cn}/\ell\alpha$ for the second and fourth modes have been plotted. Also plotted are the semi-analytical solutions of $Re_{cn}/\ell\alpha$ for the first four modes as seen in Figure 2.7. We can see in Figure 2.9 that for all the different modes, the leading-order approximations are giving good agreement with the semi-analytical results for $M > 1$. We also see in the case of the odd modes, the first-order approximations are giving good agreement with the semi-analytical results, even for some values of M smaller than $M = 1$.

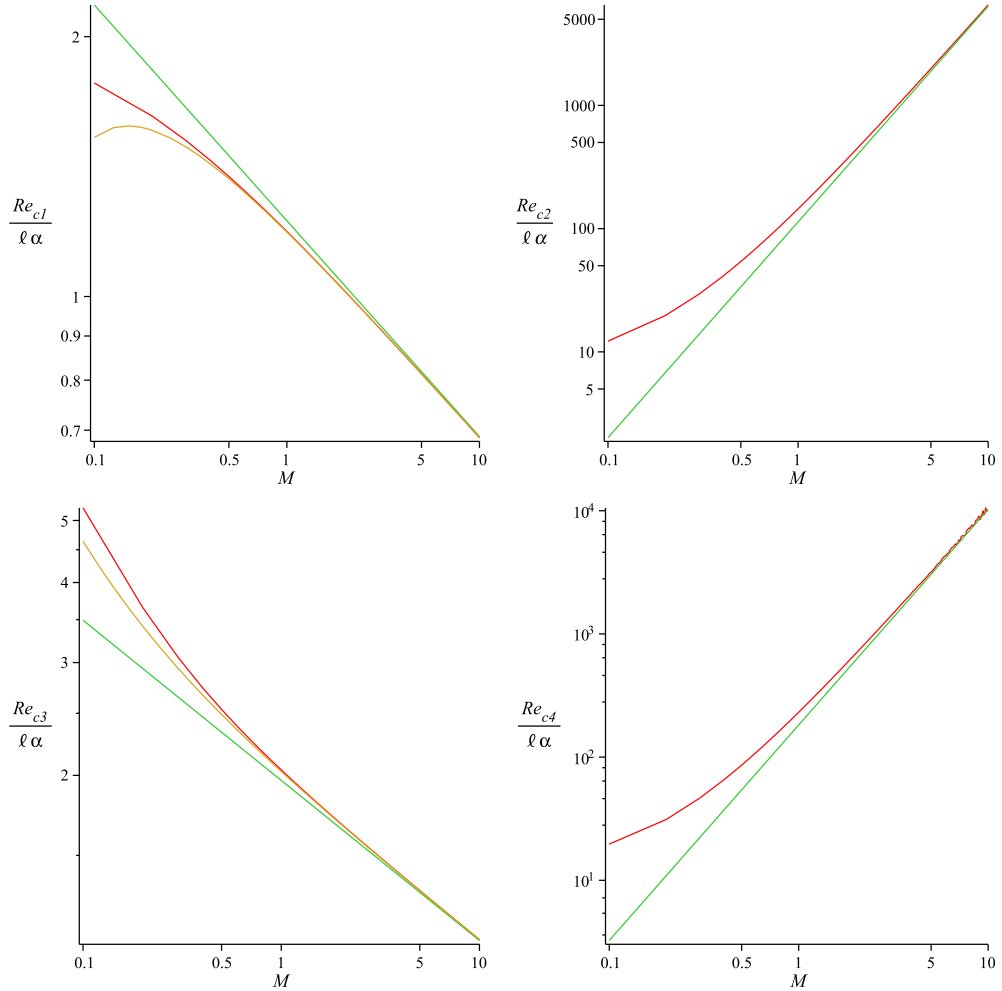


Figure 2.11: The semi-analytical critical Reynolds number $Re_{cn}/\ell\alpha$ (red) calculated in §2.7.4 along with the leading-order (green) and first-order (yellow) asymptotic approximations (2.170), (2.173) for Re_{cn} as functions of M for the first four modes. Here, $z_1 = 0.1$, $z_2 = 0.9$, $\sigma_0 = 0.6$ and $\mathcal{F} = 1$.

2.8.4 Asymptotic Approximation for Λ

We now turn our attention to deriving an asymptotic approximation for the growth rate Λ . Substituting the approximations (2.147) for ω_n , \tilde{p}_n into (2.146), it is seen that the growth rate Λ_n for the n^{th} mode may be written as

$$\Lambda_n = \frac{\pi(Re - Re_{cn}) (p'_{n0}(0) + \epsilon p'_{n1}(0) + \epsilon^2 p'_{n2}(0) + O(\epsilon^3))^2}{2A_0\ell\alpha^2 \left[1 + \int_0^1 k_2 \epsilon^{-1} (p''_{n0} + \epsilon p''_{n1} + O(\epsilon^2))^2 dz \right]}, \quad (2.174)$$

where again the normalisation condition (2.107) has been used to simplify the expression. Again, due to the fact that $p'_{n0}(0) = 0$ for even modes and

$p'_{n0}(0) \neq 0$ for odd modes, we will obtain different expansions for Λ_n for odd and even modes. It is possible to include our asymptotic expansions for Re_{cn} within this expression to obtain a full asymptotic expansion. However, the full approximation will also depend on the size of the Reynolds number Re of the flow. As such, it is more informative to determine the asymptotic expansion of Λ_n up to the value of $Re - Re_{cn}$ and we will leave this factor in our approximations.

When n is odd, (2.174) can be rewritten as

$$\Lambda_n = \frac{\pi(Re - Re_{cn})p'^2_{n0}(0) \left(1 + \epsilon \frac{p'_{n1}(0)}{p'_{n0}(0)} + O(\epsilon^2)\right)^2}{2A_0\ell\alpha^2 \left[1 + k_2\epsilon^{-1} \int_0^1 p''^2_{n0} \left(1 + \epsilon \frac{p''_{n1}}{p''_{n0}} + O(\epsilon^2)\right)^2 dz\right]}. \quad (2.175)$$

Again, we use the Binomial Theorem to evaluate terms in the numerator and denominator of (2.175). It is initially found that

$$\left(1 + \epsilon \frac{p'_{n1}(0)}{p'_{n0}(0)} + O(\epsilon^2)\right)^2 = 1 + \frac{2\epsilon p'_{n1}(0)}{p'_{n0}(0)} + O(\epsilon^2). \quad (2.176)$$

To evaluate the denominator of (2.175), we must first of all calculate the asymptotic expansion of the integral within the denominator. It is found that

$$\begin{aligned} & \int_0^1 p''^2_{n0} \left(1 + \epsilon \frac{p''_{n1}}{p''_{n0}} + O(\epsilon^2)\right)^2 dz \\ &= \int_0^1 p''^2_{n0} dz + \int_0^1 2\epsilon p''_{n0} p''_{n1} dz + O(\epsilon^2). \end{aligned} \quad (2.177)$$

Using this, we may determine the following

$$\begin{aligned} & \left[1 + k_2\epsilon^{-1} \int_0^1 p''^2_{n0} \left(1 + \epsilon \frac{p''_{n1}}{p''_{n0}} + O(\epsilon^2)\right)^2 dz\right]^{-1} \\ &= \left[1 + k_2\epsilon^{-1} \left(\int_0^1 p''^2_{n0} dz + \int_0^1 2\epsilon p''_{n0} p''_{n1} dz + O(\epsilon^2)\right)\right]^{-1} \\ &= \frac{\epsilon}{k_2 \int_0^1 p''^2_{n0} dz} \left(1 + \epsilon \frac{2k_2 \int_0^1 p''_{n0} p''_{n1} dz + 1}{k_2 \int_0^1 p''^2_{n0} dz} + O(\epsilon^2)\right)^{-1} \\ &= \frac{\epsilon}{k_2 \int_0^1 p''^2_{n0} dz} \left(1 - \epsilon \frac{2k_2 \int_0^1 p''_{n0} p''_{n1} dz + 1}{k_2 \int_0^1 p''^2_{n0} dz} + O(\epsilon^2)\right). \end{aligned} \quad (2.178)$$

Substituting (2.176) and (2.178) into the expression (2.175) for Λ_n for odd

modes, it is seen that Λ_n is determined to be

$$\Lambda_n = \frac{\epsilon \pi (Re - Re_{cn}) p_{n0}''(0)}{2A_0 \ell \alpha^2 k_2 \int_0^1 p_{n0}''^2 dz} \left[1 + \epsilon \left(\frac{2p_{n1}'(0)}{p_{n0}'(0)} - \frac{2k_2 \int_0^1 p_{n0}'' p_{n1}'' dz + 1}{k_2 \int_0^1 p_{n0}''^2 dz} \right) + O(\epsilon^2) \right] \quad \text{for odd } n. \quad (2.179)$$

When we have even n , $p_{n0}'(0) = 0$ and the expression (2.174) for Λ_n may be written as

$$\Lambda_n = \frac{\epsilon^2 \pi (Re - Re_{cn}) p_{n1}''(0) \left(1 + \epsilon \frac{p_{n2}'(0)}{p_{n1}'(0)} + O(\epsilon^2) \right)^2}{2A_0 \ell \alpha^2 \left[1 + k_2 \epsilon^{-1} \int_0^1 p_{n0}''^2 \left(1 + \epsilon \frac{p_{n1}''}{p_{n0}''} + O(\epsilon^2) \right)^2 dz \right]}. \quad (2.180)$$

As before, the Binomial Theorem is applied to find

$$\left(1 + \epsilon \frac{p_{n2}'(0)}{p_{n1}'(0)} + O(\epsilon^2) \right)^2 = 1 + \frac{2\epsilon p_{n2}'(0)}{p_{n1}'(0)} + O(\epsilon^2). \quad (2.181)$$

Substituting this and (2.178) into (2.180), the growth rate Λ_n for even modes is found to be

$$\Lambda_n = \frac{\epsilon^3 \pi (Re - Re_{cn}) p_{n1}''(0)}{2A_0 \ell \alpha^2 k_2 \int_0^1 p_{n0}''^2 dz} \left[1 + \epsilon \left(\frac{2p_{n2}'(0)}{p_{n1}'(0)} - \frac{2k_2 \int_0^1 p_{n0}'' p_{n1}'' dz + 1}{k_2 \int_0^1 p_{n0}''^2 dz} \right) + O(\epsilon^2) \right] \quad \text{for even } n. \quad (2.182)$$

In order to determine the first-order approximation of Λ_n for even modes (up to the value of $Re - Re_{cn}$), we would need to determine $p_{n2}(z)$. As this would require a lot of working this is not attempted here.

Again, we can immediately see that the approximations (2.179), (2.182) for Λ_n behave differently for odd and even modes. The leading-order approximations of $\Lambda_n / (Re - Re_{cn})$ behave as $\Lambda_n / (Re - Re_{cn}) \sim \epsilon = M^{-1}$ and $\Lambda_n / (Re - Re_{cn}) \sim \epsilon^3 = M^{-3}$ for odd and even modes respectively. Hence, as we increase M , the value of $\Lambda_n / (Re - Re_{cn})$ decreases for both odd and even

modes, but the even modes are faster to decay. Again, this is in agreement with the behaviours found in the semi-analytical results shown in §2.7.4.

We further test the accuracy of the approximations (2.179), (2.182) by plotting the leading and first-order gradient of the growth rate $\ell\alpha^2\partial\Lambda_n/\partial Re$ derived from the approximations along with the semi-analytical solution of $\ell\alpha^2\partial\Lambda_n/\partial Re$ as seen in Figure 2.8. This has been done in Figure 2.12 for the first four modes. We can see from the figure that there is good agreement between the leading-order approximations and the semi-analytical results for all four of the modes when $M > 5$. It is also seen that the first-order approximations for the odd modes have good agreement with the semi-analytical results for $M \geq O(1)$.

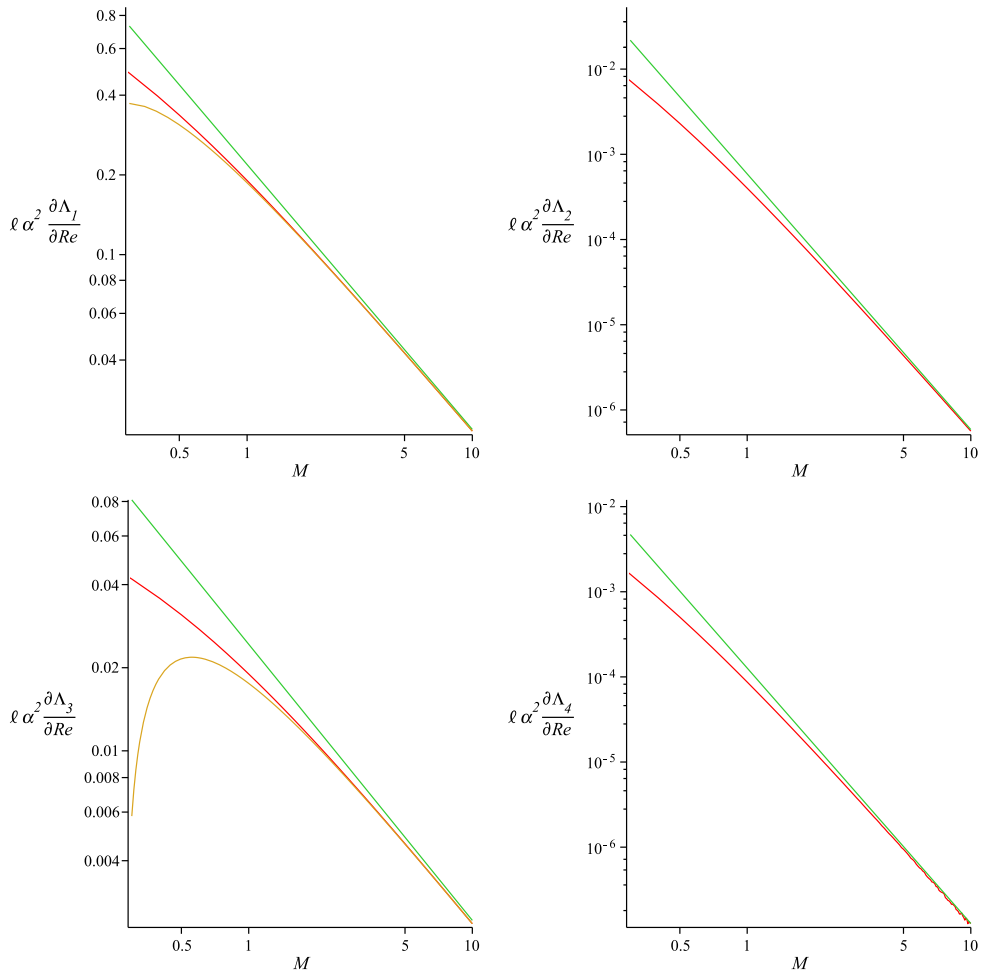


Figure 2.12: The semi-analytical gradient of the growth rate $\ell\alpha^2\partial\Lambda_n/\partial Re$ (red) calculated in §2.7.4 along with the leading-order (green) and first-order (yellow) asymptotic approximations (2.179), (2.182) for $\ell\alpha^2\partial\Lambda_n/\partial Re$ as functions of M for the first four modes. Here, $z_1 = 0.1$, $z_2 = 0.9$, $\sigma_0 = 0.6$ and $\mathcal{F} = 1$.

2.9 Conclusions

In this chapter, we have introduced wall inertia to the Whittaker *et al.* (2010c) model and quantified the effect it has on the frequency, mode shape and growth rate of the oscillations, as well as the critical Reynolds number at which oscillations occur.

The model developed here takes the form of the same differential equations and boundary conditions found by Whittaker *et al.* (2010c) except for the inclusion of a wall inertia term in the governing ODE (2.82) for the flexible part of the tube. It is noted that this wall inertia term does not enter the governing equation in the same way that the fluid inertia does, but instead combines with the azimuthal bending term. The wall inertia term is proportional to a dimensionless wall inertia parameter M which quantifies the amount of wall inertia within the system. As in the Whittaker *et al.* (2010c) model, the ordinary differential equations (2.82), (2.83) and boundary conditions (2.85)–(2.87) govern the oscillatory component of the pressure \tilde{p} as a function of the axial coordinate z .

Solving this model, we have found that increasing wall inertia yields a decrease in the eigenfrequencies ω_n , particularly for higher modes. However, the variation in ω_n with increasing M is found to be small for the fundamental $n = 1$ mode in the case $M \leq O(1)$, in comparison with higher modes. We also find that the variation of the fundamental mode shapes for the oscillatory pressure, axial velocity and area is small with increasing M (see figures 2.4, 2.5, 2.6). For higher-order modes, the mode shapes of the pressure $\tilde{p}_n(z)$ start diverging away from $\tilde{p}_n = 0$ as z increases, when M is increased (see figure 2.4).

By considering the energy budget of the system, we have been able to predict that the normal mode oscillations grow or decay exponentially with rate Λ defined by (2.146). Like the other parameters of the problem, Λ also depends on the wall inertia parameter M . We have also defined the critical mean-flow Reynolds number Re_c at which oscillations first become unstable (2.145). By calculating Re_c semi-analytically, we have found that for odd modes $n = 1, 3, \dots$, Re_c decreases for increasing M , and hence the modes become more unstable. However, for even modes $n = 2, 4, \dots$, Re_c increases rapidly with increasing M , resulting in the even modes becoming much more stable. Calculating Λ semi-analytically, we have seen that the gradient $\partial\Lambda/\partial Re$ of the growth rates for all modes decreases for increasing M . However, $\partial\Lambda/\partial Re$

decays much more rapidly to zero for even modes than for odd modes.

Through our analysis, we have determined that for all values of M , the fundamental mode is the fastest growing and most unstable mode. As it is an odd mode, its stability decreases with increasing M . Hence, the inclusion of wall inertia destabilises the oscillations within the system. This is in agreement with Luo & Pedley (1998) who found that wall inertia was also destabilising in a two-dimensional collapsible channel.

Using the model derived here, we quantify the effects of wall inertia on the frequency ω , critical Reynolds number Re_c and gradient $\partial\Lambda/\partial Re$ of the growth rate for the fundamental mode, for a couple of physical examples. We first take the example of the main pulmonary artery which carries deoxygenated blood from the heart to the lungs. The typical dimensional values of the radial scale, wall thickness and tube length (given by Pedley, 1980, p. 11) are found to be $a = 1\text{cm}$, $d = 0.03\text{cm}$, and $L = 3\text{cm}$, respectively. It is also assumed that the fluid and wall material is mostly comprised of water, yielding a density ρ of $\rho = 1\text{gcm}^{-3}$. Using the values of d and ρ , the mass $m = d\rho$ per unit area of the tube wall is determined to be $m = 0.03\text{gcm}^{-2}$. Using these values in the expression (2.9b) for the wall inertia parameter M , we find $M \approx 0.003$ for flow through the main pulmonary artery. Setting this value of M instead of $M = 0$ yields a 0.9% decrease in the frequency ω of the fundamental mode, a 0.5% decrease in the critical Reynolds number Re_c of the fundamental mode, and a 1.8% decrease in the gradient $\partial\Lambda/\partial Re$ of the growth rate for the fundamental mode. Hence, in this example the effects of wall inertia are negligible.

Another physical example that can be considered is crude oil flowing through a steel submarine pipe. Here we take the radial scale and wall thickness to be $a = 0.9\text{m}$ and $d = 0.075\text{m}$, based on values given by Gerwick (2007). The density ρ_w of the steel comprising the tube wall is approximately $\rho_w = 8000\text{kgm}^{-2}$ (see Haynes, 2012). The density ρ of the crude oil is assumed to be similar to that of water, yielding a density of $\rho = 1000\text{kgm}^{-2}$, and we consider the scenario when we have a tube of length $L = 5\text{m}$. With the values of d and ρ_w , we calculate the mass $m = d\rho_w$ per unit area of the tube wall to be $m = 600\text{kgm}^{-2}$. Substituting these values into the definition (2.9b) of M yields $M \approx 0.02$ for oil flow through a steel pipe. By changing the value of M from $M = 0$ to $M = 0.02$, it is found that the frequency ω of the fundamental mode decreases by 5.7%, the critical Reynolds number Re_c of the fundamental mode decreases by 3.2%, and the gradient $\partial\Lambda/\partial Re$ of the growth rate for the

fundamental mode decreases by 10.8%. Therefore, the effects of wall inertia in this example are more significant and cannot necessarily be neglected.

Finally, we have developed asymptotic approximations for ω , \tilde{p} , Re_c and Λ for the different modes in the parameter regime $M \gg 1$, where wall inertia dominates over fluid inertia. Using these approximations, we have seen that even and odd modes behave very differently. Our leading-order approximation (2.157) for the modes \tilde{p}_n of the pressure predicts that in the upstream region $0 \leq z \leq z_1$, odd modes have a linear rise in the pressure mode shape, whereas the even modes have no change in the pressure. This approximation also predicts that all odd modes tend to one fixed value in the downstream region $z_2 \leq z \leq 1$ and that the even modes all tend to a different fixed value (see figure 2.10). It is seen that all of these approximations are in good agreement with the previously found semi-analytical results, even for $M = O(1)$.

We have seen both in the semi-analytical results and in the asymptotic approximations that the odd and even modes of the oscillations behave very differently when $M \gg 1$. In this scenario, the primary balance in the governing ODE (2.82) for the elastic-walled region of the tube is between the axial tension, azimuthal bending and wall inertia terms. As the fluid inertia no longer has an effect on the primary balance, the odd and even modes \tilde{A}_n for the oscillatory area become symmetric and antisymmetric respectively about $z = 0.5$ at leading order. In this case, the even modes have little flux in the upstream rigid region of the tube (as the fluid predominantly moves between the crests and troughs of the oscillations in the elastic-walled region) whereas the odd modes have a significant flux in the upstream region. As such, the energy input for the odd modes takes a significant value and this energy may be used to destabilise the system. For even modes however, the energy input is small and the destabilising effect is only a weak first-order effect, meaning the even modes are much more stable.

2.A Proof That the Eigenfrequencies are Real

Here, we prove that the eigenfrequencies ω of the oscillations take real values. We start with the governing ODE (2.82) for \tilde{p} in the flexible region ($z_1 < z < z_2$) of the tube

$$k_2 \mathcal{F} \tilde{p}''' + (M\omega^2 k_2 - k_0) \tilde{p}'' - \omega^2 \tilde{p} = 0,$$

where ' denotes a derivative with respect to z . Multiplying this equation by \tilde{p}''^\dagger , where † represents the complex conjugate, the following is obtained

$$k_2 \mathcal{F} \tilde{p}''' \tilde{p}''^\dagger + (M\omega^2 k_2 - k_0) |\tilde{p}''|^2 - \omega^2 \tilde{p}''^\dagger \tilde{p} = 0.$$

The next step is to integrate between z_1 and z_2 with respect to z . Doing so, using integration by parts when needed, we calculate

$$\begin{aligned} k_2 \mathcal{F} \left(\left[\tilde{p}''' \tilde{p}''^\dagger \right]_{z_1}^{z_2} - \int_{z_1}^{z_2} |\tilde{p}'''|^2 dz \right) + (M\omega^2 k_2 - k_0) \int_{z_1}^{z_2} |\tilde{p}''|^2 dz \\ - \omega^2 \left(\left[\tilde{p}''^\dagger \tilde{p} \right]_{z_1}^{z_2} - \int_{z_1}^{z_2} |\tilde{p}'|^2 dz \right) = 0. \end{aligned}$$

From the boundary condition (2.85), we know that $\tilde{p}'' = 0$ at $z = z_1, z_2$, which implies $\left[\tilde{p}''' \tilde{p}''^\dagger \right]_{z_1}^{z_2} = 0$. Hence, the above equation now becomes

$$\begin{aligned} (M\omega^2 k_2 - k_0) \int_{z_1}^{z_2} |\tilde{p}''|^2 dz - k_2 \mathcal{F} \int_{z_1}^{z_2} |\tilde{p}'''|^2 dz \\ - \omega^2 \left(\left[\tilde{p}''^\dagger \tilde{p} \right]_{z_1}^{z_2} - \int_{z_1}^{z_2} |\tilde{p}'|^2 dz \right) = 0. \end{aligned} \quad (2.183)$$

We now look at the governing equation (2.83) in the upstream rigid part of the tube. Taking the complex conjugate of (2.83), it can be seen that

$$\tilde{p}''^\dagger \tilde{p} = 0,$$

for $0 < z < z_1$. We may integrate this expression by parts with respect to z , between $z = 0$ and $z = z_1$. Carrying this out, rearranging, then multiplying by ω^2 , we find

$$\omega^2 \int_0^{z_1} |\tilde{p}'|^2 dz - \omega^2 \left[\tilde{p}''^\dagger \tilde{p} \right]_0^{z_1} = 0. \quad (2.184)$$

Adding equations (2.183) and (2.184) together yields the following

$$(M\omega^2 k_2 - k_0) \int_{z_1}^{z_2} |\tilde{p}''|^2 dz - k_2 \mathcal{F} \int_{z_1}^{z_2} |\tilde{p}'''|^2 dz - \omega^2 \left[\tilde{p}''^\dagger \tilde{p} \right]_0^{z_2} + \omega^2 \int_0^{z_2} |\tilde{p}'|^2 dz = 0. \quad (2.185)$$

Finally, we know that $\tilde{p} = 0$ at $z = 0$ from the boundary condition (2.86). We also know from the boundary condition (2.92) that $\tilde{p}' = 0$ at $z = z_2$ and thus,

$\tilde{p}'^\dagger = 0$ at $z = z_2$. Hence, $[\tilde{p}'^\dagger \tilde{p}]_0^{z_2} = 0$ and vanishes from (2.185). Rearranging (2.185), it can be shown that

$$\omega^2 = \frac{k_2 \mathcal{F} \int_{z_1}^{z_2} |\tilde{p}'''|^2 dz + k_0 \int_{z_1}^{z_2} |\tilde{p}''|^2 dz}{\int_0^{z_2} |\tilde{p}'|^2 dz + M k_2 \int_{z_1}^{z_2} |\tilde{p}''|^2 dz}.$$

As the terms being integrated on the right-hand side are all square terms of real values, the integrals must be positive. Also, as all the constants are real and positive and the denominator is non-zero for non-trivial solutions, the right-hand side is real and positive. Hence, ω^2 is real and strictly positive, and thus ω is real and non-zero. \square

Chapter 3

Introducing an Axial-Bending Boundary Layer

3.1 Introduction

In this chapter we turn our attention to introducing the effects of axial bending to the model considered by Whittaker *et al.* (2010c) and the model derived in Chapter 2. By including axial bending in these models, it is possible to satisfy stronger and more appropriate boundary conditions at the ends of the elastic-walled tube being considered in the models.

Here, it is useful to consider three different conditions which may be applied at the end of a shell. These are the canonical ‘clamped’ and ‘pinned’ boundary conditions (Howell *et al.*, 2009, p.156), and the non-canonical ‘sliding’ boundary conditions, all of which may be viewed in Figure 3.1. The clamped boundary condition seen in Figure 3.1(a) fixes the position and the axial gradient of the shell at a fixed axial coordinate. The pinned boundary condition shown in Figure 3.1(b) again fixes the position of the shell at a fixed axial coordinate. However instead of fixing the axial gradient, this condition sets zero torque at the same axial coordinate. Finally, the sliding boundary condition viewed in Figure 3.1(c) fixes the normal and transverse components of the position of the shell, as well as sets zero axial stress perturbation and zero torque, at a fixed axial coordinate. In a typical Starling resistor set-up, the elastic-walled tube is clamped onto two rigid tubes. In order to reflect this, clamped boundary conditions should be set at the interfaces between the elastic-walled and rigid tubes.

In the model by Whittaker *et al.* (2010d) and the model derived in Chapter 2,

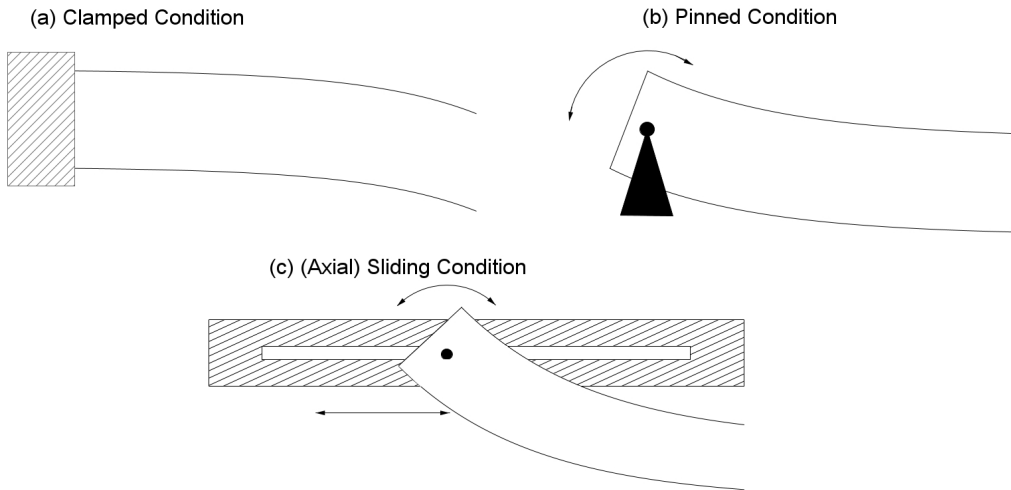


Figure 3.1: A physical representation of the canonical ‘clamped’ and ‘pinned’ boundary conditions and the non-canonical ‘sliding’ conditions, applied to a shell.

a ‘tube law’ modelling the wall mechanics and relating the transmural pressure acting on the tube to the cross-sectional area of the tube at each axial position is derived. In the derivation of this tube law, axial bending and in-plane shear effects are neglected, reducing the axial order of the problem from 8 to 2. This axial order is not high enough for the full clamped boundary conditions to be satisfied. Instead it is only possible to set the normal and azimuthal displacements to zero at the elastic-walled tube ends in these models. These conditions represent the Dirichlet parts of the sliding conditions, with the axial gradient and axial displacement not necessarily set to zero.

Whittaker (2015) takes a step towards being able to satisfy the full clamped boundary conditions by reintroducing in-plane shear effects in the model by Whittaker *et al.* (2010d). This allows the normal, azimuthal and axial displacements to be set to zero at the interface between the flexible and rigid tubes. This represents the Dirichlet parts of the pinned boundary conditions, with the axial gradient not necessarily set to zero. The inclusion of these in-plane shear effects only raises the axial order of the problem from 2 to 6, and this axial order is still not high enough for the full clamped boundary conditions to be satisfied.

In order to satisfy the clamped boundary conditions, the effects of axial bending must be included in the model. The inclusion of these effects allows the axial order of the problem to increase to 8, which is high enough for the clamped boundary conditions to be satisfied. Due to the scaling of the axial bending terms, it is found that these terms only have a significant effect

on the leading-order solution in a small boundary layer near the ends of the elastic-walled tube.

In this chapter, a brief discussion of problems with a singular limit, and of boundary layers in general, is given in §3.2. We then proceed to define the mathematical set-up of the elastic-walled tube and the parameter regime of the problem in §3.3. In §3.4, the clamped boundary conditions are defined in terms of the dimensionless deformations of the tube wall. These conditions are then compared with the ‘sliding’ conditions tested in the model by Whittaker *et al.* (2010d), and the pinned boundary conditions tested in the model by Whittaker (2015). In §3.5, we then provide an overview of the work by Whittaker (2015), where a shear-relaxation boundary layer that includes the effects of in-plane shearing is introduced.

A boundary layer that includes the effects of axial bending is then considered in §3.6. Using a simplified model based on a set of nonlinear partial differential equations known as the Föppl–von Kármán equations (Landau & Lifshitz, 1959), an estimate for the size of the bending boundary-layer width is derived. With this estimate, it is found that the problem splits into multiple regimes depending on how the size of the bending boundary layer compares with the tube wall thickness and the sub-layers that comprise the shear-relaxation layer studied by Whittaker (2015). In §3.7, a description of these different regimes is given. Finally, in §3.8 we give an overview of how each of the different regimes are modelled in Chapters 4–7.

3.2 Theory of Singular Limits and Boundary Layers

Before we begin introducing the effects of axial bending to the model derived in Chapter 2, it is necessary to have a full understanding of problems that have a singular limit and how boundary layers may be introduced in order to obtain a solution for these problems. The concepts that are discussed here may also be found in Hinch (1991).

3.2.1 Definition of a Singular Problem

We begin with stating what it means for a problem to be singular. To illustrate this, the following algebraic equation is considered

$$\epsilon x^2 + x - 1 = 0. \quad (3.1)$$

If we set $\epsilon = 0$, this equation only has one solution, $x = 1$. However, in the case $\epsilon \neq 0$ there are two solutions to (3.1), even if $\epsilon \ll 1$. This difference in behaviour when $\epsilon = 0$ and in the limit $\epsilon \rightarrow 0$ is what sets (3.1) as a singular perturbation problem.

3.2.2 Singular Differential Equations

It is also possible to have singular differential equations. An example of this is the differential equation

$$\epsilon \frac{d^2f}{dx^2} + \frac{df}{dx} + 1 = 0, \quad (3.2)$$

which has different solutions in the cases $\epsilon \rightarrow 0$ and $\epsilon = 0$. As this is a second-order differential equation, we would need two boundary conditions as well to form a solvable boundary-value problem. For example, we could have the conditions

$$f(0) = 0, \quad f(1) = 1. \quad (3.3)$$

If we naively take $\epsilon = 0$, it is not possible for a solution of (3.2) to satisfy both of these boundary conditions. However if $\epsilon \rightarrow 0$, we still have a second order equation to be solved, meaning the two boundary conditions may be satisfied. When $\epsilon \neq 0$, the exact solution of this system is dependent on ϵ and is found to be

$$f(x) = \frac{(x-2)e^{\frac{1}{\epsilon}} - x + 2e^{\frac{1-x}{\epsilon}}}{1 - e^{\frac{1}{\epsilon}}}. \quad (3.4)$$

However, in general it is not always possible to obtain an exact analytical solution of a system containing singular differential equations. It is therefore convenient to be able to form analytical approximations of the solutions of singular differential equations.

3.2.3 Introducing a Boundary Layer

For $\epsilon \ll 1$, the solution of (3.2) for most x is approximated well by the solution of

$$\frac{df}{dx} + 1 = 0.$$

However near the $x = 0$ boundary, f is found to vary on a shorter length scale. Because of this, the second-order derivative d^2f/dx^2 becomes large and the first term of (3.2) is no longer small. The region where this occurs is known as a boundary layer.

By rescaling the variable x , it is possible to determine the leading-order equation satisfied by f within the boundary layer and find an approximation for f . The approximate solutions for f within the boundary layer (inner solution) and outside the boundary layer (outer solution) will have a similar form in an intermediate region of x . By forcing these solutions to be the same in this intermediate region, any remaining unknown constants may be determined. This method is known as matching.

We now fully illustrate the method used to find an approximation to the solution of singular boundary-value problems using the system (3.2)–(3.3). In order to determine an approximate solution for f when $\epsilon \ll 1$, we split the domain of the solution into two regions; an outer region where $x = O(1)$ and a boundary layer where $x = O(\delta_B) \ll O(1)$. The boundary-layer width δ_B will be chosen so that the leading-order governing equation in the boundary layer includes the second-order derivative needed to allow the boundary condition at $x = 0$ to be satisfied.

3.2.4 Approximation in the Outer Layer

To determine an approximation for $f(x)$ in the outer region, we begin by taking the following asymptotic expansion

$$f(x) \sim f^{(0)}(x) + \epsilon f^{(1)}(x) + \epsilon^2 f^{(2)}(x) + \dots \quad (3.5)$$

Substituting this into (3.2) and equating powers of ϵ , we find the leading-order governing equation to be

$$\frac{df^{(0)}}{dx} + 1 = 0, \quad (3.6)$$

and the higher-order governing equations as

$$\frac{d^2f^{(n-1)}}{dx^2} + \frac{df^{(n)}}{dx} = 0, \quad \text{for } n \geq 1. \quad (3.7)$$

Hence, the ϵf_{xx} term only appears in the higher-order governing equations. As the leading-order equation (3.6) is first-order in x , it can only satisfy one boundary condition. We know that the behaviour of the solution changes for small x so we may ignore the $f(0) = 0$ condition. Thus, we apply the condition $f(1) = 1$ to the solutions of (3.6) and (3.7). Substituting the asymptotic expansion (3.5) into $f(1) = 1$ and equating powers of ϵ yields the following conditions

$$f^{(0)}(1) = 1, \quad f^{(n)}(1) = 0 \quad \text{for } n \geq 1. \quad (3.8)$$

Solving the leading-order system (3.6), (3.8a), $f^{(0)}(x)$ is found to be

$$f^{(0)}(x) = 2 - x. \quad (3.9)$$

Substituting this into the first-order governing equation (3.7) when $n = 1$, it is found that the second-order derivative vanishes and we are left with $df^{(1)}/dx = 0$. Solving this and applying the condition (3.8b), we obtain $f^{(1)} = 0$. We find that all the higher-order systems have the same governing equations and boundary conditions. Hence, the higher-order solutions for $f^{(n)}$ are calculated to be

$$f^{(n)}(x) = 0 \quad \text{for } n \geq 1. \quad (3.10)$$

Substituting (3.9), (3.10) into the asymptotic approximation (3.5), the full asymptotic approximation for f in the outer layer is found to be

$$f(x) \sim 2 - x. \quad (3.11)$$

3.2.5 Approximation in the Boundary Layer

We now determine an approximation for $f(x)$ in the boundary layer. We begin by introducing a new variable $x_B = \delta_B^{-1}x$, which is $O(1)$ in the boundary layer. We also determine the size of f in the boundary layer by examining the behaviour of the outer solution (3.11) as $x \rightarrow 0$. Taking the Taylor series of (3.11) about $x = 0$, it is seen that the outer solution for f behaves like an $O(1)$ constant when $x \rightarrow 0$. Hence, the magnitude of $f(x)$ in the boundary layer is $O(1)$.

Substituting $x = \delta_B x_B$ into the governing equation (3.2), we obtain

$$\frac{\epsilon}{\delta_B^2} \frac{d^2 f}{dx_B^2} + \frac{1}{\delta_B} \frac{df}{dx_B} + 1 = 0. \quad (3.12)$$

As $f = O(1)$ in the boundary layer and $\delta_B \ll 1$, the second term of (3.12) must be larger than the third constant term and these cannot balance at leading order. Hence, the only sensible dominant balance that may occur at leading order in (3.12) is between the first and second terms. For these terms to balance, we must set $\delta_B = \epsilon$ and the governing equation (3.12) becomes

$$\frac{1}{\epsilon} \frac{d^2 f}{dx_B^2} + \frac{1}{\epsilon} \frac{df}{dx_B} + 1 = 0. \quad (3.13)$$

As in the outer region, we define another asymptotic expansion for $f(x)$, this time valid in the boundary layer

$$f(x) \sim g^{(0)}(x_B) + \epsilon g^{(1)}(x_B) + \epsilon^2 g^{(2)}(x_B) + \dots \quad (3.14)$$

By substituting this into (3.13), the leading-order governing equation is found to be

$$\frac{d^2g^{(0)}}{dx_B^2} + \frac{dg^{(0)}}{dx_B} = 0. \quad (3.15)$$

As this involves different terms to the leading-order equation (3.6) in the outer region, we can see that there are different dominant mechanisms in each region giving rise to different behaviours. The higher-order governing equations are calculated to be

$$\frac{d^2g^{(1)}}{dx_B^2} + \frac{dg^{(1)}}{dx_B} + 1 = 0, \quad \frac{d^2g^{(n)}}{dx_B^2} + \frac{dg^{(n)}}{dx_B} = 0 \quad \text{for } n > 1. \quad (3.16)$$

As the boundary condition $f(1) = 1$ does not reside within this region, we do not apply this condition to the solutions of (3.15) and (3.16). Substituting the asymptotic expansion (3.14) into the condition $f(0) = 0$ gives the following conditions on the $g^{(n)}$

$$g^{(n)}(0) = 0 \quad \text{for } n \geq 0. \quad (3.17)$$

As the leading-order system and the systems higher than first order have the same governing equation and boundary conditions, the solutions for these systems will take the same form. Solving (3.15) and (3.16b) subject to the boundary conditions (3.17), it is calculated that

$$g^{(n)}(x_B) = A_n(1 - e^{-x_B}) \quad \text{for } n \neq 1, \quad (3.18)$$

where the A_n are undetermined constants. Solving the first-order governing equation (3.16a) subject to the boundary condition (3.17) when $n = 1$, $g^{(1)}$ is found to be

$$g^{(1)}(x_B) = A_1 + 1 - x_B - (A_1 + 1)e^{-x_B}. \quad (3.19)$$

Substituting the expressions (3.18) and (3.19) for the $g^{(n)}$ into the asymptotic approximation (3.14) for f in the boundary layer, we find the following approximation valid in the boundary layer

$$f(x_B) \sim \sum_{\substack{n \geq 0 \\ n \neq 1}} \epsilon^n A_n(1 - e^{-x_B}) + \epsilon [A_1 + 1 - x_B - (A_1 + 1)e^{-x_B}]. \quad (3.20)$$

3.2.6 Matching the Outer and Boundary Layer Approximations

We see that the constants A_n in (3.20) are still undetermined. This is because the governing equation (3.13) in the boundary layer is second order, but we have only applied the single boundary condition $f(0) = 0$. In order to determine the

A_n , we must somehow apply the boundary condition $f(1) = 1$. This is done by matching the solution in the boundary layer to the solution in the outer layer (which satisfies $f(1) = 1$) over some intermediate region where x is small and x_B is large.

We first express both x and x_B in terms of an intermediate variable ξ as follows

$$\epsilon^{-\alpha} x = \xi = \epsilon^{1-\alpha} x_B \quad \text{where } 0 < \alpha < 1. \quad (3.21)$$

It is seen that as $\epsilon \rightarrow 0$ with $\xi = O(1)$, we must have $x \rightarrow 0$ and $x_B \rightarrow \infty$. Substituting this variable into the approximations (3.11), (3.20) for f in the outer and boundary layers, the outer layer approximation may be rewritten as

$$f(\xi) \sim 2 - \epsilon^\alpha \xi, \quad (3.22)$$

and the boundary layer approximation becomes

$$f(\xi) \sim \sum_{\substack{n \geq 0 \\ n \neq 1}} \epsilon^n A_n - \epsilon^\alpha \xi + \epsilon(A_1 + 1), \quad (3.23)$$

where the exponential terms have become exponentially small within the intermediate region $\xi = O(1)$. As these approximations must be the same within the intermediate region, we may equate the expressions (3.22) and (3.23) to determine the unknown constants A_n . Doing so, we find

$$A_0 = 2, \quad A_1 = -1, \quad A_n = 0 \quad \text{for } n \geq 2. \quad (3.24)$$

Substituting these constants into the approximation (3.20) for f in the boundary layer, it is calculated that

$$f(x_B) \sim 2(1 - e^{-x_B}) - \epsilon x_B, \quad (3.25)$$

within the boundary layer. We also have the approximation (3.11) for f in the outer layer, given by

$$f(x) \sim 2 - x.$$

3.2.7 Comparisons of the Exact Solution and the Asymptotic Approximations

In Figure 3.2, the exact solution (3.4) of the system (3.2), (3.3) has been plotted in the case $\epsilon = 0.1$. Also plotted are the leading-order, $O(1)$ terms of the approximations (3.11), (3.25) of $f(x)$ in the outer and boundary

layers for $\epsilon = 0.1$. From the figure, it is observed that the leading-order asymptotic approximations are in good agreement with the exact solution in their respective layers. Hence, the method applied here has allowed us to approximate the behaviour of the exact solution, both in the outer layer and in a boundary layer near the $x = 0$ boundary.

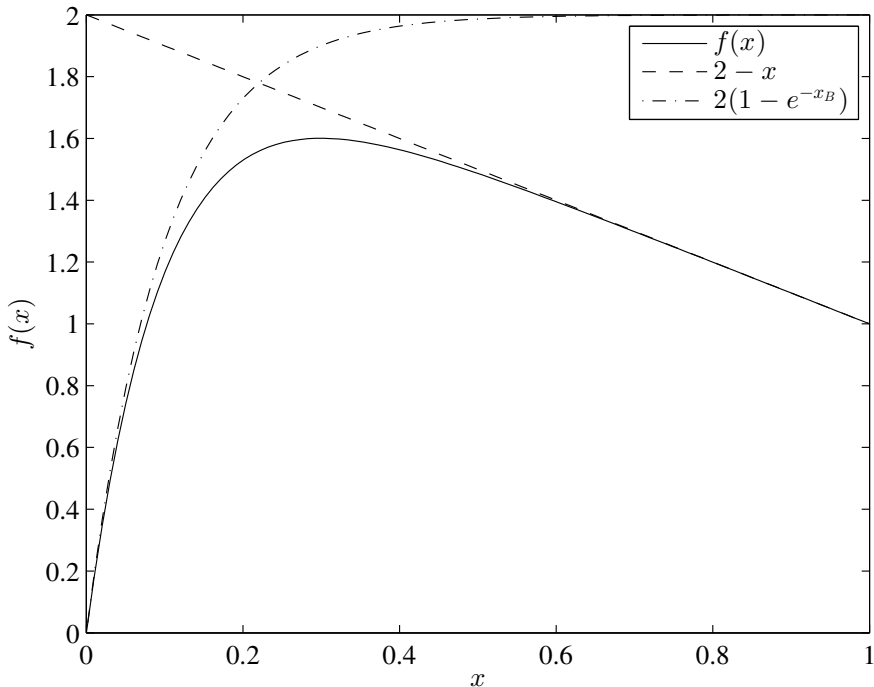


Figure 3.2: The exact solution (3.4) of the boundary-value problem (3.2), (3.3) (solid line). Also plotted are the leading-order terms of the approximations (3.11), (3.25) of $f(x)$ in the outer layer (dashed line) and boundary layer (dashed-dotted line). All the plots have been taken in the case $\epsilon = 0.1$.

3.2.8 Applications to Adding the Effects of Axial Bending to the Model in Chapter 2

Reverting back to our original problem of adding axial bending to the model derived in Chapter 2, we find that in the governing equations the axial bending terms are small enough not to contribute at leading order in the bulk of the tube. However, these bending terms have the highest axial derivatives as well, meaning it is possible to find an axial scale where the effects of axial bending become significant. As we have a term which is smaller than the dominant terms in the bulk of the tube but also has the highest derivatives, we find

ourselves in a similar situation to the example problem (3.2). Hence, we may apply the same method described here to analyse the effect axial bending has on the model.

3.3 Mathematical Set-up for the Elastic-Walled Tube

We consider the following set-up depicted in Figure 3.3. This set-up was first used by Whittaker (2015) and is similar to that used in Chapter 2. Here, we have an initially elliptical elastic-walled tube with length L , circumference $2\pi a$ and tube wall thickness d , where the ends of the tube are fixed onto rigid tubes (as in the Starling Resistor set-up depicted in Figure 1.1). The ellipticity of the tube is set by a parameter σ_0 such that the dimensional major and minor radii are given by $ac \cosh(\sigma_0)$ and $ac \sinh(\sigma_0)$. As in Chapter 2, the dimensionless parameter c is set to be

$$c = \frac{\pi \operatorname{sech}(\sigma_0)}{2E(\operatorname{sech}(\sigma_0))},$$

where $E(\phi)$ is the complete elliptic integral of the second kind, as defined in (2.2). The tube wall has incremental Young's modulus E , Poisson's ratio ν and bending stiffness K . It is also assumed that the tube wall behaves linearly elastically over the deformations that will be considered here. In its initial configuration, the tube is subject to a uniform axial pre-stress due to an axial tension $F/(2\pi ad)$. The tube will then be subject to deformations of amplitude $b(t)$ that are slowly varying in dimensionless time t , and are induced by an applied transmural pressure p_{tm}^* .

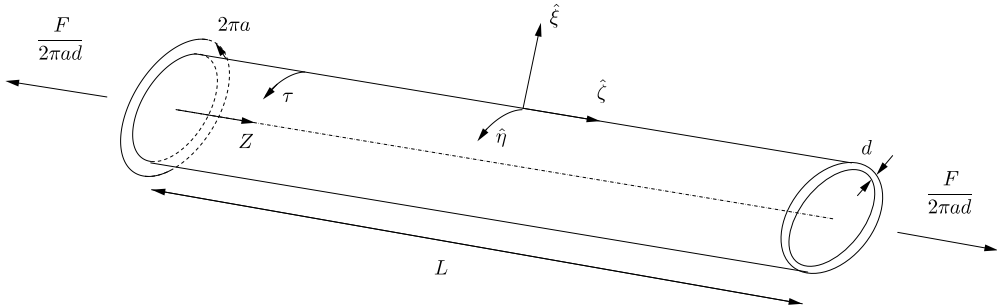


Figure 3.3: The set-up of the undeformed, elliptical, elastic-walled tube as used by Whittaker (2015).

The following dimensionless parameters, first used by Whittaker *et al.*

(2010d), are now introduced

$$\ell = \frac{L}{a} \gg 1, \quad \delta = \frac{d}{a} \ll 1, \quad \mathcal{F} = \frac{aF}{2\pi K\ell^2} = O(1), \quad \Delta(t) = \frac{b(t)}{a} \ll 1. \quad (3.26)$$

These correspond to the tube length, wall thickness, axial tension and amplitude of the deformations respectively. In this parameter regime, we have a long, thin-walled tube under large axial tension, subject to small-amplitude, slowly varying deformations that are induced by the transmural pressure.

We use a similar coordinate system to that used in Chapter 2 to describe the elastic tube wall. The midplane of the tube wall is parameterized using dimensional Lagrangian coordinates (x^1, x^2) , which measure arc length in the azimuthal and axial directions respectively, in the undeformed configuration. These are then converted into two dimensionless Lagrangian surface coordinates $\tau \in [0, 2\pi)$, $Z \in [0, \ell]$ via the relations

$$x^1 = ah(\tau)\tau, \quad x^2 = aZ, \quad (3.27)$$

where for convenience, we have introduced the scale factor $h(\tau)$ set to be

$$h(\tau) = c(\sinh^2 \sigma_0 + \sin^2 \tau)^{\frac{1}{2}}.$$

We note that Z is set so that the ends of the elastic-walled tube, which are clamped onto rigid tubes, are found at $Z = 0, \ell$. This coordinate is different to the dimensionless axial coordinate $z \in [0, 1]$ used in Chapter 2 and we may relate the two using the following

$$Z = \ell \frac{z - z_1}{z_2 - z_1},$$

where $z_1 < z_2$ are the positions in the z -coordinate where the ends of the elastic-walled tube are found.

Using the coordinates (τ, Z) , we define the position $\mathbf{r}_0(\tau, Z)$ of the tube wall in its undeformed state to be

$$\mathbf{r}_0(\tau, Z) = a \begin{pmatrix} c \cosh \sigma_0 \cos \tau \\ c \sinh \sigma_0 \sin \tau \\ Z \end{pmatrix}. \quad (3.28)$$

Denoting the position of the tube wall as \mathbf{r} , we write the deformation $\mathbf{r} - \mathbf{r}_0$ of the tube wall from its undeformed state as

$$\mathbf{r} - \mathbf{r}_0 = \frac{\Delta(t)a}{\ell} \left(\frac{1}{h(\tau)} [\hat{\xi}(\tau, Z, t)\hat{\mathbf{n}} + \hat{\eta}(\tau, Z, t)\hat{\mathbf{t}}] + \hat{\zeta}(\tau, Z, t)\hat{\mathbf{z}} \right), \quad (3.29)$$

where $\hat{\mathbf{n}}$, $\hat{\mathbf{t}}$ and $\hat{\mathbf{z}}$ are unit vectors in the normal, azimuthal and axial directions of the undeformed tube wall. The dimensionless functions $(\hat{\xi}, \hat{\eta}, \hat{\zeta})$ represent the deformations of the tube wall in the normal, azimuthal and axial directions respectively. The representation (3.29) is the same representation of the deformation used by Whittaker (2015), whose work we shall consider later on.

Comparing (3.29) with the expression (2.20) for \mathbf{r} used in §2.3, it is seen that the deformations $(\hat{\xi}, \hat{\eta}, \hat{\zeta})$ are related to their counterparts $(\xi, \eta, \zeta, \zeta_a)$ used in Chapter 2 via the following

$$\hat{\xi} = \ell \xi, \quad \hat{\eta} = \ell \eta, \quad \hat{\zeta} = \zeta + \delta^2 \ell^2 \zeta_a. \quad (3.30)$$

As $\xi, \eta, \zeta, \zeta_a$ are all $O(1)$ when $Z = O(\ell)$ (see Chapter 2), we have

$$\hat{\xi} = O(\ell), \quad \hat{\eta} = O(\ell), \quad \hat{\zeta} = O(\max(1, \delta^2 \ell^2)), \quad \text{when } Z = O(\ell). \quad (3.31)$$

3.4 Types of Boundary Conditions at the Tube Ends

Now that we have an expression for the deformation of the tube wall, we may proceed to evaluate the conditions we wish to set at the ends of the elastic-walled tube.

To reflect the fact that the ends of the elastic-walled tube are joined to rigid tubes, the canonical ‘clamped’ boundary conditions that fix the axial gradient and normal, azimuthal and axial displacement of the tube wall should be applied. In terms of the deformations $(\hat{\xi}, \hat{\eta}, \hat{\zeta})$, the clamped boundary conditions are

$$\hat{\xi} = \hat{\eta} = \hat{\zeta} = \frac{\partial \hat{\xi}}{\partial Z} = 0 \quad \text{at } Z = 0, \ell. \quad (3.32)$$

A depiction of the clamped boundary condition may be seen in Figure 3.4. In the model derived by Whittaker *et al.* (2010d) and in the model derived in Chapter 2, it is not possible to satisfy these clamped boundary conditions. In order to see why, we consider how the equations governing the wall mechanics in each model are derived.

The starting point for modelling the wall mechanics in each of the previous models is the Kirchhoff–Love shell equations (Flügge, 1972; Søndergaard, 2007), which have an axial order of 8. These equations are then reduced to a single PDE in the azimuthal deformation $\hat{\eta}$, using asymptotic methods based on the regime described in (3.26). Details of this reduction may be found in §2.3. The resulting PDE has the following form

$$\mathcal{F} \frac{\partial^2}{\partial Z^2} \mathcal{L}_2(\hat{\eta}) - \mathcal{L}_6(\hat{\eta}) = -p_{\text{tm}}(Z), \quad (3.33)$$

where \mathcal{L}_n is an n th-order linear differential operator in τ , and p_{tm} is the dimensionless transmural pressure. The normal $\hat{\xi}$ and axial $\hat{\zeta}$ displacements have been eliminated from the equation using the asymptotic result that, geometrically, the shear and azimuthal stretching in the tube wall is negligible. These constraints allow $\hat{\xi}$ and $\hat{\zeta}$ to be written in terms of $\hat{\eta}$ at leading order.

As the asymptotic analysis neglects the terms that arise from axial bending and in-plane shearing, both of which have higher-order derivatives in the axial direction, the axial order of the system is reduced from 8 to 2. Since the axial order of the system has been reduced, it is not possible for a solution of (3.33) to satisfy the clamped boundary conditions (3.32). Indeed it is only possible to set one quantity at each end of the tube. In the work by Whittaker *et al.* (2010d) and in the model in Chapter 2, the chosen conditions are

$$\hat{\eta} = 0 \quad \text{at} \quad Z = 0, \ell.$$

The fact that we have negligible azimuthal stretching also sets $\hat{\zeta} = 0$ at the tube ends. Hence, the conditions on the deformations satisfied within the two models are

$$\hat{\xi} = \hat{\eta} = 0 \quad \text{at} \quad Z = 0, \ell. \quad (3.34)$$

These form the Dirichlet parts of a non-standard condition termed ‘sliding’, which also sets zero axial stress perturbation and zero torque at the tube ends. It is noted that the solutions of the model by Whittaker *et al.* (2010d) and the model in Chapter 2 do not satisfy these conditions on the stresses exactly, but the solutions are closer to satisfying these conditions than the full clamped conditions (3.32).

Physically, these sliding conditions ensure that the normal and azimuthal displacements are set to be zero where the elastic-walled tube joins the rigid tubes in the Starling resistor. However, unlike when the clamped boundary conditions are satisfied, the axial displacements $\hat{\zeta}$ (set by zero axial stress perturbation) and the axial gradient of the tube $\partial\hat{\xi}/\partial Z$ (set by zero torque) are not necessarily set to zero at the tube ends here.

A step towards satisfying the full clamped boundary conditions (3.32) is taken by Whittaker (2015). In his work, the effects of in-plane shear are included in a shear-relaxation boundary layer at the ends of the tube. The inclusion of the in-plane shear terms raises the axial order of the system from 2 to 6, which allows the following six boundary conditions on the deformations to be satisfied

$$\hat{\xi} = \hat{\eta} = \hat{\zeta} = 0 \quad \text{at} \quad Z = 0, \ell. \quad (3.35)$$

These form the Dirichlet parts of the canonical ‘pinned’ boundary conditions, which also set the ends of the tube to have zero torque. Again, this condition on the torque is not satisfied exactly by the solution to the model derived by Whittaker (2015). However, this solution models the pinned boundary conditions more closely than the clamped boundary conditions (3.32).

A depiction of these pinned boundary conditions is seen in Figure 3.4. From the figure, we see that with these conditions, there is no displacement in the elastic-walled tube where it joins onto the rigid tube, which is an improvement on the Dirichlet parts of the sliding conditions (3.34). However, the elastic-walled tube joins the rigid tube at a non-zero axial gradient. This is in opposition with the stronger clamped boundary condition which forces the axial gradient as well as the displacements to be zero at the interfaces between the elastic and rigid tubes.

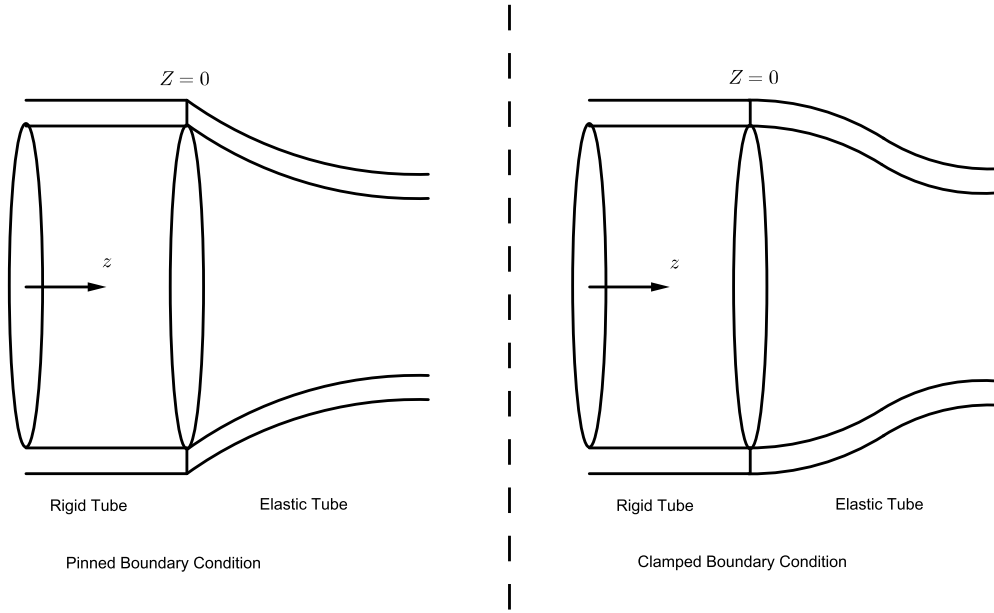


Figure 3.4: The pinned and clamped boundary conditions to be satisfied at the interfaces $Z = 0, \ell$ between the rigid and elastic regions of the tube.

In order to satisfy the condition on the axial gradient $\partial\xi/\partial Z$ within the clamped boundary conditions (3.32), we need another boundary layer where the axial bending terms are reintroduced to the problem. The inclusion of these bending terms returns the axial order of the problem to 8, which is high enough for the full clamped boundary conditions to be satisfied.

3.5 Consideration of the Shear-Relaxation Layer Found by Whittaker (2015)

The shear-relaxation boundary layer studied by Whittaker (2015) must be taken into account when attempting to satisfy the clamped boundary conditions (3.32). It is therefore convenient to review the work done by Whittaker (2015). An overview of this work is now provided.

In the study carried out by Whittaker (2015), the set-up described in §3.3 is considered. As in the model derived by Whittaker *et al.* (2010d) and derived in Chapter 2, the Kirchhoff–Love shell equations are used to model the wall mechanics, albeit using the smaller axial scale $x^2 = aZ$ as opposed to the scale $x^2 = alz$ used in previous models.

By applying an asymptotic analysis based on the parameter regime (3.26), appropriate governing equations are derived for the deformations $(\hat{\xi}, \hat{\eta}, \hat{\zeta})$ that hold true in a boundary layer near the tube ends. The boundary-layer width is chosen so that these governing equations now include terms that arise from in-plane shearing at leading order. The addition of these terms gives rise to a system that is now 6th-order in the axial direction. Hence, it is possible to satisfy the six deformation conditions (3.35) (three at each end of the tube) that form the Dirichlet parts of the pinned boundary conditions.

Within the governing equations, there are terms that are proportional to a new dimensionless parameter $\tilde{\mathcal{F}}$, related to the dimensionless axial tension \mathcal{F} by

$$\tilde{\mathcal{F}} = \frac{\delta^2 \ell^2 \mathcal{F}}{12(1 - \nu^2)}. \quad (3.36)$$

Whittaker (2015) found that the shear-relaxation layer only has a significant effect on the boundary conditions of the interior solution when $\tilde{\mathcal{F}} \ll 1$.

Taking the limit $\tilde{\mathcal{F}} \rightarrow 0$, it is found that the boundary layer here splits into two distinct sub-layers: an inner layer with thickness $O(\tilde{\mathcal{F}}^{1/2})$ and an outer layer with thickness $O(\tilde{\mathcal{F}}^{-1/2})$. It is found that the in-plane stresses have different orders of magnitude in each layer. Because of this, although the deformations $(\hat{\xi}, \hat{\eta}, \hat{\zeta})$ are the same magnitude in both the inner and outer layers, certain combinations of them have different sizes in the two layers. This results in some leading-order cancellations in the governing equations.

Solving the systems within the inner and outer shear layers, Whittaker (2015) has determined the leading-order in-plane stresses and deformations within the two layers. The Fourier coefficients of the first Fourier modes of

these stresses and deformations in the limit of a circular cross-section may be seen in Figures 3.5 and 3.6. From the figures, it is seen that the stresses and displacements have different behaviours in a small region near $Z = 0$ compared to the rest of the domain, displaying the presence of the two layers within the shear-relaxation layer.

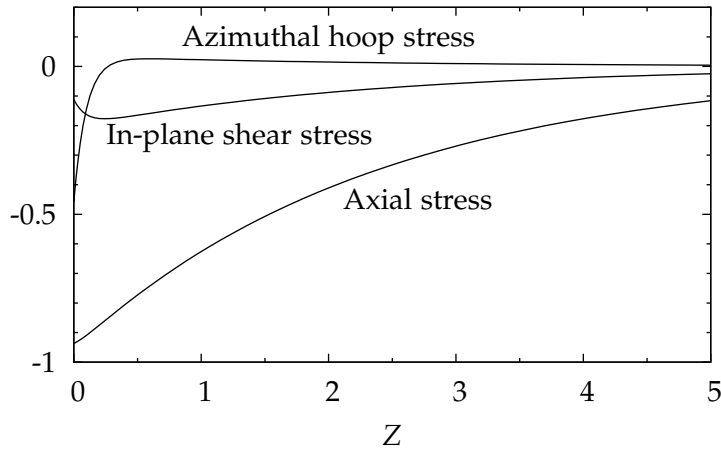


Figure 3.5: Solutions for the Fourier coefficients of the first Fourier modes of the in-plane stresses in the shear-relaxation layer, with $\tilde{\mathcal{F}} = 0.01$, in the limit of a circular cross-section.

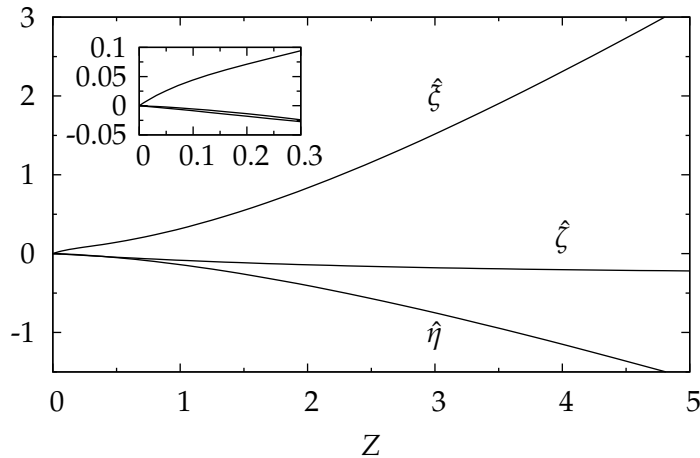


Figure 3.6: Solutions for the Fourier coefficients of the first Fourier modes of the deformations in the shear-relaxation layer, with $\tilde{\mathcal{F}} = 0.01$, in the limit of a circular cross-section. The inset displays the behaviour near $Z = 0$ more clearly.

Whittaker (2015) found that the inner shear layer allows the azimuthal hoop stress to decay to its required value in the outer layer, while leaving the shear and axial stresses approximately constant in Z . The outer shear layer then allows the decay of the shear and axial stresses so that they match with the stresses in the bulk solution as $Z \rightarrow \infty$. The outer layer also enables the axial deformation $\hat{\zeta}$ to grow to the value needed to match onto the bulk solution as $Z \rightarrow \infty$.

The solutions of the deformations and stresses within the inner and outer layers are considered later on when we introduce the new axial-bending boundary layer which must interact with the shear-relaxation layer.

3.6 Finding an Estimate for the Bending Boundary-Layer Width

We now consider a boundary layer at the ends of the elastic-walled tube with a small enough axial scale that the axial-bending terms within the Kirchhoff–Love shell equations appear at leading order. The inclusion of these axial-bending terms will ensure that the governing equations in this bending boundary layer have an axial order of 8, allowing the full clamped boundary conditions (3.32) to be satisfied.

To determine how this bending layer and the shear-relaxation layer found by Whittaker (2015) interact with each other, we must find an appropriate estimate for the width of the bending layer. This width is denoted δ_B . The size of δ_B must then be compared with the size of the inner and outer shear-relaxation layers to determine the arrangement of these boundary layers near the ends of the tube.

As a starting point for finding an estimate for δ_B , we consider a set of nonlinear partial differential equations known as the Föppl–von Kármán equations (Landau & Lifshitz, 1959). These equations are used to model the large deflections of a flat, thin plate and are as follows

$$K\nabla^4 w - d \frac{\partial}{\partial x^\beta} \left(\sigma_{\alpha\beta} \frac{\partial w}{\partial x^\alpha} \right) = P, \quad (3.37)$$

$$\frac{\partial \sigma_{\alpha\beta}}{\partial x^\beta} = 0. \quad (3.38)$$

Here d and K are the thickness and bending stiffness of the plate, w is the dimensional normal deflection of the plate, (x^1, x^2) are dimensional Lagrangian coordinates parameterizing the midplane of the thin plate and $\sigma_{\alpha\beta}$ is the Cauchy

stress tensor. (The indices α, β can take the values of 1 or 2.) The term P represents the dimensional, external, normal force on the plate.

It is noted that as we are studying a curved shell rather than a flat plate, the Föppl–von Kármán equations will not model the bending layer in the tube exactly. However, for the axial-bending terms to appear at leading order within the governing equations in the bending layer, we must have $\delta_B \ll 1$. As such, the azimuthal variation will be slow in the bending layer and we should be able to obtain the correct size of the bending boundary-layer width using this theory.

Assuming no variation in the azimuthal x^1 direction, we may reduce the Föppl–von Kármán equations (3.37), (3.38) to the following two-dimensional problem

$$K \frac{\partial^4 w}{\partial (x^2)^4} - d \frac{\partial}{\partial x^2} \left(\sigma_{22} \frac{\partial w}{\partial x^2} \right) = p_{\text{tm}}^*, \quad (3.39)$$

$$\frac{\partial \sigma_{22}}{\partial x^2} = 0, \quad (3.40)$$

where the dimensional transmural pressure p_{tm}^* has been included as the only external force.

We now nondimensionalize the terms within (3.39) and (3.40). Using the expression (3.29) for the deformation of the tube wall, the normal deformation w may be written as

$$w = (\mathbf{r} - \mathbf{r}_0) \cdot \hat{\mathbf{n}} = \frac{\Delta a}{\ell h} \hat{\xi}. \quad (3.41)$$

Although $\hat{\xi} = O(\ell)$ when $Z = O(\ell)$ from (3.31), the size of $\hat{\xi}$ will decrease to some magnitude of $O(\Delta_B)$ as we move into the bending layer, where $Z = O(\delta_B)$. To determine the sizes of the terms in (3.39) and (3.40), we must determine the size of $\hat{\xi}$ in the bending layer. Whittaker *et al.* (2010d) found that as the axial scale becomes small in the bulk solution, $\hat{\xi}$ behaves linearly in the axial direction. From this property, the ratio of the size of the deformation to the axial scale must be the same in the bending layer and outer solution. Hence, we have the relation $\Delta_B/\delta_B = 1$. Rearranging this, we find $\Delta_B = \delta_B$ which in turn gives

$$\hat{\xi} = O(\delta_B), \quad \text{when } Z = O(\delta_B).$$

For convenience, we rewrite $\hat{\xi}$ as

$$\hat{\xi} = \delta_B h \xi_B, \quad (3.42)$$

where ξ_B is $O(1)$ in the bending layer and the factor of $h(\tau)$ has been included to remove any azimuthal dependence from the reduced Föppl–von Kármán equations (3.39), (3.40). Substituting this into (3.41), it is found that

$$w = (\mathbf{r} - \mathbf{r}_0) \cdot \hat{\mathbf{n}} = \frac{\Delta a \delta_B}{\ell} \xi_B. \quad (3.43)$$

The Lagrangian coordinate x^2 is non-dimensionalized as

$$x^2 = a \delta_B z_B, \quad (3.44)$$

where $z_B = O(1)$ in the bending boundary layer. As the dominant stress in the axial direction of the tube is the axial pre-stress $F/(2\pi ad)$, we must have

$$\sigma_{22} = \frac{F}{2\pi ad} = \frac{K\ell^2 \mathcal{F}}{a^2 d}, \quad (3.45)$$

where we have used the definition of \mathcal{F} in (3.26). Finally, we non-dimensionalize the transmural pressure p_{tm}^* using the same scaling (2.17) used in §2.3, that is

$$p_{\text{tm}}^* = \frac{\Delta(t)K}{a^3} p_{\text{tm}}, \quad (3.46)$$

where we have the dimensionless transmural pressure $p_{\text{tm}} = O(1)$.

Substituting (3.43)–(3.46) into the reduced Föppl–von Kármán equations (3.39), (3.40), it is seen that (3.40) is satisfied and, after cancelling a factor of $\Delta K/a^3$, (3.39) yields

$$\frac{1}{\delta_B^3 \ell} \frac{\partial^4 \xi_B}{\partial z_B^4} - \frac{\ell}{\delta_B} \mathcal{F} \frac{\partial^2 \xi_B}{\partial z_B^2} = p_{\text{tm}}. \quad (3.47)$$

Here, the first term corresponds to axial bending and the second term is due to axial tension. It is noted that the factor of ℓ^2 in the axial tension term comes from the non-dimensionalization of the axial tension and not from the geometric properties of the tube.

As ξ_B , z_B and p_{tm} are all $O(1)$ in the bending layer, and $\ell \gg 1$, $\delta_B \ll 1$, $\mathcal{F} = O(1)$, it is seen that the axial tension term in (3.47) is much larger than the transmural pressure term. Hence, the pressure term cannot appear at leading order and the only dominant balance in (3.47) can be between the axial bending and axial tension terms. For these terms to balance, we must have

$$\delta_B = O(\mathcal{F}^{-\frac{1}{2}} \ell^{-1}) = O\left(\left(\frac{2\pi K}{aF}\right)^{\frac{1}{2}}\right), \quad (3.48)$$

where we have used (3.26c) to rewrite the value of δ_B in terms of the axial tension force F . Hence, the bending boundary-layer width is dependent upon the axial tension of the tube wall, but not on ℓ .

3.7 The Different Regimes

Using the estimate (3.48) for the width δ_B of the bending layer, it is found that the problem is split into multiple cases depending on how the estimate of δ_B compares with the sizes of the tube wall thickness and the inner and outer shear-relaxation layers studied by Whittaker (2015). These cases may be seen in Figure 3.7.

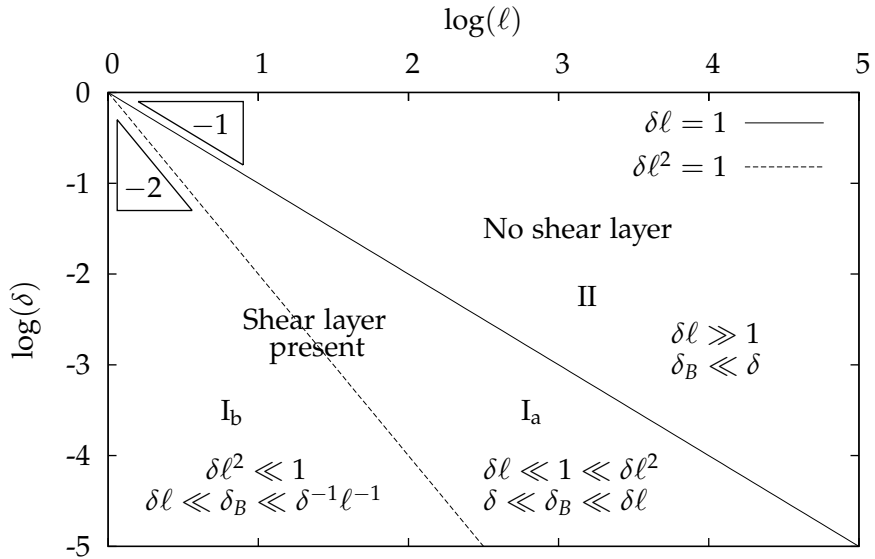


Figure 3.7: The different cases of the problem. These depend on how the estimate of the dimensionless thickness of the axial-bending boundary layer $\delta_B \sim \mathcal{F}^{-1/2}\ell^{-1}$ compares with the dimensionless wall thickness δ and the two shear-layer thicknesses $\delta^{-1}\ell^{-1}$ and $\delta\ell$.

In the first case, regime I, we consider the scenario where the thickness δ of the tube wall is much smaller than the estimate $\delta_B \sim \mathcal{F}^{-1/2}\ell^{-1}$ of the thickness of the bending layer. Thus, $\delta \ll \mathcal{F}^{-1/2}\ell^{-1}$ and as $\mathcal{F} = O(1)$, this implies $\delta\ell \ll 1$. In this case, we should still be able to use the Kirchhoff–Love shell equations to model the wall mechanics in the bending layer. This is because in order for Kirchhoff–Love shell theory to hold, the thickness of the tube wall must be the smallest geometric parameter. In this case, as the wall thickness is expected to be smaller than the bending-layer width, this property holds. The scenario $\delta\ell \ll 1$ corresponds to the limit $\tilde{\mathcal{F}} \rightarrow 0$ taken by Whittaker (2015) in his work on introducing a shear-relaxation boundary layer to the problem. In this case, the shear layer modelled by Whittaker (2015) is found to have a significant effect on the solution and must be considered.

As the shear-relaxation layer is split into an inner shear layer of width $O(\delta\ell)$ and an outer shear layer of width $O(\delta^{-1}\ell^{-1})$, regime I is split into two sub-cases. In the first sub-case, regime I_a , the estimate of the width of the bending layer is smaller than the width of the inner shear layer ($\delta \ll \delta_B \ll \delta\ell$). Hence, we have $\delta \ll \ell^{-1} \ll \delta\ell$, which implies $\delta\ell \ll 1 \ll \delta\ell^2$. In the second sub-case, regime I_b , the estimate of the bending boundary-layer width is larger than the inner shear-layer width ($\delta_B \gg \delta\ell$), and we have $\delta\ell \ll \ell^{-1}$. This in turn implies $\delta\ell^2 \ll 1$. We note that as $\delta_B \sim \ell^{-1}$ in the estimate (3.48), $\delta_B \ll \delta^{-1}\ell^{-1}$ and the bending-layer width is still smaller than the outer shear-layer width.

In the second case, regime II, the estimate of the bending layer thickness is much smaller than the tube wall thickness ($\delta_B \ll \delta$). Applying the estimate (3.48) and rearranging, it is found that in this case, $\delta\ell \gg 1$. As this corresponds to $\tilde{\mathcal{F}} \gg 1$, the shear-relaxation layer is not expected to be significant here. In this regime, it is expected that the Kirchhoff–Love shell equations can no longer be used to describe the wall mechanics within the bending layer. This is due to the fact that for the Kirchhoff–Love shell equations to accurately model the wall mechanics, the thickness of the tube wall must be smaller than the other geometric parameters of the wall. Here, the axial scale being considered is smaller than the wall thickness, and this condition is violated. Hence, a different model must be applied.

3.8 Overview of Chapters 4–7

In the next four chapters, we will concentrate on modelling the bending layer in each of the regimes I_a , I_b and II.

We first turn our attention to regime I_a in Chapter 4. Here, the Kirchhoff–Love shell equations are used to model the tube wall. By taking the parameter regime (3.26) along with $\delta\ell \ll 1 \ll \delta\ell^2$, the leading-order force-balance equations are derived. To enable a sensible dominant balance in these equations, it is found that the bending boundary-layer width δ_B must be $O(\mathcal{F}^{-1/2}\ell^{-1})$. This is in agreement with the estimate (3.48). By solving the leading-order force-balance equations, expressions for the leading-order deformations and area change within the bending layer are found.

In Chapter 5, regime I_b is considered. Again, the Kirchhoff–Love shell equations are used to model the tube wall. The parameter regime (3.26) along with $\delta\ell^2 \ll 1$ is then taken to find the leading-order force-balance equations. It

is found that in this regime, the inner-shear layer is not needed and the bending layer is situated at the elastic-walled tube ends. The bending layer then matches onto the outer shear layer. It is also found that the bending boundary-layer width is $\delta_B = O(\delta^{1/2})$ in this regime. This is different to the estimate (3.48) and the value found in regime I_a in Chapter 4. The reason for this is because we now have azimuthal and axial stretching terms appearing within the leading-order normal force-balance equation. This is different from regime I_a, where these terms are small enough that they do not appear at leading order. This is also different from the toy model in §3.6, where the reduced Föppl–von Kármán equations (3.39), (3.40) used to derive the estimate (3.48) do not capture the effects of azimuthal and axial stretching. By performing an asymptotic analysis, the leading-order deformations and their first-order corrections in the bending layer are determined.

Finally, in Chapters 6 and 7 we consider regime II. As the Kirchhoff–Love shell equations are no longer expected to be valid in this regime, we instead use a two-dimensional linear elastic model to describe the wall mechanics. The deformations that arise within this regime are then both numerically calculated and approximated analytically. With this model, a bending layer with width $\delta_B = O(\mathcal{F}^{-1/2}\ell^{-1})$ is found in the case $\delta\ell \ll 1$. This is in agreement with the boundary layer found in regime I_a in Chapter 4, and the estimate (3.48). However, in the case $\delta\ell \gg 1$, we instead find a different boundary layer with width $\delta_B = O(\delta^2\ell\mathcal{F}^{1/2})$. This is larger than the estimate (3.48) and larger than the tube wall thickness δ . Despite this, we find that Kirchhoff–Love shell theory is still unable to model this boundary layer. This is due to the fact that the particles normal to the midplane of the tube wall in the undeformed configuration must stay normal to the midplane when the tube is deformed for Kirchhoff–Love shell theory to be applicable. Within the boundary layer, this is not the case and Kirchhoff–Love shell theory cannot accurately model the boundary layer. It is found that this boundary layer is actually a transverse shear-relaxation boundary layer, although not the same as the shear-relaxation layer studied by Whittaker (2015).

Chapter 4

The Bending Boundary Layer in Regime I_a ($\delta\ell \ll 1 \ll \delta\ell^2$)

4.1 Introduction

In this chapter, we consider the problem described in Chapter 3, where we introduce an axial-bending boundary layer to the model of flow through an elastic-walled tube derived in Chapter 2. This bending layer will allow us to apply the canonical clamped boundary conditions at the ends of the elastic-walled tube, where it is clamped onto two fixed rigid tubes.

Here, we consider regime I_a where the dimensionless tube wall thickness δ and tube length ℓ are set so that $\delta\ell \ll 1 \ll \delta\ell^2$. In this case, a shear-relaxation layer studied by Whittaker (2015) (details of which may be found in §3.5) is found to have a significant effect on the solution in the bulk of the tube. Therefore, this shear layer must be considered. It is noted that the shear layer is split into two sub-layers: an inner layer of width $O(\delta\ell)$, and an outer layer of width $O(\delta^{-1}\ell^{-1})$.

From the estimate for the width of the bending layer derived from the toy model in §3.6, we expect the dimensionless bending boundary-layer width δ_B to be larger than the dimensionless tube wall thickness δ . As such, the Kirchhoff–Love shell equations (Flügge, 1972; Søndergaard, 2007) may still be used as a model for the wall mechanics. However, we also expect δ_B to be smaller than the widths of both the inner and outer shear-relaxation layers. Hence in this regime, we expect the axial-bending boundary layer to be situated at the ends of the elastic-walled tube. The bending layer then matches onto the two shear-relaxation boundary layers, which in turn match onto the bulk

solution in the main region of the tube. The arrangement of these boundary layers along the dimensionless axial coordinate $Z \in [0, \ell]$ introduced in Chapter 3 and used in the work by Whittaker (2015), may be seen in Figure 4.1.

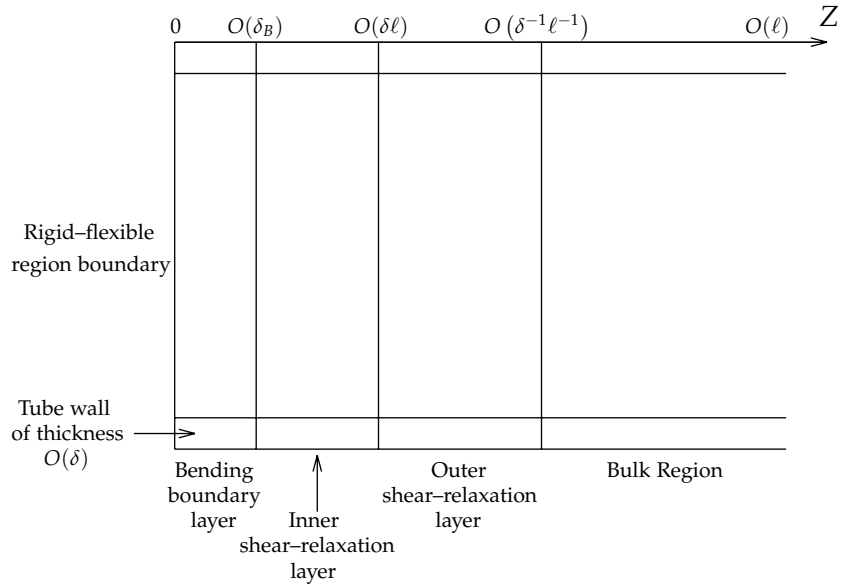


Figure 4.1: The arrangement of the boundary layers in a cross section through the centre point and along the length of the tube, in regime I_a where $\delta\ell \ll 1 \ll \delta\ell^2$. We expect to have: $\delta \ll \delta_B \ll \delta\ell \ll 1 \ll \delta^{-1}\ell^{-1} \ll \ell$.

We later find that the deformations in the bending and shear-relaxation boundary layers only depend on the properties of the tube wall, which are uniform along the wall, and not on the properties of the fluid inside the tube. As such, the boundary layers at the interfaces between the flexible and rigid parts of the tube will behave the same at both the upstream and downstream interface. Hence, we only need to calculate the deformations at one of these interfaces. In this chapter, we will concentrate on modelling the bending layer at the upstream end ($Z = 0$) of the elastic-walled tube.

This chapter is arranged as follows. In §4.2, the mathematical set-up of the tube and its deformations is provided, and in §4.3, the behaviour of the deformations within the inner shear-relaxation layer is considered. Estimates for the sizes of the deformations in the bending layer are calculated in §4.4, and the boundary and matching conditions for the deformations in the bending layer are derived in §4.5. In §4.6, the tensors and constitutive laws needed in the problem are provided, and in §4.7 the governing force-balance equations are derived and the sizes of the terms within the force-balance equations are calculated. In §4.8–§4.10, the leading-order force-balance equations are found

and the leading-order deformations within the bending layer are calculated. The area change in the bending layer due to the leading-order normal deformation is calculated in §4.11. Finally in §4.12 and §4.13, the corrections to the deformations in the inner shear, outer shear and bulk layers, due to the leading-order deformations in the bending layer, are determined.

4.2 Mathematical Set-up

We consider the set-up described in §3.3 and depicted in Figure 4.2. The full details of the non-dimensionalization of this problem may be found in §3.3. Here, we have an initially elliptical elastic-walled tube with dimensionless

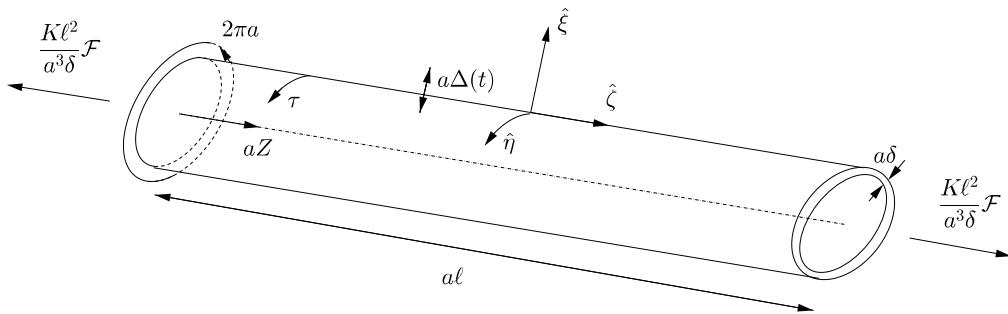


Figure 4.2: The set-up of the undeformed, elliptical, elastic-walled tube, showing the dimensionless coordinates and variables.

length $\ell \gg 1$ and dimensionless wall thickness $\delta \ll 1$. This tube is subject to a dimensionless uniform axial tension $\mathcal{F} = O(1)$ in its undeformed configuration, and deformations of dimensionless amplitude $\Delta(t) \ll 1$ are induced by a dimensionless transmural pressure p_{tm} . The amplitude $\Delta(t)$ is assumed to be slowly varying in dimensionless time t . The tube wall has dimensionless mass M per unit area, Poisson's ratio ν and bending stiffness K , and we also introduce the parameter $\tilde{\mathcal{F}}$ given by

$$\tilde{\mathcal{F}} = \frac{\delta^2 \ell^2 \mathcal{F}}{12(1 - \nu^2)} \ll 1. \quad (4.1)$$

This parameter appears in the model of the shear-relaxation layer derived by Whittaker (2015), which is considered later on.

The midplane of the tube wall is parameterized with two dimensionless Lagrangian surface coordinates $\tau \in [0, 2\pi)$, $Z \in [0, \ell]$, which represent arc length in the azimuthal and axial directions respectively. These are related to

their dimensional counterparts (x^1, x^2) by $dx^1 = ah(\tau)d\tau$, $dx^2 = adZ$, where a is the typical radial scale of the tube and the scale factor $h(\tau)$ is defined as

$$h(\tau) = c(\sinh^2 \sigma_0 + \sin^2 \tau)^{\frac{1}{2}},$$

where σ_0 is a parameter setting the ellipticity of the tube, and $c(\sigma_0)$ is a known function dependent on the ellipticity of the tube.

Using these coordinates, the dimensional position $\mathbf{r}_0(\tau, Z)$ of the tube wall in the undeformed configuration is defined to be

$$\mathbf{r}_0(\tau, Z) = a \begin{pmatrix} c \cosh \sigma_0 \cos \tau \\ c \sinh \sigma_0 \sin \tau \\ Z \end{pmatrix}. \quad (4.2)$$

Denoting the position of the tube wall in its deformed configuration as \mathbf{r} , the deformation $\mathbf{r} - \mathbf{r}_0$ of the tube wall may be written as

$$\mathbf{r} - \mathbf{r}_0 = \frac{\Delta(t)a}{\ell} \left(\frac{1}{h(\tau)} [\hat{\xi}(\tau, Z, t)\hat{\mathbf{n}} + \hat{\eta}(\tau, Z, t)\hat{\mathbf{t}}] + \hat{\zeta}(\tau, Z, t)\hat{\mathbf{z}} \right). \quad (4.3)$$

This is the same representation of the deformation used by Whittaker (2015) in his study of the shear-relaxation layer which must be considered in this regime. The vectors $\hat{\mathbf{n}}$, $\hat{\mathbf{t}}$ and $\hat{\mathbf{z}}$ are unit vectors in the normal, azimuthal and axial directions of the undeformed tube wall, and the dimensionless functions $(\hat{\xi}, \hat{\eta}, \hat{\zeta})$ represent the normal, azimuthal and axial deformations of the tube wall.

4.3 Consideration of the Inner Shear-Relaxation Layer by Whittaker (2015)

As the bending boundary layer has a smaller width than the shear-relaxation layer studied by Whittaker (2015), the bending layer must match onto a modified shear-relaxation layer. In particular, it must match onto the inner shear layer which is the smallest sub-layer within the shear-relaxation layer. Hence, to determine the sizes of the deformations within the bending layer, along with the matching conditions the deformations must satisfy as we exit the bending layer, the behaviour of the inner shear layer must be considered.

When deriving a model of the shear-relaxation layer, Whittaker (2015) used the scaled axial coordinate $\hat{z} = \tilde{\mathcal{F}}^{-\frac{1}{2}}Z$ to describe the axial behaviour of the deformations within the inner shear layer. Using this coordinate, Whittaker

(2015) found asymptotic approximations for the deformations $\hat{\xi}, \hat{\eta}, \hat{\zeta}$ within the inner shear layer. These approximations are denoted $\hat{\xi}_s, \hat{\eta}_s, \hat{\zeta}_s$ here and they satisfy the Dirichlet parts (3.35) of the pinned boundary conditions defined in §3.4. However, they do not satisfy the full clamped boundary conditions (3.32). As such, the bending boundary layer we introduce will force a correction to the approximations $\hat{\xi}_s, \hat{\eta}_s, \hat{\zeta}_s$. This correction will only take effect at higher orders in the asymptotic approximations, and thus we may still use the leading-order approximations to estimate the sizes of the deformations within the bending layer.

We consider the leading-order behaviour of the approximations $\hat{\xi}_s, \hat{\eta}_s, \hat{\zeta}_s$ as found by Whittaker (2015) when $\hat{z} \rightarrow 0$. Taking the Taylor series of $\hat{\xi}_s, \hat{\eta}_s, \hat{\zeta}_s$ about $\hat{z} = 0$ yields at leading order

$$\hat{\xi}_s \sim \frac{\tilde{\mathcal{F}}^{\frac{1}{2}} h(\tau) \nu |\bar{B}(\tau)| \hat{z}}{12(1 - \nu^2) \bar{B}(\tau)} \sum_{n=1}^{\infty} B_n(t) Y_n(\tau), \quad (4.4)$$

$$\begin{aligned} \hat{\eta}_s \sim & -\frac{\tilde{\mathcal{F}}^{\frac{3}{2}}}{12(1 - \nu^2)} \sum_{n=1}^{\infty} B_n(t) \frac{\partial}{\partial \tau} \left\{ Y_n(\tau) \left(\frac{[1 + \nu(2 + \nu)] \hat{z}^2}{2} - \frac{2\nu(1 + \nu) \hat{z}}{|\bar{B}(\tau)|} \right) \right. \\ & \left. - \frac{2(1 + \nu)}{\mu_n} \left[\frac{1}{h(\tau) |\bar{B}(\tau)|^2} \frac{\partial}{\partial \tau} \left(\frac{Y'_n(\tau)}{h(\tau)} \right) - Y_n(\tau) \right] \hat{z} \right\}, \end{aligned} \quad (4.5)$$

$$\hat{\zeta}_s \sim \frac{\tilde{\mathcal{F}}^{\frac{1}{2}}}{12} \sum_{n=1}^{\infty} B_n(t) Y_n(\tau), \quad (4.6)$$

when $\hat{z} \rightarrow 0$. Here, ' denotes the differential with respect to τ . The π -periodic, orthogonal functions $Y_n(\tau)$ are the eigenfunctions of the operator

$$\mathcal{L} \equiv \frac{1}{h} \frac{\partial}{\partial \tau} \frac{1}{h} \frac{\partial}{\partial \tau} \left(\frac{1}{\bar{B}^2 h} \frac{\partial}{\partial \tau} \frac{1}{h} \frac{\partial}{\partial \tau} - 1 \right), \quad (4.7)$$

and μ_n^2 are the corresponding distinct positive eigenvalues ordered such that $0 < \mu_1 < \mu_2 < \mu_3 \dots$. For finite σ_0 , these eigenfunctions and eigenvalues can only be found numerically. Finally, the $B_n(t)$ are arbitrary $O(1)$ functions of t setting the amplitude of each eigenmode of the deformations and $\bar{B}(\tau)$ is the dimensionless base-state azimuthal curvature, given as

$$\bar{B}(\tau) = -\frac{c^2 \sinh 2\sigma_0}{2h^3}.$$

4.4 Estimating The Sizes of the Deformations in the Bending Layer

Using the approximations (4.4)–(4.6) for the leading-order deformations in the inner shear layer as $\hat{z} \rightarrow 0$, it is possible to estimate the sizes of the deformations

in the bending layer. Denoting the width of the bending layer as δ_B , we have that $Z = O(\delta_B)$ in the bending layer, which implies $\hat{z} = O(\delta_B \tilde{\mathcal{F}}^{-\frac{1}{2}})$. The precise boundary-layer width δ_B is undetermined at this point, but will be found later in §4.8 when the normal force-balance equation is considered. Substituting the size of \hat{z} into the approximations (4.4)–(4.6) and applying the definition (4.3) for the total deformation $\mathbf{r} - \mathbf{r}_0$, we find

$$(\mathbf{r} - \mathbf{r}_0) \cdot \hat{\mathbf{n}} = O\left(\frac{\Delta a \delta_B}{\ell}\right), \quad (4.8)$$

$$(\mathbf{r} - \mathbf{r}_0) \cdot \hat{\mathbf{t}} = O\left(\frac{\Delta a \delta_B}{\ell} \tilde{\mathcal{F}}\right), \quad (4.9)$$

$$(\mathbf{r} - \mathbf{r}_0) \cdot \hat{\mathbf{z}} = O\left(\frac{\Delta a \delta_B}{\ell} \tilde{\mathcal{F}}^{\frac{1}{2}}\right), \quad (4.10)$$

within the bending layer. Using this, we rewrite the representation (4.3) of the total deformation as

$$\mathbf{r} - \mathbf{r}_0 = \frac{\Delta(t) a \delta_B}{\ell} \left(\frac{1}{h(\tau)} [\xi_B(\tau, z_B, t) \hat{\mathbf{n}} + \tilde{\mathcal{F}} \eta_B(\tau, z_B, t) \hat{\mathbf{t}}] + \tilde{\mathcal{F}}^{\frac{1}{2}} \zeta_B(\tau, z_B, t) \hat{\mathbf{z}} \right), \quad (4.11)$$

where $\xi_B(\tau, z_B, t)$, $\eta_B(\tau, z_B, t)$, $\zeta_B(\tau, z_B, t)$ are $O(1)$ functions and we have introduced the new axial coordinate

$$z_B = \delta_B^{-1} Z, \quad (4.12)$$

which satisfies $z_B = O(1)$ in the bending layer. The scale factor $h(\tau)$ has once again been included for convenience.

4.5 Boundary and Matching Conditions

The boundary and matching conditions that should be applied in the bending layer are now derived. By comparing the expressions (4.3) and (4.11) for $\mathbf{r} - \mathbf{r}_0$, it is seen that

$$\hat{\xi} = \delta_B \xi_B, \quad \hat{\eta} = \delta_B \tilde{\mathcal{F}} \eta_B, \quad \hat{\zeta} = \delta_B \tilde{\mathcal{F}}^{\frac{1}{2}} \zeta_B. \quad (4.13)$$

Hence, the approximations for the deformations in the bending and inner shear layers must satisfy the matching conditions

$$\xi_B \sim \delta_B^{-1} \hat{\xi}_s, \quad \eta_B \sim \delta_B^{-1} \tilde{\mathcal{F}}^{-1} \hat{\eta}_s, \quad \zeta_B \sim \delta_B^{-1} \tilde{\mathcal{F}}^{-\frac{1}{2}} \hat{\zeta}_s, \quad \text{as } z_B \rightarrow \infty, \hat{z} \rightarrow 0. \quad (4.14)$$

When applying these matching conditions, it is convenient to express both \hat{z} and z_B in terms of an intermediate variable z_I with size $O(1)$ in a region

between the bending and inner shear layers. We define z_I as follows

$$\left(\tilde{\mathcal{F}}^{\frac{1}{2}}\delta_B^{-1}\right)^\alpha \hat{z} = z_I = \left(\tilde{\mathcal{F}}^{\frac{1}{2}}\delta_B^{-1}\right)^{\alpha-1} z_B, \quad \text{where } \frac{1}{2} < \alpha < 1. \quad (4.15)$$

It is noted that when $z_I = O(1)$, this also sets $z_B \rightarrow \infty$ and $\hat{z} \rightarrow 0$, as $\tilde{\mathcal{F}}^{\frac{1}{2}}\delta_B^{-1} \gg 1$. The condition $1/2 < \alpha$ has been set so that the order of the terms within the expressions for the bending layer deformations is retained as $z_B \rightarrow \infty$.

Using (4.13), we also rewrite the full clamped boundary conditions (3.32), seen in §3.4, in terms of ξ_B , η_B , ζ_B and z_B as follows

$$\xi_B = \frac{\partial \xi_B}{\partial z_B} = \eta_B = \zeta_B = 0 \quad \text{at } z_B = 0. \quad (4.16)$$

4.6 Tensor Notation and Constitutive Laws

The various tensors that are needed to derive the governing force-balance equations in the bending layer are now provided. We begin with defining the basis vectors \mathbf{a}_1 , \mathbf{a}_2 , and the unit normal \mathbf{a}_3 to the tube wall in the deformed state. These were first defined in equations (2.21), (2.22) in §2.3 and are given as

$$\mathbf{a}_\alpha = \frac{\partial \mathbf{r}}{\partial x^\alpha}, \quad \mathbf{a}_3 = \frac{\mathbf{a}_1 \times \mathbf{a}_2}{|\mathbf{a}_1 \times \mathbf{a}_2|}, \quad (4.17)$$

where α spans over (1, 2). Substituting the expressions (4.2), (4.11) for \mathbf{r}_0 , \mathbf{r} into (4.17) and neglecting terms of $O(\Delta^2)$ and higher, it can be shown that

$$\begin{aligned} \mathbf{a}_1 &= \hat{\mathbf{t}} + \frac{\Delta}{\ell h} \delta_B \left(\left[-\xi_B \bar{B}(\tau) + \tilde{\mathcal{F}} \frac{\partial}{\partial \tau} \left(\frac{\eta_B}{h} \right) \right] \hat{\mathbf{t}} + \left[\tilde{\mathcal{F}} \eta_B \bar{B}(\tau) + \frac{\partial}{\partial \tau} \left(\frac{\xi_B}{h} \right) \right] \hat{\mathbf{n}} \right. \\ &\quad \left. + \tilde{\mathcal{F}}^{\frac{1}{2}} \frac{\partial \zeta_B}{\partial \tau} \hat{\mathbf{z}} \right), \end{aligned} \quad (4.18)$$

$$\mathbf{a}_2 = \hat{\mathbf{z}} + \frac{\Delta}{\ell} \left(\frac{1}{h} \left[\frac{\partial \xi_B}{\partial z_B} \hat{\mathbf{n}} + \tilde{\mathcal{F}} \frac{\partial \eta_B}{\partial z_B} \hat{\mathbf{t}} \right] + \tilde{\mathcal{F}}^{\frac{1}{2}} \frac{\partial \zeta_B}{\partial z_B} \hat{\mathbf{z}} \right), \quad (4.19)$$

$$\mathbf{a}_3 = \hat{\mathbf{n}} - \frac{\Delta}{\ell h} \left(\delta_B \left[\tilde{\mathcal{F}} \eta_B \bar{B}(\tau) + \frac{\partial}{\partial \tau} \left(\frac{\xi_B}{h} \right) \right] \hat{\mathbf{t}} + \frac{\partial \xi_B}{\partial z_B} \hat{\mathbf{z}} \right). \quad (4.20)$$

With these it is possible to evaluate the metric tensor $a_{\alpha\beta}$, curvature tensor $b_{\alpha\beta}$ and in-plane and bending strain tensors, $\gamma_{\alpha\beta}$ and $\kappa_{\alpha\beta}$, in the bending boundary layer. These tensors are defined as

$$\begin{aligned} a_{\alpha\beta} &= \mathbf{a}_\alpha \cdot \mathbf{a}_\beta, & b_{\alpha\beta} &= \mathbf{a}_3 \cdot \frac{\partial \mathbf{a}_\alpha}{\partial x^\beta}, \\ \gamma_{\alpha\beta} &= \frac{1}{2}(a_{\alpha\beta} - \bar{a}_{\alpha\beta}), & \kappa_{\alpha\beta} &= -b_{\alpha\beta} + \bar{b}_{\alpha\beta} + 2\bar{b}_\alpha^\delta \gamma_{\delta\beta}. \end{aligned} \quad (4.21)$$

The definitions (4.21) are the same as (2.23), (2.24) and (2.32), used in §2.3. Substituting (4.18)–(4.20) into (4.21) and again neglecting terms of $O(\Delta^2)$ and

higher, we find

$$a_{\alpha\beta} = \bar{a}_{\alpha\beta} + \frac{\Delta}{\ell h} \begin{bmatrix} 2\delta_B \left[-\xi_B \bar{B} + \tilde{\mathcal{F}} \frac{\partial}{\partial \tau} \left(\frac{\eta_B}{h} \right) \right] & \tilde{\mathcal{F}} \frac{\partial \eta_B}{\partial z_B} + \delta_B \tilde{\mathcal{F}} \frac{1}{2} \frac{\partial \zeta_B}{\partial \tau} \\ \tilde{\mathcal{F}} \frac{\partial \eta_B}{\partial z_B} + \delta_B \tilde{\mathcal{F}} \frac{1}{2} \frac{\partial \zeta_B}{\partial \tau} & 2h \tilde{\mathcal{F}} \frac{1}{2} \frac{\partial \zeta_B}{\partial z_B} \end{bmatrix}, \quad (4.22)$$

$$b_{\alpha\beta} = \bar{b}_{\alpha\beta} + \frac{\Delta}{a\ell h} \begin{bmatrix} \delta_B (\beta_1 + \beta_2) & \tilde{\mathcal{F}} \bar{B} \frac{\partial \eta_B}{\partial z_B} + \frac{\partial}{\partial \tau} \left(\frac{1}{h} \frac{\partial \xi_B}{\partial z} \right) \\ \tilde{\mathcal{F}} \bar{B} \frac{\partial \eta_B}{\partial z_B} + \frac{\partial}{\partial \tau} \left(\frac{1}{h} \frac{\partial \xi_B}{\partial z} \right) & \frac{1}{\delta_B} \frac{\partial^2 \zeta_B}{\partial z^2} \end{bmatrix}, \quad (4.23)$$

$$\gamma_{\alpha\beta} = \frac{\Delta}{\ell h} \begin{bmatrix} \delta_B \left[-\xi_B \bar{B} + \tilde{\mathcal{F}} \frac{\partial}{\partial \tau} \left(\frac{\eta_B}{h} \right) \right] & \frac{1}{2} \left[\tilde{\mathcal{F}} \frac{\partial \eta_B}{\partial z_B} + \delta_B \tilde{\mathcal{F}} \frac{1}{2} \frac{\partial \zeta_B}{\partial \tau} \right] \\ \frac{1}{2} \left[\tilde{\mathcal{F}} \frac{\partial \eta_B}{\partial z_B} + \delta_B \tilde{\mathcal{F}} \frac{1}{2} \frac{\partial \zeta_B}{\partial \tau} \right] & h \tilde{\mathcal{F}} \frac{1}{2} \frac{\partial \zeta_B}{\partial z_B} \end{bmatrix}, \quad (4.24)$$

$$\kappa_{\alpha\beta} = \frac{\Delta}{a\ell h} \begin{bmatrix} \delta_B (\beta_1 - \beta_2) & \delta_B \tilde{\mathcal{F}} \frac{1}{2} \bar{B} \frac{\partial \zeta_B}{\partial \tau} - \frac{\partial}{\partial \tau} \left(\frac{1}{h} \frac{\partial \xi_B}{\partial z_B} \right) \\ -\frac{\partial}{\partial \tau} \left(\frac{1}{h} \frac{\partial \xi_B}{\partial z_B} \right) - \tilde{\mathcal{F}} \bar{B} \frac{\partial \eta_B}{\partial z_B} & -\frac{1}{\delta_B} \frac{\partial^2 \zeta_B}{\partial z_B^2} \end{bmatrix}, \quad (4.25)$$

where $\bar{a}_{\alpha\beta}$ is the 2×2 identity matrix, $\bar{b}_{\alpha\beta}$ is defined as

$$\bar{b}_{\alpha}^{\beta} = \frac{1}{a} \begin{bmatrix} \bar{B}(\tau) & 0 \\ 0 & 0 \end{bmatrix},$$

and β_1, β_2 are given by

$$\beta_1 = \bar{B} \left[-\xi_B \bar{B} + \tilde{\mathcal{F}} \frac{\partial}{\partial \tau} \left(\frac{\eta_B}{h} \right) \right], \quad \beta_2 = \frac{\partial}{\partial \tau} \left(\frac{1}{h} \left[\tilde{\mathcal{F}} \eta_B \bar{B} + \frac{\partial}{\partial \tau} \left(\frac{\xi_B}{h} \right) \right] \right). \quad (4.26)$$

Using these tensors, the in-plane stresses $N^{\alpha\beta}$ and in-plane bending moments $M^{\alpha\beta}$ may be determined. Flügge (1972) found the following linear constitutive laws relating $N^{\alpha\beta}, M^{\alpha\beta}$ to $a_{\alpha\beta}, b_{\alpha\beta}, \gamma_{\alpha\beta}, \kappa_{\alpha\beta}$

$$\begin{aligned} N^{\alpha\beta} = & \delta_2^{\alpha} \delta_2^{\beta} \frac{K \ell^2 \mathcal{F}}{a^2} + \frac{12}{a^2 \delta^2} K [(1-\nu) \gamma^{\alpha\beta} + \nu \gamma_{\lambda}^{\lambda} a^{\alpha\beta}] \\ & + K \left\{ \frac{(1-\nu)}{2} [2a^{\beta\delta} b^{\alpha\gamma} + a^{\beta\gamma} b^{\alpha\gamma} + a^{\alpha\delta} b^{\beta\gamma} - b_{\lambda}^{\lambda} (a^{\alpha\delta} a^{\beta\gamma} + a^{\alpha\gamma} a^{\beta\delta})] \right. \\ & \left. + \nu [a^{\alpha\beta} b^{\gamma\delta} + a^{\gamma\delta} b^{\alpha\beta} - a^{\alpha\beta} a^{\gamma\delta} b_{\lambda}^{\lambda}] \right\} \kappa_{\lambda\delta}, \end{aligned} \quad (4.27)$$

$$\begin{aligned} M^{\alpha\beta} = & K [-(1-\nu) (b_{\gamma}^{\alpha} \gamma^{\gamma\beta} - b_{\lambda}^{\lambda} \gamma^{\alpha\beta}) - \nu (b^{\alpha\beta} - b_{\lambda}^{\lambda} a^{\alpha\beta}) \gamma_{\mu}^{\mu} \\ & + \frac{1}{2} (1-\nu) (\kappa^{\alpha\beta} + \kappa^{\beta\alpha}) + \nu a^{\alpha\beta} \kappa_{\lambda}^{\lambda}], \end{aligned} \quad (4.28)$$

where δ_j^i is the Kronecker delta. Substituting the tensors (4.22)–(4.25) into the constitutive laws (4.27)–(4.28), the leading-order components of $N^{\alpha\beta}, M^{\alpha\beta}$ are calculated to be

$$N^{\alpha\beta} = \frac{K}{a^2} \begin{pmatrix} 0 & 0 \\ 0 & \ell^2 \mathcal{F} \end{pmatrix} + \frac{\Delta K}{a^2 \delta^2 \ell} \begin{pmatrix} 12 \tilde{\mathcal{F}} \frac{1}{2} \nu \frac{\partial \zeta_B}{\partial z_B} & \frac{6(1-\nu)}{h} \tilde{\mathcal{F}} \frac{\partial \eta_B}{\partial z_B} \\ \frac{6(1-\nu)}{h} \tilde{\mathcal{F}} \frac{\partial \eta_B}{\partial z_B} & 12 \tilde{\mathcal{F}} \frac{1}{2} \frac{\partial \zeta_B}{\partial z_B} \end{pmatrix} + \dots, \quad (4.29)$$

$$M^{\alpha\beta} = \frac{\Delta K}{a\ell h} \begin{pmatrix} -\frac{1}{\delta_B} \nu \frac{\partial^2 \zeta_B}{\partial z_B^2} & -(1-\nu) \frac{\partial}{\partial \tau} \left(\frac{1}{h} \frac{\partial \xi_B}{\partial z} \right) \\ -(1-\nu) \frac{\partial}{\partial \tau} \left(\frac{1}{h} \frac{\partial \xi_B}{\partial z} \right) & -\frac{1}{\delta_B} \frac{\partial^2 \zeta_B}{\partial z_B^2} \end{pmatrix} + \dots \quad (4.30)$$

The first term of (4.29) corresponds to the axial pre-stress applied to the tube wall and the second term corresponds to stresses induced by the deformations of the tube wall.

4.7 Force-Balance Equations

To model the mechanics of the tube wall, Kirchhoff–Love shell theory is used. In §2.3, the governing force-balance equations (2.29)–(2.31) in the normal, azimuthal and axial directions were derived from the Kirchhoff–Love shell equations in covariant differential form (Flügge, 1972; Søndergaard, 2007). In terms of the deformations ξ_B , η_B , ζ_B , the force-balance equations are

$$\begin{aligned} \nabla_\alpha \nabla_\beta M^{\alpha\beta} + N^{\alpha\beta} b_{\alpha\beta} - \frac{K\delta^2 M}{12a^2} \nabla_\alpha \frac{d^2\theta^{*\alpha}}{dt^2} \\ + \frac{\Delta(t)K}{a^3} p_{\text{tm}} - \frac{\Delta(t)K}{a^3} \frac{\delta_B}{\ell} \frac{M}{h(\tau)} \frac{d^2\xi_B}{dt^2} + \dots = 0, \end{aligned} \quad (4.31)$$

$$\nabla_\beta N^{\beta 1} - b_\gamma^1 \nabla_\beta M^{\beta\gamma} + \frac{K\delta^2 M}{12a^2} b_\gamma^1 \frac{d^2\theta^{*\gamma}}{dt^2} - \frac{\Delta(t)K}{a^3} \frac{\delta_B \tilde{\mathcal{F}}}{\ell} \frac{M}{h(\tau)} \frac{d^2\eta_B}{dt^2} + \dots = 0, \quad (4.32)$$

$$\nabla_\beta N^{\beta 2} - b_\gamma^2 \nabla_\beta M^{\beta\gamma} + \frac{K\delta^2 M}{12a^2} b_\gamma^2 \frac{d^2\theta^{*\gamma}}{dt^2} - \frac{\Delta(t)K}{a^3} \frac{\delta_B \tilde{\mathcal{F}}^{\frac{1}{2}}}{\ell} M \frac{d^2\zeta_B}{dt^2} + \dots = 0, \quad (4.33)$$

where the covariant derivatives ∇_α at leading order are

$$\nabla_1 = \frac{1}{ah} \frac{\partial}{\partial \tau} + O(\Delta), \quad \nabla_2 = \frac{1}{a\delta_B} \frac{\partial}{\partial z_B} + O(\Delta), \quad (4.34)$$

and $\theta^{*\alpha}$ is the angle of rotation that the tube wall takes about an axis passing through the material in the \mathbf{a}_α direction. By considering the size of the normal deformation of the tube wall within the bending layer and the azimuthal and axial length scales being used, we find the $\theta^{*\alpha}$ may be scaled as follows

$$\theta^{*1} = \frac{\Delta}{\ell} \theta^1, \quad \theta^{*2} = \frac{\Delta \delta_B}{\ell} \theta^2, \quad (4.35)$$

where θ^1 and θ^2 are $O(1)$ in the bending layer.

It is found that we must evaluate some of the higher-order terms in the covariant derivatives of $N^{\alpha\beta}$ due to the large pre-stress term. The full expression for the covariant derivative of $N^{\alpha\beta}$ is

$$\nabla_\alpha N^{\alpha\beta} = \frac{\partial N^{\alpha\beta}}{\partial x^\alpha} + \Gamma_{\gamma\alpha}^\alpha N^{\gamma\beta} + \Gamma_{\gamma\alpha}^\beta N^{\alpha\gamma}, \quad (4.36)$$

where the Christoffel symbol $\Gamma_{\mu\nu}^\beta$ is defined as $\Gamma_{\mu\nu}^\beta \equiv a^{\alpha\beta} \mathbf{a}_\alpha \cdot \mathbf{a}_{\mu,\nu}$. Each component of $\Gamma_{\mu\nu}^\beta$ is $O(\Delta)$ and as such we need only consider terms involving

N^{22} , the only non- $O(\Delta)$ component of $N^{\alpha\beta}$. The Christoffel symbols needed are Γ_{21}^1 , Γ_{22}^1 and Γ_{22}^2 , which are calculated to be

$$\Gamma_{21}^1 = \frac{\Delta}{a\ell h\bar{B}} \frac{\partial\beta_1}{\partial z_B} + O(\Delta^2), \quad (4.37)$$

$$\Gamma_{22}^1 = \frac{\Delta\tilde{\mathcal{F}}}{a\ell\delta_B h} \frac{\partial^2\eta_B}{\partial z_B^2} + O(\Delta^2), \quad (4.38)$$

$$\Gamma_{22}^2 = \frac{\Delta\tilde{\mathcal{F}}^{\frac{1}{2}}}{a\ell\delta_B} \frac{\partial^2\zeta_B}{\partial z_B^2} + O(\Delta^2). \quad (4.39)$$

Now we substitute (4.22)–(4.30) as well as (4.34)–(4.39) into the governing force-balance equations (4.31)–(4.33). Doing so, it is possible to determine the sizes of each of the terms in the force-balance equations and see what terms contribute at leading order. The scalings of the terms within the force-balance equations can be found in Tables 4.1–4.3. It is found that the terms corresponding to angular acceleration, wall inertia and transmural pressure are not large enough to contribute at leading order and thus are not included in the tables. (In (4.31)–(4.33) these terms are at most $O(\Delta K/a^3)$, which is strictly smaller than some of the other terms in these equations when $\delta_B \ll 1$.)

To solve the force-balance equations (4.31)–(4.33), we form asymptotic approximations of the deformations ξ_B , η_B and ζ_B . By examining the scalings of the terms within the force-balance equations, it is found that these approximations should take the form

$$\xi_B = \xi_B^{(0)} + O(\delta^{-1}\ell^{-2}), \quad (4.40)$$

$$\eta_B = \eta_B^{(0)} + O(\delta^{-1}\ell^{-2}), \quad (4.41)$$

$$\zeta_B = \zeta_B^{(0)} + O(\delta^{-1}\ell^{-2}). \quad (4.42)$$

Here $\xi_B^{(0)}$, $\eta_B^{(0)}$ and $\zeta_B^{(0)}$ are the leading-order terms of the asymptotic approximations and the higher-order terms of the approximations are $O(\delta^{-1}\ell^{-2})$ at most. We proceed to solve the leading-order force-balance equations and determine expressions for the leading-order deformations $\xi_B^{(0)}$, $\eta_B^{(0)}$ and $\zeta_B^{(0)}$.

4.8 Normal Force-Balance Equation

From the scalings in Table 4.1, we find under the assumption $\delta_B \ll \delta\ell \ll 1$ that the only terms that can contribute at leading order in the normal force-balance equation are the terms from axial-bending, and pre-stress and axial curvature.

Mechanism	Strain	Dominant contribution to normal force-balance equation
Azimuthal stretching	$\gamma_{11} \sim \frac{\Delta \delta_B}{\ell}$	$\left\{ \begin{array}{l} \nabla_2 \nabla_2 M^{22} \sim \frac{\Delta K}{a^3 \ell \delta_B} (1, \tilde{\mathcal{F}}) \\ N^{11} b^{11} \sim \frac{\Delta K}{a^3 \ell \delta_B} \frac{\delta_B^2}{\delta^2} (1, \tilde{\mathcal{F}}) \end{array} \right.$
Shear stretching	$\gamma_{12}, \gamma_{21} \sim \frac{\Delta}{\ell} (\tilde{\mathcal{F}}, \delta_B \tilde{\mathcal{F}}^{\frac{1}{2}})$	$\nabla_2 \nabla_1 M^{21} \sim \frac{\Delta K}{a^3 \ell \delta_B} (\tilde{\mathcal{F}}, \delta_B \tilde{\mathcal{F}}^{\frac{1}{2}})$
Axial stretching	$\gamma_{22} \sim \frac{\Delta}{\ell} \tilde{\mathcal{F}}^{\frac{1}{2}}$	$\left\{ \begin{array}{l} \nabla_2 \nabla_2 M^{22} \sim \frac{\Delta K}{a^3 \ell \delta_B} \frac{\tilde{\mathcal{F}}^{\frac{1}{2}}}{\delta_B} \\ N^{11} b^{11} \sim \frac{\Delta K}{a^3 \ell \delta_B} \frac{\delta_B \tilde{\mathcal{F}}^{\frac{1}{2}}}{\delta^2} \end{array} \right.$
Azimuthal bending	$\kappa_{11} \sim \frac{\Delta \delta_B}{a \ell} (1, \tilde{\mathcal{F}})$	$\nabla_2 \nabla_2 M^{22} \sim \frac{\Delta K}{a^3 \ell \delta_B} (1, \tilde{\mathcal{F}})$
Torsion	$\kappa_{12} \sim \frac{\Delta}{a \ell} (1, \tilde{\mathcal{F}}^{\frac{1}{2}} \delta_B)$ $\kappa_{21} \sim \frac{\Delta}{a \ell} (1, \tilde{\mathcal{F}})$	$\nabla_1 \nabla_2 M^{12}, \nabla_2 \nabla_1 M^{21} \sim \frac{\Delta K}{a^3 \ell \delta_B} (1, \delta_B \tilde{\mathcal{F}}^{\frac{1}{2}})$ $\nabla_1 \nabla_2 M^{12}, \nabla_2 \nabla_1 M^{21} \sim \frac{\Delta K}{a^3 \ell \delta_B} (1, \tilde{\mathcal{F}})$
Axial bending	$\kappa_{22} \sim \frac{\Delta}{a \ell \delta_B}$	$\nabla_2 \nabla_2 M^{22} \sim \frac{\Delta K}{a^3 \ell \delta_B} \frac{1}{\delta_B^2}$
Pre-stress and axial curvature	$\kappa_{22} \sim \frac{\Delta}{a \ell \delta_B}$	$N^{22} b_{22} \sim \frac{\Delta K}{a^3 \ell \delta_B} \mathcal{F} \ell^2$

Table 4.1: Scaling estimates for the dominant terms contributing to the normal force-balance equation in regime I_a. The mechanisms that contribute at leading order are in bold.

(Since $\tilde{\mathcal{F}} \ll 1$, the other effects are all strictly smaller than at least one of these two terms.) These two terms must balance and thus we must have

$$\delta_B = \mathcal{F}^{-\frac{1}{2}} \ell^{-1}. \quad (4.43)$$

This is in agreement with the estimate (3.48) derived from the toy model in §3.6. Using (4.43) and the asymptotic expansion (4.40), we find the normal force-balance equation (4.31) becomes, at leading order

$$\nabla_2 \nabla_2 M^{22} + N^{22} b_{22} = 0, \quad \Rightarrow \quad \frac{\partial^4 \xi_B^{(0)}}{\partial z_B^4} - \frac{\partial^2 \xi_B^{(0)}}{\partial z_B^2} = 0. \quad (4.44)$$

The general solution for $\xi_B^{(0)}$ is therefore

$$\xi_B^{(0)} = A(\tau, t) e^{z_B} + B(\tau, t) e^{-z_B} + C(\tau, t) z_B + D(\tau, t), \quad (4.45)$$

Mechanism	Strain	Dominant contribution to azimuthal force-balance equation
Azimuthal stretching	$\gamma_{11} \sim \frac{\Delta \delta_B}{\ell}$	$\nabla_1 N^{11} \sim \frac{\Delta K}{a^3 \ell \delta_B} \delta_B^2 \delta^{-2} (1, \tilde{\mathcal{F}})$
Shear stretching	$\gamma_{12}, \gamma_{21} \sim \frac{\Delta}{\ell} (\tilde{\mathcal{F}}, \delta_B \tilde{\mathcal{F}}^{\frac{1}{2}})$	$\begin{cases} \nabla_2 N^{21} \sim \frac{\Delta K}{a^3 \ell \delta_B} \delta^{-2} (\tilde{\mathcal{F}}, \delta_B \tilde{\mathcal{F}}^{\frac{1}{2}}) \\ b_{11} \nabla_2 M^{21} \sim \frac{\Delta K}{a^3 \ell \delta_B} (\tilde{\mathcal{F}}, \delta_B \tilde{\mathcal{F}}^{\frac{1}{2}}) \end{cases}$
Axial stretching	$\gamma_{22} \sim \frac{\Delta}{\ell} \tilde{\mathcal{F}}^{\frac{1}{2}}$	$\nabla_1 N^{11} \sim \frac{\Delta K}{a^3 \ell \delta_B} \delta_B \tilde{\mathcal{F}}^{\frac{1}{2}} \delta^{-2}$
Azimuthal bending	$\kappa_{11} \sim \frac{\Delta \delta_B}{a \ell} (1, \tilde{\mathcal{F}})$	$\begin{cases} \nabla_1 N^{11} \sim \frac{\Delta K}{a^3 \ell \delta_B} \delta_B^2 (1, \tilde{\mathcal{F}}) \\ b_{11} \nabla_1 M^{11} \sim \frac{\Delta K}{a^3 \ell \delta_B} \delta_B^2 (1, \tilde{\mathcal{F}}) \end{cases}$
Torsion	$\kappa_{12} \sim \frac{\Delta}{a \ell} (1, \tilde{\mathcal{F}}^{\frac{1}{2}} \delta_B)$ $\kappa_{21} \sim \frac{\Delta}{a \ell} (1, \tilde{\mathcal{F}})$	$\begin{cases} \nabla_1 N^{11} \sim \frac{\Delta K}{a^3 \ell \delta_B} \delta_B (1, \delta_B \tilde{\mathcal{F}}^{\frac{1}{2}}) \\ b_{11} \nabla_2 M^{21} \sim \frac{\Delta K}{a^3 \ell \delta_B} (1, \delta_B \tilde{\mathcal{F}}^{\frac{1}{2}}) \end{cases}$ $\begin{cases} \nabla_2 N^{21} \sim \frac{\Delta K}{a^3 \ell \delta_B} (1, \tilde{\mathcal{F}}) \\ b_{11} \nabla_2 M^{21} \sim \frac{\Delta K}{a^3 \ell \delta_B} (1, \tilde{\mathcal{F}}) \end{cases}$
Axial bending	$\kappa_{22} \sim \frac{\Delta}{a \ell \delta_B}$	$b_{11} \nabla_1 M^{11} \sim \frac{\Delta K}{a^3 \ell \delta_B}$
Pre-stress and axial curvature	$\Gamma_{22}^1 \sim \frac{\Delta \tilde{\mathcal{F}}}{a \ell \delta_B}$	$\nabla_2 N^{21} \sim \frac{\Delta K}{a^3 \ell \delta_B} \tilde{\mathcal{F}} \mathcal{F} \ell^2$

Table 4.2: Scaling estimates for the dominant terms contributing to the azimuthal force-balance equation in regime I_a. The mechanism that contributes at leading order is in bold.

where A, B, C, D are arbitrary functions.

By examining the matching condition (4.14a) for ξ_B as well as the leading-order approximation (4.4) for $\hat{\xi}_s$ as $\hat{z} \rightarrow 0$, it is seen that for the matching condition to hold, $\xi_B^{(0)}$ cannot be exponentially growing in z_B as $z_B \rightarrow \infty$. Hence, $A(\tau, t) = 0$. Applying the clamped boundary conditions (4.16), it is also determined that

$$C(\tau, t) = B(\tau, t), \quad D(\tau, t) = -B(\tau, t). \quad (4.46)$$

Substituting the values of $A(\tau, t)$, $C(\tau, t)$ and $D(\tau, t)$ into the general solution (4.45) yields

$$\xi_B^{(0)} = B(\tau, t)(e^{-z_B} + z_B - 1). \quad (4.47)$$

Mechanism	Strain	Dominant contribution to axial force-balance equation
Azimuthal stretching	$\gamma_{11} \sim \frac{\Delta \delta_B}{\ell}$	$\nabla_2 N^{22} \sim \frac{\Delta K}{a^3 \ell} \delta^{-2} (1, \tilde{\mathcal{F}})$
Shear stretching	$\gamma_{12}, \gamma_{21} \sim \frac{\Delta}{\ell} (\tilde{\mathcal{F}}, \delta_B \tilde{\mathcal{F}}^{\frac{1}{2}})$	$\nabla_1 N^{12} \sim \frac{\Delta K}{a^3 \ell} \delta^{-2} (\tilde{\mathcal{F}}, \delta_B \tilde{\mathcal{F}}^{\frac{1}{2}})$
Axial stretching	$\gamma_{22} \sim \frac{\Delta}{\ell} \tilde{\mathcal{F}}^{\frac{1}{2}}$	$\nabla_2 N^{22} \sim \frac{\Delta K}{a^3 \ell} \delta_B^{-1} \tilde{\mathcal{F}}^{\frac{1}{2}} \delta^{-2}$
Torsion	$\kappa_{12} \sim \frac{\Delta}{a \ell} (1, \tilde{\mathcal{F}}^{\frac{1}{2}} \delta_B)$ $\kappa_{21} \sim \frac{\Delta}{a \ell} (1, \tilde{\mathcal{F}})$	$\nabla_1 N^{12} \sim \frac{\Delta K}{a^3 \ell} (1, \delta_B \tilde{\mathcal{F}}^{\frac{1}{2}})$ $\nabla_1 N^{12} \sim \frac{\Delta K}{a^3 \ell} (1, \tilde{\mathcal{F}})$
Axial bending	$\kappa_{22} \sim \frac{\Delta}{a \ell \delta_B}$	$\nabla_2 N^{22} \sim \frac{\Delta K}{a^3 \ell} \delta_B^{-2}$
Pre-stress and axial curvature	$\Gamma_{21}^1 \sim \frac{\Delta}{a \ell} (1, \tilde{\mathcal{F}})$ $\Gamma_{22}^2 \sim \frac{\Delta \tilde{\mathcal{F}}^{\frac{1}{2}}}{a \ell \delta_B}$	$\nabla_1 N^{12} \sim \frac{\Delta K}{a^3 \ell} \ell^2 (1, \tilde{\mathcal{F}})$ $\nabla_2 N^{22} \sim \frac{\Delta K}{a^3 \ell} \delta_B^{-1} \tilde{\mathcal{F}}^{\frac{1}{2}} \mathcal{F} \ell^2$

Table 4.3: Scaling estimates for the dominant terms contributing to the axial force-balance equation in regime I_a. The mechanism that contributes at leading order is in bold.

The function $B(\tau, t)$ is now set so that the matching condition (4.14a) is satisfied. As $z_B \rightarrow \infty$, $\xi_B^{(0)}$ is approximated by

$$\xi_B^{(0)} \sim B(\tau, t)(z_B - 1). \quad (4.48)$$

Substituting this and the leading-order approximation (4.4) for $\hat{\xi}_s$ as $\hat{z} \rightarrow 0$ into (4.14a) and rewriting z_B and \hat{z} in terms of the intermediate variable z_I using (4.15), it can be shown that

$$B(\tau, t) \left(\left(\tilde{\mathcal{F}}^{\frac{1}{2}} \delta_B^{-1} \right)^{1-\alpha} z_I - 1 \right) \sim - \frac{\left(\tilde{\mathcal{F}}^{\frac{1}{2}} \delta_B^{-1} \right)^{1-\alpha} h(\tau) \nu z_I}{12(1-\nu^2)} \sum_{n=1}^{\infty} B_n(t) Y_n(\tau). \quad (4.49)$$

Examining this relation, we see that the linear terms on both sides of the expression have the same size. However, the constant term on the left-hand-side is a factor of $(\tilde{\mathcal{F}}^{\frac{1}{2}} \delta_B^{-1})^{\alpha-1}$ smaller than the other terms in the relation. As such, this term will not affect the leading-order matching condition but will instead force a correction to $\hat{\xi}_s$ at a higher order. The effect of this correction is evaluated further in §4.12. As the correction does not apply at leading order,

the leading-order term of the approximation $\hat{\zeta}_s$ in the inner shear layer still behaves linearly as $z_I \rightarrow 0$ and thus it still satisfies the Dirichlet parts (3.35) of the pinned boundary conditions.

Rearranging (4.49) and neglecting the constant term on the left-hand-side, it is calculated that

$$B(\tau, t) = -\frac{h(\tau)\nu}{12(1-\nu^2)} \sum_{n=1}^{\infty} B_n(t) Y_n(\tau). \quad (4.50)$$

Hence, we find the leading-order deformation $\xi_B^{(0)}$ in the bending layer to be

$$\xi_B^{(0)} = -\frac{h(\tau)\nu}{12(1-\nu^2)} \sum_{n=1}^{\infty} B_n(t) Y_n(\tau) (e^{-z_B} + z_B - 1). \quad (4.51)$$

This is depicted in Figure 4.3 in §4.12.

4.9 Azimuthal Force-Balance Equation

Using $\delta_B = \mathcal{F}^{-\frac{1}{2}}\ell^{-1}$ and the scalings in Table 4.2, we find the only leading-order term within the azimuthal force-balance equation (4.32) to be one of the shear stretching terms, which has size $O(\frac{\Delta K}{a^3 \ell \delta_B} \delta^{-2} \tilde{\mathcal{F}})$. Substituting the asymptotic approximation (4.41) for η_B into (4.32), the leading-order azimuthal force-balance equation is determined as

$$\nabla_2 N^{21} = 0, \quad \Rightarrow \quad \frac{\partial^2 \eta_B^{(0)}}{\partial z_B^2} = 0. \quad (4.52)$$

Thus, the general solution for $\eta_B^{(0)}$ is

$$\eta_B^{(0)} = E(\tau, t) z_B + F(\tau, t), \quad (4.53)$$

where E, F are arbitrary functions.

Applying the clamped boundary condition (4.16) to (4.53) gives

$$F(\tau, t) = 0. \quad (4.54)$$

Substituting (4.53) and the approximation (4.5) for $\hat{\eta}_s$ as $\hat{z} \rightarrow 0$ into the matching condition (4.14b), and once again rewriting both z_B and \hat{z} in terms of z_I using (4.15), we find

$$\begin{aligned} E(\tau, t) z_I \sim & \frac{1}{12(1-\nu^2)} \sum_{n=1}^{\infty} B_n(t) \frac{\partial}{\partial \tau} \left\{ Y_n(\tau) \left(\frac{2\nu(1+\nu)z_I}{|\bar{B}(\tau)|} - \frac{[1+\nu(2+\nu)]z_I^2}{2(\tilde{\mathcal{F}}^{\frac{1}{2}}\delta_B^{-1})^\alpha} \right) \right. \\ & \left. + \frac{2(1+\nu)}{\mu_n} \left[\frac{1}{h(\tau)|\bar{B}(\tau)|^2} \frac{\partial}{\partial \tau} \left(\frac{Y'_n(\tau)}{h(\tau)} \right) - Y_n(\tau) \right] z_I \right\}. \end{aligned} \quad (4.55)$$

It is seen that there are terms linear in z_I with the same size on both sides of (4.55), allowing these terms to be matched. On the right-hand-side, there are also terms quadratic in z_I which are a factor of $(\tilde{\mathcal{F}}^{\frac{1}{2}}\delta_B^{-1})^{-\alpha}$ smaller than the other terms in the relation. As such these terms will not play a part in the leading-order matching and will instead match with the higher-order terms in the asymptotic approximation (4.41) for η_B . We see that there is no correction at leading order to the approximation $\hat{\eta}_s$ in the inner shear layer, and thus as $z_I \rightarrow 0$, the approximation of the leading-order term of $\hat{\eta}_s$ still contains only linear and quadratic terms in z_I . Hence, the leading-order term of $\hat{\eta}_s$ still satisfies the Dirichlet parts (3.35) of the pinned boundary conditions.

Matching the linear terms in (4.55), it is found that

$$E(\tau, t) = \frac{1}{12(1-\nu^2)} \sum_{n=1}^{\infty} B_n(t) \frac{\partial}{\partial \tau} \left\{ \frac{2\nu(1+\nu)Y_n(\tau)}{|\bar{B}(\tau)|} + \frac{2(1+\nu)}{\mu_n} \left[\frac{1}{h(\tau)|\bar{B}(\tau)|^2} \frac{\partial}{\partial \tau} \left(\frac{Y'_n(\tau)}{h} \right) - Y_n(\tau) \right] \right\}, \quad (4.56)$$

which in turn gives the leading-order azimuthal deformation $\eta_B^{(0)}$ in the bending layer as

$$\eta_B^{(0)} = \frac{z_B}{12(1-\nu^2)} \sum_{n=1}^{\infty} B_n(t) \frac{\partial}{\partial \tau} \left\{ \frac{2\nu(1+\nu)Y_n(\tau)}{|\bar{B}(\tau)|} + \frac{2(1+\nu)}{\mu_n} \left[\frac{1}{h(\tau)|\bar{B}(\tau)|^2} \frac{\partial}{\partial \tau} \left(\frac{Y'_n(\tau)}{h} \right) - Y_n(\tau) \right] \right\}. \quad (4.57)$$

This is plotted in Figure 4.4 in §4.12.

4.10 Axial Force-Balance Equation

Finally, by looking at the scalings in Table 4.3, we find the leading-order axial force-balance equation to be at $O(\frac{\Delta K}{a^3 \ell} \delta_B^{-1} \tilde{\mathcal{F}}^{\frac{1}{2}} \delta^{-2})$ and contain only the axial stretching term. Thus, by substituting in the asymptotic approximation (4.42) for ζ_B , the axial force-balance equation (4.33) becomes, at leading order

$$\nabla_2 N^{22} = 0, \quad \Rightarrow \quad \frac{\partial^2 \zeta_B^{(0)}}{\partial z_B^2} = 0. \quad (4.58)$$

Hence, the general solution for $\zeta_B^{(0)}$ is found to be

$$\zeta_B^{(0)} = G(\tau, t)z_B + H(\tau, t), \quad (4.59)$$

where G, H are arbitrary functions.

The clamped boundary condition (4.16) on ζ_B is applied to (4.59) to obtain

$$H(\tau, t) = 0. \quad (4.60)$$

By substituting (4.59) and the approximation (4.6) for $\hat{\zeta}_s$ as $\hat{z} \rightarrow 0$ into the matching condition (4.14c) for ζ_B , and again using (4.15) to rewrite z_B and \hat{z} in terms of z_I , it is shown that

$$G(\tau, t)z_I \sim \frac{z_I}{12} \sum_{n=1}^{\infty} B_n(t)Y_n(\tau). \quad (4.61)$$

Since all the terms here are the same size and are linear, we see that there is no correction at leading order to $\hat{\zeta}_s$ and the leading-order term of $\hat{\zeta}_s$ still behaves linearly in z_I as $z_I \rightarrow 0$. As such, $\hat{\zeta}_s$ still satisfies the Dirichlet parts (3.35) of the pinned boundary conditions at leading order.

As all the terms within (4.61) are linear in z_I and have the same size, we may match these terms to obtain

$$G(\tau, t) = \frac{1}{12} \sum_{n=1}^{\infty} B_n(t)Y_n(\tau), \quad (4.62)$$

and hence the leading-order axial deformation $\zeta_B^{(0)}$ in the bending layer is

$$\zeta_B^{(0)} = \frac{1}{12} \sum_{n=1}^{\infty} B_n(t)Y_n(\tau)z_B. \quad (4.63)$$

This is depicted in Figure 4.5 in §4.12.

4.11 Leading-Order Area Change in the Bending Layer

With the expression (4.51) for the leading-order normal deformation $\zeta_B^{(0)}$ in the bending layer, we can determine the leading-order area change in the bending layer. Whittaker *et al.* (2010d) found the relation between the area change and the overall deformation in the tube wall to be

$$(A(z, t) - A_0) a^2 = \oint (\mathbf{r} - \mathbf{r}_0) \cdot \hat{\mathbf{n}} a h(\tau) d\tau + O(\Delta^2), \quad (4.64)$$

where A , A_0 are the dimensionless cross-sectional areas of the tube in its deformed and undeformed state respectively. Applying the deformation (4.11) in the bending boundary layer to (4.64), we find the area change in the bending boundary layer to be

$$\begin{aligned} A(z, t) - A_0 &= \frac{\Delta}{\ell^2} \int_0^{2\pi} \xi_B d\tau + O(\Delta^2). \\ &\sim -\frac{\Delta\nu}{12\ell^2(1-\nu^2)} \sum_{n=1}^{\infty} B_n(e^{-z_B} + z_B - 1) \int_0^{2\pi} h(\tau) Y_n(\tau) d\tau \\ &\quad + O(\delta^{-1}\ell^{-2}), \end{aligned} \quad (4.65)$$

where we have substituted in the asymptotic expansion (4.40) for ξ_B . To evaluate the integral in (4.65), we use the property that the $Y_n(\tau)$ are eigenfunctions of the operator \mathcal{L} , with corresponding eigenvalues μ_n^2 . Using this property and the definition (4.7) of \mathcal{L} , we find the following

$$\begin{aligned} h(\tau)Y_n(\tau) &= \frac{h(\tau)}{\mu_n^2} \mathcal{L}Y_n(\tau) \\ &= \frac{1}{\mu_n^2} \frac{\partial}{\partial \tau} \frac{1}{h} \frac{\partial}{\partial \tau} \left(\frac{1}{\bar{B}^2 h} \frac{\partial}{\partial \tau} \frac{1}{h} \frac{\partial Y_n(\tau)}{\partial \tau} - Y_n(\tau) \right). \end{aligned} \quad (4.66)$$

Evaluating the integral in (4.65) gives

$$\int_0^{2\pi} h(\tau)Y_n(\tau) d\tau = \frac{1}{\mu_n^2} \left[\frac{1}{h} \frac{\partial}{\partial \tau} \left(\frac{1}{\bar{B}^2 h} \frac{\partial}{\partial \tau} \frac{1}{h} \frac{\partial Y_n(\tau)}{\partial \tau} - Y_n(\tau) \right) \right]_0^{2\pi} = 0, \quad (4.67)$$

since $Y_n(\tau)$, $h(\tau)$ and $\bar{B}(\tau)$ are all periodic over 2π . Hence

$$A(z, t) - A_0 = O(\delta^{-1} \ell^{-2}), \quad (4.68)$$

and there is no area change within the bending layer at leading order.

4.12 Corrections to the Inner Shear-Layer Solution

Now that we have found the leading-order deformations within the bending layer, we can use this information to determine the corrections that are imposed on the deformations $\hat{\xi}$, $\hat{\eta}$ and $\hat{\zeta}$ within the inner shear layer. To do so, we must determine the solutions of the deformations in the inner shear layer without applying the Dirichlet parts (3.35) of the pinned boundary conditions. We then match these general solutions to the leading-order bending-layer deformations.

The general solutions of the deformations in the inner shear layer, up to leading order, are derived in Appendix 4.A and shown in equations

(4.100)–(4.102). These are found to be

$$\hat{\xi} = \frac{\tilde{\mathcal{F}}^{\frac{1}{2}}h}{12\bar{B}(1-\nu^2)} \left[\nu \sum_{n=1}^{\infty} B_n(t) Y_n(\tau) \left(1 - e^{-|\bar{B}|\hat{z}} \right) - \hat{A}(\tau, t) e^{-|\bar{B}|\hat{z}} \right] + O(\tilde{\mathcal{F}}^{\frac{3}{2}}), \quad (4.69)$$

$$\begin{aligned} \hat{\eta} = & \frac{\tilde{\mathcal{F}}^{\frac{3}{2}}}{12(1-\nu^2)} \left\{ \frac{\partial}{\partial \tau} \left[-\frac{2+\nu}{|\bar{B}|^2} \left(\sum_{n=1}^{\infty} \nu B_n(t) Y_n(\tau) + \hat{A}(\tau, t) \right) e^{-|\bar{B}|\hat{z}} \right. \right. \\ & - \sum_{n=1}^{\infty} \frac{B_n(t) Y'_n(\tau)}{2} \hat{z}^2 + \frac{2(1+\nu)}{\mu_n} \sum_{n=1}^{\infty} B_n(t) \left[\frac{1}{\bar{B}^2 h} \frac{\partial}{\partial \tau} \left(\frac{Y'_n(\tau)}{h} \right) - Y_n \right] \hat{z} \\ & \left. \left. - \hat{C}(\tau, t) \hat{z} \right] + \hat{B}(\tau, t) \right\} + O(\tilde{\mathcal{F}}^{\frac{5}{2}}), \end{aligned} \quad (4.70)$$

$$\begin{aligned} \hat{\zeta} = & \frac{\tilde{\mathcal{F}}}{12(1-\nu^2)} \left[\sum_{n=1}^{\infty} B_n(t) Y_n(\tau) \left(\hat{z} + \frac{\nu^2}{|\bar{B}|} e^{-|\bar{B}|\hat{z}} \right) \right. \\ & \left. + \frac{\nu}{|\bar{B}|} \hat{A}(\tau, t) e^{-|\bar{B}|\hat{z}} + \hat{C}(\tau, t) \right] + O(\tilde{\mathcal{F}}^2), \end{aligned} \quad (4.71)$$

where \hat{A} , \hat{B} and \hat{C} are functions to be determined. In order for (4.69)–(4.71) to match onto the leading-order deformations in the bending layer, the functions \hat{A} , \hat{B} and \hat{C} must be set so that

$$\hat{\xi} \sim \delta_B \xi_B^{(0)}, \quad \hat{\eta} \sim \delta_B \tilde{\mathcal{F}} \eta_B^{(0)}, \quad \hat{\zeta} \sim \delta_B \tilde{\mathcal{F}}^{\frac{1}{2}} \zeta_B^{(0)}, \quad \text{as } z_B \rightarrow \infty, \hat{z} \rightarrow 0. \quad (4.72)$$

These conditions are derived from the relations (4.13) between the deformations in the bending and inner shear layers. For the matching conditions (4.72) to be satisfied, we must have

$$\hat{A}(\tau, t) = -\nu \bar{B} \tilde{\mathcal{F}}^{-\frac{1}{2}} \delta_B \sum_{n=1}^{\infty} B_n(t) Y_n(\tau), \quad (4.73)$$

$$\hat{B}(\tau, t) = \nu(2+\nu) \sum_{n=1}^{\infty} B_n(t) \frac{\partial}{\partial \tau} \left[\frac{Y_n(\tau)}{|\bar{B}(\tau)|} \left(\frac{1}{|\bar{B}(\tau)|} + \tilde{\mathcal{F}}^{-\frac{1}{2}} \delta_B \right) \right], \quad (4.74)$$

$$\hat{C}(\tau, t) = -\nu^2 \left(\frac{1}{|\bar{B}(\tau)|} + \tilde{\mathcal{F}}^{-\frac{1}{2}} \delta_B \right) \sum_{n=1}^{\infty} B_n(t) Y_n(\tau). \quad (4.75)$$

Substituting (4.73)–(4.75) into (4.69)–(4.71), the corrected deformations in the

inner shear layer, which we denote $\hat{\xi}_c$, $\hat{\eta}_c$ and $\hat{\zeta}_c$ are found to be

$$\hat{\xi}_c = \frac{\tilde{\mathcal{F}}^{\frac{1}{2}} h \nu}{12 \bar{B} (1 - \nu^2)} \sum_{n=1}^{\infty} B_n(t) Y_n(\tau) \left[1 - \left(1 - \bar{B} \tilde{\mathcal{F}}^{-\frac{1}{2}} \delta_B \right) e^{-|\bar{B}| \hat{z}} \right] + O(\tilde{\mathcal{F}}^{\frac{3}{2}}), \quad (4.76)$$

$$\begin{aligned} \hat{\eta}_c = & \frac{\tilde{\mathcal{F}}^{\frac{3}{2}}}{12(1 - \nu^2)} \sum_{n=1}^{\infty} B_n(t) \frac{\partial}{\partial \tau} \left\{ \frac{2(1 + \nu)}{\mu_n} \left[\frac{1}{\bar{B}^2 h} \frac{\partial}{\partial \tau} \left(\frac{Y'_n(\tau)}{h} \right) - Y_n \right] \hat{z} \right. \\ & \left. + Y_n(\tau) \left[\left(\frac{\nu(2 + \nu)}{|\bar{B}|} \left(1 - e^{-|\bar{B}| \hat{z}} \right) + \nu^2 \hat{z} \right) \left(\frac{1}{|\bar{B}(\tau)|} + \tilde{\mathcal{F}}^{-\frac{1}{2}} \delta_B \right) - \frac{\hat{z}^2}{2} \right] \right\} \\ & + O(\tilde{\mathcal{F}}^{\frac{5}{2}}), \end{aligned} \quad (4.77)$$

$$\begin{aligned} \hat{\zeta}_c = & \frac{\tilde{\mathcal{F}}}{12(1 - \nu^2)} \sum_{n=1}^{\infty} B_n(t) Y_n(\tau) \left[\hat{z} - \nu^2 \left(\frac{1}{|\bar{B}(\tau)|} + \tilde{\mathcal{F}}^{-\frac{1}{2}} \delta_B \right) \left(1 - e^{-|\bar{B}| \hat{z}} \right) \right] \\ & + O(\tilde{\mathcal{F}}^2). \end{aligned} \quad (4.78)$$

By comparing the deformations (4.76)–(4.78) to the deformations originally found in the inner shear layer by Whittaker (2015), it is seen that the correction terms are all a factor of $O(\tilde{\mathcal{F}}^{-\frac{1}{2}} \delta_B) = O(\mathcal{F}^{-1} \delta^{-1} \ell^{-2})$ smaller than the leading-order terms within the expressions. Hence, these correction terms do not alter the leading-order behaviour of the inner shear-layer deformations. Instead, they alter the deformations at a higher order so that the inner shear-layer deformations allow the bending-layer deformations to satisfy the clamped boundary conditions (4.16). In particular, they allow the new condition on the gradient of the normal deformation to be satisfied.

If the condition $\mathcal{F} = O(1)$ is relaxed so we can set $\mathcal{F} = O(\delta^{-1} \ell^{-2})$, resulting in a lower tension, the correction terms will then appear at leading order. However, by changing the value of \mathcal{F} in this way, it is seen using the definitions (4.1) and (4.43) of $\tilde{\mathcal{F}}$ and δ_B that we then have $\tilde{\mathcal{F}}^{\frac{1}{2}} = O(\delta^{\frac{1}{2}})$ and $\delta_B = O(\delta^{\frac{1}{2}})$. Hence, the bending layer and inner shear layer now have the same width. As the pre-stress contributes at leading order in the bulk layer, setting this value of \mathcal{F} could also alter the behaviour of the leading-order solution in the bulk layer. Because of these effects, further investigation is needed to evaluate what occurs in this scenario.

In Figures 4.3, 4.4 and 4.5, the first $n = 1$ modes of the leading-order approximations $\hat{\xi}_s$, $\hat{\eta}_s$ and $\hat{\zeta}_s$ of the deformations $\hat{\xi}$, $\hat{\eta}$ and $\hat{\zeta}$ in the original inner shear layer found by Whittaker (2015) have been plotted in the axial direction. Also plotted are the approximations $\delta_B \zeta_B^{(0)}$, $\delta_B \tilde{\mathcal{F}} \hat{\eta}_B^{(0)}$ and $\delta_B \tilde{\mathcal{F}}^{\frac{1}{2}} \zeta_B^{(0)}$ of the deformations in the bending layer, and the corrected approximations $\hat{\xi}_c$, $\hat{\eta}_c$ and $\hat{\zeta}_c$ in the inner shear layer. These are given by (4.51)–(4.63) and (4.76)–(4.78), respectively. It is seen that the bending-layer deformations and the

gradient of $\hat{\xi}$ are all zero at the clamped boundary $Z = 0$. It is also seen that the correction to $\hat{\xi}$ in the inner shear layer enforces a shift from the original value found by Whittaker (2015), which decreases exponentially with increasing Z . The correction to $\hat{\eta}$ in the inner shear layer is found to alter the gradient of the deformation as well as give a shift comprised of an exponentially decaying and constant part with increasing Z . Finally, the correction to $\hat{\zeta}$ in the inner shear layer is found to give a shift with an exponentially decaying and constant part with increasing Z .

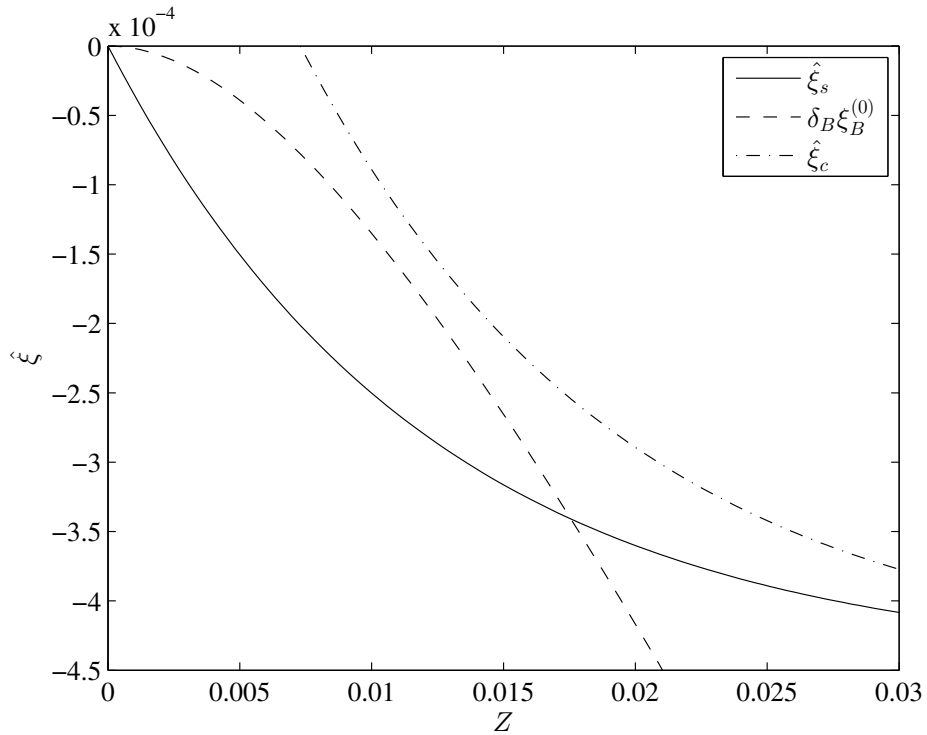


Figure 4.3: The first $n = 1$ modes of the approximations $\hat{\xi}_s$, $\delta_B \hat{\xi}_B^{(0)}$, and $\hat{\xi}_c$, of $\hat{\xi}$ in the original inner shear layer studied by Whittaker (2015), in the bending layer, and in the corrected inner shear layer, respectively. The approximations $\delta_B \hat{\xi}_B^{(0)}$ and $\hat{\xi}_c$ are given by (4.51) and (4.76), and all the approximations are plotted in the case $\sigma_0 = 0.6$, $\delta = 0.001$, $\ell = 100$, $\nu = 0.49$, $\mathcal{F} = 1$, $\tau = 0$ and $B_1(t) = 1$, with $Y_1(\tau)$ normalised such that $Y_1(0) = 1$. In this case $\delta_B = 0.01$.

In each of the deformations the new correction terms are a factor of $O(\tilde{\mathcal{F}}^{-\frac{3}{2}} \delta_B) = O(\delta^{-3} \ell^{-4})$ different from the largest of the other higher-order terms in the expressions. It is unclear whether $\delta^{-3} \ell^{-4} \ll 1$ or $\delta^{-3} \ell^{-4} \gg 1$ and as such, it is also unclear whether the new correction terms are larger or smaller than the other higher-order terms within the expressions for the deformations.

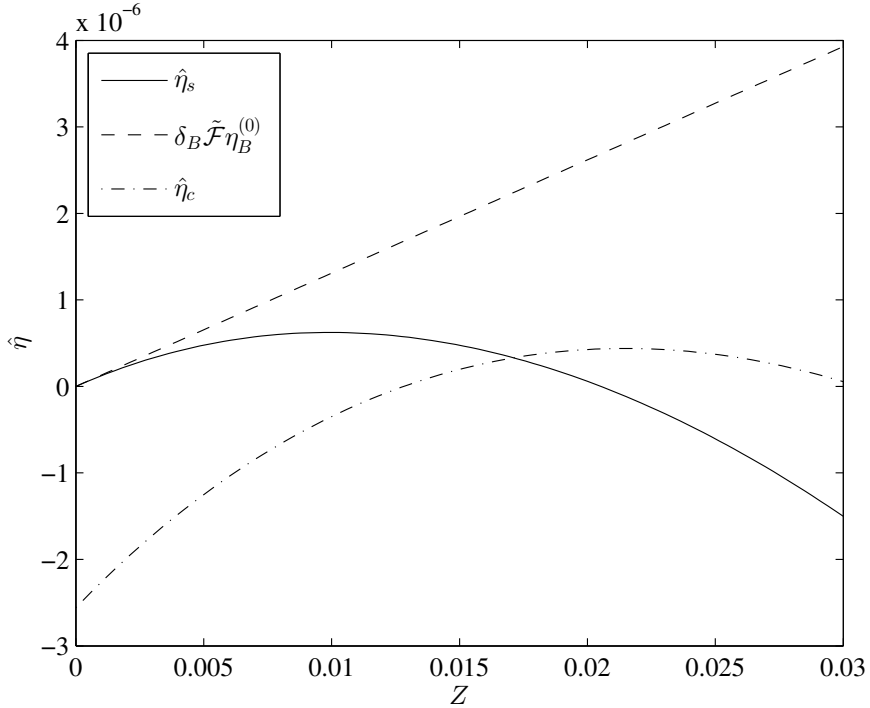


Figure 4.4: The first $n = 1$ modes of the approximations $\hat{\eta}_s$, $\delta_B \tilde{\mathcal{F}}\eta_B^{(0)}$, and $\hat{\eta}_c$, of $\hat{\eta}$ in the original inner shear layer studied by Whittaker (2015), in the bending layer, and in the corrected inner shear layer, respectively. The approximations $\delta_B \tilde{\mathcal{F}}\eta_B^{(0)}$ and $\hat{\eta}_c$ are given by (4.57) and (4.77), and all the approximations are plotted in the case $\sigma_0 = 0.6$, $\delta = 0.001$, $\ell = 100$, $\nu = 0.49$, $\mathcal{F} = 1$, $\tau = 2.6656$ (where $Y_1'(\tau)$ is near its maximum value) and $B_1(t) = 1$, with $Y_1(\tau)$ normalised such that $Y_1(0) = 1$. In this case $\delta_B = 0.01$.

Hence, whether these new correction terms are more important than the other higher-order terms depends on the values of δ and ℓ .

4.13 Corrections to the Outer Shear-Layer and Bulk-Layer Solutions

We now consider the behaviour of the deformations (4.76)–(4.78) in the inner shear layer as $\hat{z} \rightarrow \infty$. This will allow us to determine the effect that the correction terms have on the deformations in the outer shear layer studied by Whittaker (2015), and in the bulk layer modelled in Chapter 2.

In the expression (4.76) for $\hat{\xi}$, the correction term behaves exponentially in \hat{z} . As such, this term will become exponentially small as $\hat{z} \rightarrow \infty$, and this correction will have no effect on the normal deformation in the outer shear

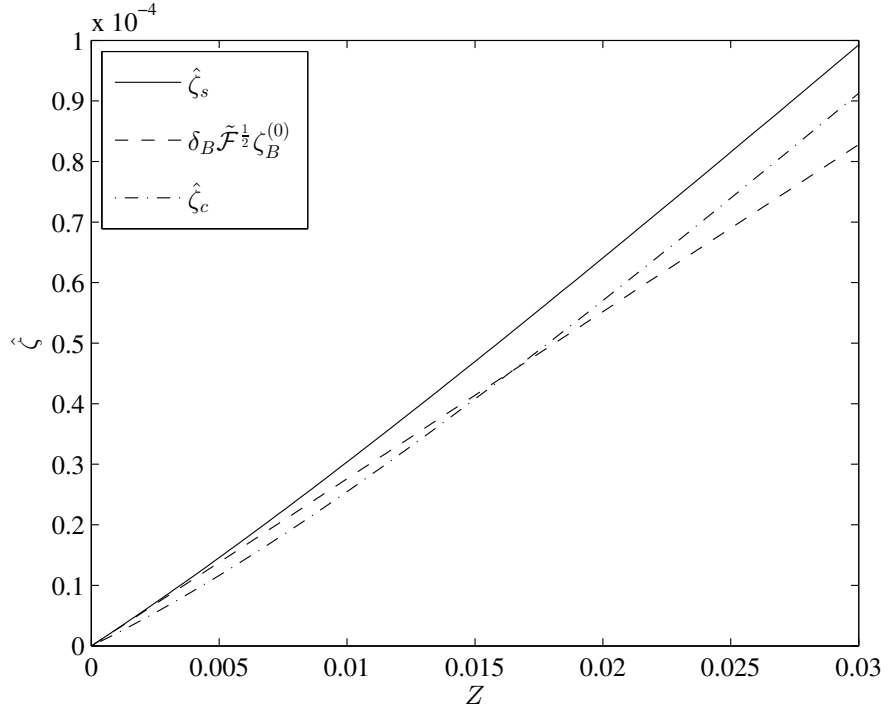


Figure 4.5: The first $n = 1$ modes of the approximations $\hat{\zeta}_s$, $\delta_B \tilde{\mathcal{F}}^{1/2} \zeta_B^{(0)}$, and $\hat{\zeta}_c$, of $\hat{\zeta}$ in the original inner shear layer studied by Whittaker (2015), in the bending layer, and in the corrected inner shear layer, respectively. The approximations $\delta_B \tilde{\mathcal{F}}^{1/2} \zeta_B^{(0)}$ and $\hat{\zeta}_c$ are given by (4.63), and (4.78), and all the approximations are plotted in the case $\sigma_0 = 0.6$, $\delta = 0.001$, $\ell = 100$, $\nu = 0.49$, $\mathcal{F} = 1$, $\tau = 0$ and $B_1(t) = 1$, with $Y_1(\tau)$ normalised such that $Y_1(0) = 1$. In this case $\delta_B = 0.01$.

layer, or in the bulk layer. From equation (4.64), it is seen that the area change of the tube is dependent only on the normal deformation. Hence, as the correction term in (4.76) does not alter the normal deformation in the outer shear or bulk layers, it will also have no effect on the area change in these layers.

In the expression (4.77) for $\hat{\eta}$, there are correction terms that behave exponentially, linearly and as a constant in \hat{z} . In the case $\hat{z} \rightarrow \infty$, the exponential terms will become exponentially small. However, the linear and constant terms will enforce a correction to the azimuthal deformation in the outer shear layer. When $\hat{z} \rightarrow \infty$, the quadratic and leading-order linear terms in (4.77) will be larger than the correction terms. As such the correction terms will enforce corrections to the outer shear-layer deformation that appear at higher orders than terms matching onto the quadratic and leading-order linear terms in the inner shear layer. As these corrections are so small we do not compute them here.

Finally, in the expression (4.78) for $\hat{\zeta}$, we have correction terms that behave exponentially and as a constant in \hat{z} . When $\hat{z} \rightarrow \infty$, again the exponential term becomes exponentially small and the constant term enforces a correction to axial deformation in the outer shear layer. The linear and leading-order constant terms in (4.78) will still be larger than the correction terms when $\hat{z} \rightarrow \infty$. Hence the corrections to the outer shear-layer deformation will appear at higher orders than terms matching onto the linear and leading-order constant terms in the inner shear layer. Again, as these corrections are so small they are not computed here.

To determine the exact sizes of the corrections to $\hat{\eta}$ and $\hat{\zeta}$ in the bulk layer, the corrections in the outer shear layer would be needed. However, the corrections in the outer shear layer are smaller than the leading-order terms, and will behave linearly or as a constant in the axial direction for $\hat{\eta}$, and as a constant in the axial direction for $\hat{\zeta}$. Hence, as there are linear and constant leading-order terms in $\hat{\eta}$ and $\hat{\zeta}$ respectively, the correction terms will not be as large as the leading-order terms as we leave the outer shear layer and enter the bulk layer. Thus, the leading-order bulk-layer deformations will not be affected.

4.14 Conclusions

In this chapter, we have introduced a bending boundary layer to the model derived in Chapter 2, in the regime I_a where $\delta\ell \ll 1 \ll \delta\ell^2$. This bending layer has enabled the full clamped boundary conditions (4.16) to be satisfied at the ends of the elastic-walled tube, and matches onto a modified version of the shear-relaxation layer studied by Whittaker (2015). We have also evaluated how this bending layer effects the solutions in the shear-relaxation layer as well as how it effects the bulk solution modelled in Chapter 2.

Here, we have used the Kirchhoff–Love shell equations to model the wall mechanics within the bending layer. Doing so, the leading-order force-balance equations in the normal, azimuthal and axial directions were derived. By examining the normal force-balance equation, we found that the only terms that could balance at leading order are terms that arise from axial bending, and pre-stress and axial curvature. In order for these terms to balance, we found that the width δ_B of the bending layer must be $\delta_B = \mathcal{F}^{-\frac{1}{2}}\ell^{-1}$. This is in agreement with the estimate (3.48) for the bending boundary-layer width derived from the toy model in §3.6. The width of the bending layer is smaller

than the width of the inner shear layer modelled by Whittaker (2015) and as such, the bending layers are situated at the ends of the elastic-walled tube, and match onto modified inner shear layers.

Solving the leading-order force-balance equations, we have determined the leading-order normal, azimuthal and axial deformations within the bending layer. We have also found that within the bending layer, the leading-order normal deformation induces no change in the cross-sectional area of the tube from its undeformed state.

Using the leading-order deformations within the bending layer, we have determined the corrections to the deformations in the inner shear layer originally found by Whittaker (2015). These corrections have been found to be a factor of $O(\mathcal{F}^{-1}\delta^{-1}\ell^{-2})$ smaller than the leading-order terms and thus do not change the leading-order behaviour of the deformations. It is also found that these correction terms may appear at either lower or higher orders than the other higher-order terms in the expressions for the inner shear-layer deformations, depending on the sizes of δ and ℓ . If the condition $\mathcal{F} = O(1)$ is relaxed and we instead set $\mathcal{F} = O(\delta^{-1}\ell^{-2})$, the corrections will be large enough to contribute at leading order. However, this may change the behaviour of the bulk solution and will also change the sizes of the bending and inner shear layers so that they become the same size. As such, further investigation is needed to determine what happens when $\mathcal{F} = O(\delta^{-1}\ell^{-2})$.

Finally, we have also determined how the corrections in the inner shear-layer deformations affect the outer shear layer modelled by Whittaker (2015), and the bulk layer modelled in Chapter 2. We have seen that the correction in the normal deformation decays exponentially as we exit the inner shear layer. As such there will be no correction to the normal deformation or the cross-sectional area change in either of the outer shear or bulk layers. We have also seen that the corrections to the azimuthal and axial deformations in the inner shear layer yield corrections to the corresponding outer shear-layer deformations at higher orders than terms matching onto some of the leading-order terms in the inner shear layer. The corrections to the azimuthal and axial deformations in the bulk layer will also apply at higher orders.

It is seen that the bending layer found here is passive and does not contribute to the leading-order deformations as $z_B \rightarrow \infty$. Instead, it simply allows the axial gradient of the tube wall to decrease to zero as the clamped boundary at $z_B = 0$ is reached.

4.A General Solutions for the Leading-Order Deformations in the Inner Shear Layer

To determine the corrections the leading-order bending-layer deformations impose on the inner shear-layer deformations, we must solve the system governing the inner shear layer without imposing the Dirichlet parts (3.35) of the pinned boundary conditions originally applied by Whittaker (2015).

4.A.1 Recasting the System in Terms of the Stresses

In order to find the deformations within the inner shear layer, Whittaker (2015) first recast the problem in terms of the leading-order azimuthal hoop stress \tilde{N} , the leading-order in-plane shear stress \tilde{S} and the leading-order axial stress $\tilde{\Sigma}$. This was to avoid leading-order degeneracies that appeared within the governing system when written in terms of the deformations. In terms of the deformations $\hat{\xi}$, $\hat{\eta}$, $\hat{\zeta}$, and the axial coordinate $\hat{z} = \tilde{\mathcal{F}}^{-\frac{1}{2}}Z$, these stresses are defined as

$$\tilde{N} = 12 \left(-\frac{\bar{B}\hat{\xi}}{h} + \frac{1}{h} \frac{\partial}{\partial \tau} \left(\frac{\hat{\eta}}{h} \right) + \tilde{\mathcal{F}}^{-\frac{1}{2}} \nu \frac{\partial \hat{\zeta}}{\partial \hat{z}} \right), \quad (4.79)$$

$$\tilde{S} = \frac{12(1-\nu)}{2h} \left(\tilde{\mathcal{F}}^{-\frac{1}{2}} \frac{\partial \hat{\eta}}{\partial \hat{z}} + \frac{\partial \hat{\zeta}}{\partial \tau} \right), \quad (4.80)$$

$$\tilde{\Sigma} = 12 \left(\tilde{\mathcal{F}}^{-\frac{1}{2}} \frac{\partial \hat{\zeta}}{\partial \hat{z}} + \nu \left(-\frac{\bar{B}\hat{\xi}}{h} + \frac{1}{h} \frac{\partial}{\partial \tau} \left(\frac{\hat{\eta}}{h} \right) \right) \right). \quad (4.81)$$

By manipulating (4.79)–(4.81), the following expressions for the deformations in terms of the stresses are found

$$\hat{\zeta} = \int \frac{\tilde{\mathcal{F}}^{\frac{1}{2}} (\tilde{\Sigma} - \nu \tilde{N})}{12(1-\nu^2)} d\hat{z} + \frac{\tilde{\mathcal{F}}}{12(1-\nu^2)} \hat{C}(\tau, t), \quad (4.82)$$

$$\hat{\eta} = \int \tilde{\mathcal{F}}^{\frac{1}{2}} \left(\frac{h\tilde{S}}{6(1-\nu)} - \frac{\partial \hat{\zeta}}{\partial \tau} \right) d\hat{z} + \tilde{\mathcal{F}}^{\frac{3}{2}} \hat{B}(\tau, t), \quad (4.83)$$

$$\hat{\xi} = -\frac{h}{\bar{B}} \left(\frac{\tilde{N} - \nu \tilde{\Sigma}}{12(1-\nu^2)} - \frac{1}{h} \frac{\partial}{\partial \tau} \left(\frac{\hat{\eta}}{h} \right) \right), \quad (4.84)$$

where \hat{B} , \hat{C} are functions that are later determined by matching to the bending-layer deformations, and their corresponding scalings have been included for convenience.

4.A.2 Determining the Leading-Order Stresses

Once the governing system for the inner shear layer was recast in terms of \tilde{N} , \tilde{S} and $\tilde{\Sigma}$, Whittaker (2015) determined solutions for the stresses by considering asymptotic expansions of the following forms

$$\tilde{N} = \tilde{\mathcal{F}}^{\frac{1}{2}} \hat{N} = \tilde{\mathcal{F}}^{\frac{1}{2}} \left(\hat{N}^{(0)} + \tilde{\mathcal{F}} \hat{N}^{(1)} + \dots \right), \quad (4.85)$$

$$\tilde{S} = \hat{S} = \left(\hat{S}^{(0)} + \tilde{\mathcal{F}} \hat{S}^{(1)} + \dots \right), \quad (4.86)$$

$$\tilde{\Sigma} = \tilde{\mathcal{F}}^{\frac{1}{2}} \hat{\Sigma} = \tilde{\mathcal{F}}^{\frac{1}{2}} \left(\hat{\Sigma}^{(0)} + \tilde{\mathcal{F}} \hat{\Sigma}^{(1)} + \dots \right). \quad (4.87)$$

Using these approximations, the following leading-order governing equations were derived in the inner shear layer

$$-\bar{B}^2 \hat{N}^{(0)} + \frac{\partial^2 \hat{N}^{(0)}}{\partial \hat{z}^2} + (2 + \nu) \frac{\partial^2 \hat{\Sigma}^{(0)}}{\partial \hat{z}^2} = 0, \quad (4.88)$$

$$\frac{\partial^2 \hat{\Sigma}^{(0)}}{\partial \hat{z}^2} = 0, \quad (4.89)$$

$$\frac{1}{h} \frac{\partial \hat{S}^{(0)}}{\partial \tau} + \frac{\partial \hat{\Sigma}^{(0)}}{\partial \hat{z}} = 0. \quad (4.90)$$

By matching the approximations (4.85)–(4.87) to the stresses in the outer shear layer, which (at leading order) only depend on the properties of the bulk of the tube and not on the properties of the inner shear layer, the following leading-order matching conditions were found

$$\hat{N}^{(0)} \rightarrow 0, \quad \hat{S}^{(0)} \rightarrow 0, \quad \hat{\Sigma}^{(0)} \rightarrow \sum_{n=1}^{\infty} B_n(t) Y_n(\tau), \quad \text{as } \hat{z} \rightarrow \infty. \quad (4.91)$$

The general solutions of the governing equations (4.88)–(4.90) are determined to be

$$\hat{N}^{(0)} = \check{A}(\tau, t) e^{-|\bar{B}|\hat{z}} + \hat{a}(\tau, t) e^{|\bar{B}|\hat{z}}, \quad (4.92)$$

$$\hat{S}^{(0)} = \hat{s}(\tau, t) + \hat{b}(\hat{z}, t), \quad (4.93)$$

$$\hat{\Sigma}^{(0)} = -\frac{1}{h} \frac{\partial \hat{s}(\tau, t)}{\partial \tau} \hat{z} + \hat{c}(\tau, t). \quad (4.94)$$

Applying the matching conditions (4.91), it is found that

$$\hat{a}(\tau, t) = \hat{s}(\tau, t) = 0, \quad \hat{c} = \sum_{n=1}^{\infty} B_n(t) Y_n(\tau).$$

In the inner shear layer, Whittaker (2015) found that \tilde{S} is odd in τ . Using this property, we must also have

$$\hat{b}(\hat{z}, t) = 0.$$

Hence, it is found that $\hat{N}^{(0)}$, $\hat{S}^{(0)}$, and $\hat{\Sigma}^{(0)}$ are given by

$$\hat{N}^{(0)} = \check{A}(\tau, t) e^{-|\bar{B}|\hat{z}}, \quad \hat{S}^{(0)} = 0, \quad \hat{\Sigma}^{(0)} = \sum_{n=1}^{\infty} B_n(t) Y_n(\tau). \quad (4.95)$$

4.A.3 Determining the First-Order Correction to \tilde{S} in the Inner Shear Layer

As $\hat{S}^{(0)} = 0$, it is found that the leading-order azimuthal displacement $\hat{\eta}$ is dependent on the first-order correction term $\hat{S}^{(1)}$ that arises in the asymptotic expansion (4.86) for \tilde{S} . Hence, we must calculate $\hat{S}^{(1)}$ to determine $\hat{\eta}$ at leading order.

Using the approximations (4.85)–(4.87), Whittaker (2015) found the following first-order governing equation in the inner shear layer

$$\frac{1}{h} \frac{\partial \hat{N}^{(0)}}{\partial \tau} + \frac{\partial \hat{S}^{(1)}}{\partial \hat{z}} + 2(1+\nu) \frac{\partial \hat{S}^{(0)}}{\partial \hat{z}} = 0. \quad (4.96)$$

By matching the approximation (4.86) for \tilde{S} to the approximation of \tilde{S} in the outer shear layer, Whittaker (2015) found the following matching condition for $\hat{S}^{(1)}$

$$\hat{S}^{(1)} \rightarrow \sum_{n=1}^{\infty} \frac{B_n(t)}{\mu_n h} \frac{\partial}{\partial \tau} \left[\frac{1}{\bar{B}^2 h} \frac{\partial}{\partial \tau} \left(\frac{1}{h} \frac{\partial Y_n}{\partial \tau} \right) - Y_n(\tau) \right], \quad \text{as } \hat{z} \rightarrow \infty. \quad (4.97)$$

Substituting the values (4.95) of $\hat{N}^{(0)}$, $\hat{S}^{(0)}$ into (4.96) and integrating with respect to \hat{z} , we find the general solution of $\hat{S}^{(1)}$ to be

$$\hat{S}^{(1)} = \frac{1}{h} \frac{\partial}{\partial \tau} \left(\frac{\check{A}(\tau, t)}{|\bar{B}|} e^{-|\bar{B}|\hat{z}} \right) + \hat{d}(\tau, t). \quad (4.98)$$

By applying the matching condition (4.97), we obtain

$$\hat{d}(\tau, t) = \sum_{n=1}^{\infty} \frac{B_n(t)}{\mu_n h} \frac{\partial}{\partial \tau} \left[\frac{1}{\bar{B}^2 h} \frac{\partial}{\partial \tau} \left(\frac{1}{h} \frac{\partial Y_n}{\partial \tau} \right) - Y_n(\tau) \right],$$

which in turn yields

$$\hat{S}^{(1)} = \frac{1}{h} \frac{\partial}{\partial \tau} \left(\frac{\check{A}(\tau, t)}{|\bar{B}|} e^{-|\bar{B}|\hat{z}} \right) + \sum_{n=1}^{\infty} \frac{B_n(t)}{\mu_n h} \frac{\partial}{\partial \tau} \left[\frac{1}{\bar{B}^2 h} \frac{\partial}{\partial \tau} \left(\frac{1}{h} \frac{\partial Y_n}{\partial \tau} \right) - Y_n(\tau) \right]. \quad (4.99)$$

4.A.4 General Solutions of the Leading-Order Deformations

Now that we have the expressions (4.95) and (4.99) for $\hat{N}^{(0)}$, $\hat{S}^{(0)}$, $\hat{\Sigma}^{(0)}$ and $\hat{S}^{(1)}$, we use these to derive the leading-order inner shear-layer deformations in

the absence of the Dirichlet parts (3.35) of the pinned boundary conditions. Substituting the asymptotic expansions (4.85)–(4.87) into the expressions (4.82)–(4.84), the general leading-order deformations in the inner shear layer are calculated to be

$$\hat{\xi} = \frac{\tilde{\mathcal{F}}^{\frac{1}{2}}h}{12\bar{B}(1-\nu^2)} \left[\nu \sum_{n=1}^{\infty} B_n(t) Y_n(\tau) \left(1 - e^{-|\bar{B}|\hat{z}} \right) - \hat{A}(\tau, t) e^{-|\bar{B}|\hat{z}} \right] + O(\tilde{\mathcal{F}}^{\frac{3}{2}}), \quad (4.100)$$

$$\begin{aligned} \hat{\eta} = & \frac{\tilde{\mathcal{F}}^{\frac{3}{2}}}{12(1-\nu^2)} \left\{ \frac{\partial}{\partial \tau} \left[-\frac{2+\nu}{|\bar{B}|^2} \left(\sum_{n=1}^{\infty} \nu B_n(t) Y_n(\tau) + \hat{A}(\tau, t) \right) e^{-|\bar{B}|\hat{z}} \right. \right. \\ & - \sum_{n=1}^{\infty} \frac{B_n(t) Y'_n(\tau)}{2} \hat{z}^2 + \frac{2(1+\nu)}{\mu_n} \sum_{n=1}^{\infty} B_n(t) \left[\frac{1}{\bar{B}^2 h} \frac{\partial}{\partial \tau} \left(\frac{Y'_n(\tau)}{h} \right) - Y_n \right] \hat{z} \\ & \left. \left. - \hat{C}(\tau, t) \hat{z} \right] + \hat{B}(\tau, t) \right\} + O(\tilde{\mathcal{F}}^{\frac{5}{2}}), \end{aligned} \quad (4.101)$$

$$\begin{aligned} \hat{\zeta} = & \frac{\tilde{\mathcal{F}}}{12(1-\nu^2)} \left[\sum_{n=1}^{\infty} B_n(t) Y_n(\tau) \left(\hat{z} + \frac{\nu^2}{|\bar{B}|} e^{-|\bar{B}|\hat{z}} \right) \right. \\ & \left. + \frac{\nu}{|\bar{B}|} \hat{A}(\tau, t) e^{-|\bar{B}|\hat{z}} + \hat{C}(\tau, t) \right] + O(\tilde{\mathcal{F}}^2), \end{aligned} \quad (4.102)$$

where for convenience, we have rewritten \check{A} as

$$\check{A}(\tau, t) = \sum_{n=1}^{\infty} \nu B_n(t) Y_n(\tau) + \hat{A}(\tau, t),$$

and \hat{A} , \hat{B} , \hat{C} are arbitrary functions. In Whittaker (2015), the conditions $\hat{\xi} = \hat{\eta} = \hat{\zeta} = 0$ at $\hat{z} = 0$ were applied to obtain the functions $\hat{A}, \hat{B}, \hat{C}$. But here $\hat{A}, \hat{B}, \hat{C}$ are determined by matching to the bending-layer deformations.

Chapter 5

The Bending Boundary Layer in Regime I_b ($\delta\ell^2 \ll 1$)

5.1 Introduction

In this chapter, we consider another regime of the general problem described in Chapter 3, where an axial-bending boundary layer is introduced to the model of flow through an elastic-walled tube. This bending layer will allow the canonical clamped boundary conditions to be satisfied at the ends of the elastic-walled tube, where it is clamped onto two fixed rigid tubes.

Here, we focus on regime I_b , where the dimensionless tube wall thickness $\delta \ll 1$ and tube length $\ell \gg 1$ are set so $\delta\ell^2 \ll 1$. In this regime, a shear-relaxation layer studied by Whittaker (2015) (details of which may be found in §3.5) is seen to have a significant effect on the bulk of the tube and must be considered. This shear layer is comprised of two sub-layers: an inner layer of width $O(\delta\ell)$, and an outer layer of width $O(\delta^{-1}\ell^{-1})$.

In §3.6, a toy model was derived which estimated the width δ_B of the bending boundary layer to be $\delta_B = O(\ell^{-1})$. Using this estimate, we expect δ_B to be larger than the tube wall thickness δ ($\ell^{-1} \gg \delta^{\frac{1}{2}} \gg \delta$). As such, we may use the Kirchhoff–Love shell equations (Flügge, 1972; Søndergaard, 2007) to model the wall mechanics. As $\ell \gg 1$, we also anticipate that $\delta_B \ll 1$. Finally, we expect δ_B to be larger than the inner shear-layer width, and smaller than the outer shear-layer width ($\delta\ell \ll \ell^{-1} \ll \delta^{-1}\ell^{-1}$).

As the bending layer is expected to be larger than the inner shear layer, we will have one of two scenarios. In the first scenario an inner shear layer, modified so that the full clamped boundary conditions are satisfied at the ends

of the elastic-walled tube, is situated at the tube ends. This inner shear layer then matches onto the bending layer which in turn matches onto the outer shear layer. The outer shear layer then matches onto the solution in the bulk layer. This scenario is unlikely as the inner shear layer would need terms with additional axial derivatives to appear at leading order in the governing equations so that the clamped boundary conditions may be satisfied.

In the second scenario, the inner shear layer is not needed and instead the bending layer is situated at the ends of the elastic-walled tube. This bending layer then matches onto the outer shear layer, which in turn matches onto the bulk layer. When the governing equations are later examined at an axial scale smaller than δ_B in §5.5, it is found that no new mechanisms contribute to the leading-order governing equations, and there are no boundary layers smaller than the bending layer. Hence, it is the second scenario that arises within the model. Figure 5.1 shows the arrangement of these boundary layers along the dimensionless, axial coordinate $Z \in [0, \ell]$ introduced in Chapter 3 and used by Whittaker (2015) to describe the inner and outer shear layers.

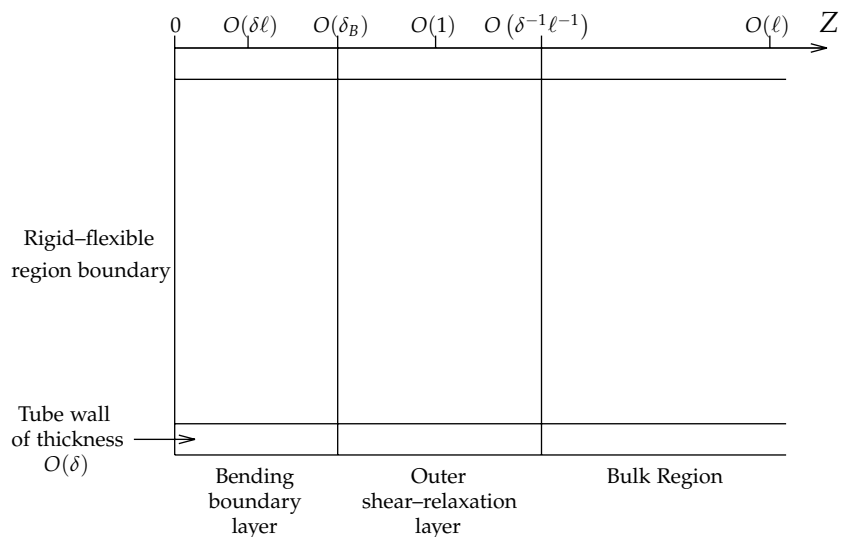


Figure 5.1: The arrangement of the boundary layers in a cross section through the centre point and along the length of the tube, in regime I_b where $\delta\ell^2 \ll 1$. We expect to have $\delta \ll \delta\ell \ll \delta_B \ll 1 \ll \delta^{-1}\ell^{-1} \ll \ell$.

We later find that the deformations in the bending and outer shear layers depend only on the uniform properties of the tube wall and not on the properties of the fluid within the tube. Therefore, the boundary layers will behave the same at the upstream and downstream ends of the elastic-walled

tube. Hence, we need only determine the behaviour of the boundary layers at one of these ends. In this chapter, we concentrate on modelling the bending layer at the upstream ($Z = 0$) end of the tube.

We arrange this chapter as follows. In §5.2 and §5.3, the mathematical set-up of the tube and its deformations, as well as the tensors and constitutive laws needed in the problem, are provided. In §5.4, the behaviour of the tube wall in the outer shear layer studied by Whittaker (2015) is reviewed. The force-balance equations governing the tube wall in the bending layer are then derived in §5.5, including all the terms that *may* contribute at leading order. The boundary and matching conditions for the system are considered in §5.6.

Due to the behaviour of the leading-order deformations within the outer shear layer, it is unclear what the matching conditions for the deformations in the bending layer should be. To resolve this problem, the system is recast in terms of the leading-order in-plane stresses acting on the tube in §5.7. The sizes of the stresses within the bending layer, as well as the magnitude of the width δ_B of the bending layer, are calculated in §5.8, and the simpler case of the limit of a circular cross-section is considered in §5.9. Asymptotic approximations for the stresses in the bending layer are calculated up to second order in §5.10, and the bending-layer deformations and area variation are determined in §5.11 and §5.12, respectively. Finally, in §5.13 and §5.14, we determine the corrections the leading-order bending-layer deformations enforce on the deformations and area change in the outer shear and bulk layers.

5.2 Mathematical Set-up

We again consider the set-up described in §3.3 and §4.2, and depicted in Figure 5.2. We begin with an initially elliptical elastic-walled tube with dimensionless

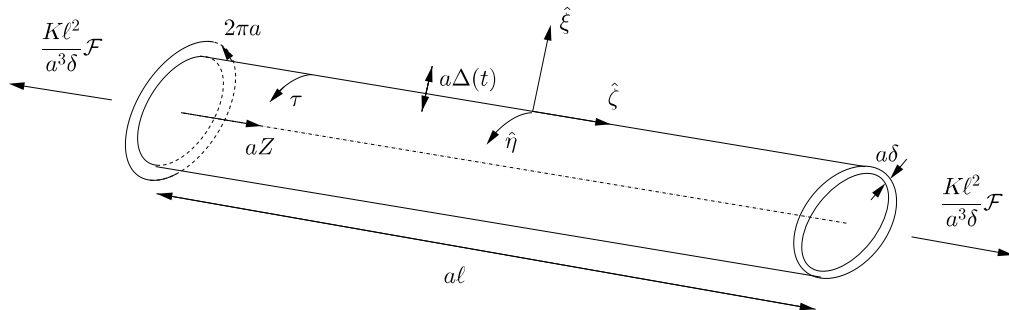


Figure 5.2: The set-up of the undeformed, elliptical, elastic-walled tube.

length $\ell \gg 1$ and dimensionless wall thickness $\delta \ll 1$. In its undeformed configuration, this tube is subject to a dimensionless uniform axial tension $\mathcal{F} = O(1)$. Deformations of dimensionless amplitude $\Delta(t) \ll 1$ are then induced by a dimensionless transmural pressure p_{tm} . We assume that the amplitude $\Delta(t)$ is slowly varying in dimensionless time t . The tube wall has dimensionless mass M per unit area, Poisson's ratio ν and bending stiffness K . We again introduce the parameter $\tilde{\mathcal{F}}$ given by

$$\tilde{\mathcal{F}} = \frac{\delta^2 \ell^2 \mathcal{F}}{12(1-\nu^2)} \ll 1. \quad (5.1)$$

This parameter appears in the model of the shear-relaxation layer derived by Whittaker (2015) considered later on.

We parameterize the midplane of the tube wall using two dimensionless Lagrangian surface coordinates $\tau \in [0, 2\pi)$, $Z \in [0, \ell]$, which represent arc length in the azimuthal and axial directions respectively. These are related to their dimensional counterparts (x^1, x^2) by $dx^1 = ah(\tau)d\tau$, $dx^2 = adZ$. Here, a is the typical radial scale of the tube and $h(\tau)$ is a scale factor defined as

$$h(\tau) = c(\sinh^2 \sigma_0 + \sin^2 \tau)^{\frac{1}{2}}, \quad (5.2)$$

where σ_0 is a parameter that sets the ellipticity of the tube and $c(\sigma_0)$ is defined as

$$c = \frac{\pi \operatorname{sech}(\sigma_0)}{2E(\operatorname{sech}(\sigma_0))}, \quad (5.3)$$

where the complete elliptic integral of the second kind $E(\phi)$ is defined as

$$E(\phi) = \int_0^{\frac{\pi}{2}} (1 - \phi^2 \sin^2 \vartheta)^{\frac{1}{2}} d\vartheta.$$

Using these coordinates, we define the position $\mathbf{r}_0(\tau, Z)$ of the tube wall in the undeformed configuration as

$$\mathbf{r}_0(\tau, Z) = a \begin{pmatrix} c \cosh \sigma_0 \cos \tau \\ c \sinh \sigma_0 \sin \tau \\ Z \end{pmatrix}. \quad (5.4)$$

Denoting the position of the tube wall in its deformed configuration as \mathbf{r} , the deformation $\mathbf{r} - \mathbf{r}_0$ of the tube wall is written as

$$\mathbf{r} - \mathbf{r}_0 = \frac{\Delta(t)a}{\ell} \left(\frac{1}{h(\tau)} [\hat{\xi}(\tau, Z, t)\hat{\mathbf{n}} + \hat{\eta}(\tau, Z, t)\hat{\mathbf{t}}] + \hat{\zeta}(\tau, Z, t)\hat{\mathbf{z}} \right), \quad (5.5)$$

based on the expected sizes of the deformations at $Z = O(1)$. This is the same representation used by Whittaker (2015) when modelling the shear-relaxation

layer. The vectors $\hat{\mathbf{n}}$, $\hat{\mathbf{t}}$ and $\hat{\mathbf{z}}$ are unit vectors in the normal, azimuthal and axial directions of the undeformed tube wall, and the dimensionless functions $(\hat{\xi}, \hat{\eta}, \hat{\zeta})$ represent the normal, azimuthal and axial deformations of the tube wall.

Finally, we introduce a new axial coordinate

$$z_B = \delta_B^{-1} Z, \quad (5.6)$$

where δ_B is the width of the axial-bending boundary layer. As such, we have that $z_B = O(1)$ within the bending layer. Here, we assume $\delta \ll \delta_B$ allowing Kirchhoff–Love shell theory to be used in deriving the governing equations within the bending layer. In order for the axial-bending terms to appear at leading order in the governing equations, we must also have $\delta_B \ll 1$.

5.3 Tensor Notation and Constitutive Laws

Using the deformation (5.5), it is now possible to calculate the tensors associated with the tube wall that are needed in the governing force-balance equations later on. These are slightly different to the tensors derived in §4.6 in Regime I_a. We begin with the basis vectors \mathbf{a}_1 , \mathbf{a}_2 , and the normal \mathbf{a}_3 to the tube wall in the deformed configuration, defined as

$$\mathbf{a}_\alpha = \frac{\partial \mathbf{r}}{\partial x^\alpha}, \quad \mathbf{a}_3 = \frac{\mathbf{a}_1 \times \mathbf{a}_2}{|\mathbf{a}_1 \times \mathbf{a}_2|}, \quad (5.7)$$

where α spans over (1, 2). Substituting the expressions (5.4)–(5.6) for \mathbf{r}_0 , \mathbf{r} and z_B into (5.7) and neglecting terms of $O(\Delta^2)$ and higher, we find

$$\begin{aligned} \mathbf{a}_1 &= \hat{\mathbf{t}} + \frac{\Delta}{\ell h} \left(\left[-\hat{\xi} \bar{B}(\tau) + \frac{\partial}{\partial \tau} \left(\frac{\hat{\eta}}{h} \right) \right] \hat{\mathbf{t}} + \left[\hat{\eta} \bar{B}(\tau) + \frac{\partial}{\partial \tau} \left(\frac{\hat{\zeta}}{h} \right) \right] \hat{\mathbf{n}} + \frac{\partial \hat{\zeta}}{\partial \tau} \hat{\mathbf{z}} \right) \\ &\quad + O(\Delta^2), \end{aligned} \quad (5.8)$$

$$\mathbf{a}_2 = \hat{\mathbf{z}} + \frac{\Delta}{\ell \delta_B} \left(\frac{1}{h} \left[\frac{\partial \hat{\zeta}}{\partial z_B} \hat{\mathbf{n}} + \frac{\partial \hat{\eta}}{\partial z_B} \hat{\mathbf{t}} \right] + \frac{\partial \hat{\zeta}}{\partial z_B} \hat{\mathbf{z}} \right) + O(\Delta^2), \quad (5.9)$$

$$\mathbf{a}_3 = \hat{\mathbf{n}} - \frac{\Delta}{\ell h} \left(\left[\hat{\eta} \bar{B}(\tau) + \frac{\partial}{\partial \tau} \left(\frac{\hat{\zeta}}{h} \right) \right] \hat{\mathbf{t}} + \frac{1}{\delta_B} \frac{\partial \hat{\zeta}}{\partial z_B} \hat{\mathbf{z}} \right) + O(\Delta^2), \quad (5.10)$$

where, as in previous chapters, $\bar{B}(\tau)$ is the dimensionless base-state azimuthal curvature, given by

$$\bar{B}(\tau) = -\frac{c^2 \sinh(2\sigma_0)}{2h^3}. \quad (5.11)$$

Using these, we evaluate the metric tensor $a_{\alpha\beta}$, curvature tensor $b_{\alpha\beta}$, and in-plane and bending strain tensors, $\gamma_{\alpha\beta}$ and $\kappa_{\alpha\beta}$, in the bending layer. As in §2.3 and §4.6, these are defined as

$$\begin{aligned} a_{\alpha\beta} &= \mathbf{a}_\alpha \cdot \mathbf{a}_\beta, & b_{\alpha\beta} &= \mathbf{a}_3 \cdot \frac{\partial \mathbf{a}_\alpha}{\partial x^\beta}, \\ \gamma_{\alpha\beta} &= \frac{1}{2}(a_{\alpha\beta} - \bar{a}_{\alpha\beta}), & \kappa_{\alpha\beta} &= -b_{\alpha\beta} + \bar{b}_{\alpha\beta} + 2\bar{b}_\alpha^\delta \gamma_{\delta\beta}. \end{aligned} \quad (5.12)$$

Substituting (5.8)–(5.10) into (5.12) and again neglecting terms that are $O(\Delta^2)$ or higher, the following is calculated

$$a_{\alpha\beta} = \bar{a}_{\alpha\beta} + \frac{\Delta}{\ell h} \begin{bmatrix} 2 \left[-\hat{\xi} \bar{B} + \frac{\partial}{\partial \tau} \left(\frac{\hat{\eta}}{h} \right) \right] & \frac{1}{\delta_B} \frac{\partial \hat{\eta}}{\partial z_B} + \frac{\partial \hat{\xi}}{\partial \tau} \\ \frac{1}{\delta_B} \frac{\partial \hat{\eta}}{\partial z_B} + \frac{\partial \hat{\xi}}{\partial \tau} & \frac{2h}{\delta_B} \frac{\partial \hat{\xi}}{\partial z_B} \end{bmatrix} + O(\Delta^2), \quad (5.13)$$

$$\begin{aligned} b_{\alpha\beta} &= \bar{b}_{\alpha\beta} + \frac{\Delta}{a\ell h} \begin{bmatrix} \beta_1 + \beta_2 & \frac{1}{\delta_B} \left[\bar{B} \frac{\partial \hat{\eta}}{\partial z_B} + \frac{\partial}{\partial \tau} \left(\frac{1}{h} \frac{\partial \hat{\xi}}{\partial z_B} \right) \right] \\ \frac{1}{\delta_B} \left[\bar{B} \frac{\partial \hat{\eta}}{\partial z_B} + \frac{\partial}{\partial \tau} \left(\frac{1}{h} \frac{\partial \hat{\xi}}{\partial z_B} \right) \right] & \frac{1}{\delta_B^2} \frac{\partial^2 \hat{\xi}}{\partial z_B^2} \end{bmatrix} \\ &\quad + O(\Delta^2), \end{aligned} \quad (5.14)$$

$$\gamma_{\alpha\beta} = \frac{\Delta}{\ell h} \begin{bmatrix} -\hat{\xi} \bar{B} + \frac{\partial}{\partial \tau} \left(\frac{\hat{\eta}}{h} \right) & \frac{1}{2} \left(\frac{1}{\delta_B} \frac{\partial \hat{\eta}}{\partial z_B} + \frac{\partial \hat{\xi}}{\partial \tau} \right) \\ \frac{1}{2} \left(\frac{1}{\delta_B} \frac{\partial \hat{\eta}}{\partial z_B} + \frac{\partial \hat{\xi}}{\partial \tau} \right) & h \frac{1}{\delta_B} \frac{\partial \hat{\xi}}{\partial z_B} \end{bmatrix} + O(\Delta^2), \quad (5.15)$$

$$\kappa_{\alpha\beta} = \frac{\Delta}{a\ell h} \begin{bmatrix} \beta_1 - \beta_2 & \bar{B} \frac{\partial \hat{\xi}}{\partial \tau} - \frac{1}{\delta_B} \frac{\partial}{\partial \tau} \left(\frac{1}{h} \frac{\partial \hat{\xi}}{\partial z_B} \right) \\ -\frac{1}{\delta_B} \left[\frac{\partial}{\partial \tau} \left(\frac{1}{h} \frac{\partial \hat{\xi}}{\partial z_B} \right) + \bar{B} \frac{\partial \hat{\eta}}{\partial z_B} \right] & -\frac{1}{\delta_B^2} \frac{\partial^2 \hat{\xi}}{\partial z_B^2} \end{bmatrix} + O(\Delta^2). \quad (5.16)$$

Here $\bar{a}_{\alpha\beta}$ is the 2×2 identity matrix, $\bar{b}_{\alpha\beta}$ is defined as

$$\bar{b}_\alpha^\beta = \frac{1}{a} \begin{bmatrix} \bar{B}(\tau) & 0 \\ 0 & 0 \end{bmatrix},$$

and β_1, β_2 are given by

$$\beta_1 = \bar{B} \left[-\hat{\xi} \bar{B} + \frac{\partial}{\partial \tau} \left(\frac{\hat{\eta}}{h} \right) \right], \quad \beta_2 = \frac{\partial}{\partial \tau} \left(\frac{1}{h} \left[\hat{\eta} \bar{B} + \frac{\partial}{\partial \tau} \left(\frac{\hat{\xi}}{h} \right) \right] \right). \quad (5.17)$$

The in-plane stresses, $N^{\alpha\beta}$, and the in-plane bending moments, $M^{\alpha\beta}$, may be determined from the following constitutive laws relating $N^{\alpha\beta}$ and $M^{\alpha\beta}$ to $a_{\alpha\beta}, b_{\alpha\beta}, \gamma_{\alpha\beta}$ and $\kappa_{\alpha\beta}$

$$\begin{aligned} N^{\alpha\beta} &= \delta_2^\alpha \delta_2^\beta \frac{K\ell^2 \mathcal{F}}{a^2} + \frac{12}{a^2 \delta^2} K[(1-\nu)\gamma^{\alpha\beta} + \nu \gamma_\lambda^\lambda a^{\alpha\beta}] \\ &\quad + K \left\{ \frac{(1-\nu)}{2} [2a^{\beta\delta} b^{\alpha\gamma} + a^{\beta\gamma} b^{\alpha\gamma} + a^{\alpha\delta} b^{\beta\gamma} - b_\lambda^\lambda (a^{\alpha\delta} a^{\beta\gamma} + a^{\alpha\gamma} a^{\beta\delta})] \right. \\ &\quad \left. + \nu [a^{\alpha\beta} b^{\gamma\delta} + a^{\gamma\delta} b^{\alpha\beta} - a^{\alpha\beta} a^{\gamma\delta} b_\lambda^\lambda] \right\} \kappa_{\lambda\delta}, \end{aligned} \quad (5.18)$$

$$\begin{aligned} M^{\alpha\beta} &= K[-(1-\nu)(b_\gamma^\alpha \gamma^{\gamma\beta} - b_\lambda^\lambda \gamma^{\alpha\beta}) - \nu(b^{\alpha\beta} - b_\lambda^\lambda a^{\alpha\beta}) \gamma_\mu^\mu \\ &\quad + \frac{1}{2}(1-\nu)(\kappa^{\alpha\beta} + \kappa^{\beta\alpha}) + \nu a^{\alpha\beta} \kappa_\lambda^\lambda], \end{aligned} \quad (5.19)$$

where δ_j^i is the Kronecker delta. These constitutive laws were originally derived by Flügge (1972). By substituting the tensors (5.13)–(5.16) into (5.18), the leading-order components of $N^{\alpha\beta}$ are determined as

$$N^{\alpha\beta} = \frac{K}{a^2} \begin{pmatrix} 0 & 0 \\ 0 & \ell^2 \mathcal{F} \end{pmatrix} + \frac{\Delta K}{a^2 \delta^2 \ell} \begin{pmatrix} \tilde{N} & \tilde{S} \\ \tilde{S} & \tilde{\Sigma} \end{pmatrix} + O\left(\frac{\Delta K}{a^2 \delta_B^2 \ell}\right), \quad (5.20)$$

where the leading-order azimuthal hoop stress \tilde{N} is defined as

$$\tilde{N} = 12 \left(-\frac{\bar{B}\hat{\xi}}{h} + \frac{1}{h} \frac{\partial}{\partial \tau} \left(\frac{\hat{\eta}}{h} \right) + \frac{\nu}{\delta_B} \frac{\partial \hat{\zeta}}{\partial z_B} \right), \quad (5.21)$$

the leading-order in-plane shear stress \tilde{S} is

$$\tilde{S} = \frac{6(1-\nu)}{h} \left(\frac{1}{\delta_B} \frac{\partial \hat{\eta}}{\partial z_B} + \frac{\partial \hat{\zeta}}{\partial \tau} \right), \quad (5.22)$$

and the leading-order axial stress $\tilde{\Sigma}$ is defined to be

$$\tilde{\Sigma} = 12 \left(\frac{1}{\delta_B} \frac{\partial \hat{\zeta}}{\partial z_B} + \nu \left(-\frac{\bar{B}\hat{\xi}}{h} + \frac{1}{h} \frac{\partial}{\partial \tau} \left(\frac{\hat{\eta}}{h} \right) \right) \right). \quad (5.23)$$

The first term of (5.20) corresponds to the axial pre-stress applied to the tube wall and the second term contains the leading-order stresses induced by the deformations of the tube wall. Substituting the tensors (5.13)–(5.16) into (5.19), we find the leading-order components of $M^{\alpha\beta}$ to be

$$M^{\alpha\beta} = -\frac{\Delta K}{a \delta_B^2 \ell} \begin{pmatrix} \frac{\nu}{h} \frac{\partial^2 \hat{\xi}}{\partial z_B^2} & 0 \\ 0 & \frac{1}{h} \frac{\partial^2 \hat{\xi}}{\partial z_B^2} \end{pmatrix} + O\left(\frac{\Delta K}{a \delta_B \ell}\right). \quad (5.24)$$

5.4 Consideration of the Outer Shear-Relaxation Layer by Whittaker (2015)

In the current regime, the size of the bending layer is expected to be in between the sizes of the two sub-layers comprising the shear-relaxation layer studied by Whittaker (2015). That is the width δ_B of the bending layer is larger than the width $\tilde{\mathcal{F}}^{\frac{1}{2}}$ of the inner shear layer, but smaller than the width $\tilde{\mathcal{F}}^{-\frac{1}{2}}$ of the outer shear layer. It is later found that in this scenario the inner shear layer is non-existent, and the bending layer is situated at the ends of the tube. The bending layer then matches onto the outer shear layer. Because of this, the outer shear layer must be considered so that the sizes of the deformations in

the bending layer, and the matching conditions the bending-layer deformations must satisfy, may be determined.

In deriving a model of the shear-relaxation layer, Whittaker (2015) rewrote the problem to be in terms of the stresses \tilde{N} , \tilde{S} and $\tilde{\Sigma}$ rather than the displacements $\hat{\xi}$, $\hat{\eta}$ and $\hat{\zeta}$. This was to avoid the leading-order cancellations that occurred in the governing equations when written in terms of the deformations. Solving the problem in terms of the stresses, Whittaker (2015) calculated asymptotic approximations for the stresses \tilde{N} , \tilde{S} and $\tilde{\Sigma}$ in the outer shear layer. Here, we shall denote these approximations as \tilde{N}_s , \tilde{S}_s and $\tilde{\Sigma}_s$.

These approximations only rely on matching to the solutions in the bulk layer and not on matching to the inner shear layer. As such, when the inner shear layer is replaced by the bending layer these approximations will still hold true, and the bending layer will not force any leading-order corrections to the stresses within the outer shear layer.

Using the approximations for the stresses, Whittaker (2015) determined asymptotic approximations for the deformations $\hat{\xi}$, $\hat{\eta}$ and $\hat{\zeta}$ within the outer shear layer. These approximations were determined using the Dirichlet parts (3.35) of the pinned boundary conditions, defined in §3.4. Hence, as we are now introducing the bending layer so the deformations satisfy the clamped boundary conditions (3.32) (defined in §3.4) instead, the bending layer will force corrections to the deformations in the outer shear layer. These corrections will only take effect at higher orders in the approximations.

By examining the approximations of the deformations in the outer shear layer, it is found that as $Z \rightarrow 0$, the leading-order term in the approximation for $\hat{\xi}$ behaves quadratically in the axial direction. However as Z is decreased, this term eventually becomes small enough that another, higher-order term (that behaves as a constant as $Z \rightarrow 0$) becomes the leading-order term in the approximation. Because of this property, it is unclear what the size and leading-order matching condition for the normal deformation $\hat{\zeta}$ in the bending layer should be.

To obtain a full set of matching conditions to be used in finding a solution for the bending layer, we later rewrite the problem in terms of the stresses \tilde{N} , \tilde{S} and $\tilde{\Sigma}$. As $Z \rightarrow 0$, the leading-order terms of the asymptotic expansions \tilde{N}_s , \tilde{S}_s and $\tilde{\Sigma}_s$ in the outer shear layer all behave as a constant in Z . Hence, even as we decrease Z , the leading-order terms do not become smaller than any other terms in the approximations, and it is these terms the bending-layer stresses

must match on to at leading order. Taking the Taylor series of \tilde{N}_s , \tilde{S}_s and $\tilde{\Sigma}_s$ about $\check{z} = 0$, where the scaled axial coordinate $\check{z} = \tilde{\mathcal{F}}^{\frac{1}{2}}Z$ is used by Whittaker (2015) to describe the axial behaviour of the stresses and deformations in the outer shear layer, we find as $\check{z} \rightarrow 0$

$$\tilde{N}_s \sim \frac{\tilde{\mathcal{F}}^{\frac{3}{2}}}{\bar{B}^2 h} \sum_{n=1}^{\infty} B_n(t) \frac{\partial}{\partial \tau} \left(\frac{1}{h} \frac{\partial Y_n}{\partial \tau} \right) (1 - \mu_n \check{z} + O(\check{z}^2)) + O(\tilde{\mathcal{F}}^{\frac{5}{2}}), \quad (5.25)$$

$$\begin{aligned} \tilde{S}_s \sim & \frac{\tilde{\mathcal{F}}}{h} \sum_{n=1}^{\infty} \frac{B_n(t)}{\mu_n} \frac{\partial}{\partial \tau} \left[\frac{1}{\bar{B}^2 h} \frac{\partial}{\partial \tau} \left(\frac{1}{h} \frac{\partial Y_n}{\partial \tau} \right) - Y_n(\tau) \right] (1 - \mu_n \check{z} + O(\check{z}^2)) \\ & + O(\tilde{\mathcal{F}}^2), \end{aligned} \quad (5.26)$$

$$\tilde{\Sigma}_s \sim \tilde{\mathcal{F}}^{\frac{1}{2}} \sum_{n=1}^{\infty} B_n(t) Y_n(\tau) (1 - \mu_n \check{z} + O(\check{z}^2)) + O(\tilde{\mathcal{F}}^{\frac{3}{2}}). \quad (5.27)$$

Here, the π -periodic, orthogonal functions $Y_n(\tau)$ are the eigenfunctions of the operator

$$\mathcal{L} \equiv \frac{1}{h} \frac{\partial}{\partial \tau} \frac{1}{h} \frac{\partial}{\partial \tau} \left(\frac{1}{\bar{B}^2 h} \frac{\partial}{\partial \tau} \frac{1}{h} \frac{\partial}{\partial \tau} - 1 \right), \quad (5.28)$$

and the μ_n^2 are the corresponding distinct positive eigenvalues ordered such that $0 < \mu_1 < \mu_2 < \mu_3 \dots$. For finite σ_0 , these eigenfunctions and eigenvalues can only be found numerically. Finally, the $B_n(t)$ are arbitrary $O(1)$ functions of t setting the amplitude of each eigenmode of the deformations.

Matching the stresses in the bending layer to the approximations (5.25)–(5.27) will allow us to determine the full leading-order solutions of the stresses in the bending layer. These solutions along with the clamped boundary conditions (3.32) will in turn allow us to determine the leading-order deformations in the bending layer. To find the corrections the leading-order bending-layer deformations force on the outer shear-layer deformations, we will need to match the bending-layer deformations to solutions of the deformations in the outer shear layer which do not depend on the Dirichlet parts (3.35) of the pinned boundary conditions. By removing these boundary conditions from the relations derived by Whittaker (2015) that relate the stresses and deformations in the outer shear layer, the most general solutions of the

deformations in the outer shear layer are found to be

$$\hat{\xi} = \frac{\tilde{\mathcal{F}}^{-\frac{1}{2}}}{12\bar{B}(1-\nu^2)} \left\{ \sum_{n=1}^{\infty} \frac{B_n(t)}{\mu_n} \frac{\partial}{\partial \tau} \left(\frac{1}{h} \frac{\partial Y_n}{\partial \tau} \right) \left[\frac{1}{\mu_n} (1 - e^{-\mu_n \check{z}}) - \check{z} \right] - \frac{\partial}{\partial \tau} \left(\frac{1}{h} \frac{\partial \check{A}(\tau, t)}{\partial \tau} \right) \check{z} + \frac{\partial}{\partial \tau} \left(\frac{\check{B}(\tau, t)}{h} \right) \right\} + O(\tilde{\mathcal{F}}^{\frac{1}{2}}), \quad (5.29)$$

$$\hat{\eta} = \frac{\tilde{\mathcal{F}}^{-\frac{1}{2}}}{12(1-\nu^2)} \left\{ \sum_{n=1}^{\infty} \frac{B_n(t)}{\mu_n} \frac{\partial Y_n}{\partial \tau} \left[\frac{1}{\mu_n} (1 - e^{-\mu_n \check{z}}) - \check{z} \right] - \frac{\partial \check{A}(\tau, t)}{\partial \tau} \check{z} + \check{B}(\tau, t) \right\} + O(\tilde{\mathcal{F}}^{\frac{1}{2}}), \quad (5.30)$$

$$\hat{\zeta} = \frac{1}{12(1-\nu^2)} \left\{ \sum_{n=1}^{\infty} \frac{B_n(t) Y_n(\tau)}{\mu_n} (1 - e^{-\mu_n \check{z}}) + \check{A}(\tau, t) \right\} + O(\tilde{\mathcal{F}}), \quad (5.31)$$

where \check{A} and \check{B} are arbitrary functions to be determined by matching to the bending-layer deformations. The corrections to the outer shear-layer deformations due to the leading-order bending-layer deformations are calculated in §5.13.

5.5 Force-Balance Equations

In order to model the mechanics of the tube wall in the bending layer, we use Kirchhoff–Love shell theory. Previously in §2.3, the governing force-balance equations (2.29)–(2.31) in the normal, azimuthal and axial directions were derived from the Kirchhoff–Love shell equations in covariant differential form (Flügge, 1972; Søndergaard, 2007). Rewriting these in terms of the deformations $\hat{\xi}$, $\hat{\eta}$ and $\hat{\zeta}$, we find

$$\nabla_{\alpha} \nabla_{\beta} M^{\alpha\beta} + N^{\alpha\beta} b_{\alpha\beta} - \frac{K\delta^2 M}{12a^2} \nabla_{\alpha} \frac{d^2 \theta^{*\alpha}}{dt^2} + \frac{\Delta(t)K}{a^3} p_{\text{tm}} - \frac{\Delta(t)K}{a^3 \ell} \frac{M}{h(\tau)} \frac{d^2 \hat{\xi}}{dt^2} = 0, \quad (5.32)$$

$$\nabla_{\beta} N^{\beta 1} - b_{\gamma}^1 \nabla_{\beta} M^{\beta\gamma} + \frac{K\delta^2 M}{12a^2} b_{\gamma}^1 \frac{d^2 \theta^{*\gamma}}{dt^2} - \frac{\Delta(t)K}{a^3 \ell} \frac{M}{h(\tau)} \frac{d^2 \hat{\eta}}{dt^2} = 0, \quad (5.33)$$

$$\nabla_{\beta} N^{\beta 2} - b_{\gamma}^2 \nabla_{\beta} M^{\beta\gamma} + \frac{K\delta^2 M}{12a^2} b_{\gamma}^2 \frac{d^2 \theta^{*\gamma}}{dt^2} - \frac{\Delta(t)K}{a^3 \ell} M \frac{d^2 \hat{\zeta}}{dt^2} = 0. \quad (5.34)$$

Here, the covariant derivatives ∇_{α} at leading order are found to be

$$\nabla_1 = \frac{1}{ah} \frac{\partial}{\partial \tau} + O(\Delta), \quad \nabla_2 = \frac{1}{a\delta_B} \frac{\partial}{\partial z_B} + O(\Delta), \quad (5.35)$$

and $\theta^{*\alpha}$ is the angle of rotation the tube wall takes about an axis passing through the wall in the \mathbf{a}_{α} direction. By considering the size of the normal deformation

in the bending layer, and the sizes of the azimuthal and axial length scales used in the bending layer, we scale the $\theta^{*\alpha}$ in the following way

$$\theta^{*1} = \frac{\Delta}{\delta_B \ell} \theta^1, \quad \theta^{*2} = \frac{\Delta}{\ell} \theta^2, \quad (5.36)$$

where θ^1, θ^2 take the same size as $\hat{\xi}$ in the bending layer.

As the in-plane stress $N^{\alpha\beta}$ contains a large pre-stress term, we must evaluate some of the higher-order terms in the covariant derivative of $N^{\alpha\beta}$. The full expression for $\nabla_\alpha N^{\alpha\beta}$ is given by

$$\nabla_\alpha N^{\alpha\beta} = \frac{\partial N^{\alpha\beta}}{\partial x^\alpha} + \Gamma_{\gamma\alpha}^\alpha N^{\gamma\beta} + \Gamma_{\gamma\alpha}^\beta N^{\alpha\gamma}, \quad (5.37)$$

where the Christoffel symbol $\Gamma_{\mu\nu}^\beta$ is given as $\Gamma_{\mu\nu}^\beta \equiv a^{\alpha\beta} \mathbf{a}_\alpha \cdot \mathbf{a}_{\mu,\nu}$. As each component of $\Gamma_{\mu\nu}^\beta$ is $O(\Delta)$, we need only consider terms involving N^{22} , the only non- $O(\Delta)$ component of $N^{\alpha\beta}$. The Christoffel symbols found to be needed are $\Gamma_{21}^1, \Gamma_{22}^1$ and Γ_{22}^2 . These are determined to be

$$\Gamma_{21}^1 = \frac{\Delta}{a\ell\delta_B h\bar{B}} \frac{\partial\beta_1}{\partial z_B} + O(\Delta^2), \quad (5.38)$$

$$\Gamma_{22}^1 = \frac{\Delta}{a\ell\delta_B^2 h} \frac{\partial^2\hat{\eta}}{\partial z_B^2} + O(\Delta^2), \quad (5.39)$$

$$\Gamma_{22}^2 = \frac{\Delta}{a\ell\delta_B^2} \frac{\partial^2\hat{\zeta}}{\partial z_B^2} + O(\Delta^2). \quad (5.40)$$

By substituting (5.13)–(5.24) and (5.35)–(5.40) into the governing force-balance equations (5.32)–(5.34), it is possible to determine the sizes of each of the terms within the force-balance equations, up to the unknown sizes of the deformations $\hat{\xi}, \hat{\eta}$ and $\hat{\zeta}$. The sizes of the terms in (5.32)–(5.34) are found in Tables 5.1–5.3. As in §4.7, the terms corresponding to angular acceleration and wall inertia are not large enough to contribute at leading order and are not included in the tables. This is because these terms are either $O(\Delta K\hat{\xi}/a^3\ell)$, $O(\Delta K\hat{\eta}/a^3\ell)$ or $O(\Delta K\hat{\zeta}/a^3\ell)$ at most, all of which are strictly smaller than some of the other terms within the governing equations when $\delta_B \ll 1$.

By examining the scalings of the terms within Tables 5.1–5.3, the terms that contribute to the leading-order force-balance equations may be determined up to the unknown sizes of the deformations $\hat{\xi}, \hat{\eta}$ and $\hat{\zeta}$. In the normal force-balance equation, the possible leading-order terms arise from azimuthal and axial stretching, axial bending, pre-stress and axial curvature, and transmural pressure. In the azimuthal and axial force-balance equations, the possible terms that contribute at leading order come from azimuthal, shear

and axial stretching. The force-balance equations including all terms that *may* contribute at leading order, as well as some higher-order terms, are found to be

$$0 = 12\bar{B} \left(-\frac{\bar{B}\hat{\xi}}{h} + \frac{1}{h} \frac{\partial}{\partial \tau} \left(\frac{\hat{\eta}}{h} \right) + \frac{\nu}{\delta_B} \frac{\partial \hat{\xi}}{\partial z_B} \right) + \frac{\delta^2 \ell^2 \mathcal{F}}{\delta_B^2} \frac{\partial^2 \hat{\xi}}{h \partial z_B^2} - \frac{\delta^2}{\delta_B^4} \frac{1}{h} \frac{\partial^4 \hat{\xi}}{\partial z_B^4} + \delta^2 \ell p_{\text{tm}} + O \left(\frac{\delta^2}{\delta_B^2} \hat{\xi}, \frac{\delta^2}{\delta_B^2} \hat{\eta}, \frac{\delta^2}{\delta_B^3} \hat{\xi} \right), \quad (5.41)$$

$$0 = \frac{\partial}{\partial \tau} \left(-\frac{\bar{B}\hat{\xi}}{h} + \frac{1}{h} \frac{\partial}{\partial \tau} \left(\frac{\hat{\eta}}{h} \right) \right) + \frac{1}{\delta_B} \frac{1+\nu}{2} \frac{\partial}{\partial z_B} \left(\frac{1}{\delta_B} \frac{\partial \hat{\eta}}{\partial z_B} + \frac{\partial \hat{\xi}}{\partial \tau} \right) - \frac{1}{\delta_B^2} \nu \frac{\partial^2 \hat{\eta}}{\partial z_B^2} - \frac{\delta^2}{\delta_B^2} \frac{\bar{B}(1+\nu)}{24} \frac{\partial}{\partial \tau} \left(\frac{1}{h} \frac{\partial^2 \hat{\xi}}{\partial z_B^2} \right) + O \left(\frac{\delta^2}{\delta_B} \hat{\xi}, \frac{\delta^2 \ell^2}{\delta_B^2} \hat{\eta}, \frac{\delta^2}{\delta_B} \hat{\xi} \right), \quad (5.42)$$

$$0 = \nu \frac{1}{\delta_B} \frac{\partial}{\partial z_B} \left(-\frac{\bar{B}\hat{\xi}}{h} + \frac{1}{h} \frac{\partial}{\partial \tau} \left(\frac{\hat{\eta}}{h} \right) \right) + \frac{1-\nu}{2h} \frac{\partial}{\partial \tau} \left(\frac{1}{h} \left(\frac{1}{\delta_B} \frac{\partial \hat{\eta}}{\partial z_B} + \frac{\partial \hat{\xi}}{\partial \tau} \right) \right) + \frac{1}{\delta_B^2} \frac{\partial^2 \hat{\xi}}{\partial z_B^2} + \frac{\delta^2}{\delta_B^3} \frac{\bar{B}}{12h} \frac{\partial^3 \hat{\xi}}{\partial z_B^3} + O \left(\frac{\delta^2 \ell^2}{\delta_B} \hat{\xi}, \frac{\delta^2 \ell^2}{\delta_B} \hat{\eta}, \frac{\delta^2 \ell^2}{\delta_B^2} \hat{\xi} \right). \quad (5.43)$$

The higher-order terms have been included so that when we later carry out an asymptotic analysis of the problem, we can determine the largest non-zero higher-order terms that appear in the bending-layer deformations. These leading-order governing equations are similar to those derived by Whittaker (2015), but they are not entirely the same. It is first seen that the normal force-balance equation (5.41) contains all the terms appearing in the normal force-balance equation found by Whittaker (2015). However, (5.41) also contains an extra axial-bending term ($\partial^4 \hat{\xi} / \partial z_B^4$) and transmural pressure term. The azimuthal force-balance equation (5.42) and the corresponding equation found by Whittaker (2015) contain the same terms apart from the pre-stress term in the equation by Whittaker (2015). This is replaced in (5.42) by the $\partial^2 \hat{\xi} / \partial z_B^2$ term which comes from the torsion mechanism. Finally, the axial force-balance equation (5.43) and the corresponding equation derived by Whittaker (2015) have the same terms apart from again the pre-stress term in the Whittaker (2015) equation. In this case, the pre-stress term is replaced in (5.43) by the $\partial^3 \hat{\xi} / \partial z_B^3$ term which comes from axial bending.

By examining the governing equations (5.41)–(5.43) and the scalings of the terms within Tables 5.1–5.3, it is seen that if we take an axial scale $Z = O(\tilde{\delta}) \leq O(\delta_B)$, we do not obtain any new terms that arise from different mechanisms at leading order. Hence, as no new mechanisms contribute at leading order for smaller axial scales, there are no boundary layers smaller than the bending boundary layer in the current scenario. Thus, we do not obtain an

inner shear-relaxation layer in the current case and we need only match the bending layer onto the outer shear layer.

To determine precisely which of the terms in (5.41)–(5.43) contribute at leading order, the sizes of $\hat{\zeta}$, $\hat{\eta}$ and $\hat{\zeta}$ within the bending layer would need to be determined. However, it is later found to be more convenient to recast the problem in terms of the stresses \tilde{N} , \tilde{S} and $\tilde{\Sigma}$, and compute their sizes instead to determine the leading-order governing equations.

Mechanism	Strain	Dominant contribution to normal force-balance equation
Azimuthal stretching	$\gamma_{11} \sim \frac{\Delta}{\ell} (O(\hat{\xi}), O(\hat{\eta}))$	$\left\{ \begin{array}{l} \nabla_2 \nabla_2 M^{22} \sim \frac{\Delta K}{a^3 \ell} \frac{1}{\delta_B^2} (O(\hat{\xi}), O(\hat{\eta})) \\ N^{11} b^{11} \sim \frac{\Delta K}{a^3 \ell} \frac{1}{\delta_B^2} (O(\hat{\xi}), O(\hat{\eta})) \end{array} \right.$
Shear stretching	$\gamma_{12}, \gamma_{21} \sim \frac{\Delta}{\ell} \left(\frac{1}{\delta_B} O(\hat{\eta}), O(\hat{\xi}) \right)$	$\nabla_2 \nabla_1 M^{21} \sim \frac{\Delta K}{a^3 \ell} \frac{1}{\delta_B} \left(\frac{1}{\delta_B} O(\hat{\eta}), O(\hat{\xi}) \right)$
Axial stretching	$\gamma_{22} \sim \frac{\Delta}{\ell \delta_B} O(\hat{\xi})$	$\left\{ \begin{array}{l} \nabla_2 \nabla_2 M^{22} \sim \frac{\Delta K}{a^3 \ell} \frac{1}{\delta_B^3} O(\hat{\xi}) \\ N^{11} b^{11} \sim \frac{\Delta K}{a^3 \ell} \frac{1}{\delta_B \delta^2} O(\hat{\xi}) \end{array} \right.$
Azimuthal bending	$\kappa_{11} \sim \frac{\Delta}{a \ell} (O(\hat{\xi}), O(\hat{\eta}))$	$\left\{ \begin{array}{l} \nabla_1 \nabla_1 M^{11} \sim \frac{\Delta K}{a^3 \ell} (O(\hat{\xi}), O(\hat{\eta})) \\ \nabla_2 \nabla_2 M^{22} \sim \frac{\Delta K}{a^3 \ell} \frac{1}{\delta_B^2} (O(\hat{\xi}), O(\hat{\eta})) \\ N^{11} b^{11} \sim \frac{\Delta K}{a^3 \ell} (O(\hat{\xi}), O(\hat{\eta})) \end{array} \right.$
Torsion	$\kappa_{12} \sim \frac{\Delta}{a \ell} \left(\frac{1}{\delta_B} O(\hat{\xi}), O(\hat{\eta}) \right)$	$\left\{ \begin{array}{l} \nabla_1 \nabla_2 M^{12}, \nabla_2 \nabla_1 M^{21} \sim \frac{\Delta K}{a^3 \ell} \frac{1}{\delta_B} \left(\frac{1}{\delta_B} O(\hat{\xi}), O(\hat{\eta}) \right) \\ N^{11} b^{11} \sim \frac{\Delta K}{a^3 \ell} \left(\frac{1}{\delta_B} O(\hat{\xi}), O(\hat{\eta}) \right) \end{array} \right.$
Axial bending	$\kappa_{21} \sim \frac{\Delta}{a \ell \delta_B} (O(\hat{\xi}), O(\hat{\eta}))$	$\left\{ \begin{array}{l} \nabla_1 \nabla_2 M^{12}, \nabla_2 \nabla_1 M^{21} \sim \frac{\Delta K}{a^3 \ell} \frac{1}{\delta_B^2} (O(\hat{\xi}), O(\hat{\eta})) \\ N^{11} b^{11} \sim \frac{\Delta K}{a^3 \ell} \left(\frac{1}{\delta_B} O(\hat{\xi}), O(\hat{\eta}) \right) \end{array} \right.$
Pre-stress and axial curvature	$\kappa_{22} \sim \frac{\Delta}{a \ell \delta_B^2} O(\hat{\xi})$	$\left\{ \begin{array}{l} \nabla_1 \nabla_1 M^{11} \sim \frac{\Delta K}{a^3 \ell} \frac{1}{\delta_B^2} O(\hat{\xi}) \\ \nabla_2 \nabla_2 M^{22} \sim \frac{\Delta K}{a^3 \ell} \frac{1}{\delta_B^4} O(\hat{\xi}) \end{array} \right.$
Transmural pressure	$p_{\text{tm}} \sim 1$	$N^{22} b_{22} \sim \frac{\Delta K}{a^3 \ell} \frac{\ell^2}{\delta_B^2} O(\hat{\xi})$
		$\frac{\Delta K}{a^3} p_{\text{tm}} \sim \frac{\Delta K}{a^3 \ell} \ell$

Table 5.1: Scaling estimates for the dominant terms contributing to the normal force-balance equation in regime I_b. The mechanisms that *may* contribute at leading order are in bold.

Mechanism	Strain	Dominant contribution to azimuthal force-balance equation
Azimuthal stretching	$\gamma_{11} \sim \frac{\Delta}{\ell} (O(\hat{\xi}), O(\hat{\eta}))$	$\nabla_1 N^{11} \sim \frac{\Delta K}{\ell^2 \delta_B^2} (O(\hat{\xi}), O(\hat{\eta}))$
Shear stretching	$\gamma_{12}, \gamma_{21} \sim \frac{\Delta}{\ell} \left(\frac{1}{\delta_B} O(\hat{\eta}), O(\hat{\xi}) \right)$	$\left\{ \begin{array}{l} \nabla_2 N^{21} \sim \frac{\Delta K}{\ell^2 \delta_B^2} \left(\frac{1}{\delta_B} O(\hat{\eta}), O(\hat{\xi}) \right) \\ b_{11} \nabla_2 M^{21} \sim \frac{\Delta K}{\ell^2 \delta_B} \left(\frac{1}{\delta_B} O(\hat{\eta}), O(\hat{\xi}) \right) \end{array} \right.$
Axial stretching	$\gamma_{22} \sim \frac{\Delta}{\ell \delta_B} O(\hat{\xi})$	$\nabla_1 N^{11} \sim \frac{\Delta K}{\ell^2 \delta_B^2} O(\hat{\xi})$
Azimuthal bending	$\kappa_{11} \sim \frac{\Delta}{a \ell} (O(\hat{\xi}), O(\hat{\eta}))$	$\left\{ \begin{array}{l} \nabla_1 N^{11} \sim \frac{\Delta K}{\ell^2} (O(\hat{\xi}), O(\hat{\eta})) \\ b_{11} \nabla_1 M^{11} \sim \frac{\Delta K}{\ell^2} (O(\hat{\xi}), O(\hat{\eta})) \end{array} \right.$
Torsion	$\kappa_{12} \sim \frac{\Delta}{a \ell} \left(\frac{1}{\delta_B} O(\hat{\xi}), O(\hat{\eta}) \right)$	$\left\{ \begin{array}{l} \nabla_1 N^{11} \sim \frac{\Delta K}{\ell^2 \delta_B} \left(\frac{1}{\delta_B} O(\hat{\xi}), O(\hat{\eta}) \right) \\ b_{11} \nabla_2 M^{21} \sim \frac{\Delta K}{\ell^2 \delta_B} \left(\frac{1}{\delta_B} O(\hat{\xi}), O(\hat{\eta}) \right) \end{array} \right.$
Axial bending	$\kappa_{21} \sim \frac{\Delta}{a \ell \delta_B} (O(\hat{\xi}), O(\hat{\eta}))$	$\left\{ \begin{array}{l} \nabla_2 N^{21} \sim \frac{\Delta K}{\ell^2 \delta_B^2} (O(\hat{\xi}), O(\hat{\eta})) \\ b_{11} \nabla_2 M^{21} \sim \frac{\Delta K}{\ell^2 \delta_B^2} (O(\hat{\xi}), O(\hat{\eta})) \end{array} \right.$
Pre-stress and axial curvature	$\Gamma_{22}^1 \sim \frac{\Delta}{a \ell \delta_B^2} O(\hat{\eta})$	$\nabla_2 N^{21} \sim \frac{\Delta K}{\ell^2 \delta_B^2} O(\hat{\eta})$

Table 5.2: Scaling estimates for the dominant terms contributing to the azimuthal force-balance equation in regime I_b. The mechanisms that *may* contribute at leading order are in bold.

Mechanism	Strain	Dominant contribution to axial force-balance equation
Azimuthal stretching	$\gamma_{11} \sim \frac{\Delta}{\ell} (O(\hat{\xi}), O(\hat{\eta}))$	$\nabla_2 N^{22} \sim \frac{\Delta K}{a^3 \ell} \frac{1}{\delta_B \delta^2} (O(\hat{\xi}), O(\hat{\eta}))$
Shear stretching	$\gamma_{12}, \gamma_{21} \sim \frac{\Delta}{\ell} \left(\frac{1}{\delta_B} O(\hat{\eta}), O(\hat{\zeta}) \right)$	$\nabla_1 N^{12} \sim \frac{\Delta K}{a^3 \ell} \frac{1}{\delta^2} \left(\frac{1}{\delta_B} O(\hat{\eta}), O(\hat{\zeta}) \right)$
Axial stretching	$\gamma_{22} \sim \frac{\Delta}{\ell \delta_B} O(\hat{\zeta})$	$\nabla_2 N^{22} \sim \frac{\Delta K}{a^3 \ell} \frac{1}{\delta_B^2 \delta^2} O(\hat{\zeta})$
Torsion	$\kappa_{12} \sim \frac{\Delta}{a \ell} \left(\frac{1}{\delta_B} O(\hat{\xi}), O(\hat{\zeta}) \right)$ $\kappa_{21} \sim \frac{\Delta}{a \ell \delta_B} (O(\hat{\xi}), O(\hat{\eta}))$	$\nabla_1 N^{12} \sim \frac{\Delta K}{a^3 \ell} \left(\frac{1}{\delta_B} O(\hat{\xi}), O(\hat{\zeta}) \right)$ $\nabla_1 N^{12} \sim \frac{\Delta K}{a^3 \ell} \frac{1}{\delta_B} (O(\hat{\xi}), O(\hat{\eta}))$
Axial bending	$\kappa_{22} \sim \frac{\Delta}{a \ell \delta_B^2} O(\hat{\xi})$	$\nabla_2 N^{22} \sim \frac{\Delta K}{a^3 \ell} \frac{1}{\delta_B^3} O(\hat{\xi})$
Pre-stress and axial curvature	$\Gamma_{21}^1 \sim \frac{\Delta}{a \ell \delta_B} (O(\hat{\xi}), O(\hat{\eta}))$ $\Gamma_{22}^2 \sim \frac{\Delta}{a \ell \delta_B^2} O(\hat{\zeta})$	$\nabla_1 N^{12} \sim \frac{\Delta K}{a^3 \ell} \frac{\ell^2}{\delta_B} (O(\hat{\xi}), O(\hat{\eta}))$ $\nabla_2 N^{22} \sim \frac{\Delta K}{a^3 \ell} \frac{\ell^2}{\delta_B^2} O(\hat{\zeta})$

Table 5.3: Scaling estimates for the dominant terms contributing to the axial force-balance equation in regime I_b. The mechanisms that *may* contribute at leading order are in bold.

5.6 Boundary and Matching Conditions

Along with the governing force-balance equations (5.41)–(5.43), we also have the clamped boundary conditions (3.32) as seen in Chapter 3. In terms of $\hat{\xi}$, $\hat{\eta}$, $\hat{\zeta}$, z_B , these become

$$\hat{\xi} = \frac{\partial \hat{\xi}}{\partial z_B} = \hat{\eta} = \hat{\zeta} = 0 \quad \text{at} \quad z_B = 0. \quad (5.44)$$

The deformations in the bending layer must also match onto the deformations (5.29)–(5.31) in the outer shear layer. However, as discussed in §5.4 in the overview of the outer shear layer studied by Whittaker (2015), the leading-order term in the approximation for the normal deformation $\hat{\xi}$ in the outer shear layer does not stay at leading order for smaller axial scales. As such, it is unclear what the matching condition for $\hat{\xi}$ in the bending layer should be.

We may resolve this problem by re-casting the problem in terms of the stresses \tilde{N} , \tilde{S} and $\tilde{\Sigma}$. Approximations for these stresses in the outer shear layer, denoted \tilde{N}_s , \tilde{S}_s and $\tilde{\Sigma}_s$ here, were derived by Whittaker (2015). The leading-order terms within these approximations stay at leading order when the axial scale is reduced, and as \tilde{N}_s , \tilde{S}_s and $\tilde{\Sigma}_s$ only depend on matching to the bulk solution and not on matching to any smaller layers, these approximations are also the most general they can be. Hence, we may obtain clear matching conditions for the stresses in the bending layer using the Taylor series (5.25)–(5.27) of \tilde{N}_s , \tilde{S}_s and $\tilde{\Sigma}_s$ as $\check{z} \rightarrow 0$.

5.7 Re-casting the Problem in Terms of the Stresses

We proceed to rewrite the bending boundary-layer system in terms of the stresses \tilde{N} , \tilde{S} and $\tilde{\Sigma}$. The details of the change of variables from the deformations $\hat{\xi}$, $\hat{\eta}$ and $\hat{\zeta}$ to the stresses \tilde{N} , \tilde{S} and $\tilde{\Sigma}$ are shown in Appendix 5.A. There, we obtain the new governing equations (5.148)–(5.150), which are

shown to be

$$0 = \tilde{N}\bar{B} - \frac{\delta^2}{\delta_B^2} \frac{1}{12\bar{B}} \left[-\frac{1}{\delta_B^2} \frac{\partial^4}{\partial z_B^4} \left(\frac{\tilde{N} - \nu\tilde{\Sigma}}{1 - \nu^2} \right) + \frac{12}{\delta_B^2 h} \frac{\partial^3}{\partial \tau \partial z_B^2} \left(\frac{1}{h} \frac{\partial^2 \hat{\eta}}{\partial z_B^2} \right) \right] \\ + \frac{\tilde{\mathcal{F}}(1 - \nu^2)h}{\bar{B}} \left[-\frac{1}{\delta_B^2} \frac{\partial^2}{\partial z_B^2} \left(\frac{\tilde{N} - \nu\tilde{\Sigma}}{1 - \nu^2} \right) + \frac{12}{\delta_B^2 h} \frac{\partial}{\partial \tau} \left(\frac{1}{h} \frac{\partial^2 \hat{\eta}}{\partial z_B^2} \right) \right] + \\ + \delta^2 \ell p_{\text{tm}} + O \left(\frac{\delta^2}{\delta_B^2} \tilde{N}, \frac{\delta^2}{\delta_B} \tilde{S}, \frac{\delta^2}{\delta_B^2} \tilde{\Sigma} \right), \quad (5.45)$$

$$0 = \frac{1}{h} \frac{\partial \tilde{N}}{\partial \tau} + \frac{1}{\delta_B} \frac{\partial \tilde{S}}{\partial z_B} \\ - \delta^2 \frac{(1 + \nu)\bar{B}}{24h} \frac{\partial}{\partial \tau} \left[\frac{1}{\bar{B}} \left[-\frac{1}{\delta_B^2} \frac{\partial^2}{\partial z_B^2} \left(\frac{\tilde{N} - \nu\tilde{\Sigma}}{1 - \nu^2} \right) + \frac{12}{\delta_B^2 h} \frac{\partial}{\partial \tau} \left(\frac{1}{h} \frac{\partial^2 \hat{\eta}}{\partial z_B^2} \right) \right] \right] + \\ + O \left(\delta^2 \left(\frac{1}{\delta_B}, \ell^2 \right) \tilde{N}, \frac{\delta^2 \ell^2}{\delta_B} \tilde{S}, \delta^2 \left(\frac{1}{\delta_B}, \ell^2 \right) \tilde{\Sigma} \right), \quad (5.46)$$

$$0 = \frac{\partial \tilde{\Sigma}}{\partial z_B} + \frac{\delta_B}{h} \frac{\partial \tilde{S}}{\partial \tau} - \frac{\delta^2}{12\delta_B^2} \frac{\partial^3}{\partial z_B^3} \left(\frac{\tilde{N} - \nu\tilde{\Sigma}}{1 - \nu^2} \right) + \frac{\delta^2}{\delta_B^2 h} \frac{\partial^2}{\partial \tau \partial z_B} \left(\frac{1}{h} \frac{\partial^2 \hat{\eta}}{\partial z_B^2} \right) + \\ + O \left(\frac{\delta^2 \ell^2}{\delta_B} \tilde{N}, \delta^2 \ell^2 \tilde{S}, \frac{\delta^2 \ell^2}{\delta_B} \tilde{\Sigma} \right), \quad (5.47)$$

where $\partial^2 \hat{\eta} / \partial z_B^2$ is defined in terms of the stresses as

$$\frac{\partial^2 \hat{\eta}}{\partial z_B^2} = \frac{\delta_B^2 h}{12} \left(\frac{2}{\delta_B(1 - \nu)} \frac{\partial \tilde{S}}{\partial z_B} - \frac{1}{h} \frac{\partial}{\partial \tau} \left(\frac{\tilde{\Sigma} - \nu\tilde{N}}{1 - \nu^2} \right) \right).$$

Also in Appendix 5.A, the clamped boundary conditions (5.44) are shown in (5.151) to impose the following conditions on the stresses

$$\tilde{N} - \nu\tilde{\Sigma} = 0, \quad \text{at } z_B = 0, \quad (5.48)$$

$$\frac{\partial \tilde{N}}{\partial z_B} - \nu \frac{\partial \tilde{\Sigma}}{\partial z_B} - \frac{2(1 + \nu)\delta_B}{h} \frac{\partial \tilde{S}}{\partial \tau} = 0, \quad \text{at } z_B = 0. \quad (5.49)$$

Finally, the stresses in the bending layer must match onto the Taylor series (5.25)–(5.27) of the stresses \tilde{N}_s , \tilde{S}_s , $\tilde{\Sigma}_s$ in the outer shear layer, in some intermediate region between the two layers. Hence, we must have the following matching conditions for the stresses in the bending layer

$$\tilde{N} \sim \tilde{N}_s, \quad \tilde{S} \sim \tilde{N}_s, \quad \tilde{\Sigma} \sim \tilde{\Sigma}_s, \quad \text{as } z_B \rightarrow \infty, \tilde{z} \rightarrow 0. \quad (5.50)$$

When applying the matching conditions, it is convenient to rewrite both \tilde{z} and z_B in terms of some intermediate variable z_I which is $O(1)$ in a region between the outer shear and bending layers. We define z_I as

$$\left(\frac{1}{\delta_B \tilde{\mathcal{F}}^{\frac{1}{2}}} \right)^\alpha \tilde{z} = z_I = \left(\frac{1}{\delta_B \tilde{\mathcal{F}}^{\frac{1}{2}}} \right)^{\alpha-1} z_B, \quad \text{where } 0 < \alpha < 1. \quad (5.51)$$

We note that as $\delta_B \tilde{\mathcal{F}}^{\frac{1}{2}} \ll 1$, setting $z_I = O(1)$ also sets $\check{z} \rightarrow 0$ and $z_B \rightarrow \infty$. By substituting the approximations (5.25)–(5.27) for \tilde{N}_s , \tilde{S}_s and $\tilde{\Sigma}_s$ as $\check{z} \rightarrow 0$ into the matching conditions (5.50), and applying the expression (5.51) for the intermediate variable z_I , the matching conditions for the stresses in the bending layer are calculated to be

$$\tilde{N} \sim \frac{\tilde{\mathcal{F}}^{\frac{3}{2}}}{\bar{B}^2 h} \sum_{n=1}^{\infty} B_n(t) \frac{\partial}{\partial \tau} \left(\frac{1}{h} \frac{\partial Y_n}{\partial \tau} \right) \left[1 - \mu_n \left(\delta_B \tilde{\mathcal{F}}^{\frac{1}{2}} \right)^{\alpha} z_I + O \left(\left(\delta_B \tilde{\mathcal{F}}^{\frac{1}{2}} \right)^{2\alpha} \right) \right] + O(\tilde{\mathcal{F}}^{\frac{5}{2}}), \quad (5.52)$$

$$\tilde{S} \sim \frac{\tilde{\mathcal{F}}}{h} \sum_{n=1}^{\infty} \frac{B_n(t)}{\mu_n} \frac{\partial}{\partial \tau} \left[\frac{1}{\bar{B}^2 h} \frac{\partial}{\partial \tau} \left(\frac{1}{h} \frac{\partial Y_n}{\partial \tau} \right) - Y_n(\tau) \right] \left[1 - \mu_n \left(\delta_B \tilde{\mathcal{F}}^{\frac{1}{2}} \right)^{\alpha} z_I + O \left(\left(\delta_B \tilde{\mathcal{F}}^{\frac{1}{2}} \right)^{2\alpha} \right) \right] + O(\tilde{\mathcal{F}}^2), \quad (5.53)$$

$$\tilde{\Sigma} \sim \tilde{\mathcal{F}}^{\frac{1}{2}} \sum_{n=1}^{\infty} B_n(t) Y_n(\tau) \left[1 - \mu_n \left(\delta_B \tilde{\mathcal{F}}^{\frac{1}{2}} \right)^{\alpha} z_I + O \left(\left(\delta_B \tilde{\mathcal{F}}^{\frac{1}{2}} \right)^{2\alpha} \right) \right] + O(\tilde{\mathcal{F}}^{\frac{3}{2}}), \quad (5.54)$$

as $z_B \rightarrow \infty$.

5.8 Determining the Sizes of the Stresses in the Bending Layer

By examining the governing equations (5.45)–(5.47), the boundary conditions (5.48)–(5.49), and the matching conditions (5.52)–(5.54), we may determine the sizes of the stresses in the bending layer.

We first of all note that for the matching conditions (5.52)–(5.54) to be satisfied, we must have in the bending layer

$$\tilde{N} \geq O(\tilde{\mathcal{F}}^{\frac{3}{2}}), \quad \tilde{S} \geq O(\tilde{\mathcal{F}}), \quad \tilde{\Sigma} \geq O(\tilde{\mathcal{F}}^{\frac{1}{2}}). \quad (5.55)$$

There must also be at least one equality in these relations to enable non-homogeneous matching between the layers. We next see that for the condition (5.48) to be satisfied, we need

$$O(\tilde{\Sigma}) = O(\tilde{N}). \quad (5.56)$$

By examining the azimuthal force-balance equation (5.46) it is seen that the only two terms that can appear at leading order are the $\partial \tilde{N} / \partial \tau$ and $\partial \tilde{S} / \partial z_B$ terms in the first line of (5.46). For these terms to balance, we must have

$$O(\tilde{S}) = \delta_B O(\tilde{N}). \quad (5.57)$$

Combining the inequality for $\tilde{\Sigma}$ in (5.55) with (5.56), it is seen that we must have

$$\tilde{N} \geq O(\tilde{\mathcal{F}}^{\frac{1}{2}}) \gg O(\tilde{\mathcal{F}}^{\frac{3}{2}}).$$

Using this along with (5.57), we also find

$$\tilde{S} \geq O(\delta_B \tilde{\mathcal{F}}^{\frac{1}{2}}) \gg O(\tilde{\mathcal{F}}),$$

as we are under the assumption $\delta_B \gg \tilde{\mathcal{F}}^{\frac{1}{2}}$. As there must be one equality within (5.55), we obtain

$$\tilde{\Sigma} = O(\tilde{\mathcal{F}}^{\frac{1}{2}}), \quad (5.58)$$

in the bending layer. Substituting this into (5.56) and (5.57), it is found that

$$\tilde{N} = O(\tilde{\mathcal{F}}^{\frac{1}{2}}), \quad \tilde{S} = O(\delta_B \tilde{\mathcal{F}}^{\frac{1}{2}}), \quad (5.59)$$

within the bending layer.

By applying the sizes (5.58), (5.59) to the normal force-balance equation (5.45), we see that the transmural pressure term is smaller than the first term in (5.45) and thus cannot appear at leading order. It is then found that the only terms that may appear at leading order are the \tilde{N} term and the axial-bending term containing the fourth axial derivative of $\tilde{N} - \nu \tilde{\Sigma}$. To ensure that these terms balance, we must have $\delta_B = O(\delta^{\frac{1}{2}})$. With this new information, it is found that the first of the pre-stress terms in (5.45) is larger than the transmural pressure term. Hence, the pressure term contributes to the normal force-balance equation at a higher order than the azimuthal hoop stress term, the axial bending term, and the first pre-stress term.

Now that the sizes (5.58), (5.59) of the stresses \tilde{N} , \tilde{S} and $\tilde{\Sigma}$ have been determined, it is possible to determine the sizes of the terms within the governing equations (5.45)–(5.47) and boundary conditions (5.48), (5.49). Using this knowledge, it is then possible to calculate asymptotic approximations for the solutions to the governing system (5.45)–(5.54).

5.9 Solution in the Limit of a Circular Cross-Section ($\sigma_0 \rightarrow \infty$)

To gain a quick idea of how the stresses and deformations behave within the bending layer, we consider the limit $\sigma_0 \rightarrow \infty$, where the elliptical cross-section

of the tube becomes circular. In this limit, we have from (5.2), (5.3) and (5.11) that

$$c \sim 2e^{-\sigma_0}, \quad h(\tau) \rightarrow 1, \quad \bar{B} \rightarrow -1,$$

and Whittaker (2015) also found in this limit

$$Y_n(\tau) \rightarrow \cos(2n\tau), \quad \mu_n \rightarrow 2n(4n^2 + 1)^{\frac{1}{2}}.$$

This greatly simplifies the system (5.45)–(5.54) and it is possible to determine analytical leading-order expressions for the stresses \tilde{N} , \tilde{S} , $\tilde{\Sigma}$, and deformations $\hat{\zeta}$, $\hat{\eta}$, $\hat{\zeta}$ by using Fourier expansions in τ .

The details of finding the leading-order solution in the limit $\sigma_0 \rightarrow \infty$ are found in Appendix 5.B. There, we set the bending boundary-layer width δ_B to be

$$\delta_B = \frac{\sqrt{2}\delta^{\frac{1}{2}}}{(12(1-\nu^2))^{\frac{1}{4}}},$$

which is consistent with the $O(\delta^{\frac{1}{2}})$ scaling identified in §5.8 for the full system (5.45)–(5.54) with an elliptical cross-section. This has a different scaling from the value (3.48) predicted by the toy model in §3.6, but we still have $\delta\ell \ll \delta_B \ll \delta^{-1}\ell^{-1}$. Therefore the size of the bending-layer width lies in between the sizes of the inner and outer shear layers found by Whittaker (2015). The different scaling arises because the toy model cannot capture the azimuthal and axial stretching mechanisms which are found to contribute at leading order here.

By examining the solutions in the circular limit, it is seen that $\tilde{N}, \tilde{\Sigma} = O(\tilde{\mathcal{F}}^{\frac{1}{2}})$ and $\tilde{S} = O(\delta_B \tilde{\mathcal{F}}^{\frac{1}{2}})$, which is in agreement with the sizes (5.58), (5.59) calculated in §5.8. The sizes of the deformations within the bending layer are then calculated to be $\hat{\zeta} = O(\tilde{\mathcal{F}}^{\frac{1}{2}})$, $\hat{\eta} = O(\delta_B^2 \tilde{\mathcal{F}}^{\frac{1}{2}})$ and $\hat{\zeta} = O(\delta_B \tilde{\mathcal{F}}^{\frac{1}{2}})$ in the circular limit, and the same sizes are expected in the elliptical case.

It is found in the circular limit that the leading-order \tilde{N} and \tilde{S} both decay to zero as $z_B \rightarrow \infty$ in the bending layer. The leading-order $\tilde{\Sigma}$ instead remains constant in the axial direction for all values of z_B . Converting the leading-order stresses into the deformations $\hat{\zeta}$, $\hat{\eta}$, $\hat{\zeta}$, it is verified that the clamped boundary conditions (5.44) are satisfied at leading order. It is also seen that as $z_B \rightarrow \infty$, the sizes of the deformations increase to different values, and $\hat{\zeta}$, $\hat{\eta}$ and $\hat{\zeta}$ behave as a constant, quadratically and linearly, respectively, in the axial direction.

5.10 Asymptotic Analysis for $\tilde{\mathcal{F}} \ll 1, \delta_B \ll 1$

We proceed to solve the system (5.45)–(5.54) by forming asymptotic expansions for the stresses \tilde{N} , \tilde{S} and $\tilde{\Sigma}$. It is first convenient to rewrite these stresses in terms of some new functions N_B , S_B and Σ_B as follows

$$\tilde{N} = \tilde{\mathcal{F}}^{\frac{1}{2}} N_B, \quad \tilde{S} = \delta_B \tilde{\mathcal{F}}^{\frac{1}{2}} S_B, \quad \tilde{\Sigma} = \tilde{\mathcal{F}}^{\frac{1}{2}} \Sigma_B. \quad (5.60)$$

Comparing these expressions with the sizes (5.58), (5.59) of the stresses in the bending layer, we see that N_B , S_B and Σ_B must all be $O(1)$ in the bending layer. With these new representations and the fact that $\delta_B = O(\delta^{\frac{1}{2}})$ for a sensible dominant balance in the normal force-balance equation, we may rewrite the governing equations (5.45)–(5.47) as

$$0 = N_B \bar{B} + \frac{\delta^2}{\delta_B^4} \frac{1}{12 \bar{B}} \frac{\partial^4}{\partial z_B^4} \left(\frac{N_B - \nu \Sigma_B}{1 - \nu^2} \right) - \frac{\tilde{\mathcal{F}} h}{\delta_B^2 \bar{B}} \frac{\partial^2}{\partial z_B^2} (N_B - \nu \Sigma_B) + O\left(\frac{\delta^2}{\delta_B^2}\right), \quad (5.61)$$

$$0 = \frac{1}{h} \frac{\partial N_B}{\partial \tau} + \frac{\partial S_B}{\partial z_B} + O\left(\frac{\delta^2}{\delta_B^2}\right), \quad (5.62)$$

$$0 = \frac{\partial \Sigma_B}{\partial z_B} + O\left(\frac{\delta^2}{\delta_B^2}, \frac{\delta^2 \ell^2}{\delta_B}\right). \quad (5.63)$$

The boundary conditions (5.48) and (5.49) may also be rewritten as

$$N_B - \nu \Sigma_B = 0, \quad \text{and} \quad \frac{\partial N_B}{\partial z_B} - \nu \frac{\partial \Sigma_B}{\partial z_B} - \delta_B^2 \frac{2(1+\nu)}{h} \frac{\partial S_B}{\partial \tau} = 0, \quad \text{at} \quad z_B = 0, \quad (5.64)$$

and the matching conditions (5.52)–(5.54) are rewritten as

$$N_B \sim \frac{\tilde{\mathcal{F}}}{\bar{B}^2 h} \sum_{n=1}^{\infty} B_n(t) \frac{\partial}{\partial \tau} \left(\frac{1}{h} \frac{\partial Y_n}{\partial \tau} \right) \left[1 - \mu_n \left(\delta_B \tilde{\mathcal{F}}^{\frac{1}{2}} \right)^{\alpha} z_I + O\left(\left(\delta_B \tilde{\mathcal{F}}^{\frac{1}{2}}\right)^{2\alpha}\right) \right] + O(\tilde{\mathcal{F}}^2), \quad (5.65)$$

$$S_B \sim \frac{\tilde{\mathcal{F}}^{\frac{1}{2}}}{\delta_B h} \sum_{n=1}^{\infty} \frac{B_n(t)}{\mu_n} \frac{\partial}{\partial \tau} \left[\frac{1}{\bar{B}^2 h} \frac{\partial}{\partial \tau} \left(\frac{1}{h} \frac{\partial Y_n}{\partial \tau} \right) - Y_n(\tau) \right] \left[1 - \mu_n \left(\delta_B \tilde{\mathcal{F}}^{\frac{1}{2}} \right)^{\alpha} z_I + O\left(\left(\delta_B \tilde{\mathcal{F}}^{\frac{1}{2}}\right)^{2\alpha}\right) \right] + O\left(\frac{\tilde{\mathcal{F}}^{\frac{3}{2}}}{\delta_B}\right), \quad (5.66)$$

$$\Sigma_B \sim \sum_{n=1}^{\infty} B_n(t) Y_n(\tau) \left[1 - \mu_n \left(\delta_B \tilde{\mathcal{F}}^{\frac{1}{2}} \right)^{\alpha} z_I + O\left(\left(\delta_B \tilde{\mathcal{F}}^{\frac{1}{2}}\right)^{2\alpha}\right) \right] + O(\tilde{\mathcal{F}}), \quad (5.67)$$

as $z_B \rightarrow \infty$. When the leading-order normal force-balance equation is considered later on, it is found to be convenient to set δ_B to be

$$\delta_B = \frac{\sqrt{2} \delta^{\frac{1}{2}}}{(12(1-\nu^2))^{\frac{1}{4}}}. \quad (5.68)$$

This is the same value of δ_B used in the work on the circular limit $\sigma_0 \rightarrow \infty$ in Appendix 5.B.

A solution for the system (5.61)–(5.67) is now found by considering the following asymptotic expansions of N_B , S_B , and Σ_B

$$N_B = N_B^{(0)} + \frac{\tilde{\mathcal{F}}^{\frac{1}{2}}}{\delta_B} N_B^{(1)} + \frac{\tilde{\mathcal{F}}}{\delta_B^2} N_B^{(2)} + O\left(\frac{\tilde{\mathcal{F}}^{\frac{3}{2}}}{\delta_B^3}, \frac{\delta^2}{\delta_B^2}\right), \quad (5.69)$$

$$S_B = S_B^{(0)} + \frac{\tilde{\mathcal{F}}^{\frac{1}{2}}}{\delta_B} S_B^{(1)} + \frac{\tilde{\mathcal{F}}}{\delta_B^2} S_B^{(2)} + O\left(\frac{\tilde{\mathcal{F}}^{\frac{3}{2}}}{\delta_B^3}, \frac{\delta^2}{\delta_B^2}\right), \quad (5.70)$$

$$\Sigma_B = \Sigma_B^{(0)} + \frac{\tilde{\mathcal{F}}^{\frac{1}{2}}}{\delta_B} \Sigma_B^{(1)} + \frac{\tilde{\mathcal{F}}}{\delta_B^2} \Sigma_B^{(2)} + O\left(\frac{\tilde{\mathcal{F}}^{\frac{3}{2}}}{\delta_B^3}, \frac{\delta^2}{\delta_B^2}\right). \quad (5.71)$$

Including an expansion in powers of $\tilde{\mathcal{F}}^{\frac{1}{2}}/\delta_B$ within the approximations (5.69)–(5.71) supplies terms that can balance the $O(\tilde{\mathcal{F}}/\delta_B^2)$ terms in the normal force-balance equation (5.61), as well as supplies a higher-order term that can satisfy the matching condition (5.66) for S_B . It is noted that these approximations will need expansions in other parameters as well to satisfy all the higher-order governing equations and conditions within the system (5.61)–(5.67). However, these parameters will be $O(\tilde{\mathcal{F}}^{\frac{3}{2}}/\delta_B^3)$ or $O(\delta^2/\delta_B^2)$ at most. As these size terms are smaller than the $O(\tilde{\mathcal{F}}/\delta_B^2)$ terms included in the approximations (5.69)–(5.71) (as $\tilde{\mathcal{F}}^{\frac{1}{2}}/\delta_B \ll 1$ and $\tilde{\mathcal{F}} \gg \delta^2$), they will only appear at third order at most and thus will not be considered.

Using the approximations (5.69)–(5.71), approximations for the stresses \tilde{N} , \tilde{S} and $\tilde{\Sigma}$ in the bending layer may be easily found. These stresses may then be substituted into the expressions (5.141)–(5.143) to determine approximations for the deformations $\hat{\xi}$, $\hat{\eta}$, $\hat{\zeta}$ in the bending layer. It is later found that the largest non-zero higher-order terms in the approximations of these deformations involve some second-order terms from the approximations (5.69)–(5.71) of N_B , S_B and Σ_B , due to some of the first-order terms in (5.69)–(5.71) turning out to be zero. Hence, in order to determine the largest non-zero higher-order terms in the expressions for the deformations, we will consider the approximations for N_B , S_B and Σ_B up to second order.

5.10.1 Leading-Order Solution

Substituting the asymptotic approximations (5.69)–(5.71) and the value (5.68) of δ_B into the governing equations (5.61)–(5.63), the boundary conditions (5.64), and the matching conditions (5.65)–(5.67), we obtain the following,

leading-order governing equations at $O(1)$

$$0 = \bar{B}N_B^{(0)} + \frac{1}{4\bar{B}} \left(\frac{\partial^4 N_B^{(0)}}{\partial z_B^4} - \nu \frac{\partial^4 \Sigma_B^{(0)}}{\partial z_B^4} \right), \quad (5.72)$$

$$0 = \frac{1}{h} \frac{\partial N_B^{(0)}}{\partial \tau} + \frac{\partial S_B^{(0)}}{\partial z_B}, \quad (5.73)$$

$$0 = \frac{\partial \Sigma_B^{(0)}}{\partial z_B}, \quad (5.74)$$

the following leading-order boundary conditions

$$N_B^{(0)} - \nu \Sigma_B^{(0)} = 0, \quad \text{and} \quad \frac{\partial N_B^{(0)}}{\partial z_B} - \nu \frac{\partial \Sigma_B^{(0)}}{\partial z_B} = 0 \quad \text{at} \quad z_B = 0, \quad (5.75)$$

and the following leading-order matching conditions

$$N_B^{(0)} \rightarrow 0, \quad S_B^{(0)} \rightarrow 0, \quad \Sigma_B^{(0)} \rightarrow \sum_{n=1}^{\infty} B_n(t) Y_n(\tau), \quad \text{as} \quad z_B \rightarrow \infty. \quad (5.76)$$

The matching conditions on $N_B^{(0)}$ and $S_B^{(0)}$ arise from the fact that these functions, which are $O(1)$ in the bending layer, are too large to match onto any of the terms within the matching conditions (5.65), (5.66) for N_B, S_B . Hence, $N_B^{(0)}$ and $S_B^{(0)}$ must decay to zero as $z_B \rightarrow \infty$. On the other hand, $\Sigma_B^{(0)}$ has the same size as the leading-order constant term in the matching condition (5.67) for Σ_B , and may match onto it.

Immediately, it is seen that the general solution of (5.74) is

$$\Sigma_B^{(0)} = A_1(\tau, t), \quad (5.77)$$

where A_1 is an arbitrary function of τ and t . Substituting this into (5.72) gives the following ODE for $N_B^{(0)}$

$$\frac{\partial^4 N_B^{(0)}}{\partial z_B^4} + 4\bar{B}^2 N_B^{(0)} = 0, \quad (5.78)$$

which has the general solution

$$\begin{aligned} N_B^{(0)} = & \left[A_2(\tau, t) \cos \left(|\bar{B}|^{\frac{1}{2}} z_B \right) + A_3(\tau, t) \sin \left(|\bar{B}|^{\frac{1}{2}} z_B \right) \right] e^{-|\bar{B}|^{\frac{1}{2}} z_B} \\ & + \left[A_4(\tau, t) \cos \left(|\bar{B}|^{\frac{1}{2}} z_B \right) + A_5(\tau, t) \sin \left(|\bar{B}|^{\frac{1}{2}} z_B \right) \right] e^{|\bar{B}|^{\frac{1}{2}} z_B}, \end{aligned} \quad (5.79)$$

where A_2, \dots, A_5 are arbitrary functions of τ and t . From the matching conditions (5.76), it is clear that $N_B^{(0)}$ cannot be exponentially growing as $z_B \rightarrow \infty$. Hence, we must set

$$A_4(\tau, t) = A_5(\tau, t) = 0. \quad (5.80)$$

Finally, substituting (5.79) and (5.80) into (5.73) gives a complicated but solvable ODE for $S_B^{(0)}$. Solving this ODE, we find

$$S_B^{(0)} = \frac{1}{4h\bar{B}^2} \mathcal{A}(\tau, z_B, t) e^{-|\bar{B}|^{\frac{1}{2}}z_B} + A_6(\tau, t), \quad (5.81)$$

where A_6 is an arbitrary function of τ and t , and $\mathcal{A}(\tau, z_B, t)$ is given by

$$\begin{aligned} \mathcal{A}(\tau, z_B, t) = & 2|\bar{B}|^{\frac{3}{2}} \left[(A'_2 + A'_3) \cos \left(|\bar{B}|^{\frac{1}{2}}z_B \right) + (A'_3 - A'_2) \sin \left(|\bar{B}|^{\frac{1}{2}}z_B \right) \right] \\ & - |\bar{B}|' \left(2|\bar{B}|z_B + |\bar{B}|^{\frac{1}{2}} \right) \left[A_2 \cos \left(|\bar{B}|^{\frac{1}{2}}z_B \right) + A_3 \sin \left(|\bar{B}|^{\frac{1}{2}}z_B \right) \right] \\ & + |\bar{B}|^{\frac{1}{2}}|\bar{B}|' \left[A_2 \sin \left(|\bar{B}|^{\frac{1}{2}}z_B \right) - A_3 \cos \left(|\bar{B}|^{\frac{1}{2}}z_B \right) \right], \end{aligned} \quad (5.82)$$

where ' denotes a derivative with respect to τ .

We proceed to use the boundary and matching conditions (5.75), (5.76) to find the full solutions of $N_B^{(0)}$, $S_B^{(0)}$ and $\Sigma_B^{(0)}$. Applying the matching conditions (5.76) as $z_B \rightarrow \infty$, it is found that

$$A_1(\tau, t) = \sum_{n=1}^{\infty} B_n(t) Y_n(\tau), \quad A_6(\tau, t) = 0. \quad (5.83)$$

The boundary conditions (5.75) are then applied to find

$$A_2(\tau, t) = A_3(\tau, t) = \sum_{n=1}^{\infty} \nu B_n(t) Y_n(\tau). \quad (5.84)$$

Substituting (5.83) and (5.84) into the expressions (5.77), (5.79) and (5.81), we find the full solutions for $N_B^{(0)}$, $S_B^{(0)}$ and $\Sigma_B^{(0)}$ to be

$$N_B^{(0)} = \sum_{n=1}^{\infty} \nu B_n(t) Y_n(\tau) \left[\cos \left(|\bar{B}|^{\frac{1}{2}}z_B \right) + \sin \left(|\bar{B}|^{\frac{1}{2}}z_B \right) \right] e^{-|\bar{B}|^{\frac{1}{2}}z_B}, \quad (5.85)$$

$$\begin{aligned} S_B^{(0)} = & \sum_{n=1}^{\infty} \frac{\nu B_n(t)}{2h|\bar{B}|^{\frac{3}{2}}} \left\{ 2|\bar{B}|Y'_n(\tau) \cos \left(|\bar{B}|^{\frac{1}{2}}z_B \right) - |\bar{B}|'Y_n(\tau) \left[\cos \left(|\bar{B}|^{\frac{1}{2}}z_B \right) \right. \right. \\ & \left. \left. + |\bar{B}|^{\frac{1}{2}}z_B \left(\cos \left(|\bar{B}|^{\frac{1}{2}}z_B \right) + \sin \left(|\bar{B}|^{\frac{1}{2}}z_B \right) \right) \right] \right\} e^{-|\bar{B}|^{\frac{1}{2}}z_B}, \end{aligned} \quad (5.86)$$

$$\Sigma_B^{(0)} = \sum_{n=1}^{\infty} B_n(t) Y_n(\tau). \quad (5.87)$$

In Figure 5.3, the leading-order approximations $\tilde{\mathcal{F}}^{\frac{1}{2}}N_B^{(0)}$, $\delta_B\tilde{\mathcal{F}}^{\frac{1}{2}}S_B^{(0)}$, $\tilde{\mathcal{F}}^{\frac{1}{2}}\Sigma_B^{(0)}$ of \tilde{N} , \tilde{S} , $\tilde{\Sigma}$ in the bending layer, and the approximations \tilde{N}_s , \tilde{S}_s and $\tilde{\Sigma}_s$ of \tilde{N} , \tilde{S} , $\tilde{\Sigma}$ in the outer shear layer, found by Whittaker (2015), are plotted. It is seen that the bending layer allows the stresses \tilde{N} and \tilde{S} to decay from their values at $Z = 0$ to the smaller values needed in the outer shear layer, while keeping $\tilde{\Sigma}$ approximately constant in Z .

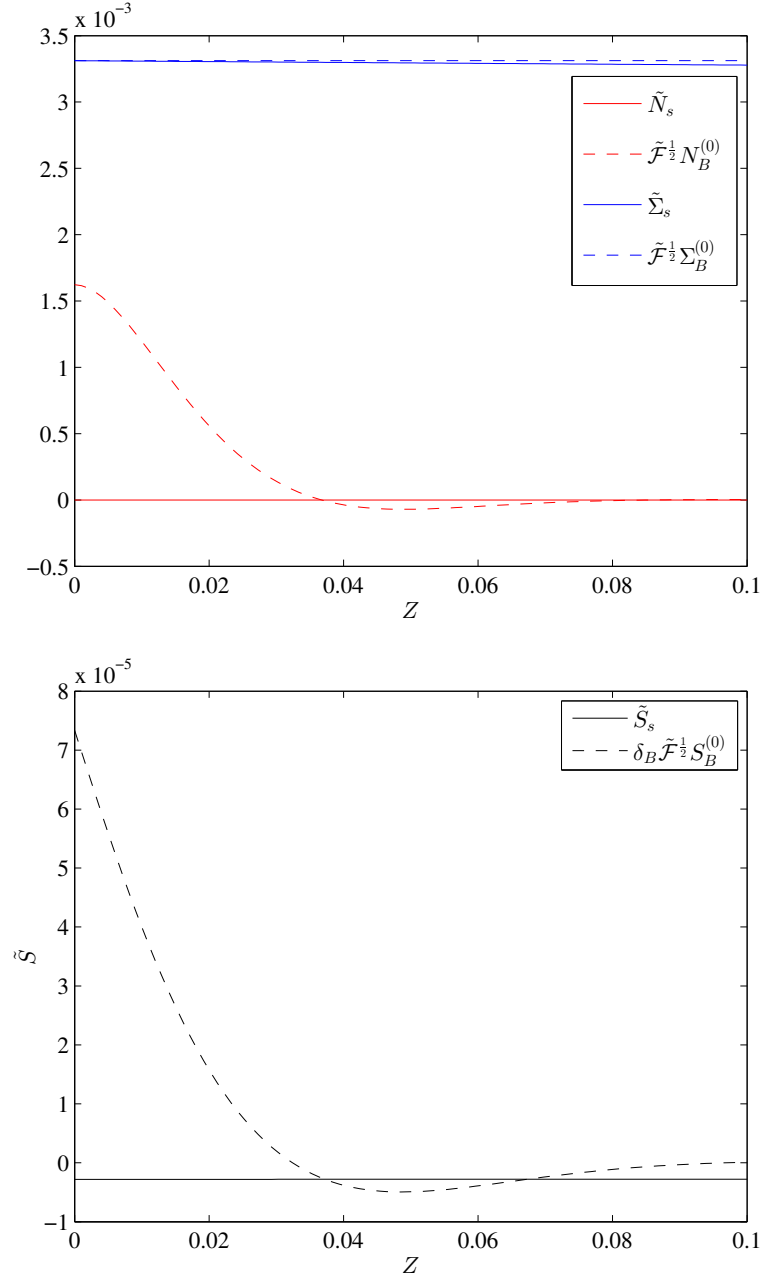


Figure 5.3: The first $n = 1$ modes of the leading-order approximations $\tilde{\mathcal{F}}^{\frac{1}{2}} N_B^{(0)}$, $\delta_B \tilde{\mathcal{F}}^{\frac{1}{2}} S_B^{(0)}$, $\tilde{\mathcal{F}}^{\frac{1}{2}} \Sigma_B^{(0)}$ of \tilde{N} , \tilde{S} , $\tilde{\Sigma}$ in the bending layer. Also plotted are the approximations \tilde{N}_s , \tilde{S}_s and $\tilde{\Sigma}_s$ of \tilde{N} , \tilde{S} , $\tilde{\Sigma}$ in the outer shear layer, found by Whittaker (2015). All approximations are plotted in the case $\sigma_0 = 0.6$, $\delta = 0.001$, $\ell = 10$, $\nu = 0.49$, $\mathcal{F} = 1$, and $B_1(t) = 1$, with $Y_1(\tau)$ normalised such that $Y_1(0) = 1$. In this case $\delta_B \approx 0.026$. To maximise the amplitudes of the plots, we set $\tau = 0$ in the approximations for \tilde{N} and $\tilde{\Sigma}$ and $\tau = 2.6656$, where $Y'_1(\tau)$ is near its maximum value, in the approximations for \tilde{S} .

5.10.2 First-Order Solution

We now consider the first-order solution of the system (5.61)–(5.67). By substituting the approximations (5.69)–(5.71) for N_B , S_B , Σ_B into the system (5.61)–(5.67) we obtain the first-order system for the problem. The first-order governing equations are at $O(\tilde{\mathcal{F}}^{\frac{1}{2}}/\delta_B)$ and are determined to be

$$0 = \bar{B}N_B^{(1)} + \frac{1}{4\bar{B}} \left(\frac{\partial^4 N_B^{(1)}}{\partial z_B^4} - \nu \frac{\partial^4 \Sigma_B^{(1)}}{\partial z_B^4} \right), \quad (5.88)$$

$$0 = \frac{1}{h} \frac{\partial N_B^{(1)}}{\partial \tau} + \frac{\partial S_B^{(1)}}{\partial z_B}, \quad (5.89)$$

$$0 = \frac{\partial \Sigma_B^{(1)}}{\partial z_B}, \quad (5.90)$$

the first-order boundary conditions are calculated as

$$N_B^{(1)} - \nu \Sigma_B^{(1)} = 0, \quad \text{and} \quad \frac{\partial N_B^{(1)}}{\partial z_B} - \nu \frac{\partial \Sigma_B^{(1)}}{\partial z_B} = 0 \quad \text{at} \quad z_B = 0, \quad (5.91)$$

and the first-order matching conditions are found to be

$$N_B^{(1)} \rightarrow 0, \quad S_B^{(1)} \rightarrow \sum_{n=1}^{\infty} \frac{B_n(t)}{\mu_n h} \frac{\partial}{\partial \tau} \left[\frac{1}{\bar{B}^2 h} \frac{\partial}{\partial \tau} \left(\frac{1}{h} \frac{\partial Y_n}{\partial \tau} \right) - Y_n(\tau) \right], \quad \Sigma_B^{(1)} \rightarrow 0, \quad (5.92)$$

as $z_B \rightarrow \infty$. The matching condition on $N_B^{(1)}$ arises from the fact that the first-order $N_B^{(1)}$ term in the expansion (5.69) for N_B is too large to match onto any of the terms in the matching condition (5.65), and thus must decay to zero as $z_B \rightarrow \infty$. The first-order $S_B^{(1)}$ term in the expansion (5.70) for S_B has the same size as the leading-order constant term in the matching condition (5.66), and so $S_B^{(1)}$ must match onto this constant term. Finally, the size of the first-order $\Sigma_B^{(1)}$ term in the expansion (5.71) for Σ_B is too small to match onto the leading-order constant term in the matching condition (5.67), which has already been matched with $\Sigma_B^{(0)}$. However, the size of this first-order $\Sigma_B^{(1)}$ term is also too large for any linear or higher-order terms in z_B that may arise in $\Sigma_B^{(1)}$ to match with any of the higher-order terms in (5.67). Hence, $\Sigma_B^{(1)}$ must tend to zero as $z_B \rightarrow \infty$.

As the first-order governing equations (5.88)–(5.90) take the same form as the leading-order governing equations (5.72)–(5.74), the general solutions for $N_B^{(1)}$, $S_B^{(1)}$ and $\Sigma_B^{(1)}$ will be the same as the general solutions (5.77), (5.79), (5.81) for $N_B^{(0)}$, $S_B^{(0)}$ and $\Sigma_B^{(0)}$. Applying the homogeneous boundary conditions (5.91) and the matching conditions (5.92), the following first-order solutions are found

$$N_B^{(1)} = 0, \quad S_B^{(1)} = \sum_{n=1}^{\infty} \frac{B_n(t)}{\mu_n h} \frac{\partial}{\partial \tau} \left[\frac{1}{\bar{B}^2 h} \frac{\partial}{\partial \tau} \left(\frac{1}{h} \frac{\partial Y_n}{\partial \tau} \right) - Y_n(\tau) \right], \quad \Sigma_B^{(1)} = 0. \quad (5.93)$$

5.10.3 Second-Order Solution

The second-order solution of the system (5.61)–(5.67) is now considered. Substituting the approximations (5.69)–(5.71) for N_B, S_B, Σ_B into (5.61)–(5.67), we find the second-order governing equations at $\mathcal{O}(\tilde{\mathcal{F}}/\delta_B^2)$ to be

$$0 = 4\bar{B}^2 N_B^{(2)} + \left(\frac{\partial^4 N_B^{(2)}}{\partial z_B^4} - \nu \frac{\partial^4 \Sigma_B^{(2)}}{\partial z_B^4} \right) - 4h \left(\frac{\partial^2 N_B^{(0)}}{\partial z_B^2} - \nu \frac{\partial^2 \Sigma_B^{(0)}}{\partial z_B^2} \right), \quad (5.94)$$

$$0 = \frac{1}{h} \frac{\partial N_B^{(2)}}{\partial \tau} + \frac{\partial S_B^{(2)}}{\partial z_B}, \quad (5.95)$$

$$0 = \frac{\partial \Sigma_B^{(2)}}{\partial z_B}, \quad (5.96)$$

the second-order boundary conditions as

$$N_B^{(2)} - \nu \Sigma_B^{(2)} = 0, \quad \text{and} \quad \frac{\partial N_B^{(2)}}{\partial z_B} - \nu \frac{\partial \Sigma_B^{(2)}}{\partial z_B} = 0 \quad \text{at} \quad z_B = 0, \quad (5.97)$$

and the second-order matching conditions to be

$$N_B^{(2)} \rightarrow 0, \quad S_B^{(2)} \rightarrow 0, \quad \Sigma_B^{(2)} \rightarrow 0, \quad \text{as} \quad z_B \rightarrow \infty. \quad (5.98)$$

We have these matching conditions for the following reasons. Like the leading and first-order terms in the expansion (5.69) for N_B , the second-order $N_B^{(2)}$ term is too large to match onto any of the terms in the matching condition (5.65) and thus must decay to zero as $z_B \rightarrow \infty$. The second-order $S_B^{(2)}$ and $\Sigma_B^{(2)}$ terms in the expansions (5.70), (5.71) for S_B and Σ_B are both too small to match with the (already matched) leading-order constant terms in their respective matching conditions (5.66) and (5.67). These second-order terms are also too big for any of the linear or higher-order terms in z_B that $S_B^{(2)}$ and $\Sigma_B^{(2)}$ may contain to match onto any of the higher-order terms within (5.66) and (5.67). Hence, both $S_B^{(2)}$ and $\Sigma_B^{(2)}$ must decay to zero as $z_B \rightarrow \infty$.

Solving the governing equation (5.96) we see that the general solution of $\Sigma_B^{(2)}$ must be

$$\Sigma_B^{(2)} = C_1(\tau, t), \quad (5.99)$$

where C_1 is an arbitrary function of τ and t . Applying the matching condition (5.98) for $\Sigma_B^{(2)}$, it is seen that

$$C_1(\tau, t) = 0, \quad (5.100)$$

which implies

$$\Sigma_B^{(2)} = 0.$$

Substituting (5.99) and the expressions (5.79), (5.77) for $N_B^{(0)}$, $\Sigma_B^{(0)}$ into (5.94), the following ODE for $N_B^{(2)}$ is obtained

$$\frac{\partial^4 N_B^{(2)}}{\partial z_B^4} + 4\bar{B}^2 N_B^{(2)} = \sum_{n=1}^{\infty} 8h|\bar{B}|\nu B_n(t)Y_n(\tau) \left[\sin\left(|\bar{B}|^{\frac{1}{2}}z_B\right) - \cos\left(|\bar{B}|^{\frac{1}{2}}z_B\right) \right] e^{-|\bar{B}|^{\frac{1}{2}}z_B}. \quad (5.101)$$

It is seen that the homogeneous version of this ODE has the same form as the governing ODE (5.78) for $N_B^{(0)}$. As such the complementary function of $N_B^{(2)}$, denoted $N_{B\text{CF}}^{(2)}$ here, will have the same form as the general solution (5.79) of $N_B^{(0)}$ and we have

$$N_{B\text{CF}}^{(2)} = \left[C_2(\tau, t) \cos\left(|\bar{B}|^{\frac{1}{2}}z_B\right) + C_3(\tau, t) \sin\left(|\bar{B}|^{\frac{1}{2}}z_B\right) \right] e^{-|\bar{B}|^{\frac{1}{2}}z_B} + \left[C_4(\tau, t) \cos\left(|\bar{B}|^{\frac{1}{2}}z_B\right) + C_5(\tau, t) \sin\left(|\bar{B}|^{\frac{1}{2}}z_B\right) \right] e^{|\bar{B}|^{\frac{1}{2}}z_B}, \quad (5.102)$$

where C_2, \dots, C_5 are arbitrary functions of τ and t . Applying the matching condition (5.98) for $N_B^{(2)}$, we see that the solution for $N_B^{(2)}$ cannot be exponentially growing as $z_B \rightarrow \infty$ and we must set

$$C_4(\tau, t) = C_5(\tau, t) = 0. \quad (5.103)$$

To find the particular integral of $N_B^{(2)}$, denoted $N_{B\text{PI}}^{(2)}$ here, we try a solution of the form

$$N_{B\text{PI}}^{(2)} = \left[\mathcal{B}(\tau, t) \sin\left(|\bar{B}|^{\frac{1}{2}}z_B\right) - \mathcal{C}(\tau, t) \cos\left(|\bar{B}|^{\frac{1}{2}}z_B\right) \right] z_B e^{-|\bar{B}|^{\frac{1}{2}}z_B},$$

where $\mathcal{B}(\tau, t)$, $\mathcal{C}(\tau, t)$ are functions to be found. Substituting this into the ODE (5.101) and equating coefficients, we find

$$\mathcal{B}(\tau, t) = 0, \quad \mathcal{C}(\tau, t) = \sum_{n=1}^{\infty} \frac{h}{|\bar{B}|^{\frac{1}{2}}} \nu B_n(t) Y_n(\tau),$$

which yields

$$N_{B\text{PI}}^{(2)} = - \sum_{n=1}^{\infty} \frac{h}{|\bar{B}|^{\frac{1}{2}}} \nu B_n(t) Y_n(\tau) z_B \cos\left(|\bar{B}|^{\frac{1}{2}}z_B\right) e^{-|\bar{B}|^{\frac{1}{2}}z_B}. \quad (5.104)$$

Adding the complementary function (5.102) to the particular integral (5.104), the general solution of $N_B^{(2)}$ is found to be

$$N_B^{(2)} = \left[\left(C_2(\tau, t) - \sum_{n=1}^{\infty} \frac{h}{|\bar{B}|^{\frac{1}{2}}} \nu B_n(t) Y_n(\tau) z_B \right) \cos\left(|\bar{B}|^{\frac{1}{2}}z_B\right) + C_3(\tau, t) \sin\left(|\bar{B}|^{\frac{1}{2}}z_B\right) \right] e^{-|\bar{B}|^{\frac{1}{2}}z_B}. \quad (5.105)$$

Finally, we rearrange and integrate (5.95) to obtain the following expression for $S_B^{(2)}$

$$S_B^{(2)} = \int_{z_B}^{\infty} \frac{1}{h} \frac{\partial N_B^{(2)}(\tau, z', t)}{\partial \tau} dz'. \quad (5.106)$$

It is noted that the matching condition (5.98) for $S_B^{(2)}$ has been incorporated into this expression.

We now use the boundary conditions (5.97) to derive the full solution of $N_B^{(2)}$. Applying these boundary conditions to the general solution (5.105) of $N_B^{(2)}$, it is found that

$$C_2(\tau, t) = 0, \quad C_3(\tau, t) = \sum_{n=1}^{\infty} \frac{h}{|\bar{B}|} v B_n(t) Y_n(\tau).$$

Substituting these into (5.105), the full solution of $N_B^{(2)}$ is found to be

$$N_B^{(2)} = \sum_{n=1}^{\infty} \frac{h}{|\bar{B}|^{\frac{1}{2}}} v B_n(t) Y_n(\tau) \left[\frac{\sin(|\bar{B}|^{\frac{1}{2}} z_B)}{|\bar{B}|^{\frac{1}{2}}} - z_B \cos(|\bar{B}|^{\frac{1}{2}} z_B) \right] e^{-|\bar{B}|^{\frac{1}{2}} z_B}. \quad (5.107)$$

It is now possible to derive $S_B^{(2)}$ by substituting the value for $N_B^{(2)}$ into (5.106). Doing so gives the following solution for $S_B^{(2)}$

$$S_B^{(2)} = \frac{v B_n(t)}{4h|\bar{B}|^{\frac{5}{2}}} \left\{ \sin\left(|\bar{B}|^{\frac{1}{2}} z_B\right) \left[\left(2(hY_n)'|\bar{B}|^{\frac{3}{2}} - 5hY_n|\bar{B}|^{\frac{1}{2}}|\bar{B}'\right) z_B + 4(hY_n)'|\bar{B}| - 6hY_n|\bar{B}' \right] \right. \\ \left. + \cos\left(|\bar{B}|^{\frac{1}{2}} z_B\right) \left[2hY_n|\bar{B}||\bar{B}'|z_B^2 + \left(3hY_n|\bar{B}|^{\frac{1}{2}}|\bar{B}' - 2(hY_n)'|\bar{B}|^{\frac{3}{2}}\right) z_B + 2(hY_n)'|\bar{B}| - 3hY_n|\bar{B}' \right] \right\} e^{-|\bar{B}|^{\frac{1}{2}} z_B}, \quad (5.108)$$

where once again, ' denotes a derivative with respect to τ .

Finally, we recall that

$$\Sigma_B^{(2)} = 0. \quad (5.109)$$

5.11 Bending-Layer Deformations

Now that the asymptotic expansions (5.69)–(5.71) for N_B , S_B and Σ_B have been calculated up to second order, we may use these to calculate approximations for the deformations $\hat{\xi}$, $\hat{\eta}$, $\hat{\zeta}$ in the bending layer, up to the largest non-zero higher-order term. Substituting (5.69)–(5.71) into the expressions (5.60) allows us to find \tilde{N} , \tilde{S} and $\tilde{\Sigma}$ in the bending layer. We may then substitute these stresses into the expressions (5.141)–(5.143) for the deformations $\hat{\xi}$, $\hat{\eta}$, $\hat{\zeta}$ in terms of \tilde{N} , \tilde{S}

and $\tilde{\Sigma}$. Doing so and noting that $N_B^{(1)} = \Sigma_B^{(1)} = \Sigma_B^{(2)} = 0$, the approximations of the deformations including the largest non-zero higher-order terms are found to be

$$\hat{\xi} = \tilde{\mathcal{F}}^{\frac{1}{2}} \left[\hat{\xi}^{(0)} + \frac{\tilde{\mathcal{F}}}{\delta_B^2} \hat{\xi}^{(1)} + O\left(\frac{\tilde{\mathcal{F}}^{\frac{3}{2}}}{\delta_B^3}, \frac{\delta^2}{\delta_B^2}\right) \right], \quad (5.110)$$

$$\hat{\eta} = \delta_B^2 \tilde{\mathcal{F}}^{\frac{1}{2}} \left[\hat{\eta}^{(0)} + \frac{\tilde{\mathcal{F}}^{\frac{1}{2}}}{\delta_B} \hat{\eta}^{(1)} + O\left(\frac{\tilde{\mathcal{F}}}{\delta_B^2}\right) \right], \quad (5.111)$$

$$\hat{\zeta} = \delta_B \tilde{\mathcal{F}}^{\frac{1}{2}} \left[\hat{\zeta}^{(0)} + \frac{\tilde{\mathcal{F}}}{\delta_B^2} \hat{\zeta}^{(1)} + O\left(\frac{\tilde{\mathcal{F}}^{\frac{3}{2}}}{\delta_B^3}, \frac{\delta^2}{\delta_B^2}\right) \right], \quad (5.112)$$

where the leading-order terms $\hat{\xi}^{(0)}$, $\hat{\eta}^{(0)}$ and $\hat{\zeta}^{(0)}$ are given by

$$\hat{\xi}^{(0)} = \frac{h}{12\bar{B}(1-\nu^2)} \left(\nu \Sigma_B^{(0)} - N_B^{(0)} \right), \quad (5.113)$$

$$\begin{aligned} \hat{\eta}^{(0)} = & \int_0^{z_B} \left(\frac{h S_B^{(0)}(\tau, z', t)}{6(1-\nu)} \right. \\ & \left. - \frac{\partial}{\partial \tau} \int_0^{z'} \frac{\Sigma_B^{(0)}(\tau, z'', t) - \nu N_B^{(0)}(\tau, z'', t)}{12(1-\nu^2)} dz'' \right) dz', \end{aligned} \quad (5.114)$$

$$\hat{\zeta}^{(0)} = \int_0^{z_B} \frac{\Sigma_B^{(0)}(\tau, z', t) - \nu N_B^{(0)}(\tau, z', t)}{12(1-\nu^2)} dz', \quad (5.115)$$

and the higher-order terms $\hat{\xi}^{(1)}$, $\hat{\eta}^{(1)}$ and $\hat{\zeta}^{(1)}$ are defined as

$$\hat{\xi}^{(1)} = -\frac{h}{12\bar{B}(1-\nu^2)} N_B^{(2)}, \quad (5.116)$$

$$\hat{\eta}^{(1)} = \int_0^{z_B} \frac{h S_B^{(1)}(\tau, z', t)}{6(1-\nu)} dz', \quad (5.117)$$

$$\hat{\zeta}^{(1)} = - \int_0^{z_B} \frac{\nu N_B^{(2)}(\tau, z', t)}{12(1-\nu^2)} dz'. \quad (5.118)$$

Applying the expressions (5.85)–(5.87), (5.93) and (5.107)–(5.109) for $N_B^{(0)}, \dots, \Sigma_B^{(2)}$ to the approximations (5.110)–(5.112), the bending-layer

deformations up to the largest non-zero higher-order term are found to be

$$\begin{aligned} \hat{\xi} &= \tilde{\mathcal{F}}^{\frac{1}{2}} \sum_{n=1}^{\infty} \frac{h\nu B_n(t) Y_n(\tau)}{12\bar{B}(1-\nu^2)} \left[1 - \left(\cos\left(|\bar{B}|^{\frac{1}{2}} z_B\right) + \sin\left(|\bar{B}|^{\frac{1}{2}} z_B\right) \right) e^{-|\bar{B}|^{\frac{1}{2}} z_B} \right] \\ &\quad + \frac{\tilde{\mathcal{F}}^{\frac{3}{2}}}{\delta_B^2} \sum_{n=1}^{\infty} \frac{h^2 \nu B_n(t) Y_n(\tau)}{12|\bar{B}|^{\frac{3}{2}}(1-\nu^2)} \left[\frac{\sin\left(|\bar{B}|^{\frac{1}{2}} z_B\right)}{|\bar{B}|^{\frac{1}{2}}} - z_B \cos\left(|\bar{B}|^{\frac{1}{2}} z_B\right) \right] e^{-|\bar{B}|^{\frac{1}{2}} z_B} \\ &\quad + O\left(\frac{\tilde{\mathcal{F}}^2}{\delta_B^3}, \frac{\tilde{\mathcal{F}}^{\frac{1}{2}} \delta^2}{\delta_B^2}\right), \end{aligned} \quad (5.119)$$

$$\begin{aligned} \hat{\eta} &= \delta_B^2 \tilde{\mathcal{F}}^{\frac{1}{2}} \sum_{n=1}^{\infty} \frac{B_n(t)}{24(1-\nu^2)} \left\{ (\nu^2 + 2\nu) \left[\left(\frac{Y_n}{|\bar{B}|} \right)' \sin\left(|\bar{B}|^{\frac{1}{2}} z_B\right) \right. \right. \\ &\quad \left. \left. + \left(\frac{Y_n}{|\bar{B}|^{\frac{3}{2}}} |\bar{B}|' z_B - \left(\frac{Y_n}{|\bar{B}|} \right)' \right) \cos\left(|\bar{B}|^{\frac{1}{2}} z_B\right) \right] e^{-|\bar{B}|^{\frac{1}{2}} z_B} \right. \\ &\quad \left. - Y_n' z_B^2 + 2 \left(\frac{Y_n}{|\bar{B}|^{\frac{1}{2}}} \right)' \nu^2 z_B + (\nu^2 + 2\nu) \left(\frac{Y_n}{|\bar{B}|} \right)' \right\} \\ &\quad + \delta_B \tilde{\mathcal{F}} \sum_{n=1}^{\infty} \frac{B_n(t)}{6\mu_n(1-\nu)} \frac{\partial}{\partial \tau} \left[\frac{1}{\bar{B}^2 h} \frac{\partial}{\partial \tau} \left(\frac{1}{h} \frac{\partial Y_n}{\partial \tau} \right) - Y_n(\tau) \right] z_B + O\left(\tilde{\mathcal{F}}^{\frac{3}{2}}\right), \end{aligned} \quad (5.120)$$

$$\begin{aligned} \hat{\zeta} &= \delta_B \tilde{\mathcal{F}}^{\frac{1}{2}} \sum_{n=1}^{\infty} \frac{B_n(t) Y_n(\tau)}{12(1-\nu^2)} \left[z_B + \frac{\nu^2}{|\bar{B}|^{\frac{1}{2}}} \left(\cos\left(|\bar{B}|^{\frac{1}{2}} z_B\right) e^{-|\bar{B}|^{\frac{1}{2}} z_B} - 1 \right) \right] \\ &\quad - \frac{\tilde{\mathcal{F}}^{\frac{3}{2}}}{\delta_B} \sum_{n=1}^{\infty} \frac{h\nu^2 B_n(t) Y_n(\tau)}{24|\bar{B}|^{\frac{3}{2}}(1-\nu^2)} \left\{ 1 - \left[(1 - |\bar{B}|^{\frac{1}{2}} z_B) \cos\left(|\bar{B}|^{\frac{1}{2}} z_B\right) \right. \right. \\ &\quad \left. \left. + (2 + |\bar{B}|^{\frac{1}{2}} z_B) \sin\left(|\bar{B}|^{\frac{1}{2}} z_B\right) \right] e^{-|\bar{B}|^{\frac{1}{2}} z_B} \right\} + O\left(\frac{\tilde{\mathcal{F}}^2}{\delta_B^2}, \frac{\tilde{\mathcal{F}}^{\frac{1}{2}} \delta^2}{\delta_B}\right). \end{aligned} \quad (5.121)$$

The sizes of these deformations are in agreement with the sizes of the deformations (5.174)–(5.176) calculated in the limit of a circular cross-section in Appendix 5.B. The leading-order terms of these expressions are depicted in Figures 5.5, 5.6 and 5.7 in §5.13.

5.12 Leading-Order Area Change in the Bending Layer

Using the expression (5.119) for the normal deformation $\hat{\xi}$ in the bending layer, it is possible to determine the leading-order variation in the cross-sectional area of the tube within the bending layer. We begin with the following relation between the area change and deformation $\mathbf{r} - \mathbf{r}_0$ in the tube wall, found by

Whittaker *et al.* (2010d)

$$(A(z_B, t) - A_0) a^2 = \oint (\mathbf{r} - \mathbf{r}_0) \cdot \hat{\mathbf{n}} a h d\tau + O(\Delta^2), \quad (5.122)$$

where A , A_0 are the dimensionless cross-sectional areas of the tube in its deformed and undeformed state respectively. Applying the expression (5.5) for $\mathbf{r} - \mathbf{r}_0$, we find the leading-order area change in the bending layer is given by

$$\begin{aligned} A(z_B, t) - A_0 &= \frac{\Delta}{\ell} \int_0^{2\pi} \hat{\zeta} d\tau + O(\Delta^2), \\ &= \frac{\Delta \tilde{\mathcal{F}}^{\frac{1}{2}}}{\ell} \sum_{n=1}^{\infty} \frac{\nu B_n(t)}{12(1-\nu^2)} \mathcal{C}_n(z_B) + O\left(\frac{\Delta \tilde{\mathcal{F}}^{\frac{3}{2}}}{\delta_B^2 \ell}\right), \end{aligned} \quad (5.123)$$

where

$$\mathcal{C}_n(z_B) = \int_0^{2\pi} \frac{h Y_n}{\bar{B}} \left[1 - \left(\cos\left(|\bar{B}|^{\frac{1}{2}} z_B\right) + \sin\left(|\bar{B}|^{\frac{1}{2}} z_B\right) \right) e^{-|\bar{B}|^{\frac{1}{2}} z_B} \right] d\tau. \quad (5.124)$$

The function $\mathcal{C}_n(z_B)$ cannot be determined analytically and so instead we find a numerical solution for the function. We begin by numerically determining the eigenfunctions $Y_n(\tau)$ of the operator \mathcal{L} defined in (5.28). This may be done in MATLAB using the “BVP4C” solver, documented in Kierzenka & Shampine (2001). Once the eigenfunctions are calculated, it is then possible to numerically evaluate the integral within (5.124) by applying the trapezium rule with the “trapz” function in MATLAB.

In Figure 5.4, the numerical solution of $\mathcal{C}_n(z_B)$ for the first $n = 1$ mode has been plotted in the case $\sigma_0 = 0.6$. In this case, the eigenfunction $Y_1(\tau)$ has been normalised such that $Y_1(0) = 1$. From the figure, we see that as $z_B \rightarrow 0$, the value and axial gradient of $\mathcal{C}_1(z_B)$ both tend to zero as expected. We also see that as $z_B \rightarrow \infty$, $\mathcal{C}_1(z_B)$ tends to some constant $O(1)$ value. By examining (5.124) and noting the exponential decay of the sinusoidal terms, we may deduce that

$$\mathcal{C}_n(z_B) \rightarrow \int_0^{2\pi} \frac{h Y_n}{\bar{B}} d\tau, \quad \text{as } z_B \rightarrow \infty.$$

In the case $\sigma_0 = 0.6$, it is found that for the normalisation $Y_1(0) = 1$,

$$\mathcal{C}_1(z_B) \sim 2.399, \quad \text{as } z_B \rightarrow \infty.$$

Finally, we note that there is a maximum in $\mathcal{C}_1(z_B)$ at $z_B \sim 4.5$ which is slightly larger than the value $\mathcal{C}_1(z_B)$ takes as $z_B \rightarrow \infty$.

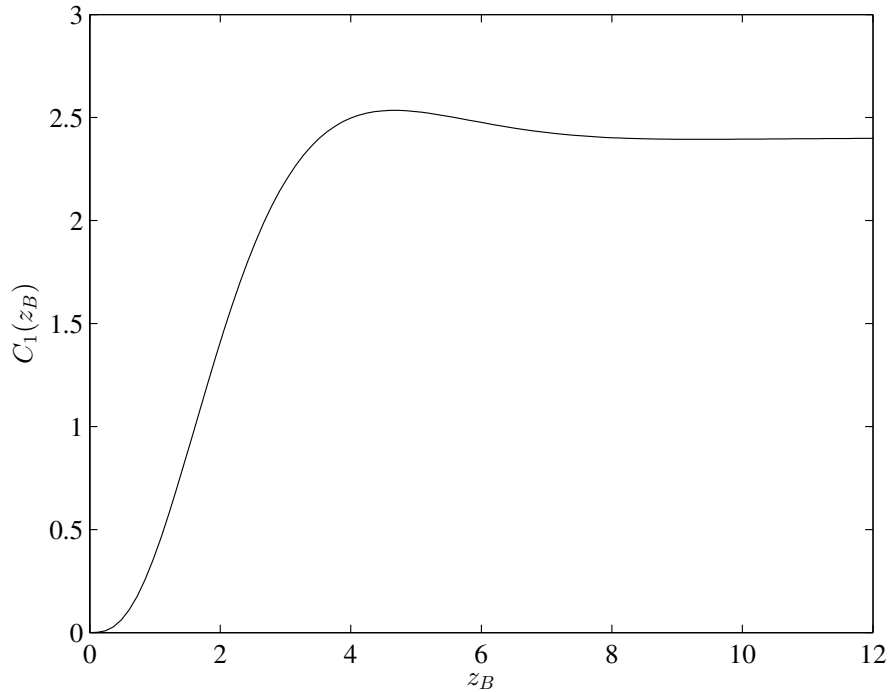


Figure 5.4: The numerical solution of the first $n = 1$ mode of the function $C_n(z_B)$ defined in (5.124), in the case $\sigma_0 = 0.6$. Here we have normalised $Y_1(\tau)$ such that $Y_1(0) = 1$.

Examining the expression (5.123) for the area change along with the behaviour of the functions $C_n(z_B)$, it is seen that within the bending layer $A(z_B, t) - A_0 = O(\Delta \tilde{\mathcal{F}}^{\frac{1}{2}}/\ell)$. It can also be shown that

$$A(z_B, t) - A_0 \rightarrow \frac{\Delta \tilde{\mathcal{F}}^{\frac{1}{2}}}{\ell} \sum_{n=1}^{\infty} \frac{\nu B_n(t)}{12(1-\nu^2)} \int_0^{2\pi} \frac{h Y_n}{\bar{B}} d\tau, \quad \text{as } z_B \rightarrow \infty. \quad (5.125)$$

Hence, as we exit the bending layer the change in area tends to some $O(\Delta \tilde{\mathcal{F}}^{\frac{1}{2}}/\ell)$ constant in z_B .

5.13 Corrections to the Outer Shear-Layer Solution

Now that we have obtained the expressions (5.119)–(5.121) for the deformations $\hat{\xi}$, $\hat{\eta}$ and $\hat{\zeta}$ in the bending layer, we determine what corrections the leading-order terms of these expressions impose on the deformations in the outer shear layer. To do this, we must match the general leading-order solutions (5.29)–(5.31) for the deformations in the outer shear layer to the expressions (5.119)–(5.121) as $\check{z} \rightarrow 0, z_B \rightarrow \infty$.

Taking the Taylor series of (5.29)–(5.31) about $\check{z} = 0$ and rewriting the axial coordinate in terms of the intermediate variable z_I defined in (5.51), we find the asymptotic behaviour of the deformations in the outer shear layer as $\check{z} \rightarrow 0$ to be

$$\hat{\xi} \sim \frac{\tilde{\mathcal{F}}^{-\frac{1}{2}}}{12\bar{B}(1-\nu^2)} \left\{ -\sum_{n=1}^{\infty} B_n(t) \frac{\partial}{\partial \tau} \left(\frac{1}{h} \frac{\partial Y_n}{\partial \tau} \right) \left[\frac{1}{2} \left(\delta_B \tilde{\mathcal{F}}^{\frac{1}{2}} \right)^{2\alpha} z_I^2 + O \left(\left(\delta_B \tilde{\mathcal{F}}^{\frac{1}{2}} \right)^{3\alpha} \right) \right] \right. \\ \left. - \frac{\partial}{\partial \tau} \left(\frac{1}{h} \frac{\partial \check{A}(\tau, t)}{\partial \tau} \right) \left(\delta_B \tilde{\mathcal{F}}^{\frac{1}{2}} \right)^{\alpha} z_I + \frac{\partial}{\partial \tau} \left(\frac{\check{B}(\tau, t)}{h} \right) \right\} + O(\tilde{\mathcal{F}}^{\frac{1}{2}}), \quad (5.126)$$

$$\hat{\eta} \sim \frac{\tilde{\mathcal{F}}^{-\frac{1}{2}}}{12(1-\nu^2)} \left\{ -\sum_{n=1}^{\infty} B_n(t) \frac{\partial Y_n}{\partial \tau} \left[\frac{1}{2} \left(\delta_B \tilde{\mathcal{F}}^{\frac{1}{2}} \right)^{2\alpha} z_I^2 + O \left(\left(\delta_B \tilde{\mathcal{F}}^{\frac{1}{2}} \right)^{3\alpha} \right) \right] \right. \\ \left. - \frac{\partial \check{A}(\tau, t)}{\partial \tau} \left(\delta_B \tilde{\mathcal{F}}^{\frac{1}{2}} \right)^{\alpha} z_I + \check{B}(\tau, t) \right\} + O(\tilde{\mathcal{F}}^{\frac{1}{2}}), \quad (5.127)$$

$$\hat{\zeta} \sim \frac{1}{12(1-\nu^2)} \left\{ \sum_{n=1}^{\infty} B_n(t) Y_n(\tau) \left[\left(\delta_B \tilde{\mathcal{F}}^{\frac{1}{2}} \right)^{\alpha} z_I + O \left(\left(\delta_B \tilde{\mathcal{F}}^{\frac{1}{2}} \right)^{2\alpha} \right) \right] + \check{A}(\tau, t) \right\} \\ + O(\tilde{\mathcal{F}}). \quad (5.128)$$

As $z_B \rightarrow \infty$, the asymptotic behaviours of the deformations (5.119)–(5.121) are found to be

$$\hat{\xi} \sim \frac{\tilde{\mathcal{F}}^{\frac{1}{2}}}{12\bar{B}(1-\nu^2)} \sum_{n=1}^{\infty} h\nu B_n(t) Y_n(\tau) \\ + O \left(\frac{\tilde{\mathcal{F}}^{\frac{2-k}{2}}}{\delta_B^{3+k}} \left(\delta_B \tilde{\mathcal{F}}^{\frac{1}{2}} \right)^{k\alpha}, \frac{\tilde{\mathcal{F}}^{\frac{1-k}{2}} \delta^2}{\delta_B^{2+k}} \left(\delta_B \tilde{\mathcal{F}}^{\frac{1}{2}} \right)^{k\alpha} \right), \quad (5.129)$$

$$\hat{\eta} \sim \sum_{n=1}^{\infty} \frac{B_n(t)}{24(1-\nu^2)} \left\{ -\tilde{\mathcal{F}}^{-\frac{1}{2}} Y'_n \left(\delta_B \tilde{\mathcal{F}}^{\frac{1}{2}} \right)^{2\alpha} z_I^2 + 2\delta_B \nu^2 \left(\frac{Y_n}{|\bar{B}|^{\frac{1}{2}}} \right)' \left(\delta_B \tilde{\mathcal{F}}^{\frac{1}{2}} \right)^{\alpha} z_I \right. \\ \left. + \delta_B^2 \tilde{\mathcal{F}}^{\frac{1}{2}} (\nu^2 + 2\nu) \left(\frac{Y_n}{|\bar{B}|} \right)' \right\} \\ + O \left(\tilde{\mathcal{F}}^{\frac{1}{2}} \left(\delta_B \tilde{\mathcal{F}}^{\frac{1}{2}} \right)^{\alpha}, \frac{\tilde{\mathcal{F}}^{\frac{3-k}{2}}}{\delta_B^k} \left(\delta_B \tilde{\mathcal{F}}^{\frac{1}{2}} \right)^{k\alpha} \right), \quad (5.130)$$

$$\hat{\zeta} \sim \sum_{n=1}^{\infty} \frac{B_n(t) Y_n(\tau)}{12(1-\nu^2)} \left[\left(\delta_B \tilde{\mathcal{F}}^{\frac{1}{2}} \right)^{\alpha} z_I - \delta_B \tilde{\mathcal{F}}^{\frac{1}{2}} \frac{\nu^2}{|\bar{B}|} \right] \\ + O \left(\frac{\tilde{\mathcal{F}}^{\frac{3}{2}}}{\delta_B}, \frac{\tilde{\mathcal{F}}^{\frac{2-k}{2}}}{\delta_B^{2+k}} \left(\delta_B \tilde{\mathcal{F}}^{\frac{1}{2}} \right)^{k\alpha}, \frac{\tilde{\mathcal{F}}^{\frac{1-k}{2}} \delta^2}{\delta_B^{1+k}} \left(\delta_B \tilde{\mathcal{F}}^{\frac{1}{2}} \right)^{k\alpha} \right). \quad (5.131)$$

Here, the integer k is the highest power of z_I that appears at higher orders in the approximations. For (5.126)–(5.128) to match with (5.129)–(5.131), we must have

$$\check{A}(\tau, t) = -\delta_B \tilde{\mathcal{F}}^{\frac{1}{2}} \sum_{n=1}^{\infty} \frac{\nu^2 B_n(t) Y_n(\tau)}{|\bar{B}|^{\frac{1}{2}}}, \quad \check{B}(\tau, t) = 0. \quad (5.132)$$

We note that the quadratic and linear terms in the asymptotic behaviour (5.126) for $\hat{\xi}$ in the outer shear layer match onto higher-order terms in the approximation (5.129) for $\hat{\xi}$ in the bending layer as $z_B \rightarrow \infty$. We also note that the constant term in (5.129) matches with higher-order terms in (5.126). Finally, the constant term in the approximation (5.130) for $\hat{\eta}$ in the bending layer as $z_B \rightarrow \infty$ matches with higher-order terms in the outer shear-layer approximation (5.127) as $\check{z} \rightarrow 0$.

Substituting (5.132) into (5.29)–(5.31), the corrected deformations in the outer shear layer are found to be

$$\begin{aligned} \hat{\xi} = & \frac{1}{12\bar{B}(1-\nu^2)} \sum_{n=1}^{\infty} B_n(t) \left\{ \frac{\tilde{\mathcal{F}}^{-\frac{1}{2}}}{\mu_n} \frac{\partial}{\partial \tau} \left(\frac{1}{h} \frac{\partial Y_n}{\partial \tau} \right) \left[\frac{1}{\mu_n} (1 - e^{-\mu_n \check{z}}) - \check{z} \right] \right. \\ & \left. + \delta_B \nu^2 \frac{\partial}{\partial \tau} \left[\frac{1}{h} \frac{\partial}{\partial \tau} \left(\frac{Y_n(\tau)}{|\bar{B}|^{\frac{1}{2}}} \right) \right] \check{z} \right\} + O(\tilde{\mathcal{F}}^{\frac{1}{2}}), \end{aligned} \quad (5.133)$$

$$\begin{aligned} \hat{\eta} = & \frac{1}{12(1-\nu^2)} \sum_{n=1}^{\infty} B_n(t) \left\{ \frac{\tilde{\mathcal{F}}^{-\frac{1}{2}}}{\mu_n} \frac{\partial Y_n}{\partial \tau} \left[\frac{1}{\mu_n} (1 - e^{-\mu_n \check{z}}) - \check{z} \right] \right. \\ & \left. + \delta_B \nu^2 \frac{\partial}{\partial \tau} \left(\frac{Y_n(\tau)}{|\bar{B}|^{\frac{1}{2}}} \right) \check{z} \right\} + O(\tilde{\mathcal{F}}^{\frac{1}{2}}), \end{aligned} \quad (5.134)$$

$$\hat{\zeta} = \sum_{n=1}^{\infty} \frac{B_n(t) Y_n(\tau)}{12(1-\nu^2)} \left[\frac{1}{\mu_n} (1 - e^{-\mu_n \check{z}}) - \delta_B \tilde{\mathcal{F}}^{\frac{1}{2}} \frac{\nu^2}{|\bar{B}|^{\frac{1}{2}}} \right] + O(\tilde{\mathcal{F}}). \quad (5.135)$$

Comparing these deformations with those originally found by Whittaker (2015), we see that the correction terms are all a factor of $O(\delta_B \tilde{\mathcal{F}}^{\frac{1}{2}}) = O(\mathcal{F}^{\frac{1}{2}} \delta^{\frac{3}{2}} \ell)$ smaller than the leading-order terms, and the leading-order behaviour of the deformations in the outer shear layer is not altered. However as $\delta_B \gg \tilde{\mathcal{F}}^{\frac{1}{2}}$, these correction terms are larger than the other higher-order terms within the expressions and thus are more important than the other higher-order terms. In $\hat{\xi}$ and $\hat{\eta}$, the correction terms are linear in \check{z} and thus alter the axial gradient of the normal and azimuthal deformations. In $\hat{\zeta}$, the correction term is instead constant in \check{z} and imposes a constant shift in the axial deformation.

By relaxing the condition $\mathcal{F} = O(1)$ and setting $\mathcal{F} = O(\delta^{-3} \ell^{-2})$, the correction terms become large enough to contribute at leading order. However, substituting this value of \mathcal{F} into the definition (5.1) of $\tilde{\mathcal{F}}$, we instead find $\tilde{\mathcal{F}} = O(\delta^{-1})$. As $\delta \ll 1$, we have $\tilde{\mathcal{F}} \gg 1$ in this scenario, and the shear layer studied by Whittaker (2015) no longer has a significant effect on the bulk solution and does not need to be considered. Hence, further investigation is required to see what happens in this case.

In Figures 5.5, 5.6 and 5.7, the first $n = 1$ mode of the leading-order

approximations for $\hat{\xi}$, $\hat{\eta}$ and $\hat{\zeta}$ in the original outer shear layer studied by Whittaker (2015), which we denote as $\hat{\xi}_s$, $\hat{\eta}_s$ and $\hat{\zeta}_s$, are plotted in the axial direction for fixed τ . Also plotted is the first $n = 1$ mode of the leading-order approximations $\tilde{\mathcal{F}}^{\frac{1}{2}}\hat{\zeta}^{(0)}$, $\delta_B^2\tilde{\mathcal{F}}^{\frac{1}{2}}\hat{\eta}^{(0)}$, $\delta_B\tilde{\mathcal{F}}^{\frac{1}{2}}\hat{\zeta}^{(0)}$ for the deformations in the bending layer, as found in (5.119)–(5.121), and the first mode of the corrected outer shear-layer deformations (5.133)–(5.135), which we denote as $\hat{\xi}_c$, $\hat{\eta}_c$ and $\hat{\zeta}_c$. It is seen that the bending-layer deformations and axial gradient are all zero at the clamped boundary $Z = 0$, and the clamped boundary conditions are satisfied. The linear corrections to $\hat{\xi}$ and $\hat{\eta}$ and the constant shift to $\hat{\zeta}$ in the outer shear layer is also observed. Finally, it is noted that the correction to the outer shear-layer $\hat{\xi}$ behaves differently from the far-field behaviour of the approximation for $\hat{\xi}$ in the bending layer. This is because the leading-order terms in the bending layer match with higher-order terms in the outer shear layer, with axially uniform behaviour in the intermediate region. Conversely the leading-order terms in the outer shear layer match with the higher-order terms in the bending boundary layer, with axially quadratic behaviour in the intermediate region. Hence, the leading-order bending-layer $\hat{\xi}$ does not alter the leading-order shear-layer $\hat{\xi}$, and the correction seen in the shear layer is due to terms that arise at higher-order in the bending layer.

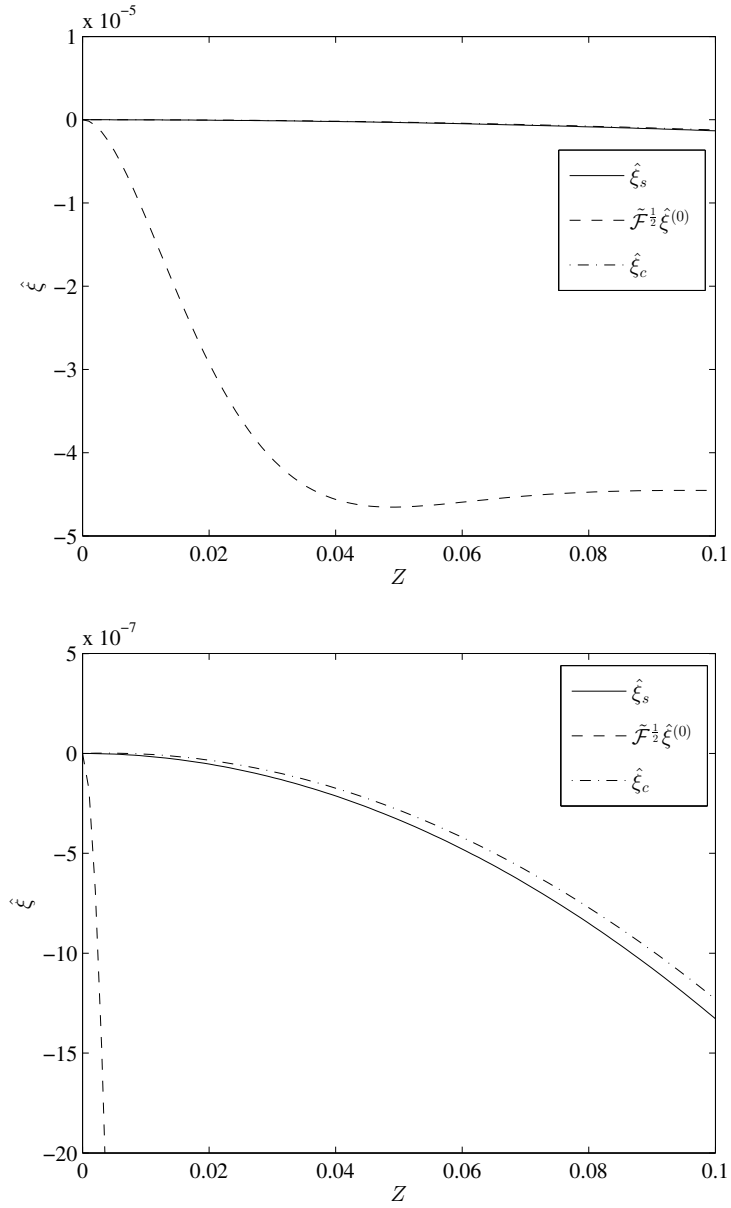


Figure 5.5: The first $n = 1$ modes of the approximations $\hat{\xi}_s$, $\tilde{\mathcal{F}}^{1/2}\hat{\xi}^{(0)}$, and $\hat{\xi}_c$, of $\hat{\xi}$ in the original outer shear layer studied by Whittaker (2015), in the bending layer, and in the corrected outer shear layer, respectively. The approximations $\tilde{\mathcal{F}}^{1/2}\hat{\xi}^{(0)}$ and $\hat{\xi}_c$ are found in (5.119) and (5.133), and all the approximations are plotted in the case $\sigma_0 = 0.6$, $\delta = 0.001$, $\ell = 10$, $\nu = 0.49$, $\mathcal{F} = 1$, $\tau = 0$ and $B_1(t) = 1$, with $Y_1(\tau)$ normalised such that $Y_1(0) = 1$. In this case $\delta_B = 0.026$.

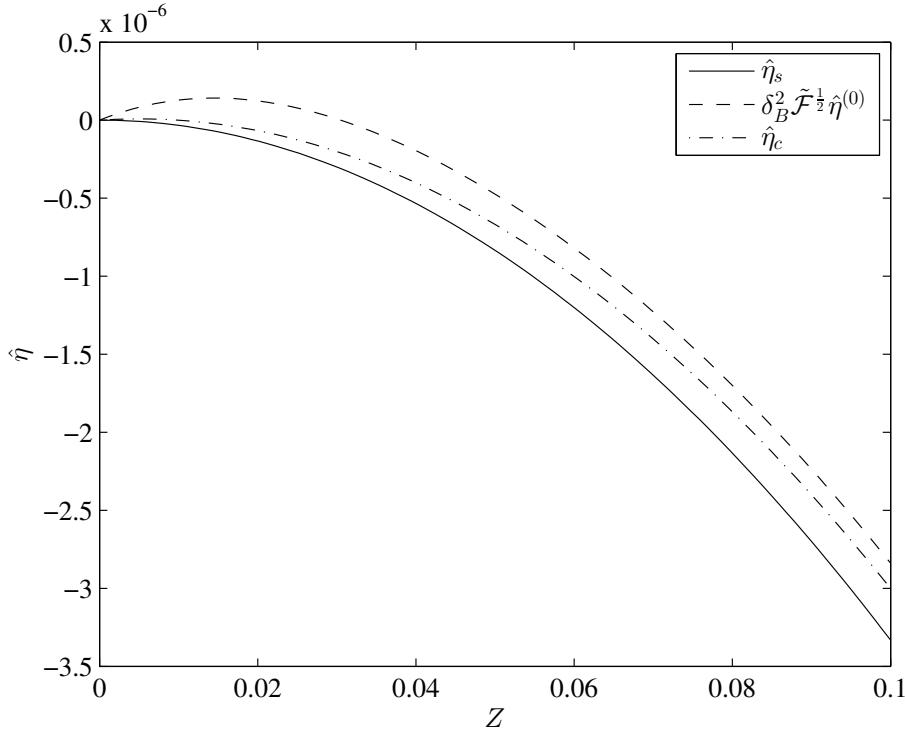


Figure 5.6: The first $n = 1$ modes of the approximations $\hat{\eta}_s$, $\delta_B^2 \tilde{\mathcal{F}}^{1/2} \hat{\eta}^{(0)}$, and $\hat{\eta}_c$, of $\hat{\eta}$ in the original outer shear layer studied by Whittaker (2015), in the bending layer, and in the corrected outer shear layer, respectively. The approximations $\delta_B^2 \tilde{\mathcal{F}}^{1/2} \hat{\eta}^{(0)}$ and $\hat{\eta}_c$ are found in (5.120) and (5.134), and all the approximations are plotted in the case $\sigma_0 = 0.6$, $\delta = 0.001$, $\ell = 10$, $\nu = 0.49$, $\mathcal{F} = 1$, $\tau = 2.6656$ (where $Y'_1(\tau)$ is near its maximum value) and $B_1(t) = 1$, with $Y_1(\tau)$ normalised such that $Y_1(0) = 1$. In this case $\delta_B = 0.026$.

With the expression (5.133) for $\hat{\xi}$ in the outer shear layer, it is also possible to determine the correction to the cross-sectional area change within the outer shear layer. Substituting (5.133) into the expression (5.122), the area change $A(\check{z}, t) - A_0$ in the outer shear layer is found to be

$$A(\check{z}, t) - A_0 = \sum_{n=1}^{\infty} \frac{\Delta B_n(t)}{12\ell(1-\nu^2)} \left\{ \frac{\tilde{\mathcal{F}}^{-\frac{1}{2}}}{\mu_n} \left[\frac{1}{\mu_n} (1 - e^{-u_n \check{z}}) - \check{z} \right] \int_0^{2\pi} \frac{1}{\bar{B}} \left(\frac{Y'_n}{h} \right)' d\tau \right. \\ \left. + \delta_B \nu^2 \check{z} \int_0^{2\pi} \frac{1}{\bar{B}} \left(\frac{1}{h} \left(\frac{Y_n}{|\bar{B}|^{\frac{1}{2}}} \right)' \right)' d\tau \right\} + O\left(\frac{\Delta \tilde{\mathcal{F}}^{\frac{1}{2}}}{\ell}\right). \quad (5.136)$$

As with the normal deformation $\hat{\xi}$, the correction term is a factor of $O(\delta_B \tilde{\mathcal{F}}^{\frac{1}{2}})$ smaller than the leading-order term so does not alter the leading-order behaviour of the area variation. However, this term is larger than the other higher-order terms, meaning the correction term is more important than the

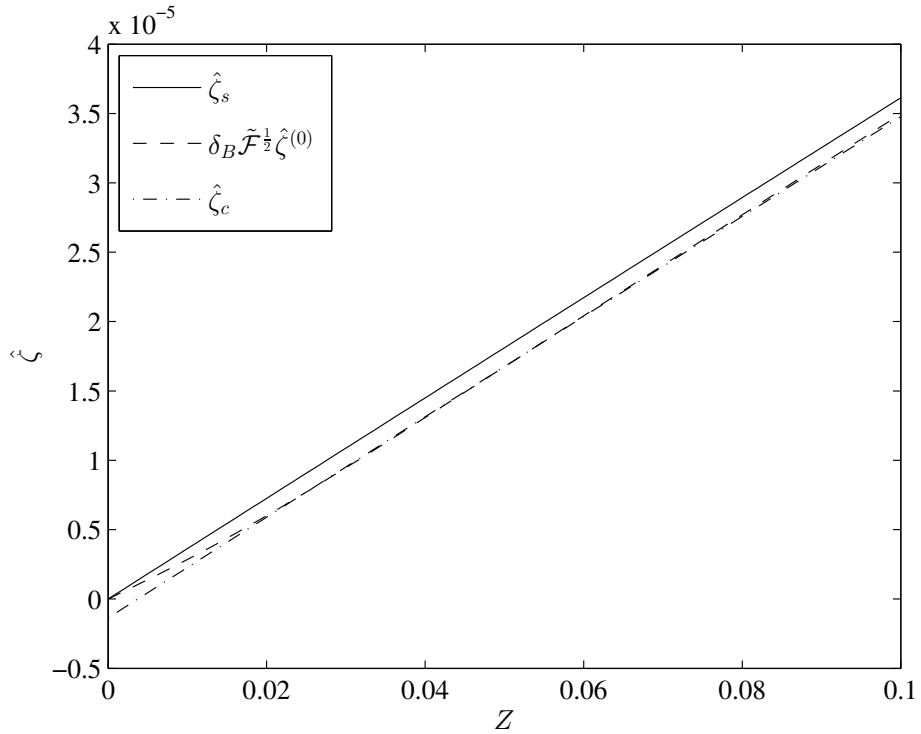


Figure 5.7: The first $n = 1$ modes of the approximations $\hat{\zeta}_s$, $\delta_B \tilde{\mathcal{F}}^{\frac{1}{2}} \hat{\zeta}^{(0)}$, and $\hat{\zeta}_c$, of $\hat{\zeta}$ in the original outer shear layer studied by Whittaker (2015), in the bending layer, and in the corrected outer shear layer, respectively. The approximations $\delta_B \tilde{\mathcal{F}}^{\frac{1}{2}} \hat{\zeta}^{(0)}$ and $\hat{\zeta}_c$ are found in (5.121) and (5.135), and all the approximations are plotted in the case $\sigma_0 = 0.6$, $\delta = 0.001$, $\ell = 10$, $\nu = 0.49$, $\mathcal{F} = 1$, $\tau = 0$ and $B_1(t) = 1$, with $Y_1(\tau)$ normalised such that $Y_1(0) = 1$. In this case $\delta_B = 0.026$.

other higher-order terms. This correction is linear in \check{z} and thus gives a correction to the axial gradient of the area change.

5.14 Corrections to the Bulk-Layer Solution

Now we determine what effect the bending layer has on the bulk solution by considering the behaviour of the deformations (5.133)–(5.135) in the outer shear layer as $\check{z} \rightarrow \infty$. It is first convenient to express \check{z} and Z in terms of some intermediate variable z_m . By considering the typical axial scales in the outer shear layer and bulk solution, we define z_m as

$$\left(\ell \tilde{\mathcal{F}}^{\frac{1}{2}}\right)^{-\beta} Z = z_m = \left(\ell \tilde{\mathcal{F}}^{\frac{1}{2}}\right)^{1-\beta} \check{z}, \quad \text{where } 0 < \beta < 1. \quad (5.137)$$

It is seen that when $z_m = O(1)$, we must have $Z \rightarrow 0$ and $\check{z} \rightarrow \infty$ due to the fact that $\ell \tilde{\mathcal{F}}^{\frac{1}{2}} = O(\delta \ell^2) \ll 1$.

As $\check{z} \rightarrow \infty$ the deformations (5.133)–(5.135) in the outer shear layer become

$$\begin{aligned} \hat{\xi} \sim & \frac{1}{12\bar{B}(1-\nu^2)} \sum_{n=1}^{\infty} B_n(t) \left\{ \frac{1}{\mu_n} \frac{\partial}{\partial \tau} \left(\frac{1}{h} \frac{\partial Y_n}{\partial \tau} \right) \left[\frac{\tilde{\mathcal{F}}^{-\frac{1}{2}}}{\mu_n} - \frac{1}{\ell \tilde{\mathcal{F}}} (\ell \tilde{\mathcal{F}}^{\frac{1}{2}})^{\beta} z_m \right] \right. \\ & \left. + \frac{\delta_B}{\ell \tilde{\mathcal{F}}^{\frac{1}{2}}} \nu^2 \frac{\partial}{\partial \tau} \left[\frac{1}{h} \frac{\partial}{\partial \tau} \left(\frac{Y_n(\tau)}{|\bar{B}|^{\frac{1}{2}}} \right) \right] (\ell \tilde{\mathcal{F}}^{\frac{1}{2}})^{\beta} z_m \right\} \\ & + O\left(\frac{\tilde{\mathcal{F}}^{\frac{1-s}{2}}}{\ell^s} (\ell \tilde{\mathcal{F}}^{\frac{1}{2}})^{s\beta}\right), \end{aligned} \quad (5.138)$$

$$\begin{aligned} \hat{\eta} \sim & \frac{1}{12(1-\nu^2)} \sum_{n=1}^{\infty} B_n(t) \left\{ \frac{1}{\mu_n} \frac{\partial Y_n}{\partial \tau} \left[\frac{\tilde{\mathcal{F}}^{-\frac{1}{2}}}{\mu_n} - \frac{1}{\ell \tilde{\mathcal{F}}} (\ell \tilde{\mathcal{F}}^{\frac{1}{2}})^{\beta} z_m \right] \right. \\ & \left. + \frac{\delta_B}{\ell \tilde{\mathcal{F}}^{\frac{1}{2}}} \nu^2 \frac{\partial}{\partial \tau} \left(\frac{Y_n(\tau)}{|\bar{B}|^{\frac{1}{2}}} \right) (\ell \tilde{\mathcal{F}}^{\frac{1}{2}})^{\beta} z_m \right\} + O\left(\frac{\tilde{\mathcal{F}}^{\frac{1-s}{2}}}{\ell^s} (\ell \tilde{\mathcal{F}}^{\frac{1}{2}})^{s\beta}\right), \end{aligned} \quad (5.139)$$

$$\hat{\zeta} \sim \sum_{n=1}^{\infty} \frac{B_n(t) Y_n(\tau)}{12(1-\nu^2)} \left[\frac{1}{\mu_n} - \delta_B \tilde{\mathcal{F}}^{\frac{1}{2}} \frac{\nu^2}{|\bar{B}|^{\frac{1}{2}}} \right] + O\left(\frac{\tilde{\mathcal{F}}^{\frac{2-s}{2}}}{\ell^s} (\ell \tilde{\mathcal{F}}^{\frac{1}{2}})^{s\beta}\right), \quad (5.140)$$

where we have rewritten \check{z} in terms of the intermediate variable z_m using (5.137), and the integer s is the highest power of z_m that appears at higher orders within the deformations (5.133)–(5.135) in the outer shear layer.

In the approximations (5.138), (5.139) for $\hat{\xi}$, $\hat{\eta}$ as we exit the outer shear layer, we see that the axially linear correction terms in the second lines of the expressions are smaller than the leading-order axially linear terms in the first lines of the expressions. As such the correction terms will affect the bulk solution at a higher order than the leading-order linear terms. As the axially constant terms are $O(\tilde{\mathcal{F}}^{-\frac{1}{2}})$ within (5.138), (5.139), they must match onto terms that have the same size in the bulk layer. However, by noting that $Z = (\ell \tilde{\mathcal{F}}^{\frac{1}{2}})^{\beta} z_m$ in the bulk layer, we see that the linear correction terms, which are $O(\tilde{\mathcal{F}}^{-\frac{1}{2}} \delta_B \ell^{-1} (\ell \tilde{\mathcal{F}}^{\frac{1}{2}})^{\beta})$ in the intermediate region, must instead match onto terms in the bulk solution that are $O(\tilde{\mathcal{F}}^{-\frac{1}{2}} \delta_B \ell^{-1})$. As $\delta_B \ell^{-1} \ll 1$, the terms in the bulk region that match onto the linear correction terms are smaller than the terms that match onto the constant terms. Hence, the bending layer induces corrections to $\hat{\xi}$ and $\hat{\eta}$ in the bulk solution that appear at higher orders than terms matching onto the leading-order axially constant and linear terms in the outer shear layer, seen in (5.133), (5.134). From (5.122) the cross-sectional area variation is dependent only on the normal deformation $\hat{\xi}$. Hence, the bending layer also induces corrections to the area change in the bulk solution that appear at higher orders than terms matching onto the leading-order axially constant

and linear terms in the outer shear layer, seen in (5.136). As these corrections are so small, they are not computed here.

In the approximation (5.140) for $\hat{\zeta}$ as we exit the outer shear layer, there is a leading-order constant term in z_m and a smaller correction term also constant in z_m . Hence the correction term will not affect the leading-order solution in the bulk layer, but instead induce a correction to the bulk solution at a higher order. As determining the correction would require calculating a general solution of $\hat{\zeta}$ in the bulk layer which does not depend on any boundary conditions at the tube ends, we do not calculate the correction to $\hat{\zeta}$ here.

5.15 Conclusions

In this chapter, we have introduced a bending boundary layer to the model in Chapter 2, in regime I_b where $\delta\ell^2 \ll 1$, and the width δ_B of this bending layer lies in between the widths $\tilde{\mathcal{F}}^{\frac{1}{2}}, \tilde{\mathcal{F}}^{-\frac{1}{2}}$ of the inner and outer shear layers found by Whittaker (2015). It is found that the inner shear layer is no longer needed in this scenario. As such, the bending layer is situated at the ends of the elastic-walled tube and matches onto the outer shear layer. In introducing this bending layer, the full clamped boundary conditions (5.44) have been satisfied at the ends of the elastic-walled tube. The effects this bending layer induces on the outer shear layer studied by Whittaker (2015) and the bulk solution modelled in Chapter 2 have also been evaluated.

As in Regime I_a studied in Chapter 4, we have used Kirchhoff–Love shell theory to model the wall mechanics in the bending layer. In doing so, the force-balance equations in the normal, azimuthal and axial directions were derived. It was initially unclear however what matching conditions the deformations should have as we exit the bending layer. To resolve this problem, the system was recast in terms of the in-plane stresses \tilde{N}, \tilde{S} and $\tilde{\Sigma}$. By examining the resulting normal force-balance equation, it was found that the only terms that contribute at leading order are terms that arise from azimuthal and axial stretching mechanisms, and axial bending mechanisms. For these terms to balance, we found that the width δ_B of the bending layer must be $\delta_B = O(\delta^{\frac{1}{2}})$. This does not agree with the estimate (3.48) for the bending-layer width derived in the toy model in §3.6. This is due to the fact that the toy model does not capture the effects of azimuthal and axial stretching, which are found to contribute at leading order in this regime. Although δ_B is different

from the value predicted by the toy model, we still have $\tilde{\mathcal{F}}^{\frac{1}{2}} \ll \delta_B \ll \tilde{\mathcal{F}}^{-\frac{1}{2}}$ and the bending-layer width is still larger than the inner shear layer, and smaller than the outer shear layer, both modelled by Whittaker (2015).

To determine a solution for the system, asymptotic expansions of the stresses \tilde{N} , \tilde{S} and $\tilde{\Sigma}$ within the bending layer were considered. These approximations were solved up to second order and, using these stresses, the normal, azimuthal and axial deformations within the bending layer were derived up to the largest non-zero higher-order term. The normal deformation was then used to derive an expression for the leading-order area change within the bending layer. This area change was determined to be $O(\Delta \tilde{\mathcal{F}}^{\frac{1}{2}} \ell^{-1})$ in the bending layer, and it was also found that as $z_B \rightarrow \infty$, the area variation tends to a constant in z_B .

Using the leading-order deformations in the bending layer, the corrections to the deformations in the outer shear layer have been determined. These corrections have been found to be a factor of $O(\delta_B \tilde{\mathcal{F}}^{\frac{1}{2}})$ smaller than the leading-order terms and as such do not alter the leading-order behaviour of the deformations. However the correction terms are larger than the other higher-order terms by a factor of $O(\tilde{\mathcal{F}}^{\frac{1}{2}} \delta_B^{-1})$ and so these corrections are more important than the other higher-order terms. In the normal and azimuthal deformations, $\hat{\xi}$ and $\hat{\eta}$, these corrections are linear in \hat{z} and so alter the axial gradient of the deformations, whereas in the axial deformation $\hat{\zeta}$ the correction term is constant in \hat{z} and forces a constant shift in the axial direction. Using the expression for $\hat{\xi}$, the correction to the area variation in the outer shear layer has also been calculated. Like in $\hat{\xi}$, the correction does not affect the leading-order behaviour of the area variation. Instead the correction appears at a higher order and alters the axial gradient of the area change at a lower order than any of the other non-zero higher-order terms. If we relax the condition $\mathcal{F} = O(1)$ and instead set $\mathcal{F} = O(\delta^{-3} \ell^{-2})$, these correction terms become large enough to contribute at leading order. However, this also sets $\tilde{\mathcal{F}} \gg 1$, and in this case the shear layer studied by Whittaker (2015) no longer has a significant effect on the bulk solution and does not need to be considered. Further investigation is required to see what happens in the case with $\mathcal{F} = O(\delta^{-3} \ell^{-2})$.

Finally, we have evaluated how the corrections to the deformation in the outer shear layer affect the bulk layer modelled in Chapter 2. In the normal, azimuthal and axial deformations $\hat{\xi}$, $\hat{\eta}$, $\hat{\zeta}$, as well as the cross-sectional area variation $A - A_0$, the corrections in the outer shear layer enforce corrections to

the corresponding variables in the bulk layer that appear at a higher order than terms matching onto the leading-order terms in the outer shear layer.

It is seen here that the bending layer in this regime is passive and does not contribute to the leading-order deformations in the outer and bulk layers. However it allows the axial gradient of the tube wall to decrease to zero as the clamped boundary at $Z = 0$ is reached. This bending layer also allows the stresses \tilde{N} and \tilde{S} to decay from their respective $O(\tilde{\mathcal{F}}^{\frac{1}{2}})$ and $O(\delta_B \tilde{\mathcal{F}}^{\frac{1}{2}})$ values at $Z = 0$ to the $O(\tilde{\mathcal{F}}^{\frac{3}{2}})$ and $O(\tilde{\mathcal{F}})$ values needed in the outer shear layer, while keeping $\tilde{\Sigma}$ approximately constant in Z . The decay of \tilde{N} and the conservation of the size of $\tilde{\Sigma}$ was originally accomplished by the inner shear layer. However, the value of \tilde{S} in the original inner shear layer was the same size as the corresponding value in the outer shear layer. As such, the bending layer has increased the size of this in-plane shear stress near the clamped boundary by a factor of $\delta_B / \tilde{\mathcal{F}}^{\frac{1}{2}}$.

5.A Reformulation in Terms of Stress Variables

To determine a solvable system with a complete set of matching conditions, valid within the bending boundary layer, we consider a change of variables from the deformations $\hat{\zeta}$, $\hat{\eta}$ and $\hat{\xi}$, to the leading-order azimuthal hoop stress \tilde{N} , the leading-order in-plane shear stress \tilde{S} , and the leading-order axial stress $\tilde{\Sigma}$. These stresses are defined in terms of the deformations $\hat{\zeta}$, $\hat{\eta}$ and $\hat{\xi}$ in equations (5.21)–(5.23). This reformulation follows closely the reformulation carried out by Whittaker (2015).

Manipulating (5.21)–(5.23) and applying the clamped boundary conditions (5.44) allows the following expressions for the displacements in terms of the stresses to be found

$$\hat{\zeta}(\tau, z_B, t) = \int_0^{z_B} \frac{\delta_B}{12(1-\nu^2)} (\tilde{\Sigma}(\tau, z', t) - \nu \tilde{N}(\tau, z', t)) \, dz', \quad (5.141)$$

$$\hat{\eta}(\tau, z_B, t) = \int_0^{z_B} \delta_B \left(\frac{h(\tau) \tilde{S}(\tau, z', t)}{6(1-\nu)} - \frac{\partial \hat{\zeta}(\tau, z', t)}{\partial \tau} \right) \, dz', \quad (5.142)$$

$$\hat{\xi}(\tau, z_B, t) = \frac{h(\tau)}{\bar{B}(\tau)} \left(\frac{\nu \tilde{\Sigma}(\tau, z_B, t) - \tilde{N}(\tau, z_B, t)}{12(1-\nu^2)} + \frac{1}{h(\tau)} \frac{\partial}{\partial \tau} \left(\frac{\hat{\eta}(\tau, z_B, t)}{h(\tau)} \right) \right). \quad (5.143)$$

With these expressions, we rewrite the terms within the force-balance equations (5.41)–(5.43) in terms of the stresses. It is found that all the terms in (5.41)–(5.43) may be rewritten using the following expressions and their derivatives

$$\frac{\partial \hat{\zeta}}{\partial z_B} = \frac{\delta_B(\tilde{\Sigma} - \nu \tilde{N})}{12(1-\nu^2)}, \quad (5.144)$$

$$\frac{\partial^2 \hat{\eta}}{\partial z_B^2} = \frac{\delta_B^2 h}{12} \left(\frac{2}{\delta_B(1-\nu)} \frac{\partial \tilde{S}}{\partial z_B} - \frac{1}{h} \frac{\partial}{\partial \tau} \left(\frac{\tilde{\Sigma} - \nu \tilde{N}}{1-\nu^2} \right) \right), \quad (5.145)$$

$$\begin{aligned} \frac{\partial^2 \hat{\xi}}{\partial z_B^2} = & \frac{\delta_B^2 h}{12 \bar{B}} \left(-\frac{1}{\delta_B^2} \frac{\partial^2}{\partial z_B^2} \left(\frac{\tilde{N} - \nu \tilde{\Sigma}}{1-\nu^2} \right) \right. \\ & \left. + \frac{1}{h} \frac{\partial}{\partial \tau} \left(\frac{2}{\delta_B(1-\nu)} \frac{\partial \tilde{S}}{\partial z_B} - \frac{1}{h} \frac{\partial}{\partial \tau} \left(\frac{\tilde{\Sigma} - \nu \tilde{N}}{1-\nu^2} \right) \right) \right), \end{aligned} \quad (5.146)$$

$$-\frac{\bar{B} \hat{\xi}}{h} + \frac{1}{h} \frac{\partial}{\partial \tau} \left(\frac{\hat{\eta}}{h} \right) = \frac{\tilde{N} - \nu \tilde{\Sigma}}{12(1-\nu^2)}. \quad (5.147)$$

Substituting these expressions and their derivatives into (5.41)–(5.43), we find

the governing force-balance equations in terms of the stresses to be

$$0 = \tilde{N}\bar{B} - \frac{\delta^2}{\delta_B^2} \frac{1}{12\bar{B}} \left[-\frac{1}{\delta_B^2} \frac{\partial^4}{\partial z_B^4} \left(\frac{\tilde{N} - \nu\tilde{\Sigma}}{1 - \nu^2} \right) + \frac{12}{\delta_B^2 h} \frac{\partial^3}{\partial \tau \partial z_B^2} \left(\frac{1}{h} \frac{\partial^2 \hat{\eta}}{\partial z_B^2} \right) \right] \\ + \frac{\tilde{\mathcal{F}}(1 - \nu^2)h}{\bar{B}} \left[-\frac{1}{\delta_B^2} \frac{\partial^2}{\partial z_B^2} \left(\frac{\tilde{N} - \nu\tilde{\Sigma}}{1 - \nu^2} \right) + \frac{12}{\delta_B^2 h} \frac{\partial}{\partial \tau} \left(\frac{1}{h} \frac{\partial^2 \hat{\eta}}{\partial z_B^2} \right) \right] \\ + \delta^2 \ell p_{\text{tm}} + O \left(\frac{\delta^2}{\delta_B^2} \tilde{N}, \frac{\delta^2}{\delta_B} \tilde{S}, \frac{\delta^2}{\delta_B^2} \tilde{\Sigma} \right), \quad (5.148)$$

$$0 = \frac{1}{h} \frac{\partial \tilde{N}}{\partial \tau} + \frac{1}{\delta_B} \frac{\partial \tilde{S}}{\partial z_B} \\ - \delta^2 \frac{(1 + \nu)\bar{B}}{24h} \frac{\partial}{\partial \tau} \left[\frac{1}{\bar{B}} \left[-\frac{1}{\delta_B^2} \frac{\partial^2}{\partial z_B^2} \left(\frac{\tilde{N} - \nu\tilde{\Sigma}}{1 - \nu^2} \right) + \frac{12}{\delta_B^2 h} \frac{\partial}{\partial \tau} \left(\frac{1}{h} \frac{\partial^2 \hat{\eta}}{\partial z_B^2} \right) \right] \right] \\ + O \left(\delta^2 \left(\frac{1}{\delta_B}, \ell^2 \right) \tilde{N}, \frac{\delta^2 \ell^2}{\delta_B} \tilde{S}, \delta^2 \left(\frac{1}{\delta_B}, \ell^2 \right) \tilde{\Sigma} \right), \quad (5.149)$$

$$0 = \frac{\partial \tilde{\Sigma}}{\partial z_B} + \frac{\delta_B}{h} \frac{\partial \tilde{S}}{\partial \tau} - \frac{\delta^2}{12\delta_B^2} \frac{\partial^3}{\partial z_B^3} \left(\frac{\tilde{N} - \nu\tilde{\Sigma}}{1 - \nu^2} \right) + \frac{\delta^2}{\delta_B^2 h} \frac{\partial^2}{\partial \tau \partial z_B} \left(\frac{1}{h} \frac{\partial^2 \hat{\eta}}{\partial z_B^2} \right) \\ + O \left(\frac{\delta^2 \ell^2}{\delta_B} \tilde{N}, \delta^2 \ell^2 \tilde{S}, \frac{\delta^2 \ell^2}{\delta_B} \tilde{\Sigma} \right), \quad (5.150)$$

where $\partial^2 \hat{\eta} / \partial z_B^2$ is given in terms of the stresses by (5.145).

The clamped boundary conditions (5.44) are now converted into conditions on the stresses. From the expressions (5.141) and (5.142) for the deformations $\hat{\zeta}$ and $\hat{\eta}$, we see that when $z_B = 0$, $\hat{\eta} = \hat{\zeta} = 0$ automatically. Using (5.143), it can then be shown that for the remaining clamped boundary conditions ($\hat{\zeta} = \partial \hat{\zeta} / \partial z_B = 0$ at $z_B = 0$) to be satisfied, we must have

$$\tilde{N} - \nu\tilde{\Sigma} = 0, \quad \text{and} \quad \frac{\partial \tilde{N}}{\partial z_B} - \nu \frac{\partial \tilde{\Sigma}}{\partial z_B} - \frac{2(1 + \nu)\delta_B}{h} \frac{\partial \tilde{S}}{\partial \tau} = 0, \quad \text{at } z_B = 0. \quad (5.151)$$

5.B Limit of a Circular Cross-Section ($\sigma_0 \rightarrow \infty$)

Here, we determine the leading-order stresses and deformations in the bending layer in the limit where the undeformed tube has a circular cross-section as opposed to an elliptical cross-section. We first use Fourier series in the azimuthal coordinate τ to obtain solutions for stresses \tilde{N} , \tilde{S} , $\tilde{\Sigma}$, that satisfy (5.45)–(5.54) at leading order. These stresses are then used to determine the deformations $\hat{\xi}$, $\hat{\eta}$ and $\hat{\zeta}$ at leading order in the circular limit.

5.B.1 Governing Equations as ($\sigma_0 \rightarrow \infty$)

As $\sigma_0 \rightarrow \infty$ and the undeformed cross-section of the tube becomes circular, we have from (5.2), (5.3) and (5.11) that

$$c \sim 2e^{-\sigma_0}, \quad h(\tau) \rightarrow 1, \quad \bar{B} \rightarrow -1. \quad (5.152)$$

Whittaker (2015) also found that as $\sigma_0 \rightarrow \infty$, the functions $Y_n(\tau)$ seen in the matching conditions (5.52)–(5.54) are given by

$$Y_n(\tau) \rightarrow \cos(2n\tau). \quad (5.153)$$

Substituting these approximations, as well as the sizes (5.58), (5.59) of \tilde{N} , \tilde{S} and $\tilde{\Sigma}$ into the force-balance equations (5.45)–(5.47), we find the leading-order force-balance equations as $\sigma_0 \rightarrow \infty$ to be

$$\tilde{N} + \frac{\delta^2}{\delta_B^4} \frac{1}{12(1-\nu^2)} \frac{\partial^4}{\partial z_B^4} (\tilde{N} - \nu \tilde{\Sigma}) = 0, \quad (5.154)$$

$$\frac{\partial \tilde{N}}{\partial \tau} + \frac{1}{\delta_B} \frac{\partial \tilde{S}}{\partial z_B} = 0, \quad (5.155)$$

$$\frac{\partial \tilde{\Sigma}}{\partial z_B} = 0. \quad (5.156)$$

As seen in §5.8, we need $\delta_B = O(\delta^{\frac{1}{2}})$ for the axial-bending term in (5.154) to balance the first term in the equation. We set

$$\delta_B = \frac{\sqrt{2}\delta^{\frac{1}{2}}}{(12(1-\nu^2))^{\frac{1}{4}}}, \quad (5.157)$$

where the factor of $\sqrt{2}(12(1-\nu^2))^{-\frac{1}{4}}$ has been included to simplify the following analysis.

5.B.2 Fourier Representation

We see that (5.154)–(5.156) have no explicit dependence on τ . We also note that these equations are linear and so we expect to find solutions that are sinusoidal in τ . Whittaker *et al.* (2010d) found that in the bulk layer, the deformations $\hat{\xi}$, $\hat{\eta}$ and $\hat{\zeta}$ are periodic over π , and $\hat{\eta}$ is odd in τ , whereas $\hat{\xi}$ and $\hat{\zeta}$ are even in τ . So the deformations in the outer shear layer could match onto these bulk layer deformations, Whittaker (2015) only considered outer shear layer deformations with these same properties. Similarly, here we will only consider deformations in the bending layer with these properties so that they may match onto the deformations in the outer shear layer. By considering these properties and the expressions (5.21)–(5.23) for the stresses \tilde{N} , \tilde{S} and $\tilde{\Sigma}$ in terms of the deformations, it is found that the stresses are also all periodic over π , and \tilde{S} is odd in τ , whereas \tilde{N} and $\tilde{\Sigma}$ are even in τ . We therefore look for solutions of the form

$$\tilde{N} = \sum_{n=0}^{\infty} \alpha_n(z_B) \cos(2n\tau), \quad \tilde{S} = \sum_{n=0}^{\infty} \beta_n(z_B) \sin(2n\tau), \quad \tilde{\Sigma} = \sum_{n=0}^{\infty} \gamma_n(z_B) \cos(2n\tau). \quad (5.158)$$

Substituting (5.158) into (5.154)–(5.156), we find that the different Fourier modes decouple, and for each mode n we have

$$\alpha_n'''' + 4\alpha_n - \nu\gamma_n'''' = 0, \quad (5.159)$$

$$-2n\alpha_n + \frac{1}{\delta_B} \beta_n' = 0, \quad (5.160)$$

$$\gamma_n' = 0, \quad (5.161)$$

where ' denotes a derivative with respect to z_B . We also substitute (5.158) into the boundary conditions (5.48), (5.49) to obtain the following, leading-order conditions at $z_B = 0$

$$\alpha_n - \nu\gamma_n = 0 \quad \text{and} \quad \alpha_n' - \nu\gamma_n' = 0 \quad \text{at} \quad z_B = 0. \quad (5.162)$$

It is noted that in the condition (5.49), the $\partial\tilde{S}/\partial\tau$ term is a factor of δ_B^2 smaller than the other terms in the condition (due to the sizes (5.58), (5.59) of the stresses), and has been neglected in the leading-order condition here.

Finally, we determine the leading-order matching conditions for α_n , β_n and γ_n . By comparing the size (5.58) of $\tilde{\Sigma}$ in the bending layer to the size of the leading-order term in the matching condition (5.54) for $\tilde{\Sigma}$, it is seen that these sizes are the same and the matching condition (5.54) may be used here.

Substituting the approximations (5.152), (5.153) and the Fourier series (5.158) for $\tilde{\Sigma}$ into (5.54), we find the following leading-order condition for γ_n as $z_B \rightarrow \infty$

$$\gamma_n \sim \tilde{\mathcal{F}}^{\frac{1}{2}} B_n(t) \quad \text{for } n \geq 1, \quad (5.163)$$

where all the higher-order terms within (5.54) have been neglected here. We note that when $n = 0$, we obtain the matching condition $\gamma_0 \sim 0$ as $z_B \rightarrow \infty$. It is found that this condition combined with the rest of the system sets $\alpha_0 = \beta_0 = \gamma_0 = 0$. As such, we now only consider the scenario $n \geq 1$.

Unlike $\tilde{\Sigma}$, the sizes (5.59) of \tilde{N} and \tilde{S} are larger than the sizes of the leading-order terms in their corresponding matching conditions (5.52) and (5.53). As such, the leading-order \tilde{N} and \tilde{S} must tend to zero as $z_B \rightarrow \infty$. Hence, we have the following leading-order matching conditions for α_n, β_n

$$\alpha_n, \beta_n \rightarrow 0 \quad \text{as } z_B \rightarrow \infty. \quad (5.164)$$

5.B.3 General Solution

We proceed to find the solution of the system (5.159)–(5.164), starting with the general solutions of $\alpha_n(z_B)$, $\beta_n(z_B)$ and $\gamma_n(z_B)$. First, by integrating (5.161), we find

$$\gamma_n = C_{1n}, \quad (5.165)$$

where C_{1n} is a constant to be found. Substituting this into (5.159) gives the following ODE for α_n

$$\alpha_n'''' + 4\alpha_n = 0, \quad (5.166)$$

which has the general solution

$$\alpha_n = [C_{2n} \cos(z_B) + C_{3n} \sin(z_B)] e^{-z_B} + [C_{4n} \cos(z_B) + C_{5n} \sin(z_B)] e^{z_B}, \quad (5.167)$$

where C_{2n} – C_{5n} are constants to be found. Finally, by substituting (5.167) into (5.160), an ODE for β_n is obtained. Solving this ODE, the general solution of β_n is found to be

$$\begin{aligned} \beta_n = C_{6n} + n\delta_B & \{ [-(C_{2n} + C_{3n}) \cos(z_B) + (C_{2n} - C_{3n}) \sin(z_B)] e^{-z_B} \\ & + [(C_{4n} - C_{5n}) \cos(z_B) + (C_{4n} + C_{5n}) \sin(z_B)] e^{z_B} \}, \end{aligned} \quad (5.168)$$

where C_{6n} is a constant to be found.

5.B.4 Applying Boundary and Matching Conditions

We now apply the boundary conditions (5.162) and matching conditions (5.163), (5.164) to the solutions (5.165), (5.167), (5.168) for γ_n , α_n , β_n . Applying the matching conditions (5.163) and (5.164) to (5.165), (5.167) and (5.168) allows us to find

$$C_{1n} = \tilde{\mathcal{F}}^{\frac{1}{2}} B_n(t), \quad C_{4n} = C_{5n} = C_{6n} = 0. \quad (5.169)$$

Substituting (5.165) and (5.167) into the clamped boundary conditions (5.162) then yields

$$C_{2n} = C_{3n} = \nu \tilde{\mathcal{F}}^{\frac{1}{2}} B_n(t). \quad (5.170)$$

5.B.5 Full Solution of the Modes

We now substitute (5.169) and (5.170) into the expressions (5.165), (5.167) and (5.168) for γ_n , α_n and β_n . Doing so, we find the full, leading-order solutions of α_n , β_n , γ_n to be

$$\alpha_n(z_B) = \nu \tilde{\mathcal{F}}^{\frac{1}{2}} B_n(t) [\cos(z_B) + \sin(z_B)] e^{-z_B}, \quad (5.171)$$

$$\beta_n(z_B) = -2n\delta_B \nu \tilde{\mathcal{F}}^{\frac{1}{2}} B_n(t) \cos(z_B) e^{-z_B}, \quad (5.172)$$

$$\gamma_n(z_B) = \tilde{\mathcal{F}}^{\frac{1}{2}} B_n(t). \quad (5.173)$$

The first $n = 1$ modes of these Fourier coefficients have been plotted in Figure 5.8, in the case $\delta = 0.001$, $\ell = 10$, $\nu = 0.49$ and $B_n(t) = 1$. From the figure, it is seen that the leading-order coefficients α_1 and β_1 , which relate to the azimuthal hoop stress \tilde{N} and in-plane shear stress \tilde{S} , both decay to zero as $z_B \rightarrow \infty$. This reduction in size is particularly apparent for α_1 . However, the leading-order coefficient γ_1 , which relates to the axial stress $\tilde{\Sigma}$, is seen to remain constant within the bending layer.

Using (5.171)–(5.173), we may calculate and substitute the leading-order stresses \tilde{N} , \tilde{S} , $\tilde{\Sigma}$ into the expressions (5.141)–(5.143) in Appendix 5.A to find the leading-order values of the deformations $\hat{\xi}$, $\hat{\eta}$ and $\hat{\zeta}$ in the circular limit.

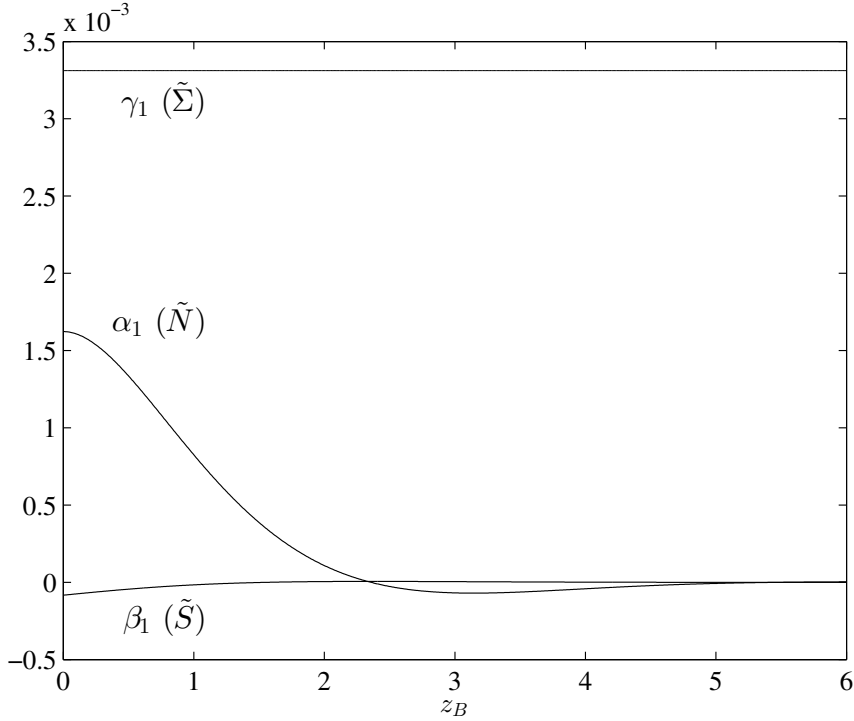


Figure 5.8: The leading-order solutions (5.171)–(5.173) for the first $n = 1$ Fourier coefficients α_1 , β_1 , γ_1 in the expansions (5.158) for the stresses \tilde{N} , \tilde{S} , $\tilde{\Sigma}$, in the case $\delta = 0.001$, $\ell = 10$, $\nu = 0.49$. These coefficients have been normalised such that $B_1(t) = 1$.

Doing so, the leading-order deformations are found to be

$$\hat{\xi} = \sum_{n=1}^{\infty} \frac{\nu \tilde{\mathcal{F}}^{\frac{1}{2}} B_n(t) \cos(2n\tau)}{12(1-\nu^2)} [(\cos(z_B) + \sin(z_B)) e^{-z_B} - 1], \quad (5.174)$$

$$\begin{aligned} \hat{\eta} = \sum_{n=1}^{\infty} \frac{\delta_B^2 \tilde{\mathcal{F}}^{\frac{1}{2}} n B_n(t) \sin(2n\tau)}{12(1-\nu^2)} & \left\{ \nu(\nu+2) [(\cos(z_B) - \sin(z_B)) e^{-z_B} - 1] \right. \\ & \left. + z_B^2 - 2\nu^2 z_B \right\}, \end{aligned} \quad (5.175)$$

$$\hat{\zeta} = \sum_{n=1}^{\infty} \frac{\delta_B \tilde{\mathcal{F}}^{\frac{1}{2}} B_n(t) \cos(2n\tau)}{12(1-\nu^2)} [z_B + \nu^2 (\cos(z_B) e^{-z_B} - 1)]. \quad (5.176)$$

The axial behaviour of these leading-order deformations for the first $n = 1$ mode has been plotted in Figure 5.9, in the case $\delta = 0.001$, $\ell = 10$, $\nu = 0.49$ and $B_n(t) = 1$. In the plots, we have also set $\tau = 0$ in $\hat{\xi}$, $\hat{\zeta}$, and $\tau = \pi/4$ in $\hat{\eta}$, to ensure these deformations demonstrate their maximum amplitude in the τ coordinate. From the figure, it is seen that all the leading-order deformations and the leading-order axial gradient $\partial \hat{\zeta} / \partial z_B$ take the value of zero at $z_B = 0$,

and the full clamped boundary conditions (5.44) are satisfied at leading order. As $z_B \rightarrow \infty$, the sizes of all the deformations increase to different values. It is also seen that $\hat{\xi}$, $\hat{\eta}$ and $\hat{\zeta}$ behave as a constant, quadratically and linearly respectively, in the axial direction when $z_B \rightarrow \infty$.

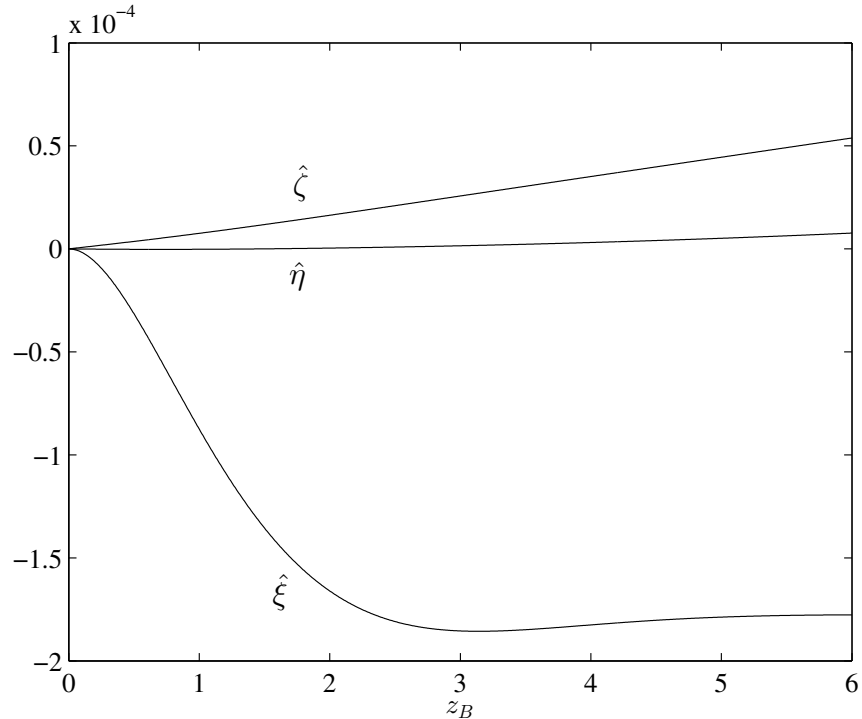


Figure 5.9: The leading-order axial behaviour of the solutions (5.174)–(5.176) for the first $n = 1$ mode of the deformations $\hat{\xi}$, $\hat{\eta}$, $\hat{\zeta}$, in the case $\delta = 0.001$, $\ell = 10$, $\nu = 0.49$. These deformations have been normalised such that $B_1(t) = 1$, and we have set $\tau = 0$ in $\hat{\xi}$, $\hat{\zeta}$, and $\tau = \pi/4$ in $\hat{\eta}$.

Chapter 6

The Boundary Layer in Regime II $(\delta\ell \gg 1)$

6.1 Introduction

In this chapter, another regime of the general problem described in Chapter 3, where a boundary layer is introduced to the model derived in Chapter 2 describing flow through an elastic-walled tube, is considered. This boundary layer will allow the canonical clamped boundary conditions to be satisfied at the ends of the elastic-walled tube, where it is clamped onto two fixed rigid tubes.

The regime considered here is regime II, where the dimensionless tube wall thickness $\delta \ll 1$ and tube length $\ell \gg 1$ are set so that $\delta\ell \gg 1$. Unlike in regimes I_a and I_b considered in Chapters 4 and 5, the shear-relaxation layer studied by Whittaker (2015) does not have a significant effect on the solution in the bulk of the tube and does not need to be considered here. In the toy model in §3.6, it was estimated that an axial-bending boundary layer would have dimensionless width $\delta_B = O(\ell^{-1})$. Hence, in this regime it is expected that $\delta_B \ll \delta$, and the boundary-layer width is smaller than the thickness of the tube wall. As the tube wall thickness is no longer the smallest geometric parameter, the Kirchhoff–Love shell equations (Flügge, 1972; Søndergaard, 2007) can no longer be used to model the mechanics of the tube wall and a new model must be derived.

As it is expected that $\delta_B \ll \delta$, the transmural pressure will not have an effect at leading-order in the boundary layer. This is because terms from other mechanisms such as axial bending and pre-stress and axial curvature will grow

to be larger than the transmural pressure in the boundary layer. Also, since the axial scale $a\delta_B$ is much smaller than the azimuthal scale a , we expect to be able to neglect the effects of azimuthal variation when studying the boundary layer. As such, it is possible that the wall mechanics can be modelled using a 2D model in the normal and axial directions only. We consider modelling a cross section of the tube wall in the normal and axial directions near the interfaces between the elastic and rigid-walled tubes, as seen in Figure 6.1. In the boundary layer, the tube wall must transition from being clamped horizontally at the rigid wall, to being bent at an angle in order to match on to the bulk solution. Since the wall is thin, it cannot sustain large transverse forces. The large axial tension force F must therefore be aligned with the angle of the wall in the far-field, as shown in Figure 6.1.

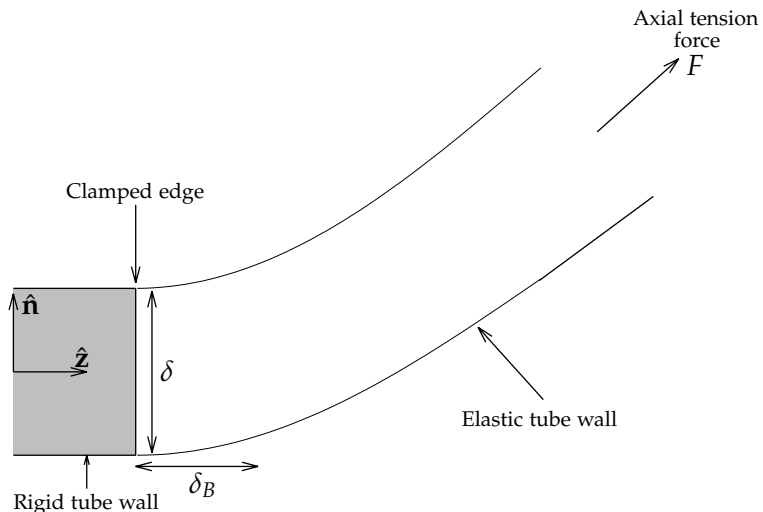


Figure 6.1: Two-dimensional cross section of the tube wall in the normal and axial directions near the clamped edge.

This scenario is equivalent to a 2D semi-infinite block that is clamped along its short edge and bent by applying a large axial tension. In this chapter, we concentrate on deriving and solving a model for this scenario. As the original tube wall is subject only to small amplitude deformations, the deformations considered in this model will also be small, allowing us to linearise the problem. However, this model must also include the effect of the large pre-stress, which will add additional terms relating to rotations of the pre-stress as the block deforms.

By deriving and solving this model, it is found that in the case $\delta\ell \ll 1$,

we obtain an axial-bending boundary layer with the same size width as that predicted by the toy model in §3.6. This magnitude of the bending layer is also in agreement with the size of the bending layer in regime I_a considered in Chapter 4. However, in the regime we are considering here, $\delta\ell \gg 1$, a different boundary layer with a much larger width is found. This boundary layer is found to be a transverse shear-relaxation layer (different from the shear layer modelled by Whittaker (2015)), instead of the expected bending layer.

This chapter is organised as follows. In §6.2, the mathematical set-up of the semi-infinite block under tension is provided, along with its deformations, necessary tensors, governing equation and boundary conditions. In §6.3, a linearised constitutive law is derived for the Cauchy stress tensor σ of the block, and in §6.4, the linearised governing equation and boundary conditions for the problem are derived. §6.5 focuses on rewriting the governing system in a form that can be solved numerically by the numerical finite-element differential equation solver "FEniCS" (Dupont *et al.*, 2003), and in §6.6 an analytic solution in terms of normal modes is sought. Although progress has been made in finding an analytic solution, it has not been possible to determine the amplitudes of the modes explicitly. Even though these amplitudes have not yet been found, it is possible that a modification of a method used by Shankar (2003) could be used to determine these amplitudes.

In §6.7 approximations for the deformations in the far-field are derived, and in §6.8 these approximations are compared with the numerical solutions of the problem found using FEniCS. The effect that varying the axial tension imposed on the block has on the deformations is evaluated in §6.9. This 2D model is then applied to the elastic-walled tube in §6.10 and the corrections to the boundary conditions on the bulk layer modelled in Chapter 2 are calculated. Finally, in §6.11, a physical interpretation of the boundary layers that arise in the cases $\delta\ell \ll 1$ and $\delta\ell \gg 1$ is provided.

6.2 Mathematical Set-Up

6.2.1 Set-Up of the Semi-Infinite Block

A two-dimensional scenario as seen in Figure 6.2 is considered. Here we have an almost incompressible, semi-infinite block of dimensional thickness d , and we set dimensional Eulerian coordinates in the normal and semi-infinite (axial) direction to be x_1 and x_2 respectively. These coordinates are encapsulated in

the vector representation $\mathbf{x} = (x_1, x_2)$. The block initially occupies the region $x_1 \in [0, d], x_2 \in [0, \infty)$ and is subject to a large dimensional axial tension of size \mathbb{F} . For convenience, the coordinates have been set so that x_2 is aligned with the far-field axial tension \mathbb{F} , even after the block undergoes the deformations considered here. Hence, the deformations are induced by changing the angle of the clamped boundary at $x_2 = 0$ instead of changing the angle of \mathbb{F} . The boundaries of the block are denoted $\gamma_1, \gamma_2, \gamma_3$ and γ_4 , where

- γ_1 is initially at $0 \leq x_1 \leq d, x_2 = 0$,
- γ_2 is initially at $x_1 = 0, 0 \leq x_2$,
- γ_3 is initially at $0 \leq x_1 \leq d, x_2 \rightarrow \infty$,
- γ_4 is initially at $x_1 = d, 0 \leq x_2$.

This block is set to have Lamé's first parameter λ and Lamé's second parameter μ . From these, the incremental Young's modulus E , Poisson's ratio ν and bending stiffness K can be derived.

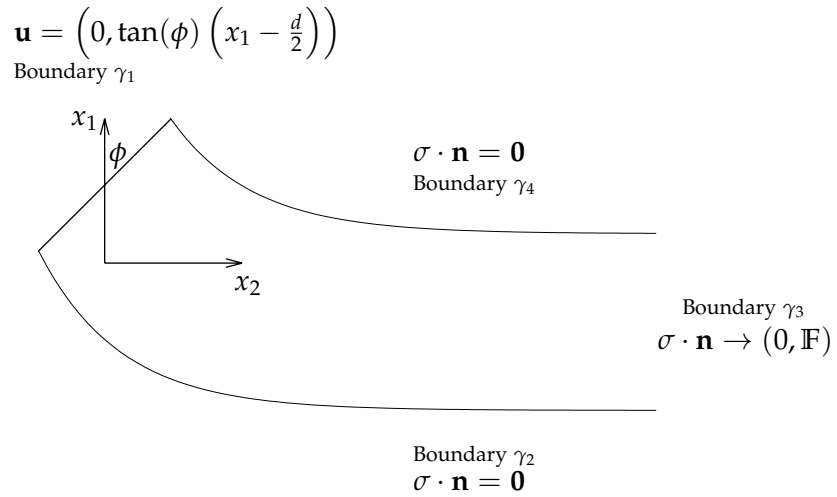


Figure 6.2: The set-up of the semi-infinite block subject to the deformation \mathbf{u} and axial tension \mathbb{F} .

In order to relate this semi-infinite block to the elastic-walled tube modelled in Chapters 2–5, we set the axial tension \mathbb{F} to have the same value as the pre-stress in the elastic-walled tube. That is

$$\mathbb{F} = \frac{K\ell^2}{a^3\delta} \mathcal{F}, \quad (6.1)$$

where a is the typical radial scale of the tube, $\ell \gg 1$ is the dimensionless length of the tube, $\delta = d/a \ll 1$ is the dimensionless thickness of the tube wall, and $\mathcal{F} = O(1)$ is the dimensionless axial tension of the tube.

A small amplitude deformation

$$\mathbf{u} = \begin{pmatrix} u_1 \\ u_2 \end{pmatrix},$$

is induced on the block by clamping boundary γ_1 (initially at $0 \leq x_1 \leq d$, $x_2 = 0$) at an angle ϕ to the x_1 -axis. We have stress-free boundary conditions on boundaries γ_2 and γ_4 (initially at $x_1 = 0, d$, $x_2 \geq 0$) and no change to the pre-stress \mathbb{F} on boundary γ_3 (initially at $0 \leq x_1 \leq d$, $x_2 \rightarrow \infty$). The boundaries and their associated conditions may be seen in Figure 6.2. Owing to the symmetry of the boundary conditions and the form of the linearised elastic model which we derive in §6.3–§6.4, the component u_1 of \mathbf{u} in the x_1 -direction is found to be symmetric about $x_1 = d/2$, and the component u_2 of \mathbf{u} in the x_2 -direction is found to be antisymmetric about $x_1 = d/2$. Since the deformation is assumed to be small, we will later linearise the problem back to the domain $0 \leq x_1 \leq d$, $0 \leq x_2$.

6.2.2 Lagrangian Representation of the System

The corresponding Lagrangian coordinates of this system are denoted $\mathbf{X} = (X_1, X_2)$, where X_1 , X_2 represent Lagrangian coordinates in the normal and axial directions of the block respectively. Using this coordinate system, we define the applied deformation on the block in the Lagrangian coordinate system as \mathbf{U} , where

$$\mathbf{U} = \begin{pmatrix} U_1 \\ U_2 \end{pmatrix},$$

and U_i is the component of the deformation in the X_i -direction. Howell *et al.* (2009) show that the Eulerian coordinates \mathbf{x} may be expressed in terms of the Lagrangian coordinates \mathbf{X} as follows

$$\delta\mathbf{x} = \delta\mathbf{X} + (\delta\mathbf{X} \cdot \nabla)\mathbf{U}(\mathbf{X}) + \dots, \quad (6.2)$$

where, in two dimensions

$$(\delta\mathbf{X} \cdot \nabla) = \delta X_1 \frac{\partial}{\partial X_1} + \delta X_2 \frac{\partial}{\partial X_2}. \quad (6.3)$$

6.2.3 Tensor Notation

The various tensors that are needed to derive a suitable model for this problem are now defined. Firstly, the strain tensor \mathcal{E} is defined as

$$\mathcal{E}_{ij} = \frac{1}{2} \left(\frac{\partial u_i}{\partial X_j} + \frac{\partial u_j}{\partial X_i} + \sum_{k=1}^2 \frac{\partial u_k}{\partial X_i} \frac{\partial u_k}{\partial X_j} \right). \quad (6.4)$$

Next, we define the deformation gradient tensor \mathcal{G} to be

$$\mathcal{G}_{ij} = \frac{\partial x_i}{\partial X_j}, \quad (6.5)$$

and let σ be the Cauchy stress tensor of the block. Finally we introduce the second Piola–Kirchhoff stress tensor \mathcal{S} of the block, which is related to the Cauchy stress tensor σ by

$$\mathcal{S} = \det(\mathcal{G}) \mathcal{G}^{-1} \sigma \left(\mathcal{G}^T \right)^{-1}. \quad (6.6)$$

Rearranging (6.6), it is seen that

$$\sigma = \frac{\mathcal{G} \mathcal{S} \mathcal{G}^T}{\det(\mathcal{G})}, \quad (6.7)$$

and we will later use this expression to derive an appropriate constitutive law for σ .

6.2.4 Governing Equation and Boundary Conditions

To model the mechanics within the block, we use the static version of Cauchy's momentum equation in absence of external forces (Howell *et al.*, 2009, p. 10) given by

$$\nabla \cdot \sigma = \mathbf{0}. \quad (6.8)$$

In terms of σ , the boundary conditions may be written as follows

$$\begin{aligned} \mathbf{u} = \begin{pmatrix} 0 \\ \tan(\phi) \left(x_1 - \frac{d}{2} \right) \end{pmatrix} \quad &\text{on } \gamma_1, \quad \sigma \cdot \mathbf{n} \rightarrow \begin{pmatrix} 0 \\ \mathbf{F} \end{pmatrix} \quad \text{on } \gamma_3, \\ \sigma \cdot \mathbf{n} = \mathbf{0} \quad &\text{on } \gamma_2, \gamma_4, \end{aligned} \quad (6.9)$$

where \mathbf{n} is the outward unit normal to the block. We note that the factor of $-d/2$ in the condition on boundary γ_1 forces the shift in the x_2 -direction to be antisymmetric about the centre of the block. It is also noted that as this system is going to be converted into a linear problem, the choice of the (small) angle ϕ of clamping only alters the amplitude of the deformations.

6.3 Constitutive Law for σ

Before we can derive solutions for the system (6.8)–(6.9), we must determine a constitutive law for σ . In this constitutive law, we must include the pre-stress \mathbb{F} applied to the block and create a linear model for small deformations to the pre-stressed state. The naive option of simply adding a pre-stress to the constitutive law for an isotropic linearly elastic solid fails as this does not take into account rotations in the tension as the material deforms. In particular for an $O(\epsilon)$ deformation, the interactions between the $O(1)$ tension and $O(\epsilon)$ rotations of the material will be $O(\epsilon)$ and should be included in a linear model. However, these interactions would be omitted from a model derived in the above way.

6.3.1 A Modified Saint Venant–Kirchhoff Model

Instead we consider using a different model applicable to hyperelastic materials, where a material is deemed to be hyperelastic if its stress-strain relationship is dependent on some strain energy density function which is different for each material. The model in question is the nonlinear Saint Venant–Kirchhoff model (Howell *et al.*, 2009, p. 230) for hyperelastic materials, which gives the second Piola–Kirchhoff stress tensor \mathcal{S} as

$$\mathcal{S} = \lambda \text{Tr}(\mathcal{E}) I + 2\mu \mathcal{E}, \quad (6.10)$$

where I is the identity matrix.

In its current form, the Saint Venant–Kirchhoff model (6.10) does not include the effects of the pre-stress \mathbb{F} . However, we may easily modify this model to obtain an appropriate constitutive law for \mathcal{S} that includes the effects of the pre-stress in the following way

$$\mathcal{S} = \mathcal{S}_0 + \lambda \text{Tr}(\mathcal{E}) I + 2\mu \mathcal{E}, \quad (6.11)$$

where

$$\mathcal{S}_0 = \begin{pmatrix} 0 & 0 \\ 0 & \mathbb{F} \end{pmatrix}.$$

6.3.2 Approximations for \mathcal{G} , \mathcal{G}^T and $\det(\mathcal{G})^{-1}$

By examining the relationship (6.7), it can be seen that the constitutive law (6.11) for \mathcal{S} can be used to derive an appropriate constitutive law for σ . However, it is

observed that applicable expressions are also needed for \mathcal{G} , \mathcal{G}^T and $\det(\mathcal{G})^{-1}$ to derive an expression for σ . Approximations for these terms are now derived.

Firstly, applying the relation (6.2) between the Eulerian coordinates \mathbf{x} and the Lagrangian coordinates \mathbf{X} to the expression (6.5) for \mathcal{G}_{ij} , the following approximation is obtained

$$\mathcal{G}_{ij} = \frac{\partial x_i}{\partial X_j} = \frac{\delta x_i}{\delta X_j} \approx \delta_{ij} + \frac{\partial U_i}{\partial X_j}, \quad (6.12)$$

where δ_{ij} is the Kronecker delta. Using this approximation, it is seen that \mathcal{G}^T may be approximated by

$$\mathcal{G}_{ij}^T \approx \delta_{ij} + \frac{\partial U_j}{\partial X_i}. \quad (6.13)$$

The determinant $\det(\mathcal{G})$ may be calculated by using the following definition for the determinant of a 3×3 matrix in index notation

$$\det(\mathcal{G}) = \epsilon_{ijk} \mathcal{G}_{i1} \mathcal{G}_{j2} \mathcal{G}_{k3}, \quad (6.14)$$

where the permutation symbol ϵ_{ijk} is given by

$$\epsilon_{ijk} = \begin{cases} 1 & i, j, k = 1, 2, 3 \quad 2, 3, 1 \quad \text{or} \quad 3, 1, 2 \\ -1 & i, j, k = 3, 2, 1 \quad 2, 1, 3 \quad \text{or} \quad 1, 3, 2 \\ 0 & \text{otherwise} \end{cases}. \quad (6.15)$$

Substituting the approximation (6.12) of \mathcal{G} into (6.14), noting that $\mathcal{G}_{33} = 1$ and $\mathcal{G}_{i3} = \mathcal{G}_{3i} = 0$ for $i \neq 3$ as we are considering a two-dimensional problem, we find

$$\det(\mathcal{G}) \approx 1 + \frac{\partial U_1}{\partial X_1} + \frac{\partial U_2}{\partial X_2} + O(\mathbf{U}^2). \quad (6.16)$$

Finally, taking the inverse of (6.16) and calculating the binomial expansion yields

$$\det(\mathcal{G})^{-1} \approx 1 - \frac{\partial U_1}{\partial X_1} - \frac{\partial U_2}{\partial X_2} + O(\mathbf{U}^2). \quad (6.17)$$

6.3.3 Linearising the Problem

Using the constitutive law (6.11) for \mathcal{S} , along with the approximations (6.12), (6.13), (6.17), for \mathcal{G} , \mathcal{G}^T and $\det(\mathcal{G})^{-1}$, it is now possible to determine a constitutive law for σ . Before we do so, we simplify these expressions by linearising for small $|\mathbf{u}|$ and $|\mathbf{U}|$. This allows us to neglect any terms that are quadratic or higher order in these deformations. As we have a small displacement \mathbf{u} compared to any other length scale, we also have that the Eulerian and Lagrangian coordinates, \mathbf{x} and \mathbf{X} , are equal to lowest order in

\mathbf{u} . Hence, as we are only considering terms linear in the deformations, we may replace \mathbf{X} by \mathbf{x} and $\partial/\partial X_i$ by $\partial/\partial x_i$ throughout our expressions. It is also the case that the components u_i of \mathbf{u} in the x_i -direction are equal to the components U_i of \mathbf{U} in the X_i -direction, at leading order in the deformations. Hence, we may linearise the expressions (6.11)–(6.13), (6.17) for \mathcal{S} , \mathcal{G} , \mathcal{G}^T and $\det(\mathcal{G})^{-1}$ as follows

$$\mathcal{S} = \mathcal{S}_0 + \lambda \text{Tr}(\bar{\mathcal{E}}) I + 2\mu \bar{\mathcal{E}}, \quad (6.18)$$

$$\mathcal{G}_{ij} \approx \delta_{ij} + \frac{\partial u_i}{\partial x_j}, \quad (6.19)$$

$$\mathcal{G}_{ij}^T \approx \delta_{ij} + \frac{\partial u_j}{\partial x_i}, \quad (6.20)$$

$$\det(\mathcal{G})^{-1} \approx 1 - \frac{\partial u_1}{\partial x_1} - \frac{\partial u_2}{\partial x_2}, \quad (6.21)$$

where $\bar{\mathcal{E}}$ is the linearised strain tensor

$$\bar{\mathcal{E}}_{ij} = \frac{1}{2} \left(\frac{\partial u_i}{\partial x_j} + \frac{\partial u_j}{\partial x_i} \right). \quad (6.22)$$

6.3.4 A Linearised Constitutive Law for σ

We now substitute (6.18)–(6.22) into the expression (6.7) for σ . Doing so, we find the constitutive law for σ to be

$$\sigma = \sigma_0 + \sigma_1, \quad (6.23)$$

where

$$\sigma_0 = \begin{pmatrix} 0 & 0 \\ 0 & \mathbb{F} \end{pmatrix}, \quad (6.24)$$

$$\sigma_1 = \begin{pmatrix} \lambda \left(\frac{\partial u_1}{\partial x_1} + \frac{\partial u_2}{\partial x_2} \right) + 2\mu \frac{\partial u_1}{\partial x_1} & \mu \left(\frac{\partial u_1}{\partial x_2} + \frac{\partial u_2}{\partial x_1} \right) \\ \mu \left(\frac{\partial u_1}{\partial x_2} + \frac{\partial u_2}{\partial x_1} \right) & \lambda \left(\frac{\partial u_1}{\partial x_1} + \frac{\partial u_2}{\partial x_2} \right) + 2\mu \frac{\partial u_2}{\partial x_2} \end{pmatrix} \\ + \mathbb{F} \begin{pmatrix} 0 & \frac{\partial u_1}{\partial x_2} \\ \frac{\partial u_1}{\partial x_2} & \frac{\partial u_2}{\partial x_2} - \frac{\partial u_1}{\partial x_1} \end{pmatrix}. \quad (6.25)$$

We note that σ_0 represents the constant pre-stress, whereas σ_1 contains all the terms linear in the deformations u_i . We can see that the pre-stress \mathbb{F} makes contributions to σ_1 as well as σ_0 . It is also noted that in the limit $\mathbb{F} \rightarrow 0$, the usual constitutive law for a linearly elastic isotropic material is recovered.

6.4 Linearising the Governing Equation and Boundary Conditions

Now that we have a suitable constitutive law for σ , we may evaluate and linearise the governing equation (6.8) and boundary conditions (6.9) imposed on the semi-infinite block. Substituting (6.23) into (6.8) and noting that σ_0 is a constant tensor, the following governing equation is obtained

$$\nabla \cdot \sigma_1 = \mathbf{0}. \quad (6.26)$$

The boundary conditions (6.9) are now linearised back to the rectangular boundaries $\bar{\gamma}_1$, $\bar{\gamma}_2$, $\bar{\gamma}_3$ and $\bar{\gamma}_4$ where

$$\begin{aligned} \bar{\gamma}_1 &\text{ is at } 0 \leq x_1 \leq d, \quad x_2 = 0, \\ \bar{\gamma}_2 &\text{ is at } x_1 = 0, \quad 0 \leq x_2, \\ \bar{\gamma}_3 &\text{ is at } 0 \leq x_1 \leq d, \quad x_2 \rightarrow \infty, \\ \bar{\gamma}_4 &\text{ is at } x_1 = d, \quad 0 \leq x_2. \end{aligned}$$

Hence, in the following, the γ_i denote the non-linearised boundaries whereas the quantities $\bar{\gamma}_i$ with the overbars denote the corresponding linearised boundaries.

Firstly, the boundary condition (6.9a) on γ_1 is linearised back to the boundary $\bar{\gamma}_1$ to give

$$\mathbf{u} = \begin{pmatrix} 0 \\ \tan(\phi) \left(x_1 - \frac{d}{2} \right) \end{pmatrix} \quad \text{at } x_2 = 0. \quad (6.27)$$

We now focus on linearising the more complicated conditions on the other boundaries of the block.

6.4.1 Boundary Conditions on Boundaries $\bar{\gamma}_2$ and $\bar{\gamma}_4$

We recall the following stress-free conditions on boundaries γ_2 and γ_4

$$\sigma \cdot \mathbf{n} = \mathbf{0} \quad \text{on } \gamma_2, \gamma_4, \quad (6.28)$$

where \mathbf{n} is the outward unit normal to the material. We must be careful with how this normal is treated as it will take different values before and after the problem has been linearised. In the linearised case, the normal \mathbf{n}_0 to boundaries $\bar{\gamma}_2$ and $\bar{\gamma}_4$ will be $(-1, 0)$ and $(1, 0)$ respectively. However, in the non-linearised

case there will be a correction to the normal linear in the deformation \mathbf{u} , as well as higher-order corrections in \mathbf{u} . Hence, we may decompose the normal \mathbf{n} to the non-linearised boundary as follows

$$\mathbf{n} = \mathbf{n}_0 + \mathbf{n}_1 + \dots, \quad (6.29)$$

where \mathbf{n}_0 is the unit normal to the boundary in the linearised case and \mathbf{n}_1 is a correction term linear in \mathbf{u} .

To evaluate the components within (6.29), we first consider a unit vector \mathbf{t} that is tangential to boundary γ_2 , as shown in Figure 6.3. We can see from the figure that the ratio of the x_1 and x_2 components of \mathbf{t} must be $\partial u_1 / \partial x_2$, evaluated at the appropriate point on the boundary. We then normalise \mathbf{t} in the following way to ensure that it is a unit vector

$$\begin{aligned} \mathbf{t} &= \left(1 + \left(\frac{\partial u_1}{\partial x_2} \right)^2 \right)^{-\frac{1}{2}} \begin{pmatrix} \frac{\partial u_1}{\partial x_2} \\ 1 \end{pmatrix}, \\ &= \begin{pmatrix} 0 \\ 1 \end{pmatrix} + \begin{pmatrix} \frac{\partial u_1}{\partial x_2} \\ 0 \end{pmatrix} + O\left(\left| \frac{\partial u_1}{\partial x_2} \right|^2\right). \end{aligned} \quad (6.30)$$

Hence, we may decompose \mathbf{t} as follows

$$\mathbf{t} = \mathbf{t}_0 + \mathbf{t}_1 + \dots, \quad (6.31)$$

where

$$\mathbf{t}_0 = \begin{pmatrix} 0 \\ 1 \end{pmatrix}, \quad \mathbf{t}_1 = \begin{pmatrix} \frac{\partial u_1}{\partial x_2} \\ 0 \end{pmatrix}.$$

As \mathbf{t} and \mathbf{n} are unit vectors that are perpendicular to each other, we rotate \mathbf{t} by $\pi/2$ to obtain the unit normal \mathbf{n} and thus its components. Doing so, the components \mathbf{n}_0 , \mathbf{n}_1 of the unit normal to boundary γ_2 are found to be

$$\mathbf{n}_0 = \begin{pmatrix} -1 \\ 0 \end{pmatrix}, \quad \mathbf{n}_1 = \begin{pmatrix} 0 \\ \frac{\partial u_1}{\partial x_2} \end{pmatrix}. \quad (6.32)$$

Using a similar argument, the components \mathbf{n}_0 , \mathbf{n}_1 of the unit normal to boundary γ_4 are calculated as

$$\mathbf{n}_0 = \begin{pmatrix} 1 \\ 0 \end{pmatrix}, \quad \mathbf{n}_1 = \begin{pmatrix} 0 \\ -\frac{\partial u_1}{\partial x_2} \end{pmatrix}. \quad (6.33)$$

With the expressions (6.29), (6.32), (6.33) of the normal and its components on boundaries γ_2 and γ_4 , we linearise the boundary conditions (6.28) back to

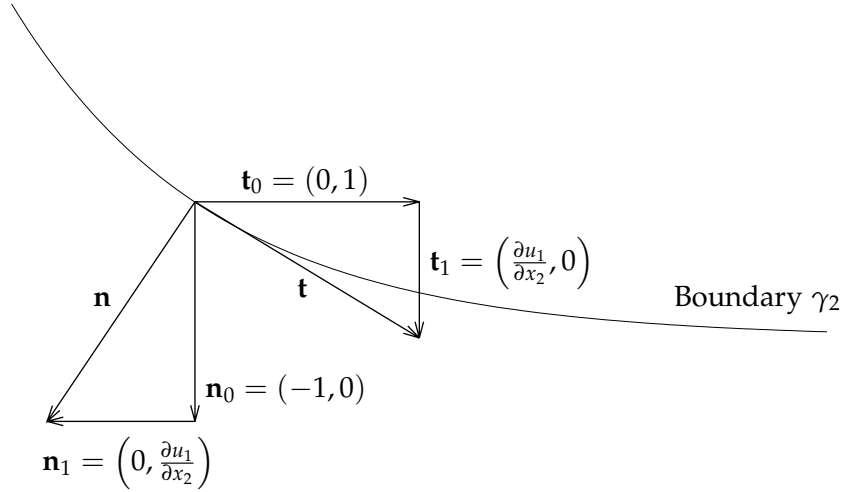


Figure 6.3: Components of the unit tangent vector \mathbf{t} and unit outward normal \mathbf{n} of boundary γ_2 .

the linearised boundaries $\bar{\gamma}_2$ and $\bar{\gamma}_4$. We first express $\sigma \cdot \mathbf{n}$ in the following way

$$\sigma \cdot \mathbf{n} = \sigma_0 \cdot (\mathbf{n}_0 + \mathbf{n}_1) + \sigma_1 \cdot (\mathbf{n}_0 + \mathbf{n}_1) + \dots \quad (6.34)$$

$$\approx \sigma_0 \cdot \mathbf{n}_1 + \sigma_1 \cdot \mathbf{n}_0 \quad \text{on} \quad \gamma_2, \gamma_4. \quad (6.35)$$

Here we have used the fact that $\sigma_0 \cdot \mathbf{n}_0 = \mathbf{0}$ for the values of \mathbf{n}_0 in (6.32) and (6.33), and $\sigma_1 \cdot \mathbf{n}_1$ contains only terms that are quadratic in the deformation \mathbf{u} and may be neglected. Substituting (6.35) into the boundary conditions (6.28) along with the definitions (6.24), (6.32) and (6.33) for σ_0 and \mathbf{n}_1 along each boundary, the following linearised boundary conditions along boundaries $\bar{\gamma}_2$ and $\bar{\gamma}_4$ are found

$$\sigma_1 \cdot \mathbf{n}_0 = \begin{pmatrix} 0 \\ -\mathbb{F} \frac{\partial u_1}{\partial x_2} \end{pmatrix} \quad \text{at} \quad x_1 = 0, \quad (6.36)$$

$$\sigma_1 \cdot \mathbf{n}_0 = \begin{pmatrix} 0 \\ \mathbb{F} \frac{\partial u_1}{\partial x_2} \end{pmatrix} \quad \text{at} \quad x_1 = d. \quad (6.37)$$

6.4.2 Boundary Condition on Boundary $\bar{\gamma}_3$

On boundary γ_3 , we have the following condition of no stress perturbation

$$\sigma \cdot \mathbf{n} \rightarrow \begin{pmatrix} 0 \\ \mathbb{F} \end{pmatrix} \quad \text{as} \quad x_2 \rightarrow \infty, \quad (6.38)$$

where now \mathbf{n} is a unit vector in the same direction as the axial tension \mathbb{F} , as $x_2 \rightarrow \infty$. This vector can be decomposed as in (6.29), where \mathbf{n}_0 is now the unit vector in the same direction as \mathbb{F} as $x_2 \rightarrow \infty$ in the linearised case, and \mathbf{n}_1 is a correction term linear in the deformation \mathbf{u} . Using a similar argument to that used to determine the components of the normal to boundaries γ_2 and γ_4 , we find at boundary γ_3

$$\mathbf{n}_0 = \begin{pmatrix} 0 \\ 1 \end{pmatrix}, \quad \mathbf{n}_1 = \begin{pmatrix} \frac{\partial u_2}{\partial x_1} \\ 0 \end{pmatrix}. \quad (6.39)$$

Substituting the expression (6.24) for σ_0 and (6.39) into (6.34), $\sigma \cdot \mathbf{n}$ may be rewritten as

$$\sigma \cdot \mathbf{n} \approx \sigma_0 \cdot \mathbf{n}_0 + \sigma_1 \cdot \mathbf{n}_0 \quad \text{on } \gamma_3, \quad (6.40)$$

where $\sigma_0 \cdot \mathbf{n}_1 = \mathbf{0}$ and $\sigma_1 \cdot \mathbf{n}_1$ is again composed of terms quadratic in \mathbf{u} and is neglected. It is also found that $\sigma_0 \cdot \mathbf{n}_0 = (0, \mathbb{F})$ on boundary γ_3 . Substituting (6.40) into the boundary condition (6.38) and rearranging, the linearised boundary condition to be applied at $\bar{\gamma}_3$ is calculated as

$$\sigma_1 \cdot \mathbf{n}_0 \rightarrow \mathbf{0} \quad \text{as } x_2 \rightarrow \infty. \quad (6.41)$$

6.4.3 The Linearised Problem

Combining the governing equation (6.26) with the boundary conditions (6.27), (6.36), (6.37) and (6.41), the full linearised problem is

$$\nabla \cdot \sigma_1 = \mathbf{0} \quad \text{for } 0 \leq x_1 \leq d, x_2 \geq 0, \quad (6.42)$$

$$\mathbf{u} = \begin{pmatrix} 0 \\ \tan(\phi) \left(x_1 - \frac{d}{2} \right) \end{pmatrix} \quad \text{at } x_2 = 0, \quad (6.43)$$

$$\sigma_1 \cdot \mathbf{n}_0 = \begin{pmatrix} 0 \\ -\mathbb{F} \frac{\partial u_1}{\partial x_2} \end{pmatrix} \quad \text{at } x_1 = 0, \quad (6.44)$$

$$\sigma_1 \cdot \mathbf{n}_0 = \begin{pmatrix} 0 \\ \mathbb{F} \frac{\partial u_1}{\partial x_2} \end{pmatrix} \quad \text{at } x_1 = d, \quad (6.45)$$

$$\sigma_1 \cdot \mathbf{n}_0 \rightarrow \mathbf{0} \quad \text{as } x_2 \rightarrow \infty. \quad (6.46)$$

This system is depicted in Figure 6.4. We now proceed to solve this linearised problem, both numerically and using analytical techniques.

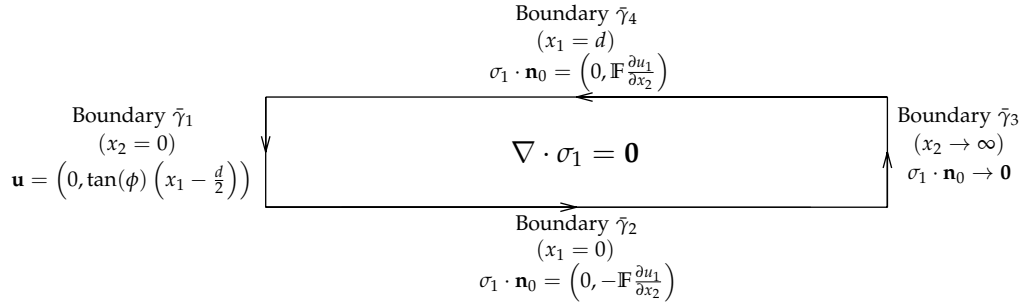


Figure 6.4: The linearised problem of a semi-infinite block being bent under axial tension. The domain is given by $A = \{(x_1, x_2) : 0 \leq x_1 \leq d, 0 \leq x_2\}$ and the total boundary of the domain is given by $\partial A = \bar{\gamma}_1 \cup \bar{\gamma}_2 \cup \bar{\gamma}_3 \cup \bar{\gamma}_4$.

6.5 Numerical Solution

Here, a numerical solution of the system (6.42)–(6.46) is determined using the numerical finite-element differential equation solver “FEniCS” (Dupont *et al.*, 2003). As FEniCS can only solve problems within a finite domain, we must restrict the range of x_2 to $0 \leq x_2 \leq x_{\max}$, where x_{\max} is some fixed, finite value. As long as a large enough value for x_{\max} is chosen, along with a suitable number of grid points, the numerical solution will still accurately simulate the deformation. The numerical scheme used by FEniCS is the finite element method, an overview of which is given by Iserles (1996).

For FEniCS to be able to apply the finite element method to a problem, the problem must be written in variational form. That is

$$a(\mathbf{u}, \mathbf{v}) = L(\mathbf{v}), \quad (6.47)$$

where \mathbf{u} is the unknown function to be found, known as a trial function, \mathbf{v} is an arbitrary function known as a test function, and a, L are differential operators. Hence, in order to use FEniCS to find a numerical solution for the system (6.42)–(6.46), we must rewrite the system in variational form.

We begin by taking the dot product of the governing equation (6.42) with a test function \mathbf{v} , and integrating over the (linearised) area A of the block, given by $A = \{(x_1, x_2) : 0 \leq x_1 \leq d, 0 \leq x_2 \leq x_{\max}\}$. Doing so, we obtain

$$\iint_A (\nabla \cdot \sigma_1) \cdot \mathbf{v} \, dA = 0. \quad (6.48)$$

This may be rewritten as

$$\iint_A \nabla \cdot (\sigma_1 \cdot \mathbf{v}) - \sigma_1 : (\nabla \mathbf{v}) \, dA = 0, \quad (6.49)$$

where the Frobenius inner product : of two tensors M, N is defined by

$$M : N = \sum_i \sum_j M_{ij} N_{ij}, \quad (6.50)$$

and the gradient $\nabla \mathbf{a}$ of a vector \mathbf{a} is given by

$$\nabla \mathbf{a} = \frac{\partial a_i}{\partial x_j} \mathbf{e}_i \mathbf{e}_j, \quad (6.51)$$

where \mathbf{e}_i is a unit vector in the x_i -direction. Applying the divergence theorem to the first term in (6.49), we find

$$\oint_{\partial A} (\sigma_1 \cdot \mathbf{n}_0) \cdot \mathbf{v} \, ds - \iint_A \sigma_1 : (\nabla \mathbf{v}) \, dA = 0, \quad (6.52)$$

where \mathbf{n}_0 is the unit normal to the boundary of the linearised domain.

6.5.1 Evaluating the Integrals in (6.52)

The integrals in (6.52) are now evaluated. We start by evaluating the line integral over the linearised boundaries $\bar{\gamma}_1, \bar{\gamma}_2, \bar{\gamma}_3$ and $\bar{\gamma}_4$ separately.

On $\bar{\gamma}_1$, we have the boundary condition (6.43) for \mathbf{u} . In the finite-element formulation, the test function \mathbf{v} must vanish on the segments of the boundary where \mathbf{u} is known. As such, we must have $\mathbf{v} = \mathbf{0}$ along $\bar{\gamma}_1$, and the line integral along $\bar{\gamma}_1$ vanishes from (6.52).

Along boundaries $\bar{\gamma}_2$ and $\bar{\gamma}_4$, we have the boundary conditions (6.44) and (6.45). Using the values of $\sigma_1 \cdot \mathbf{n}_0$ within these conditions and noting that we must take our integrals in the anticlockwise direction around the boundary ∂A as in Figure 6.4, we find the line integrals along boundaries $\bar{\gamma}_2$ and $\bar{\gamma}_4$ become

$$\int_{\bar{\gamma}_2} (\sigma_1 \cdot \mathbf{n}_0) \cdot \mathbf{v} \, ds = \int_{\bar{\gamma}_2} -\mathbb{F} \left(\frac{\partial u_1}{\partial x_2} v_2 \right) \, ds, = \int_{x_{\max}}^0 \mathbb{F} \left(\frac{\partial u_1}{\partial x_2} v_2 \right) \Big|_{x_1=0} \, dx_2, \quad (6.53)$$

$$\int_{\bar{\gamma}_4} (\sigma_1 \cdot \mathbf{n}_0) \cdot \mathbf{v} \, ds = \int_{\bar{\gamma}_4} \mathbb{F} \left(\frac{\partial u_1}{\partial x_2} v_2 \right) \, ds, = \int_{x_{\max}}^0 \mathbb{F} \left(\frac{\partial u_1}{\partial x_2} v_2 \right) \Big|_{x_1=d} \, dx_2, \quad (6.54)$$

where v_1, v_2 are the components of the test function \mathbf{v} in the x_1 and x_2 -directions respectively.

Finally, on boundary $\bar{\gamma}_3$ we have the boundary condition $\sigma_1 \cdot \mathbf{n}_0 = \mathbf{0}$. Hence, the line integral along $\bar{\gamma}_3$ vanishes. Combining the line integrals along each boundary, the total line integral around the domain is determined to be

$$\oint_{\partial A} (\sigma_1 \cdot \mathbf{n}_0) \cdot \mathbf{v} \, ds = - \int_0^{x_{\max}} \mathbb{F} \left(\frac{\partial u_1}{\partial x_2} v_2 \Big|_{x_1=0} + \frac{\partial u_1}{\partial x_2} v_2 \Big|_{x_1=d} \right) \, dx_2. \quad (6.55)$$

The surface integral within (6.52) is now evaluated. Using, the expression (6.25) for σ_1 , it is found that

$$\begin{aligned} \iint_A \sigma_1 : (\nabla \mathbf{v}) \, dA &= \iint_A \frac{\partial v_1}{\partial x_1} \left[(\lambda + 2\mu) \frac{\partial u_1}{\partial x_1} + \lambda \frac{\partial u_2}{\partial x_2} \right] \\ &\quad + \left(\frac{\partial v_1}{\partial x_2} + \frac{\partial v_2}{\partial x_1} \right) \left[(\mu + \mathbb{F}) \frac{\partial u_1}{\partial x_2} + \mu \frac{\partial u_2}{\partial x_1} \right] \\ &\quad + \frac{\partial v_2}{\partial x_2} \left[(\lambda - \mathbb{F}) \frac{\partial u_1}{\partial x_1} + (\lambda + 2\mu + \mathbb{F}) \frac{\partial u_2}{\partial x_2} \right] \, dA. \end{aligned} \quad (6.56)$$

6.5.2 Rewriting the Problem in Terms of E and ν

The expressions (6.55) and (6.56) can now be used to derive the variational form of the problem. However, it is found to be convenient to first rewrite the problem in terms of the Young's modulus E , and Poisson's ratio ν of the block. The parameters λ and μ can be rewritten in terms of E and ν as follows

$$\lambda = \frac{E\nu}{(1+\nu)(1-2\nu)}, \quad \mu = \frac{E}{2(1+\nu)}. \quad (6.57)$$

It is also found to be convenient to rewrite axial tension \mathbb{F} as

$$\mathbb{F} = \frac{E\bar{\mathcal{F}}}{2(1+\nu)(1-2\nu)}, \quad (6.58)$$

where $\bar{\mathcal{F}}$ is a dimensionless parameter, the size of which we determine later on. The factor of $[2(1+\nu)(1-2\nu)]^{-1}$ has been included for mathematical convenience in the following calculations. Rewriting (6.55) and (6.56) in terms of these parameters yields

$$\oint_{\partial A} (\sigma_1 \cdot \mathbf{n}_0) \cdot \mathbf{v} \, ds = - \int_0^{x_{\max}} \frac{E\bar{\mathcal{F}}}{2(1+\nu)(1-2\nu)} \left(\frac{\partial u_1}{\partial x_2} v_2 \Big|_{x_1=0} + \frac{\partial u_1}{\partial x_2} v_2 \Big|_{x_1=d} \right) \, dx_2, \quad (6.59)$$

$$\begin{aligned} \iint_A \sigma_1 : (\nabla \mathbf{v}) \, dA &= \iint_A E \left\{ \frac{\partial v_1}{\partial x_1} \left[\frac{\nu}{(1+\nu)(1-2\nu)} \left(\frac{\partial u_1}{\partial x_1} + \frac{\partial u_2}{\partial x_2} \right) + \frac{1}{1+\nu} \frac{\partial u_1}{\partial x_1} \right] \right. \\ &\quad + \left(\frac{\partial v_1}{\partial x_2} + \frac{\partial v_2}{\partial x_1} \right) \left[\frac{1}{2(1+\nu)} \left(\frac{\partial u_1}{\partial x_2} + \frac{\partial u_2}{\partial x_1} \right) \right. \\ &\quad \left. \left. + \frac{\bar{\mathcal{F}}}{2(1+\nu)(1-2\nu)} \frac{\partial u_1}{\partial x_2} \right] \right. \\ &\quad + \frac{\partial v_2}{\partial x_2} \left[\frac{\nu}{(1+\nu)(1-2\nu)} \left(\frac{\partial u_1}{\partial x_1} + \frac{\partial u_2}{\partial x_2} \right) + \frac{1}{1+\nu} \frac{\partial u_2}{\partial x_2} \right. \\ &\quad \left. \left. + \frac{\bar{\mathcal{F}}}{2(1+\nu)(1-2\nu)} \left(\frac{\partial u_2}{\partial x_2} - \frac{\partial u_1}{\partial x_1} \right) \right] \right\} \, dA. \end{aligned} \quad (6.60)$$

Rewriting the problem in this way has two advantages. First of all, this ensures that all terms within the components (6.59) and (6.60) of the governing equation (6.52) have a single factor of the Young's modulus E within them. This factor of E can then later be eliminated from (6.52) leaving us with only one parameter to set, the Poisson's ratio ν .

The second advantage of rewriting the problem is that we have a clear choice of value for ν . If the block was perfectly incompressible, a natural choice of the Poisson's ratio would be $\nu = 0.5$, corresponding to a perfectly incompressible material. However, this value would form singularities within the numerical solutions. We instead choose a Poisson's ratio of $\nu = 0.49$ to correspond to an almost incompressible material and avoid any singularities. This is a common choice of Poisson's Ratio used by other authors. When we later plot the numerical and analytical solutions for the deformations in §6.8, we will set $\nu = 0.49$.

It is noted that although $\bar{\mathcal{F}}$ is dimensionless, it is not necessarily $O(1)$. To find the size of $\bar{\mathcal{F}}$, we recall the expression (6.1) for the dimensional axial tension \mathbb{F} , which is

$$\mathbb{F} = \frac{K\ell^2}{a^3\delta} \mathcal{F},$$

where K is the bending stiffness of the block, $\mathcal{F} = O(1)$ is a scaled dimensionless axial tension, a is the typical radial scale of the original tube and $\delta = d/a \ll 1$, $\ell \gg 1$ are the dimensionless wall thickness and length of the original tube. Substituting the expression (6.58) for \mathbb{F} into (6.1), rearranging and using the fact that the bending stiffness K may be rewritten in terms of E and ν as

$$K = \frac{Ed^3}{12(1-\nu^2)},$$

we find

$$\bar{\mathcal{F}} = \frac{(1-2\nu)\mathcal{F}\delta^2\ell^2}{6(1-\nu)}. \quad (6.61)$$

Hence as $\mathcal{F} = O(1)$, we have $\bar{\mathcal{F}} = O(\delta^2\ell^2)$. In regime II considered here, we have $\delta\ell \gg 1$, which corresponds to the limit $\bar{\mathcal{F}} \rightarrow \infty$. We can also consider regime I in this model by taking the limit $\bar{\mathcal{F}} \rightarrow 0$, which corresponds to $\delta\ell \ll 1$. We note that although $\bar{\mathcal{F}}$ has the same scaling as the parameter $\tilde{\mathcal{F}}$ defined in (3.36) and used to describe the axial tension in the study of regimes I_a and I_b in Chapters 4 and 5, $\bar{\mathcal{F}}$ and $\tilde{\mathcal{F}}$ do not have the exact same value. It is found to be mathematically convenient to write the following equations in terms of $\bar{\mathcal{F}}$, rather than \mathcal{F} or $\tilde{\mathcal{F}}$.

6.5.3 Variational Form of the Problem

By substituting (6.59) and (6.60) into (6.52), a numerically solvable equation is obtained. To enable FEniCS to solve this equation, we rewrite it in the variational form given in (6.47). Rewriting (6.52) in this form, dividing through by the Young's modulus E and multiplying by $2(1 + \nu)(1 - 2\nu)$ yields

$$\begin{aligned} a(\mathbf{u}, \mathbf{v}) &= \iint_A \frac{\partial v_1}{\partial x_1} \left[2\nu \left(\frac{\partial u_1}{\partial x_1} + \frac{\partial u_2}{\partial x_2} \right) + 2(1 - 2\nu) \frac{\partial u_1}{\partial x_1} \right] \\ &\quad + \left(\frac{\partial v_1}{\partial x_2} + \frac{\partial v_2}{\partial x_1} \right) \left[(1 - 2\nu) \left(\frac{\partial u_1}{\partial x_2} + \frac{\partial u_2}{\partial x_1} \right) + \bar{\mathcal{F}} \frac{\partial u_1}{\partial x_2} \right] \\ &\quad + \frac{\partial v_2}{\partial x_2} \left[2\nu \left(\frac{\partial u_1}{\partial x_1} + \frac{\partial u_2}{\partial x_2} \right) + 2(1 - 2\nu) \frac{\partial u_2}{\partial x_2} \right. \\ &\quad \left. + \bar{\mathcal{F}} \left(\frac{\partial u_2}{\partial x_2} - \frac{\partial u_1}{\partial x_1} \right) \right] \, dA \\ &\quad + \int_{\bar{\gamma}_2} -\bar{\mathcal{F}} \left(\frac{\partial u_1}{\partial x_2} v_2 \right) \, ds + \int_{\bar{\gamma}_4} \bar{\mathcal{F}} \left(\frac{\partial u_1}{\partial x_2} v_2 \right) \, ds, \end{aligned} \quad (6.62)$$

$$L(\mathbf{v}) = 0. \quad (6.63)$$

This is the form of the problem needed for FEniCS to compute the solution. This is because FEniCS uses a domain specified in the code to evaluate the limits of the surface and line integrals, as well as the direction of the line integral around ∂A . Including the limits of the integrals in the definition (6.62), the analytical form of $a(\mathbf{u}, \mathbf{v})$ is found to be

$$\begin{aligned} a(\mathbf{u}, \mathbf{v}) &= \int_0^{x_{\max}} \int_0^d \frac{\partial v_1}{\partial x_1} \left[2\nu \left(\frac{\partial u_1}{\partial x_1} + \frac{\partial u_2}{\partial x_2} \right) + 2(1 - 2\nu) \frac{\partial u_1}{\partial x_1} \right] \\ &\quad + \left(\frac{\partial v_1}{\partial x_2} + \frac{\partial v_2}{\partial x_1} \right) \left[(1 - 2\nu) \left(\frac{\partial u_1}{\partial x_2} + \frac{\partial u_2}{\partial x_1} \right) + \bar{\mathcal{F}} \frac{\partial u_1}{\partial x_2} \right] \\ &\quad + \frac{\partial v_2}{\partial x_2} \left[2\nu \left(\frac{\partial u_1}{\partial x_1} + \frac{\partial u_2}{\partial x_2} \right) + 2(1 - 2\nu) \frac{\partial u_2}{\partial x_2} \right. \\ &\quad \left. + \bar{\mathcal{F}} \left(\frac{\partial u_2}{\partial x_2} - \frac{\partial u_1}{\partial x_1} \right) \right] \, dx_1 dx_2 \\ &\quad - \int_0^{x_{\max}} \bar{\mathcal{F}} \left(\frac{\partial u_1}{\partial x_2} v_2 \Big|_{x_1=0} + \frac{\partial u_1}{\partial x_2} v_2 \Big|_{x_1=d} \right) \, dx_2. \end{aligned} \quad (6.64)$$

It is now possible to input the expressions (6.62), (6.63), along with the boundary condition (6.27) at $x_2 = 0$ into FEniCS and calculate the numerical solution to the system (6.42)–(6.46). This solution is shown in §6.8, where it is compared with the analytical approximations for the solution derived in §6.6.

6.6 Analytical Treatment

Analytical techniques are now used to determine a solution to the system (6.42)–(6.46). As a starting point, we eliminate u_2 from the system, leaving us with a governing system to be solved for the deformation u_1 .

6.6.1 Eliminating u_2 from the Governing Equation

We begin by eliminating u_2 from the governing equation (6.42). The two components of (6.42) yield

$$2(1-\nu) \frac{\partial^2 u_1}{\partial x_1^2} + \frac{\partial^2 u_2}{\partial x_1 \partial x_2} + (1-2\nu + \bar{F}) \frac{\partial^2 u_1}{\partial x_2^2} = 0, \quad (6.65)$$

$$(1-2\nu) \frac{\partial^2 u_2}{\partial x_1^2} + \frac{\partial^2 u_1}{\partial x_1 \partial x_2} + (2(1-\nu) + \bar{F}) \frac{\partial^2 u_2}{\partial x_2^2} = 0. \quad (6.66)$$

where again the Lamé constants λ, μ have been rewritten in terms of the Young's modulus E and Poisson's ratio ν using (6.57), and the axial tension \mathbb{F} has been rewritten in terms of \bar{F} using (6.58). This has provided a factor of E in each term in (6.42) allowing this parameter to be cancelled entirely from the governing equations. For mathematical convenience, the governing equations have also been multiplied by $2(1+\nu)(1-2\nu)$.

Rearranging (6.65), we obtain

$$\frac{\partial^2 u_2}{\partial x_1 \partial x_2} = - \left[2(1-\nu) \frac{\partial^2 u_1}{\partial x_1^2} + (1-2\nu + \bar{F}) \frac{\partial^2 u_1}{\partial x_2^2} \right], \quad (6.67)$$

and differentiating (6.66) with respect to x_1 and x_2 yields

$$(1-2\nu) \frac{\partial^4 u_2}{\partial x_1^3 \partial x_2} + \frac{\partial^4 u_1}{\partial x_1^2 \partial x_2^2} + (2(1-\nu) + \bar{F}) \frac{\partial^4 u_2}{\partial x_1 \partial x_2^3} = 0. \quad (6.68)$$

To eliminate u_2 from (6.68), we may differentiate (6.67) twice with respect to x_1 , and twice with respect to x_2 , to obtain expressions for $\partial^4 u_2 / \partial x_1^3 \partial x_2$ and $\partial^4 u_2 / \partial x_1 \partial x_2^3$ in terms of u_1 . These expressions may then be substituted into (6.68). This gives the following fourth-order governing PDE for u_1

$$0 = \frac{\partial^4 u_1}{\partial x_1^4} + \left[\frac{2(1-\nu) + \bar{F}}{2(1-\nu)} + \frac{1-2\nu + \bar{F}}{1-2\nu} \right] \frac{\partial^4 u_1}{\partial x_1^2 \partial x_2^2} + \frac{(2(1-\nu) + \bar{F})(1-2\nu + \bar{F})}{2(1-\nu)(1-2\nu)} \frac{\partial^4 u_1}{\partial x_2^4}. \quad (6.69)$$

6.6.2 Eliminating u_2 from the Boundary Conditions

We now determine conditions on u_1 from the prescribed boundary conditions (6.43)–(6.46) shown in Figure 6.4. Some of these boundary conditions will translate to traditional boundary conditions on u_1 . However, others will become integral constraints on u_1 which must be satisfied so that a corresponding solution for u_2 exists. In order to convert the boundary conditions into a suitable form, we must find an expression for u_2 in terms of u_1 and see what constraints are necessary for u_2 to satisfy the boundary conditions.

By integrating (6.67) with respect to x_2 and then x_1 , we obtain

$$u_2 = \int_{\frac{d}{2}}^{x_1} \left(\int_{x_2}^{\infty} \left[2(1-\nu) \frac{\partial^2 u_1}{\partial x_1^2} + (1-2\nu + \bar{\mathcal{F}}) \frac{\partial^2 u_1}{\partial x_2^2} \right] dx'_2 + C(x_1) \right) dx'_1 + K(x_2), \quad (6.70)$$

where $C(x_1)$ and $K(x_2)$ are functions to be determined by the boundary conditions of the problem. It is convenient to set these particular limits for the integrals as they simplify the form of $C(x_1)$ as well as ensure that u_2 is antisymmetric about $x_1 = d/2$. We note that as we have switched the limits in the x_2 integral, the minus sign from (6.67) vanishes.

We begin by evaluating the boundary condition (6.46) as $x_2 \rightarrow \infty$. In Appendix 6.A, the boundary conditions (6.43)–(6.46) have been used to show that the condition (6.46) is equivalent to

$$\nabla u_1, \nabla u_2 \rightarrow \mathbf{0} \quad \text{as} \quad x_2 \rightarrow \infty. \quad (6.71)$$

The first of these conditions is a condition on u_1 which may be applied to the problem immediately. The second of these conditions is a condition on u_2 which must be applied to the expression (6.70) for u_2 , to find a corresponding integral condition on u_1 . When $x_2 \rightarrow \infty$, (6.70) yields

$$u_2 \Big|_{x_2 \rightarrow \infty} = \int_{\frac{d}{2}}^{x_1} C(x_1) dx'_1 + K(x_2) \Big|_{x_2 \rightarrow \infty}. \quad (6.72)$$

As $u_2 \rightarrow \text{constant}$ as $x_2 \rightarrow \infty$ from (6.71), we cannot have any x_1 dependence in (6.72). Hence, we must have

$$C(x_1) = 0. \quad (6.73)$$

For (6.71) to be satisfied, we must also have

$$K \rightarrow \text{constant} \quad \text{as} \quad x_2 \rightarrow \infty. \quad (6.74)$$

We now evaluate the boundary condition (6.43) at $x_2 = 0$. Straight away, we have the boundary condition on u_1

$$u_1 = 0 \quad \text{at} \quad x_2 = 0. \quad (6.75)$$

From (6.43), there is also the condition

$$u_2 = \tan(\phi) \left(x_1 - \frac{d}{2} \right) \quad \text{at} \quad x_2 = 0.$$

Applying this condition to the expression (6.70) for u_2 , it is found that

$$\tan(\phi) \left(x_1 - \frac{d}{2} \right) = \int_{\frac{d}{2}}^{x_1} \int_0^\infty \left[2(1-\nu) \frac{\partial^2 u_1}{\partial x_1^2} + (1-2\nu+\bar{\mathcal{F}}) \frac{\partial^2 u_1}{\partial x_2^2} \right] dx_2 dx_1' + K(0). \quad (6.76)$$

Differentiating (6.76) with respect to x_1 and evaluating the x_2 integral, we obtain the following integral condition on u_1

$$\tan(\phi) = (1-2\nu+\bar{\mathcal{F}}) \left[\frac{\partial u_1}{\partial x_2} \right]_{x_2=0}^{x_2 \rightarrow \infty} + 2(1-\nu) \int_0^\infty \frac{\partial^2 u_1}{\partial x_1^2} dx_2. \quad (6.77)$$

Substituting (6.77) into (6.76), we find

$$K(0) = 0. \quad (6.78)$$

Finally, we evaluate the stress-free conditions (6.44), (6.45) at $x_1 = 0, d$, rewriting these conditions in terms of E , ν and $\bar{\mathcal{F}}$. Evaluating the first components of these conditions and multiplying by $(1+\nu)(1-2\nu)$ gives

$$(1-\nu) \frac{\partial u_1}{\partial x_1} + \nu \frac{\partial u_2}{\partial x_2} = 0 \quad \text{at} \quad x_1 = 0, d. \quad (6.79)$$

Substituting the expression (6.70) for u_2 into the conditions (6.79), we obtain

$$(1-\nu) \frac{\partial u_1}{\partial x_1} \Big|_{x_1=d} - \nu \int_0^{\frac{d}{2}} 2(1-\nu) \frac{\partial^2 u_1}{\partial x_1^2} + (1-2\nu+\bar{\mathcal{F}}) \frac{\partial^2 u_1}{\partial x_2^2} dx_1 + \nu \frac{dK}{dx_2} = 0, \quad (6.80)$$

$$(1-\nu) \frac{\partial u_1}{\partial x_1} \Big|_{x_1=0} + \nu \int_{\frac{d}{2}}^d 2(1-\nu) \frac{\partial^2 u_1}{\partial x_1^2} + (1-2\nu+\bar{\mathcal{F}}) \frac{\partial^2 u_1}{\partial x_2^2} dx_1 + \nu \frac{dK}{dx_2} = 0. \quad (6.81)$$

By subtracting (6.81) from (6.80) and rearranging, another integral condition on u_1 is determined

$$\int_0^d \left((1-\nu)(1-2\nu) \frac{\partial^2 u_1}{\partial x_1^2} - \nu(1-2\nu+\bar{\mathcal{F}}) \frac{\partial^2 u_1}{\partial x_2^2} \right) dx_1 = 0. \quad (6.82)$$

If we instead add together (6.80) and (6.81) and integrate the resulting expression with respect to x_2 , the following expression for $K(x_2)$ is found after

rearranging

$$K(x_2) = \int_0^{x_2} \left[\frac{\nu-1}{2\nu} \left(\frac{\partial u_1(x_1, x'_2)}{\partial x_1} \Big|_{x_1=d} + \frac{\partial u_1(x_1, x'_2)}{\partial x_1} \Big|_{x_1=0} \right) + \int_{\frac{d}{2}}^d (1-\nu) \frac{\partial^2 u_1(x_1, x'_2)}{\partial x_1^2} + \frac{1-2\nu+\bar{\mathcal{F}}}{2} \frac{\partial^2 u_1(x_1, x'_2)}{\partial x'_2^2} dx_1 \right. \\ \left. - \int_0^{\frac{d}{2}} (1-\nu) \frac{\partial^2 u_1(x_1, x'_2)}{\partial x_1^2} + \frac{1-2\nu+\bar{\mathcal{F}}}{2} \frac{\partial^2 u_1(x_1, x'_2)}{\partial x'_2^2} dx_1 \right] dx'_2. \quad (6.83)$$

Here we have used the property (6.78) to set the limits of the x'_2 integral.

The second components of the stress-free conditions (6.44), (6.45) are

$$\frac{\partial u_1}{\partial x_2} + \frac{\partial u_2}{\partial x_1} = 0 \quad \text{at} \quad x_1 = 0, d. \quad (6.84)$$

As the boundaries of the block at $x_1 = 0, d$ are parallel to the x_2 -direction, we may differentiate (6.84) with respect to x_2 . Doing so, we obtain

$$\frac{\partial^2 u_1}{\partial x_2^2} + \frac{\partial^2 u_2}{\partial x_1 \partial x_2} = 0 \quad \text{at} \quad x_1 = 0, d. \quad (6.85)$$

Substituting the expression (6.67) for $\partial^2 u_2 / \partial x_1 \partial x_2$ into (6.85), the following boundary condition for u_1 is found

$$2(1-\nu) \frac{\partial^2 u_1}{\partial x_1^2} - (2\nu - \bar{\mathcal{F}}) \frac{\partial^2 u_1}{\partial x'_2^2} = 0 \quad \text{at} \quad x_1 = 0, d. \quad (6.86)$$

The boundary and integral conditions on u_1 are thus (6.71a), (6.75), (6.77), (6.82) and (6.86).

Substituting the expressions (6.73), (6.83) for the functions $C(x_1)$ and $K(x_2)$ into (6.70), we find the full expression for u_2 in terms of u_1 to be

$$u_2 = \int_{\frac{d}{2}}^{x_1} \int_{x_2}^{\infty} 2(1-\nu) \frac{\partial^2 u_1(x'_1, x'_2)}{\partial x'_1^2} + (1-2\nu+\bar{\mathcal{F}}) \frac{\partial^2 u_1(x'_1, x'_2)}{\partial x'_2^2} dx'_2 dx'_1 + K(x_2), \quad (6.87)$$

where $K(x_2)$ is defined by (6.83). As long as the integral conditions (6.77) and (6.82) are satisfied, this u_2 along with the corresponding u_1 will automatically satisfy all the boundary conditions (6.43)–(6.46). Hence, once a solution for u_1 is calculated, we may use (6.87) to find u_2 as well.

6.6.3 Governing System for u_1

Combining the governing equation (6.69) with the boundary conditions (6.71), (6.75), (6.86) and integral conditions (6.77), (6.82), we obtain the following

system to be solved for u_1 .

$$0 = \frac{\partial^4 u_1}{\partial x_1^4} + \left[\frac{2(1-\nu) + \bar{\mathcal{F}}}{2(1-\nu)} + \frac{1-2\nu+\bar{\mathcal{F}}}{1-2\nu} \right] \frac{\partial^4 u_1}{\partial x_1^2 \partial x_2^2} + \frac{(2(1-\nu) + \bar{\mathcal{F}})(1-2\nu+\bar{\mathcal{F}})}{2(1-\nu)(1-2\nu)} \frac{\partial^4 u_1}{\partial x_2^4}, \quad (6.88)$$

$$\nabla u_1 \rightarrow \mathbf{0} \quad \text{as} \quad x_2 \rightarrow \infty, \quad (6.89)$$

$$u_1 = 0 \quad \text{at} \quad x_2 = 0, \quad (6.90)$$

$$2(1-\nu) \frac{\partial^2 u_1}{\partial x_1^2} - (2\nu - \bar{\mathcal{F}}) \frac{\partial^2 u_1}{\partial x_2^2} = 0 \quad \text{at} \quad x_1 = 0, d, \quad (6.91)$$

$$(1-2\nu+\bar{\mathcal{F}}) \left[\frac{\partial u_1}{\partial x_2} \right]_{x_2=0}^{x_2 \rightarrow \infty} + 2(1-\nu) \int_0^\infty \frac{\partial^2 u_1}{\partial x_1^2} dx_2 = \tan(\phi), \quad (6.92)$$

$$\int_0^d \left((1-\nu)(1-2\nu) \frac{\partial^2 u_1}{\partial x_1^2} - \nu(1-2\nu+\bar{\mathcal{F}}) \frac{\partial^2 u_1}{\partial x_2^2} \right) dx_1 = 0. \quad (6.93)$$

We now proceed to solve the system (6.88)–(6.93). As the governing equation (6.88) is fourth-order and linear with constant coefficients, we expect solutions for u_1 to be exponential, trigonometric or up to cubic in x_1, x_2 . As we must have solutions that tend to a constant as $x_2 \rightarrow \infty$, due to the boundary condition (6.89), we seek separable solutions of the forms

$$u_1 = \hat{u}_1 \left(x_1 - \frac{d}{2} \right) \tan(\phi) e^{-\Omega x_2}, \quad (6.94)$$

where \hat{u}_1 is an unknown function to be found, and

$$u_1 = H \tan(\phi), \quad (6.95)$$

where H is a constant to be found. The real parameter $\Omega > 0$ is the rate of decay in the x_2 -direction and the function \hat{u}_1 gives the behaviour in the normal x_1 -direction. The factor of $-d/2$ will later allow symmetry conditions about the midpoint of the block in the x_1 -direction to be applied. As the problem is linear, the resulting deformations will be proportional to $\tan(\phi)$. Using this property, we have written explicitly this dependence on $\tan(\phi)$ and thus removed all ϕ dependence from \hat{u}_1 and the constant solution (6.95). It is noted that we do not look for solutions that are proportional to $\exp(\Omega x_2)$ or are linear or higher order in x_1 or x_2 as these will not satisfy the boundary condition (6.89) as $x_2 \rightarrow \infty$. It is noted that the full solution of u_1 will comprise a summation of all the valid solutions that have the same form as either (6.94) or (6.95).

6.6.4 General Solution for \hat{u}_1

Substituting the expression (6.94) for u_1 into the governing equation (6.88), the following ODE for \hat{u}_1 is derived

$$0 = \hat{u}_1''' + \left[\frac{2(1-\nu)+\bar{\mathcal{F}}}{2(1-\nu)} + \frac{1-2\nu+\bar{\mathcal{F}}}{1-2\nu} \right] \Omega^2 \hat{u}_1'' + \frac{(2(1-\nu)+\bar{\mathcal{F}})(1-2\nu+\bar{\mathcal{F}})}{2(1-\nu)(1-2\nu)} \Omega^4 \hat{u}_1, \quad (6.96)$$

where ' represents a derivative with respect to x_1 . As this is a fourth-order linear ODE with constant coefficients, we seek solutions of the form

$$\hat{u}_1 \left(x_1 - \frac{d}{2} \right) = e^{i\Lambda\Omega(x_1 - \frac{d}{2})}, \quad (6.97)$$

where $\Lambda \in \mathbb{C}$ is to be determined. The factor of Ω is included in the exponential to simplify the calculations that follow. Substituting (6.97) into (6.96), a quadratic equation to be solved for Λ^2 is derived. Solving this quadratic, it is determined that

$$\Lambda^2 = \frac{2(1-\nu)+\bar{\mathcal{F}}}{2(1-\nu)}, \frac{1-2\nu+\bar{\mathcal{F}}}{1-2\nu}. \quad (6.98)$$

As all the parameters within (6.98) are real and $\bar{\mathcal{F}} > 0, \nu < 1/2$, we find $\Lambda^2 > 0$ and thus Λ must be real. Taking the square root of (6.98) yields

$$\Lambda = \pm \sqrt{\frac{2(1-\nu)+\bar{\mathcal{F}}}{2(1-\nu)}}, \pm \sqrt{\frac{1-2\nu+\bar{\mathcal{F}}}{1-2\nu}}. \quad (6.99)$$

Hence, for every value of Ω , we have four corresponding values of Λ , and we find

$$\begin{aligned} \hat{u}_1 = & A \cos \left(\Omega \Lambda_1 \left(x_1 - \frac{d}{2} \right) \right) + B \cos \left(\Omega \Lambda_2 \left(x_1 - \frac{d}{2} \right) \right) \\ & + C \sin \left(\Omega \Lambda_1 \left(x_1 - \frac{d}{2} \right) \right) + D \sin \left(\Omega \Lambda_2 \left(x_1 - \frac{d}{2} \right) \right), \end{aligned} \quad (6.100)$$

where Λ_1, Λ_2 are given by

$$\Lambda_1 = \sqrt{\frac{2(1-\nu)+\bar{\mathcal{F}}}{2(1-\nu)}}, \quad \Lambda_2 = \sqrt{\frac{1-2\nu+\bar{\mathcal{F}}}{1-2\nu}}, \quad (6.101)$$

and A, B, C, D are real constants to be found.

The expression (6.100) for \hat{u}_1 may be simplified further by using the fact that the deformation in the x_1 -direction is symmetric about $x_1 = d/2$. This implies

$$C = D = 0, \quad (6.102)$$

which, when applied to (6.100), yields

$$\hat{u}_1 = A \cos \left(\Omega \Lambda_1 \left(x_1 - \frac{d}{2} \right) \right) + B \cos \left(\Omega \Lambda_2 \left(x_1 - \frac{d}{2} \right) \right). \quad (6.103)$$

Substituting (6.103) into the definition (6.94) of u_1 , the following solution for u_1 is obtained

$$u_1 = \left[A \cos \left(\Omega \Lambda_1 \left(x_1 - \frac{d}{2} \right) \right) + B \cos \left(\Omega \Lambda_2 \left(x_1 - \frac{d}{2} \right) \right) \right] \tan \phi e^{-\Omega x_2}. \quad (6.104)$$

6.6.5 Determining the Decay Rate Ω

The boundary condition (6.91) and integral condition (6.93) on u_1 are now used to find the possible values of the decay rate Ω . Substituting u_1 into both of these and rearranging gives the following relations to be satisfied

$$A[(1-\nu)\Lambda_1 + \nu\alpha] \sin \left(\frac{d\Omega\Lambda_1}{2} \right) + B(1-2\nu)\Lambda_2 \sin \left(\frac{d\Omega\Lambda_2}{2} \right) = 0, \quad (6.105)$$

$$A(1-\alpha\Lambda_1) \cos \left(\frac{d\Omega\Lambda_1}{2} \right) + B(1+\Lambda_2^2) \cos \left(\frac{d\Omega\Lambda_2}{2} \right) = 0, \quad (6.106)$$

where

$$\alpha = (1-2\nu + \bar{\mathcal{F}})\Lambda_1^{-1} - 2(1-\nu)\Lambda_1. \quad (6.107)$$

It is noted that due to the symmetry of u_1 , the boundary condition (6.91) gives the same condition (6.106) at $x_1 = 0$ and $x_1 = d$. The homogeneous conditions (6.105), (6.106) may be written in matrix form like so

$$\begin{pmatrix} \bar{a} & \bar{b} \\ \bar{c} & \bar{d} \end{pmatrix} \begin{pmatrix} A \\ B \end{pmatrix} = \mathbf{0}. \quad (6.108)$$

where

$$\begin{aligned} \bar{a} &= [(1-\nu)\Lambda_1 + \nu\alpha] \sin \left(\frac{d\Omega\Lambda_1}{2} \right), \\ \bar{b} &= (1-2\nu)\Lambda_2 \sin \left(\frac{d\Omega\Lambda_2}{2} \right), \\ \bar{c} &= (1-\alpha\Lambda_1) \cos \left(\frac{d\Omega\Lambda_1}{2} \right), \\ \bar{d} &= (1+\Lambda_2^2) \cos \left(\frac{d\Omega\Lambda_2}{2} \right). \end{aligned}$$

For a non-trivial solution for the constants A, B to exist, we need the determinant of the matrix in (6.108) to be zero. Setting this, we obtain the following eigenvalue equation for Ω

$$\psi_1 \sin \left(\frac{d\Omega\Lambda_1}{2} \right) \cos \left(\frac{d\Omega\Lambda_2}{2} \right) - \psi_2 \sin \left(\frac{d\Omega\Lambda_2}{2} \right) \cos \left(\frac{d\Omega\Lambda_1}{2} \right) = 0, \quad (6.109)$$

where

$$\begin{aligned}\psi_1 &= [(1 - \nu)\Lambda_1 + \nu\alpha](1 + \Lambda_2^2), \\ \psi_2 &= (1 - \alpha\Lambda_1)(1 - 2\nu)\Lambda_2.\end{aligned}$$

Solving the eigenvalue equation (6.109) numerically using Maple, we find countably many eigenvalues for the decay rate Ω . We denote the n th eigenvalue of the decay rate as Ω_n , with Ω_0 being the fundamental eigenvalue. As we have countably many eigenvalues, there are countably many modes for the deformations, each with their own distinct decay rate along the x_2 -direction. Solutions of the first five eigenvalues Ω_n for different values of the scaled pre-stress $\bar{\mathcal{F}}$ in the case $d = 1$, $\nu = 0.49$ are given in Table 6.1. The decay rates Ω_n of the first four modes of the deformations have also been plotted in Figure 6.5. We see from the table and plots that in general, as the pre-stress is increased, the decay rate of all the different modes decreases. The only exception is the fundamental mode where, for small values of $\bar{\mathcal{F}}$, there is an increase in Ω_0 when $\bar{\mathcal{F}}$ is increased. We elaborate on this more in §6.9.

$\bar{\mathcal{F}}$	Ω_0	Ω_1	Ω_2	Ω_3	Ω_4	Ω_5
0.01	0.9343	28.36	58.146	85.10	115.0	141.9
0.1	0.9978	3.939	8.976	14.01	16.94	18.02
1	0.4265	1.317	2.200	3.082	3.971	4.470
10	0.1399	0.4209	0.7017	0.9825	1.263	1.544
100	0.04441	0.1333	0.2221	0.3110	0.3998	0.4887

Table 6.1: The eigenvalues Ω_n of the decay rate in the x_2 -direction for different values of $\bar{\mathcal{F}}$, when $d = 1$, $\nu = 0.49$.

6.6.6 General Solutions for u_1 and u_2

As there are countably many modes for u_1 of the form (6.104), the general solution of the deformation u_1 will be comprised of the summation of all of these modes and the constant solution (6.95) given by $u_1 = H \tan \phi$. It is noted that the constant solution (6.95) satisfies the boundary condition (6.91) on $x_1 = 0, d$ and the integral condition (6.93). Combining these solutions, the

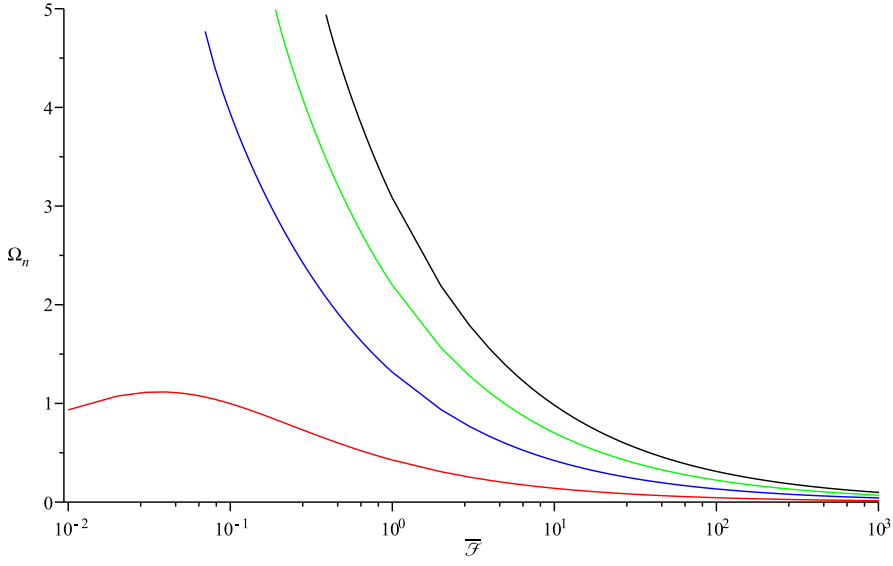


Figure 6.5: The decay rates Ω_n of the first four modes of the deformations u_1, u_2 , against \bar{F} , for $\nu = 0.49, d = 1$. The red, blue, green and black curves correspond to the fundamental, second, third and fourth modes respectively.

general solution of the deformation u_1 is found to be

$$u_1 = \left(\sum_{n=0}^{\infty} A_n \left[\cos \left(\Omega_n \Lambda_1 \left(x_1 - \frac{d}{2} \right) \right) - \frac{\bar{a}_n}{\bar{b}_n} \cos \left(\Omega_n \Lambda_2 \left(x_1 - \frac{d}{2} \right) \right) \right] e^{-\Omega_n x_2} + H \right) \tan \phi. \quad (6.110)$$

The constants A_n are the coefficients corresponding to the n th modes of the deformation, and by relating the coefficients of the two cosine terms within the expression (6.104) for the modes of u_1 using (6.108), we set

$$\begin{aligned} \bar{a}_n &= [(1 - \nu) \Lambda_1 + \nu \alpha] \sin \left(\frac{d \Omega_n \Lambda_1}{2} \right), \\ \bar{b}_n &= (1 - 2\nu) \Lambda_2 \sin \left(\frac{d \Omega_n \Lambda_2}{2} \right). \end{aligned}$$

Substituting the expression (6.110) for u_1 into (6.87), the following general solution for u_2 is derived

$$\begin{aligned} u_2 = \sum_{n=0}^{\infty} A_n \tan(\phi) & \left[\alpha \sin \left(\Omega_n \Lambda_1 \left(x_1 - \frac{d}{2} \right) \right) \right. \\ & \left. + \frac{\bar{a}_n}{\bar{b}_n} \Lambda_2 \sin \left(\Omega_n \Lambda_2 \left(x_1 - \frac{d}{2} \right) \right) \right] e^{-\Omega_n x_2}. \quad (6.111) \end{aligned}$$

6.6.7 Applying the Remaining Conditions

The remaining conditions are now applied to the general solution (6.110) for u_1 . These conditions are the boundary condition (6.90) at $x_2 = 0$ and the integral condition (6.92) over x_2 .

Applying the boundary condition (6.90) to (6.110), we find the following expression for H in terms of the coefficients A_n

$$H = \sum_{n=0}^{\infty} A_n \left[\frac{\bar{a}_n}{\bar{b}_n} \cos \left(\Omega_n \Lambda_2 \left(x_1 - \frac{d}{2} \right) \right) - \cos \left(\Omega_n \Lambda_1 \left(x_1 - \frac{d}{2} \right) \right) \right]. \quad (6.112)$$

This represents both a condition on the coefficients A_n , since the right-hand-side of (6.112) must be constant in x_1 , as well as an expression to determine H . By differentiating (6.112) with respect to x_1 , and setting $x_1 = d/2$ within (6.112), the two conditions may be explicitly shown. Applying these calculations, the following is obtained

$$0 = \sum_{n=0}^{\infty} A_n \Omega_n \left[\Lambda_1 \sin \left(\Omega_n \Lambda_1 \left(x_1 - \frac{d}{2} \right) \right) - \frac{\bar{a}_n}{\bar{b}_n} \Lambda_2 \sin \left(\Omega_n \Lambda_2 \left(x_1 - \frac{d}{2} \right) \right) \right], \quad (6.113)$$

$$H = \sum_{n=0}^{\infty} A_n \left(\frac{\bar{a}_n}{\bar{b}_n} - 1 \right). \quad (6.114)$$

The first of these relations (6.113) is a condition on the coefficients A_n , while (6.114) allows H to be found once the A_n are known.

Substituting the general solution (6.110) for u_1 into the integral condition (6.92), another condition on the coefficients A_n is obtained

$$1 = \sum_{n=0}^{\infty} A_n \Omega_n \left[\alpha \Lambda_1 \cos \left(\Omega_n \Lambda_1 \left(x_1 - \frac{d}{2} \right) \right) + \frac{\bar{a}_n}{\bar{b}_n} \Lambda_2^2 \cos \left(\Omega_n \Lambda_2 \left(x_1 - \frac{d}{2} \right) \right) \right]. \quad (6.115)$$

At first, it appears that we do not have enough degrees of freedom to satisfy the two Fourier like conditions (6.113), (6.115) on A_n , since we have just a single countable set of eigenvalues. However, by following the calculations in Appendix 6.B, it is found that for large \mathcal{F} the eigenvalue equation (6.109) can be approximated by (6.206), that is

$$\psi_1 \sin \left(\frac{d \Omega \Lambda_1}{2} \right) \cos \left(\frac{d \Omega \Lambda_2}{2} \right) \approx 0.$$

Hence, we actually get two coupled sets of solutions for the eigenvalues which correspond to the zeroes of the sine and cosine functions respectively. Although

the two sets are less apparent for $\bar{\mathcal{F}} \lesssim O(1)$, we expect similar behaviour in this case. Because of this, finding a solution may be possible.

A similar situation arises in finding the solution of the biharmonic equation in a semi-infinite strip. This has been studied by Shankar (2003) and details of his work may be found in Appendix 6.C. Shankar (2003) shows how it is possible to decouple the governing biharmonic equation into two coupled ODEs, and find a biorthogonality relation between the eigenfunctions that arise. Using this biorthogonality relation, it is possible to find a solution that satisfies two independent boundary conditions imposed on the short edge of the strip. Thus far, we have been unable to find a similar decomposition and biorthogonality relation for the system (6.42)–(6.46) considered here due to the increased complexity of the governing equation and boundary conditions. However, the same underlying principles hold and may allow a solution to be found.

6.7 Far-field Approximation for $x_2 \rightarrow \infty$

Although a full analytic solution to the system (6.42)–(6.46) has not yet been found, it is possible to determine an approximation for the deformation \mathbf{u} away from $x_2 = 0$, up to a multiplicative constant and constant shift. Near $x_2 = 0$, all modes will be having an effect on the overall deformation. However as we move away from $x_2 = 0$, the higher-order modes all decay more rapidly, so the solution becomes dominated by the fundamental mode. Hence, away from the $x_2 = 0$ boundary we may approximate the deformation using this mode. Taking the fundamental modes of the expressions (6.110) and (6.111) for u_1 and u_2 , we determine approximations for the components of the deformation up to a constant A_0 setting the amplitude of the deformation, and a constant shift H in u_1 . These approximations are given by

$$u_1 = \left(A_0 \left[\cos \left(\Omega_0 \Lambda_1 \left(x_1 - \frac{d}{2} \right) \right) - \frac{\bar{a}_0}{\bar{b}_0} \cos \left(\Omega_0 \Lambda_2 \left(x_1 - \frac{d}{2} \right) \right) \right] e^{-\Omega_0 x_2} + H \right) \tan \phi, \quad (6.116)$$

$$u_2 = A_0 \left[\alpha \sin \left(\Omega_0 \Lambda_1 \left(x_1 - \frac{d}{2} \right) \right) + \frac{\bar{a}_0 \Lambda_2}{\bar{b}_0} \sin \left(\Omega_0 \Lambda_2 \left(x_1 - \frac{d}{2} \right) \right) \right] \tan \phi e^{-\Omega_0 x_2}, \quad (6.117)$$

where H is a constant dependent on all of the A_n via the relation (6.114).

6.8 Comparison of Analytical and Numerical Results

We now see how well the fundamental mode approximations (6.116), (6.117) of the components u_1, u_2 of the deformation agree with the numerical simulations developed in §6.5, away from the clamped $x_2 = 0$ boundary. In order to compare the numerical solutions and analytical approximations, we first define u_1^∞ and u_2^∞ to be

$$u_1^\infty = u_1(x_1, x_{\max}), \quad u_2^\infty = u_2(x_1, x_{\max}), \quad (6.118)$$

in the numerical simulations, and

$$u_1^\infty = H \tan \phi, \quad u_2^\infty = 0, \quad (6.119)$$

in the analytical approximations. Using these definitions, $u_1 - u_1^\infty$ and $u_2 - u_2^\infty$ will tend to zero as $x_2 \rightarrow \infty$ in both the numerical simulations and analytical approximations, and any constant shift in the deformations is removed. The only parameter that then needs to be set is the amplitude A_0 of the analytical approximations. This constant may be set to best fit the amplitude of the analytic approximations to the amplitude of the numerical solutions. In Figures 6.6 and 6.7, the numerical solutions and analytical approximations of $u_1 - u_1^\infty$ and $u_2 - u_2^\infty$ have been plotted.

In Figure 6.6, $u_1 - u_1^\infty$ and $u_2 - u_2^\infty$ have been plotted as functions of x_1 for fixed values of x_2 , and in Figure 6.7, $u_1 - u_1^\infty$ and $u_2 - u_2^\infty$ have been plotted as functions of x_2 for fixed values of x_1 . For both the analytical and numerical results, we have set the width of the block as $d = 1$, the angle of clamping to satisfy $\tan \phi = 1$, the axial tension as $\bar{\mathcal{F}} = 1$ and the Poisson's ratio to be $\nu = 0.49$. In the numerical simulations, the mesh over the domain in question is set to have 100 points in the x_1 -direction and 1000 points in the x_2 -direction. It is also found that $x_{\max} = 20$ is a large enough choice of x_{\max} to simulate the deformations accurately for the chosen parameters. In the analytical approximations, the amplitude A_0 of the deformations is set to be $A_0 = 0.08072$ to fit the analytical approximations to the numerical simulations.

We see from Figure 6.6 that in the x_1 -direction, the numerical solutions and analytical approximations are almost identical to each other, apart from some slight deviation when $x_2 = 2$. This deviation is found near the midpoint of the block for $u_1 - u_1^\infty$ and near the stress-free boundaries for $u_2 - u_2^\infty$. Figure 6.7 again displays that the numerical results and analytical approximations are in good agreement in the x_2 -direction, apart from in a small region near

the clamped boundary $x_2 = 0$. The differences between the two solutions near $x_2 = 0$ are expected due to the higher-order modes, that are neglected in the analytical approximations, having a significant effect on the overall solution for smaller values of x_2 . Hence, by setting the single parameter A_0 in the analytical approximations (6.116) and (6.117) for u_1 and u_2 , we have excellent agreement between the numerical solutions developed in §6.5 and the analytical approximations away from $x_2 = 0$, in both the x_1 and x_2 -directions. This demonstrates that the analytical approximations accurately capture the behaviour of the deformations.

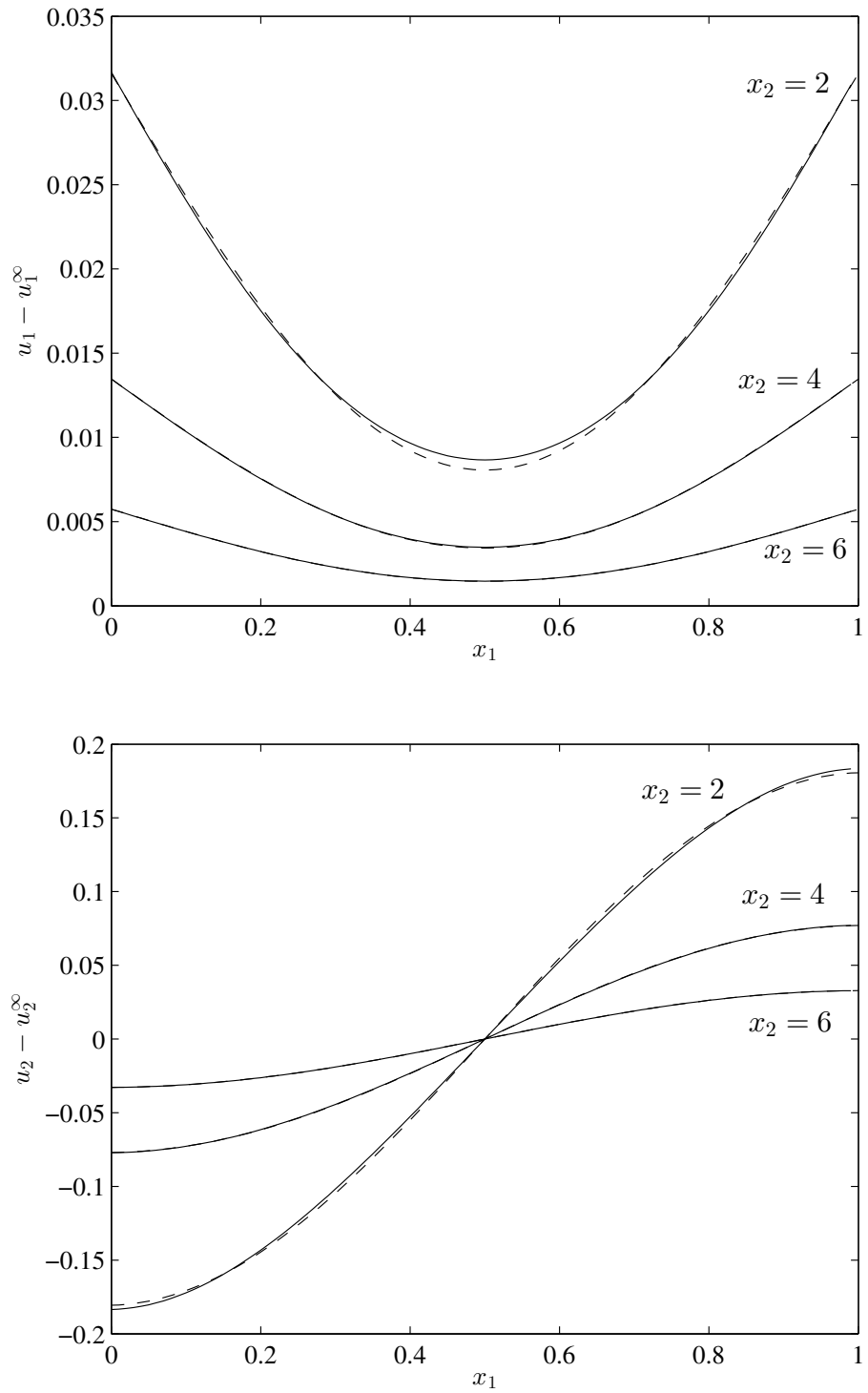


Figure 6.6: The numerical solutions for $u_1 - u_1^\infty$ and $u_2 - u_2^\infty$ across x_1 for fixed values of x_2 , in the case $d = 1$, $\bar{\mathcal{F}} = 1$, $\nu = 0.49$, $\tan \phi = 1$ (solid lines). Also shown are the corresponding analytical approximations (6.116), (6.117) for $u_1 - H \tan \phi$, u_2 , with $A_0 = 0.08072$ (dashed lines).

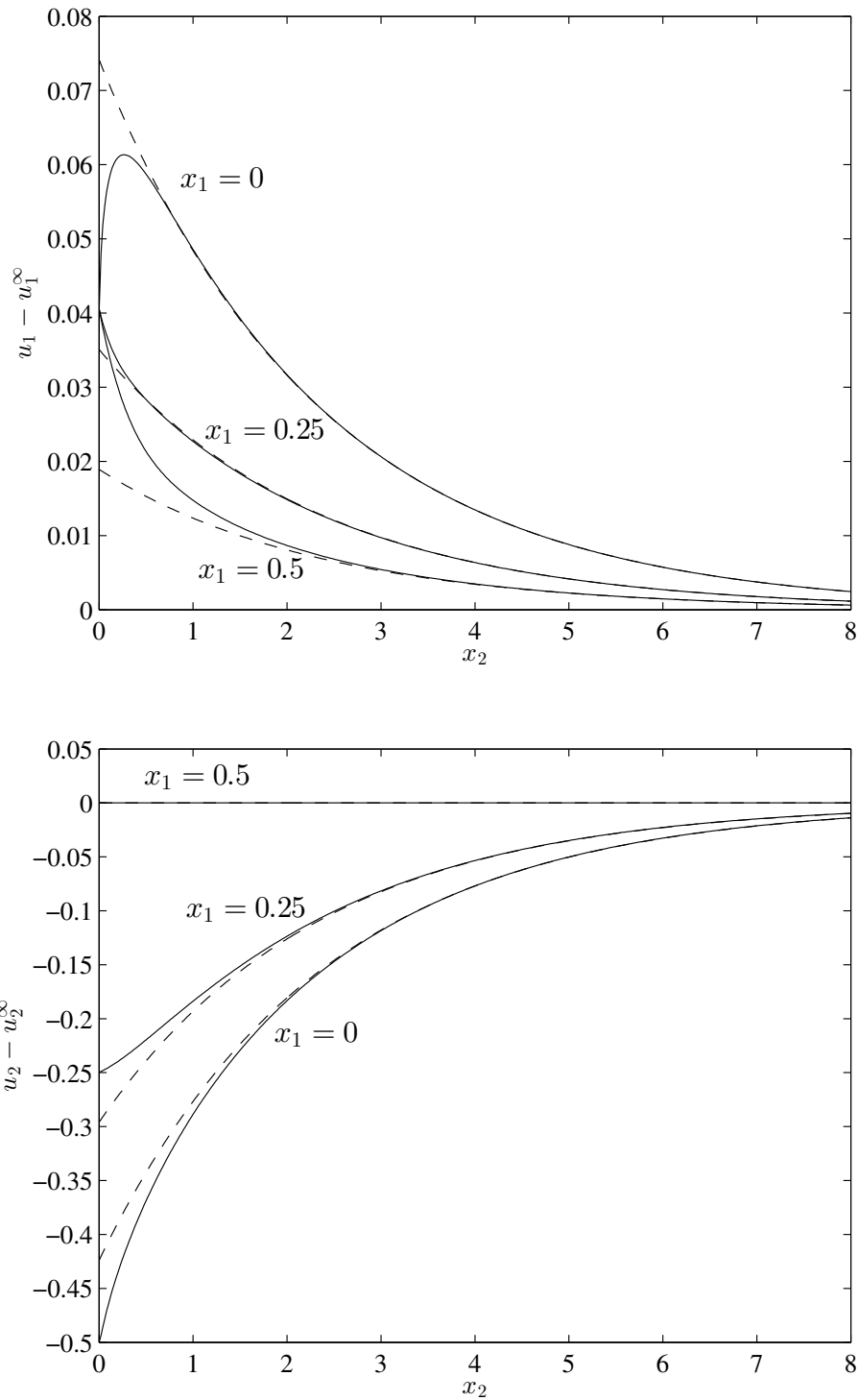


Figure 6.7: The numerical solutions for $u_1 - u_1^\infty$ and $u_2 - u_2^\infty$ across x_2 for fixed values of x_1 , in the case $d = 1$, $\bar{\mathcal{F}} = 1$, $\nu = 0.49$, $\tan \phi = 1$ (solid lines). Also shown are the corresponding analytical approximations (6.116), (6.117) for $u_1 - H \tan \phi$, u_2 , with $A_0 = 0.08072$ (dashed lines).

6.9 The Effect of Varying Axial Tension on the Deformations

We now evaluate the effect that varying the axial tension $\bar{\mathcal{F}}$ has on the deformations. In particular, we focus on how the boundary-layer width of the deformations, and the value u_1^∞ that u_1 takes as $x_2 \rightarrow \infty$, changes as we vary $\bar{\mathcal{F}}$. The behaviour of the boundary-layer width is important as this will let us know if we have an axial-bending layer with the width predicted in the toy model in §3.6, or if we have a different boundary layer with a different width. The value of u_1^∞ is also important as this determines what boundary conditions should be applied to the bulk solution modelled in Chapter 2 at the ends of the elastic-walled tube in the 3D case. As the limits $\bar{\mathcal{F}} \rightarrow 0$ and $\bar{\mathcal{F}} \rightarrow \infty$ correspond to the regimes I ($\delta\ell \ll 1$) and II ($\delta\ell \gg 1$), we can determine if the behaviour of the boundary layer derived here matches with the behaviour of the bending layers found in regime I, studied in Chapters 4 and 5. We can also find what the behaviour of the boundary layer is in regime II, as well as how this boundary layer affects the bulk layer.

6.9.1 Effect of Varying $\bar{\mathcal{F}}$ on the Decay Rate and Boundary-Layer Width

We begin by evaluating the effect that varying $\bar{\mathcal{F}}$ has on the decay rate of the deformations as $x_2 \rightarrow \infty$, and hence the boundary-layer width of the deformations. As the fundamental mode has the smallest value of Ω , it is this mode that has the slowest decay rate. Hence, it is this mode that we need to examine to determine the overall boundary-layer width.

In Figure 6.5, it is observed that for large values of $\bar{\mathcal{F}}$, the fundamental decay rate Ω_0 is always decreasing as $\bar{\mathcal{F}}$ increases. However when $\bar{\mathcal{F}}$ is small, it is seen that Ω_0 increases with increasing $\bar{\mathcal{F}}$. In Appendix 6.B, asymptotic approximations of Ω_0 in the limits $\bar{\mathcal{F}} \rightarrow \infty$ and $\bar{\mathcal{F}} \rightarrow 0$ have been calculated. It is found that

$$\Omega_0 \sim \frac{\pi\sqrt{1-2\nu}}{d} \bar{\mathcal{F}}^{-\frac{1}{2}} \quad \text{as } \bar{\mathcal{F}} \rightarrow \infty, \quad (6.120)$$

and

$$\Omega_0 \sim \left(\frac{6(1-\nu)}{d^2(1-2\nu)} \right)^{\frac{1}{2}} \bar{\mathcal{F}}^{\frac{1}{2}} \quad \text{as } \bar{\mathcal{F}} \rightarrow 0. \quad (6.121)$$

These approximations are in agreement with the behaviour shown by the decay rate Ω_0 of the fundamental mode in Figure 6.5.

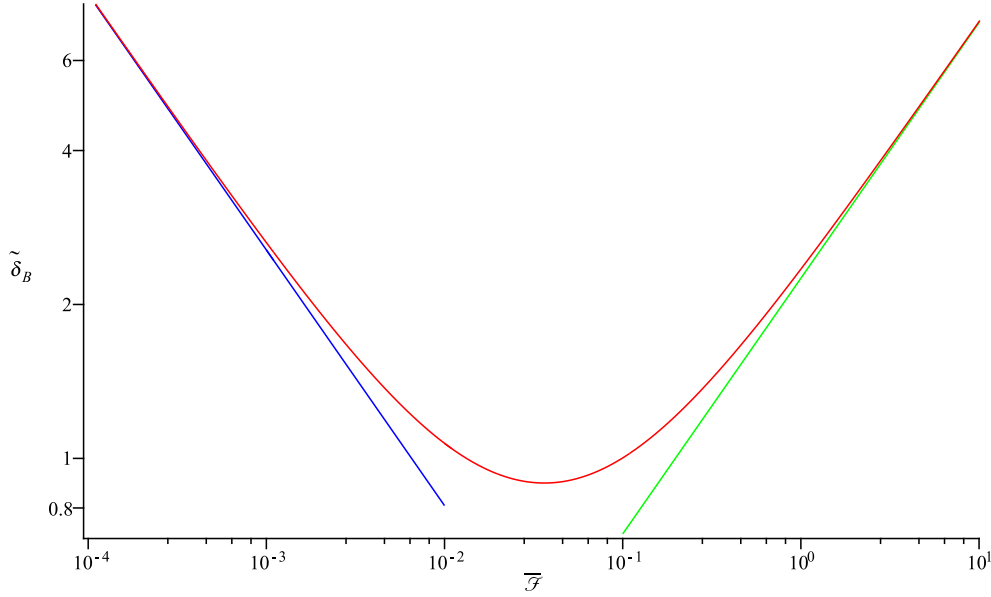


Figure 6.8: The boundary-layer width $\tilde{\delta}_B = 1/\Omega_0$ of the fundamental mode against $\bar{\mathcal{F}}$, for $\nu = 0.49$, $d = 1$ (red line). The asymptotic approximations (6.122), (6.123) of $\tilde{\delta}_B$ in the limits $\bar{\mathcal{F}} \rightarrow \infty$ and $\bar{\mathcal{F}} \rightarrow 0$ have also been plotted in green and blue respectively.

We define the boundary-layer width of the fundamental mode to be $\tilde{\delta}_B = 1/\Omega_0$. Using the numerically found values of Ω_0 calculated in §6.6 and shown in Figure 6.5, $\tilde{\delta}_B$ is calculated and plotted against $\bar{\mathcal{F}}$ in Figure 6.8. From the figure, it is observed that for large tension values, the boundary-layer width is increasing for increasing $\bar{\mathcal{F}}$. However for small enough $\bar{\mathcal{F}}$, the behaviour of the fundamental mode changes, and the boundary-layer width decreases with increasing $\bar{\mathcal{F}}$. Also plotted in Figure 6.8 are the following asymptotic approximations

$$\tilde{\delta}_B \sim \frac{d}{\pi\sqrt{1-2\nu}} \bar{\mathcal{F}}^{\frac{1}{2}} \quad \text{as } \bar{\mathcal{F}} \rightarrow \infty, \quad (6.122)$$

$$\tilde{\delta}_B \sim \left(\frac{1-2\nu}{6(1-\nu)} \right)^{\frac{1}{2}} d \bar{\mathcal{F}}^{-\frac{1}{2}} \quad \text{as } \bar{\mathcal{F}} \rightarrow 0, \quad (6.123)$$

as calculated in Appendix 6.B. We see that there is excellent agreement between the numerically found boundary-layer width and the analytic approximations (6.122), (6.123) for the corresponding sizes of $\bar{\mathcal{F}}$.

We note that in the limits $\bar{\mathcal{F}} \rightarrow 0$ and $\bar{\mathcal{F}} \rightarrow \infty$ (which, by using the expression (6.61) for $\bar{\mathcal{F}}$, correspond to $\delta\ell \ll 1$ and $\delta\ell \gg 1$ respectively), the boundary-layer width $\tilde{\delta}_B$ is larger than the thickness d of the semi-infinite block. This property is also demonstrated by the estimate (3.48) of the boundary-layer

width derived from the toy model in §3.6 when $\delta\ell \ll 1$, as well as by the bending layer widths (4.43), (5.68) derived in regimes I_a and I_B, where $\delta\ell \ll 1$, in Chapters 4 and 5. However, when $\delta\ell \gg 1$, the toy-model estimate (3.48) of the boundary-layer width is smaller than the tube wall thickness, which is different from how $\tilde{\delta}_B$ actually behaves in the limit $\bar{\mathcal{F}} \rightarrow \infty$.

6.9.2 Effect of Varying $\bar{\mathcal{F}}$ on u_1^∞

We now evaluate the effect $\bar{\mathcal{F}}$ has on the limiting value u_1^∞ , defined in (6.118) and (6.119) for the numerical simulations and analytical approximations respectively. We note that in both these cases, the value of u_1^∞ corresponds to the limit $\lim_{x_2 \rightarrow \infty} u_1$. In Figure 6.9, the numerical value of u_1^∞ , given by (6.118), has been plotted against $\bar{\mathcal{F}}$ for two different sets of values for x_{\max} , the largest x_2 value in the numerical domain. This is to ensure that the solutions for these two sets of x_{\max} agree, and the choice of values for x_{\max} is high enough for the numerical simulations to model the deformations accurately. The first set of values we choose for x_{\max} , which we denote $x_{\max 1}$, are

$$x_{\max 1} = \begin{cases} 200 & 10^{-6} \leq \bar{\mathcal{F}} \leq 10^{-4} \\ 20 & 10^{-4} \leq \bar{\mathcal{F}} \leq 1 \\ 50 & 1 \leq \bar{\mathcal{F}} \leq 10^2 \\ 400 & 10^2 \leq \bar{\mathcal{F}} \leq 10^4 \end{cases} \quad (6.124)$$

The second set of values chosen for x_{\max} , which we denote $x_{\max 2}$, are

$$x_{\max 2} = \begin{cases} 400 & 10^{-6} \leq \bar{\mathcal{F}} \leq 10^{-4} \\ 40 & 10^{-4} \leq \bar{\mathcal{F}} \leq 1 \\ 100 & 1 \leq \bar{\mathcal{F}} \leq 10^2 \\ 800 & 10^2 \leq \bar{\mathcal{F}} \leq 10^4 \end{cases} \quad (6.125)$$

We note that $x_{\max 2} = 2x_{\max 1}$. Finally, we have set $\nu = 0.49$, $d = 1$, $\tan(\phi) = 1$ for both cases of x_{\max} .

It is seen in Figure 6.9 that there is excellent agreement between the plots using the two sets of values (6.124) and (6.125) for x_{\max} . As such, the plots are accurately representing the values of u_1^∞ . For both small and large $\bar{\mathcal{F}}$, it is seen that $\log(u_1^\infty)$ increases linearly with increasing $\log(\bar{\mathcal{F}})$. It is later found that these plots have a gradient of $-1/2$ in both cases, meaning that u_1^∞ is behaving like $\bar{\mathcal{F}}^{-1/2}$, for small and large $\bar{\mathcal{F}}$. It is also observed that between $10^{-2} \leq \bar{\mathcal{F}} \leq 1$, there is a transitional region that joins the linearly behaving plots found in the regions with smaller and larger $\bar{\mathcal{F}}$. Within this transitional region, the gradient

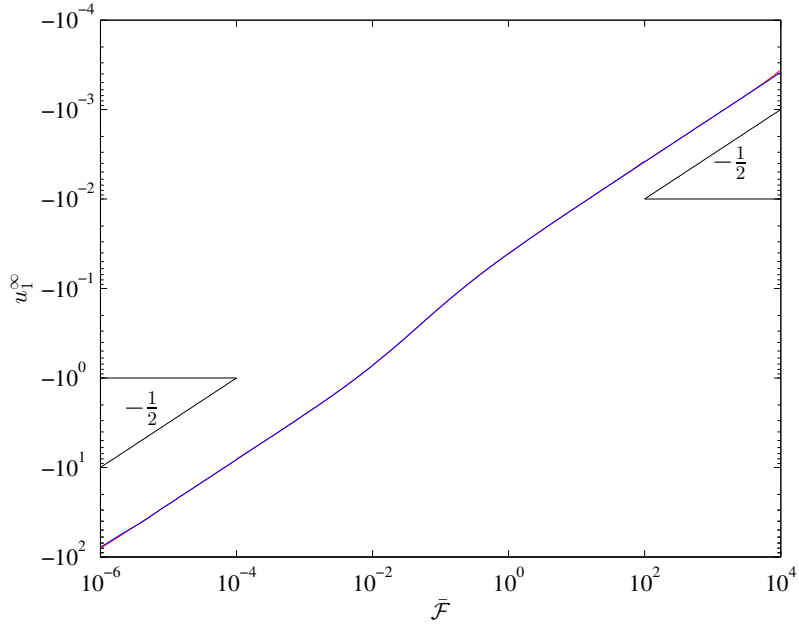


Figure 6.9: The numerical value of u_1^∞ , defined in (6.118), against $\bar{\mathcal{F}}$ for $\nu = 0.49$, $d = 1$, $\tan \phi = 1$. The red line corresponds to setting $x_{\max} = x_{\max 1}$, defined in (6.124), in the numerical simulations, whereas the blue line corresponds to setting $x_{\max} = x_{\max 2}$, defined in (6.125).

of the curve is slowly varying. We now consider further how u_1^∞ behaves for small and large $\bar{\mathcal{F}}$.

6.9.3 Fundamental-Mode Approximation for u_1^∞

We first investigate a possible approximation for u_1^∞ in the limits $\bar{\mathcal{F}} \rightarrow 0$ and $\bar{\mathcal{F}} \rightarrow \infty$. In order for the conditions (6.113), (6.115) on A_n , as well as the relation (6.114) between the A_n and the finite constant H to hold, the sum of the coefficients A_n must converge. It is then assumed that the coefficient A_0 of the fundamental mode is much larger than than coefficients A_n of the higher-order modes that comprise the deformations u_1 and u_2 . (This may or may not be a good assumption.) Making this assumption, we may neglect the higher-order coefficients A_n . This simplifies the expressions (6.113)–(6.115) and allows approximations for A_0 and H to be formed. These approximations may then be used to derive an approximation for u_1^∞ which can be tested against numerical values of u_1^∞ .

Neglecting all the A_n with $n \geq 1$ in the condition (6.115), rearranging, and

setting $x_1 = d/2$ yields the following approximation for A_0

$$A_0 \sim \Omega_0^{-1} \left(\alpha \Lambda_1 + \frac{\bar{a}_0}{\bar{b}_0} \Lambda_2^2 \right)^{-1}, \quad (6.126)$$

where \bar{a}_0, \bar{b}_0 are defined as

$$\bar{a}_0 = [(1 - \nu) \Lambda_1 + \nu \alpha] \sin \left(\frac{d \Omega_0 \Lambda_1}{2} \right), \quad \bar{b}_0 = (1 - 2\nu) \Lambda_2 \sin \left(\frac{d \Omega_0 \Lambda_2}{2} \right), \quad (6.127)$$

as before. It is also found that neglecting all the A_n apart from A_0 in (6.114) gives the following approximation for H

$$H \sim A_0 \left(\frac{\bar{a}_0}{\bar{b}_0} - 1 \right). \quad (6.128)$$

Substituting (6.126), (6.128) into the analytic definition (6.119) for u_1^∞ , we derive the following approximation for u_1^∞

$$u_1^\infty = H \tan \phi \sim \frac{\left(\frac{\bar{a}_0}{\bar{b}_0} - 1 \right) \tan \phi}{\Omega_0 \left(\alpha \Lambda_1 + \frac{\bar{a}_0}{\bar{b}_0} \Lambda_2^2 \right)}. \quad (6.129)$$

To determine how this approximation behaves in the limits $\bar{\mathcal{F}} \rightarrow \infty$ and $\bar{\mathcal{F}} \rightarrow 0$, we use the asymptotic approximations (6.120) and (6.121) of the fundamental decay rate Ω_0 in the limits $\bar{\mathcal{F}} \rightarrow \infty$ and $\bar{\mathcal{F}} \rightarrow 0$, respectively. Substituting (6.120) and (6.121) into (6.129) yields the approximations

$$u_1^\infty \sim \frac{\left(\frac{\bar{a}_0}{\bar{b}_0} - 1 \right) d \bar{\mathcal{F}}^{\frac{1}{2}} \tan \phi}{\pi (1 - 2\nu)^{\frac{1}{2}} \left(\alpha \Lambda_1 + \frac{\bar{a}_0}{\bar{b}_0} \Lambda_2^2 \right)} \quad \text{as} \quad \bar{\mathcal{F}} \rightarrow \infty, \quad (6.130)$$

and

$$u_1^\infty \sim \left(\frac{(1 - 2\nu) \left(\frac{\bar{a}_0}{\bar{b}_0} - 1 \right)^2}{6(1 - \nu) \left(\alpha \Lambda_1 + \frac{\bar{a}_0}{\bar{b}_0} \Lambda_2^2 \right)^2} \right)^{\frac{1}{2}} d \bar{\mathcal{F}}^{-\frac{1}{2}} \tan \phi \quad \text{as} \quad \bar{\mathcal{F}} \rightarrow 0. \quad (6.131)$$

6.9.4 Behaviour of u_1^∞ for Small and Large $\bar{\mathcal{F}}$

The approximations (6.130), (6.131) are now tested against the numerical simulations, starting with the approximation (6.131) as $\bar{\mathcal{F}} \rightarrow 0$. In Figure 6.10, the numerical value of u_1^∞ has been plotted for small $\bar{\mathcal{F}}$, along with the approximation (6.131) of u_1^∞ . From the figure, we see that there is excellent agreement between the numerical solution and the approximation of u_1^∞ , up until we exit the regime of small $\bar{\mathcal{F}}$ at $\bar{\mathcal{F}} = O(10^{-3})$. This indicates that

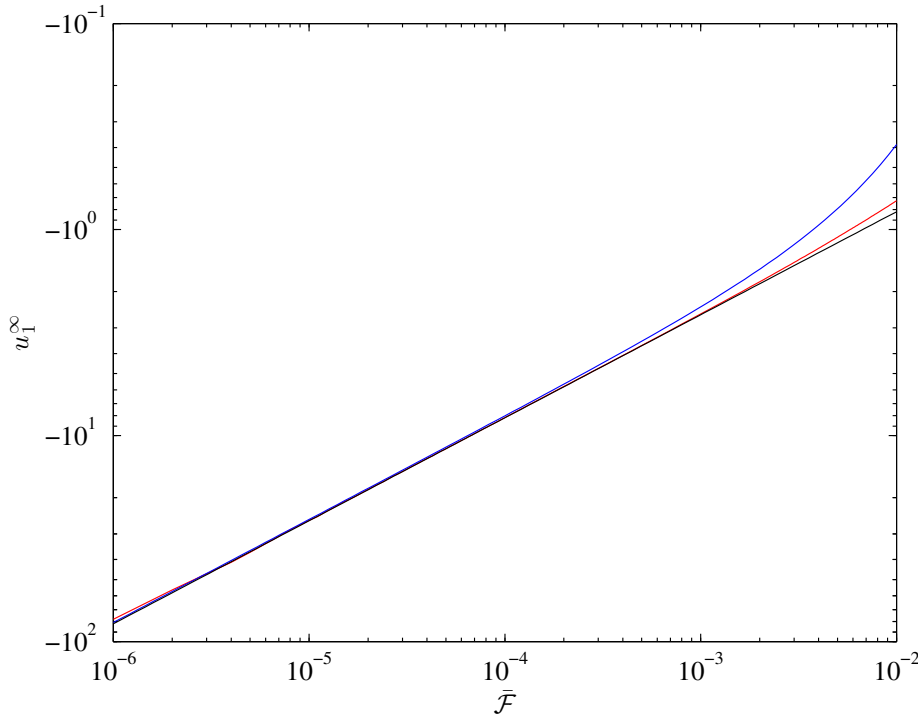


Figure 6.10: The numerical solution for u_1^∞ for small $\bar{\mathcal{F}}$ when $\nu = 0.49$, $d = 1$, $\tan \phi = 1$ (red line). Also plotted is the fundamental-mode approximation (6.131) of u_1^∞ (blue line) and $-0.082\bar{\mathcal{F}}^{-\frac{1}{2}}$ (black line).

simply taking the fundamental mode of the deformation yields an accurate approximation for u_1^∞ when $\bar{\mathcal{F}}$ is small.

Also plotted in Figure 6.10 is $-0.082\bar{\mathcal{F}}^{-\frac{1}{2}}$. It is seen that both the numerical simulation and analytical approximation have the same gradient as $\bar{\mathcal{F}}^{-\frac{1}{2}}$. It is also noted that u_1 , and thus u_1^∞ , must contain a single dimensional parameter d in order for the dimensional deformation to have the dimensions required. This is in agreement with the approximation (6.131). Using this information, it is concluded that

$$u_1^\infty = O(d\bar{\mathcal{F}}^{-\frac{1}{2}}) = O(a\bar{\mathcal{F}}^{-\frac{1}{2}}\ell^{-1}) \quad \text{as } \bar{\mathcal{F}} \rightarrow 0, \quad (6.132)$$

where we have used (6.61) to evaluate the size of $\bar{\mathcal{F}}$. As $u_1^\infty = H \tan \phi$, it is also seen that

$$H = O(a\bar{\mathcal{F}}^{-\frac{1}{2}}\ell^{-1}) \quad \text{as } \bar{\mathcal{F}} \rightarrow 0. \quad (6.133)$$

We now test the approximation (6.130) for u_1^∞ in the limit $\bar{\mathcal{F}} \rightarrow \infty$. In Figure 6.11, the numerical solution of u_1^∞ as well as the approximation (6.130) has been plotted for large $\bar{\mathcal{F}}$. It is seen from the figure that although the curves of the

numerical solution and approximation of u_1^∞ have the same gradient, there is a constant difference between the two. As such the numerical solution and analytical approximation have the same power of $\bar{\mathcal{F}}$ but a different coefficient. This is likely to be due to using only the coefficient A_0 of the fundamental mode when deriving approximation (6.130) of u_1^∞ . As all the other coefficients A_n are neglected, it is possible that a contributing term that has the same order as the true value of u_1^∞ has been lost. This implies that although the fundamental mode gives the correct qualitative behaviour for u_1^∞ as $\bar{\mathcal{F}} \rightarrow \infty$, there are other modes that contribute to u_1^∞ which cannot be neglected.

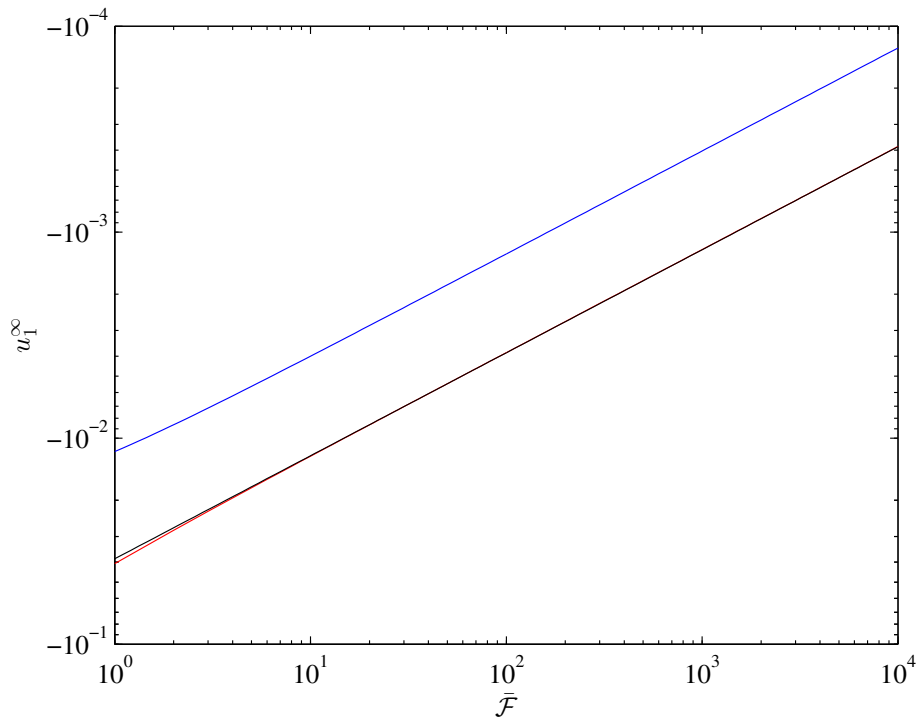


Figure 6.11: The numerical solution for u_1^∞ for large $\bar{\mathcal{F}}$ when $\nu = 0.49$, $d = 1$, $\tan \phi = 1$ (red line). Also plotted is the fundamental-mode approximation (6.130) of u_1^∞ (blue line) and $-0.0385\bar{\mathcal{F}}^{-\frac{1}{2}}$ (black line).

We have also plotted $-0.0385\bar{\mathcal{F}}^{-\frac{1}{2}}$ in Figure 6.11, and we see that the numerical value of u_1^∞ has the same gradient as $\bar{\mathcal{F}}^{-\frac{1}{2}}$. As such, by again noting that u_1^∞ must contain a single dimensional parameter d for the dimensions of u_1^∞ to be consistent, it is concluded that

$$u_1^\infty = O\left(d\bar{\mathcal{F}}^{-\frac{1}{2}}\right) = O\left(a\bar{\mathcal{F}}^{-\frac{1}{2}}\ell^{-1}\right) \quad \text{as } \bar{\mathcal{F}} \rightarrow \infty, \quad (6.134)$$

where once again (6.61) has been applied to evaluate the size of $\bar{\mathcal{F}}$. Again, we

use the fact that $u_1^\infty = H \tan \phi$ to determine

$$H = O\left(a\mathcal{F}^{-\frac{1}{2}}\ell^{-1}\right) \quad \text{as} \quad \mathcal{F} \rightarrow \infty. \quad (6.135)$$

6.10 Applying the 2D Model to the Elastic-Walled Tube

The model for bending a semi-infinite block under tension is now used to model a boundary layer at the ends of the elastic-walled tube considered in Chapters 2 and 3, in the case $\delta\ell \gg 1$ which corresponds to having a large axial tension $\bar{\mathcal{F}}$. By doing so, it is seen what corrections this boundary layer imposes on the bulk solution modelled in Chapter 2. It is noted that contrary to the original estimation of the boundary-layer width (3.48) derived in §3.6, the boundary-layer width grows with increasing $\bar{\mathcal{F}}$ instead of decreases with increasing $\bar{\mathcal{F}}$. Because of this the boundary-layer width is larger than expected and azimuthal variation in the tube wall may not necessarily be small in the boundary layer. As such, it is possible the 2D model studied here may neglect some significant effects arising from azimuthal variation, and it may not model the tube wall correctly near the tube ends. However, it is still informative to apply this model to the tube wall as it will give corrections to the bulk solution which may be tested against numerical simulations of the tube to see if the 2D model is accurately modelling the tube near the tube ends.

6.10.1 Summary of the Set-up of the Elastic-Walled Tube

Before we apply the 2D model to the elastic-walled tube, it is convenient to review the set-up of the tube as described in §2.2.1 (also used by Whittaker *et al.* (2010c)) and depicted in Figure 6.12. As the properties of the fluid within the tube do not contribute to the boundary layer at leading order, or the correction in the bulk layer, we do not describe the properties of the fluid here.

Here, an initially elliptical tube of length L , wall thickness d and circumference $2\pi a$ is set so that the tube axis is aligned with the z^* -axis. We also set x^* to be the dimensional coordinate normal to the undeformed tube wall and perpendicular to z^* . The point $x^* = 0$ is set to be on the inner surface of the tube wall. The ellipticity of the tube is set by a parameter σ_0 , and the tube is split into three regions: two rigid sections occupying $0 < z^* < z_+^*$ and $z_-^* < z^* < 1$, and an elastic-walled section within $z_+^* < z^* < z_-^*$ which is clamped onto the rigid tubes at $z^* = z_+^*, z_-^*$. (It is noted that z_+^* and z_-^* correspond to $z_1 L$ and $z_2 L$ in Chapter 2.)

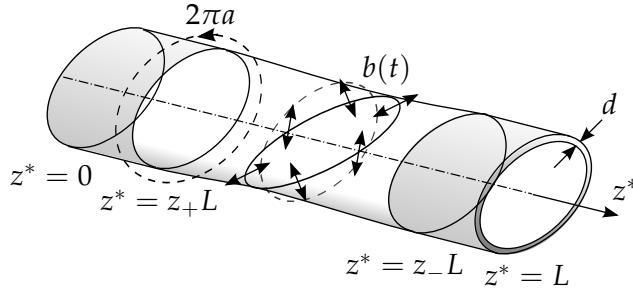


Figure 6.12: The set-up of the tube used by Whittaker *et al.* (2010c). An initially elliptical elastic-walled tube is clamped between two rigid tubes, and oscillates with amplitude $b(t)$.

The elastic-walled region is subject to both a steady deformation and an oscillatory deformation of frequency ω and amplitude $b(t)$, where t is non-dimensional time. (Full details of the non-dimensionalization are found in §2.2.3.) It is assumed that the elastic wall behaves linearly elastically over the range of deformations considered here, and has Poisson's ratio ν , incremental Young's modulus E and bending stiffness K . An axial tension force F is applied at the ends of the elastic-walled tube, yielding a uniform axial pre-stress of $\mathbb{F} = F/(2\pi ad)$ in the undeformed configuration.

The dimensional cross-sectional area of the tube in its deformed and undeformed state is A^* and A_0^* respectively, and \mathbf{r} , \mathbf{r}_0 are the dimensional positions of the tube wall in the deformed and undeformed configuration. The component of the dimensional deformation normal to the tube wall (in the x^* -direction) is then denoted ξ^* .

The following dimensionless parameters are also introduced

$$\ell = \frac{L}{a} \gg 1, \quad \delta = \frac{d}{a} \ll 1, \quad \mathcal{F} = \frac{aF}{2\pi K\ell^2} = O(1), \quad \Delta(t) = \frac{b(t)}{a} \ll 1, \quad (6.136)$$

which correspond to the tube length, wall thickness, axial tension and amplitude of the deformations respectively. In this parameter regime, we have a long, thin-walled tube under large axial tension, subject to small-amplitude, slowly varying deformations. Using the definition of \mathcal{F} , the pre-stress \mathbb{F} may be rewritten as

$$\mathbb{F} = \frac{K\ell^2}{a^3\delta} \mathcal{F},$$

which matches with the pre-stress (6.1) applied to the semi-infinite block in the 2D model.

The dimensional axial coordinate z^* , the axial coordinates z_{\pm}^* of the clamped ends of the elastic-walled tube, and cross-sectional areas A^* , A_0^* in the

deformed and undeformed states are non-dimensionalized with the following scalings

$$z^* = a\ell z, \quad z_\pm^* = a\ell z_\pm, \quad A_0^* = a^2 A_0, \quad A^* = a^2 A. \quad (6.137)$$

As the tube wall is subject first to a steady deformation, and then oscillatory deformations of dimensionless amplitude $\Delta(t)$ about the steady deformed state, Whittaker *et al.* (2010c) decomposed the non-dimensional area variation $A - A_0$ in the following way

$$A(z, t) - A_0 = \frac{1}{\alpha^2 \ell St} \bar{A}(z) + \Delta(t) \operatorname{Re}(\tilde{A}(z) e^{i\omega t}), \quad (6.138)$$

where \bar{A} , \tilde{A} are the non-dimensional components of the area change due to the steady and oscillatory deformations respectively. Multiplying (6.138) by a^2 gives the following dimensional expression for the area variation

$$A^*(z^*, t) - A_0^* = \frac{a^2}{\alpha^2 \ell St} \bar{A}(z^*) + \Delta(t) a^2 \operatorname{Re}(\tilde{A}(z^*) e^{i\omega t}). \quad (6.139)$$

Finally, the midplane of the tube wall is parameterized with dimensional Lagrangian coordinates (x^1, x^2) , which are measures of arc length in the azimuthal and axial directions respectively, in the undeformed state. These are then converted into two dimensionless Lagrangian surface coordinates $\tau \in [0, 2\pi]$, $z \in [0, 1]$ using the relations

$$x^1 = ah(\tau)\tau, \quad x^2 = a\ell z, \quad (6.140)$$

where the scale factor $h(\tau)$ is defined as

$$h(\tau) = c(\sinh^2 \sigma_0 + \sin^2 \tau)^{\frac{1}{2}},$$

and $c(\sigma_0)$ is a known function of the ellipticity parameter σ_0 , defined in (2.1) in §2.2.1.

6.10.2 Relating the Coordinate Systems and Deformations in the 2D and 3D models

One important difference between the 2D model of the semi-infinite block, and the 3D model of the elastic-walled tube, is that the coordinates (x_1, x_2) and normal deformation u_1 used in the 2D model are not aligned with the coordinates (x^*, z^*) and normal deformation ξ^* used in the 3D model. Hence, to apply the 2D model to the 3D model of the elastic-walled tube, relations

must be found between these coordinate systems and deformations. It is noted that as the 3D model is described in terms of the area variation, which only depends on the normal deformation ξ^* , we need only consider determining a relation between ξ^* and the deformations u_1, u_2 in order to determine the corrections to the bulk layer. The azimuthal and axial deformations in the 3D model are therefore not considered here.

In the 2D model, the deformations u_1 and u_2 in the x_1 and x_2 -directions have been defined in (6.110) and (6.111) in terms of the dimensional coordinates x_1 and x_2 . These coordinates are oriented such that x_2 is in the direction of the tension acting on the block (and so in the direction of the centre line of the block at the exit of the boundary layer) and x_1 is perpendicular to x_2 . The origin of this coordinate system is set to be at the bottom corner of the short edge of the block in its undeformed configuration. In the 3D model in Chapter 2, z^* is defined to be the dimensional coordinate aligned with the tube axis, and x^* is a dimensional coordinate both perpendicular to z^* and normal to the surface of the tube wall in its undeformed configuration. The dimensional normal deformation ξ^* is then set as the deformation in the x^* -direction. In Figure 6.13, we see how these sets of coordinates are oriented relative to a 2D cross-section of the elastic tube wall near the clamped boundary $z^* = z_+^*$. The components u_1 and u_2 of the deformation \mathbf{u} of the point \mathbf{O} in the undeformed 2D block to a point \mathbf{P} , as well as the component ξ^* of the deformation $\mathbf{r} - \mathbf{r}_0$ of the point \mathbf{Q} in the undeformed tube wall to the point \mathbf{P} are also displayed. The components of \mathbf{O} , \mathbf{P} and \mathbf{Q} are (x_{1O}, x_{2O}) , (x_{1P}, x_{2P}) and (x_{1Q}, x_{2Q}) in the (x_1, x_2) coordinate system, and (x_{O}^*, z_{O}^*) , (x_{P}^*, z_{P}^*) and (x_{Q}^*, z_{Q}^*) in the (x^*, z^*) coordinate system.

From the figure, it is observed that near the end of the tube wall situated at $z^* = z_+^*$, the coordinates $(x^*, z^* - z_+^*)$ are simply rotations of the coordinates (x_1, x_2) by the small angle of clamping ϕ , about the point $x_1 = x^* = d/2$, $x_2 = z^* - z_+^* = 0$, where the flexible tube joins the rigid tube. Conversely, if we instead consider the end of the tube $z^* = z_-^*$, the coordinates $(x^*, z^* - z_-^*)$ are rotations of (x_1, x_2) by an angle ϕ about $x_1 = x^* = d/2$, $x_2 = z^* - z_-^* = 0$. It is noted that as the angle ϕ is dependent on the azimuthally varying, time-dependent deformations acting on the tube, $\phi = \phi(\tau, t)$ is a function of both τ and t . Using this information, x^* and z^* may be written as the following

$$x^* = \left(x_1 - \frac{d}{2} \right) \cos \phi + x_2 \sin \phi + \frac{d}{2}, \quad z^* - z_{\pm}^* = \pm \left(x_2 \cos \phi - \left(x_1 - \frac{d}{2} \right) \sin \phi \right). \quad (6.141)$$

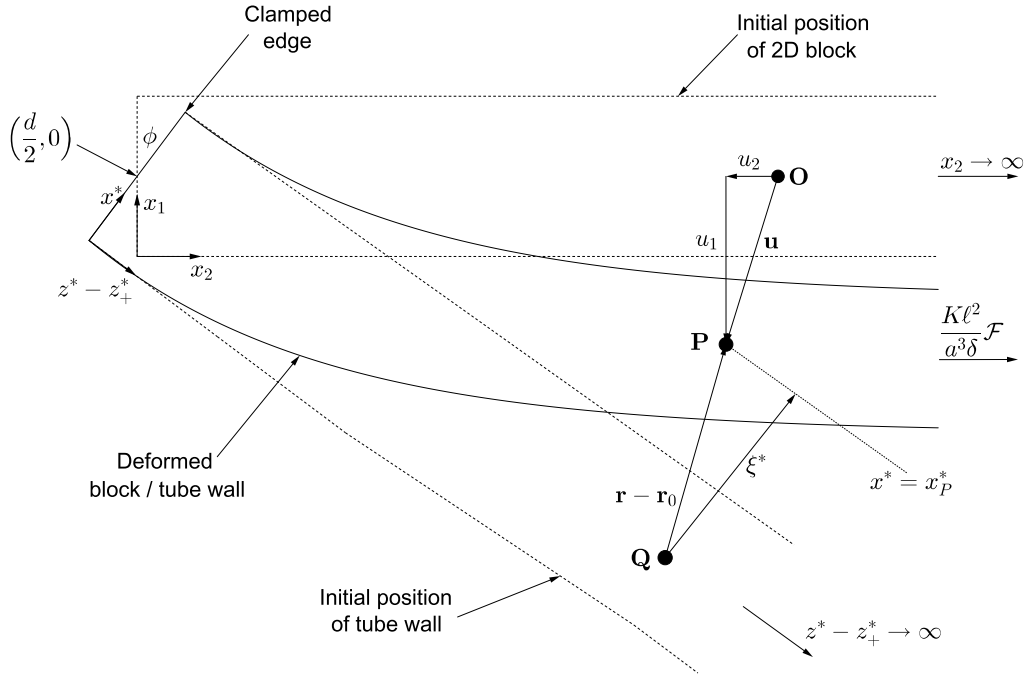


Figure 6.13: Orientation of the coordinates (x_1, x_2) and $(x^*, z^* - z_{\pm}^*)$, as well as the deformations u_1 , u_2 and ξ^* , relative to a 2D cross-section of the tube wall, near the rigid-flexible wall boundary at $z^* = z_{\pm}^*$.

The sign of the rotation in the definition (6.141) of z^* depends on which clamped boundary we are rotating from. At z_{\pm}^* , the flexible tube is in the positive z^* -direction so we must have a positive sign. Conversely, the flexible tube is in the negative z^* -direction from z_{\pm}^* and so the rotation must have a minus sign.

6.10.3 An Expression for ξ^*

We now consider deriving an expression for the normal component ξ^* of the deformation of a point **Q** in the tube wall to some point **P**. To do so, we introduce a point **O** in the undeformed 2D block equivalent to **Q** in the undeformed tube wall. The point **O** then undergoes a deformation **u** to deform to the point **P**. We first set the components of **O** in the (x_1, x_2) coordinate system to be the general points $x_{1O} = x_1$ and $x_{2O} = x_2$. Hence, the coordinates of **O** in the $(x^*, z^* - z_{\pm}^*)$ system are given by the expressions (6.141). In order for **Q** to be the point in the undeformed tube wall equivalent to the point **O** in the 2D block, the components of **Q** in the $(x^*, z^* - z_{\pm}^*)$ system are set to be

$$x_Q^* = x_1, \quad z_Q^* - z_{\pm}^* = \pm x_2. \quad (6.142)$$

As the point \mathbf{P} is a deformation of \mathbf{O} by \mathbf{u} , the coordinates of the deformed point \mathbf{P} in the (x_1, x_2) system are $x_{1P} = x_1 + u_1(x_1, x_2)$ and $x_{2P} = x_2 + u_2(x_1, x_2)$. By applying the expressions (6.141), these coordinates are given in the $(x^*, z^* - z_{\pm}^*)$ system by

$$x_P^* = \left(x_1 + u_1 - \frac{d}{2} \right) \cos \phi + (x_2 + u_2) \sin \phi + \frac{d}{2}, \quad (6.143)$$

$$z_P^* - z_{\pm}^* = \pm \left[(x_2 + u_2) \cos \phi - \left(x_1 + u_1 - \frac{d}{2} \right) \sin \phi \right]. \quad (6.144)$$

The normal component ξ^* of the deformation from \mathbf{Q} to \mathbf{P} is simply

$$\xi^* = x_P^* - x_Q^*. \quad (6.145)$$

Substituting the definitions (6.142) and (6.143) of x_Q^* and x_P^* into (6.145) and rearranging yields

$$\xi^* = \left(x_1 - \frac{d}{2} \right) (\cos \phi - 1) + u_1 \cos \phi + (x_2 + u_2) \sin \phi. \quad (6.146)$$

This expression may be simplified further by rewriting x_2 in terms of $z^* - z_{\pm}^*$. Rearranging the expression (6.141) for z^* gives

$$x_2 = \pm \frac{z^* - z_{\pm}^*}{\cos \phi} + \left(x_1 - \frac{d}{2} \right) \frac{\sin \phi}{\cos \phi}. \quad (6.147)$$

Substituting (6.147) into (6.146), we obtain

$$\begin{aligned} \xi^* &= \left(x_1 - \frac{d}{2} \right) \left(\cos \phi - 1 + \frac{\sin^2 \phi}{\cos \phi} \right) + u_1 \cos \phi + u_2 \sin \phi \pm (z^* - z_{\pm}^*) \tan \phi, \\ &= \left(x_1 - \frac{d}{2} \right) \left(\frac{1 - \cos \phi}{\cos \phi} \right) + u_1 \cos \phi + u_2 \sin \phi \pm (z^* - z_{\pm}^*) \tan \phi. \end{aligned} \quad (6.148)$$

As the range of deformations considered here are assumed to be small, the angle ϕ of clamping is also assumed to be small. With this assumption, we can make the approximation

$$\cos \phi \sim 1. \quad (6.149)$$

Applying this to (6.148), we find

$$\xi^* = u_1 + u_2 \sin \phi \pm (z^* - z_{\pm}^*) \tan \phi, \quad (6.150)$$

and substituting the expressions (6.110) and (6.111) for u_1 and u_2 into (6.150) gives the full expression for ξ^* in the boundary layer as

$$\begin{aligned} \xi^* &= \sum_{n=0}^{\infty} A_n \tan \phi e^{-\Omega_n x_2} \left\{ \cos \left(\Omega_n \Lambda_1 \left(x_1 - \frac{d}{2} \right) \right) - \frac{\bar{a}_n}{\bar{b}_n} \cos \left(\Omega_n \Lambda_2 \left(x_1 - \frac{d}{2} \right) \right) \right. \\ &\quad \left. + \sin \phi \left[\alpha \sin \left(\Omega_n \Lambda_1 \left(x_1 - \frac{d}{2} \right) \right) + \frac{\bar{a}_n}{\bar{b}_n} \Lambda_2 \sin \left(\Omega_n \Lambda_2 \left(x_1 - \frac{d}{2} \right) \right) \right] \right\} \\ &\quad + [H \pm (z^* - z_{\pm}^*)] \tan \phi. \end{aligned} \quad (6.151)$$

In order to use the expression (6.151) for ξ^* to match the boundary layers to the bulk solution, we must determine the behaviour of ξ^* as we exit the boundary layers situated near z_+^* and z_-^* . This corresponds to the limit $x_2 \rightarrow \infty$. By examining the relation (6.141) between z^* and x_2 , it is seen that as $x_2 \rightarrow \infty$, $z^* \rightarrow \infty$ in the boundary layer near z_+^* , and $z^* \rightarrow -\infty$ in the boundary layer near z_-^* . Hence, ξ^* must be evaluated within the boundary layers near z_+^* and z_-^* as $z^* \rightarrow \infty$ and as $z^* \rightarrow -\infty$ respectively. Using the expression (6.147) for x_2 , we find

$$\exp(-\Omega_n x_2) = \exp\left(\mp\Omega_n \frac{z^* - z_\pm^*}{\cos\phi}\right) \exp\left(-\Omega_n \left(x_1 - \frac{d}{2}\right) \tan\phi\right), \quad (6.152)$$

in the boundary layers near $z^* = z_\pm^*$. As $z^* \rightarrow \pm\infty$ within the boundary layers situated near $z^* = z_\pm^*$, (6.152) tends to zero. Hence as we exit the boundary layers, ξ^* behaves as

$$\xi^* \sim [H \pm (z^* - z_\pm^*)] \tan\phi. \quad (6.153)$$

6.10.4 Area Change at the Exit of the Boundary Layers

Now that the behaviour of ξ^* as we exit the boundary layers has been determined, we use this behaviour to see what corrections the boundary layers impose on the bulk region of the tube modelled in Chapter 2. As the model for the bulk region describes the tube in terms of the cross-sectional area variation of the tube, as well as in terms of the pressure and axial velocity of the fluid passing through the tube, it is convenient to determine the area change as we exit the boundary layers so that the corrections to the area change in the bulk solution can be determined.

As a starting point, we use the following relation found by Whittaker *et al.* (2010d) between the cross-sectional area of the elastic-walled tube and the deformation of the tube wall

$$A^*(z^*) - A_0^* = \oint (\mathbf{r} - \mathbf{r}_0) \cdot \hat{\mathbf{n}} a h(\tau) d\tau + O(\Delta^2), \quad (6.154)$$

where $\hat{\mathbf{n}}$ is the outward, normal unit vector to the tube wall in its undeformed state. As the normal component of $\mathbf{r} - \mathbf{r}_0$ is the normal deformation ξ^* , (6.154) is rewritten as

$$A^*(z) - A_0^* = a \int_0^{2\pi} \xi^* h(\tau) d\tau + O(\Delta^2). \quad (6.155)$$

Substituting the expression (6.153) for ξ^* at the exit of the boundary layers into (6.155) gives

$$A^*(z) - A_0^* \sim a \int_0^{2\pi} [H \pm (z^* - z_\pm^*)] h(\tau) \tan\phi d\tau \quad \text{as } z^* \rightarrow \pm\infty, \quad (6.156)$$

in the boundary layers near $z^* = z_\pm^*$. The only parameter in (6.156) that depends on the transverse variable τ , other than $h(\tau)$, is the angle of clamping ϕ , and any term that does not depend on ϕ or $h(\tau)$ may be extracted from the integral. Doing so, (6.156) is rewritten as

$$A^*(z^*) - A_0^* \sim a[H \pm (z^* - z_\pm^*)] \int_0^{2\pi} h(\tau) \tan \phi \, d\tau \quad \text{as } z^* \rightarrow \pm\infty, \quad (6.157)$$

in the boundary layers near $z^* = z_\pm^*$.

As the area change within the bulk region is decomposed into a steady component and oscillatory component, it is convenient to decompose (6.157) into steady and oscillatory components. This can be done by splitting the gradient of clamping $\tan \phi$ as follows

$$\tan \phi = \frac{1}{\alpha^2 \ell S t} \tan \phi_s + \Delta(t) \operatorname{Re}(\tan \phi_o e^{i\omega t}), \quad (6.158)$$

where $\tan \phi_s$ is the gradient of clamping after the steady deformation, and $\tan \phi_o$ is the mode shape of the oscillatory gradient of clamping about the steady configuration. Substituting (6.158) into (6.157) yields

$$A^*(z^*) - A_0^* \sim a[H \pm (z^* - z_\pm^*)] \int_0^{2\pi} h(\tau) \left(\frac{1}{\alpha^2 \ell S t} \tan \phi_s + \Delta(t) \operatorname{Re}(\tan \phi_o e^{i\omega t}) \right) \, d\tau, \quad (6.159)$$

as $z^* \rightarrow \pm\infty$ within the boundary layers near $z^* = z_\pm^*$. Comparing the steady and oscillatory components of (6.159) to the corresponding components in (6.139), we find

$$\bar{A} \sim \frac{H \pm (z^* - z_\pm^*)}{a} \int_0^{2\pi} h(\tau) \tan \phi_s \, d\tau, \quad (6.160)$$

$$\tilde{A} \sim \frac{H \pm (z^* - z_\pm^*)}{a} \int_0^{2\pi} h(\tau) \tan \phi_o \, d\tau, \quad (6.161)$$

as $z^* \rightarrow \pm\infty$ in the boundary layers near $z^* = z_\pm^*$.

6.10.5 Matching the Boundary-Layer Area Change to the Bulk Solution

To match the area change (6.159) as we exit the boundary layers to the area change in the bulk solution, the limit of the area variation in the bulk solution as $z^* \rightarrow z_\pm^*$ must first be determined. From the expression (6.139), the area variation in the bulk layer has a steady component \bar{A} and an oscillatory component \tilde{A} to match onto the boundary layer. These components may be considered separately and we focus first on matching the oscillatory area variation \tilde{A} .

Taking the Taylor series of the oscillatory area \tilde{A} about $z^* = z_\pm^*$, where the clamped boundaries are located, gives

$$\tilde{A}(z^*) = \tilde{A}(z_\pm^*) + (z^* - z_\pm^*) \frac{d\tilde{A}}{dz^*}(z_\pm^*) + \dots \quad \text{as } z^* \rightarrow z_\pm^*. \quad (6.162)$$

By truncating (6.162) after the first-order term and substituting into the oscillatory component (6.161) of the area change as we exit the boundary layers, we obtain

$$\frac{H \pm (z^* - z_\pm^*)}{a} \int_0^{2\pi} h(\tau) \tan \phi_0 d\tau \sim \tilde{A}(z_\pm^*) + (z^* - z_\pm^*) \frac{d\tilde{A}}{dz^*}(z_\pm^*). \quad (6.163)$$

Equating the leading and first-order terms in $z^* - z_\pm^*$ in (6.163) and rearranging gives the following relations

$$\int_0^{2\pi} h(\tau) \tan \phi_0 d\tau = \frac{a}{H} \tilde{A}(z_\pm^*), \quad (6.164)$$

$$\int_0^{2\pi} h(\tau) \tan \phi_0 d\tau = \pm a \frac{d\tilde{A}}{dz^*}(z_\pm^*). \quad (6.165)$$

Eliminating the integral from (6.164) and (6.165) yields the following conditions on \tilde{A}

$$\tilde{A}(z_\pm^*) \mp H \frac{d\tilde{A}}{dz^*}(z_\pm^*) = 0. \quad (6.166)$$

Following a similar method, the new conditions on the steady component \bar{A} of the area variation in the bulk layer are found to be

$$\bar{A}(z_\pm^*) \mp H \frac{d\bar{A}}{dz^*}(z_\pm^*) = 0. \quad (6.167)$$

Hence the new conditions on \bar{A} and \tilde{A} have the same form. As the original conditions imposed by Whittaker *et al.* (2010c) on \bar{A} and \tilde{A} also have the same form as each other, the corrections to the original conditions will take the same form in both the steady and oscillatory components. Thus, we need only consider the corrections to one of these components. Here, we focus on determining the corrections to the boundary conditions on the oscillatory component.

6.10.6 Corrections to the Original Boundary Conditions in the Bulk Layer

To see how the new conditions (6.166) on \tilde{A} are different from the original boundary conditions, and see how large the correction term is, we must non-dimensionalize (6.166). The axial coordinates z^* and z_\pm^* are

non-dimensionalized as in (6.137) and the only parameter left that needs non-dimensionalizing is the dimensional constant H . It was found in §6.9.2 that for $\bar{\mathcal{F}} \rightarrow \infty$

$$H = O\left(a\mathcal{F}^{-\frac{1}{2}}\ell^{-1}\right). \quad (6.168)$$

A sensible scaling for the dimensional constant H is therefore

$$H = \frac{a}{\mathcal{F}^{\frac{1}{2}}\ell}\bar{H}, \quad (6.169)$$

where \bar{H} is an $O(1)$ dimensionless constant. Using the scalings (6.137) and (6.169) in (6.166), the new non-dimensional boundary condition on \tilde{A} in the bulk solution is found to be

$$\tilde{A}(z_{\pm}) \mp \frac{1}{\mathcal{F}^{\frac{1}{2}}\ell^2}\bar{H}\frac{d\tilde{A}}{dz}(z_{\pm}) = 0. \quad (6.170)$$

This condition may be rewritten in terms of the oscillatory transmural pressure $\tilde{p}(z)$ using the following relation

$$\tilde{A} = -\frac{A_0}{\omega^2}\frac{d^2\tilde{p}}{dz^2}, \quad (6.171)$$

which was derived in §2.4. Applying (6.171) to (6.170) and rearranging gives the following boundary conditions on \tilde{p}

$$\frac{d^2\tilde{p}}{dz^2}(z_{\pm}) \mp \frac{1}{\mathcal{F}^{\frac{1}{2}}\ell^2}\bar{H}\frac{d^3\tilde{p}}{dz^3}(z_{\pm}) = 0. \quad (6.172)$$

The original boundary conditions at the clamped ends of the tube, given by (2.85) in §2.5.2, were

$$\frac{d^2\tilde{p}}{dz^2}(z_{\pm}) = 0. \quad (6.173)$$

The new boundary condition (6.172) has a correction term proportional to $d^3\tilde{p}/dz^3$, which has size $O(\mathcal{F}^{\frac{1}{2}}\ell^{-2})$. As $\ell \gg 1$, we have $\ell^{-2} \ll 1$, and as $\mathcal{F} = O(1)$, the new boundary condition (6.172) can only be applied at higher orders within the bulk solution. Hence, there is no change to the original boundary condition (6.173) at leading order, and we would need to calculate the asymptotic solution of the bulk region up to $O(\ell^{-2})$ to evaluate the effects of the correction term. However, if the condition $\mathcal{F} = O(1)$ is relaxed and we allow $\mathcal{F} = O(\ell^{-4})$ or smaller (corresponding to a smaller axial tension force), the correction terms then become significant at leading order. However, as the restoring forces due to pre-stress contribute at leading order in the bulk layer, it is possible that reducing the size of the axial tension will alter the behaviour in the bulk layer, as the axial tension will no longer contribute at leading order there.

6.11 Physical Interpretation

In the model for bending a semi-infinite block under tension, different behaviours are witnessed for small $\bar{\mathcal{F}}$ and large $\bar{\mathcal{F}}$. From (6.123) in §6.9.1, it is seen that in the limit $\bar{\mathcal{F}} \rightarrow 0$, the dimensional boundary-layer width $\tilde{\delta}_B$ has magnitude $O(d\bar{\mathcal{F}}^{-\frac{1}{2}})$. Using the expression (6.61) for $\bar{\mathcal{F}}$, and the dimensionless parameter $\delta = d/a$, this can be rewritten as

$$\tilde{\delta}_B = O\left(\frac{a}{\mathcal{F}^{\frac{1}{2}}\ell}\right). \quad (6.174)$$

By comparing this with the dimensionless bending-layer widths (3.48) from the toy model in §3.6, and (4.43) in regime I_a studied in Chapter 4 (which are dimensionalized by simply multiplying by a), it is seen for small $\bar{\mathcal{F}}$ that the boundary layer here has the same size as the bending layers found in the toy model and in regime I_a, where $\delta\ell \ll 1 \ll \delta\ell^2$. It is also seen later that the axial deformation u_2 is approximately a uniform shear across the width of the block for small $\bar{\mathcal{F}}$, meaning that any transverse shear stresses are negligible. Hence, the deformation of the block must be due to bending effects and the boundary layer modelled here must be an axial-bending boundary layer.

In the limit $\bar{\mathcal{F}} \rightarrow \infty$, it is seen from (6.122) in §6.9.1 that $\tilde{\delta}_B = O(d\bar{\mathcal{F}}^{\frac{1}{2}})$. Again using (6.61) and $\delta = d/a$, this is rewritten as

$$\tilde{\delta}_B = O\left(a\mathcal{F}^{\frac{1}{2}}\delta^2\ell\right). \quad (6.175)$$

This behaviour is different to the behaviour in the limit $\bar{\mathcal{F}} \rightarrow 0$, as well as the behaviours displayed by the toy model in §3.6 and the bending layers modelled in regime I_a ($\delta\ell \ll 1 \ll \delta\ell^2$) and regime I_b ($\delta\ell^2 \ll 1$), in Chapters 4 and 5 respectively. Hence, the boundary layer for large $\bar{\mathcal{F}}$ is due to a different mechanism.

To see what this new mechanism is, the behaviour of u_2 is examined for both small and large $\bar{\mathcal{F}}$ values. In Figure 6.14, the numerical solution for u_2 in the x_1 -direction has been plotted for $\bar{\mathcal{F}} = 10^{-4}$, and $\bar{\mathcal{F}} = 10$. This has been done for $x_2 = 0, 1$ and $x_2 = 75^{\frac{n}{5}}$ where $n = 1, 2, 3, 4$, in the case $d = 1$, $\nu = 0.49$, $\tan(\phi) = 1$. From the figure, it is seen for small $\bar{\mathcal{F}}$ that in the x_1 -direction, there is little deviation in u_2 from a uniform shear over the width of the block, for all values of x_2 . However, in the case with large $\bar{\mathcal{F}}$, for all values of x_2 apart from at the clamped boundary $x_2 = 0$, u_2 appears to be behaving sinusoidally across x_1 , and there is a much larger deviation from uniform shear.

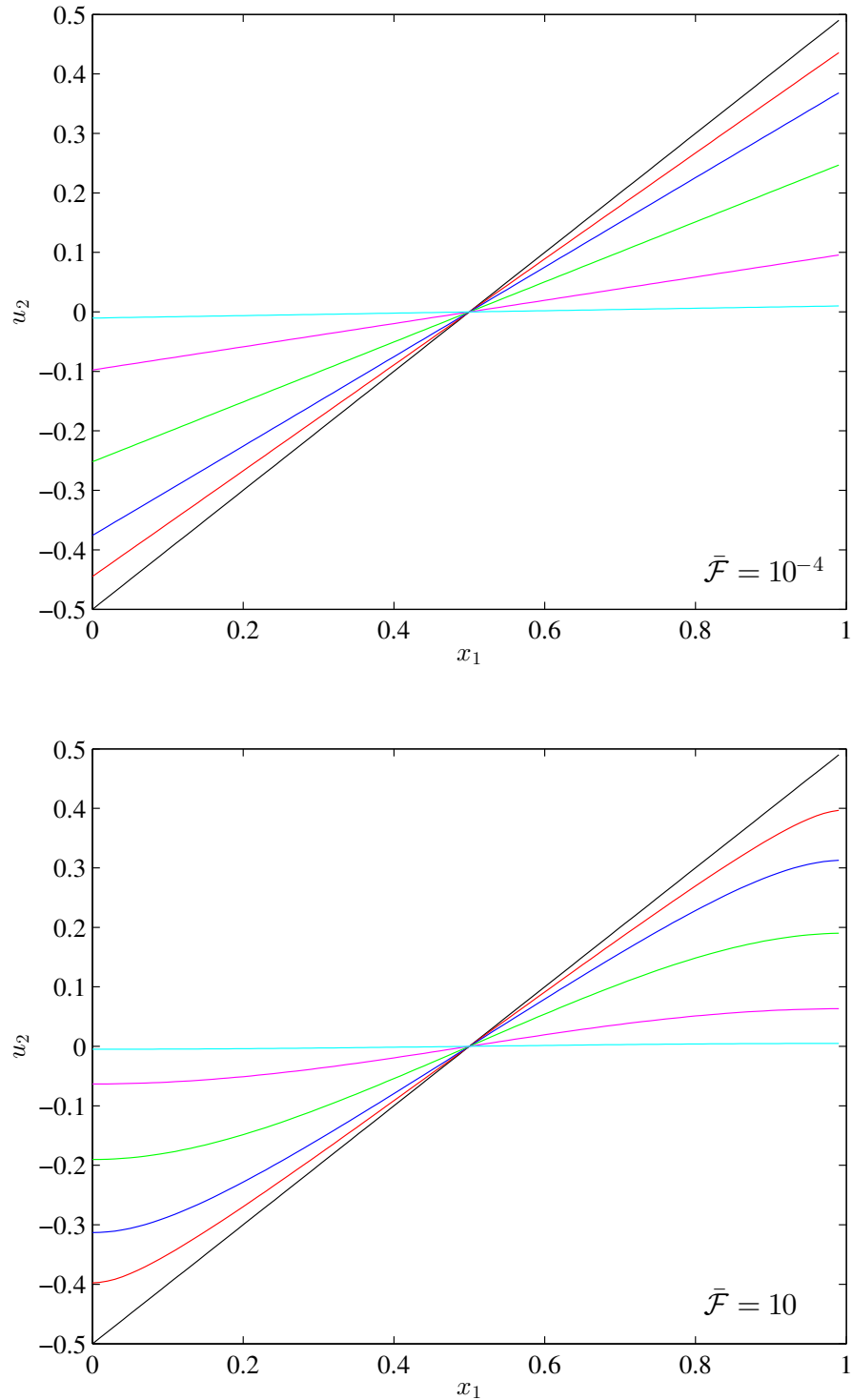


Figure 6.14: The numerical solution of u_2 in the x_1 -direction for small $\bar{\mathcal{F}}$ ($\bar{\mathcal{F}} = 10^{-4}$) and large $\bar{\mathcal{F}}$ ($\bar{\mathcal{F}} = 10$), in the case $d = 1$, $\nu = 0.49$, $\tan(\phi) = 1$, for fixed values of x_2 . The black and red lines correspond to $x_2 = 0, 1$ and the blue, green, pink and cyan lines correspond to $x_2 = 75^{\frac{n}{5}}$, for $n = 1, 2, 3, 4$.

To obtain more information about the deviation from uniform shear for small and large $\bar{\mathcal{F}}$, the following normalisation of u_2 is employed

$$u_2^{(n)} = \frac{u_2(x_1, x_2)}{u_2(d, x_2)} - \frac{2}{d} \left(x_1 - \frac{d}{2} \right). \quad (6.176)$$

In this normalisation, the deformation u_2 is divided by $u_2(d, x_2)$ to ensure that the deformation has the same amplitude at the stress-free boundaries $x_1 = 0, d$, for all values of x_2 . A uniform shear of the same amplitude is then subtracted so the resulting function shows the normalised deviation from a uniform shear.

In Figure 6.15, the numerical solution for $u_2^{(n)}$ in the x_1 -direction is displayed in the case $\bar{\mathcal{F}} = 10$ (large $\bar{\mathcal{F}}$), $d = 1$, $\nu = 0.49$ and $\tan(\phi) = 1$, for $x_2 = 0, 1$ and $x_2 = 75^{\frac{n}{5}}$ where $n = 1, 2, 3, 4$. It is observed from the figure that as the value of x_2 is increased, $u_2^{(n)}$ deviates away from the uniform shear set at the clamped boundary $x_2 = 0$, and tends towards a self-similar form of sinusoidal shape. This self-similar form corresponds to the fundamental mode of the deformation. It is found for small $\bar{\mathcal{F}}$ ($\bar{\mathcal{F}} = 10^{-4}$) that $u_2^{(n)}$ is almost indistinguishable from $u_2^{(n)} = 0$ on the scale used in Figure 6.15, and thus the normalised deviation from uniform shear is negligible.

Finally, the decay of this shear as x_2 is increased is evaluated. This is done by observing the following three quantities. The first quantity is $u_2(d, x_2)$, which corresponds to the amplitude of the deformation u_2 at the stress-free boundary $x_1 = d$. The second quantity is du_2/dx_1 at $x_1 = d/2$, which is the gradient of the deformation in the x_1 -direction at the midpoint of the block, where the gradient is at its highest. The final quantity is

$$\frac{du_2^{(n)}}{dx_1} \left(\frac{d}{2}, x_2 \right) = \frac{\frac{du_2}{dx_1} \left(\frac{d}{2}, x_2 \right)}{u_2(d, x_2)} - \frac{2}{d}, \quad (6.177)$$

which corresponds to the gradient of the normalised deviation from uniform shear, in the x_1 -direction at the midpoint of the block. It is noted that the calculation of this consists of the ratio of the previous two quantities, $u_2(d, x_2)$ and du_2/dx_1 at $x_1 = d/2$, with a constant subtracted.

In Figure 6.16, these three quantities have been plotted for $\bar{\mathcal{F}} = 10$ (large $\bar{\mathcal{F}}$), $d = 1$, $\nu = 0.49$ and $\tan(\phi) = 1$. From the figure, it is seen that u_2 and du_2/dx_1 , at $x_1 = d$ and $x_1 = d/2$ respectively, both decay to zero as x_2 is increased. Hence, the amplitude of the deformation and its gradient in the x_1 -direction are both decaying for increasing x_2 . It is also seen that $du_2^{(n)}/dx_1$ at the midpoint of the block tends to a constant as $x_2 \rightarrow \infty$. Hence, the gradient

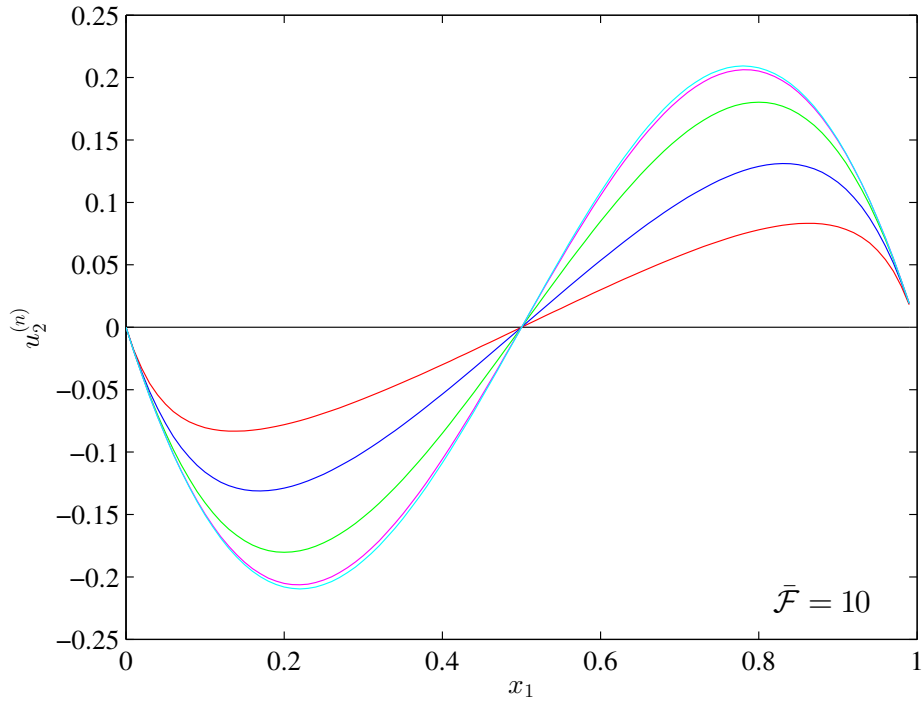


Figure 6.15: The numerical solution of $u_2^{(n)}$ in the x_1 -direction for $\bar{\mathcal{F}} = 10$ (large $\bar{\mathcal{F}}$), in the case $d = 1$, $\nu = 0.49$, $\tan(\phi) = 1$, for fixed values of x_2 . The black and red lines correspond to $x_2 = 0, 1$ and the blue, green, pink and cyan lines correspond to $x_2 = 75^{\frac{n}{5}}$, for $n = 1, 2, 3, 4$.

of the normalised deviation from uniform shear tends to a constant, and the deformation u_2 is indeed tending to a self-similar form.

Overall, it is seen that for small $\bar{\mathcal{F}}$, the boundary layer that occurs is a bending layer. In this bending layer, the deformation u_2 is indistinguishable from a uniform shear across the width of the block that decays as $x_2 \rightarrow \infty$. However when $\bar{\mathcal{F}}$ is large, u_2 varies sinusoidally about a uniform shear across the width of the block. These deviations from uniform shear arise so that the stress-free conditions on the top and bottom boundaries of the block are still satisfied. The variations tend towards a self-similar solution as $x_2 \rightarrow \infty$ and the boundary layer then allows for the decay of this self-similar solution in the axial direction. Hence, the boundary layer is allowing u_2 to deviate away from uniform shear across the width of the block, and thus we have a transverse shear-relaxation layer. It is noted that this boundary layer is different from the shear-relaxation boundary layer studied by Whittaker (2015), which deals with shear in the azimuthal direction of the elastic-walled tube. The difference

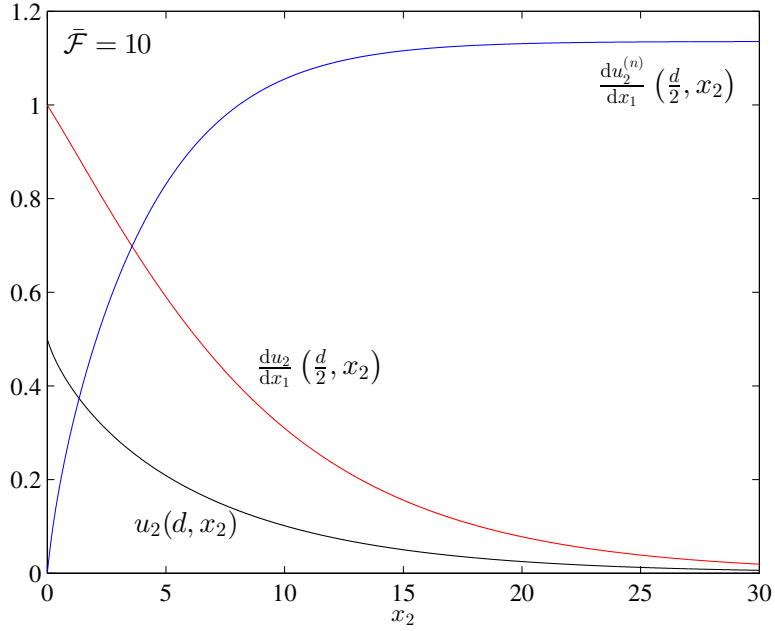


Figure 6.16: The numerical solutions of u_2 (black line) at $x_1 = d$, du_2/dx_1 (red line) at $x_1 = d/2$, and $du_2^{(n)}/dx_1$ (blue line) at $x_1 = d/2$, in the x_2 -direction, for $\bar{\mathcal{F}} = 10$ (large $\bar{\mathcal{F}}$), $d = 1$, $\nu = 0.49$ and $\tan(\phi) = 1$.

between the boundary layers for small and large $\bar{\mathcal{F}}$ is depicted in Figure 6.17.

6.12 Conclusions

In this chapter, we have considered deriving a model to describe the behaviour near the clamped ends of the elastic-walled tube modelled in Chapter 2, in regime II where $\delta\ell \gg 1$. In this regime, it was originally predicted by the toy model in §3.6 that a bending layer of dimensionless width $\delta_B \ll \delta$ would reside at the tube ends. As such, it was originally expected that the boundary layer would be smaller than the thickness of the block, and Kirchhoff–Love shell theory (Flügge, 1972; Søndergaard, 2007) could not be used to model the mechanics of the tube wall. Instead, a linearised 2D model describing the mechanics of a semi-infinite block being bent under tension has been derived. It was initially expected that this would be a good representation of a cross-section of the tube wall in the normal and axial directions, as there would be slow azimuthal variation within a boundary layer of width $\delta_B \ll \delta$. However, in this 2D model, a larger transverse shear-relaxation layer has been

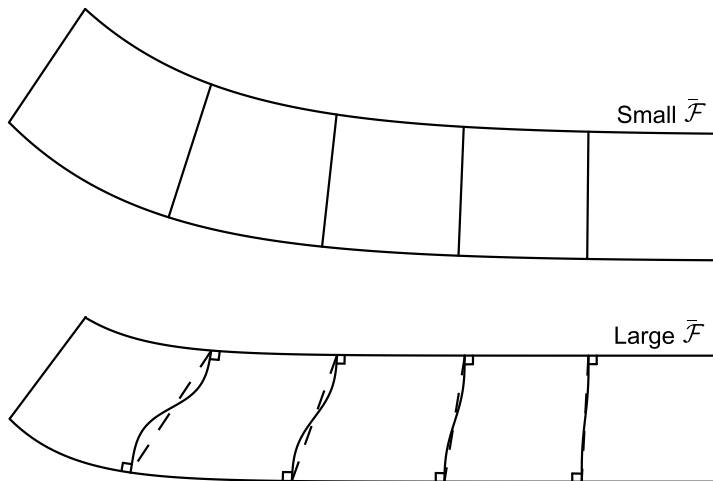


Figure 6.17: Sketch of the different shapes of u_2 for small and large \bar{F} . For small \bar{F} , u_2 is indistinguishable from a uniform shear. For large \bar{F} , u_2 first evolves into a sinusoidal deviation from uniform shear, which then decays as $x_2 \rightarrow \infty$.

found when $\delta\ell \gg 1$. The properties of this shear layer have been evaluated, and although this layer is of a size that azimuthal variation may be important, the 2D model has been applied to the elastic-walled tube and corrections to the boundary conditions of the bulk layer have been calculated. These corrections can be tested against numerical simulations in future work.

In the 2D model, Cauchy's momentum equation in absence of external forces (Howell *et al.*, 2009) is used as a governing equation for the wall mechanics, and a modified Saint Venant–Kirchhoff model (Howell *et al.*, 2009, p. 230) is used to derive an appropriate constitutive law for the Cauchy stress tensor σ . This linearised 2D model has been solved numerically using the numerical finite-element differential equation solver "FEniCS" (Dupont *et al.*, 2003), and analytical techniques have also been applied to the model. With these analytical techniques, approximations for the normal deformation u_1 and axial deformation u_2 , away from the clamped boundary $x_2 = 0$, have been derived and these have been shown to be in agreement with the numerical solutions. A full analytical solution satisfying the clamped boundary conditions (6.43) at $x_2 = 0$ has not yet been derived. However, it is possible that a similar technique to that used by Shankar (2003) to solve the biharmonic equation in a semi-infinite strip, detailed in Appendix 6.C, could be used to obtain the full solution.

It has been found that the deformations u_1 and u_2 are composed of a series of modes, each of which decay exponentially in the axial direction with

their own unique decay rate. It was determined that for all values of the scaled pre-stress $\bar{\mathcal{F}} = O(\delta^2 \ell^2 \mathcal{F})$, the decay rates of the higher-order modes all decrease with increasing $\bar{\mathcal{F}}$. However, the decay rate Ω_0 of the fundamental mode, is found to have different behaviours for small and large $\bar{\mathcal{F}}$. By forming asymptotic approximations of Ω_0 for small and large $\bar{\mathcal{F}}$, it was found that in the limit $\bar{\mathcal{F}} \rightarrow 0$, Ω_0 behaves as $\Omega_0 \sim d^{-1} \bar{\mathcal{F}}^{\frac{1}{2}}$, and in the limit $\bar{\mathcal{F}} \rightarrow \infty$, the asymptotic behaviour of Ω_0 is given by $\Omega_0 \sim d^{-1} \bar{\mathcal{F}}^{-\frac{1}{2}}$.

Using the approximations for Ω_0 , the dimensional boundary-layer width $\tilde{\delta}_B$ was determined to behave as $\tilde{\delta}_B \sim d \bar{\mathcal{F}}^{-\frac{1}{2}}$ as $\bar{\mathcal{F}} \rightarrow 0$, and $\tilde{\delta}_B \sim d \bar{\mathcal{F}}^{\frac{1}{2}}$ as $\bar{\mathcal{F}} \rightarrow \infty$. Using the expression (6.61) and noting that d can be written as $d = a\delta$, the asymptotic behaviours of $\tilde{\delta}_B$ may be rewritten as

$$\tilde{\delta}_B \sim O(a\ell^{-1} \mathcal{F}^{-\frac{1}{2}}) \quad \text{as } \delta\ell \rightarrow 0, \quad (6.178)$$

$$\tilde{\delta}_B \sim O(a\delta^2 \ell \mathcal{F}^{\frac{1}{2}}) \quad \text{as } \delta\ell \rightarrow \infty. \quad (6.179)$$

The behaviour (6.178) for $\delta\ell \rightarrow 0$ is the same as the behaviours (3.48) and (4.43) of the widths of the bending layers in the toy model in §3.6 and the bending layer in regime I_a ($\delta\ell \ll 1 \ll \delta\ell^2$). This behaviour is also different from the behaviour (5.68) of the bending layer in regime I_b ($\delta\ell^2 \ll 1$). This is because azimuthal effects that are neglected in this model are found to contribute at leading-order in regime I_b. However, the behaviour (6.179) of $\tilde{\delta}_B$ as $\delta\ell \rightarrow \infty$ does not match with the behaviour of any of the previous boundary layers considered.

It has also been found that as $x_2 \rightarrow \infty$, u_1 tends to some constant u_1^∞ whereas $u_2 \rightarrow 0$. It is determined that for both small and large $\bar{\mathcal{F}}$, $u_1^\infty = O(d \bar{\mathcal{F}}^{-\frac{1}{2}})$ and the asymptotic behaviour of u_1^∞ does not differ between the cases with small and large $\bar{\mathcal{F}}$.

This 2D model has been used to determine corrections to the boundary conditions imposed on the bulk layer of the elastic-walled tube modelled in Chapter 2. It is found that when $\mathcal{F} = O(1)$, the corrections are a factor of ℓ^{-2} smaller than the leading-order boundary condition. Hence, the correction term does not affect the leading-order bulk layer solution, but does affect the solution at $O(\ell^{-2})$ and higher. Hence, to determine the effects of this correction, an asymptotic solution of the bulk layer would need to be calculated up to $O(\ell^{-2})$. To increase the size of these corrections so that they have an effect at leading order in the bulk of the tube, it was seen that the condition $\mathcal{F} = O(1)$ must be replaced with $\mathcal{F} = O(\ell^{-4})$, corresponding to a smaller axial tension force. Introducing this parameter regime may however change the behaviour

of the bulk solution. It is noted that as there is a possibility that azimuthal variation, neglected in the 2D model, could have a leading-order effect at the scale of the boundary layer, these corrections may not be accurate. To determine the validity of these corrections, the corrected solution could be tested against numerical simulations, or the sizes of the neglected azimuthal effects could be evaluated to see if they contribute at leading order on the axial scale of the boundary layer. Even if this 2D model does not yield valid corrections to the bulk layer of the elastic-walled tube, this model can still be applied to more general problems of clamped shells under tension.

Finally, by examining the behaviour of u_2 for both small and large $\bar{\mathcal{F}}$, the dominant mechanism within this boundary layer has been found. For small $\bar{\mathcal{F}}$, there is very little difference between u_2 and a uniform shear across the width of the block. However for large $\bar{\mathcal{F}}$, the deviation of u_2 from a uniform shear is much larger and tends towards a decaying self-similar solution as $x_2 \rightarrow \infty$. Hence, the boundary layer in the case $\delta\ell \gg 1$ allows deviation away from uniform shear across the block, and we have a transverse shear-relaxation layer. This shear layer is different from that modelled by Whittaker (2015).

6.A Deriving the Boundary Condition (6.71) as $x_2 \rightarrow \infty$

Here, the governing equation (6.42) and boundary conditions (6.44)–(6.46) are used to prove that in the current problem the original boundary condition (6.46), which states

$$\sigma_1 \cdot \begin{pmatrix} 0 \\ 1 \end{pmatrix} \rightarrow \mathbf{0} \quad \text{as } x_2 \rightarrow \infty, \quad (6.180)$$

is equivalent to the condition (6.71) used in §6.6, which is

$$\nabla u_1, \nabla u_2 \rightarrow \mathbf{0} \quad \text{as } x_2 \rightarrow \infty. \quad (6.181)$$

We note that if $\nabla u_1, \nabla u_2 \rightarrow \mathbf{0}$ as $x_2 \rightarrow \infty$, then from the definition (6.25) of σ_1 we must have $\sigma_1 \rightarrow 0$ as $x_2 \rightarrow \infty$, and this implies the condition (6.180). Now we consider proving that (6.180) implies (6.181).

We start with the governing equation (6.42) which is valid in all areas of the block

$$\nabla \cdot \sigma_1 = \frac{\partial}{\partial x_1} \left(\sigma_1 \cdot \begin{pmatrix} 1 \\ 0 \end{pmatrix} \right) + \frac{\partial}{\partial x_2} \left(\sigma_1 \cdot \begin{pmatrix} 0 \\ 1 \end{pmatrix} \right) = \mathbf{0}. \quad (6.182)$$

In §6.6, it was shown that the deformation u_2 can be eliminated from the components of (6.42), leaving a homogeneous, fourth-order PDE with constant coefficients to be solved for u_1 . Similarly, it can be shown that eliminating u_1 from the components of (6.42) yields a homogeneous, fourth-order PDE with constant coefficients to be solved for u_2 . For u_1 and u_2 to satisfy their corresponding governing PDEs, they must have either sinusoidal or exponential behaviour in the x_1 and x_2 -directions, or be cubic or lower order in x_1, x_2 . With this information, the condition (6.180) then implies

$$\frac{\partial}{\partial x_2} \left(\sigma_1 \cdot \begin{pmatrix} 0 \\ 1 \end{pmatrix} \right) \rightarrow \mathbf{0} \quad \text{as } x_2 \rightarrow \infty. \quad (6.183)$$

Applying (6.183) to (6.182), it is found that

$$\frac{\partial}{\partial x_1} \left(\sigma_1 \cdot \begin{pmatrix} 1 \\ 0 \end{pmatrix} \right) \rightarrow \mathbf{0} \quad \text{as } x_2 \rightarrow \infty,$$

and hence

$$\sigma_1 \cdot \begin{pmatrix} 1 \\ 0 \end{pmatrix} \sim \mathbf{A}(x_2) \quad \text{as } x_2 \rightarrow \infty, \quad (6.184)$$

where \mathbf{A} is a function of x_2 . To determine \mathbf{A} , we use the stress-free boundary conditions (6.44), (6.45), which state

$$\sigma_1 \cdot \begin{pmatrix} 1 \\ 0 \end{pmatrix} = \begin{pmatrix} 0 \\ \mathbb{F} \frac{\partial u_1}{\partial x_2} \end{pmatrix} \quad \text{at} \quad x_1 = 0, d. \quad (6.185)$$

As \mathbf{A} is independent of x_1 , applying (6.185) to (6.184) yields

$$\mathbf{A} = \begin{pmatrix} 0 \\ \mathbb{F} \frac{\partial u_1}{\partial x_2} \Big|_{x_1=0} \end{pmatrix}. \quad (6.186)$$

(It is noted that due to the symmetry of the boundary conditions (6.43)–(6.46) and the form of the governing equation (6.42), u_1 is symmetric about $x_1 = d/2$, and hence $\partial u_1 / \partial x_2$ is also symmetric about $x_1 = d/2$. Because of this the value of $\partial u_1 / \partial x_2$ is the same at $x_1 = 0, d$, and both the conditions within (6.185) give the value (6.186) for $\mathbf{A}(x_2)$.)

Using the definition (6.186) of \mathbf{A} along with the conditions (6.180) and (6.184), it is determined that

$$\sigma_1 \sim \begin{pmatrix} 0 & 0 \\ \mathbb{F} \frac{\partial u_1}{\partial x_2} \Big|_{x_1=0} & 0 \end{pmatrix}, \quad \text{as} \quad x_2 \rightarrow \infty. \quad (6.187)$$

Substituting the definition (6.25) of σ_1 into (6.187), each of the components of (6.187) give a condition to be satisfied as $x_2 \rightarrow \infty$. These conditions are

$$(\lambda + 2\mu) \frac{\partial u_1}{\partial x_1} + \lambda \frac{\partial u_2}{\partial x_2} \rightarrow 0 \quad \text{as} \quad x_2 \rightarrow \infty, \quad (6.188)$$

$$(\lambda - \mathbb{F}) \frac{\partial u_1}{\partial x_1} + (\lambda + 2\mu + \mathbb{F}) \frac{\partial u_2}{\partial x_2} \rightarrow 0 \quad \text{as} \quad x_2 \rightarrow \infty, \quad (6.189)$$

$$(\mu + \mathbb{F}) \frac{\partial u_1}{\partial x_2} + \mu \frac{\partial u_2}{\partial x_1} \rightarrow 0 \quad \text{as} \quad x_2 \rightarrow \infty, \quad (6.190)$$

$$(\mu + \mathbb{F}) \frac{\partial u_1}{\partial x_2} + \mu \frac{\partial u_2}{\partial x_1} \rightarrow \mathbb{F} \frac{\partial u_1}{\partial x_2} \Big|_{x_1=0} \quad \text{as} \quad x_2 \rightarrow \infty. \quad (6.191)$$

As the conditions (6.188) and (6.189) are homogeneous conditions involving the terms $\partial u_1 / \partial x_1$ and $\partial u_2 / \partial x_2$, these may be combined and written in matrix form. Doing so gives

$$\begin{pmatrix} \lambda + 2\mu & \lambda \\ \lambda - \mathbb{F} & \lambda + 2\mu + \mathbb{F} \end{pmatrix} \cdot \begin{pmatrix} \frac{\partial u_1}{\partial x_1} \\ \frac{\partial u_2}{\partial x_2} \end{pmatrix} \rightarrow \mathbf{0} \quad \text{as} \quad x_2 \rightarrow \infty. \quad (6.192)$$

Taking the determinant of the matrix within (6.192), we obtain

$$\begin{aligned} \begin{vmatrix} \lambda + 2\mu & \lambda \\ \lambda - \mathbb{F} & \lambda + 2\mu + \mathbb{F} \end{vmatrix} &= (\lambda + 2\mu)(\lambda + 2\mu + \mathbb{F}) - \lambda(\lambda - \mathbb{F}) \\ &= 2(\lambda + \mu)(\mathbb{F} + 2\mu). \end{aligned}$$

In the current scenario, the Lamé parameters satisfy $\mu, \lambda + \mu > 0$. Hence, as long as the axial tension is set such that $\mathbb{F} > 0$, corresponding to a stretching force rather than a compression force, we have

$$\begin{vmatrix} \lambda + 2\mu & \lambda \\ \lambda - \mathbb{F} & \lambda + 2\mu + \mathbb{F} \end{vmatrix} = 2(\lambda + \mu)(\mathbb{F} + 2\mu) \neq 0.$$

Thus, for (6.192) to be satisfied, it follows that

$$\frac{\partial u_1}{\partial x_1}, \frac{\partial u_2}{\partial x_2} \rightarrow 0 \quad \text{as } x_2 \rightarrow \infty. \quad (6.193)$$

We now proceed to apply a similar method to the conditions (6.190), (6.191) to obtain similar constraints on $\partial u_1 / \partial x_2$ and $\partial u_2 / \partial x_1$. We first use the condition (6.193) on $\partial u_1 / \partial x_1$ to rewrite the term on the right-hand-side of (6.191) in a way that it can be combined with the terms on the left-hand-side. Using the fact that $\partial u_1 / \partial x_1 \rightarrow 0$ as $x_2 \rightarrow \infty$, and that u_1 has sinusoidal or exponential behaviour, or is cubic or lower order in x_1, x_2 , this implies

$$\frac{\partial}{\partial x_2} \left(\frac{\partial u_1}{\partial x_1} \right) \rightarrow 0 \quad \text{as } x_2 \rightarrow \infty, \quad \Rightarrow \quad \frac{\partial}{\partial x_1} \left(\frac{\partial u_1}{\partial x_2} \right) \rightarrow 0 \quad \text{as } x_2 \rightarrow \infty.$$

From this, we see that there is negligible variation in $\partial u_1 / \partial x_2$ in the x_1 -direction as $x_2 \rightarrow \infty$. Hence, we must have

$$\frac{\partial u_1}{\partial x_2} \Big|_{x_1=0} \sim \frac{\partial u_1}{\partial x_2} \quad \text{as } x_2 \rightarrow \infty. \quad (6.194)$$

Substituting (6.194) into the condition (6.191) and rearranging yields

$$\mu \frac{\partial u_1}{\partial x_2} + \mu \frac{\partial u_2}{\partial x_1} \rightarrow 0 \quad \text{as } x_2 \rightarrow \infty. \quad (6.195)$$

This can be combined with the condition (6.190) and rewritten in matrix form to give

$$\begin{pmatrix} \mu + \mathbb{F} & \mu \\ \mu & \mu \end{pmatrix} \cdot \begin{pmatrix} \frac{\partial u_1}{\partial x_2} \\ \frac{\partial u_2}{\partial x_1} \end{pmatrix} \rightarrow \mathbf{0} \quad \text{as } x_2 \rightarrow \infty. \quad (6.196)$$

We take the determinant of the matrix in (6.196) to find

$$\begin{vmatrix} \mu + \mathbb{F} & \mu \\ \mu & \mu \end{vmatrix} = \mu \mathbb{F} \neq 0,$$

provided $\mu, \mathbb{F} \neq 0$. Hence, for (6.196) to be satisfied, we must have

$$\frac{\partial u_1}{\partial x_2}, \frac{\partial u_2}{\partial x_1} \rightarrow 0 \quad \text{as } x_2 \rightarrow \infty. \quad (6.197)$$

Combining (6.193) and (6.197), it is seen that

$$\frac{\partial u_i}{\partial x_j} \rightarrow 0 \quad \text{as} \quad x_2 \rightarrow \infty,$$

for all i, j . Thus

$$\nabla u_1, \nabla u_2 \rightarrow \mathbf{0} \quad \text{as} \quad x_2 \rightarrow \infty,$$

holds true. \square

6.B Asymptotic Analysis of the Fundamental Decay Rate Ω_0 for $\bar{\mathcal{F}} \gg 1$ and $\bar{\mathcal{F}} \ll 1$

Here, we formulate asymptotic approximations for the decay rate Ω_0 of the fundamental modes of the deformations u_1, u_2 for both large and small axial pre-stress $\bar{\mathcal{F}}$. We begin by considering the eigenvalue problem (6.109) to be solved for Ω

$$\psi_1 \sin\left(\frac{d\Omega\Lambda_1}{2}\right) \cos\left(\frac{d\Omega\Lambda_2}{2}\right) - \psi_2 \sin\left(\frac{d\Omega\Lambda_2}{2}\right) \cos\left(\frac{d\Omega\Lambda_1}{2}\right) = 0, \quad (6.198)$$

where

$$\psi_1 = [(1 - \nu)\Lambda_1 + \nu\alpha](1 + \Lambda_2^2) \quad \psi_2 = (1 - \alpha\Lambda_1)(1 - 2\nu)\Lambda_2, \quad (6.199)$$

$$\Lambda_1 = \sqrt{\frac{2(1 - \nu) + \bar{\mathcal{F}}}{2(1 - \nu)}}, \quad \Lambda_2 = \sqrt{\frac{1 - 2\nu + \bar{\mathcal{F}}}{1 - 2\nu}}, \quad (6.200)$$

$$\alpha = (1 - 2\nu + \bar{\mathcal{F}})\Lambda_1^{-1} - 2(1 - \nu)\Lambda_1. \quad (6.201)$$

By substituting the expression (6.200a) for Λ_1 into (6.201), it is found that α may be rewritten as

$$\alpha = -\sqrt{\frac{2(1 - \nu)}{2(1 - \nu) + \bar{\mathcal{F}}}}. \quad (6.202)$$

To evaluate (6.198) for different sizes of $\bar{\mathcal{F}}$, we must consider the behaviour of the parameters $\Lambda_1, \Lambda_2, \alpha, \psi_1$ and ψ_2 as $\bar{\mathcal{F}}$ varies.

When $\bar{\mathcal{F}} \rightarrow \infty$, we find the following approximations for the parameters (6.199)–(6.201)

$$\Lambda_1 \sim \frac{\bar{\mathcal{F}}^{\frac{1}{2}}}{\sqrt{2(1 - \nu)}}, \quad \Lambda_2 \sim \frac{\bar{\mathcal{F}}^{\frac{1}{2}}}{\sqrt{1 - 2\nu}}, \quad \alpha \sim -\sqrt{2(1 - \nu)}\bar{\mathcal{F}}^{-\frac{1}{2}}, \quad (6.203)$$

$$\psi_1 \sim \frac{\sqrt{1 - \nu}\bar{\mathcal{F}}^{\frac{3}{2}}}{\sqrt{2(1 - 2\nu)}}, \quad \psi_2 \sim 2\sqrt{1 - 2\nu}\bar{\mathcal{F}}^{\frac{1}{2}}. \quad (6.204)$$

From (6.204), it is seen that in the case of large $\bar{\mathcal{F}}$, $\psi_1 = O(\bar{\mathcal{F}}^{\frac{3}{2}})$ and $\psi_2 = O(\bar{\mathcal{F}}^{\frac{1}{2}})$. Hence, $\psi_1 \gg \psi_2$. However, in the limit $\bar{\mathcal{F}} \rightarrow 0$, we instead have the following approximations

$$\Lambda_1 \sim 1, \quad \Lambda_2 \sim 1, \quad \alpha \sim -1, \quad \psi_1 \sim 2(1 - 2\nu), \quad \psi_2 \sim 2(1 - 2\nu). \quad (6.205)$$

We see from (6.205) that $\Lambda_1 \sim \Lambda_2$ and $\psi_1 \sim \psi_2$ when $\bar{\mathcal{F}}$ is small. Using the approximations (6.203)–(6.205), we now evaluate the eigenvalue equation (6.198) in the limits $\bar{\mathcal{F}} \rightarrow \infty$ and $\bar{\mathcal{F}} \rightarrow 0$.

6.B.1 Decay Rate Ω_0 as $\bar{\mathcal{F}} \rightarrow \infty$

In the limit $\bar{\mathcal{F}} \rightarrow \infty$, we have $\psi_1 \gg \psi_2$. Hence, the first term in (6.198) is the dominant term, and we may approximate the eigenvalues of Ω using

$$\psi_1 \sin\left(\frac{d\Omega\Lambda_1}{2}\right) \cos\left(\frac{d\Omega\Lambda_2}{2}\right) \approx 0. \quad (6.206)$$

The roots of (6.206) occur when

$$\frac{d\Omega\Lambda_1}{2} \approx n\pi, \quad \text{and} \quad \frac{d\Omega\Lambda_2}{2} \approx \left(n + \frac{1}{2}\right)\pi, \quad (6.207)$$

where n is a positive integer. Rearranging the expressions within (6.207), we find

$$\Omega \approx \frac{2n\pi}{d\Lambda_1}, \quad \text{and} \quad \Omega \approx \frac{2\left(n + \frac{1}{2}\right)\pi}{d\Lambda_2}. \quad (6.208)$$

To determine the fundamental decay rate Ω_0 , we must determine what the smallest, non-trivial solution of Ω is. By inspection, we see that the smallest solution will be either

$$\Omega_0 \approx \frac{2\pi}{d\Lambda_1}, \quad \text{or} \quad \Omega_0 \approx \frac{\pi}{d\Lambda_2}. \quad (6.209)$$

To determine which of these is smaller, we examine the behaviour of $2/\Lambda_1$ and $1/\Lambda_2$ for large $\bar{\mathcal{F}}$. Using the expressions (6.200) for Λ_1, Λ_2 , it is seen that $2\Lambda_2/\Lambda_1$ is given by

$$\frac{2\Lambda_2}{\Lambda_1} = 2\sqrt{\frac{1 + \bar{\mathcal{F}}(1 - 2\nu)^{-1}}{1 + \bar{\mathcal{F}}(2 - 2\nu)^{-1}}} > 2, \quad (6.210)$$

for $\bar{\mathcal{F}} > 0, \nu < 1/2$. The inequality within (6.210) holds as $(1 - 2\nu)^{-1} > (2 - 2\nu)^{-1}$, which implies that the square root in (6.210) is greater than 1. From this inequality, it is deduced that

$$\frac{2}{\Lambda_1} > \frac{2}{\Lambda_2} > \frac{1}{\Lambda_2}. \quad (6.211)$$

Hence, applying this inequality to (6.209), it is seen that the decay rate Ω_0 of the fundamental mode for large $\bar{\mathcal{F}}$ must be

$$\Omega_0 \approx \frac{\pi}{d\Lambda_2}. \quad (6.212)$$

Substituting the approximation (6.203b) for Λ_2 when $\bar{\mathcal{F}} \rightarrow \infty$ into (6.212), we find Ω_0 may be approximated by

$$\Omega_0 \sim \frac{\pi\sqrt{1 - 2\nu}}{d} \bar{\mathcal{F}}^{-\frac{1}{2}} \quad \text{as} \quad \bar{\mathcal{F}} \rightarrow \infty. \quad (6.213)$$

Finally, by defining the boundary-layer width of the fundamental mode as $\tilde{\delta}_B = 1/\Omega_0$, the boundary-layer width is approximated by

$$\tilde{\delta}_B \sim \frac{d}{\pi\sqrt{1-2\nu}} \bar{\mathcal{F}}^{\frac{1}{2}} \quad \text{as } \bar{\mathcal{F}} \rightarrow \infty. \quad (6.214)$$

In §6.9, the expression (6.214) is plotted in Figure 6.8 along with the numerically found boundary-layer width. It is observed that there is excellent agreement between the two solutions for large $\bar{\mathcal{F}}$.

6.B.2 Decay Rate Ω_0 as $\bar{\mathcal{F}} \rightarrow 0$

In the limit $\bar{\mathcal{F}} \rightarrow 0$, we have that $\psi_1 \sim \psi_2$ and thus both terms within the eigenvalue equation (6.198) contribute at leading order. We also have that $\Lambda_1 \sim \Lambda_2$ for small $\bar{\mathcal{F}}$. As a starting point for evaluating the eigenvalue equation (6.198), we take the Taylor series of the expressions (6.199), (6.200) for Λ_1 , Λ_2 , ψ_1 , ψ_2 about $\bar{\mathcal{F}} = 0$. Doing so, we find

$$\Lambda_1 = 1 + \frac{1}{4(1-\nu)} \bar{\mathcal{F}} - \frac{1}{32(\nu-1)^2} \bar{\mathcal{F}}^2 + O(\bar{\mathcal{F}}^3), \quad (6.215)$$

$$\Lambda_2 = 1 + \frac{1}{2(1-2\nu)} \bar{\mathcal{F}} - \frac{1}{8(2\nu-1)^2} \bar{\mathcal{F}}^2 + O(\bar{\mathcal{F}}^3), \quad (6.216)$$

$$\psi_1 = 2 - 4\nu + \frac{3-2\nu}{2(1-\nu)} \bar{\mathcal{F}} + \frac{3-4\nu+4\nu^2}{16(1-2\nu)(1-\nu)^2} \bar{\mathcal{F}}^2 + O(\bar{\mathcal{F}}^3), \quad (6.217)$$

$$\psi_2 = 2 - 4\nu + \bar{\mathcal{F}} - \frac{1}{4(1-2\nu)} \bar{\mathcal{F}}^2 + O(\bar{\mathcal{F}}^3). \quad (6.218)$$

We also find it convenient to rewrite the eigenvalue equation (6.198) as

$$\frac{\psi_1 + \psi_2}{2} \sin\left(\frac{d\Omega}{2}(\Lambda_1 - \Lambda_2)\right) + \frac{\psi_1 - \psi_2}{2} \sin\left(\frac{d\Omega}{2}(\Lambda_1 + \Lambda_2)\right) = 0, \quad (6.219)$$

where we have used the identities

$$\sin\left(\frac{d\Omega}{2}(\Lambda_1 \pm \Lambda_2)\right) = \sin\left(\frac{d\Omega\Lambda_1}{2}\right) \cos\left(\frac{d\Omega\Lambda_2}{2}\right) \pm \cos\left(\frac{d\Omega\Lambda_1}{2}\right) \sin\left(\frac{d\Omega\Lambda_2}{2}\right).$$

The following asymptotic expansions are now considered

$$\Lambda_1 + \Lambda_2 = \alpha^{(0)} + \alpha^{(1)} \bar{\mathcal{F}} + \alpha^{(2)} \bar{\mathcal{F}}^2 + O(\bar{\mathcal{F}}^3), \quad (6.220)$$

$$\Lambda_1 - \Lambda_2 = \beta^{(0)} + \beta^{(1)} \bar{\mathcal{F}} + \beta^{(2)} \bar{\mathcal{F}}^2 + O(\bar{\mathcal{F}}^3), \quad (6.221)$$

$$\psi_1 + \psi_2 = \gamma^{(0)} + \gamma^{(1)} \bar{\mathcal{F}} + \gamma^{(2)} \bar{\mathcal{F}}^2 + O(\bar{\mathcal{F}}^3), \quad (6.222)$$

$$\psi_1 - \psi_2 = \delta^{(0)} + \delta^{(1)} \bar{\mathcal{F}} + \delta^{(2)} \bar{\mathcal{F}}^2 + O(\bar{\mathcal{F}}^3), \quad (6.223)$$

where $\alpha^{(0)}, \alpha^{(1)}, \dots, \delta^{(2)}$, are $O(1)$ constants that are determined from the Taylor series (6.215)–(6.218) of Λ_1 , Λ_2 , ψ_1 and ψ_2 , about $\bar{\mathcal{F}} = 0$. Using these Taylor

series, it is immediately observed that $\beta^{(0)} = \delta^{(0)} = 0$. We also calculate the following coefficients

$$\alpha^{(0)} = 2, \quad \alpha^{(1)} = \frac{3 - 4\nu}{4(1 - \nu)(1 - 2\nu)}, \quad (6.224)$$

$$\beta^{(1)} = -\frac{1}{4(1 - \nu)(1 - 2\nu)}, \quad \beta^{(2)} = \frac{3 - 4\nu}{32(1 - \nu)^2(1 - 2\nu)^2}, \quad (6.225)$$

$$\gamma^{(0)} = 4(1 - 2\nu), \quad \gamma^{(1)} = \frac{5 - 4\nu}{2(1 - \nu)}, \quad (6.226)$$

$$\delta^{(1)} = \frac{1}{2(1 - \nu)}, \quad \delta^{(2)} = \frac{7 - 12\nu + 8\nu^2}{16(1 - \nu)^2(1 - 2\nu)}. \quad (6.227)$$

Finally, we assume that the decay rate Ω behaves like an unknown power of $\bar{\mathcal{F}}$ at leading order as $\bar{\mathcal{F}} \rightarrow 0$, and set

$$\Omega = \bar{\Omega} \bar{\mathcal{F}}^n, \quad (6.228)$$

where n is real and $\bar{\Omega} = O(1)$ as $\bar{\mathcal{F}} \rightarrow 0$. Substituting the asymptotic expansions (6.220)–(6.223) and the expression (6.228) into the eigenvalue equation (6.219), we obtain

$$\begin{aligned} 0 = & \frac{\gamma^{(0)} + \gamma^{(1)} \bar{\mathcal{F}} + \gamma^{(2)} \bar{\mathcal{F}}^2 + O(\bar{\mathcal{F}}^3)}{2} \sin \left(\frac{d\bar{\Omega} \bar{\mathcal{F}}^n}{2} \left(\beta^{(1)} \bar{\mathcal{F}} + \beta^{(2)} \bar{\mathcal{F}}^2 + O(\bar{\mathcal{F}}^3) \right) \right) \\ & + \frac{\delta^{(1)} \bar{\mathcal{F}} + \delta^{(2)} \bar{\mathcal{F}}^2 + O(\bar{\mathcal{F}}^3)}{2} \sin \left(\frac{d\bar{\Omega} \bar{\mathcal{F}}^n}{2} \left(\alpha^{(0)} + \alpha^{(1)} \bar{\mathcal{F}} + \alpha^{(2)} \bar{\mathcal{F}}^2 + O(\bar{\mathcal{F}}^3) \right) \right). \end{aligned} \quad (6.229)$$

This problem is now split into three separate cases; $n < 0$, $n = 0$ and $n > 0$.

Case when $n < 0$

When $n < 0$, the leading-order component of (6.229) becomes

$$\frac{\gamma^{(0)}}{2} \sin \left(\frac{d\bar{\Omega} \beta^{(1)} \bar{\mathcal{F}}^{n+1}}{2} \right) = 0. \quad (6.230)$$

For (6.230) to be satisfied, we need

$$\frac{d\bar{\Omega} \beta^{(1)} \bar{\mathcal{F}}^{n+1}}{2} = k\pi, \quad (6.231)$$

where k is an integer. For this to be the case, we must have $n = -1$ and

$$\bar{\Omega} = \frac{2k\pi}{d\beta^{(1)}}, \quad \text{for } k = 1, 2, 3, \dots \quad (6.232)$$

Hence, by applying the expression (6.225a) for $\beta^{(1)}$ to (6.232) and substituting into (6.228), the following leading-order approximations for the eigenvalues Ω are calculated

$$\Omega \sim 8k\pi(1-\nu)(1-2\nu)d^{-1}\bar{\mathcal{F}}^{-1} \quad \text{for } k = 1, 2, 3, \dots \quad \text{as } \bar{\mathcal{F}} \rightarrow 0. \quad (6.233)$$

This yields countably many solutions, all of which are decreasing with increasing $\bar{\mathcal{F}}$.

In Figure 6.18, the approximations (6.233) for $k = 1, 2$, and 3 are plotted for small $\bar{\mathcal{F}}$, in the case $\nu = 0.49$, $d = 1$. Also plotted are the numerically determined solutions Ω_1 , Ω_2 and Ω_3 of the eigenvalue equation (6.198) for the first, second and third modes, as seen in Figure 6.5 in §6.6. It is seen that the approximations and numerical solutions are in strong agreement for $\bar{\mathcal{F}} \ll 1$. We note that the small-amplitude, high-frequency variations seen in the numerical solutions for larger values of $\bar{\mathcal{F}}$ are part of the solution rather than any numerical deficiency. These high-frequency variations arise from the second term in the rewritten eigenvalue equation (6.219), which is found to be negligible at leading order in the limit $\bar{\mathcal{F}} \rightarrow 0$.

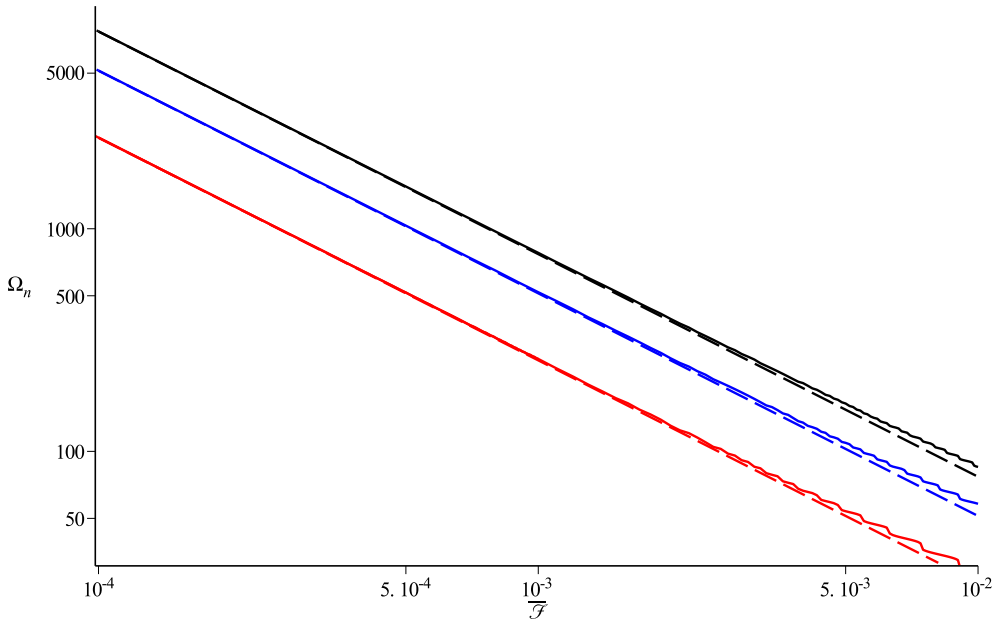


Figure 6.18: The asymptotic approximations (6.233) of Ω in the limit $\bar{\mathcal{F}} \rightarrow 0$, for $\nu = 0.49$, $d = 1$ (dashed lines). The approximations when $k = 1, 2$ and 3 are plotted in red, blue and black, respectively. Also shown are the numerically determined solutions Ω_1 (red solid line), Ω_2 (blue solid line) and Ω_3 (black solid line), of the eigenvalue equation (6.198) for the first, second and third modes, as seen in Figure 6.5.

Case when $n = 0$

In the case $n = 0$, (6.229) becomes

$$0 = \frac{\gamma^{(0)} + \gamma^{(1)}\bar{\mathcal{F}} + \gamma^{(2)}\bar{\mathcal{F}}^2 + O(\bar{\mathcal{F}}^3)}{2} \sin\left(\frac{d\bar{\Omega}}{2} \left(\beta^{(1)}\bar{\mathcal{F}} + \beta^{(2)}\bar{\mathcal{F}}^2 + O(\bar{\mathcal{F}}^3)\right)\right) \\ + \frac{\delta^{(1)}\bar{\mathcal{F}} + \delta^{(2)}\bar{\mathcal{F}}^2 + O(\bar{\mathcal{F}}^3)}{2} \sin\left(\frac{d\bar{\Omega}}{2} \left(\alpha^{(0)} + \alpha^{(1)}\bar{\mathcal{F}} + \alpha^{(2)}\bar{\mathcal{F}}^2 + O(\bar{\mathcal{F}}^3)\right)\right). \quad (6.234)$$

Taking the Taylor series of

$$\sin\left(\frac{d\bar{\Omega}}{2} \left(\beta^{(1)}\bar{\mathcal{F}} + \beta^{(2)}\bar{\mathcal{F}}^2\right)\right)$$

about $\bar{\mathcal{F}} = 0$ and substituting into (6.234), the leading-order eigenvalue problem at $O(\bar{\mathcal{F}})$ is determined to be

$$\frac{d\gamma^{(0)}\beta^{(1)}}{4}\bar{\Omega} + \frac{\delta^{(1)}}{2} \sin\left(\frac{d\alpha^{(0)}}{2}\bar{\Omega}\right) = 0. \quad (6.235)$$

Substituting in the expressions (6.224)–(6.227) for the constants $\alpha^{(0)}$, $\beta^{(1)}$, $\gamma^{(0)}$ and $\delta^{(1)}$ into (6.235) and rearranging, we obtain

$$\sin(d\bar{\Omega}) = d\bar{\Omega}. \quad (6.236)$$

The only (real) solution of (6.236) is the trivial solution $\bar{\Omega} = 0$. However, as $\bar{\mathcal{F}} \rightarrow 0$, $\bar{\Omega} = O(1)$, and so $\bar{\Omega} = 0$ cannot be a valid solution. Thus, there are no non-trivial solutions that arise from this scenario.

Case when $n > 0$

In the final case $n > 0$, we take the Taylor series of both sine functions within (6.229) to obtain

$$0 = \frac{d\bar{\Omega}}{4} \left[\left(\delta^{(1)}\alpha^{(0)} + \gamma^{(0)}\beta^{(1)} \right) \bar{\mathcal{F}}^{n+1} \right. \\ \left. + \left(\delta^{(2)}\alpha^{(0)} + \delta^{(1)}\alpha^{(1)} + \gamma^{(0)}\beta^{(2)} + \gamma^{(1)}\beta^{(1)} \right) \bar{\mathcal{F}}^{n+2} \right] \\ - \frac{1}{12}\delta^{(1)} \left(\frac{d\bar{\Omega}}{2}\alpha^{(0)} \right)^3 \bar{\mathcal{F}}^{3n+1} + \dots \quad (6.237)$$

Using (6.224)–(6.227), we note that

$$\delta^{(1)}\alpha^{(0)} + \gamma^{(0)}\beta^{(1)} = 0.$$

Hence, there is no $O(\bar{\mathcal{F}}^{n+1})$ term in (6.237) and we must examine the next order to find the leading-order equation. To find non-trivial solutions for $\bar{\Omega}$, we need the $O(\bar{\mathcal{F}}^{n+2})$ and $O(\bar{\mathcal{F}}^{3n+1})$ terms to have the same size, allowing them to balance at leading order. To enable this, we set $n = 1/2$. At leading order, found to be at $O(\bar{\mathcal{F}}^{\frac{5}{2}})$, (6.237) then becomes after rearranging

$$\frac{d\bar{\Omega}}{4} \left(\delta^{(2)}\alpha^{(0)} + \delta^{(1)}\alpha^{(1)} + \gamma^{(0)}\beta^{(2)} + \gamma^{(1)}\beta^{(1)} \right) = \frac{1}{12}\delta^{(1)} \left(\frac{d\bar{\Omega}}{2}\alpha^{(0)} \right)^3. \quad (6.238)$$

Substituting the constants (6.224)–(6.227) into (6.238) and rearranging, we obtain

$$\bar{\Omega} = \left(\frac{6(1-\nu)}{d^2(1-2\nu)} \right)^{\frac{1}{2}}, \quad (6.239)$$

and hence, substituting (6.239) into (6.228) yields the following leading-order approximation for Ω

$$\Omega \sim \left(\frac{6(1-\nu)}{d^2(1-2\nu)} \right)^{\frac{1}{2}} \bar{\mathcal{F}}^{\frac{1}{2}} \quad \text{as} \quad \bar{\mathcal{F}} \rightarrow 0. \quad (6.240)$$

Unlike the solutions (6.233) for Ω found for the case when $n < 0$, the solution (6.240) increases with increasing $\bar{\mathcal{F}}$. This solution is also the smallest possible value of Ω in the case $\bar{\mathcal{F}} \rightarrow 0$ and so must be the approximation for the decay rate Ω_0 of the fundamental mode. As such, it is this mode that has the largest boundary-layer width $\tilde{\delta}_B = 1/\Omega_0$. Hence, we find the boundary-layer width of the deformations in the limit $\bar{\mathcal{F}} \rightarrow 0$ to be approximated by

$$\tilde{\delta}_B \sim \left(\frac{1-2\nu}{6(1-\nu)} \right)^{\frac{1}{2}} d\bar{\mathcal{F}}^{-\frac{1}{2}} \quad \text{as} \quad \bar{\mathcal{F}} \rightarrow 0. \quad (6.241)$$

The approximation (6.241) for the boundary-layer width has been plotted in Figure 6.8 in §6.9, along with the numerically found boundary-layer width. It is seen that there is excellent agreement between the two solutions for small $\bar{\mathcal{F}}$.

6.C Finding the Solution of the Biharmonic Equation

Here we give a summary of the work of Shankar (2003), which looks at the problem of solving the biharmonic equation

$$\nabla^4 \Psi(x, y) = 0, \quad (6.242)$$

in the semi-infinite strip $x \in (-1/2, +1/2)$, $y \in (-\infty, 0)$. This problem has the prescribed boundary conditions

$$\Psi(x, 0) = p(x), \quad \nabla^2 \Psi(x, 0) = q(x), \quad (6.243)$$

along the short edge $y = 0$, where $p(x)$, $q(x)$ are known functions, and $p(x)$ satisfies the compatibility conditions $p(\pm 1/2) = p'(\pm 1/2) = 0$, where ' denotes a derivative with respect to x . The following homogeneous boundary conditions are also prescribed

$$\Psi = 0 \quad \text{and} \quad \frac{\partial \Psi}{\partial x} = 0 \quad \text{at} \quad x = \pm \frac{1}{2}, \quad (6.244)$$

$$\Psi \rightarrow 0 \quad \text{as} \quad y \rightarrow -\infty. \quad (6.245)$$

To simplify the problem, it is assumed that $p(x)$, $q(x)$ and $\Psi(x, y)$ are all symmetric in x . However, the method applied here can also be applied to the case of general $p(x)$, $q(x)$ and $\Psi(x, y)$.

To solve the linear system (6.242)–(6.245), separable solutions of the form

$$\Psi(x, y) = \phi(x) e^{\kappa y}, \quad (6.246)$$

are sought, where κ is a complex scalar. In order for this type of solution to satisfy the boundary condition (6.245) as $y \rightarrow -\infty$, it is assumed that $\text{Re}(\kappa) > 0$.

6.C.1 Solution for $\phi(x)$

Substituting (6.246) into (6.242) and (6.244), the following fourth-order ODE governing $\phi(x)$ is found

$$\frac{d^4 \phi}{dx^4} + 2\kappa^2 \frac{d^2 \phi}{dx^2} + \kappa^4 \phi = 0, \quad (6.247)$$

as well as the following homogeneous boundary conditions

$$\phi(x) = 0 \quad \text{and} \quad \frac{d\phi}{dx} = 0 \quad \text{at} \quad x = \pm \frac{1}{2}. \quad (6.248)$$

Solving the governing ODE (6.247) and using the fact that $\phi(x)$ is assumed to be symmetric about $x = 0$, the following general solution for $\phi(x)$ is derived

$$\phi(x) = Ax \sin(\kappa x) + B \cos(\kappa x), \quad (6.249)$$

where A, B are constants to be found.

Substituting (6.249) into the boundary conditions (6.248) and rewriting in matrix form yields

$$\begin{pmatrix} \frac{1}{2} \sin\left(\frac{\kappa}{2}\right) & \cos\left(\frac{\kappa}{2}\right) \\ \sin\left(\frac{\kappa}{2}\right) + \frac{\kappa}{2} \cos\left(\frac{\kappa}{2}\right) & -\kappa \sin\left(\frac{\kappa}{2}\right) \end{pmatrix} \begin{pmatrix} A \\ B \end{pmatrix} = \mathbf{0}. \quad (6.250)$$

It is noted that by rearranging the first component of (6.250), the constant B may be rewritten in terms of A as follows

$$B = -\frac{A}{2} \tan\left(\frac{\kappa}{2}\right). \quad (6.251)$$

For non-trivial solutions for A and B to exist, the determinant of the matrix within (6.250) must be zero. By setting this, the following eigenvalue equation for κ is derived

$$\sin(\kappa) = -\kappa. \quad (6.252)$$

This has countably many solutions for κ which we label as κ_n , where $n \geq 0$.

As we have countably many solutions for κ , we also have countably many modes $\phi_n(x)$ given by

$$\phi_n(x) = A_n \left(x \sin(\kappa_n x) - \frac{1}{2} \tan\left(\frac{\kappa_n}{2}\right) \cos(\kappa_n x) \right), \quad (6.253)$$

where the coefficients A_n are to be determined using the boundary conditions (6.243) at $y = 0$. The solution of $\phi(x)$ is comprised of the sum of the modes $\phi_n(x)$ as follows

$$\phi(x) = \sum_{n=0}^{\infty} \phi_n(x). \quad (6.254)$$

We then substitute (6.254) into (6.246) to obtain the following for $\Psi(x, y)$

$$\Psi(x, y) = \sum_{n=0}^{\infty} \phi_n(x) e^{\kappa_n y}. \quad (6.255)$$

6.C.2 A Biorthogonality Relation Between the Eigenfunctions $\phi_n(x)$

In order for $\Psi(x, y)$ to be fully determined, the coefficients A_n must be determined. Shankar (2003) achieves this using a biorthogonal relation between

the eigenfunctions $\phi_n(x)$. The derivation of this biorthogonal relation is now provided.

The first step in deriving the biorthogonal relation is to decompose the governing ODE (6.247) for $\phi(x)$ (also satisfied by each of the modes $\phi_n(x)$) into a pair of coupled, second-order ODEs. Replacing κ and $\phi(x)$ by the n th eigenvalue κ_n and n th mode $\phi_n(x)$ in (6.247), it is seen that (6.247) may be factorized as follows

$$\left(\frac{d^2}{dx^2} + \kappa_n^2 \right)^2 \phi_n = 0. \quad (6.256)$$

Using this factorization, we see that it is convenient to introduce a new function $u_n(x)$ defined as

$$u_n(x) = \frac{d^2\phi_n}{dx^2} + \kappa_n^2\phi_n. \quad (6.257)$$

Substituting (6.257) into (6.256) yields

$$\frac{d^2u_n}{dx^2} + \kappa_n^2u_n = 0. \quad (6.258)$$

Hence, the original governing ODE (6.247) has been decomposed into the coupled pair of equations (6.257) and (6.258). Rearranging and rewriting these in matrix form gives

$$L\mathbf{U}_n = \kappa_n^2\mathbf{U}_n, \quad (6.259)$$

where

$$L = \begin{pmatrix} -\frac{d^2}{dx^2} & 1 \\ 0 & -\frac{d^2}{dx^2} \end{pmatrix}, \quad \mathbf{U}_n = \begin{pmatrix} \phi_n(x) \\ u_n(x) \end{pmatrix}. \quad (6.260)$$

We now define the dual space vectors \mathbf{V}_n and the dual space inner product of two vectors. We first set

$$\mathbf{V}_n = \begin{pmatrix} \chi_n(x) \\ v_n(x) \end{pmatrix}, \quad (6.261)$$

where $\chi_n(x)$, $v_n(x)$ are arbitrary functions of x , and the $v_n(x)$ are chosen to satisfy the same homogeneous boundary conditions (6.248) as $\phi_n(x)$ along the long edges at $x = \pm 1/2$. The dual space inner product of \mathbf{U}_n and \mathbf{V}_n is defined by

$$\langle \mathbf{U}_n, \mathbf{V}_n \rangle = \int_{-1/2}^{1/2} \phi_n(x)\chi_n(x) + u_n(x)v_n(x)dx. \quad (6.262)$$

Taking the inner product of $L\mathbf{U}_n$ and \mathbf{V}_n yields

$$\begin{aligned} \langle L\mathbf{U}_n, \mathbf{V}_n \rangle &= \int_{-1/2}^{1/2} \left(u_n(x) - \frac{d^2\phi_n}{dx^2} \right) \chi_n(x) - \frac{d^2u_n}{dx^2} v_n(x) dx, \\ &= \int_{-1/2}^{1/2} -\phi_n(x) \frac{d^2\chi_n}{dx^2} + u_n(x) \left(\chi_n(x) - \frac{d^2v_n}{dx^2} \right) dx, \end{aligned} \quad (6.263)$$

where we have used integration by parts to move the derivatives from the functions $\phi_n(x)$, $u_n(x)$ to the functions $\chi_n(x)$, $v_n(x)$. We have also used the fact that $\phi_n(x)$ and $v_n(x)$ both satisfy the homogeneous boundary conditions (6.248) at $x = \pm 1/2$ to eliminate the boundary terms that arise through integration by parts. The expression (6.263) may be rewritten using an adjoint operator L^* in the following way

$$\langle L\mathbf{U}_n, \mathbf{V}_n \rangle = \langle \mathbf{U}_n, L^*\mathbf{V}_n \rangle \quad \forall \mathbf{U}_n, \mathbf{V}_n, \quad (6.264)$$

where

$$L^* = \begin{pmatrix} -\frac{d^2}{dx^2} & 0 \\ 1 & -\frac{d^2}{dx^2} \end{pmatrix}. \quad (6.265)$$

We now set \mathbf{V}_n to be an eigenvector of L^* such that

$$L^*\mathbf{V}_n = \iota_n^2 \mathbf{V}_n, \quad (6.266)$$

where ι_n are the corresponding eigenvalues of \mathbf{V}_n . It is seen that the components of (6.266) have the same form as the components of the relation $L\mathbf{U}_n = \kappa_n^2 \mathbf{U}_n$, only with $v_n(x)$, $\chi_n(x)$ and ι_n taking the place of $\phi_n(x)$, $u_n(x)$ and κ_n , respectively. Hence, the eigenvectors \mathbf{V}_n of L^* , and their corresponding eigenvectors ι_n must be

$$\mathbf{V}_n = \begin{pmatrix} u_n(x) \\ \phi_n(x) \end{pmatrix}, \quad \iota_n = \kappa_n, \quad (6.267)$$

and we have from (6.266)

$$L^*\mathbf{V}_n = \kappa_n^2 \mathbf{V}_n. \quad (6.268)$$

Using the relations (6.259), (6.264) and (6.268), the following is found

$$\begin{aligned} \langle L\mathbf{U}_n, \mathbf{V}_m \rangle &= \langle \kappa_n^2 \mathbf{U}_n, \mathbf{V}_m \rangle = \kappa_n^2 \langle \mathbf{U}_n, \mathbf{V}_m \rangle \\ &= \langle \mathbf{U}_n, L^*\mathbf{V}_m \rangle = \langle \mathbf{U}_n, \kappa_m^2 \mathbf{V}_m \rangle = \kappa_m^2 \langle \mathbf{U}_n, \mathbf{V}_m \rangle. \end{aligned} \quad (6.269)$$

Hence, we have $\kappa_n^2 \langle \mathbf{U}_n, \mathbf{V}_m \rangle = \kappa_m^2 \langle \mathbf{U}_n, \mathbf{V}_m \rangle$, which implies

$$(\kappa_n^2 - \kappa_m^2) \langle \mathbf{U}_n, \mathbf{V}_m \rangle = 0. \quad (6.270)$$

Hence if $\kappa_m \neq \kappa_n$, then $\langle \mathbf{U}_n, \mathbf{V}_m \rangle = 0$ and (6.270) is the biorthogonality relation needed to derive the unknown constants A_n in the expression (6.253) for the modes $\phi_n(x)$.

6.C.3 Determining the Constants A_n

Using the biorthogonality relation (6.270) between the eigenfunctions $\phi_n(x)$, it is now possible to apply the boundary conditions (6.243) at $y = 0$ and determine the unknown constants A_n .

Substituting the representation (6.255) for $\Psi(x, y)$ into the boundary conditions (6.243), we obtain

$$p(x) = \sum_{n=0}^{\infty} \phi_n(x), \quad q(x) = \sum_{n=0}^{\infty} \frac{d^2 \phi_n}{dx^2} + \kappa_n^2 \phi_n(x) = \sum_{n=0}^{\infty} u_n(x), \quad (6.271)$$

where we have used (6.257) to rewrite the second condition in terms of the functions $u_n(x)$. We recall that the general solution (6.253) for the $\phi_n(x)$ is

$$\phi_n(x) = A_n \left(x \sin(\kappa_n x) - \frac{1}{2} \tan\left(\frac{\kappa_n}{2}\right) \cos(\kappa_n x) \right),$$

and substituting (6.253) into (6.257), we find

$$u_n(x) = 2A_n \kappa_n \cos(\kappa_n x). \quad (6.272)$$

The conditions (6.271) may be rewritten in the following form

$$\begin{pmatrix} p(x) \\ q(x) \end{pmatrix} = \sum_{n=0}^{\infty} \mathbf{U}_n, \quad (6.273)$$

where we have set $\mathbf{U}_n^T = (\phi_n(x), u_n(x))$.

We now set $\mathbf{V}_m^T = (u_m(x), \phi_m(x))$ and take the inner product of (6.273) with \mathbf{V}_m . Doing so yields

$$\left\langle \begin{pmatrix} p(x) \\ q(x) \end{pmatrix}, \mathbf{V}_m \right\rangle = \sum_{n=0}^{\infty} \langle \mathbf{U}_n, \mathbf{V}_m \rangle. \quad (6.274)$$

Using the biorthogonality relation (6.270), it is seen that all the modes on the right-hand-side of (6.274) vanish apart from the mode $n = m$. With the definition (6.262), the inner product of \mathbf{U}_m and \mathbf{V}_m can be directly calculated to be

$$\langle \mathbf{U}_m, \mathbf{V}_m \rangle = -2A_m^2 \cos^2\left(\frac{\kappa_m}{2}\right), \quad (6.275)$$

where the eigenvalue equation (6.252) has been used to simplify this expression.

It is also calculated that

$$\begin{aligned} \left\langle \begin{pmatrix} p(x) \\ q(x) \end{pmatrix}, \mathbf{V}_m \right\rangle &= \left\langle \begin{pmatrix} p(x) \\ q(x) \end{pmatrix}, \begin{pmatrix} 2A_m \kappa_m \cos(\kappa_m x) \\ A_m (x \sin(\kappa_m x) - \frac{1}{2} \tan(\frac{\kappa_m}{2}) \cos(\kappa_m x)) \end{pmatrix} \right\rangle \\ &= A_m \int_{-\frac{1}{2}}^{\frac{1}{2}} q(x) \left(x \sin(\kappa_m x) - \frac{1}{2} \tan\left(\frac{\kappa_m}{2}\right) \cos(\kappa_m x) \right) \\ &\quad + 2p(x) \kappa_m \cos(\kappa_m x) dx. \end{aligned} \quad (6.276)$$

Substituting (6.275) and (6.276) into (6.274) and rearranging, the following expression for the constants A_m is obtained

$$A_m = -\frac{1}{2 \cos^2\left(\frac{\kappa_m}{2}\right)} \int_{-\frac{1}{2}}^{\frac{1}{2}} 2p(x)\kappa_m \cos(\kappa_m x) + q(x) \left(x \sin(\kappa_m x) - \frac{1}{2} \tan\left(\frac{\kappa_m}{2}\right) \cos(\kappa_m x) \right) dx. \quad (6.277)$$

It is noted that (6.277) is different from the expression for A_m derived by Shankar (2003) by a factor of $4\kappa_m$. However, (6.277) is consistent with the computed values of A_m presented in the work of Shankar (2003), leading us to believe that the expression (6.277) for A_m is correct. Using this expression, the modes $\phi_n(x)$ can be fully calculated using (6.253). Provided that the set of eigenfunctions ϕ_n is complete, these eigenfunctions along with the expression (6.255) give the complete analytical solution of $\Psi(x, y)$. For more details on the completeness of the set of biharmonic eigenfunctions, also known as the Papkovich–Fadle eigenfunctions, see Gregory (1980).

6.C.4 Application to the Semi-Infinite Block Under Tension

The work of Shankar (2003) summarised here gives an idea of how it may be possible to find the full analytical solution for the problem of bending a semi-infinite block under tension. Unfortunately, as the governing equation (6.88) and boundary and integral conditions (6.89)–(6.93) for the normal deformation u_1 are more complicated than the system considered by Shankar (2003), a biorthogonality relation allowing us to determine the constants A_n in the expressions (6.110), (6.111) for the deformations u_1, u_2 has not yet been found. However, if such a relation is found, it would allow a complete analytical solution to the problem to be determined.

Chapter 7

A One-Dimensional Model for Bending a Semi-Infinite Block Under Tension

7.1 Introduction

In this chapter, we examine the possibility of using a 1D model to describe a semi-infinite block being bent under tension, which is modelled in 2D in Chapter 6. By considering different methods of deriving a 1D model for this problem, more details of the underlying mechanisms occurring within the boundary layers found in the model in Chapter 6 are revealed.

In §3.6, a toy model was derived that modelled an axial-bending boundary layer near the ends of the elastic-walled tube modelled in Chapter 2. This model predicted that the dimensionless bending boundary-layer width δ_B has magnitude $\delta_B = O(\mathcal{F}^{-\frac{1}{2}}\ell^{-1})$, where $\mathcal{F} = O(1)$ and $\ell \gg 1$ are dimensionless parameters representing the axial tension and tube length. The problem of adding an axial-bending boundary layer to the model in Chapter 2 was then split into two regimes depending on the sizes of the length of the tube ℓ and the dimensionless tube wall thickness $\delta \ll 1$. In the first of these regimes, regime I, the case where δ and ℓ are set such that $\delta\ell \ll 1$ is considered. Using the estimate from the toy model, it was predicted that $\delta_B \gg \delta$ and the bending layer would be larger than the tube wall thickness. This implied that the Kirchhoff–Love shell equations (Flügge, 1972; Søndergaard, 2007) used to model the wall mechanics in the bulk of the tube in Chapter 2 could still be applied to the bending layer. This regime was studied in Chapters 4 and 5. In

the second of these regimes, regime II, we considered the scenario where δ and ℓ are set to satisfy $\delta\ell \gg 1$. In this case, the toy model estimates that $\delta_B \ll \delta$ and the bending layer is smaller than the tube wall thickness. As it was predicted that δ was no longer the smallest geometric parameter, Kirchhoff–Love shell theory could not be used in this regime to model the expected bending layer.

Instead of using Kirchhoff–Love shell theory to model the tube wall in regime II, we returned to first principles and derived a 2D model for a semi-infinite block being bent under tension in Chapter 6. This block represented a two-dimensional cross-section of the tube wall in the normal and axial directions, near the ends of the elastic-walled tube where it is clamped onto fixed rigid tubes. In solving this model, it was found that in the case $\delta\ell \gg 1$, the dimensional boundary-layer width $\tilde{\delta}_B$ had size $\tilde{\delta}_B = O(d\delta\ell)$, where d is the width of the block. Hence, it was seen that $\tilde{\delta}_B \gg d$ and the boundary-layer width is larger than the width of the block. It was found that this boundary layer is in fact a transverse shear-relaxation layer as opposed to an axial-bending layer.

As $\tilde{\delta}_B \gg d$, it is possible that Kirchhoff–Love shell theory, or some other approximation applying the fact that d is small compared to the other geometric parameters, can be used to derive a 1D model for this shear layer. This possibility is investigated in this chapter by deriving and testing three different one-dimensional models against the 2D model derived in Chapter 6. In doing so, more information about the mechanics within the shear layer is obtained.

This chapter is arranged as follows. In §7.2, a recap of the mathematical set-up of the linearised model of bending a semi-infinite block under tension, as derived in §6.4, is provided. In §7.3, the possibility of deriving an appropriate 1D model for the linearised problem using Kirchhoff–Love shell theory is investigated. It is found that an accurate 1D model cannot be derived using this theory as one of the assumptions made in Kirchhoff–Love shell theory is violated. In §7.4, a 1D model is derived by averaging the components of Cauchy’s momentum equation, the governing equation for the linearised system in §6.4. This model yields exponentially decaying deformations as the axial coordinate $x_2 \rightarrow \infty$. The decay rates of these deformations have the same qualitative behaviour as the decay rate of the fundamental mode found in the 2D model, but there is still a discrepancy between these decay rates. The final 1D model considered here is derived in §7.5, which is formed using the system (6.88)–(6.93) governing the semi-infinite block with the axial deformation u_2

eliminated. This model produces deformations consisting of exponentially decaying modes, and the decay rate of the slowest decaying of these modes matches the decay rate of the fundamental mode in the 2D model. However, there are still large discrepancies between the deformations from the 1D and 2D models. Finally, to explain these discrepancies, the behaviour of the normal deformation u_1 near the clamped boundary of the block is evaluated in §7.6. Here a 2D compression effect not incorporated into the 1D models is found near the clamped boundary.

7.2 Mathematical Set-Up

We recall the linearised model derived in §6.4 and depicted in Figure 7.1. Full details of the original set-up can be found in §6.2. Here, we have an almost incompressible semi-infinite block of dimensional thickness d . Dimensional Eulerian coordinates in the normal and semi-infinite (axial) direction have been set to be x_1 and x_2 respectively. The block is set to occupy the region $x_1 \in [0, d]$, $x_2 \in [0, \infty)$, and has incremental Young's modulus E and Poisson's ratio ν . The block is subject to a scaled dimensionless axial tension $\bar{\mathcal{F}}$. It is noted that $\bar{\mathcal{F}} = O(\delta^2 \ell^2)$, where $\delta \ll 1$ and $\ell \gg 1$ are the dimensionless tube wall thickness and tube length in the model of the elastic-walled tube in Chapter 2. In the original set-up before the linearisation, a small amplitude deformation

$$\mathbf{u} = \begin{pmatrix} u_1 \\ u_2 \end{pmatrix},$$

is induced on the block by clamping the boundary at $x_2 = 0$ at an angle ϕ to the x_1 -axis. Here, u_1 and u_2 are the components of the deformation in the x_1 and x_2 -directions respectively.

$$\boxed{\begin{aligned} & (x_1 = d) \\ & (1 - \nu) \frac{\partial u_1}{\partial x_1} + \nu \frac{\partial u_2}{\partial x_2} = 0, \quad \frac{\partial u_1}{\partial x_2} + \frac{\partial u_2}{\partial x_1} = 0 \\ & (x_2 = 0) \\ & \mathbf{u} = \left(0, \tan(\phi) \left(x_1 - \frac{d}{2} \right) \right) \\ & 2(1 - \nu) \frac{\partial^2 u_1}{\partial x_1^2} + \frac{\partial^2 u_2}{\partial x_1 \partial x_2} + (1 - 2\nu + \bar{\mathcal{F}}) \frac{\partial^2 u_1}{\partial x_2^2} = 0 \\ & (1 - 2\nu) \frac{\partial^2 u_2}{\partial x_1^2} + \frac{\partial^2 u_1}{\partial x_1 \partial x_2} + (2(1 - \nu) + \bar{\mathcal{F}}) \frac{\partial^2 u_2}{\partial x_2^2} = 0 \\ & (x_2 \rightarrow \infty) \\ & \nabla u_1, \nabla u_2 \rightarrow \mathbf{0} \\ & (x_1 = 0) \\ & (1 - \nu) \frac{\partial u_1}{\partial x_1} + \nu \frac{\partial u_2}{\partial x_2} = 0, \quad \frac{\partial u_1}{\partial x_2} + \frac{\partial u_2}{\partial x_1} = 0 \end{aligned}}$$

Figure 7.1: The linearised problem of a semi-infinite block being bent under axial tension. The domain is given by $A = \{(x_1, x_2) : 0 \leq x_1 \leq d, 0 \leq x_2\}$.

The linearised governing system is given by (6.42)–(6.46). It can be shown that this system may be rewritten in the following way

$$2(1-\nu) \frac{\partial^2 u_1}{\partial x_1^2} + \frac{\partial^2 u_2}{\partial x_1 \partial x_2} + (1-2\nu + \bar{\mathcal{F}}) \frac{\partial^2 u_1}{\partial x_2^2} = 0 \quad \text{for } 0 < x_1 < d, x_2 > 0, \quad (7.1)$$

$$(1-2\nu) \frac{\partial^2 u_2}{\partial x_1^2} + \frac{\partial^2 u_1}{\partial x_1 \partial x_2} + (2(1-\nu) + \bar{\mathcal{F}}) \frac{\partial^2 u_2}{\partial x_2^2} = 0 \quad \text{for } 0 < x_1 < d, x_2 > 0, \quad (7.2)$$

$$u_1 = 0, \quad \text{and} \quad u_2 = \tan(\phi) \left(x_1 - \frac{d}{2} \right) \quad \text{at} \quad x_2 = 0, \quad (7.3)$$

$$(1-\nu) \frac{\partial u_1}{\partial x_1} + \nu \frac{\partial u_2}{\partial x_2} = 0 \quad \text{at} \quad x_1 = 0, d, \quad (7.4)$$

$$\frac{\partial u_1}{\partial x_2} + \frac{\partial u_2}{\partial x_1} = 0 \quad \text{at} \quad x_1 = 0, d, \quad (7.5)$$

$$\nabla u_1, \nabla u_2 \rightarrow \mathbf{0} \quad \text{as} \quad x_2 \rightarrow \infty. \quad (7.6)$$

It is noted that (6.46) was found to be equivalent to (7.6) in Appendix 6.A. Due to the form of the governing equations (7.1) and (7.2), and the symmetry of the boundary conditions (7.3)–(7.6), it is found that u_1 and u_2 are symmetric and antisymmetric about $x_1 = d/2$, respectively. Finally, it is noted that as this system is linear, the angle of clamping ϕ only alters the overall amplitude of the deformations.

7.3 Application of Kirchhoff–Love Shell Theory

We now consider deriving an appropriate 1D model for the problem of bending a semi-infinite block under tension using Kirchhoff–Love shell theory.

In §6.9.1, it was found that the boundary-layer width $\tilde{\delta}_B$ of the deformations is larger than the thickness d of the block in both the regimes $\bar{\mathcal{F}} \rightarrow 0$ and $\bar{\mathcal{F}} \rightarrow \infty$. As such, the thickness of the block is smaller than any of the other geometric properties of the block, which is necessary for the use of Kirchhoff–Love shell theory. Because this condition is met, it initially appears that Kirchhoff–Love shell theory may be applied to the current problem when the axial tension is both small and large. (This is contrary to the prediction of the toy model in §3.6, which estimated that for large tension the boundary-layer width would be too small for Kirchhoff–Love shell theory to be applicable.)

Using Kirchhoff–Love shell theory, a 1D model can be derived for bending a semi-infinite block under tension. This is done by first using the Kirchhoff–Love

shell equations (Flügge, 1972; Søndergaard, 2007) to derive axial force-balance, normal force-balance and moment-balance equations, averaged over the width of the block. Usually, these equations are derived using a Cauchy stress tensor σ with a constitutive law for an isotropic linearly elastic solid. However, a different constitutive law must be used here that incorporates the pre-stress and its interactions with the rotations of the material (see §6.3). As such, in the 1D model the linearised constitutive law (6.23) for σ , derived using a modified Saint Venant–Kirchhoff model (Howell *et al.*, 2009, p. 230) in §6.3, is applied instead of the constitutive law for an isotropic linearly elastic solid. In doing so, the effects of the pre-stress are included in the modified force and moment-balance equations.

A pair of truncated Taylor series about $x_1 = d/2$ are then used to approximate the deformations u_1 and u_2 . By substituting these truncated series into the modified force and moment-balance equations, as well as into the linearised boundary conditions (7.3)–(7.6) of the linearised system (7.1)–(7.6) governing the block, a new one-dimensional governing system is formed.

Solving this new system, deformations that decay exponentially in the axial direction are found. However, the boundary-layer width of these deformations is found to behave vastly differently to the boundary-layer width found in the 2D model in Chapter 6, for large values of $\bar{\mathcal{F}}$. As this 1D model does not produce deformations that accurately display the behaviour shown in the 2D model, the details of the 1D model are omitted here.

This discrepancy in the boundary-layer widths occurs because in the case $\bar{\mathcal{F}} \rightarrow \infty$ ($\delta\ell \gg 1$), another of the assumptions needed in Kirchhoff–Love shell theory is violated. The full set of assumptions are listed by Søndergaard (2007), and one of the necessary assumptions is that the normal to the centre line of the material is preserved after a deformation. That is, the linearised strain tensor of the material e_{ij} , defined by

$$e_{ij} = \frac{1}{2} \left(\frac{\partial u_i}{\partial x_j} + \frac{\partial u_j}{\partial x_i} \right),$$

must satisfy

$$e_{i1} = 0,$$

where the x_1 -direction is normal to the shell. Hence, we must have

$$\frac{\partial u_1}{\partial x_2} = -\frac{\partial u_2}{\partial x_1}, \quad (7.7)$$

for Kirchhoff–Love shell theory to hold.

In Figure 7.2, $\partial u_1 / \partial x_2$ and $-\partial u_2 / \partial x_1$ have been plotted against x_1 , at a fixed x_2 within the boundary layer, for small and large $\bar{\mathcal{F}}$. In the plot with small $\bar{\mathcal{F}}$ ($\bar{\mathcal{F}} = 10^{-4}$), it is seen that although the two curves behave slightly differently, the difference in the amplitudes of the curves is very small, and both are well approximated by being uniform in x_1 . Hence, we have

$$\frac{\partial u_1}{\partial x_2} \sim -\frac{\partial u_2}{\partial x_1},$$

and the assumption of preservation of normals holds. Thus, the Kirchhoff–Love shell equations can accurately model the mechanics within the boundary layer for small $\bar{\mathcal{F}}$. In the plot with large $\bar{\mathcal{F}}$ ($\bar{\mathcal{F}} = 10^2$) however, there is a large difference between the values of $\partial u_1 / \partial x_2$ and $-\partial u_2 / \partial x_1$. As such

$$\frac{\partial u_1}{\partial x_2} \not\sim -\frac{\partial u_2}{\partial x_1},$$

and the assumption of preservation of normals is violated. Because of this, Kirchhoff–Love shell theory cannot be used to model the mechanics within the boundary layer for large $\bar{\mathcal{F}}$.

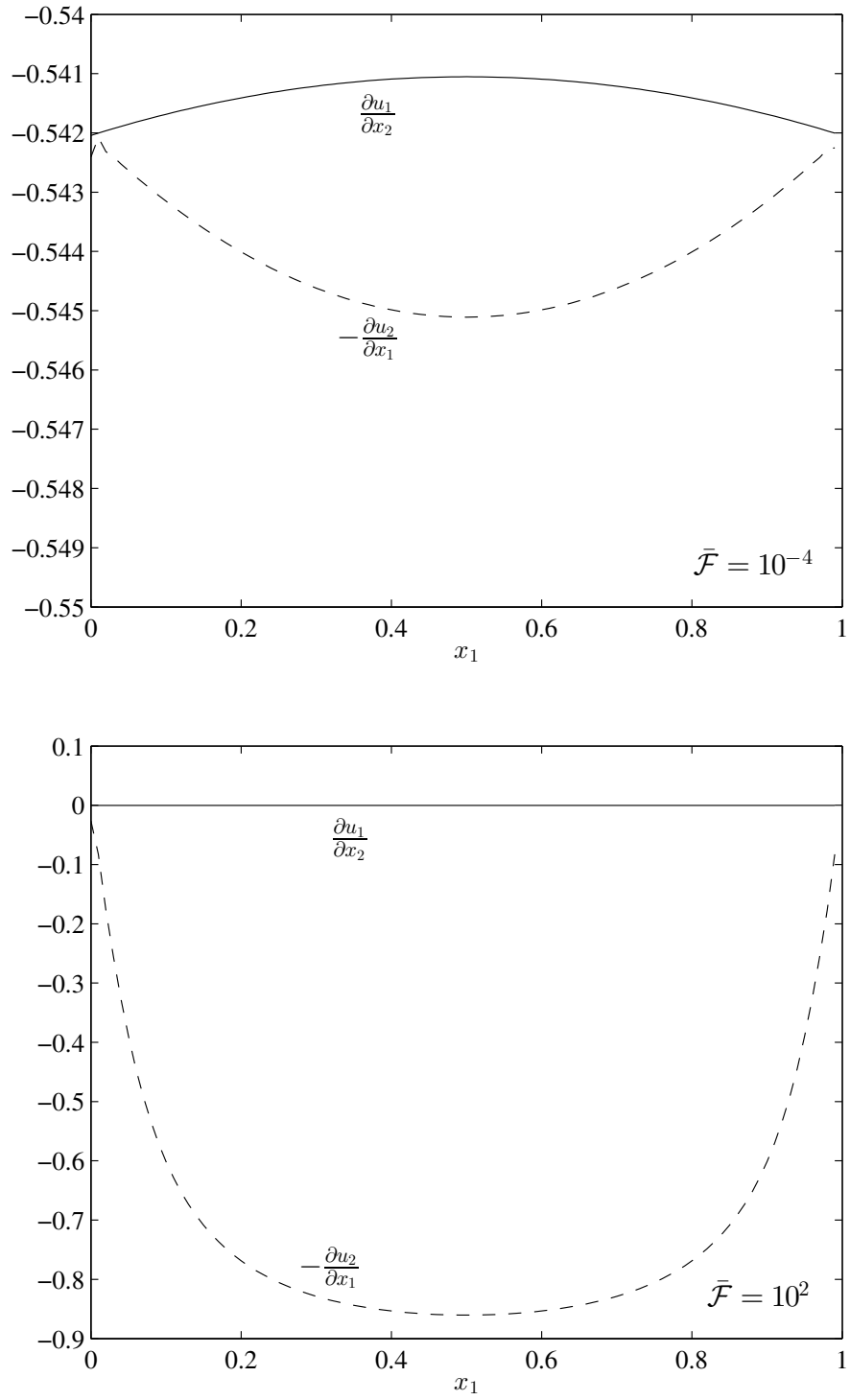


Figure 7.2: The numerical solutions for $\partial u_1 / \partial x_2$ (solid lines) and $-\partial u_2 / \partial x_1$ (dashed lines) across x_1 for $x_2 = 5$, in the case of small $\bar{\mathcal{F}}$ ($\bar{\mathcal{F}} = 10^{-4}$) and large $\bar{\mathcal{F}}$ ($\bar{\mathcal{F}} = 10^2$). Here, $d = 1$, $\nu = 0.49$, $\tan(\phi) = 1$ and $x_{\max} = 100$. The boundary-layer widths $\tilde{\delta}_B$ in the cases of small and large $\bar{\mathcal{F}}$ are calculated to be $\tilde{\delta}_B \approx 8.1$ and $\tilde{\delta}_B \approx 22.5$ respectively.

7.4 A 1D Model Derived from the Averaged Cauchy's Momentum Equation

Another potential 1D model that is considered is one that is derived from the components (6.65), (6.66) of Cauchy's momentum equation. The full details of the derivation of the model and its solution are found in Appendix 7.A. In summary, a pair of governing equations that are only dependent on the x_2 coordinate are derived by averaging the normal force-balance equation (6.65) as well as the moment-balance equation (derived by multiplying the axial-force balance equation (6.66) by $x_1 - d/2$) over the width of the block. Taylor series of u_1 and u_2 are then taken about $x_1 = d/2$. These series are truncated after the first non-zero terms and then substituted into the averaged normal force-balance and moment-balance equations, yielding a pair of coupled ODEs in terms of two variables. Boundary conditions are then obtained by substituting the truncated series into the boundary conditions (7.3)–(7.6) of the linearised system (7.1)–(7.6) governing the block.

Solving this model, it is found that u_1 and u_2 are approximated by

$$u_1 \sim \frac{(1-2\nu) \tan \phi}{(1-2\nu+\bar{\mathcal{F}})\bar{\Lambda}} \left(e^{-\bar{\Lambda}x_2} - 1 \right), \quad (7.8)$$

$$u_2 \sim \left(x_1 - \frac{d}{2} \right) \tan \phi e^{-\bar{\Lambda}x_2}. \quad (7.9)$$

Hence, both u_1 and u_2 decay exponentially to a constant, with decay rate

$$\bar{\Lambda} = \frac{1}{d} \left(\frac{12(1-2\nu)\bar{\mathcal{F}}}{(1-2\nu+\bar{\mathcal{F}})(2(1-\nu)+\bar{\mathcal{F}})} \right)^{\frac{1}{2}}, \quad (7.10)$$

as $x_2 \rightarrow \infty$. Denoting the boundary-layer width from this 1D model as $\tilde{\delta}_{CM} = 1/\bar{\Lambda}$, it is found that

$$\tilde{\delta}_{CM} = d \left(\frac{(1-2\nu+\bar{\mathcal{F}})(2(1-\nu)+\bar{\mathcal{F}})}{12(1-2\nu)\bar{\mathcal{F}}} \right)^{\frac{1}{2}}. \quad (7.11)$$

This is plotted against $\bar{\mathcal{F}}$ in Figure 7.3, along with the boundary-layer width $\tilde{\delta}_B$ from the 2D model, as seen in Figure 6.8. In both plots, $d = 1$ and $\nu = 0.49$. It is seen that although $\tilde{\delta}_{CM}$ has the same gradient (and thus the same power of $\bar{\mathcal{F}}$) as $\tilde{\delta}_B$ in the limits $\bar{\mathcal{F}} \rightarrow 0$ and $\bar{\mathcal{F}} \rightarrow \infty$, there is a constant difference between the two widths in both of these limits. This difference is particularly large for small values of $\bar{\mathcal{F}}$. As the decay rate $\bar{\Lambda}$ and boundary-layer width $\tilde{\delta}_{CM}$ are not matching with the fundamental decay rate Ω_0 and boundary-layer

width $\tilde{\delta}_B$ from the 2D model, the 1D model in Appendix 7.A is not accurately representing the deformations, even if it is displaying the right qualitative behaviour for the boundary-layer width.

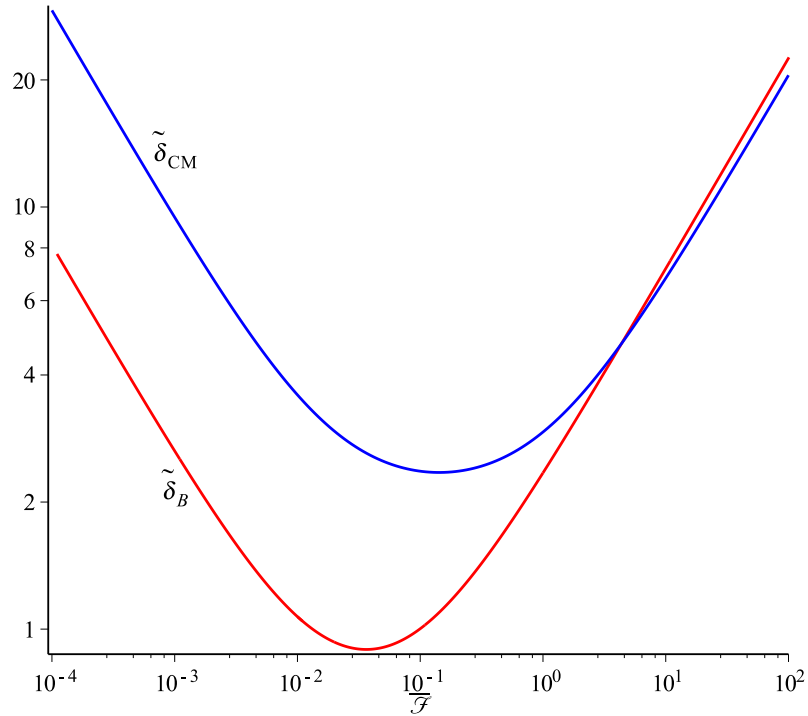


Figure 7.3: The boundary-layer width $\tilde{\delta}_{CM} = \bar{\Lambda}^{-1}$ given by (7.11), obtained from the 1D model in Appendix 7.A, against $\bar{\mathcal{F}}$ for $d = 1$, $\nu = 0.49$ (blue line). The solution of the boundary-layer width $\tilde{\delta}_B$ obtained from the 2D model, as seen in Figure 6.8, is plotted in red.

One cause of the differences between the 1D model in Appendix 7.A and the 2D model is the use of the truncated Taylor series to approximate the deformations u_1 and u_2 . As these Taylor series are truncated, information from the higher-order terms, which can significantly contribute to the overall solution, is lost. In particular, in the 1D model derived here, the deformations u_1 and u_2 are assumed to be constant and linear respectively in the x_1 -direction. However in the 2D model, u_1 and u_2 behave as trigonometric functions over the width of the block. This behaviour can be clearly seen in Figure 6.6. In order to better model this behaviour, higher-order terms are needed in the truncated Taylor series for u_1 and u_2 . Hence, one way to improve on the model in Appendix 7.A is to derive a 1D model that incorporates more terms from the Taylor series of u_1 and u_2 . Such a model is derived in §7.5.

7.5 Deriving a 1D Model from the System (6.88)–(6.93)

A new one-dimensional model for u_1 is now derived from the governing system (6.88)–(6.93). By using this system instead of the system (7.1)–(7.6) written in terms of u_1 and u_2 , it is possible to derive a system with three non-trivial governing equations instead of the two found in the 1D model in §7.4. Using this extra governing equation, three terms from a Taylor series of u_1 are incorporated into this model, as opposed to just the pair of leading-order terms in the Taylor series of u_1 and u_2 that were incorporated into the model in §7.4. As the model considered here incorporates more terms from the Taylor series, the deformations found in this 1D model are found to match the deformations in the 2D model better than either of the previous 1D models considered.

The system (6.88)–(6.93) once again is

$$0 = \frac{\partial^4 u_1}{\partial x_1^4} + \left[\frac{2(1-\nu) + \bar{\mathcal{F}}}{2(1-\nu)} + \frac{1-2\nu + \bar{\mathcal{F}}}{1-2\nu} \right] \frac{\partial^4 u_1}{\partial x_1^2 \partial x_2^2} + \frac{(2(1-\nu) + \bar{\mathcal{F}})(1-2\nu + \bar{\mathcal{F}})}{2(1-\nu)(1-2\nu)} \frac{\partial^4 u_1}{\partial x_2^4}, \quad (7.12)$$

$$\nabla u_1 \rightarrow \mathbf{0} \quad \text{as} \quad x_2 \rightarrow \infty, \quad (7.13)$$

$$u_1 = 0 \quad \text{at} \quad x_2 = 0, \quad (7.14)$$

$$2(1-\nu) \frac{\partial^2 u_1}{\partial x_1^2} - (2\nu - \bar{\mathcal{F}}) \frac{\partial^2 u_1}{\partial x_2^2} = 0 \quad \text{at} \quad x_1 = 0, d, \quad (7.15)$$

$$(1-2\nu + \bar{\mathcal{F}}) \left[\frac{\partial u_1}{\partial x_2} \right]_{x_2=0}^{x_2 \rightarrow \infty} + 2(1-\nu) \int_0^\infty \frac{\partial^2 u_1}{\partial x_1^2} dx_2 = \tan(\phi), \quad (7.16)$$

$$\int_0^d \left((1-\nu)(1-2\nu) \frac{\partial^2 u_1}{\partial x_1^2} - \nu(1-2\nu + \bar{\mathcal{F}}) \frac{\partial^2 u_1}{\partial x_2^2} \right) dx_1 = 0. \quad (7.17)$$

To derive a 1D model from this system, a Taylor series for u_1 about $x_1 = d/2$ is again considered. This series will instead be truncated after the third non-zero term, as opposed to truncating after the first non-zero terms in the Taylor series for u_1 and u_2 in the 1D model in §7.4. Truncating the Taylor series for u_1 at this higher order allows constant, quadratic and quartic variation in u_1 across the width of the block to be incorporated into the model. This is different from the model in §7.4 that instead incorporates only constant behaviour in u_1 and linear behaviour in u_2 across the width of the block. Although it is possible to include even more higher-order terms from the Taylor series of u_1 within the model, it is found that only the first three terms of the Taylor series appear at leading

order in d and $x_1 - d/2$ in the governing equations. Hence, the higher-order governing equations in the system are needed to find the higher-order terms in the Taylor series. As such, to derive the simplest complete governing system, only the first three terms of the Taylor series for u_1 are considered.

7.5.1 Governing Equations, Boundary and Integral Conditions

As a starting point for deriving a one-dimensional model from the system (7.12)–(7.17), the following Taylor series for u_1 about $x_1 = d/2$ is considered

$$u_1 = u_1^{(0)}(x_2) + \left(x_1 - \frac{d}{2}\right)^2 u_1^{(2)}(x_2) + \left(x_1 - \frac{d}{2}\right)^4 u_1^{(4)}(x_2) + \dots, \quad (7.18)$$

where we set $u_1^{(1)} = u_1^{(3)} = \dots = 0$ so that u_1 is symmetric about $x_1 = d/2$, as required by the symmetry of the system (see §6.2). To obtain the governing equations for the one-dimensional model, (7.18) is substituted into the governing equation (7.12), the boundary condition (7.15) at $x_1 = 0, d$ and the integral condition (7.17) in the x_1 -direction. Doing so yields

$$\begin{aligned} 0 = & \Lambda_1^2 \Lambda_2^2 \frac{d^4 u_1^{(0)}}{dx_2^4} + 2(\Lambda_1^2 + \Lambda_2^2) \frac{d^2 u_1^{(2)}}{dx_2^2} + 24 u_1^{(4)} \\ & + \left(x_1 - \frac{d}{2}\right)^2 \left(\Lambda_1^2 \Lambda_2^2 \frac{d^4 u_1^{(2)}}{dx_2^4} + 12(\Lambda_1^2 + \Lambda_2^2) \frac{d^2 u_1^{(4)}}{dx_2^2} + \dots \right) \\ & + \left(x_1 - \frac{d}{2}\right)^4 \left(\Lambda_1^2 \Lambda_2^2 \frac{d^4 u_1^{(4)}}{dx_2^4} + \dots \right) + O\left(\left(x_1 - \frac{d}{2}\right)^6\right), \end{aligned} \quad (7.19)$$

$$\begin{aligned} 0 = & -(2\nu - \bar{\mathcal{F}}) \frac{d^2 u_1^{(0)}}{dx_2^2} + 4(1-\nu) u_1^{(2)} + d^2 \left(-\frac{(2\nu - \bar{\mathcal{F}})}{4} \frac{d^2 u_1^{(2)}}{dx_2^2} + 6(1-\nu) u_1^{(4)} \right) \\ & + d^4 \left(-\frac{(2\nu - \bar{\mathcal{F}})}{16} \frac{d^2 u_1^{(4)}}{dx_2^2} + \dots \right) + O(d^6), \end{aligned} \quad (7.20)$$

$$\begin{aligned} 0 = & d \left(-\nu(1-2\nu + \bar{\mathcal{F}}) \frac{d^2 u_1^{(0)}}{dx_2^2} + 2(1-\nu)(1-2\nu) u_1^{(2)} \right) \\ & + d^3 \left(-\frac{\nu(1-2\nu + \bar{\mathcal{F}})}{12} \frac{d^2 u_1^{(2)}}{dx_2^2} + (1-\nu)(1-2\nu) u_1^{(4)} \right) \\ & + d^5 \left(-\frac{\nu(1-2\nu + \bar{\mathcal{F}})}{80} \frac{d^2 u_1^{(4)}}{dx_2^2} + \dots \right) + O(d^7), \end{aligned} \quad (7.21)$$

where Λ_1 and Λ_2 are given by

$$\Lambda_1 = \sqrt{\frac{2(1-\nu) + \bar{\mathcal{F}}}{2(1-\nu)}}, \quad \Lambda_2 = \sqrt{\frac{1-2\nu + \bar{\mathcal{F}}}{1-2\nu}},$$

as in (6.101), and the dots represent the $u_1^{(6)}$ and higher-order terms from the Taylor series (7.18) of u_1 . Substituting the Taylor series (7.18) into the remaining conditions (7.13), (7.14) and (7.16) of the system (7.12)–(7.17) yields the following conditions

$$2 \left(x_1 - \frac{d}{2} \right) u_1^{(2)} + 4 \left(x_1 - \frac{d}{2} \right)^3 u_1^{(4)} + \dots \rightarrow 0 \quad \text{as } x_2 \rightarrow \infty, \quad (7.22)$$

$$\frac{du_1^{(0)}}{dx_2} + \left(x_1 - \frac{d}{2} \right)^2 \frac{du_1^{(2)}}{dx_2} + \left(x_1 - \frac{d}{2} \right)^4 \frac{du_1^{(4)}}{dx_2} + \dots \rightarrow 0 \quad \text{as } x_2 \rightarrow \infty, \quad (7.23)$$

$$u_1^{(0)} + \left(x_1 - \frac{d}{2} \right)^2 u_1^{(2)} + \left(x_1 - \frac{d}{2} \right)^4 u_1^{(4)} + \dots = 0 \quad \text{at } x_2 = 0, \quad (7.24)$$

$$\begin{aligned} \tan \phi = & (1 - 2\nu + \bar{\mathcal{F}}) \left[\frac{du_1^{(0)}}{dx_2} \right]_{x_2=0}^{x_2 \rightarrow \infty} + 4(1 - \nu) \int_0^\infty u_1^{(2)} dx_2 \\ & + \left(x_1 - \frac{d}{2} \right)^2 \left[(1 - 2\nu + \bar{\mathcal{F}}) \left[\frac{du_1^{(2)}}{dx_2} \right]_{x_2=0}^{x_2 \rightarrow \infty} + 24(1 - \nu) \int_0^\infty u_1^{(4)} dx_2 \right] \\ & + \left(x_1 - \frac{d}{2} \right)^4 \left[(1 - 2\nu + \bar{\mathcal{F}}) \left[\frac{du_1^{(4)}}{dx_2} \right]_{x_2=0}^{x_2 \rightarrow \infty} + \dots \right] \\ & + O \left(\left(x_1 - \frac{d}{2} \right)^6 \right), \end{aligned} \quad (7.25)$$

where once again the dots represent the $u_1^{(6)}$ and higher-order terms from the Taylor series (7.18) of u_1 .

It is seen that substituting the Taylor series (7.18) into the system (7.12)–(7.17) gives a set of three coupled governing equations for the functions $u_1^{(0)}(x_2), u_1^{(2)}(x_2), u_1^{(4)}(x_2), \dots$ comprising the Taylor series, as well as some boundary and integral conditions for these functions. As we only have three governing equations, the leading-order equations in d and $x_1 - d/2$ can only be fully solved for three of the functions within the Taylor series. As such, the Taylor series is truncated after the $u_1^{(4)}$ term to obtain the following approximation for u_1

$$u_1 \sim u_1^{(0)}(x_2) + \left(x_1 - \frac{d}{2} \right)^2 u_1^{(2)}(x_2) + \left(x_1 - \frac{d}{2} \right)^4 u_1^{(4)}(x_2), \quad (7.26)$$

and the system (7.19)–(7.25) must be converted into a system to be solved for $u_1^{(0)}$, $u_1^{(2)}$ and $u_1^{(4)}$.

First, the governing equations (7.19)–(7.21) are converted into a set of three coupled ODEs for $u_1^{(0)}$, $u_1^{(2)}$ and $u_1^{(4)}$. This is achieved by neglecting the terms of

$O((x_1 - d/2)^2)$, $O(d^4)$ and $O(d^5)$ in (7.19), (7.20) and (7.21) respectively. Doing so, we neglect all the $u_1^{(6)}$ and higher-order terms from the Taylor series (7.18) that appear within (7.19)–(7.21) at these sizes. Neglecting these terms yields the following coupled ODEs

$$0 = \Lambda_1^2 \Lambda_2^2 \frac{d^4 u_1^{(0)}}{dx_2^4} + 2(\Lambda_1^2 + \Lambda_2^2) \frac{d^2 u_1^{(2)}}{dx_2^2} + 24 u_1^{(4)}, \quad (7.27)$$

$$0 = -(2\nu - \bar{\mathcal{F}}) \frac{d^2 u_1^{(0)}}{dx_2^2} + 4(1 - \nu) u_1^{(2)} + d^2 \left(-\frac{(2\nu - \bar{\mathcal{F}})}{4} \frac{d^2 u_1^{(2)}}{dx_2^2} + 6(1 - \nu) u_1^{(4)} \right), \quad (7.28)$$

$$0 = -\nu(1 - 2\nu + \bar{\mathcal{F}}) \frac{d^2 u_1^{(0)}}{dx_2^2} + 2(1 - \nu)(1 - 2\nu) u_1^{(2)} + d^2 \left(-\frac{\nu(1 - 2\nu + \bar{\mathcal{F}})}{12} \frac{d^2 u_1^{(2)}}{dx_2^2} + (1 - \nu)(1 - 2\nu) u_1^{(4)} \right), \quad (7.29)$$

where (7.21) has been divided by a factor of d to give (7.29).

Next, the boundary conditions (7.22)–(7.24) are converted to conditions on $u_1^{(0)}$, $u_1^{(2)}$ and $u_1^{(4)}$. By neglecting terms involving $u_1^{(6)}, u_1^{(8)}, \dots$ within (7.22)–(7.24), and equating the coefficients of $(x_1 - d/2)^n$, it is found that

$$\frac{du_1^{(0)}}{dx_2}, u_1^{(2)}, u_1^{(4)} \rightarrow 0 \quad \text{as} \quad x_2 \rightarrow \infty, \quad (7.30)$$

$$u_1^{(0)}(0) = u_1^{(2)}(0) = u_1^{(4)}(0) = 0. \quad (7.31)$$

It is also found from (7.23) that

$$\frac{du_1^{(2)}}{dx_2}, \frac{du_1^{(4)}}{dx_2} \rightarrow 0 \quad \text{as} \quad x_2 \rightarrow \infty. \quad (7.32)$$

However, it is later found that the governing equations (7.27)–(7.29) of this system can be reduced to a homogeneous, sixth-order ODE with constant coefficients for $u_1^{(0)}$. This form of ODE has exponential, sinusoidal, linear and constant solutions, and it is also later found that the functions $u_1^{(2)}$ and $u_1^{(4)}$ have these behaviours as well. As such, any solution of (7.27)–(7.29) that satisfies the conditions (7.30) also satisfies the conditions (7.32). Hence, the conditions (7.32) are superfluous.

Finally, two suitable integral conditions are obtained from (7.25) by equating the coefficients of $(x_1 - d/2)^0$ and $(x_1 - d/2)^2$, and neglecting terms of $O((x_1 - d/2)^4)$ as the functions $u_1^{(6)}, u_1^{(8)}, \dots$ appear at this order. The two

integral conditions are found to be

$$\tan \phi = (1 - 2\nu + \bar{\mathcal{F}}) \left[\frac{du_1^{(0)}}{dx_2} \right]_{x_2=0}^{x_2 \rightarrow \infty} + 4(1 - \nu) \int_0^\infty u_1^{(2)} dx_2, \quad (7.33)$$

$$0 = (1 - 2\nu + \bar{\mathcal{F}}) \left[\frac{du_1^{(2)}}{dx_2} \right]_{x_2=0}^{x_2 \rightarrow \infty} + 24(1 - \nu) \int_0^\infty u_1^{(4)} dx_2. \quad (7.34)$$

It is later found that the boundary and integral conditions (7.30)–(7.34) impose nine constraints on a system with only eight degrees of freedom. Hence, one of these constraints will have to be dropped to enable a solution for the system (7.27)–(7.34) to be found. This is considered further in §7.5.5, but for the time being we will only apply the conditions (7.30) to ensure the arising deformations decay as $x_2 \rightarrow \infty$.

7.5.2 Eliminating $u_1^{(2)}$ and $u_1^{(4)}$ from the Governing Equations

To solve the system (7.27)–(7.34), $u_1^{(2)}(x_2)$ and $u_1^{(4)}(x_2)$ are first eliminated from the governing equations (7.27)–(7.29) to form a single ODE for $u_1^{(0)}(x_2)$. Rearranging (7.27) gives

$$u_1^{(4)} = -\frac{\Lambda_1^2 \Lambda_2^2}{24} \frac{d^4 u_1^{(0)}}{dx_2^4} - \frac{(\Lambda_1^2 + \Lambda_2^2)}{12} \frac{d^2 u_1^{(2)}}{dx_2^2}. \quad (7.35)$$

Substituting (7.35) into (7.28) and (7.29) and rearranging yields the following

$$\mathcal{A}u_1^{(2)} = \mathcal{B}u_1^{(0)}, \quad (7.36)$$

$$\mathcal{C}u_1^{(2)} = \mathcal{D}u_1^{(0)}, \quad (7.37)$$

where the operators \mathcal{A} , \mathcal{B} , \mathcal{C} and \mathcal{D} are defined as

$$\mathcal{A} = 4(1 - \nu) - \frac{d^2}{4} [2\nu - \bar{\mathcal{F}} + 2(1 - \nu)(\Lambda_1^2 + \Lambda_2^2)] \frac{d^2}{dx_2^2}, \quad (7.38)$$

$$\mathcal{B} = (2\nu - \bar{\mathcal{F}}) \frac{d^2}{dx_2^2} + \frac{d^2}{4} (1 - \nu) \Lambda_1^2 \Lambda_2^2 \frac{d^4}{dx_2^4}, \quad (7.39)$$

$$\mathcal{C} = 2(1 - \nu)(1 - 2\nu) - \frac{d^2}{12} [\nu(1 - 2\nu + \bar{\mathcal{F}}) + (1 - \nu)(1 - 2\nu)(\Lambda_1^2 + \Lambda_2^2)] \frac{d^2}{dx_2^2}, \quad (7.40)$$

$$\mathcal{D} = \nu(1 - 2\nu + \bar{\mathcal{F}}) \frac{d^2}{dx_2^2} + \frac{d^2}{24} (1 - \nu)(1 - 2\nu) \Lambda_1^2 \Lambda_2^2 \frac{d^4}{dx_2^4}. \quad (7.41)$$

We now eliminate $u_1^{(2)}$ from (7.36) and (7.37). To do so, we apply the operator \mathcal{C} to (7.36), as well as apply the operator \mathcal{A} to (7.37). The difference between

these expressions then gives

$$(\mathcal{BC} - \mathcal{AD}) u_1^{(0)} = 0. \quad (7.42)$$

Substituting the definitions (7.38)–(7.41) for the operators \mathcal{A} , \mathcal{B} , \mathcal{C} and \mathcal{D} into (7.42) and rearranging, the following ODE for $u_1^{(0)}$ is obtained

$$\frac{d^6 u_1^{(0)}}{dx_2^6} - \frac{\bar{M}}{d^2} \frac{d^4 u_1^{(0)}}{dx_2^4} + \frac{\bar{N}}{d^4} \frac{d^2 u_1^{(0)}}{dx_2^2} = 0, \quad (7.43)$$

where \bar{M} and \bar{N} are set to be

$$\bar{M} = \frac{64 \left((1-2\nu)^2 + \bar{\mathcal{F}}(1-2\nu)(2-\nu) + \bar{\mathcal{F}}^2 \left(\frac{7}{8} - \nu \right) \right)}{\bar{\mathcal{F}}(2(1-\nu) + \bar{\mathcal{F}})(1-2\nu+\bar{\mathcal{F}})}, \quad (7.44)$$

$$\bar{N} = \frac{384(1-\nu)(1-2\nu)}{(2(1-\nu) + \bar{\mathcal{F}})(1-2\nu+\bar{\mathcal{F}})}. \quad (7.45)$$

It is noted that as the Poisson's ratio ν must satisfy $-1 < \nu < 1/2$, and $\bar{\mathcal{F}} > 0$, we have $\bar{M}, \bar{N} > 0$.

7.5.3 General Solution for $u_1^{(0)}$

The general solution of (7.43) is calculated to be

$$u_1^{(0)}(x_2) = A_1 e^{\frac{r_+}{d} x_2} + A_2 e^{-\frac{r_+}{d} x_2} + A_3 e^{\frac{r_-}{d} x_2} + A_4 e^{-\frac{r_-}{d} x_2} + A_5 x_2 + A_6, \quad (7.46)$$

where

$$r_{\pm} = \left(\frac{\bar{M} \pm \sqrt{\bar{M}^2 - 4\bar{N}}}{2} \right)^{\frac{1}{2}}, \quad (7.47)$$

and A_1, \dots, A_6 are constants to be found. Without loss of generality, we take $\text{Re}(r_{\pm}) \geq 0$. To determine the behaviour of the modes, we must find whether r_+ and r_- are real or complex.

We first determine whether r_+^2 and r_-^2 are real or complex. Using the definitions (7.44) and (7.45) of \bar{M} and \bar{N} , the discriminant $\bar{M}^2 - 4\bar{N}$ found within the definition (7.47) for r_{\pm} is calculated to be

$$\begin{aligned} \bar{M}^2 - 4\bar{N} = & \frac{64}{\bar{\mathcal{F}}^2(2(1-\nu) + \bar{\mathcal{F}})^2(1-2\nu+\bar{\mathcal{F}})^2} \left[\bar{\mathcal{F}}^4(4\nu-5)^2 \right. \\ & + 8\bar{\mathcal{F}}^3(1-2\nu)(4\nu^2-25\nu+19) + 16\bar{\mathcal{F}}^2(1-2\nu)^2(\nu^2-18\nu+20) \\ & \left. + 128\bar{\mathcal{F}}(1-2\nu)^3(2-\nu) + 64(1-2\nu)^4 \right]. \end{aligned} \quad (7.48)$$

As $\bar{\mathcal{F}} > 0$ and $-1 < \nu < 1/2$, all the coefficients of the powers of $\bar{\mathcal{F}}$ in (7.48), as well as the fraction multiplying the power series of $\bar{\mathcal{F}}$ within (7.48), are positive

and we have $\bar{M}^2 - 4\bar{N} > 0$. Hence, from the definition (7.47), it is seen that $r_{\pm}^2 \in \mathbb{R}$.

Now we determine whether r_+ and r_- are real or complex. As $\bar{M}, \bar{N} > 0$ and $\bar{M}^2 - 4\bar{N} > 0$ for $\bar{\mathcal{F}} > 0$ and $-1 < \nu < 1/2$, we must have

$$\bar{M} > \sqrt{\bar{M}^2 - 4\bar{N}},$$

which in turn yields

$$\bar{M} \pm \sqrt{\bar{M}^2 - 4\bar{N}} > 0.$$

Hence, we have $r_{\pm} \in \mathbb{R}$ for $\bar{\mathcal{F}} > 0$, $-1 < \nu < 1/2$, and the modes in the general solution (7.46) are exponentially growing and decaying, with no oscillatory behaviour.

As r_+ and r_- are both real and positive, it is seen that for (7.46) to satisfy the boundary condition (7.30), the exponentially growing modes must be eliminated and we must set

$$A_1 = A_3 = A_5 = 0. \quad (7.49)$$

Substituting (7.49) into (7.46), we obtain the following expression for $u_1^{(0)}$

$$u_1^{(0)}(x_2) = A_2 e^{-\frac{r_+}{d} x_2} + A_4 e^{-\frac{r_-}{d} x_2} + A_6. \quad (7.50)$$

7.5.4 General Solutions for $u_1^{(2)}$ and $u_1^{(4)}$

Using the expression (7.50) for $u_1^{(0)}(x_2)$, it is possible to obtain the general solutions for $u_1^{(2)}(x_2)$ and $u_1^{(4)}(x_2)$. Substituting (7.50) into (7.36) and rearranging, the following ODE for $u_1^{(2)}$ is obtained

$$\frac{d^2 u_1^{(2)}}{dx_2^2} - \frac{C_1^2}{d^2 C_0^2} u_1^{(2)} = -\frac{1}{d^4 C_0^2} \left(A_2 C_+ e^{-\frac{r_+}{d} x_2} + A_4 C_- e^{-\frac{r_-}{d} x_2} \right), \quad (7.51)$$

where

$$C_0 = \left(\frac{2((1-2\nu)(2-\nu) + \bar{\mathcal{F}}(1-\nu))}{1-2\nu} \right)^{\frac{1}{2}}, \quad C_1 = 4(1-\nu)^{\frac{1}{2}}, \quad (7.52)$$

and

$$C_{\pm} = 4(2\nu - \bar{\mathcal{F}})r_{\pm}^2 + (1-\nu)\Lambda_1^2\Lambda_2^2r_{\pm}^4. \quad (7.53)$$

It is noted that as $\bar{\mathcal{F}} > 0$ and $-1 < \nu < 1/2$, we have $C_0, C_1 > 0$. The general solution of (7.51) is calculated to be

$$u_1^{(2)}(x_2) = B_1 e^{\frac{C_1}{dC_0} x_2} + B_2 e^{-\frac{C_1}{dC_0} x_2} + \frac{1}{d^2} \left(A_2 K_+ e^{-\frac{r_+}{d} x_2} + A_4 K_- e^{-\frac{r_-}{d} x_2} \right), \quad (7.54)$$

where

$$K_{\pm} = \frac{C_{\pm}}{C_1^2 - C_0^2 r_{\pm}}, \quad (7.55)$$

and B_1, B_2 are constants to be found. For (7.54) to satisfy the condition (7.30) as $x_2 \rightarrow \infty$, $u_1^{(2)}$ cannot be exponentially growing. Hence as $C_0, C_1 > 0$, we must have $B_1 = 0$ and the first term of (7.54) vanishes.

Finally, using the expressions (7.50) and (7.54) for $u_1^{(0)}$ and $u_1^{(2)}$, an expression for $u_1^{(4)}$ is derived. Substituting (7.50) and (7.54) into (7.35) gives for $u_1^{(4)}$

$$u_1^{(4)}(x_2) = \frac{A_2 L_+}{d^4} e^{-\frac{r_+}{d} x_2} + \frac{A_4 L_-}{d^4} e^{-\frac{r_-}{d} x_2} - \frac{B_2 (\Lambda_1^2 + \Lambda_2^2) C_1^2}{12 d^2 C_0^2} e^{-\frac{C_1}{d C_0} x_2}, \quad (7.56)$$

where

$$L_{\pm} = -\frac{1}{12} \left((\Lambda_1^2 + \Lambda_2^2) K_{\pm} r_{\pm}^2 + \frac{\Lambda_1^2 \Lambda_2^2 r_{\pm}^4}{2} \right). \quad (7.57)$$

7.5.5 Finding the Full Solution of the 1D Model

Now that expressions for $u_1^{(0)}(x_2)$, $u_1^{(2)}(x_2)$ and $u_1^{(4)}(x_2)$ have been derived, the next step is to apply the remaining boundary and integral conditions (7.31), (7.33) and (7.34), in order to obtain values for the four unknown constants A_2 , A_4 , A_6 and B_2 . It is first noted that (7.31), (7.33) and (7.34) give five different conditions. As we only have 4 unknown constants to be found within the 1D model, there are not enough degrees of freedom to satisfy all the conditions. As such, one of these conditions must be neglected to ensure the degrees of freedom and conditions imposed in the model are consistent. In the following, we neglect the condition $u_1^{(4)}(0) = 0$ so there is an equal number of boundary conditions at $x_2 = 0$ and integral conditions across the length of the block. It is found that neglecting the condition $u_1^{(4)}(0) = 0$, as opposed to neglecting the other conditions, yields the solution that closest resembles the results from the 2D model. However, we will see in §7.5.7 that there are still significant discrepancies between the two results.

Applying the conditions (7.31) for $u_1^{(0)}$ and $u_1^{(2)}$ at $x_2 = 0$ to the expressions (7.50) and (7.54) for $u_1^{(0)}$ and $u_1^{(2)}$ gives the following relations after rearranging

$$A_6 = -(A_2 + A_4), \quad (7.58)$$

$$B_2 = -\frac{1}{d^2} (A_2 K_+ + A_4 K_-). \quad (7.59)$$

Substituting (7.50), (7.54) and the expression (7.59) for B_2 into the first integral

condition (7.33) and rearranging yields

$$A_4 = \frac{d \tan \phi}{\chi_-} - \frac{A_2 \chi_+}{\chi_-}, \quad (7.60)$$

where the χ_{\pm} are defined as

$$\chi_{\pm} = (1 - 2\nu + \bar{\mathcal{F}})r_{\pm} + 4(1 - \nu)K_{\pm} \left(\frac{1}{r_{\pm}} - \frac{C_0}{C_1} \right). \quad (7.61)$$

Finally, the expressions (7.54) and (7.56) for $u_1^{(2)}$ and $u_1^{(4)}$, and the expressions (7.59) and (7.60) for B_2 and A_4 , are substituted into the second integral condition (7.34) to yield the following expression for A_2 after rearranging

$$A_2 = -\frac{d \tan \phi \chi_1}{\chi_- \chi_2}, \quad (7.62)$$

where

$$\chi_1 = (1 - 2\nu + \bar{\mathcal{F}})K_- \left(r_- - \frac{C_1}{C_0} \right) + 24(1 - \nu) \left(\frac{L_-}{r_-} + \frac{(\Lambda_1^2 + \Lambda_2^2)C_1K_-}{12C_0} \right), \quad (7.63)$$

$$\begin{aligned} \chi_2 = & (1 - 2\nu + \bar{\mathcal{F}}) \left[K_+ \left(r_+ - \frac{C_1}{C_0} \right) + \frac{K_- \chi_+}{\chi_-} \left(\frac{C_1}{C_0} - r_- \right) \right] \\ & + 24(1 - \nu) \left[\frac{L_+}{r_+} - \frac{\chi_+ L_-}{\chi_- r_-} + \frac{(\Lambda_1^2 + \Lambda_2^2)C_1}{12C_0} \left(K_+ - \frac{K_- \chi_+}{\chi_-} \right) \right]. \end{aligned} \quad (7.64)$$

Substituting the solutions (7.50), (7.54) and (7.56) for $u_1^{(0)}$, $u_1^{(2)}$ and $u_1^{(4)}$ into the truncated Taylor series (7.26), the 1D-model approximation for u_1 is found to be

$$\begin{aligned} u_1 = & A_2 e^{-\frac{r_+}{d} x_2} + A_4 e^{-\frac{r_-}{d} x_2} + A_6 \\ & + \left(x_1 - \frac{d}{2} \right)^2 \left[B_2 e^{-\frac{C_1}{dC_0} x_2} + \frac{1}{d^2} \left(A_2 K_+ e^{-\frac{r_+}{d} x_2} + A_4 K_- e^{-\frac{r_-}{d} x_2} \right) \right] \\ & + \left(x_1 - \frac{d}{2} \right)^4 \left(\frac{A_2 L_+}{d^4} e^{-\frac{r_+}{d} x_2} + \frac{A_4 L_-}{d^4} e^{-\frac{r_-}{d} x_2} - \frac{B_2 (\Lambda_1^2 + \Lambda_2^2) C_1^2}{12d^2 C_0^2} e^{-\frac{C_1}{dC_0} x_2} \right), \end{aligned} \quad (7.65)$$

where A_2 , A_4 , A_6 and B_2 are given by (7.58)–(7.60) and (7.62).

7.5.6 Comparing the Decay Rates in the 1D and 2D models

We now compare the deformations obtained from this 1D model to the deformations obtained from the 2D model, starting with the decay rates of the modes. In the 2D model we obtain countably many modes, whereas in the

1D model we have three modes with three distinct decay rates. In Figure 7.4, the decay rate Ω_0 of the fundamental mode found from the 2D model, as seen in Figure 6.5, is plotted against $\bar{\mathcal{F}}$. Also plotted are the following decay rates from the 1D model: r_+ and r_- as defined in (7.47), and C_1/C_0 where C_0, C_1 are defined in (7.52). It is seen from the figure that there is good agreement between Ω_0 , r_- and C_1/C_0 in the limit $\bar{\mathcal{F}} \rightarrow \infty$. The decay rate r_- is still in strong agreement with Ω_0 in the limit $\bar{\mathcal{F}} \rightarrow 0$, and it is only in the transitional region between the two limits where there is a slight difference between r_- and Ω_0 . However, in the limit $\bar{\mathcal{F}} \rightarrow 0$, the value of C_1/C_0 diverges away from the values of r_- and Ω_0 to a larger constant value. Finally, it is seen that the decay rate r_+ is much larger than any of the other decay rates for all values of $\bar{\mathcal{F}} > 0$.

From this, it is concluded that the decay rate of the fundamental (and slowest decaying) mode is being captured by the 1D model, either using one mode in the case of small $\bar{\mathcal{F}}$, or two modes for large $\bar{\mathcal{F}}$. As it is the fundamental mode that determines the boundary-layer width, we also conclude that the 1D model is accurately representing the boundary-layer width.

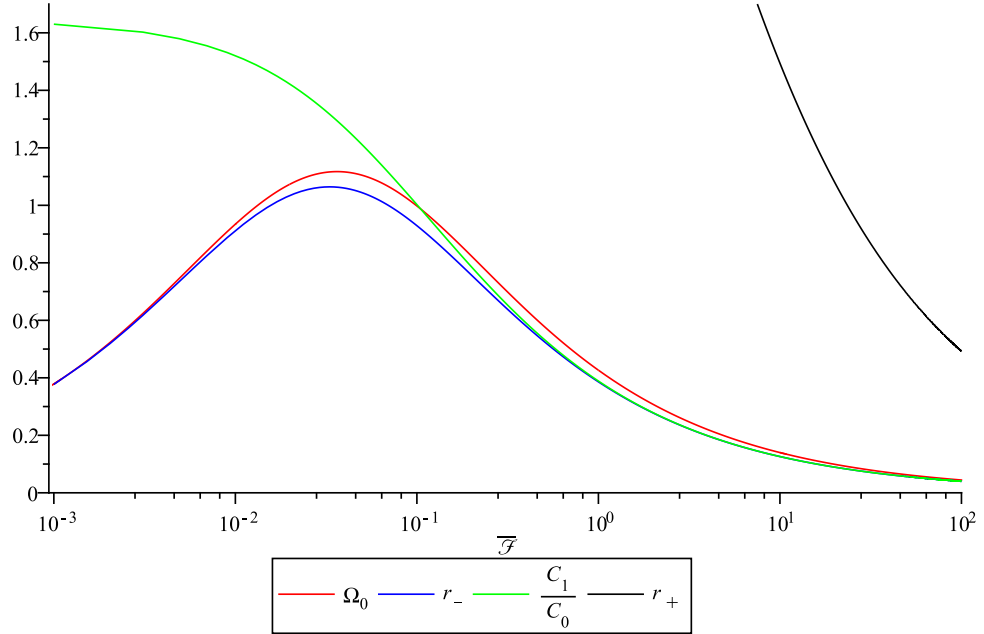


Figure 7.4: The solution of the fundamental decay rate Ω_0 from the 2D model (red line) against $\bar{\mathcal{F}}$, as seen in Figure 6.5. Also plotted are the following decay rates from the 1D model: r_+ and r_- as defined in (7.47) and C_1/C_0 (where C_0, C_1 are defined in (7.52)), in black, blue and green respectively.

In Figure 7.5, the decay rates Ω_1 , Ω_2 and Ω_3 of the first, second and third

modes from the 2D model, as well as the decay rate r_+ from the 1D model, have been plotted against $\bar{\mathcal{F}}$. It is observed that the decay rate r_+ has a higher value than the decay rates from the 2D model in the limit $\bar{\mathcal{F}} \rightarrow \infty$. However as $\bar{\mathcal{F}} \rightarrow 0$, r_+ becomes smaller than the decay rates from the 2D model. As such, r_+ does not appear to be reflecting any of the decay rates found in the 2D model. This is likely due to only incorporating the first three terms of the Taylor series (7.18) for u_1 within the 1D model, whereas in reality the higher-order terms of the Taylor series play a part in capturing the decay rates of the higher-order modes. We note that the variations seen in Ω_1 , Ω_2 and Ω_3 are part of the solution and not down to some numerical deficiency. Further details of these variations can be found in Appendix 6.B.

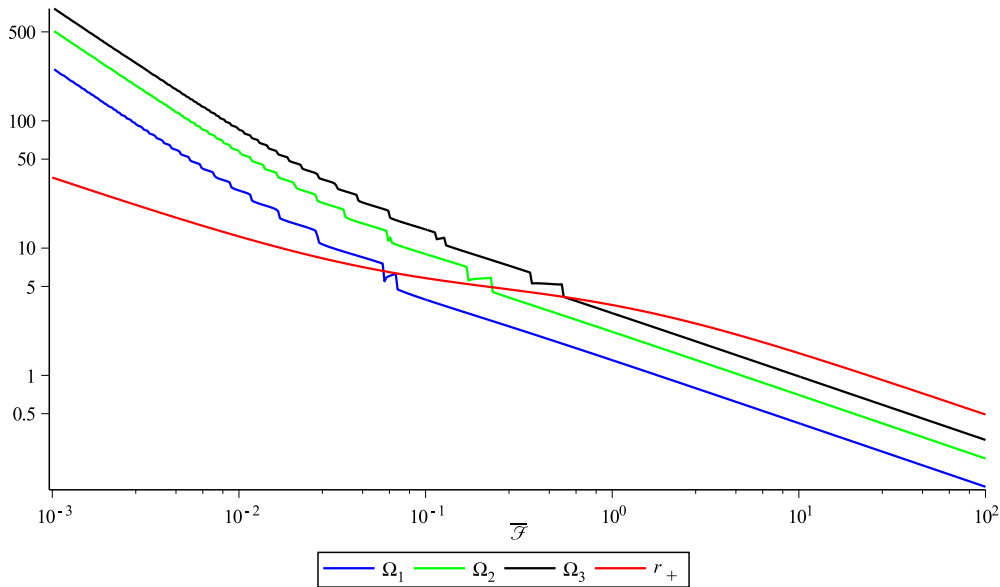


Figure 7.5: The solutions of the decay rates Ω_1 , Ω_2 and Ω_3 of the first, second and third modes from the 2D model (blue, green and black lines respectively) against $\bar{\mathcal{F}}$, as seen in Figure 6.5. Also plotted is the decay rate r_+ from the 1D model as defined in (7.47) (red line).

7.5.7 Comparing the Deformations in the 1D and 2D models

We now compare the deformations numerically obtained from the 2D model and those obtained from the 1D model, for different values of $\bar{\mathcal{F}}$. In Figure 7.6, the numerical solution of u_1 from the 2D model and the analytic solution of u_1 from the 1D model have been plotted in the x_1 and x_2 -directions, for $d = 1$, $\nu = 0.49$, $\tan(\phi) = 1$ and $\bar{\mathcal{F}} = 0.001$. In the plot in the x_1 -direction, the 2D and

1D model solutions of the normalised function $u_1 - u_1(0, x_2)$ have been plotted at the values $x_2 = 2, 4, 6$. This normalisation has been chosen as it forces the deformations from the 2D and 1D models to have a value of 0 when $x_1 = 0$, allowing for easier comparison between the two solutions in the x_1 -direction. It is seen that in the x_1 -direction, the deformation u_1 is behaving the same in both the 2D and 1D models, but the amplitude of the deformation is slightly larger in the 1D model. In the plot in the x_2 -direction, the values of u_1 from the 2D and 1D models have been plotted at $x_1 = 0.5$. As in the x_1 -direction, we find that the deformation u_1 behaves the same in the 2D and 1D models in the x_2 -direction, but again with a larger amplitude in the 1D model.

In Figure 7.7, we have again plotted the numerical solution of u_1 from the 2D model and the analytic solution of u_1 from the 1D model along the x_1 and x_2 -directions, only now with $\bar{\mathcal{F}} = 1$ along with $d = 1$, $\tan(\phi) = 1$ and $\nu = 0.49$. The plot in the x_1 -direction again has values of the normalised function $u_1 - u_1(0, x_2)$ from the 2D and 1D models, at the points $x_2 = 2, 4$. From this plot, it is observed that the two models behave differently for small values of x_2 , with the 1D model giving a positive normalised deformation and the 2D model giving a negative normalised deformation. As we increase the value of x_2 however, the deformations behave in a similar way again. Unlike the case with $\bar{\mathcal{F}} = 0.001$ depicted in Figure 7.6, the amplitude of the normalised deformation is larger in the 2D model than in the 1D model. The plot in the x_2 -direction displays the value of u_1 in both models, at $x_1 = 0.5$. It is seen from this plot that although both models are yielding a deformation decaying to a constant as $x_2 \rightarrow \infty$, the amplitude of the deformation in the 1D model is much larger than that of the deformation in the 2D model.

Finally, in Figures 7.8 and 7.9, the numerical and analytical solutions of u_1 from the 2D and 1D models respectively have been plotted in the x_1 and x_2 -directions, for $\bar{\mathcal{F}} = 1000$, $d = 1$, $\tan(\phi) = 1$ and $\nu = 0.49$. In Figure 7.8, once again the values of the normalised function $u_1 - u_1(0, x_2)$ from the 2D and 1D models have been plotted in the x_1 -direction, but this time at the points $x_2 = 20, 40, 60$. We observe from this figure that the normalised deformation behaves differently in both models, with the solution from the 1D model being positive and the solution from the 2D model being negative. We also note that the amplitude of the normalised deformation is much larger in the 1D model. In Figure 7.9, again the plot in the x_2 -direction shows the values of u_1 in both models, at $x_1 = 0.5$. This figure shows that the deformations have

similar behaviour in both the 2D and 1D models in the x_2 -direction, although the amplitude is much larger in the 1D model.

Overall, we see that for small $\bar{\mathcal{F}}$, although the 1D model does not match the 2D model exactly, it does display similar behaviour and the amplitude of the deformations has the right order of magnitude. However, for larger values of $\bar{\mathcal{F}}$, we start getting discrepancies between the two models for the behaviour of u_1 in the x_1 -direction. We also find that the amplitudes of the deformations become much larger in the 1D model than in the 2D model. To determine why we are getting such large differences between the two models, we first see if it is possible to arbitrarily set the constants A_2 , A_4 , A_6 and B_2 , found in the solution (7.65) for u_1 in the 1D model, so that the 1D model matches the behaviour of the 2D model away from the clamped boundary $x_2 = 0$.

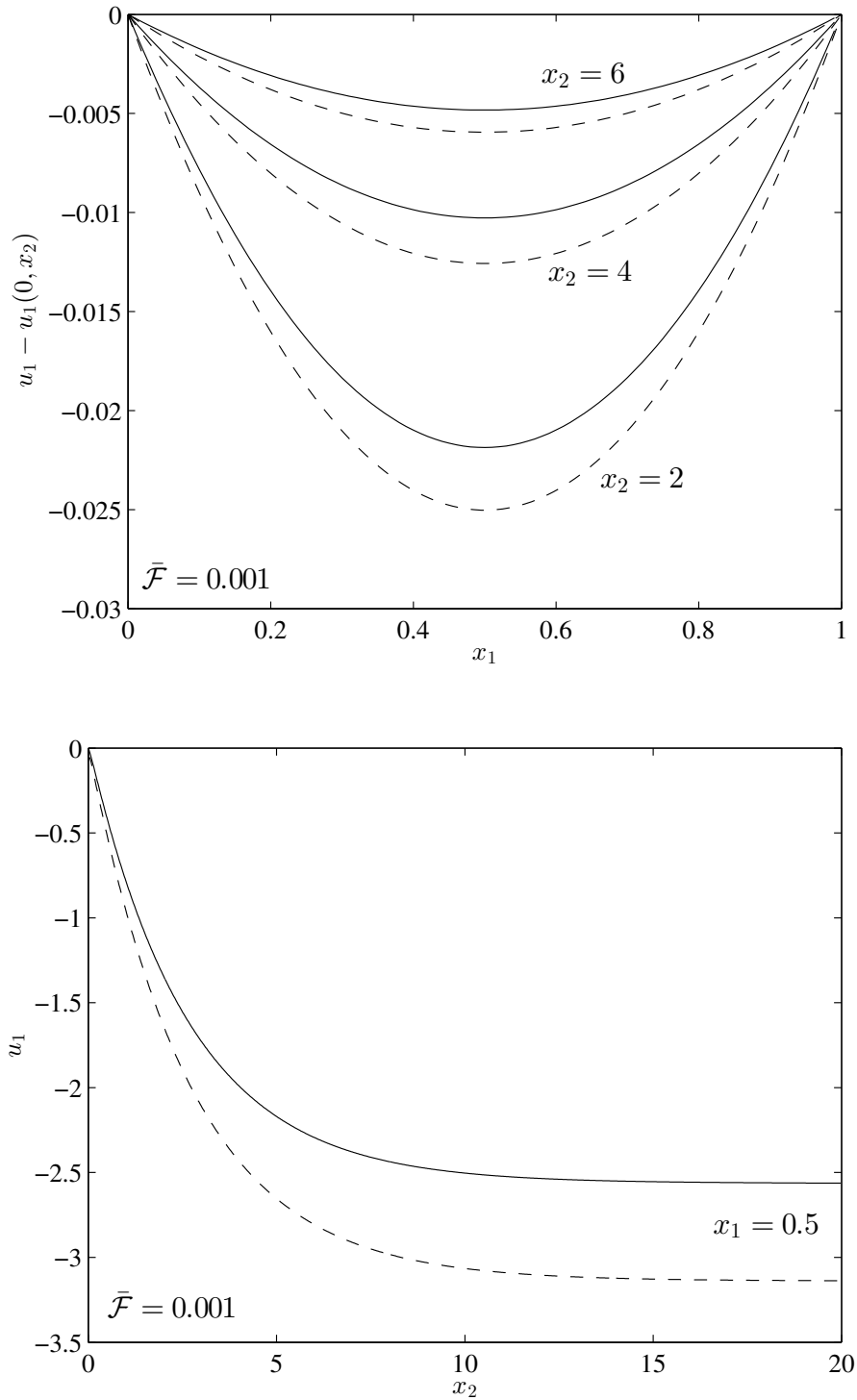


Figure 7.6: The numerical solution of the 2D model (solid lines) and the analytic solution (7.65) of the 1D model (dashed lines) for u_1 , when $\bar{\mathcal{F}} = 0.001$, $d = 1$, $\tan(\phi) = 1$ and $\nu = 0.49$. In the plot in the x_1 -direction, $u_1(x_1, x_2) - u_1(0, x_2)$ has been plotted at $x_2 = 2, 4, 6$, and in the x_2 -direction, u_1 has been plotted at $x_1 = 0.5$.

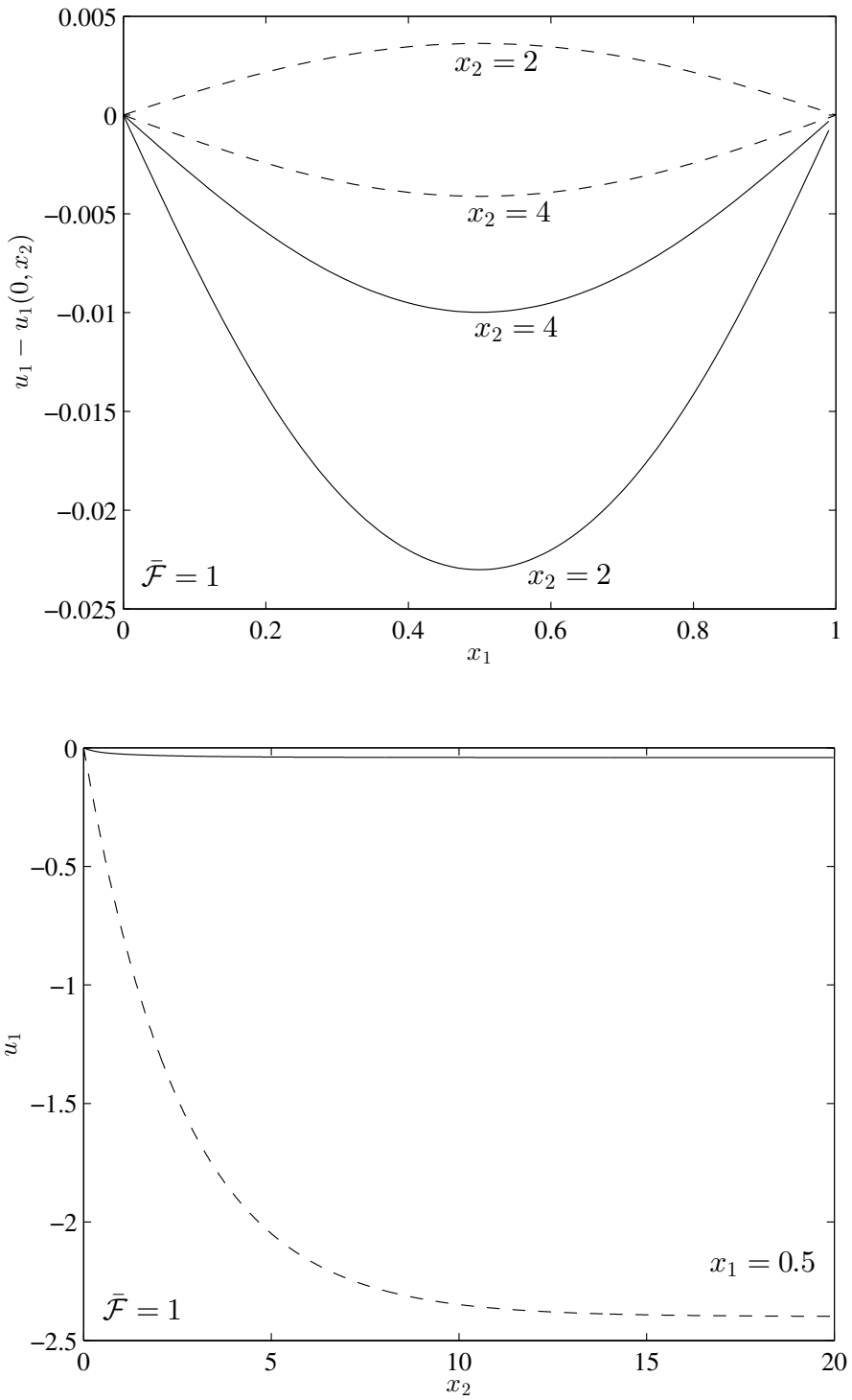


Figure 7.7: The numerical solution of the 2D model (solid lines) and the analytic solution (7.65) of the 1D model (dashed lines) for u_1 , when $\bar{\mathcal{F}} = 1$, $d = 1$, $\tan(\phi) = 1$ and $\nu = 0.49$. In the plot in the x_1 -direction, $u_1(x_1, x_2) - u_1(0, x_2)$ has been plotted at $x_2 = 2, 4$, and in the plot in the x_2 -direction, u_1 has been plotted at $x_1 = 0.5$.

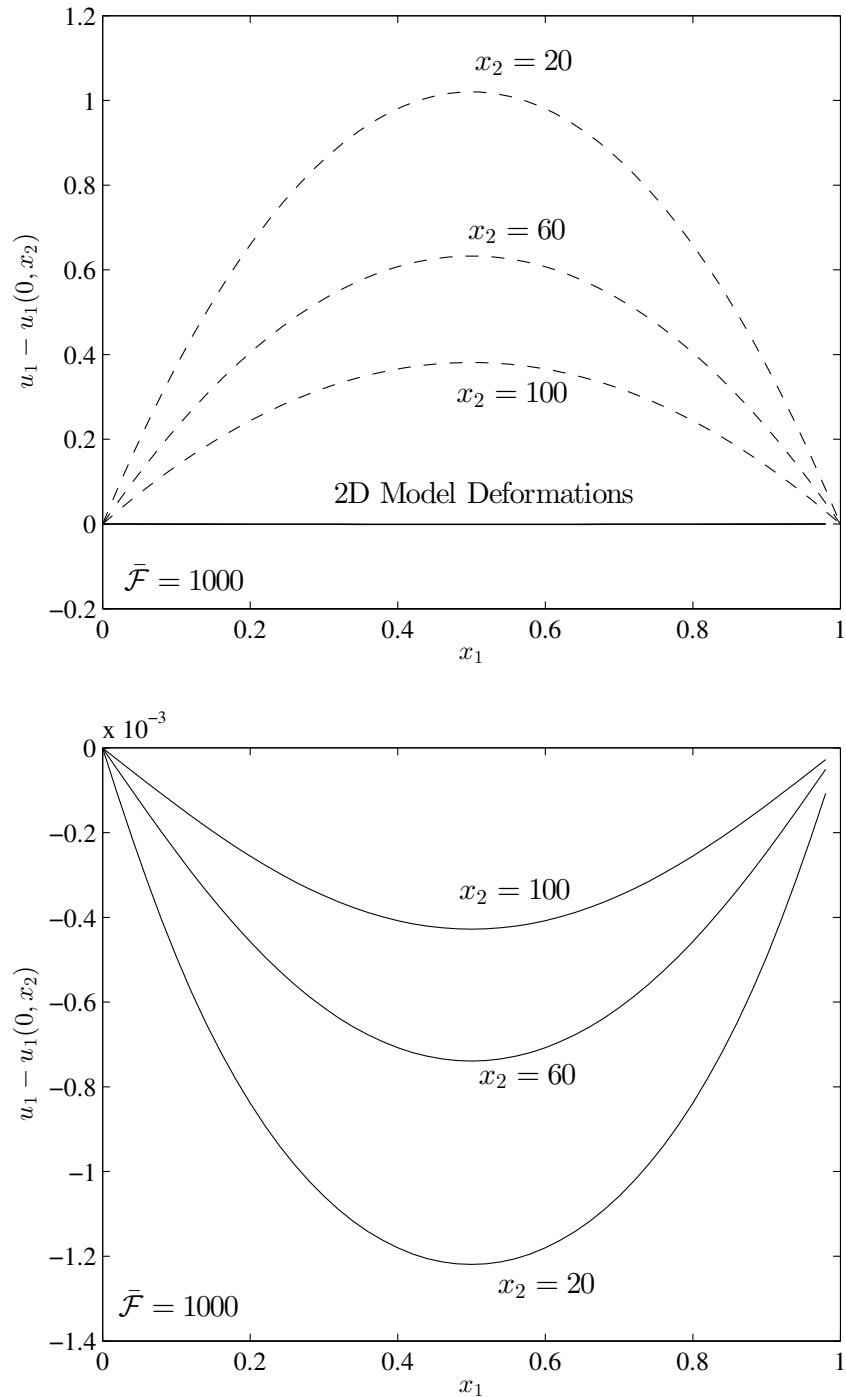


Figure 7.8: The numerical solution of the 2D model (solid lines) and the analytic solution (7.65) of the 1D model (dashed lines) for $u_1(x_1, x_2) - u_1(0, x_2)$ in the x_1 -direction at $x_2 = 20, 40, 60$, when $\bar{\mathcal{F}} = 1000$, $d = 1$, $\tan(\phi) = 1$ and $\nu = 0.49$. It is noted that both figures show the same plots, but with different scales along the vertical axis.

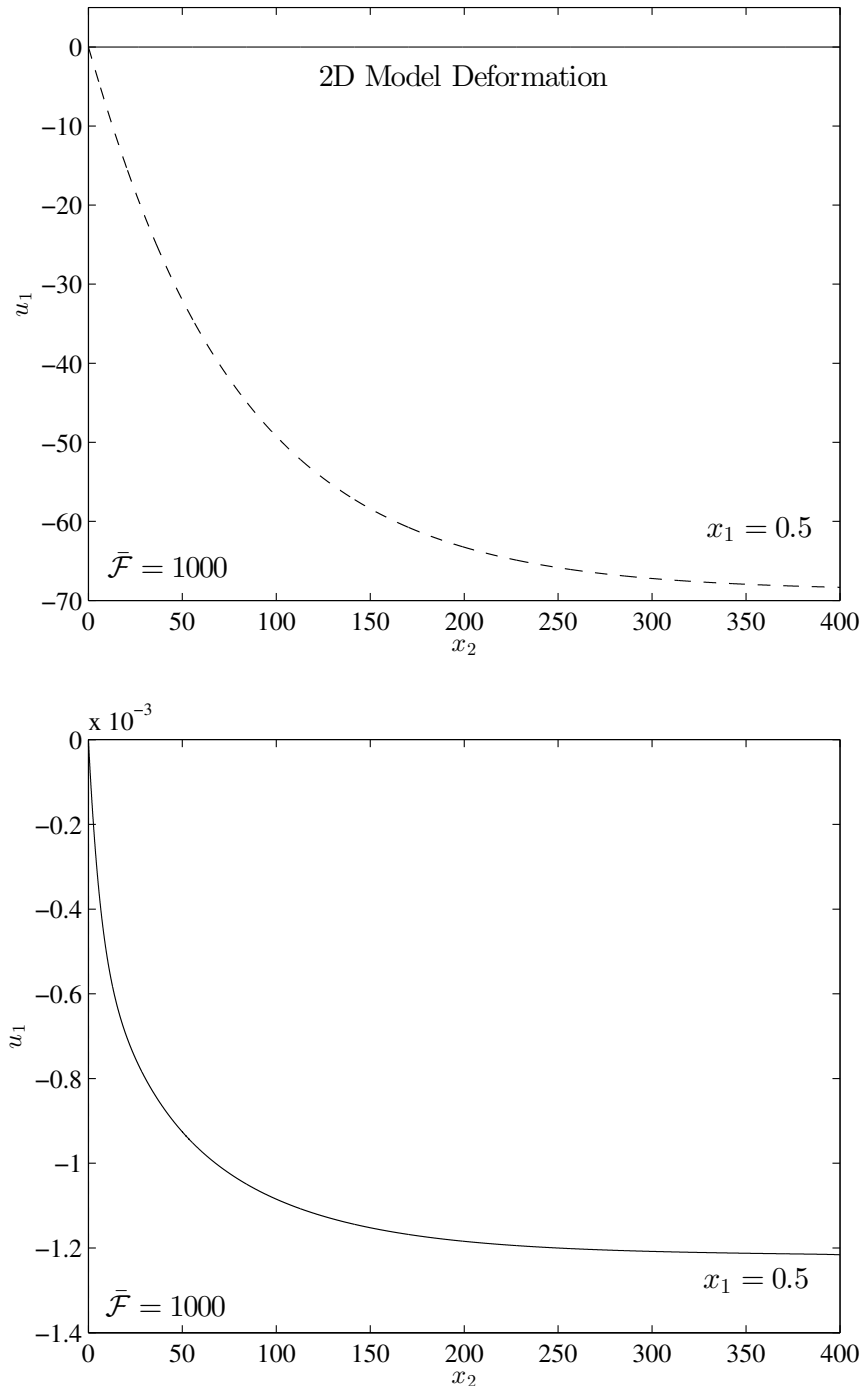


Figure 7.9: The numerical solution of the 2D model (solid lines) and the analytic solution (7.65) of the 1D model (dashed lines) for u_1 in the x_2 -direction at $x_1 = 0.5$, when $\bar{\mathcal{F}} = 1000$, $d = 1$, $\tan(\phi) = 1$ and $\nu = 0.49$. It is noted that both figures show the same plots, but with different scales along the vertical axis.

7.5.8 Matching the 1D Model to the 2D Model

In §7.5.7, it is seen that there are large discrepancies between the numerical solutions for the deformations of the 2D model and the analytical solutions for the deformations of the 1D model. In order to see why these discrepancies arise, it is first seen how well the 1D-model solution matches the 2D-model solution when the constants A_2 , A_4 , A_6 and B_2 in the general solution (7.65) for u_1 are chosen to provide a better fit. If these constants can be set so that the 2D and 1D model give similar solutions away from the clamped boundary $x_2 = 0$, then it can be concluded that some effect near the boundary, not captured by the 1D model, is giving rise to the large difference in the amplitudes of the deformations in the two models. Otherwise, the discrepancy will be due to an incorrect assumption made in the derivation of the governing system (7.27)–(7.34) for the 1D model, such as the truncation of the Taylor series (7.18) of u_1 .

Procedure for Setting A_2 – B_2

To choose the constants A_2 , A_4 , A_6 and B_2 that appear in the solution (7.65) for u_1 in the 1D model, the following procedure is used. First of all, the constant term A_6 that determines the value that u_1 decays to as $x_2 \rightarrow \infty$ is set to be $A_6 = u_1(d/2, x_{\max})$; the numerical value of u_1 at $x_1 = d/2$, $x_2 = x_{\max}$, in the 2D model.

The next constant that is determined is A_4 , which is the coefficient of the slowest decaying mode within the solution (7.65) for u_1 in the 1D model. This is done by considering $\log(u_1(d/2, x_2) - A_6)$ from the 1D model and $\log(u_1(d/2, x_2) - u_1(d/2, x_{\max}))$ from the 2D model. Substituting (7.65) into the first expression yields

$$\log(u_1(d/2, x_2) - A_6) = \log \left(A_2 e^{-\frac{r_+}{d} x_2} + A_4 e^{-\frac{r_-}{d} x_2} \right), \quad (7.66)$$

and the constant A_6 , as well as the terms involving the constant B_2 which are only found at $O((x_1 - d/2)^2)$, vanish. As such, only the two exponentially decaying modes with decay rates r_+ and r_- remain. It was determined in §7.5.6 that $r_- < r_+$ and so the mode with the decay rate r_- is the slowest decaying and fundamental mode. Hence, away from $x_2 = 0$, u_1 is dominated by this mode and (7.66) is approximated by

$$\log(u_1(d/2, x_2) - A_6) \sim \log \left(A_4 e^{-\frac{r_-}{d} x_2} \right) = \log(A_4) - \frac{r_-}{d} x_2 \quad \text{as } x_2 \rightarrow \infty. \quad (7.67)$$

Therefore, away from $x_2 = 0$, the function (7.67) gives linear behaviour with a constant shift $\log(A_4)$. The constant A_4 can then be chosen to best shift $\log(u_1(d/2, x_2) - A_6)$ from the 1D model so that it matches $\log(u_1(d/2, x_2) - u_1(d/2, x_{\max}))$ from the 2D model, away from $x_2 = 0$.

Once A_4 is set, A_2 can then be chosen to alter the behaviour of $u_1(0.5, x_2)$ near $x_2 = 0$ (as it alters the amplitude of the quickest decaying mode in the 1D model). This is chosen so that in the 1D model, $u_1(0.5, 0) \approx 0$.

The final constant to be set is B_2 and this is done by looking at logarithmic plots of $\partial^2 u_1 / \partial x_1^2$ at $x_1 = d/2$ in the 1D and 2D models. Substituting the expression (7.65) for u_1 in the 1D model into $\partial^2 u_1 / \partial x_1^2$ gives at $x_1 = d/2$

$$\left. \frac{\partial^2 u_1}{\partial x_1^2} \right|_{x_1=\frac{d}{2}} = 2B_2 e^{-\frac{C_1}{dC_0}x_2} + \frac{2}{d^2} \left(A_2 K_+ e^{-\frac{r_+}{d}x_2} + A_4 K_- e^{-\frac{r_-}{d}x_2} \right), \quad (7.68)$$

and we are left with three exponentially decaying modes with decay rates r_+ , r_- and C_1/C_0 . It was found in §7.5.6 that for small $\bar{\mathcal{F}}$, $C_1/C_0 > r_-$ and so the mode with decay rate C_1/C_0 decays faster than the fundamental mode with decay rate r_- . Hence, in this case, B_2 is chosen so that the value of $\partial^2 u_1 / \partial x_1^2$ at $x_1 = d/2$ in the 1D model best fits the corresponding 2D-model value near $x_2 = 0$. For large $\bar{\mathcal{F}}$ however, it was found in §7.5.6 that $C_1/C_0 \sim r_-$, and thus the modes with these two decay rates both contribute to the fundamental mode of the deformation u_1 in the 1D model. Hence, by taking the logarithm of (7.68), we find the following approximation as $x_2 \rightarrow \infty$

$$\begin{aligned} \log \left(\left. \frac{\partial^2 u_1}{\partial x_1^2} \right|_{x_1=\frac{d}{2}} \right) &\sim \log \left[\left(2B_2 + \frac{2A_4 K_-}{d^2} \right) e^{-\frac{r_-}{d}x_2} \right] \quad \text{as } x_2 \rightarrow \infty, \\ &\sim \log \left(2B_2 + \frac{2A_4 K_-}{d^2} \right) - \frac{r_-}{d}x_2 \quad \text{as } x_2 \rightarrow \infty. \end{aligned} \quad (7.69)$$

Again, away from $x_2 = 0$, the function (7.69) behaves linearly and the constant B_2 gives a constant shift in the function. Thus for large values of $\bar{\mathcal{F}}$, B_2 is chosen to shift the value of the function (7.69) from the 1D model so that it matches with the corresponding value from the 2D model away from $x_2 = 0$.

Comparing the New 1D-Model Deformation with the 2D Model

By following this procedure, the constants A_2 – B_2 have been chosen to match the solution for the deformation u_1 in the 1D model to its 2D-model counterpart, in the cases $\bar{\mathcal{F}} = 0.001, 1, 1000$, with $d = 1$, $\tan(\phi) = 1$ and $\nu = 0.49$. In Figures 7.10–7.12, we see how the analytical solution for u_1 in 1D model now

compares to the 2D-model solution. In each of these figures, Figure A has plots of $u_1 - u_1(0, x_2)$ from the 1D and 2D models, along the x_1 -direction for different values of x_2 . Figure B has plots of $u_1(0, x_2)$ from both models in the x_2 -direction, and Figure C contains plots of $u_1(d/2, x_2) - A_6$ and $u_1(d/2, x_2) - u_1(d/2, x_{\max})$ from the 1D and 2D models respectively, in the x_2 -direction with a logarithmic scale on the vertical axis.

From Figure 7.10, it is observed that in the case with small $\bar{\mathcal{F}}$ ($\bar{\mathcal{F}} = 0.001$), the solution from the 1D model now matches the numerical solution well in both the x_1 and x_2 -directions, apart from in a very small region near $x_2 = 0$. It is also seen in Figure 7.10C that the gradient of the curves from the 1D and 2D models is the same apart from at a region near $x_2 = 20$, where the numerical scheme is forcing the solution from the 2D model to decay to zero at $x_2 = x_{\max}$ rather than as $x_2 \rightarrow \infty$. As such, we find that the solutions from the 1D and 2D models are exhibiting the same behaviour for small $\bar{\mathcal{F}}$. Hence, it is only the conditions (7.31)–(7.34) forcing the choice of constants A_2 – B_2 within the expression (7.65) for u_1 that are causing inaccuracies between the 1D and 2D models. As the inaccuracies are reasonably small for small $\bar{\mathcal{F}}$, it is possible that this issue can be resolved by simply including more terms from the Taylor series (7.18) of u_1 within the model and determining these extra terms.

In Figures 7.11 and 7.12, the behaviour of the solution from the 1D model is compared to the behaviour of the 2D model for large $\bar{\mathcal{F}}$ ($\bar{\mathcal{F}} = 1, 1000$). Figures 7.11A and 7.12A show that although the amplitudes of the deformations from the 1D and 2D models do not match exactly in the x_1 -direction, the overall behaviour is similar and the amplitudes are much better than those derived from the conditions (7.31)–(7.34). This is particularly evident for larger values of x_2 .

In Figures 7.11B and 7.12B, similar results are seen in the x_2 -direction. Again the amplitudes of the deformations from the two models are not matching exactly, but the overall behaviour is similar apart from in a region near $x_2 = 0$.

Finally, in Figures 7.11C and 7.12C, it is seen that the gradients of the curves from the 1D and 2D models are not quite equal, meaning that the decay rates of the deformations are not the same. However the gradients are similar apart from near $x_2 = 0$ (where higher-order modes are having an effect), and near $x_2 = x_{\max}$ (where the numerical scheme is forcing the solution from the 2D model to decay to zero at $x_2 = x_{\max}$ rather than as $x_2 \rightarrow \infty$). As such, we conclude that for large $\bar{\mathcal{F}}$, the 1D model has the correct behaviour to emulate

the 2D model away from $x_2 = 0$, and the conditions (7.31)–(7.34) are forcing the constants A_2 – B_2 to take significantly incorrect values in the 1D model.

We have found that the discrepancies between the expression (7.65) for u_1 in the 1D model and the deformation in the 2D model are very large for large values of $\bar{\mathcal{F}}$. We have also found that it does not seem to be possible to set the constants A_2 – B_2 so that the behaviour near the $x_2 = 0$ boundary is accurately represented at the same time as the behaviour away from $x_2 = 0$. Hence, there may be an effect near the $x_2 = 0$ boundary in the 2D model that is particularly significant for large $\bar{\mathcal{F}}$, which is not captured by the 1D model. To see if this is the case, the behaviour of u_1 near $x_2 = 0$ in the 2D model is evaluated for both small and large $\bar{\mathcal{F}}$ in §7.6.

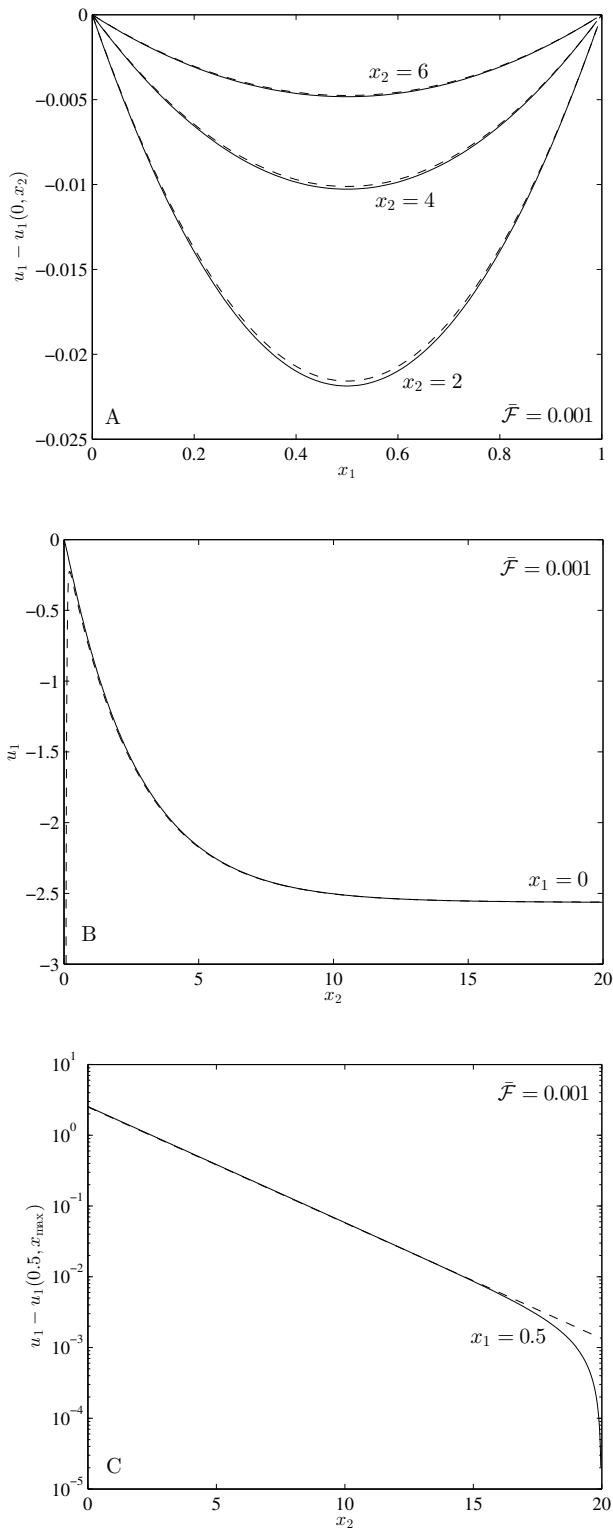


Figure 7.10: The analytical solution (7.65) for u_1 in the 1D model (dashed lines) in the x_1 and x_2 -directions, for $\bar{\mathcal{F}} = 0.001$, $d = 1$, $\tan(\phi) = 1$, $\nu = 0.49$, $A_2 = 0.03$, $A_4 = 2.51$, $A_6 = -2.5629$ and $B_2 = 0.01$. Also plotted is the corresponding solution from the 2D model (solid lines).

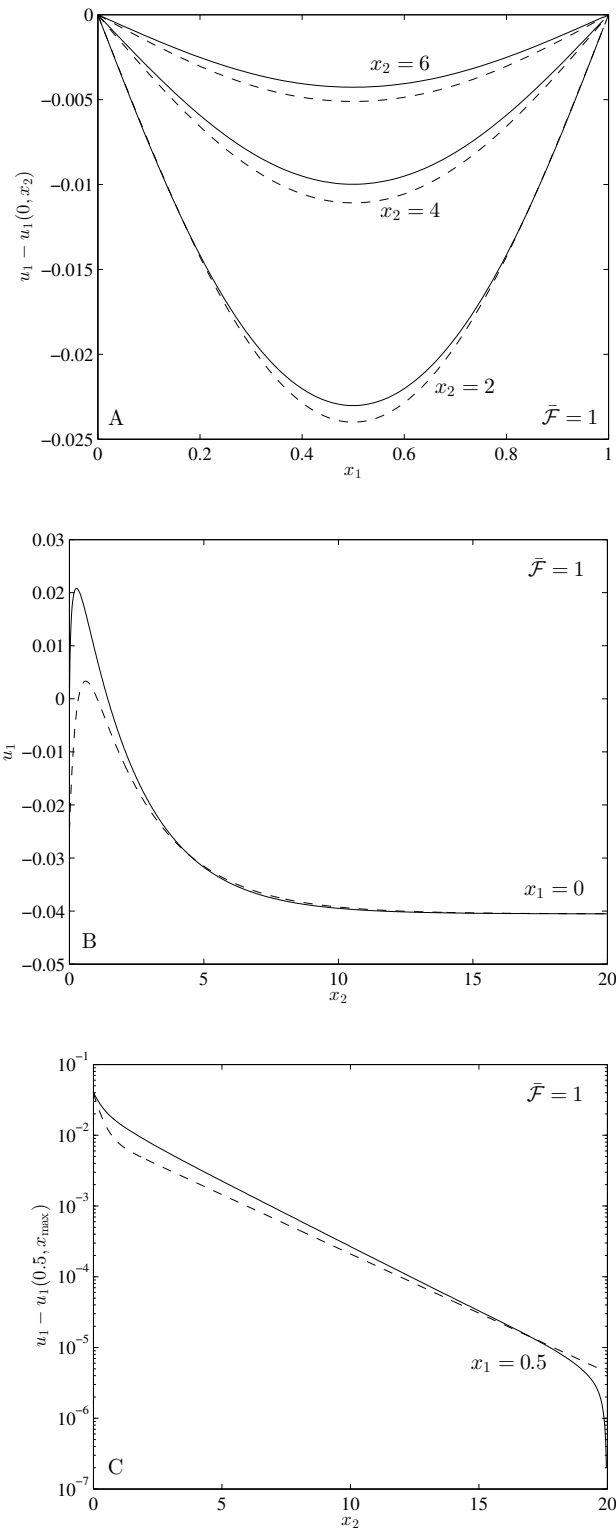


Figure 7.11: The analytical solution (7.65) for u_1 in the 1D model (dashed lines) in the x_1 and x_2 -directions, for $\bar{\mathcal{F}} = 1$, $d = 1$, $\tan(\phi) = 1$, $\nu = 0.49$, $A_2 = 0.03$, $A_4 = 0.01$, $A_6 = -0.04053$ and $B_2 = 0.15$. Also plotted is the corresponding solution from the 2D model (solid lines).

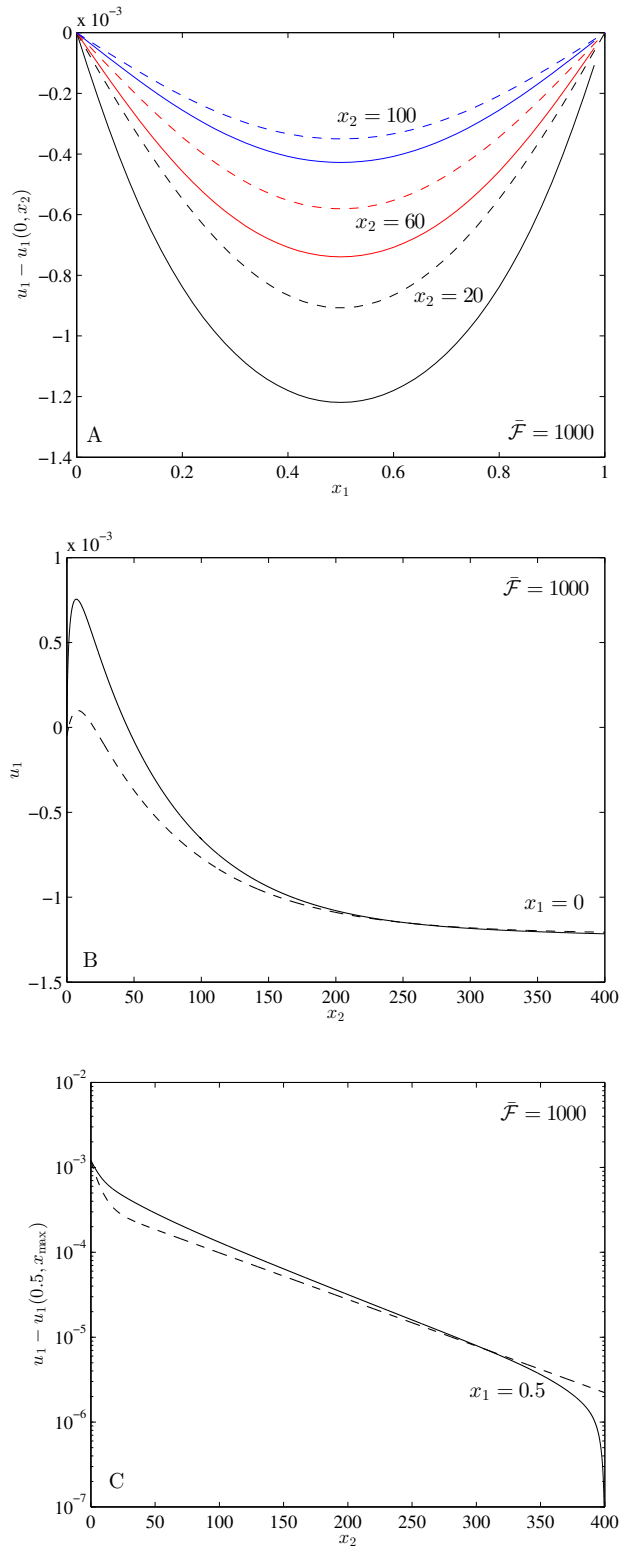


Figure 7.12: The analytical solution (7.65) for u_1 in the 1D model (dashed lines) in the x_1 and x_2 -directions, for $\bar{F} = 1000$, $d = 1$, $\tan(\phi) = 1$, $\nu = 0.49$, $A_2 = 0.00085$, $A_4 = 0.00035$, $A_6 = -0.0012162$ and $B_2 = 0.002$. Also plotted is the corresponding solution from the 2D model (solid lines).

7.6 Behaviour of u_1 for Small x_2

In §7.5, a one-dimensional model was derived for the problem of bending a semi-infinite block under tension. It was found that although this 1D model was able to accurately emulate the fundamental decay rate of the deformations found in the 2D model derived in §6.4, the amplitudes of the deformations themselves differed between the two models, particularly for large values of the axial tension $\bar{\mathcal{F}}$. It was also found that, even when arbitrarily setting the coefficients of the modes found in the 1D model, it was not possible to accurately model the behaviour of the normal deformation u_1 near $x_2 = 0$ and away from $x_2 = 0$ at the same time, in the case of large $\bar{\mathcal{F}}$. As such, it is possible that an effect in the 2D model near the clamped boundary is not captured by the 1D model. This possibility is now evaluated.

In Figure 7.13, the numerical solution of u_1 in the 2D model has been plotted for small tension ($\bar{\mathcal{F}} = 0.001$) and large tension ($\bar{\mathcal{F}} = 1$), in the x_1 -direction at $x_2 = 0.02$. Hence, we are evaluating u_1 near the clamped boundary $x_2 = 0$. From the figure, it is observed that for $\bar{\mathcal{F}} = 0.001$, the value of u_1 is always negative. However, in the case $\bar{\mathcal{F}} = 1$, it is seen that the value of u_1 rises to a positive value near the stress free boundaries, for small x_2 . The reason for this is that as the axial tension bends the block, one side of the block near the clamped boundary compresses whereas the opposing side expands. For small values of $\bar{\mathcal{F}}$, this 2D compression effect is negligible as the block smoothly bends over a relatively long distance. However for large values of $\bar{\mathcal{F}}$, the block bends over a much shorter distance, meaning that this 2D compression effect has a significant effect on the deformations. It is not possible for the 1D model in §7.5 to capture this 2D effect and as such, the conditions (7.31)–(7.34) in the 1D model do not set the correct amplitudes for the deformation. However, the 1D model does still capture the correct behaviour of the deformation away from the clamped boundary $x_2 = 0$ when we choose appropriate values for the constants A_2 – B_2 .

7.7 Conclusions

In this chapter, we have considered three possible methods for deriving an appropriate 1D model for the linearised system (6.42)–(6.46) modelling a semi-infinite block being bent under tension. The accuracy of each of these models has been evaluated.

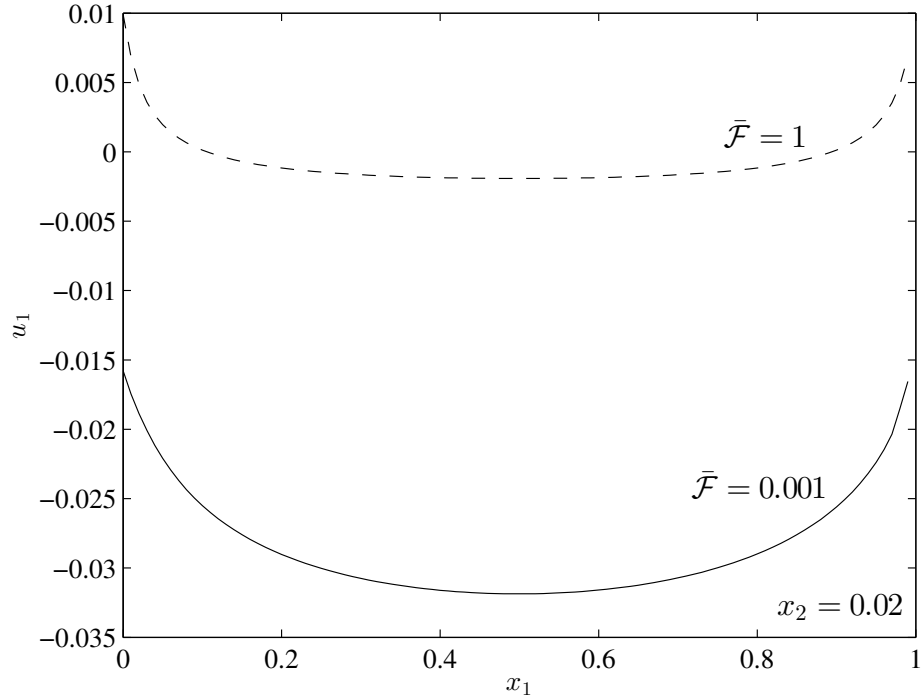


Figure 7.13: The numerical solution for u_1 in the 2D model along the x_1 -direction, at $x_2 = 0.02$, for the tensions $\bar{\mathcal{F}} = 0.001$ and $\bar{\mathcal{F}} = 1$, and $d = 1$, $\tan(\phi) = 1$, $\nu = 0.49$.

The first 1D model that was considered was one derived from Kirchhoff–Love shell theory. It was found in §6.9 that in the limit $\bar{\mathcal{F}} \rightarrow \infty$, corresponding to the regime $\delta\ell \gg 1$, the boundary-layer width $\tilde{\delta}_B$ has size $\tilde{\delta}_B = O(d\bar{\mathcal{F}}^{\frac{1}{2}}) \gg O(d)$. Hence, the boundary-layer width is larger than the width of the block, and it initially appears that Kirchhoff–Love shell theory can be used to model the problem. A model has been derived from Kirchhoff–Love shell theory, but the boundary-layer width derived from this model behaves vastly differently from the boundary-layer width calculated in the 2D model, for large values of $\bar{\mathcal{F}}$. The reason for this was found to be due to the violation of one of the assumptions made in Kirchhoff–Love shell theory within the boundary layer. The assumption violated was the preservation of the normal to the centre line of the material after a deformation, which is due to the fact that the boundary layer in question is a transverse shear-relaxation layer for large values of $\bar{\mathcal{F}}$.

The second 1D model to be considered was a model derived by averaging the components of Cauchy’s momentum equation over the width of the block. This model approximated the deformations u_1 and u_2 using the leading-order

terms from the Taylor series of the deformations about the midpoint $x_1 = d/2$ of the block. This model yielded exponentially decaying deformations in the axial direction, with a decay rate that has the same qualitative behaviour as the fundamental decay rate from the 2D model. There was however still a constant difference between the decay rates, for both small and large $\bar{\mathcal{F}}$. This difference was particularly large for small $\bar{\mathcal{F}}$. The reason for this large discrepancy is likely due to the truncation of the Taylor series used to approximate u_1 and u_2 .

The final 1D model to be considered was one derived from the system (6.88)–(6.93), where u_2 has been eliminated from the governing system. In this model, the deformation u_1 is approximated with the first three non-zero terms of the Taylor series of u_1 about the midpoint $x_1 = d/2$ of the block. The inclusion of these extra terms, corresponding to a constant, quadratic and quartic variation in u_1 in the x_1 -direction, improves the accuracy of this 1D model compared to the model derived from averaging Cauchy's momentum equation, which only accounts for constant behaviour of u_1 and linear behaviour of u_2 in the x_1 -direction.

Three exponentially decaying modes are found within this final 1D model, all with their own distinct decay rates. The first and smallest decay rate r_- obtained from this model was found to be in good agreement with the fundamental decay rate from the 2D model. The second decay rate C_1/C_0 was also found to imitate the fundamental decay rate for large $\bar{\mathcal{F}}$, but diverge to a larger value for small $\bar{\mathcal{F}}$. This implies that only one mode from the 1D model is involved in simulating the fundamental mode in the 2D model for small values of $\bar{\mathcal{F}}$, but for larger values of $\bar{\mathcal{F}}$, two modes from the 1D model combine to simulate the fundamental mode. The final decay rate r_+ from the 1D model is much larger than the other decay rates r_- and C_1/C_0 , for all values of $\bar{\mathcal{F}}$. It is found that r_+ does not accurately model any of the decay rates of the modes obtained in the 2D model. The reason for this is most likely down to higher-order terms from the Taylor series of u_1 , which are neglected in this model, being needed to accurately simulate the higher-order modes in the 2D model.

By fully solving this model and applying conditions at $x_2 = 0$, an approximation for the deformation u_1 has been derived. For small $\bar{\mathcal{F}}$, there is a small discrepancy in the amplitude of the deformations in the 1D and the 2D model, but the overall behaviour is similar. However, as $\bar{\mathcal{F}}$ is increased, the amplitude of the 1D-model deformation becomes much larger than that of the

2D-model deformation. The direction of the deformation in the x_1 -direction also differs between the two models for smaller values of x_2 . By arbitrarily choosing the constants that appear in the general solution of u_1 instead of applying the boundary conditions at $x_2 = 0$ to find them, it was found that it is possible for this 1D model to obtain much better agreement with the 2D model away from $x_2 = 0$. This implies that the 1D model is capturing the necessary mechanisms in the far-field away from $x_2 = 0$, but it is not able to model the deformations well near $x_2 = 0$.

Finally, the behaviour of u_1 for small values of x_2 has been evaluated to determine why the final 1D model cannot accurately simulate the deformations near $x_2 = 0$. It was found that for small values of $\bar{\mathcal{F}}$, the deformation always has the same sign, and the block is always being deformed in the same direction. Conversely, for large $\bar{\mathcal{F}}$, it was seen that near the stress-free boundaries $x_1 = 0, d$ close to the clamped boundary $x_2 = 0$, the value of u_1 has a different sign from the value of u_1 in the bulk of the block around $x_1 = d/2$. Hence, the block is deforming in a different direction at the edges of the block compared to the centre of the block. This is due to a 2D compression effect which arises from one side of the block expanding and the other contracting near $x_2 = 0$, as the block is bent. This compression effect is much more significant for larger values of $\bar{\mathcal{F}}$ as the block bends over a much shorter distance compared to the case with small $\bar{\mathcal{F}}$. It is not possible for the final 1D model to capture this 2D effect, and as such, this explains the discrepancies between the final 1D model and the 2D model, which are particularly large for large values of $\bar{\mathcal{F}}$.

It is possible that the 1D models considered here may be improved upon further by using modes motivated by the transition to, and decay of, the self-similar solution observed in §6.11, instead of the Taylor series of the deformations. These modes are not independent of x_1 and so would add new effects that the current models have not included. It is also possible that by using these modes based on the self-similar solutions, a new model could be derived to describe the behaviour of the block close to the clamped edge of the block. Further investigation is needed to evaluate these possibilities.

7.A Deriving a 1D Model from the Averaged Cauchy's Momentum Equation

Here, we derive a 1D model for the problem of bending a semi-infinite block under tension. This model is derived from the components (7.1), (7.2) of the linearised Cauchy's momentum equation (6.42), which are

$$2(1-\nu)\frac{\partial^2 u_1}{\partial x_1^2} + \frac{\partial^2 u_2}{\partial x_1 \partial x_2} + (1-2\nu+\bar{\mathcal{F}})\frac{\partial^2 u_1}{\partial x_2^2} = 0 \quad \text{for } 0 \leq x_1 \leq d, x_2 \geq 0, \quad (7.70)$$

$$(1-2\nu)\frac{\partial^2 u_2}{\partial x_1^2} + \frac{\partial^2 u_1}{\partial x_1 \partial x_2} + (2(1-\nu)+\bar{\mathcal{F}})\frac{\partial^2 u_2}{\partial x_2^2} = 0 \quad \text{for } 0 \leq x_1 \leq d, x_2 \geq 0. \quad (7.71)$$

The components of the linearised boundary conditions (7.3)–(7.6), given by

$$u_1 = 0, \quad \text{and} \quad u_2 = \tan(\phi) \left(x_1 - \frac{d}{2} \right) \quad \text{at} \quad x_2 = 0, \quad (7.72)$$

$$(1-\nu)\frac{\partial u_1}{\partial x_1} + \nu\frac{\partial u_2}{\partial x_2} = 0 \quad \text{at} \quad x_1 = 0, d, \quad (7.73)$$

$$\frac{\partial u_1}{\partial x_2} + \frac{\partial u_2}{\partial x_1} = 0 \quad \text{at} \quad x_1 = 0, d, \quad (7.74)$$

$$\nabla u_1, \nabla u_2 \rightarrow \mathbf{0} \quad \text{as} \quad x_2 \rightarrow \infty, \quad (7.75)$$

are later applied to this model.

7.A.1 Averaged Force-Balance and Moment-Balance Equations

To create an appropriate 1D model, we need to average the force-balance equations and moment-balance equation over the width of the block. These averaged equations are now derived. First, it is convenient to rewrite (7.70) and (7.71) in the following way

$$2 \left[(1-\nu)\frac{\partial^2 u_1}{\partial x_1^2} + \nu\frac{\partial^2 u_2}{\partial x_1 \partial x_2} \right] + (1-2\nu)\frac{\partial^2 u_2}{\partial x_1 \partial x_2} + (1-2\nu+\bar{\mathcal{F}})\frac{\partial^2 u_1}{\partial x_2^2} = 0, \quad (7.76)$$

$$(1-2\nu) \left(\frac{\partial^2 u_2}{\partial x_1^2} + \frac{\partial^2 u_1}{\partial x_1 \partial x_2} \right) + 2\nu\frac{\partial^2 u_1}{\partial x_1 \partial x_2} + (2(1-\nu)+\bar{\mathcal{F}})\frac{\partial^2 u_2}{\partial x_2^2} = 0. \quad (7.77)$$

This will later allow us to apply the boundary conditions (7.73) and (7.74) at the stress-free boundaries of the block. By integrating (7.76) and (7.77) over the width of the block and dividing by d , we find the averaged normal force-balance

and axial force-balance equations to be

$$\frac{2}{d} \left[(1 - \nu) \frac{\partial u_1}{\partial x_1} + \nu \frac{\partial u_2}{\partial x_2} \right]_{x_1=0}^{x_1=d} + (1 - 2\nu) \left\langle \frac{\partial^2 u_2}{\partial x_1 \partial x_2} \right\rangle + (1 - 2\nu + \bar{\mathcal{F}}) \left\langle \frac{\partial^2 u_1}{\partial x_2^2} \right\rangle = 0, \quad (7.78)$$

$$\frac{1 - 2\nu}{d} \left[\frac{\partial u_1}{\partial x_2} + \frac{\partial u_2}{\partial x_1} \right]_{x_1=0}^{x_1=d} + 2\nu \left\langle \frac{\partial^2 u_1}{\partial x_1 \partial x_2} \right\rangle + (2(1 - \nu) + \bar{\mathcal{F}}) \left\langle \frac{\partial^2 u_2}{\partial x_2^2} \right\rangle = 0, \quad (7.79)$$

where

$$\langle \mathbb{A} \rangle = \frac{1}{d} \int_0^d \mathbb{A} \, dx_1$$

is the average of a function \mathbb{A} over the width of the block. Applying the boundary conditions (7.73) and (7.74) for u_1 and u_2 at $x_1 = 0, d$, it is found that the first terms of (7.78) and (7.79) vanish, leaving

$$(1 - 2\nu) \left\langle \frac{\partial^2 u_2}{\partial x_1 \partial x_2} \right\rangle + (1 - 2\nu + \bar{\mathcal{F}}) \left\langle \frac{\partial^2 u_1}{\partial x_2^2} \right\rangle = 0, \quad (7.80)$$

$$2\nu \left\langle \frac{\partial^2 u_1}{\partial x_1 \partial x_2} \right\rangle + (2(1 - \nu) + \bar{\mathcal{F}}) \left\langle \frac{\partial^2 u_2}{\partial x_2^2} \right\rangle = 0. \quad (7.81)$$

We later find when applying the symmetry and antisymmetry properties of the deformations that (7.81) becomes a trivial equation. In order for the axial force-balance equation (7.77) to be captured in the 1D model, we convert (7.77) into a moment-balance equation, and average over the width of the block. This is done by multiplying (7.77) by $x_1 - d/2$, integrating the resulting equation over the width of the block, and dividing by d . This yields the following

$$0 = (1 - 2\nu) \left\langle \left(x_1 - \frac{d}{2} \right) \left(\frac{\partial^2 u_2}{\partial x_1^2} + \frac{\partial^2 u_1}{\partial x_1 \partial x_2} \right) \right\rangle + 2\nu \left\langle \left(x_1 - \frac{d}{2} \right) \frac{\partial^2 u_1}{\partial x_1 \partial x_2} \right\rangle + (2(1 - \nu) + \bar{\mathcal{F}}) \left\langle \left(x_1 - \frac{d}{2} \right) \frac{\partial^2 u_2}{\partial x_2^2} \right\rangle. \quad (7.82)$$

This expression may be simplified further by evaluating the first averaged term. Using integration by parts, we find

$$\begin{aligned} \left\langle \left(x_1 - \frac{d}{2} \right) \left(\frac{\partial^2 u_2}{\partial x_1^2} + \frac{\partial^2 u_1}{\partial x_1 \partial x_2} \right) \right\rangle &= \frac{1}{d} \left[\left(x_1 - \frac{d}{2} \right) \left(\frac{\partial u_1}{\partial x_2} + \frac{\partial u_2}{\partial x_1} \right) \right]_{x_1=0}^{x_1=d} \\ &\quad - \left\langle \frac{\partial u_1}{\partial x_2} + \frac{\partial u_2}{\partial x_1} \right\rangle \\ &= \frac{1}{2} \left[\frac{\partial u_1}{\partial x_2} + \frac{\partial u_2}{\partial x_1} \right]_{x_1=0}^{x_1=d} - \left\langle \frac{\partial u_1}{\partial x_2} + \frac{\partial u_2}{\partial x_1} \right\rangle. \end{aligned} \quad (7.83)$$

Using the boundary condition (7.74), it is seen that the boundary term within (7.83) vanishes, leaving

$$\left\langle \left(x_1 - \frac{d}{2} \right) \left(\frac{\partial^2 u_2}{\partial x_1^2} + \frac{\partial^2 u_1}{\partial x_1 \partial x_2} \right) \right\rangle = - \left\langle \frac{\partial u_1}{\partial x_2} + \frac{\partial u_2}{\partial x_1} \right\rangle. \quad (7.84)$$

Substituting (7.84) into (7.82) yields the following averaged moment-balance equation

$$\begin{aligned} 0 = 2\nu \left\langle \left(x_1 - \frac{d}{2} \right) \frac{\partial^2 u_1}{\partial x_1 \partial x_2} \right\rangle + (2(1 - \nu) + \bar{F}) \left\langle \left(x_1 - \frac{d}{2} \right) \frac{\partial^2 u_2}{\partial x_2^2} \right\rangle \\ - (1 - 2\nu) \left\langle \frac{\partial u_1}{\partial x_2} + \frac{\partial u_2}{\partial x_1} \right\rangle. \end{aligned} \quad (7.85)$$

7.A.2 Deriving the 1D Model

Using the force-balance equations (7.80), (7.81) and the moment-balance equation (7.85), a 1D model is now derived. We first recall that u_1 is symmetric and u_2 is antisymmetric about $x_1 = d/2$ (see §6.2). As such, we have that

$$\frac{\partial^2 u_1}{\partial x_1 \partial x_2} \quad \text{and} \quad \frac{\partial^2 u_2}{\partial x_2^2},$$

are antisymmetric about $x_1 = d/2$, and thus

$$\left\langle \frac{\partial^2 u_1}{\partial x_1 \partial x_2} \right\rangle = 0 \quad \text{and} \quad \left\langle \frac{\partial^2 u_2}{\partial x_2^2} \right\rangle = 0. \quad (7.86)$$

Substituting (7.86) into the axial force-balance equation (7.81) yields a trivial equation which cannot be used in deriving a 1D model. Contrariwise, the terms

$$\frac{\partial^2 u_2}{\partial x_1 \partial x_2}, \quad \frac{\partial^2 u_1}{\partial x_2^2}, \quad \frac{\partial u_1}{\partial x_2}, \quad \frac{\partial u_2}{\partial x_1}, \quad \left(x_1 - \frac{d}{2} \right) \frac{\partial^2 u_1}{\partial x_1 \partial x_2} \quad \text{and} \quad \left(x_1 - \frac{d}{2} \right) \frac{\partial^2 u_2}{\partial x_2^2},$$

are all symmetric about $x_1 = d/2$, and thus averaging these terms over the width of the block yields non-zero values. Hence, all the terms within the normal force-balance equation (7.80) and the moment-balance equation (7.85) are non-zero, and these equations may be used to derive a 1D model.

It is convenient to rewrite (7.80) and (7.85) in the following way

$$(1 - 2\nu) \frac{\partial}{\partial x_2} \left\langle \frac{\partial u_2}{\partial x_1} \right\rangle + (1 - 2\nu + \bar{\mathcal{F}}) \frac{\partial^2}{\partial x_2^2} \langle u_1 \rangle = 0, \quad (7.87)$$

$$\begin{aligned} 2\nu \frac{\partial}{\partial x_2} \left\langle \left(x_1 - \frac{d}{2} \right) \frac{\partial u_1}{\partial x_1} \right\rangle + (2(1 - \nu) + \bar{\mathcal{F}}) \frac{\partial^2}{\partial x_2^2} \left\langle \left(x_1 - \frac{d}{2} \right) u_2 \right\rangle \\ - (1 - 2\nu) \left(\frac{\partial}{\partial x_2} \langle u_1 \rangle + \left\langle \frac{\partial u_2}{\partial x_1} \right\rangle \right) = 0. \end{aligned} \quad (7.88)$$

Doing so, the equations (7.87), (7.88) are now written in terms of four averaged variables instead of the six variables found in (7.80), (7.85). We now rewrite (7.87) and (7.88) as a pair of coupled ODEs governing two variables that are only dependent on x_2 . To achieve this, we consider the following Taylor series for u_1 and u_2 about $x_1 = d/2$

$$u_1 = u_1^{(0)}(x_2) + \left(x_1 - \frac{d}{2} \right)^2 u_1^{(2)}(x_2) + \dots, \quad (7.89)$$

$$u_2 = \left(x_1 - \frac{d}{2} \right) u_2^{(1)}(x_2) + \left(x_1 - \frac{d}{2} \right)^3 u_2^{(3)}(x_2) + \dots, \quad (7.90)$$

where $u_1^{(1)}, u_1^{(3)}, \dots = 0$ and $u_2^{(0)}, u_2^{(2)}, \dots = 0$, so that u_1 and u_2 are symmetric and antisymmetric about $x_1 = d/2$, respectively. To obtain only two x_2 -dependent variables from these series, we truncate (7.89) after $u_1^{(0)}$, and (7.90) after $u_2^{(1)}$ to yield

$$u_1 \sim u_1^{(0)}(x_2), \quad u_2 \sim \left(x_1 - \frac{d}{2} \right) u_2^{(1)}(x_2). \quad (7.91)$$

Using these approximations, we determine the averaged terms within (7.87) and (7.88) to be

$$\begin{aligned} \langle u_1 \rangle = u_1^{(0)}(x_2), \quad \left\langle \frac{\partial u_2}{\partial x_1} \right\rangle = u_2^{(1)}(x_2), \quad \left\langle \left(x_1 - \frac{d}{2} \right) \frac{\partial u_1}{\partial x_1} \right\rangle = 0, \\ \left\langle \left(x_1 - \frac{d}{2} \right) u_2 \right\rangle = \left\langle \left(x_1 - \frac{d}{2} \right)^2 \right\rangle u_2^{(1)} = \frac{d^2}{12} u_2^{(1)}(x_2). \end{aligned} \quad (7.92)$$

Substituting (7.92) into (7.87) and (7.88) yields the following pair of coupled ODEs in terms of $u_1^{(0)}$ and $u_2^{(1)}$

$$(1 - 2\nu) \frac{du_2^{(1)}}{dx_2} + (1 - 2\nu + \bar{\mathcal{F}}) \frac{d^2 u_1^{(0)}}{dx_2^2} = 0, \quad (7.93)$$

$$(2(1 - \nu) + \bar{\mathcal{F}}) \frac{d^2}{dx_2^2} \frac{d^2 u_2^{(1)}}{dx_2^2} - (1 - 2\nu) \left(\frac{du_1^{(0)}}{dx_2} + u_2^{(1)} \right) = 0. \quad (7.94)$$

We also substitute the truncated Taylor series (7.91) into the remaining boundary conditions (7.72) and (7.75), at $x_2 = 0$ and $x_2 \rightarrow \infty$ respectively, to obtain

$$u_1^{(0)} = 0 \quad \text{at} \quad x_2 = 0, \quad \frac{du_1^{(0)}}{dx_2} \rightarrow 0 \quad \text{as} \quad x_2 \rightarrow \infty, \quad (7.95)$$

$$u_2^{(1)} = \tan \phi \quad \text{at} \quad x_2 = 0, \quad u_2^{(1)} \rightarrow 0 \quad \text{as} \quad x_2 \rightarrow \infty. \quad (7.96)$$

7.A.3 Solution of the System (7.93)–(7.96)

To solve the system (7.93)–(7.96), $u_2^{(1)}(x_2)$ is first eliminated from the governing equations (7.93) and (7.94). Differentiating (7.94) with respect to x_2 yields the following

$$\frac{(2(1-\nu) + \bar{\mathcal{F}})d^2}{12} \frac{d^3 u_2^{(1)}}{dx_2^3} - (1-2\nu) \frac{d^2 u_1^{(0)}}{dx_2^2} - (1-2\nu) \frac{du_2^{(1)}}{dx_2} = 0. \quad (7.97)$$

Rearranging (7.93), and differentiating (7.93) with respect to x_2 twice, gives the relations

$$\frac{du_2^{(1)}}{dx_2} = -\frac{1-2\nu + \bar{\mathcal{F}}}{1-2\nu} \frac{d^2 u_1^{(0)}}{dx_2^2}, \quad (7.98)$$

$$\frac{d^3 u_2^{(1)}}{dx_2^3} = -\frac{1-2\nu + \bar{\mathcal{F}}}{1-2\nu} \frac{d^4 u_1^{(0)}}{dx_2^4}. \quad (7.99)$$

Substituting (7.98) and (7.99) into (7.97), we obtain the following ODE for $u_1^{(0)}(x_2)$

$$\frac{d^4 u_1^{(0)}}{dx_2^4} - \bar{\Lambda}^2 \frac{d^2 u_1^{(0)}}{dx_2^2} = 0, \quad (7.100)$$

where

$$\bar{\Lambda} = \frac{1}{d} \left(\frac{12(1-2\nu)\bar{\mathcal{F}}}{(1-2\nu + \bar{\mathcal{F}})(2(1-\nu) + \bar{\mathcal{F}})} \right)^{\frac{1}{2}}. \quad (7.101)$$

The ODE (7.100) has the general solution

$$u_1^{(0)}(x_2) = A e^{\bar{\Lambda} x_2} + B e^{-\bar{\Lambda} x_2} + C x_2 + D, \quad (7.102)$$

where A, B, C, D are constants to be found. Applying the boundary conditions (7.95) to (7.102) yields

$$A = C = 0, \quad D = -B, \quad (7.103)$$

and substituting the constants (7.103) into (7.102), it is found that

$$u_1^{(0)}(x_2) = B \left(e^{-\bar{\Lambda} x_2} - 1 \right). \quad (7.104)$$

Substituting the expression (7.104) into (7.98) and integrating, it is calculated that

$$u_2^{(1)}(x_2) = \frac{(1 - 2\nu + \bar{\mathcal{F}})\bar{\Lambda}B}{1 - 2\nu} e^{-\bar{\Lambda}x_2} + E, \quad (7.105)$$

where E is a constant to be found. The boundary conditions (7.96) can then be applied to (7.105) to find

$$B = \frac{(1 - 2\nu) \tan \phi}{(1 - 2\nu + \bar{\mathcal{F}})\bar{\Lambda}}, \quad E = 0. \quad (7.106)$$

Applying (7.106) to the expressions (7.104) and (7.105), $u_1^{(0)}$ and $u_2^{(1)}$ are determined to be

$$u_1^{(0)}(x_2) = \frac{(1 - 2\nu) \tan \phi}{(1 - 2\nu + \bar{\mathcal{F}})\bar{\Lambda}} (e^{-\bar{\Lambda}x_2} - 1), \quad (7.107)$$

$$u_2^{(1)}(x_2) = \tan \phi e^{-\bar{\Lambda}x_2}, \quad (7.108)$$

and thus, by substituting (7.107) and (7.108) into the truncated Taylor series (7.91), u_1 and u_2 are found to be approximated by

$$u_1 \sim \frac{(1 - 2\nu) \tan \phi}{(1 - 2\nu + \bar{\mathcal{F}})\bar{\Lambda}} (e^{-\bar{\Lambda}x_2} - 1), \quad (7.109)$$

$$u_2 \sim \left(x_1 - \frac{d}{2} \right) \tan \phi e^{-\bar{\Lambda}x_2}. \quad (7.110)$$

Chapter 8

Conclusions and Future Work

8.1 Conclusions

In this thesis, the effects of wall inertia and axial bending have been added to the model by Whittaker *et al.* (2010c) which describes instabilities in flow through an elastic-walled tube. The changes to the instabilities and stability criteria due to the addition of wall inertia and axial bending have been evaluated.

We first added wall inertia to the Whittaker *et al.* (2010c) model in Chapter 2. In forming the new model, it was found that the wall inertia term does not enter the governing equation in the same way the fluid inertia does, but instead combines with the azimuthal bending term. In this new model we found that, as in the Whittaker *et al.* (2010c) model, countably many oscillatory modes exist, each with its own distinct eigenfrequency. These modes are distinguished by having different numbers of spatial oscillations in the axial direction. As the amount of wall inertia increases, it is found that the eigenfrequencies of all the modes decrease, but this decrease is more rapid for higher-order modes than for lower-order modes. We have discovered that the axial mode shapes of the higher-order modes for the pressure and axial velocity start spatially oscillating about a non-zero value, when wall inertia is increased to a non-zero value. We have also found that the axial mode shapes of the area change tend towards being symmetric about the axial midpoint of the tube, as the wall inertia is increased. The properties of the axial mode shapes are witnessed in Figures 2.4–2.6.

By examining the stability criterion and growth rates of the different modes, it was seen that odd modes (including the fundamental mode) become more

unstable for increasing wall inertia, whereas the even modes become more stable for increasing wall inertia. The reason for this is because as wall inertia is increased, it dominates over the fluid inertia terms and the leading-order balance is found to be between axial tension, azimuthal bending and wall inertia. As the fluid inertia no longer contributes at leading-order, the odd and even modes for the oscillatory area variation become symmetric and antisymmetric respectively in the axial direction about the midpoint of the tube. As such, the even modes have little flux within the upstream rigid region of the tube as the fluid predominantly moves between the crests and troughs of the oscillations in the elastic-walled tube. Because of this, the energy influx into the system is small, and as there is not as much energy available to drive the instabilities, the modes are much more stable. For the odd modes however, there is a larger flux in the upstream rigid region resulting in a greater influx of energy into the system. Because of this increase in available energy to drive the instabilities, the odd modes are more unstable.

It is also seen that the growth rates of all the modes decrease with increasing wall inertia, but the growth rates of the even modes decrease much faster. It is shown that the fundamental mode is always the most unstable and has the highest growth rate. As this mode also becomes more unstable with increasing wall inertia, it is found that wall inertia is a destabilising effect on the system.

Finally, the size of the effect wall inertia has on the frequency, critical Reynolds number (the Reynolds number at which the growth rate of a mode is zero), and the growth rate (differentiated with respect to the Reynolds number) of the fundamental mode has been quantified for a couple of physical examples. In the case of blood flow through the main pulmonary artery, it was found that the wall inertia parameter M takes the value $M \approx 0.003$. Using this value of M instead of $M = 0$ yielded a 0.9% decrease in the frequency of the fundamental mode, a 0.5% decrease in the critical Reynolds number of the fundamental mode, and a 1.8% decrease in the gradient of the growth rate for the fundamental mode. Hence in this case, the effects of wall inertia are negligible. The example of crude oil flowing through a steel submarine pipe was also considered. Here, we instead have $M \approx 0.02$, which yields a 5.7% decrease in the frequency of the fundamental mode, a 3.2% decrease in the critical Reynolds number of the fundamental mode, and a 10.8% decrease in the gradient of the growth rate for the fundamental mode. Thus, the effects of wall inertia are more significant here and cannot necessarily be neglected.

The problem of expanding the Whittaker *et al.* (2010c) model so that the canonical clamped boundary conditions are satisfied at the ends of the elastic-walled tube was then considered in Chapters 3–7. In the original Whittaker *et al.* (2010c) model, only the normal and azimuthal displacements of the tube wall were fixed to be zero at the tube ends. Whittaker (2015) extended this model further to allow the Dirichlet parts of the pinned boundary conditions, which fix the normal, azimuthal and axial displacements to be zero, to be satisfied at the tube ends. This was done by introducing a shear-relaxation boundary layer near the ends of the tube. Whittaker (2015) found that this shear layer splits into an inner and outer shear-relaxation layer, and that the shear layer only has a significant effect on the bulk solution when $\delta\ell \ll 1$, where $\delta \ll 1$, $\ell \gg 1$ are dimensionless parameters representing the tube wall thickness and tube length respectively.

In this thesis, it was determined that an axial-bending boundary layer must be introduced to raise the axial order of the system enough for the full clamped boundary conditions to be satisfied. In Chapter 3, a toy model was constructed from the Föppl–von Kármán equations (Landau & Lifshitz, 1959), and using this model the bending-layer width δ_B was predicted to be $\delta_B = O(\mathcal{F}^{-\frac{1}{2}}\ell^{-1})$, where $\mathcal{F} = O(1)$ is a dimensionless parameter representing the axial tension acting on the tube wall. With this estimate, it was found in Chapter 3 that this problem splits into three different regimes.

In the first of these regimes, regime I_a, we have $\delta\ell \ll 1 \ll \delta\ell^2$. In this case, the shear-relaxation layer studied by Whittaker (2015) has a significant effect on the bulk solution, and so must be considered. Using the predictions of the toy model in Chapter 3, the bending layer was expected to be larger than the tube wall thickness δ , but smaller than the inner and outer shear layers. In the second regime, regime I_b, $\delta\ell^2 \ll 1$ and again the shear layer found by Whittaker (2015) must be considered. In this case, the toy model predicted that the bending layer would be larger than the tube wall thickness and inner shear layer, but smaller than the outer shear layer. In both regimes I_a and I_b, Kirchhoff–Love shell theory could be used to model the wall mechanics. In the final regime, regime II, the case where $\delta\ell \gg 1$ was considered. In this case, the shear layer studied by Whittaker (2015) no longer has a significant effect on the bulk solution and does not need to be considered. The toy model predicts that the bending layer would be smaller than the tube wall thickness in this regime, and as such Kirchhoff–Love shell theory can no longer be used to model the

wall mechanics.

In Chapter 4, regime I_a where $\delta\ell \ll 1 \ll \delta\ell^2$ was considered. Here a bending layer with width $\delta_B = \mathcal{F}^{-\frac{1}{2}}\ell^{-1}$ was found, which is in agreement with the prediction from the toy model. Hence, this bending layer is larger than the tube wall thickness, and smaller than both the inner and outer shear layers. As such, the bending layer was found to be situated at the ends of the elastic-walled tube and matches onto a modified inner shear layer. The dominant balance within the bending layer was found to be between axial bending and pre-stress and axial curvature.

The leading-order deformations within this bending layer have been calculated, and it was found that there was no change in the cross-sectional area at leading order within this layer. The corrections to the inner shear-layer deformations were also calculated and were found to be $O(\mathcal{F}^{-1}\delta^{-1}\ell^{-2})$ smaller than the leading-order terms. These corrections may appear at lower or higher orders than the other higher-order terms in the approximations for the inner shear-layer deformations, depending on sizes of δ and ℓ . If the condition $\mathcal{F} = O(1)$ is relaxed and we instead have $\mathcal{F} = O(\delta^{-1}\ell^{-2})$ yielding a smaller tension, this will allow the correction terms to contribute at leading order. However, this may also alter the behaviour of the bulk solution, and will change the widths of the bending and inner shear layers so that they become the same size. As such, further investigation is needed to see what happens in this case. Returning to the case where $\mathcal{F} = O(1)$, it was calculated that there would be no corrections to the normal deformation or area change in the outer shear and bulk layers due to the leading-order deformations in the bending layer. It was also seen that the leading-order bending-layer deformations induce higher-order corrections to the azimuthal and axial deformations in the outer shear and bulk layers.

Overall, the bending layer in regime I_a is found to be passive and not contribute to the leading-order displacements or area change in the other layers. Instead, it simply allows the axial gradient to decrease to zero as the clamped end of the tube is reached. Hence, the effects of this bending layer on the shear layers and bulk solution may be safely neglected in the case $\delta\ell \ll 1 \ll \delta\ell^2$, $\delta \ll 1$, $\ell \gg 1$, $\mathcal{F} = O(1)$. This is consistent with numerical results published by Whittaker (2015), which are calculated in regime I_a.

Chapter 5 concentrates on regime I_b where $\delta\ell^2 \ll 1$. In this regime, a bending layer of width $\delta_B = O(\delta^{\frac{1}{2}})$ was found, and the dominant balance

within this bending layer was determined to be between axial bending, azimuthal stretching and axial stretching. This width is different from the one predicted by the toy model in Chapter 3 because of the effects of azimuthal stretching, which are not included in the toy model. However, this width is still in between the widths of the inner and outer shear layers. It was determined that the inner shear layer is no longer present. Instead there is a bending layer situated at the ends of the elastic-walled tube which matches onto a modified outer shear layer. Asymptotic approximations for the in-plane stresses within the bending layer have been calculated up to second order, and using these, approximations for the bending-layer deformations have been calculated up to the largest non-zero higher-order term. It is also found that the area variation in the bending layer is $O(\Delta \tilde{\mathcal{F}}^{\frac{1}{2}} \ell^{-1})$, where $\Delta(t)$ is the dimensionless, slowly varying amplitude of the oscillation, and $\tilde{\mathcal{F}} = O(\mathcal{F} \delta^2 \ell^2)$ is a scaled axial tension. This area variation tends to a constant multiple of $\Delta(t)$ as we exit the bending layer.

The leading-order bending-layer deformations in regime I_b then induce corrections to the outer shear-layer deformations that are found to be a factor of $O(\mathcal{F}^{\frac{1}{2}} \delta^{\frac{3}{2}} \ell)$ smaller than leading-order terms. These corrections were also determined to be larger than the other higher-order terms in the expressions for the deformations. The corrections to the normal and azimuthal deformations in the outer shear layer were found to be linear in the axial coordinate, affecting their axial gradient, and the correction to the outer shear-layer axial deformation was found to be constant in the axial coordinate, yielding a constant shift. Also calculated was the correction to the area change in the outer shear layer, which was found to be smaller than the leading-order terms but larger than the other higher-order terms. This correction was seen to behave linearly in the axial direction, affecting the axial gradient of the area change. If the condition $\mathcal{F} = O(1)$ is relaxed and we instead have $\mathcal{F} = O(\delta^{-3} \ell^{-2})$, resulting in a larger tension, the correction terms will contribute at leading order. However, this will also set $\tilde{\mathcal{F}} \gg 1$, and in this scenario the shear layer found by Whittaker (2015) does not have a significant effect on the bulk solution and does not need to be considered. Hence, further investigation is needed to determine what happens for this scenario. Returning to the case where $\mathcal{F} = O(1)$, it was found that the bending layer enforces corrections to the bulk-layer deformations and area variation that apply at higher orders.

Overall, the bending layer in regime I_b is found to be passive and not

contribute to the leading-order displacements or area change in the larger layers. Instead it allows the axial gradient to decrease to zero at the clamped boundary, and allows for the decay of the leading-order in-plane azimuthal hoop stress \tilde{N} and shear stress \tilde{S} from their values at the clamped boundary to the smaller values needed in the outer shear layer. The bending layer also keeps the leading-order in-plane axial stress $\tilde{\Sigma}$ approximately constant in the axial direction. As such, the effects of this bending layer on the outer shear layer and bulk solution may be safely neglected in the case $\delta\ell^2 \ll 1$, $\delta \ll 1$, $\ell \gg 1$, $\mathcal{F} = O(1)$.

The final regime, regime II where $\delta\ell \gg 1$, is studied in Chapters 6 and 7. In Chapter 6, a new model was derived to describe the wall mechanics as the toy model in Chapter 3 predicted that the bending layer would be too small for Kirchhoff–Love shell theory to be valid. This model is a linearised two-dimensional model describing bending a semi-infinite block under tension. The block in question corresponds to a 2D cross-section of the tube wall in the normal and axial directions. This model is based on the assumption that azimuthal variation is slow on the scale of the bending layer predicted by the toy model. Numerical solutions for this model have been constructed, and by applying analytical techniques, it was found that the deformations of the block are composed of countably many modes that decay exponentially in the axial direction, each with their own distinct decay rate. Analytical far-field approximations for the deformations have been developed and are found to be in agreement with the numerical solutions. A full analytical solution to this model has not yet been found, but it was seen that it may be possible to apply a method similar to that used by Shankar (2003) to determine the coefficients of the modes of the deformations.

In this 2D model, different behaviours were found in the cases $\delta\ell \ll 1$ and $\delta\ell \gg 1$. In the case $\delta\ell \ll 1$, corresponding to regimes I_a and I_b , a bending layer with dimensionless width $\delta_B = O(\mathcal{F}^{-\frac{1}{2}}\ell^{-1})$ is found, which is in agreement with the bending layers found in the toy model and in regime I_a . However when $\delta\ell \gg 1$, corresponding to regime II, a new boundary layer is found with dimensionless width $\delta_B = O(\mathcal{F}^{\frac{1}{2}}\delta^2\ell)$, suggesting that a different dominant mechanism is occurring within this boundary layer. In both cases however, the dimensional normal deformation u_1 is found to behave as $u_1 = O(a\mathcal{F}^{-\frac{1}{2}}\ell^{-1})$ (where a is the typical radial scale of the elastic-walled tube) as we exit the boundary layer.

Applying this 2D model to the elastic walled tube in regime II, where $\delta\ell \gg 1$, it was found that the corrections to the boundary conditions in the bulk layer are a factor of $O(\mathcal{F}^{-\frac{1}{2}}\ell^{-2})$ smaller than the leading-order conditions. It is noted that these corrections may not be accurate as the boundary layer is larger than originally expected in this regime, and azimuthal variation which is neglected by the 2D model may be significant on this scale. Further work is required to check the validity of these corrections, but even if these corrections are incorrect, this model is still applicable to more general problems of clamped shells under tension. Providing these corrections are accurate, then by relaxing the condition $\mathcal{F} = O(1)$ and instead setting $\mathcal{F} = O(\ell^{-4})$ corresponding to a smaller axial tension, the correction terms become large enough to contribute at leading order. However, applying this change may alter the behaviour of the solution in the bulk layer. As such, further work is needed to analyse what happens for this smaller tension. It is seen that in the case $\delta\ell \gg 1$, $\delta \ll 1$, $\ell \gg 1$, $\mathcal{F} = O(1)$, the correction terms are small enough that the effects of the bending layer can be safely neglected in the bulk layer. The fact that these corrections may be neglected is consistent with numerical simulations run by Whittaker *et al.* (2010d).

By examining the new boundary layer that occurs in the 2D model for $\delta\ell \gg 1$, it was found that the axial deformations of the block deviate away from a uniform shear across the width of the block and tend towards a sinusoidal self-similar solution as the axial coordinate is increased. As such, this new boundary layer was found to be a transverse shear-relaxation layer. This shear layer is different from the one modelled by Whittaker (2015), which arises due to azimuthal shear.

Finally in Chapter 7, the 2D model in Chapter 6 is considered further and the possibility of using a one-dimensional model to describe bending a semi-infinite block under tension is investigated. Here, three possible one-dimensional models are considered. The first model is one derived from Kirchhoff–Love shell theory. It is found that although the shear-layer width in regime II is larger than the block thickness, indicating that Kirchhoff–Love shell theory is applicable, applying this theory yields a model which does not give the right behaviour for the boundary-layer width when $\delta\ell \gg 1$. This is because another assumption made in Kirchhoff–Love shell theory, which is the preservation of the normal to the centre line of the block after a deformation, is violated in the shear layer that appears in this regime. The second model

considered is one derived by averaging the components of the governing Cauchy's momentum equation over the width of the block. Although this model is able to yield the right qualitative behaviour for the boundary-layer width, there are still quantitative discrepancies between the boundary-layer width from this model and the boundary-layer width from the 2D model, particularly for $\delta\ell \ll 1$.

The final model considered in Chapter 7 is one derived by solving the 2D governing system (6.88)–(6.93) for the block written solely in terms of the normal deformation u_1 , using a truncated Taylor series to approximate u_1 . This model yields three exponentially decaying modes for the deformation, each with their own distinct decay rate. The smallest of these decay rates, corresponding to the slowest decaying mode, is found to be in good agreement with the fundamental decay rate in the 2D model. The next smallest decay rate also agrees with the fundamental decay rate in the 2D model for $\delta\ell \gg 1$, but diverges away from the fundamental decay rate for $\delta\ell \ll 1$. This implies that for $\delta\ell \ll 1$, only one of the modes in the 1D model contributes in modelling the fundamental mode, whereas for $\delta\ell \gg 1$, two of the modes in the 1D model contribute in describing the fundamental mode. The largest of these decay rates, corresponding to the quickest decaying mode, does not appear to model any of the modes found in the 2D model. This is likely due to more terms from the Taylor series of u_1 being needed to capture the behaviour of the higher-order modes in the 2D model.

It is found that this model is able to capture the behaviour of the deformations away from the clamped edge of the block using arbitrary conditions set at the clamped edge. However, the behaviour near the clamped edge cannot be modelled accurately at the same time, and the discrepancies in the behaviour of the 1D and 2D models near the clamped edge are particularly large for $\delta\ell \gg 1$. This was found to be due to a 2D compression effect that occurs near the clamped boundary which cannot be captured by the 1D model. As this compression effect is particularly significant for $\delta\ell \gg 1$, the discrepancies between the solutions in the 1D and 2D models are distinctly large in this case.

It is possible that these models can be improved upon further by using modes motivated by the self-similar solution found in Chapter 6 to approximate the deformations instead of using truncated Taylor series. It may also be possible to use these modes to derive a new model for the behaviour of the

block near the clamped boundary. Further investigation is needed to examine these possibilities.

The boundary layers needed for the clamped boundary conditions to be satisfied in regimes I_a, I_b and II are summarised in table 8.1. We have determined that in the case $\delta \ll 1, \ell \gg 1$, $\mathcal{F} = O(1)$, the boundary layers introduced to satisfy the clamped boundary conditions in each of the regimes do not apply any leading-order effects to the larger boundary layers in their respective regimes, or the bulk solution. As such, the effects of the bending layer can safely be neglected in these larger boundary layers and in the bulk solution. We have also seen that by relaxing the condition $\mathcal{F} = O(1)$ and instead setting $\mathcal{F} = O(\delta^{-1}\ell^{-2})$ in regime I_a, $\mathcal{F} = O(\delta^{-3}\ell^{-2})$ in regime I_b, and $\mathcal{F} = O(\ell^{-4})$ in regime II, the effects of the axial-bending and transverse-shear layers on the larger layers become significant at leading order. In setting these tensions, the properties of the inner and outer shear layers and the bulk layer also change. As such, further study is required to determine what effects the axial-bending and transverse-shear layers have on the larger layers when we have different values of \mathcal{F} .

Regime	I _a	I _b	II
δ, ℓ Bounds	$\delta\ell \ll 1 \ll \delta\ell^2$	$\delta\ell^2 \ll 1$	$\delta\ell \gg 1$
Physical Mechanism of Inner Boundary Layer	Axial Bending	Axial Bending	Transverse Shear-Relaxation
Width of Inner Boundary Layer	$O(\mathcal{F}^{-\frac{1}{2}}\ell^{-1})$	$O(\delta^{\frac{1}{2}})$	$O(\mathcal{F}^{\frac{1}{2}}\delta^2\ell)$
Type of Outer Boundary Layers	$\begin{cases} \text{Inner Shear} \\ \text{Outer Shear} \end{cases}$	Outer Shear	None
Width of Outer Boundary Layers	$\begin{cases} O(\mathcal{F}^{\frac{1}{2}}\delta\ell) \\ O(\mathcal{F}^{-\frac{1}{2}}\delta^{-1}\ell^{-1}) \end{cases}$	$O(\mathcal{F}^{-\frac{1}{2}}\delta^{-1}\ell^{-1})$	—

Table 8.1: Summary of the boundary layers needed to satisfy the full clamped boundary conditions in regimes I_a, I_b and II.

8.2 Recommendations for Future Work

Some recommendations for future work to be carried out on the models developed here are now suggested. Firstly, numerical simulations of flow through an elastic-walled tube can be run to test the accuracy of the analytical results determined in Chapter 2, where the effects of wall inertia are evaluated. In particular, the frequency, axial mode shape, growth rate and stability criterion of the fundamental mode may be checked against the numerical simulations. This work is ongoing in collaboration with Matthias Heil of the University of Manchester.

Numerical simulations of the elastic-walled tube can also be used to check the effects induced by introducing a bending layer in the case $\delta\ell \ll 1$, $\delta \ll 1$, $\ell \gg 1$, $\mathcal{F} = O(1)$. Using these simulations, the bending layer and the corrections to the inner and outer shear layers can be tested against the numerical simulations of the elastic-walled tube near the clamped ends. These numerical simulations can be carried out by combining Kirchhoff–Love shell theory with the use of the object-oriented multi-physics finite-element library, `oomph-lib`, developed by Heil & Hazel (2006). Such numerical simulations were used by Whittaker *et al.* (2010d) to evaluate the validity of their tube law.

In the case $\delta\ell \gg 1$, $\delta \ll 1$, $\ell \gg 1$, $\mathcal{F} = O(1)$, it is possible that azimuthally dependent effects could be significant on the scale of the transverse shear-relaxation layer found in Chapter 6. To evaluate this possibility, the scalings of the azimuthally dependent effects neglected in the derivation of the 2D model in Chapter 6 can be determined to see if they appear at leading order on the axial scale of the boundary layer. If these effects do not appear at leading order, then the 2D model in Chapter 6 will be applicable to the 3D elastic-walled tube, and the shear layer will exist in the 3D case. Numerical simulations can then be used to test the properties of this shear layer and determine the validity of the corrections to the bulk solution predicted by the 2D model. These simulations will have to be constructed in a different way to the simulations described for the case $\delta\ell \ll 1$, as it was witnessed in §7.3 that Kirchhoff–Love shell theory cannot accurately model the transverse shear-relaxation layer. One possible way of constructing these simulations is to combine `oomph-lib` with a modified Saint Venant–Kirchhoff model similar to that used in deriving the 2D model in Chapter 6.

It has been seen that when $\mathcal{F} = O(1)$ in each of the regimes of introducing a boundary layer to satisfy the clamped boundary conditions, the effects of each

of the new boundary layers are not significant at leading order in the other layers. However, if we vary \mathcal{F} , it is possible that these effects will become significant at leading order. Varying \mathcal{F} to force these effects to be significant may also change various properties of the problem, such as the behaviour of the bulk layer, and the sizes and behaviours of the inner and outer shear-relaxation layers studied by Whittaker (2015). As such, further study is required to see if it is possible to vary \mathcal{F} so that the bending layers in regimes I_a and I_b , and the transverse shear layer in regime II, yield corrections at leading order to the other layers. This can be investigated by setting \mathcal{F} to be the predicted values at which the bending layers and transverse shear layer affect the leading-order behaviour in the other layers in their respective regimes, and then resolving the governing systems in each layer.

To further extend the models derived here, non-linear effects in the tube wall can be considered. This can be done by keeping the assumption that wall displacements are small, but instead of neglecting terms which are quadratic and higher-order in the deformations, some of these non-linear terms are retained. The resulting governing equations can then be solved by forming a perturbation solution for the deformations. In extending the model in this way, the sizes of the non-linear effects can be evaluated and possible regimes where these effects may become significant can be found.

Another effect that can be considered is larger amplitude oscillations. This can be included in the models considered here by removing the assumption that the wall displacements are small compared to the tube diameter. In doing so, the dimensionless parameter $\Delta(t)$ representing the dimensionless amplitude of the instabilities will now be $O(1)$, and terms that are quadratic and higher-order in the deformations will be significant at leading order. Due to the increased complexity of the governing system, it may be that a solution can only be found numerically. This situation corresponds to the case where the amplitude of the instabilities in the models considered here have grown large enough to be comparable to the tube radius.

Finally, axially varying tube properties such as wall thickness and stiffness may also be incorporated into the model by setting these properties to be known functions of the axial coordinate z . By doing so, it is possible to evaluate what happens if there is a sudden jump in these properties between two regions of the flexible tube, which may correspond to, for example, a flexible tube comprised of two regions made of different materials. In this case, different

governing systems will need to be derived in each region using similar methods to those applied in the current models, and the solutions of the two regions will have to match at the interface between the two regions.

Bibliography

AITTOKALLIO, T., GYLLENBERG, M. & POLO, O. 2001 A model of a snorer's upper airway. *Mathematical biosciences* **170** (1), 79–90.

BATCHELOR, G. K. 1967 *An introduction to fluid dynamics*, paperback edn. Cambridge University Press, Cambridge.

BERKE, G. S., GREEN, D. C., SMITH, M. E., ARNSTEIN, D. P., HONRUBIA, V., NATIVIDAD, M. & CONRAD, W. A. 1991 Experimental evidence in the in vivo canine for the collapsible tube model of phonation. *J. Acoust. Soc. Am.* **89** (3), 1358–63.

BERTRAM, C. & TSCHERRY, J. 2006 The onset of flow-rate limitation and flow-induced oscillations in collapsible tubes. *Journal of Fluids and Structures* **22** (8), 1029 – 1045.

BERTRAM, C. D. 1986 Unstable equilibrium behaviour in collapsible tubes. *Journal of biomechanics* **19** (1), 61–69.

BERTRAM, C. D. 2003 Experimental studies of collapsible tubes. In *Flow past highly compliant boundaries and in collapsible tubes* (ed. P. W. Carpenter & T. J. Pedley), chap. 3, pp. 51–65. Springer, Dordrecht, The Netherlands: Kluwer Academic.

BERTRAM, C. D. 2008 Flow-induced oscillation of collapsed tubes and airway structures. *Respir. Physiol. Neurobiol.* **163**, 256–265.

BERTRAM, C. D. & GODBOLE, S. A. 1997 Lda measurements of velocities in a simulated collapsed tube. *Journal of biomechanical engineering* **119** (3), 357–363.

BERTRAM, C. D. & NUGENT, A. H. 2005 The flow field downstream of an oscillating collapsed tube. *Journal of biomechanical engineering* **127** (1), 39–45.

BERTRAM, C. D., RAYMOND, C. J. & BUTCHER, K. S. A. 1989 Oscillations in a collapsed-tube analog of the brachial artery under a sphygmomanometer cuff. *ASME J. Biomech. Engng.* **111**, 185–191.

BERTRAM, C. D., RAYMOND, C. J. & PEDLEY, T. J. 1990 Mapping of instabilities for flow through collapsed tubes of differing length. *Journal of Fluids and Structures* **4** (2), 125–153.

BERTRAM, C. D., RAYMOND, C. J. & PEDLEY, T. J. 1991 Application of nonlinear dynamics concepts to the analysis of self-excited oscillations of a collapsible tube conveying a fluid. *Journal of Fluids and Structures* **5** (4), 391–426.

BINNS, R. L. & KU, D. N. 1989 Effect of stenosis on wall motion. a possible mechanism of stroke and transient ischemic attack. *Arteriosclerosis, Thrombosis, and Vascular Biology* **9** (6), 842–847.

BULL, J. L., REICKERT, C. A., TREDICI, S., KOMORI, E., FRANK, E. L., BRANT, D. O., GROTBORG, J. B. & HIRSCHL, R. B. 2005 Flow limitation in liquid-filled lungs: effects of liquid properties. *J. Biomech. Eng.* **127**, 630–636.

CANCELLI, C. & PEDLEY, T. J. 1985 A separated-flow model for collapsible-tube oscillations. *Journal of Fluid Mechanics* **157**, 375–404.

CAREW, E. O. & PEDLEY, T. J. 1997 An active membrane model for peristaltic pumping: Part i—periodic activation waves in an infinite tube. *Journal of biomechanical engineering* **119** (1), 66–76.

CARPENTER, P. W. & GARRAD, A. D. 1985 The hydrodynamic stability of flow over kramer-type compliant surfaces. part 1. tollmien-schlichting instabilities. *Journal of Fluid Mechanics* **155**, 465–510.

CARPENTER, P. W. & GARRAD, A. D. 1986 The hydrodynamic stability of flow over kramer-type compliant surfaces. part 2. flow-induced surface instabilities. *Journal of Fluid Mechanics* **170**, 199–232.

CONRAD, W. A. 1969 Pressure-flow relationships in collapsible tubes. *Biomedical Engineering, IEEE Transactions on* (4), 284–295.

DANAHY, D. T. & RONAN, J. A. 1974 Cervical venous hums in patients on chronic hemodialysis. *New England Journal of Medicine* **291** (5), 237–239.

DAVIES, C. & CARPENTER, P. W. 1997 Instabilities in a plane channel flow between compliant walls. *Journal of Fluid Mechanics* **352**, 205–243.

DUPONT, T., HOFFMAN, J., JOHNSON, C., KIRBY, R. C., LARSON, M. G., LOGG, A. & SCOTT, L. R. 2003 *The FEniCS project*. Chalmers Finite Element Centre, Chalmers University of Technology.

ELAD, D., KAMM, R. D. & SHAPIRO, A. H. 1987 Choking phenomena in a lung-like model. *Journal of biomechanical engineering* **109** (1), 1–9.

FEE, M. S., SHRAIMAN, B., PESARAN, B. & MITRA, P. 1998 The role of nonlinear dynamics of the syrinx in the vocalizations of a songbird. *Nature* **395** (6697), 67–71.

FLÜGGE, W. 1972 *Tensor analysis and Continuum Mechanics*. Springer, Berlin.

FULLANA, J.-M. & ZALESKI, S. 2009 A branched one-dimensional model of vessel networks. *J. Fluid Mech.* **621**, 183–204.

GAVRIELY, N. & JENSEN, O. 1993 Theory and measurements of snores. *Journal of Applied Physiology* **74** (6), 2828–2837.

GAVRIELY, N., PALTI, Y., ALROY, G. & GROTBORG, J. B. 1984 Measurement and theory of wheezing breath sounds. *J. Appl. Physiol.* **57**, 481–492.

GAVRIELY, N., SHEE, T. R., CUGELL, D. W. & GROTBORG, J. B. 1989 Flutter in flow-limited collapsible tubes: a mechanism for the generation of wheezes. *J. Appl. Physiol.* **66**, 2251–2261.

GERWICK, B. C. 2007 *Construction of marine and offshore structures*. CRC Press, New York.

GREGORY, R. D. 1980 The semi-infinite strip $x \geq 0$, $-1 \leq y \leq 1$; completeness of the Papkovitch-Fadde eigenfunctions when $\varphi_{xx}(0, y)$, $\varphi_{yy}(0, y)$ are prescribed. *J. Elasticity* **10** (1), 57–80.

GRIFFITHS, D. J. 1969 Urethral elasticity and micturition hydrodynamics in females. *Medical and biological engineering* **7** (2), 201–215.

GRIFFITHS, D. J. 1971 Hydrodynamics of male micturition—i theory of steady flow through elastic-walled tubes. *Medical and Biological Engineering* **9** (6), 581–588.

GROTBORG, J. B. & JENSEN, O. E. 2004 Biofluid mechanics in flexible tubes. In *Annual review of fluid mechanics. Vol. 36, Annu. Rev. Fluid Mech.*, vol. 36, pp. 121–147. Annual Reviews, Palo Alto, CA.

GUNERATNE, J. C. 1999 *High Reynolds number flow in a collapsible channel..* PhD Thesis, University of Cambridge.

HAYASHI, S., HAYASE, T. & KAWAMURA, H. 1998 Numerical analysis for stability and self-excited oscillation in collapsible tube flow. *Journal of biomechanical engineering* **120** (4), 468–475.

HAYNES, W. 2012 *CRC Handbook of Chemistry and Physics, 93rd Edition.* Taylor & Francis.

HAZEL, A. L. & HEIL, M. 2003 Steady finite-reynolds-number flows in three-dimensional collapsible tubes. *Journal of fluid Mechanics* **486**, 79–103.

HEIL, M. 1997 Stokes flow in collapsible tubes: computation and experiment. *Journal of Fluid Mechanics* **353** (1), 285–312.

HEIL, M. & BOYLE, J. 2010 Self-excited oscillations in three-dimensional collapsible tubes: simulating their onset and large-amplitude oscillations. *Journal of Fluid Mechanics* **652**, 405–426.

HEIL, M. & HAZEL, A. L. 2006 oomph-lib an Object-Oriented Multi-Physics finite-element Library. In *Fluid-structure interaction, Lect. Notes Comput. Sci. Eng.*, vol. 53, pp. 19–49. Springer, Berlin.

HEIL, M. & HAZEL, A. L. 2011 Fluid-structure interaction in internal physiological flows. In *Annual review of fluid mechanics. Volume 43, 2011, Annu. Rev. Fluid Mech.*, vol. 43, pp. 141–162. Annual Reviews, Palo Alto, CA.

HEIL, M. & JENSEN, O. E. 2003 Flows in deformable tubes and channels: theoretical models and biological applications. In *Flow past highly compliant boundaries and in collapsible tubes* (ed. P. W. Carpenter & T. J. Pedley), chap. 2, pp. 15–49. Springer, Dordrecht, The Netherlands: Kluwer Academic.

HEIL, M. & PEDLEY, T. J. 1996 Large post-buckling deformations of cylindrical shells conveying viscous flow. *Journal of Fluids and Structures* **10** (6), 565–599.

HEIL, M. & WATERS, S. L. 2008 How rapidly oscillating collapsible tubes extract energy from a viscous mean flow. *J. Fluid Mech.* **601**, 199–227.

HINCH, E. J. 1991 *Perturbation methods.* Cambridge University Press, Cambridge.

HOWELL, P., KOZYREFF, G. & OCKENDON, J. 2009 *Applied Solid Mechanics.* Cambridge University Press, Cambridge.

HSIUNG, S., LEE, C., LIN, J. & LEE, G. 2007 Active micro-mixers utilizing moving wall structures activated pneumatically by buried side chambers. *Journal of Micromechanics and Microengineering* **17** (1), 129.

HUANG, L. 1995 Flutter of cantilevered plates in axial flow. *Journal of Fluids and Structures* **9** (2), 127–147.

HUANG, L. 2001 Viscous flutter of a finite elastic membrane in poiseuille flow. *Journal of fluids and structures* **15** (7), 1061–1088.

ISERLES, A. 1996 *A first course in the numerical analysis of differential equations*. Cambridge University Press, Cambridge.

JENSEN, O. E. 1990 Instabilities of flow in a collapsed tube. *Journal of Fluid Mechanics* **220**, 623–659.

JENSEN, O. E. 1992 Chaotic oscillations in a simple collapsible-tube model. *Journal of biomechanical engineering* **114** (1), 55–59.

JENSEN, O. E. & HEIL, M. 2003 High-frequency self-excited oscillations in a collapsible-channel flow. *J. Fluid Mech.* **481**, 235–268.

KAMM, R. D. 1982 Bioengineering studies of periodic external compression as prophylaxis against deep vein thrombosis - part i: numerical studies. *ASME J. Biomech. Engng.* **104**, 87–95.

KECECIOGLU, I., MCCLURKEN, M. E., KAMM, R. D. & SHAPIRO, A. H. 1981 Steady, supercritical flow in collapsible tubes. part 1. experimental observations. *Journal of Fluid Mechanics* **109**, 367–389.

KIERZENKA, J. & SHAMPINE, L. F. 2001 A bvp solver based on residual control and the maltab pse. *ACM Trans. Math. Softw.* **27** (3), 299–316.

KNOWLTON, F. P. & STARLING, E. H. 1912 The influence of variations in temperature and blood pressure on the performance of the isolated mammalian heart. *J. Physiol. London* **44**, 206–219.

KOUNANIS, K. & MATHIOULAKIS, D. S. 1999 Experimental flow study within a self oscillating collapsible tube. *Journal of fluids and structures* **13** (1), 61–73.

KU, D. N. 1997 Blood flow in arteries. *Annual Review of Fluid Mechanics* **29** (1), 399–434.

KUMARAN, V. 2000 Classification of instabilities in the flow past flexible surfaces. *Current Science* **79** (6), 766–773.

KUMARAN, V. 2003 Hydrodynamic stability of flow through compliant channels and tubes. In *Flow Past Highly Compliant Boundaries and in Collapsible Tubes*, pp. 95–118. Springer.

LANDAU, L. D. & LIFSHITZ, E. M. 1959 *Theory of elasticity*. Pergamon Press, London-Paris-Frankfurt; Addison-Wesley Publishing Co., Inc., Reading, Mass.

LAROSE, P. G. & GROTBORG, J. B. 1997 Flutter and long-wave instabilities in compliant channels conveying developing flows. *Journal of Fluid Mechanics* **331**, 37–58.

LIGHTHILL, J. 1975 *Mathematical biofluidynamics*. Society for Industrial and Applied Mathematics, Philadelphia, Pa. Based on the lecture course delivered to the Mathematical Biofluidynamics Research Conference of the National Science Foundation held from July 16–20, 1973, at Rensselaer Polytechnic Institute, Troy, New York, Regional Conference Series in Applied Mathematics, No. 17.

LUO, X. Y. & PEDLEY, T. J. 1995 A numerical simulation of steady flow in a 2-d collapsible channel. *Journal of Fluids and Structures* **9** (2), 149–174.

LUO, X. Y. & PEDLEY, T. J. 1996 A numerical simulation of unsteady flow in a two-dimensional collapsible channel. *Journal of Fluid Mechanics* **314**, 191–225.

LUO, X. Y. & PEDLEY, T. J. 1998 The effects of wall inertia on flow in a two-dimensional collapsible channel. *J. Fluid Mech.* **363**, 253–280.

LUO, X. Y. & PEDLEY, T. J. 2000 Multiple solutions and flow limitation in collapsible channel flows. *Journal of Fluid Mechanics* **420**, 301–324.

MATSUZAKI, Y., IKEDA, T., KITAGAWA, T. & SAKATA, S. 1994 Analysis of flow in a two-dimensional collapsible channel using universal “tube” law. *Journal of biomechanical engineering* **116** (4), 469–476.

McCLURKEN, M. E., KECECIOGLU, I., KAMM, R. D. & SHAPIRO, A. H. 1981 Steady, supercritical flow in collapsible tubes. part 2. theoretical studies. *Journal of Fluid Mechanics* **109**, 391–415.

McDONALD, D. A. 1974 *Blood flow in arteries*, 2nd edn. Edward Arnold, London.

OHBA, K., SAKURAI, A. & OKA, J. 1997 Laser doppler measurement of local flow field in collapsible tube during self-excited oscillation. *JSME International Journal Series C* **40** (4), 665–670.

OLSON, D. A., KAMM, R. D. & SHAPIRO, A. H. 1982 Bioengineering studies of periodic external compression as prophylaxis against deep vein thrombosis - part ii: experimental studies on a simulated leg. *ASME J. Biomech. Engng.* **104**, 96–104.

PEDLEY, T. J. 1980 *The fluid mechanics of large blood vessels*. Cambridge University Press, Cambridge.

PEDLEY, T. J. 1992 Longitudinal tension variation in collapsible channels: A new mechanism for the breakdown of steady flow. *ASME J. Biomech. Engng.* **114**, 60–67.

PEDLEY, T. J., BROOK, B. S. & SEYMOUR, R. S. 1996 Blood pressure and flow rate in the giraffe jugular vein. *Philosophical Transactions of the Royal Society B: Biological Sciences* **351** (1342), 855–866.

RAST, M. P. 1994 Simultaneous solution of the navier-stokes and elastic membrane equations by a finite element method. *International journal for numerical methods in fluids* **19** (12), 1115–1135.

REYN, J. W. 1987 Multiple solutions and flow limitation for steady flow through a collapsible tube held open at the ends. *Journal of Fluid Mechanics* **174**, 467–493.

RODBARD, S. 1966 A hydrodynamics mechanism for the autoregulation of flow. *Cardiologia* **48**, 532–535.

RODBARD, S. & TAKACS, L. 1966 Hydrodynamics of autoregulation. *Cardiologia* **48**, 433–440.

SELVEROV, K. P. & STONE, H. A. 2001 Peristaltically driven channel flows with applications toward micromixing. *Physics of Fluids (1994-present)* **13** (7), 1837–1859.

SHANKAR, P. N. 2003 On the use of biorthogonality relations in the solution of some boundary value problems for the biharmonic equation. *Current Sci.* **85** (7), 975–979.

SHANKAR, V. & KUMARAN, V. 1999 Stability of non-parabolic flow in a flexible tube. *Journal of Fluid Mechanics* **395**, 211–236.

SHAPIRO, A. H. 1977 Steady flow in collapsible tubes. *Journal of Biomechanical Engineering* **99** (3), 126–147.

SHIM, E. B. & KAMM, R. D. 2002 Numerical simulation of steady flow in a compliant tube or channel with tapered wall thickness. *Journal of fluids and structures* **16** (8), 1009–1027.

SØNDERGAARD, N. 2007 Moving frames applied to shell elasticity. *J. Phys. A* **40** (19), 5067–5081.

STEWART, P. S., WATERS, S. L. & JENSEN, O. E. 2009 Local and global instabilities of flow in a flexible-walled channel. *Eur. J. Mech. B Fluids* **28** (4), 541–557.

TRUONG, N. K. & BERTRAM, C. D. 2009 The flow-field downstream of a collapsible tube during oscillation onset. *Communications in Numerical Methods in Engineering* **25** (5), 405–428.

TSUJI, T., NAKAJIM, K., TAKEUCHI, Y., INOUE, K., SHIOMA, K., KOYAMA, Y., TOKUCHI, K., YOSHIKAWA, T. & SUMA, K. 1978 Study on haemodynamics during cardiopulmonary bypass (in Japanese). *Artificial Organs* **7**, 435–438.

UR, A. & GORDON, M. 1970 Origin of korotkoff sounds. *American Journal of Physiology* **218**, 524–529.

VENUGOPAL, A. M., QUICK, C. M., LAINE, G. A. & STEWART, R. H. 2009 Optimal postnodal lymphatic network structure that maximizes active propulsion of lymph. *Am. J. Physiol. Heart Circ. Physiol.* **296**, H303–H309.

WALSH, C. 1995 Flutter in one-dimensional collapsible tubes. *Journal of fluids and structures* **9** (4), 393–408.

WHITTAKER, R. J. 2015 A shear-relaxation boundary layer near the pinned ends of a buckled elastic-walled tube. *IMA Journal of Applied Mathematics* .

WHITTAKER, R. J., WATERS, S. L., JENSEN, O. E., BOYLE, J. & HEIL, M. 2010a The energetics of flow through a rapidly oscillating tube. I. General theory. *J. Fluid Mech.* **648**, 83–121.

WHITTAKER, R. J., HEIL, M., BOYLE, J., JENSEN, O. E. & WATERS, S. L. 2010b The energetics of flow through a rapidly oscillating tube. II. Application to an elliptical tube. *J. Fluid Mech.* **648**, 123–153.

WHITTAKER, R. J., HEIL, M., JENSEN, O. E. & WATERS, S. L. 2010c Predicting the onset of high-frequency self-excited oscillations in elastic-walled tubes. *Proc. R. Soc. Lond. Ser. A Math. Phys. Eng. Sci.* **466** (2124), 3635–3657.

WHITTAKER, R. J., HEIL, M., JENSEN, O. E. & WATERS, S. L. 2010d A rational derivation of a tube law from shell theory. *Quart. J. Mech. Appl. Math.* **63** (4), 465–496.

YI, M., BAU, H. H. & HU, H. 2002 Peristaltically induced motion in a closed cavity with two vibrating walls. *Physics of Fluids (1994-present)* **14** (1), 184–197.